Advanced pre-clinical and pre-surgical assessment of musculo-skeletal medical devices

Edited by
Richard Mark Hall, Stephen Ferguson, Benedikt Helgason and Michael G. Bryant

About Frontiers

Frontiers is more than just an open access publisher of scholarly articles: it is a pioneering approach to the world of academia, radically improving the way scholarly research is managed. The grand vision of Frontiers is a world where all people have an equal opportunity to seek, share and generate knowledge. Frontiers provides immediate and permanent online open access to all its publications, but this alone is not enough to realize our grand goals.

Frontiers journal series

The Frontiers journal series is a multi-tier and interdisciplinary set of open-access, online journals, promising a paradigm shift from the current review, selection and dissemination processes in academic publishing. All Frontiers journals are driven by researchers for researchers; therefore, they constitute a service to the scholarly community. At the same time, the *Frontiers journal series* operates on a revolutionary invention, the tiered publishing system, initially addressing specific communities of scholars, and gradually climbing up to broader public understanding, thus serving the interests of the lay society, too.

Dedication to quality

Each Frontiers article is a landmark of the highest quality, thanks to genuinely collaborative interactions between authors and review editors, who include some of the world's best academicians. Research must be certified by peers before entering a stream of knowledge that may eventually reach the public - and shape society; therefore, Frontiers only applies the most rigorous and unbiased reviews. Frontiers revolutionizes research publishing by freely delivering the most outstanding research, evaluated with no bias from both the academic and social point of view. By applying the most advanced information technologies, Frontiers is catapulting scholarly publishing into a new generation.

What are Frontiers Research Topics?

Frontiers Research Topics are very popular trademarks of the *Frontiers journals series*: they are collections of at least ten articles, all centered on a particular subject. With their unique mix of varied contributions from Original Research to Review Articles, Frontiers Research Topics unify the most influential researchers, the latest key findings and historical advances in a hot research area.

Find out more on how to host your own Frontiers Research Topic or contribute to one as an author by contacting the Frontiers editorial office: frontiersin.org/about/contact

Advanced pre-clinical and pre-surgical assessment of musculo-skeletal medical devices

Topic editors

Richard Mark Hall — University of Leeds, United Kingdom
Stephen Ferguson — ETH Zürich, Switzerland
Benedikt Helgason — ETH Zürich, Switzerland
Michael G. Bryant — University of Leeds, United Kingdom

Table of contents

Editorial: Advanced pre-clinical and pre-surgical assessment of musculo-skeletal medical devices

Benedikt Helgason[1,2]*, Michael G. Bryant[3], Stephen J. Ferguson[1,2] and Richard M. Hall[3]

[1]Institute for Biomechanics, ETH Zurich, Zurich, Switzerland, [2]Future Health Technologies, Singapore-ETH Centre, Campus for Research Excellence and Technological Enterprise (CREATE), Singapore, Singapore, [3]School of Mechanical Engineering, Faculty of Engineering and Physical Sciences, University of Leeds, Leeds, United Kingdom

---

Editorial on the Research Topic
Advanced pre-clinical and pre-surgical assessment of musculo-skeletal medical devices

---

The orthopaedic implant market is worth in excess of €30B per annum globally with articulating joint replacements representing the largest orthopaedic sector. Growth in the sector of between 2% and 5% is expected over the near term due to the rapid demographic shift. Pre-clinical assessment, both experimental and *in silico*, is a series of necessary steps for the development, optimisation and validation of medical devices. It comprises the testing of implants using assessments that conform to agreed standards as well as those that are more bespoke and focus on the specific requirements and perceived usage of the device. However, once introduced the new technologies are not always successful clinically and may harm the patient. This may require an expensive intervention to correct the loss in the patient's quality of life and greater mortality risk. These deficits in implant outcomes have brought into focus the role of pre-clinical simulation and the wider regulatory science that supports these activities.

The theme of the research included in this Research Topic, which is driven by our experience within the EU MSCA European Training Network, BioTrib, is how best to facilitate improvements in pre-clinical *in silico*, *in vitro* and *in vivo* testing within an orthopaedic context to allow a reduction in the adverse events that occur in implants once marketed. The studies cover techniques such as artificial intelligence, image processing, laboratory and computer simulations, to achieve this end.

Several of the studies are focused on addressing the limitations of using a "human in the loop" for, e.g., diagnosis or implant selection. Qu et al. used a deep learning approach for localizing cruciate ligament rupture on knee MRI images. The over all aim of such work is to identify the location and tissue quality of injured ACLs to determine if the ACL repair surgery can be performed. The goal of the work of Burge et al. was to develop a computational tool for automatic selection of total knee replacement implant size using X-ray images. Both studies support the use of algorithms to achieve repeatable outcomes to reduce operator dependency.

Some of the studies are comparing the biomechanical efficacy of two or more surgical procedures or devices, with the overall aim of ranking the procedures or improving device design. Here the benefit of preclinical *in silico* testing can be utilized to avoid subjecting patients to clinical trials of devices or procedures that may involve elevated risk. Fung et al., e.g., studied the efficacy

of prophylactic ceramic-based cement augmentation of the proximal femur to prevent hip fracture. The authors provide insight into the potential efficacy of such a procedure, but prophylaxis for fracture prevention is a controversial Research Topic among clinicians. Using an advanced experimental model, Techens et al. studied the biomechanical consequences of cement discoplasty. This surgical procedure is relatively novel, and experimental models that can provide insight into, e.g., the changes in spine kinematics following the treatment, are needed.

Another important aspect of pre-clinical testing of orthopaedic devices is addressed in the study by Kohli et al. Here, a bioreactor analyses of tissue ingrowth, ongrowth and remodelling around implants is used to reduce the need for animal testing. Some of the studies in this Research Topic, fall under the category of novel measurement techniques and protocols. In the study of Kandel et al., an automated system is introduced for polymer wear debris analysis in total disc arthroplasty using convolution neural network. Using dual-plane fluoroscopy to observe treadmill walking, Zhou et al. investigate whether multi-planar instability, laxity and reduced knee flexion during the support phase of walking are determinants of return to sports. On the other hand, D'Isidoro et al. use dual plane moving fluoroscopy-based analysis, to study total hip arthroplasty kinematics during unrestricted activities of daily living. These advanced measurement techniques are providing novel insights into aspects of total joint replacements that are difficult to achieve with other, more conventional methods.

Overall, the papers on this Research Topic cover some recent advances in preclinical testing of musculoskeletal devices. The editors hope that this Research Topic will contribute to advancing the field of orthopaedics, by inspiring researchers, clinicians and industry alike, towards reduction in the need for animal testing, improving patient safety and lowering healthcare costs.

Author contributions

BH: Writing–review and editing. MB: Writing–review and editing. SF: Writing–review and editing. RH: Writing–review and editing.

Funding

This project has received funding from the European Union's Horizon 2020 research and innovation programme under the Marie Skłodowska-Curie grant agreement No 956004.

Conflict of interest

The authors declare that the research was conducted in the absence of any commercial or financial relationships that could be construed as a potential conflict of interest.

The author(s) declared that they were an editorial board member of Frontiers, at the time of submission. This had no impact on the peer review process and the final decision

Publisher's note

frontiers | Frontiers in Bioengineering and Biotechnology

A computational tool for automatic selection of total knee replacement implant size using X-ray images

Thomas A. Burge[1]*, Gareth G. Jones[2], Christopher M. Jordan[3], Jonathan R.T. Jeffers[4] and Connor W. Myant[1]

[1]Dyson School of Design Engineering, Imperial College, London, United Kingdom, [2]MSk Lab, Imperial College, London, United Kingdom, [3]Imperial College Healthcare, London, United Kingdom, [4]Department of Mechanical Engineering, Imperial College, London, United Kingdom

Purpose: The aim of this study was to outline a fully automatic tool capable of reliably predicting the most suitable total knee replacement implant sizes for patients, using bi-planar X-ray images. By eliminating the need for manual templating or guiding software tools via the adoption of convolutional neural networks, time and resource requirements for pre-operative assessment and surgery could be reduced, the risk of human error minimized, and patients could see improved outcomes.

Methods: The tool utilizes a machine learning-based 2D—3D pipeline to generate accurate predictions of subjects' distal femur and proximal tibia bones from X-ray images. It then virtually fits different implant models and sizes to the 3D predictions, calculates the implant to bone root-mean-squared error and maximum over/under hang for each, and advises the best option for the patient. The tool was tested on 78, predominantly White subjects (45 female/33 male), using generic femur component and tibia plate designs scaled to sizes obtained for five commercially available products. The predictions were then compared to the ground truth best options, determined using subjects' MRI data.

Results: The tool achieved average femur component size prediction accuracies across the five implant models of 77.95% in terms of global fit (root-mean-squared error), and 71.79% for minimizing over/underhang. These increased to 99.74% and 99.49% with ±1 size permitted. For tibia plates, the average prediction accuracies were 80.51% and 72.82% respectively. These increased to 99.74% and 98.98% for ±1 size. Better prediction accuracies were obtained for implant models with fewer size options, however such models more frequently resulted in a poor fit.

Conclusion: A fully automatic tool was developed and found to enable higher prediction accuracies than generally reported for manual templating techniques, as well as similar computational methods.

1 Introduction

Prior to total knee replacement (TKR) procedures, surgeons often manually evaluate the size and morphology of patient femur and tibia bones using X-rays taken during preoperative assessment (Tanzer and Makhdom, 2016). This information is used to estimate the most appropriately sized TKR implant components that will be required to achieve both a good global fit, and minimize local areas of over/underhang (OUH), typically from between 5 – 8 sizes (Hitt et al., 2003; Wernecke et al., 2012). Poor implant size selection can result in increased rates of complications, revisions, and patient pain post-surgery (Culler et al., 2017; Schroeder and Martin, 2019; Buller et al., 2018). The presence of regions of OUH ≥3 mm in particular is highlighted as being clinically significant and directly linked with cases of increased soft-tissue irritation, bleeding, osteolysis, laxity in flexion, subsidence, and instability (Schroeder and Martin, 2019; Dai et al., 2014; Shao et al., 2020). Despite the importance of achieving a good fit, the accuracy of manual X-ray assessment and templating, for both femur components and tibia plates, can be poor. Hernández-Vaquero et al. (2019) summarized the reported accuracies from 10 different studies and found mean selection accuracies of 59.2% for femur components and 60.7% for tibia plates. With ±1 size permitted, mean scores of 97.4% and 96.4% were recorded respectively. Consequently, surgeons often opt to implant a different size than estimated during preoperative assessment (Sheth et al., 2017). This could lead to a higher chance of human error, as well as longer procedures.

To attempt to improve the accuracy and reliability of pre-operative size selection, other techniques besides manual X-ray assessment and templating have been explored. Using computerized tomography (CT) imaging was investigated by Vaishya et al. (2018) and Kobayashi et al. (2012). The former reported accuracies of 66% for femur components and 72% for tibia plates, whilst the latter reported an accuracy of just 59% for both. Using demographic factors such as patient height and shoe size as a means of predicting implant size was investigated by Trainor et al. (2018). They reported accuracies of 56/58% for femur components and 56/63% for tibia plates respectively. Sershon et al. (2017) used a combination of demographic variables including height, weight, and sex to build a multivariate linear regression model that achieved ±1 size prediction accuracies of 71–92% and 81–97% for a range of femur component and tibia plate models. Optimum size prediction accuracies were not reported. Limited computational tools capable of predicting TKR implant sizes from X-rays were identified. Zheng et al. (2018) developed an X-ray based tool for pre-operative knee prosthesis planning named "3X." The authors reported size selection accuracies of 78% for

femur components and 70% for tibia plates, based on a study featuring 23 subjects. Massé and Ghate (2021) more recently developed a similar tool named "X-Atlas", primarily aimed at creating patient-matched cutting guides from X-ray images. The study involved 45 subjects and utilized the Zimmer Biomet "Persona" knee implant. Size selection accuracies of 53.3% for femur components and 57.8% for tibia plates were reported. Both these tools feature "semi-automatic" workflows that require users to manually identify landmarks on the inputted X-ray images and guide "live-wire algorithms" to extract the required bone contours.

In recent years, prediction and classification tools have been developed in other biomedical imaging applications using machine learning techniques to enable automatic workflows. U-Net convolutional neural networks (CNNs) in particular are growing in popularity as highly accurate classification and segmentation models can be trained with a relatively low number of reference images (Ronneberger et al., 2015). Example applications that have adopted this technology include in the diagnosis of COVID-19 (Mohammed et al., 2021) (Narin et al., 2021) and for detecting tuberculosis (Liu et al., 2018). In these studies, CNNs were trained to recognize features and patterns in X-ray images and extract the necessary information for diagnosis, all without requiring any guidance from the user. Furthermore, Cernazanu-Glavan and Holban (2013) demonstrated the benefits of usings CNNs for X-ray-based bone segmentation over alternative methods such as artificial neural networks, principal component analysis and fuzzy clustering. The authors highlighted the superior accuracy of CNNs and that all other methods investigated required some level of human intervention. In the case of computer assisted TKR implant size selection, the tools outlined in previous studies all featured workflows requiring trained users' feedback (Zheng et al., 2018; Massé and Ghate, 2021). Consequently, the authors do not believe that these "semi-automatic" solutions adequately address the issues preventing widespread adoption of computer assisted sizing tools in TKR. The aim of this study was therefore to develop a proof-of-concept, "fully" automatic alternative, facilitated by employing CNNs in the workflow. Such a tool could lower the possibility of human error, whilst reducing the burden on hospitals relating to training, completing manual X-ray templating, and driving software packages. Necessitating no more imaging requirements over conventional manual X-ray based methods would help avoid additional costs, radiation exposure, and resource/time. Lastly, an automatic, X-ray based tool could also be of benefit in less developed
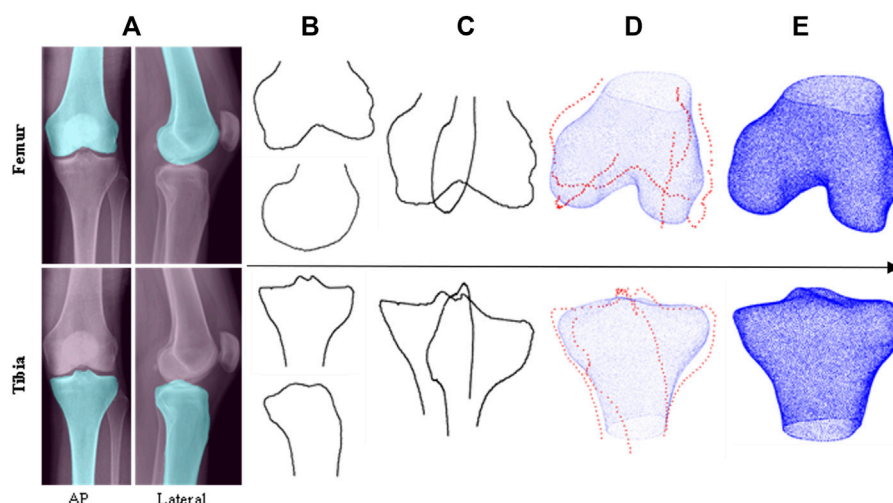
FIGURE 1
Top level workflow of the automatic 2D—3D reconstruction pipeline (top row—femur, bottom row—tibia): **(A)** CNN segmentation of input X-rays, **(B)** extracted bone contours, **(C)** contours aligned in 3D space, **(D)** PDMs used to transform contours into sparse point clouds which are then fitted to base shapes of SSMs, **(E)** 3D model predictions.

countries where implant variety and access to 3D imaging would likely be more limited. The workflow of the developed size prediction tool, from inputted X-rays to size selection, is outlined. Its performance for the dimensions of five manufacturer models is then analyzed via various fit metrics and compared to the manual and semi-automatic solutions detailed above.

2 Materials and methods

2.1 Datasets

Two datasets were utilized to train and test the size prediction tool. Anterior-posterior (AP) and lateral X-ray images, as well as high resolution (3T) magnetic resonance imaging (MRI) scans, of knee joints were obtained from the Osteoarthritis Initiative (OAI) (Nevitt et al., 2006). This facilitated data to train image segmentation models within the tool and provided the necessary pairing of X-rays with 3D ground truth data to test the accuracy of the full workflow. 3D Slicer was used to segment the OAI MRI data and generate 3D bone models (Fedorov et al., 2012). Scaling of the X-ray data retrieved from the OAI dataset was completed to address geometric magnification effects and ensure consistency with the MRI data in lieu of calibration artifacts being included. CT scans with pre-segmented 3D femur and tibia models were sourced from the Korea Institute of Science and Technology Information (KISTI) (Lee and Lee, 2010). This data was used for training aspects of the size selection tool as detailed in

TABLE 1 Test subject demographical information.

	Total, (%)
Overall	78
Sex	
Female	45 (57.7)
Male	33 (42.3)
Ethnicity	
White	73 (93.6)
Black	4 (5.1)
Asian	1 (1.3)
Knee	
Left	40 (51.3)
Right	38 (48.7)

Section 2.3. Both datasets consisted of male and female subjects with a broad range of ages. The KISTI dataset consisted purely of Asian Korean subjects, while the OAI contained White, Black and Asian Americans. No subjects used in training or testing had above mild levels of arthritis (above grade 2 out of 4) according to Kellgren and Lawrence (1956).

2.2 Test subjects

Due to the retrospective nature of the study, it was not possible to control the X-ray imaging process. Subjects' X-rays were instead

FIGURE 2
Architecture of U-Net CNN X-ray segmentation models from inputted X-ray image (left) to predicted mask (right). Each box corresponds to a multi-channel feature map with those shaded grey indicating where channels have been copied from previous layers. The number of channels is denoted on top of each box with the size provided at the lower left ($256^2 = 256 \times 256$ pixels). Arrows denote different operations such as convolutions.

visually screened to ensure appropriate anatomical alignment and clarity in both AP and lateral projections. Figure 1 illustrates correctly captured X-rays with the scan taken straight on with both the medial and lateral condyles pointing forward in the AP projection, and side on with the posterior surfaces of the femur condyles aligned in the lateral view. 78 subjects were found to be suitable and were taken from the OAI dataset to test the size prediction tool. The test subjects ranged from 46 to 79 years old, and their demographics are summarized in Table 1. KISTI subjects were used purely for training the tool as the dataset only contained CT data without accompanying X-ray images.

2.3 2D—3D pipeline

Like in Zheng et al. (2018) and Massé and Ghate (2021), the size prediction tool initially utilizes inputted AP and lateral X-ray images to generate 3D estimations of patients' femur and tibia bones before component size predictions can be made. To achieve this automatically, the 2D—3D pipeline developed in Burge et al. (2022a), Burge et al. (2022b) was utilized. The key aspects of the workflow, built using Python 3, are summarized below and illustrated in Figure 1.

The first step of the 2D—3D process utilizes CNNs to isolate the femur and tibia bones from the surrounding soft tissue in the inputted X-ray images, as shown in Figure 1A.

Four U-Net CNN image segmentation models (one for each X-ray projection of each bone) are used in the tool. The models were built using TensorFlow and a U-Net architecture, based on Ronneberger et al. (2015), was adopted (illustrated in Figure 2). To better capture the bone profiles occupying a large proportion of the X-ray images, an additional filter resolution level (16 x 16 pixels) was incorporated. The number of filter channels used in each layer and learning rate were adjusted to achieve the best validation results. Batch size was set at 10 with 100 epochs and model weights were saved after each iteration. Once training had finished, the weights with the lowest validation loss were selected for each model to minimize overfitting. 176 X-ray image/mask pairs were developed from the OAI dataset to train each model. 20 of these (~10%) were reserved for validation (separate to those used to test the full tool). It is noted that to build well generalized CNN models, capable of reliably segmenting any inputted X-ray, thousands of varied training images would likely be required (Liu et al., 2018). Due to the proof-of-concept nature of this study, and lack of suitable training data, it was deemed acceptable to mitigate this by adjusting the contrast/brightness settings of the inputted subject X-ray images to improve compatibility with the CNN models when testing the size prediction tool.

After segmentation, a Cany edge detector is applied to extract the four bone contours (Figure 1B) which are then aligned in 3D space as

FIGURE 3
Method for evaluating fit of implant model on subject ground truth anatomy (top row−femur, bottom row−tibia): **(A)** Generic implant component designs, **(B)** edges of scaled components, **(C)** scaled components fitted to subject 3D model predictions, **(D)** scaled components fitted to subject ground truth anatomy. Dashed box in **(A)** shows detail not included in fit analysis. Red squares in **(C)** and **(D)** show the location of the maximum OUH.

TABLE 2 Femur component sizing chart, detailing the manufacturer, model, size identifier, and ML/AP dimensions (obtained from respective surgical technique manuals).

Zimmer Biomet (NexGen)			DePuy (Sigma)			Smith & Nephew (Legion)			Maxx Orthopedics (Freedom)			Stryker (Scorpio)		
Id.	ML (mm)	AP (mm)	Id.	ML (mm)	AP (mm)	Id.	ML (mm	AP (mm)	Id.	ML (mm)	AP (mm)	Id.	ML (mm)	AP (mm)
'B'	58	50	'1.5'	57	53	'2'	58	50	'A'	54	51	'3'	57	51
'C'	64	54.5	'2'	60	56	'3'	62	55	'B'	58	54	'4'	60	54
'D'	68	58	'2.5'	63	58	'4'	66	59	'C'	62	58	'5'	62	56
'E'	72	62	'3'	66	61	'5'	70	62	'D'	64	60	'6'	65	58
'F'	76	66	'4'	71	65	'6'	73	66	'E'	66	62	'7'	67	61
			'5'	73	69	'7'	77	70	'F'	70	66	'8'	70	63
						'8'	80	75	'G'	74	70	'9'	72	65
									'H'	78	74	'11'	77	70
												'13'	82	75

shown in Figure 1C. Point depth models (PDMs) are applied to estimate the third dimension of the points along each contour and create a sparse 3D point cloud of reference coordinates (Figure 1D). The femur and tibia reference point clouds are independently fitted to two statistical shape models (SSMs) (one for each bone) via an iterative point method. The SSMs then morph base femur and tibia shape models to fit the reference points as closely as possible. For the PDMs and SSMs, 3D bone models (20 and 100 respectively) were used from the KISTI dataset for training.

The outputs from the 2D—3D pipeline are predictions of subjects' distal femur and proximal tibia anatomies in the form of

3D surface mesh models (Figure 1E). These can subsequently be used by the tool to approximate the most appropriately sized implant components.

2.4 Implant designs and sizes

Generic base models of TKR femur components and tibia plates were designed based on widely used commercial products (Figure 3A). The base models were scaled (Figure 3B) to the sizes listed for five manufacturers' models as reported in size charts within

TABLE 3 Tibia plate sizing chart, detailing the manufacturer, model, size identifier, and ML/AP dimensions (obtained from respective surgical technique manuals).

Zimmer Biomet (NexGen)			DePuy (Sigma)			Smith & Nephew (Legion)			Maxx Orthopedics (Freedom)			Stryker (Scorpio)		
Id.	ML (mm	AP (mm)	Id.	ML (mm)	AP (mm)	Id.	ML (mm)	AP (mm)	Id.	ML (mm)	AP (mm)	Id.	ML (mm	AP (mm)
'1'	56	41	'1'	59.2	39	'1'	60	42	'1'	59	40	'3'	61	40
'2'	62	41	'1.5'	61.8	40.7	'2'	64	45	'2'	62	40	'4'	63	42
'3'	67	46	'2'	64.6	42.6	'3'	68	48	'3'	66	42	'5'	66	44
'4'	70	46	'2.5'	67.1	44.2	'4'	71	50	'4'	66	46	'6'	68	45
'5'	74	50	'3'	69.6	45.8	'5'	74	52	'5'	71	48	'7'	71	47
'6'	77	50	'4'	74.9	49.3	'6'	77	54	'6'	72	50	'9'	77	51
			'5'	80.6	53.1	'7'	81	56	'7'	76	52	'11'	82	54
			'6'	86.8	57.2	'8'	85	59	'8'	78	54	'13'	88	58

their respective surgical technique manuals (Tables 2 and 3). This method was used as access to the official geometry of all the manufacturer models and sizes utilized within the study was not possible. Nor was acquiring physical samples for reverse engineering. Utilizing generic implant shapes also allowed for the test models to be easily controlled/edited for the purposes of the study.

The height of the 3D femur components was kept proportional by scaling the Z dimension in line with the AP and ML dimensions. The design of the base femur component was subtly adjusted for each model to reflect differences in transepicondylar (ML) width between the designs and ensure consistency with the dimensioning used in each of the surgical manuals. The design of the base tibia plate was kept constant and only the 2D profile was used like in prior studies (Shao et al., 2020; Clary et al., 2014). A 2D analysis was sufficient for the tibia plate because the components only interface with the resected bone on a singular 2D face.

2.5 Size prediction and accuracy calculation

To predict which femur component and tibia plate sizes are the most suited for a subject, the tool systematically fits each implant model and size to the 3D estimates of the subject's anatomy using an iterative closest point method (Figure 3C). Two fit metrics were calculated after each size fitting including the global root-mean-squared error (RMSE), and local maximum OUH. The RMSE calculation was performed between the surface of the positioned component and the subject anatomy as described by Eq. 1:

$$RMS\ error = \sqrt{\frac{\sum_{i=1}^{N} (x_i - \hat{x}_i)^2}{N}} \qquad (1)$$

where N is the number of points and $x_i - \hat{x}_i$ is the Euclidian distance between each point of the component surface and the bone. The maximum OUH was reported as the Hausdorff

distance (h) anywhere between the edges of the component (C) to the edges of the bone (B), as described by Eq. 2 and shown in Figure 3. The distance (d) between each point along the component edges (c) and the bone (b) was calculated as the Euclidian distance.

$$h(C, B) = max_{c \in C} \{min_{b \in B} \{d(c, b)\}\} \qquad (2)$$

For the femur, the fit analysis was completed in 3D assuming that the bone would be resected from the lateral view to the same standard dimensions as the mating faces on the femur component being fitted. For the tibia, the RMSE and maximum OUH were calculated using the 2D profile of the tibia plate and a cross-section profile taken at the intended resection point on the tibia bone. In practice, the necessary resection depth is determined by the surgeon, however, for the purposes of this study, the resection plane was located 2 mm below the height of the widest point of the tibia medial condyle, parallel with the surface of the medial plateau. Rotation of the tibia plate was limited to about its central axis and no flexion or extension was permitted. This approach consistently facilitated the largest possible surface area for stability, minimized bone loss (Schnurr et al., 2011), and enabled a continuous, flat resection plane to be created through the bone. Once RMSE and maximum OUH were recorded for each component size, the options for each model that achieved the lowest errors were outputted as the tool predictions.

2.6 Results analysis

After predictions were made, all sizes for each implant model were positioned on 3D ground truth models via an iterative closest point method and the resultant RMSE and maximum OUH values were calculated (Figure 3D). Ground truth models were created for each test subject by manually segmenting their MRI data as

TABLE 4 Femur component size prediction accuracies for each manufacturer model sizings. Size prediction accuracy is shown in terms of RMSE and maximum OUH, as well as allowing for ± one model size.

Model (no. Sizes)	RMSE correct (%)	RMSE ±1 correct (%)	Max OUH correct (%)	Max OUH ±1 correct (%)
Zimmer Biomet (5)	85.90	100.00	75.64	100.00
DePuy (6)	84.62	100.00	83.33	100.00
Smith & Nephew (7)	75.64	100.00	64.10	100.00
Maxx Orthopedics (8)	73.08	100.00	65.38	100.00
Stryker (9)	70.51	98.72	70.51	97.44
Mean	77.95	99.74	71.79	99.49

TABLE 5 Tibia plate size prediction accuracies for each manufacturer model sizings. Size prediction accuracy is shown in terms of RMSE and maximum OUH, as well as allowing for ± one model size.

Model (no. Sizes)	RMSE correct (%)	RMSE ±1 correct (%)	Max OUH correct (%)	Max OUH ±1 correct (%)
Zimmer Biomet (6)	87.18	100.00	74.36	98.72
DePuy (8)	85.90	100.00	82.05	100.00
Smith & Nephew (8)	65.38	100.00	62.82	98.72
Maxx Orthopedics (8)	83.33	98.72	69.23	97.44
Stryker (8)	80.77	100.00	75.64	100.00
Mean	80.51	99.74	72.82	98.98

described previously. The "ground truth best" size for the individual (in terms of each fit metric, implant component, and model) was recorded as the option which resulted in the lowest calculated error when fitted to the subject's 3D ground truth model. If the tool predicted the same as the ground truth best, the prediction was deemed to be correct. Spearman's correlation coefficients were calculated and used to evaluate the impact on performance due to continuous variables such as subject age.

3 Results

3.1 2D—3D model generation

The accuracy of the 2D—3D process was evaluated by Burge et al. (2022b) by comparing the tool's bone surface estimations with subjects' 3D ground truth models. A mean RMSE of 1.09 mm (SD 0.18 mm) for the femur and 0.98 mm (SD 0.15 mm) for the tibia across the 78 subjects were reported.

3.2 Size selection accuracy

The accuracy of the femur component size selection for each model is reported in Table 4 and in Table 5 for tibia plates. Tables 4 and 5 demonstrate that high levels of

accuracy for the size selection tool across the five implant model sizes for both implant components were obtained in terms of RMSE and maximum OUH. Minimal difference in prediction accuracy was observed across the five tibia plate models for males and females. For femur components however, males achieved 87.27% for both RMSE and maximum OUH, whilst accuracies of 71.11% and 60.44% were recorded for females respectively. Calculating Spearman's correlation coefficients showed no strong correlations between prediction accuracies and subject age for both femur components (RMSE = −0.03, maximum OUH = 0.02) and tibia plates (RMSE = 0.21, maximum OUH = 0.25) were present.

3.3 Implant fit

For the sizes deemed to be the best by the size prediction tool for each model and each of the test subjects, the resulting fit on the ground truth models were recorded for both metrics. These results are shown in Table 6 for femur components and Table 7 for tibia plates, alongside the best possible results. The tables show that the results obtained using the predictions made by the tool for both component types were on average only marginally inferior to the best possible outcomes in terms of both RMSE and maximum OUH.

TABLE 6 Femur component mean RMSE and mean maximum OUH results for ground truth (GT) best sizes and predictions, split by manufacturer model sizings.

Model (no. Sizes)	Mean GT best RMSE (mm)	Mean prediction RMSE (mm)	Mean GT best max OUH (mm)	Mean prediction max OUH (mm)
Zimmer Biomet (5)	1.26	1.31	3.55	3.70
DePuy (6)	1.06	1.09	2.95	3.02
Smith & Nephew (7)	1.05	1.14	2.89	3.29
Maxx Orthopedics (8)	0.99	1.04	2.67	2.91
Stryker (9)	1.03	1.10	2.87	3.16
Mean	1.08	1.13	2.99	3.22

TABLE 7 Tibia plate mean RMSE and mean maximum OUH results for ground truth (GT) best sizes and predictions, split by manufacturer model sizings.

Model (no. Sizes)	Mean GT best RMSE (mm)	Mean prediction RMSE (mm)	Mean GT best max OUH (mm)	Mean prediction max OUH (mm)
Zimmer Biomet (6)	1.73	1.77	3.48	3.63
DePuy (8)	1.11	1.19	2.52	2.70
Smith & Nephew (8)	1.11	1.25	2.53	2.85
Maxx Orthopedics (8)	1.31	1.38	2.91	3.20
Stryker (8)	1.10	1.21	2.48	2.71
Mean	1.27	1.36	2.78	3.02
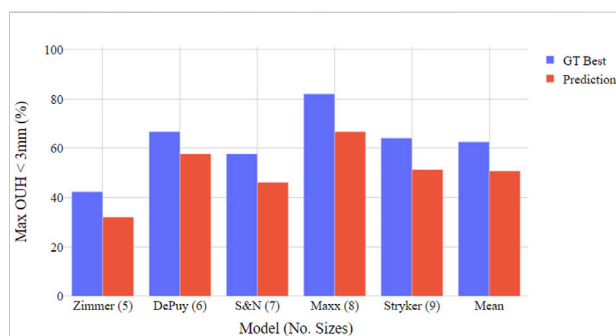
FIGURE 4
Boxplot illustrating proportion of test subjects achieving maximum OUH < 3 mm for various femur component model sizings. Both ground truth (GT) best possible size and tool prediction results shown.
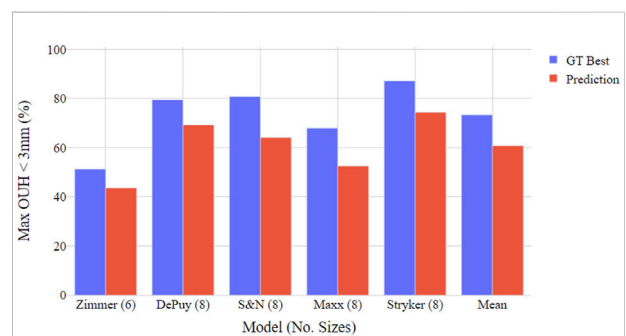
FIGURE 5
Boxplot illustrating proportion of test subjects achieving maximum OUH < 3 mm for various tibia plate model sizings. Both ground truth (GT) best possible size and tool prediction results shown.

Figures 4, 5 show the proportion of subjects achieving maximum OUH <3 mm for the various femur component and tibia plate model sizes. The figures demonstrate that the level of subjects attaining below the threshold was on average 10% less for femur components compared to tibia plates and the levels varied significantly between the different manufacturer model sizes. The proportion of subjects seeing maximum OUH of ≥3 mm was on average 12% higher than the ground truth best when the tool's size predictions were used.

4 Discussion

The most important outcome from this study is that a fully automatic, X-ray based TKR size prediction tool was developed and shown to be reliable for a range of implant model sizes and test subjects. For both femur components and tibia plates, the tool more accurately predicted the ground truth best size in terms of RMSE compared to maximum OUH. Nevertheless, the accuracies for both metrics were consistently high with the ground truth best size

predicted on average 78% of the time (in terms of RMSE) and 72% of the time (in terms of maximum OUH) for femur components. For tibia plates the prediction accuracies were 81% in terms of RMSE and 73% in terms of maximum OUH. These increased to 99–100% for ±1 size for both metrics and component types. The prediction accuracy of the tool was not found to be sensitive to subject age, nor was it sensitive to sex for predicting tibia plate size. However, 16–27% higher accuracies were achieved for male subject femur component size selection. This was likely due to the large White American male dimensions in the test population– often requiring the upper limits of the femur component size ranges or beyond. Females on the other hand utilized a broader range of smaller sizes which made predicting the correct option more challenging. Using a more balanced group of subjects, featuring ethnicities typically requiring smaller implant sizes such as Asian Chinese (Li et al., 2019), would likely reduce this effect and result in similar prediction accuracies between sexes.

Another key finding was the proportion of subjects obtaining clinically significant levels of OUH, even when the best possible sizes were used, was above 30% for all implant models evaluated. This aligns with results reported by previous studies (Wernecke et al., 2012; Mahoney and Kinsey, 2010) where the performance of non-customised implants, particularly with a limited number of size options, was shown to be poor. In this study, the model with the fewest number of sizes (the Zimmer Biomet NexGen), performed the worst in terms of the resulting mean RMSE, maximum OUH, and proportion of subjects achieving maximum OUH <3mm, whilst models with more sizes generally performed better. Nevertheless, for the tool's size prediction accuracies, the opposite was found. The Zimmer Biomet NexGen (5/6 sizes) obtained the best results, whilst the Stryker Scorpio (9 sizes) achieved the lowest accuracy for femur components (both in terms of RMSE). Comparing the results for the Smith & Nephew Legion and the Maxx Orthopedics Freedom tibia plate sizes showed considerable differences in prediction accuracies and resulting fits, despite an equal number of sizes. It is again emphasized that these results do not reflect the true performance of the named manufacturer models as generic base models were used in the analysis. However, the importance of selecting the optimum sizing dimensions, not just enough options, is highlighted. For models with many similar sizes, it was often observed that when the tool failed to predict the best possible size, the optimal component dimensions would have been close to the center of two options. As a result, the resulting RMSE and/or maximum OUH for the predicted size were only marginally worse. To better align with the approach taken by surgeons in said scenarios, the tool could be configured to always downsize the component when minimal difference in fit is predicted between two sizes (Dai et al., 2014).

Comparing the results to those available in the literature for manual planning/templating, the size prediction accuracy of the tool was shown to be considerably better than the average reported across the 10 studies summarized by Hernández-Vaquero et al.

(2019). This was also true when compared to studies that utilized CT data for manual templating (Vaishya et al., 2018; Kobayashi et al., 2012). Therefore, due to the high accuracies obtained without the need for user feedback or training, it is anticipated that hospitals could realize considerable time and resource savings and reduce the possibility of human error by adopting the tool. In terms of other computational approaches, comparing the tool to results detailed previously for prediction models based on subject demographics (Trainor et al., 2018; Sershon et al., 2017) showed significantly improved performance was possible by using the approach outlined in this study. The tool achieved a better average tibia plate size prediction accuracy and matched the level reported for femur components (in terms of RMSE) when compared to the solution published by Zheng et al. (2018). When compared to the results reported by Massé and Ghate (2021), the tool was on average >20% more accurate in selecting the best size for both component types. This study has therefore shown that fully automating the size prediction tool did not compromise accuracy, but similar or better results were in fact obtained. Moreover, the tools developed by Zheng et al. (2018) and Massé and Ghate (2021) were only tested on 23 and 45 subjects respectively, compared to 78 in this work. The authors also only used single implant models and one global fit metric in the cited studies. By exploring a range of implant model sizes and employing both global and clinical fit metrics to evaluate performance, this study has provided a more comprehensive assessment of the developed tool's robustness and applicable use with various products.

The performance of the tool could be further improved by controlling the alignment and quality of the inputted X-ray images to ensure compatibility with the 2D—3D pipeline (Burge et al., 2022b). Due to the datasets available, the testing of the tool was limited to predominantly White Americans without severe arthritis degeneration, whilst the modules of the tool were principally trained using Asian Korean data. Differences in performance between sexes and with age were evaluated in the study, however, with the data available it was not possible to analyze potential biases across ethnicities and/or the impact of arthritis severity on performance. For the development of future implant size prediction tools, it is encouraged that larger datasets, featuring hundreds of subjects with various ethnicities, ages, sexes and Kellgren and Lawrence grades, all imaged with consistent alignments/scan settings, be obtained. This would help better generalize the CNN models and improve robustness across the full range of potential patient demographics. Moreover, to further reduce overfitting, regularization techniques such as drop-out layers could be incorporated into the CNN model architecture. It should be noted that the method for determining the best fitting implant designs varied between the studies referenced. The best size in most of the referenced studies was determined by a medical professional during or after surgery. This study however was completed without clinical work and used computational fit metrics to determine performance (like in Zheng et al. (2018)). Future work could seek to test the size prediction tool against size choices made

during real surgical procedures to provide a more realistic means for comparison. Furthermore, generic implant designs, scaled to published manufacturer model size charts, were used instead of official geometries. Going forwards, it is hoped manufacturers will adapt the framework of the tool for use with commercially available products.

5 Conclusion

In this study a computational TKR size prediction tool was developed that uses two X-ray images to assist clinicians with selecting the best implant sizes for patients. The tool achieved selection accuracies superior to those reported for manual templating, as well as when compared to other computational alternatives. By removing the need for manual templating or guiding semi-automatic software tools, the tool could minimize the time and resource required for TKR preoperative assessment, increase surgeons' confidence in the outcomes, and minimize the possibility of size changes during surgery, whilst still achieving reliable size prediction results. This could also help reduce surgery time, minimize the level of component inventory required, lessen surgeon accountability for determining the right size implants, and ultimately improve outcomes for patients. Finally, the tool could be used to assess the need for customised solutions, or for a bespoke selection of implants depending on patient morphology.

Data availability statement

The datasets presented in this article are not readily available because access to the data used in the study is restricted and controlled by the OAI and KISTI. Requests to access the datasets should be directed to https://nda.nih.gov/oai/and https://www.kisti.re.kr/eng/.

Author contributions

TB: study design, algorithm development, data generation, results processing, manuscript writing. GJ and CJ: study design, advice on current templating and surgical procedures, reviewing manuscript/results. JJ and CM:

project supervision, study design, reviewing manuscript/results.

Conflict of interest

The authors declare that the research was conducted in the absence of any commercial or financial relationships that could be construed as a potential conflict of interest.

Publisher's note

All claims expressed in this article are solely those of the authors and do not necessarily represent those of their affiliated organizations, or those of the publisher, the editors and the reviewers. Any product that may be evaluated in this article, or claim that may be made by its manufacturer, is not guaranteed or endorsed by the publisher.

References

Buller, L. T., Menken, L., and Rodriguez, J. A. (2018). The custom total knee replacement: A bespoke solution. *Seminars Arthroplasty* 29 (3), 209–213. doi:10.1053/j.sart.2019.01.006

Burge, T. A., Jeffers, J. R. T., and Myant, C. W. (2022a). Development of an automated mass-customization pipeline for knee replacement surgery using biplanar X-rays *J. Mech. Des.* 144 (2), 1–11. doi:10.1115/1.4052192

Burge, T. A., Jeffers, J. R. T., and Myant, C. W. (2022b). Performance and sensitivity analysis of an automated X-ray based total knee replacement mass-customization pipeline. *J. Med. Devices.*, 1–12. doi:10.1115/1.4055000

Cernazanu-Glavan, C., and Holban, S. (2013). Segmentation of bone structure in X-ray images using convolutional neural network. *Adv. Electr. Comput. Eng.* 13 (1), 87–94. doi:10.4316/AECE.2013.01015

Clary, C., Aram, L., Deffenbaugh, D., and Heldreth, M. (2014). Tibial base design and patient morphology affecting tibial coverage and rotational alignment after total knee arthroplasty. *Knee Surg. Sports Traumatol. Arthrosc.* 22 (12), 3012–3018. doi:10.1007/s00167-014-3402-x

Culler, S. D., Martin, G. M., and Swearingen, A. (2017). Comparison of adverse events rates and hospital cost between customized individually made implants and standard off-the-shelf implants for total knee arthroplasty. *Arthroplasty Today* 3 (4), 257–263. doi:10.1016/j.artd.2017.05.001

Dai, Y., Scuderi, G. R., Penninger, C., Bischoff, J. E., and Rosenberg, A. (2014). Increased shape and size offerings of femoral components improve fit during total knee arthroplasty. *Knee Surg. Sports Traumatol. Arthrosc.* 22, 2931–2940. doi:10.1007/s00167-014-3163-6

Fedorov, A., Beichel, R., Kalpathy-Cramer, J., Finet, J., Fillion-Robin, J. C., Pujol, S., et al. (2012). 3D slicer as an image computing platform for the quantitative imaging network. *Magn. Reson. Imaging* 30 (9), 1323–1341. doi:10.1016/j.mri.2012.05.001

Hernández-Vaquero, D., Noriega-Fernandez, A., Roncero-Gonzalez, S., Perez-Coto, I., Sierra-Pereira, A. A., and Sandoval-Garcia, M. A. (2019). Agreement in component size between preoperative measurement, navigation and final implant in total knee replacement. *J. Orthop. Transl.* 18, 84–91. doi:10.1016/j.jot.2018.10.006

Hitt, K., Shurman, J. R., Greene, K., McGarthy, J., Moskal, J., Hoeman, T., et al. (2003). Anthropometric measurements of the human knee: Correlation to the sizing of current knee arthroplasty systems. *J. Bone Jt. Surgery-American* 85, 115–122. doi:10.2106/00004623-200300004-00015

Kellgren, J. H., and Lawrence, J. S. (1956) 'Radiological assessment of osteo-arthrosis', *Ann. Rheumatic Dis.*, 16(4), pp. 494–502. doi:10.1136/ard.16.4.494

Kobayashi, A., Ishii, Y., Takeda, M., Noguchi, H., Higuchi, H., and Toyabe, S. (2012). Comparison of analog 2D and digital 3D preoperative templating for predicting implant size in total knee arthroplasty. *Comput. Aided Surg.* 17 (2), 96–101. doi:10.3109/10929088.2011.651488

Lee, S. H., and Lee, S. B. (2010). Production and usage of Korean human information in KISTI. *J. Korea Contents Assoc.* 10 (5), 416–421. doi:10.5392/jkca.2010.10.5.416

Li, K., Saffarini, M., Valluy, J., Desseroit, M. C., Morvan, Y., Telmon, N., et al. (2019). Sexual and ethnic polymorphism render prosthetic overhang and under-coverage inevitable using off-the shelf TKA implants. *Knee Surg. Sports Traumatol. Arthrosc.* 27 (7), 2130–2139. doi:10.1007/s00167-019-05410-9

Liu, C., Cao, Y., Alcantara, M., Liu, B., Brunette, M., Peinado, J., et al. (2018). "TX-CNN: Detecting tuberculosis in chest X-ray images using convolutional neural network," in Proceedings - International Conference on Image Processing, Beijing, China, 17-20 September 2017. IEEE, 2314–2318. doi:10.1109/ICIP.2017.8296695

Mahoney, O. M., and Kinsey, T. (2010). Overhang of the femoral component in total knee arthroplasty: Risk factors and clinical consequences. *J. Bone Jt. Surgery-American* 92 (5), 1115–1121. doi:10.2106/JBJS.H.00434

Massé, V., and Ghate, R. S. (2021). Using standard X-ray images to create 3D digital bone models and patient-matched guides for aiding implant positioning and sizing in total knee arthroplasty. *Comput. Assist. Surg.* 26 (1), 31–40. doi:10.1080/24699322.2021.1894239

Mohammed, M. A., Abdulkareem, K. H., Garcia-Zapirain, B., Mostafa, S. A., Maashi, M. S., Al-Waisy, A. S., et al. (2021). A comprehensive investigation of machine learning feature extraction and classification methods for automated diagnosis of COVID-19 based on X-ray images. *Comput. Mat. Contin.* 66 (3), 3289–3310. doi:10.32604/cmc.2021.012874

Narin, A., Kaya, C., and Pamuk, Z. (2021). Automatic detection of coronavirus disease (COVID-19) using X-ray images and deep convolutional neural networks. *Pattern Anal. Appl.* 24 (3), 1207–1220. doi:10.1007/s10044-021-00984-y

Nevitt, M., Felson, D., and Lester, G. (2006). The osteoarthritis initiative: Protocol for the cohort study. *Osteoarthr. Initiative* 16, 1–74.

Ronneberger, O., Fischer, P., and Brox, T. (2015). U-Net: Convolutional networks for biomedical image segmentation. *Med. Image Comput. Computer-Assisted Intervention – MICCAI 2015* 9351, 234–241. doi:10.1007/978-3-319-24574-4

Schnurr, C., Csécsei, G., Nessler, J., Eysel, P., and König, D. P. (2011). How much tibial resection is required in total knee arthroplasty? *Int. Orthop.* 35 (7), 989–994. doi:10.1007/s00264-010-1025-5

Schroeder, L., and Martin, G. (2019). *In vivo* tibial fit and rotational analysis of a customized, patient-specific TKA versus off-the-shelf TKA. *J. Knee Surg.* 32 (6), 499–505. doi:10.1055/s-0038-1653966

Sershon, R. A., Courtney, P. M., Rosenthal, B. D., Sporer, S. M., and Levine, B. R. (2017). Can demographic variables accurately predict component sizing in primary total knee arthroplasty? *J. Arthroplasty* 32 (10), 3004–3008. doi:10.1016/j.arth.2017.05.007

Shao, L., Wu, X. D., Wang, T., Liu, X. K., Xu, W., Huang, W., et al. (2020). Approximating the maximum tibial coverage in total knee arthroplasty does not necessarily result in implant malrotation. *Sci. Rep.* 10, 10529–9. doi:10.1038/s41598-020-67613-2

Sheth, N. P., Husain, A., and Nelson, C. L. (2017). Surgical techniques for total knee arthroplasty: Measured resection. *J. Am. Acad. Orthop. Surg.* 25 (7), 499–508. doi:10.5435/JAAOS-D-14-00320

Tanzer, M., and Makhdom, A. M. (2016). Preoperative planning in primary total knee arthroplasty. *J. Am. Acad. Orthop. Surg.* 24 (4), 220–230. doi:10.5435/JAAOS-D-14-00332

Trainor, S., Collins, J., Mulvey, H., and Fitz, W. (2018). Total knee replacement sizing: Shoe size is a better predictor for implant size than body height. *Arch. Bone Jt. Surg.* 6 (2), 100–104. doi:10.22038/abjs.2017.22499.1603

Vaishya, R., Vijay, V., Krishnan, M., and Agarwal, A. K. (2018). Fallacies of CT based component size prediction in total knee arthroplasty – are patient specific instruments the answer? *J. Clin. Orthop. Trauma* 9 (1), 34–39. doi:10.1016/j.jcot.2017.11.001

Wernecke, G. C., Harris, I. A., Houang, M. T. W., Seeto, B. G., Chen, D. B., and MacDessi, S. J. (2012). Comparison of tibial bone coverage of 6 knee prostheses: A magnetic resonance imaging study with controlled rotation. *J. Orthop. Surg. Hong. Kong.* 20 (2), 143–147. doi:10.1177/230949901202000201

Zheng, G., Hommel, H., Akcoltekin, A., Thelen, B., Stifter, J., and Peersman, G. (2018). A novel technology for 3D knee prosthesis planning and treatment evaluation using 2D X-ray radiographs: A clinical evaluation. *Int. J. Comput. Assist. Radiol. Surg.* 13 (8), 1151–1158. doi:10.1007/s11548-018-1789-4

Check for updates

*CORRESPONDENCE
Tsung-Yuan Tsai,
tytsai@sjtu.edu.cn
Xudong Liu,
xdliu@sjtu.edu.cn

†These authors have contributed equally
to this work and share first authorship

A deep learning approach for anterior cruciate ligament rupture localization on knee MR images

Cheng Qu[1†], Heng Yang[2†], Cong Wang[3], Chongyang Wang[1], Mengjie Ying[1], Zheyi Chen[4], Kai Yang[5], Jing Zhang[2], Kang Li[6], Dimitris Dimitriou[7], Tsung-Yuan Tsai[3]* and Xudong Liu[1]*

[1]Department of Orthopedics, Shanghai Sixth People's Hospital Affiliated to Shanghai Jiao Tong University School of Medicine, Shanghai, China, [2]College of Electrical Engineering, Sichuan University, Chengdu, China, [3]School of Biomedical Engineering and Med-X Research Institute, Shanghai Jiao Tong University, Shanghai, China, [4]Department of Radiology, Shanghai Municipal Eighth People's Hospital, Shanghai, China, [5]Department of Radiology, Shanghai Sixth People's Hospital Affiliated to Shanghai Jiao Tong University School of Medicine, Shanghai, China, [6]West China Hospital, Sichuan University, Chengdu, China, [7]Department of Orthopedics, Balgrist University Hospital, University of Zürich, Zurich, Switzerland

Purpose: To develop and evaluate a deep learning-based method to localize and classify anterior cruciate ligament (ACL) ruptures on knee MR images by using arthroscopy as the reference standard.

Methods: We proposed a fully automated ACL rupture localization system to localize and classify ACL ruptures. The classification of ACL ruptures was based on the projection coordinates of the ACL rupture point on the line connecting the center coordinates of the femoral and tibial footprints. The line was divided into three equal parts and the position of the projection coordinates indicated the classification of the ACL ruptures (femoral side, middle and tibial side). In total, 85 patients (mean age: 27; male: 56) who underwent ACL reconstruction surgery under arthroscopy were included. Three clinical readers evaluated the datasets separately and their diagnostic performances were compared with those of the model. The performance metrics included the accuracy, error rate, sensitivity, specificity, precision, and F1-score. A one-way ANOVA was used to evaluate the performance of the convolutional neural networks (CNNs) and clinical readers. Intraclass correlation coefficients (ICC) were used to assess interobserver agreement between the clinical readers.

Results: The accuracy of ACL localization was 3.77 ± 2.74 and 4.68 ± 3.92 (mm) for three-dimensional (3D) and two-dimensional (2D) CNNs, respectively. There was no significant difference in the ACL rupture location performance between the 3D and 2D CNNs or among the clinical readers (Accuracy, $p < 0.01$). The 3D CNNs performed best among the five evaluators in classifying the femoral side (sensitivity of 0.86 and specificity of 0.79), middle side (sensitivity of 0.71 and specificity of 0.84) and tibial side ACL rupture (sensitivity of 0.71 and specificity of 0.99), and the overall accuracy for sides classifying of ACL rupture achieved 0.79.

Conclusion: The proposed deep learning-based model achieved high diagnostic performances in locating and classifying ACL fractures on knee MR images.

1 Introduction

Anterior cruciate ligament (ACL) injuries are common sports-related musculoskeletal diseases (Spindler and Wright, 2008) that increase the risk of developing posttraumatic osteoarthritis and require an early diagnosis and intervention (Wang et al., 2020). In current clinical practice, most orthopedic surgeons will perform ACL reconstruction in patients with ACL injuries (Reijman et al., 2021). However, reconstruction surgery has many disadvantages, such as anterior knee pain (Janani et al., 2020), muscle atrophy (Lindström et al., 2013), and loss of proprioception at the reconstructed surgical site. In addition, native gait kinematics cannot be restored and revision surgery, if necessary, can be difficult due to tunnel widening and malpositioning (Aga et al., 2017; Kraeutler et al., 2017). In the 1970s and 1980s, open primary ACL repair was commonly performed but was eventually abandoned due to poor surgical results and complications (Feagin and Curl, 1976; Taylor et al., 2009). With the development and application of arthroscopy, biotechnology, stronger internal fixation techniques, and more rational postoperative rehabilitation, ACL repair has received renewed attention from orthopedic surgeons (van der List and DiFelice, 2017; DiFelice and van der List, 2018; Mahapatra et al., 2018; Ahmad et al., 2019; Hoogeslag et al., 2019; Murray et al., 2020; Li, 2022). Isolated ACL repair has been reported using various techniques including suture anchor primary ACL repair, internal brace ligament augmentation, bridge-enhanced ACL repair (BEAR), and dynamic intraligamentary stabilization (DIS) methods (Heusdens, 2021). Sherman et al. (Sherman et al., 1991) were the first to classify ACL tears arthroscopically according to both tear location and tissue quality and named it "Sherman classifications" in 1991. More recently, Van der List et al. (van der List and DiFelice, 2016) proposed a treatment algorithm based on the modified Sherman classification and suggested that only proximal ACL tears with good to excellent tissue quality should be repaired. Note that the key question now is how to identify the location and tissue quality of the injured ACL to determine if ACL repair surgery can be performed. Currently, MRI is a non-invasive method that demonstrates excellent sensitivity and specificity for the diagnosis of ACL injuries (Odgaard et al., 2002). Several studies have suggested that MRI may help surgeons to predict the reparability of ACL tears (van der List et al., 2017; van der List and DiFelice, 2018; Mehier et al., 2022). Mehier, C. et al. (Mehier et al., 2022) proposed three classification criteria for ACL tears

based on tear location and tissue quality, including MRI Sherman tear location (MSTL), MRI Sherman tissue quality (MSTQ), and simplified MRI Sherman tissue quality (S-MSTQ) classifications. The diagnostic accuracy of the three criteria was 70% (50/71), 52% (15/29), and 90% (26/29), respectively. Interobserver agreement was good for MSTL ($\kappa = 0.78$) and moderate-to-good for the MSTQ and S-MSTQ classifications ($\kappa = 0.44$ and 0.63 respectively). Based on the above studies (Sherman et al., 1991; van der List and DiFelice, 2016; van der List et al., 2017; van der List and DiFelice, 2018; Mehier et al., 2022), we focused primarily on the localization of ACL injuries, and we simplified the classification of ACL injury sites to the femoral side, middle and tibial side, with each classification accounting for one-third of the entire ACL.

Deep learning has notable advantages in helping clinicians with limited experience or time in reading MR images and increasing the accuracy of the MR imaging interpretations (Shin et al., 2016). Several previous studies have focused on the application of deep learning for disease diagnoses in medical imaging; the applications include lung adenocarcinoma (Yu et al., 2021), abnormal pulmonary nodules (Sim et al., 2020), and breast masses (Caballo et al., 2020). In the case of diagnosing ACL injuries, previous work has been limited to the use of deep learning methods to detect the presence or absence of ACL injuries (Bien et al., 2018; Liu et al., 2019) and grading the hierarchical severity staging of ACL injuries on knee MR images (Namiri et al., 2020; Awan et al., 2021; Javed Awan et al., 2021). However, deep learning methods have yet to be applied to localizing the ACL rupture.

The main purpose of our study was to develop and evaluate a deep learning-based method to localize and classify ACL ruptures (femoral side, middle and tibial side) (Sherman et al., 1991; van der List and DiFelice, 2016; van der List et al., 2017; van der List and DiFelice, 2018; Mehier et al., 2022) on knee MR images by using arthroscopy as the reference standard.

The remainder of this article is structured as follows. Some of the recent work closely related to this study will be discussed in Section 2. In Section 3, the details of the MRI datasets are presented, and the architecture, implementation details, and performance metrics of the fully automated ACL rupture localization system are presented. The experimental results are analyzed in Section 4. The advantages and limitations of the proposed method are discussed in Section 5. Finally, the conclusion of our study is given in Section 6.

2 Recent works

In recent years, various deep learning-based methods have been developed in ACL segmentation and injury assessment. In 2021, Flannery et al. (Flannery et al., 2021) developed an automated intact ACL segmentation model based on 2D U-Net. The reference standard for training the model was the results of segmentation by an experienced (>5 years) physician, and the model was evaluated for anatomical similarity and the accuracy of quantitative metrics (i.e., signal intensity and volume). The model performed well on anatomical performance metrics (Dice coefficient = 0.84, precision = 0.82, and sensitivity = 0.85). The median signal intensities and volumes of the model were not significantly different from the ground truth. Recently, the team used a transfer learning approach to segment the surgically treated ACL automatically (Flannery et al., 2022). Compared with the intact ACL segmentation model, the anatomical performance of the automated segmentation model for surgically treated ACLs was slightly decreased (repairs/grafts: Dice coefficient = 0.80/ 0.78, precision = 0.79/0.78, sensitivity = 0.82/0.80). There were no significant differences in quantitative metrics between the ground truth and automatic segmentation of surgically treated ACLs. In 2018, Bien et al. (Bien et al., 2018) developed MRNet for detecting ACL tears on knee MR images. Using the labels of three musculoskeletal radiologists with an average of 12 years of experience as a reference standard, researchers evaluated the performance of MRNet and compared it with the performances of nine other physicians (model/physicians: sensitivity = 0.76/ 0.91, specificity = 0.97/0.93). In addition, the area under the receiver operating characteristic (ROC) curve (AUC) reached 0.82 when validated directly with MRNet on a public dataset from Clinical Hospital Centre Rijeka, Croatia, and improved to 0.91 after retraining. MRNet took less than 30 min to train on and less than 2 min to evaluate the public dataset, indicating that MRNet can improve clinician performance in the interpretation of medical imaging on both internal and external datasets. In 2019, Liu et al. (Liu et al., 2019) proposed a fully automated ACL tear detection system by using two convolutional neural networks (CNNs) to isolate the ACL on knee MR images followed by a classification CNN to detect ACL injuries on the selected image sections. A retrospective study of 350 subjects was conducted to evaluate the sensitivity and specificity of the model and those of the five radiologists in detecting ACL tears using arthroscopy as the reference standard. The overall training time was 11.62 h, while the average time for the model to detect an ACL tear for one subject was 9 s. The sensitivity and specificity of the model at the optimal threshold were 0.96 and 0.96, respectively. In contrast, the sensitivity of the radiologists ranged between 0.96 and 0.98, while the specificity ranged between 0.90 and 0.98. In 2020, Namiri et al. (Namiri et al., 2020) proposed a deep learning-based pipeline to isolate the ACL region of interest (ROI), detect abnormal ACL, and stage

lesion severity using three-dimensional (3D) and two-dimensional (2D) CNN, respectively. The overall accuracy of the 3D and 2D CNN in classifying ACL injuries (reconstructed, fully torn, partially torn, and intact ACLs) was 0.89 and 0.92, respectively. In a recent study, Namiri et al. (Astuto et al., 2021) developed a 3D CNN model for full-knee ROI (cartilage, bone marrow, menisci, and ACL) detection and lesion classification. Binary injury sensitivity reported for all tissues was between 0.70 and 0.88, while the specificity ranged from 0.85 to 0.89.

3 Materials and methods

3.1 MRI datasets

This retrospective study was performed with approval from our institutional internal review boards and ethical committees (Ethics Committee Northeast and Central Switzerland 2018-01410). The MRI datasets were obtained from 85 patients with ACL ruptures (Male: 56, Female: 29) with an average age of 27 (range: 10–57) years who underwent knee MRI examination and subsequent ACL reconstruction surgery under arthroscopy between January 2010 and April 2018 (Figure 1). Inclusion criteria were patients younger than 57 years, with no history of previous trauma or surgery on the injured knee, and MRIs that were performed within 1 month of injury. The patient exclusion criteria were as follows: (a) partial tear; (b) multiple ligamentous knee injuries; (c) MRI unavailable or of insufficient quality; (d) significant lacking information.

All the patients were scanned using a 3.0-T MR Scanner (Achieva; Philips Healthcare, Netherlands). The MRI datasets consisted of sagittal T2-weighted turbo spin-echo and coronal T1–weighted high spatial resolution turbo spin-echo sequences. The detailed imaging parameters of the sequences are summarized in Table 1.

3.2 Fully automated anterior cruciate ligament rupture localization system

In this study, we propose a two-step, coarse-to-fine deep learning-based pipeline to isolate the specific areas that contain ACL in the knee and we locate the ACL rupture site using 2D and 3D convolutions with MR images.

Our deep learning framework consists of the segmentation network that categorizes the knee into 4 distinct anatomic components and the landmark detection network to localize the centroid of an ACL rupture (Figure 2). The first segmentation network was implemented to approximately narrow the specific areas that contain ACLs; this network was based on a 3D U-Net architecture (Cicek et al., 2016). Based on the position of the femoral footprint and tibial footprint, we cropped the patches containing the ACL from the MR images to eliminate the

FIGURE 1
Inclusion and exclusion criteria. ACL, anterior cruciate ligament.
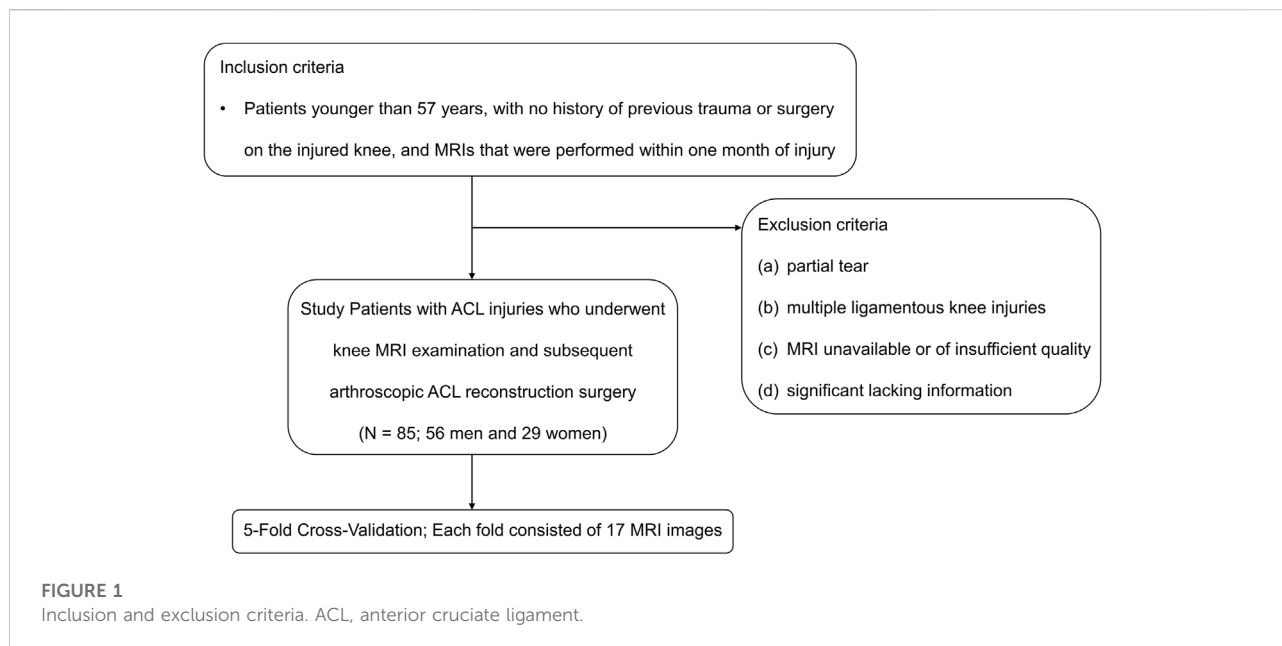
TABLE 1 Parameters for the knee MRI sequences used to locate ACL rupture.

Parameter	T1-weighted high spatial resolution turbo spin-echo sequence (min-max, avg)	T2-weighted turbo spin-echo sequence (min-max, avg)
Repetition time (msec)	567-2000 (691)	652-4714.74 (3165.65)
Echo time(s) (msec)	10-15 (14.847)	13-100 (98.74)
Flip angle (degrees)	90	90
Pixel bandwidth (Hz)	110-239 (213.108)	130-293 (288.23)
Echo train length	1-9 (8.08)	1-17
Section thickness (mm)	2.5-3 (2.525)	3-3.3
No. of sections	24-39	22-39
Signal averages	1,2,3	1,2
Acquisition matrix size	320 × 320 - 1600 × 1600	400 × 400 - 1024 × 1024
Reconstruction matrix size	256 × 256	256 × 256
File type	DICOM	DICOM
Bit depth (bit)	16	16

DICOM, digital imaging and communications in medicine.

unnecessary details and used them as input images to the localization CNNs. In the second stage, we compared the localization performance of the CNNs on 2D slices with 3D cropped images. All CNNs were developed through a cascaded approach to create a fully automated processing pipeline. The detailed network structure for the CNNs is summarized in Supplementary Table S1 (Litjens et al., 2017).

3.2.1 2D

This scheme consists of two stages, a slice selection and landmark localization. The slice selection network was constructed by a 3D full CNN (Figure 3) with an input size of $6 \times 256 \times 256$, and it had nine sets of convolutional layers and eight pooling layers. The first eight sets of convolutional layers were used to extract features with two $1 \times 3 \times 3$ convolution operations in each layer, while the last convolutional layer was used for reducing the feature dimension to one channel. The image size became $6 \times 1 \times 1$ through eight max pooling layers, which only implemented downsampling on the slice size, followed by a softmax layer, and the network was trained by the cross-entropy loss values between the output vector and standard vector.

FIGURE 2

The convolutional neural network (CNN) pipeline for the deep learning-based fully automated ACL rupture localization system. The proposed methods including 2D and 3D CNNs consisted of segmentation and landmark detection network connected in a cascaded fashion to create a fully automated image processing pipeline. ACL, anterior cruciate ligament; BN, batch normalization; Conv, convolution; Norm, normalization; LReLU, Leaky-ReLU; ReLU, rectified-linear activation; 2D, two-dimensional; 3D, three-dimensional.

FIGURE 3

Flow chart for the slice detection network of 2D CNNs.

The landmark detection stage of our method is mainly based on YOLOF, which is formulated to predict keypoint coordinates by the bounding box center. YOLOF is one of the latest single-level detectors, which only uses the final low resolution feature map C5 to detect objects. We used the ResNet-101 network (Ranjan et al., 2019) as the backbone network in our training phase. Based on the real pixel coordinates (usually decimal) of the rupture point on the axis of the high-resolution slice in the cropped MRI images, we select the integers on both sides of the decimal as the slices (2 slices) where the real rupture point is located. We maintained the slice resolution as 0.25 mm * 0.25 mm in order to use high-precision images that would ensure the accuracy of the results. We utilized random rotation, flipping and elastic transformation to enhance the data and expand our training dataset.

In sum, the selected slice was adopted as the z value of the final coordinate, and the coordinates (x, y) were obtained by the predicted bounding box center. After mapping the obtained pixel coordinates into the physical coordinates of the original MRI image, the automatic localization of the ACL rupture point was completed.

3.2.2 3D

The 3D localization scheme was based on the heatmap regression network, which was adapted from a 3D full resolution nnU-Net (Isensee et al., 2021). The network has an encoder-decoder structure. The encoder is comprised of a sequence of convolution layers with strided convolution downsampling, which compresses the original input volume into low-resolution and highly abstracted feature maps. The

decoder has the same structure with a transpose convolution upsampling, which processes the downsampling abstracted feature maps into outputs with the same resolution as the input, in a way that is symmetrical to what is done in the compression layers. The feature maps of the same level are concatenated by a skip connection. All batch normalizations were replaced by group normalizations, and we used the combination of Dice loss and focal loss (Lin et al., 2020) as the loss function to train the model.

In particular, in the training phase, we use a 3D Gaussian function, centered at the manually labeled rupture position, as a probability heatmap. The probability values are multiplied by a constant to scale the maximum to 1 (the groundtruth of the landmark). In the landmark mask, the probability value gradually decreases from 1 at the center position in the voxel range of the Gaussian heatmap distribution (the landmark voxels), and the value of the background voxels is set to zero. Note that we incorporate a false-positive suppression strategy during the training phase to make our model more robust. Specifically, we force the values that are very close to the landmark voxels (e.g., < 2 mm) to be negative rather than zero, so they are regarded as invalid voxels to avoid being calculated in the loss function. Finally, we mark the rupture voxels by using the standard probability threshold of 0.5 and calculate the centroid of the whole region as the output coordinate. The heatmaps were generated using the Matplotlib library (https://matplotlib.org/).

3.3 Definition of simplified classification of anterior cruciate ligament injury sites on our deep learning-based model

The ACL rupture was approximately described based on the line connecting the center coordinates of the femoral and tibial footprints. The line was divided into three equal parts to indicate which section (femoral side, middle, and tibial side) the rupture area was located on, while the rupture area was interpreted as the coordinate of the perpendicular foot between the rupture point and the ACL line.

The entire ACL measures approximately 38 mm in length and 11 mm in width (Girgis et al., 1975). According to our simplified classification of ACL injury sites, each section accounts for one-third of the entire ACL, which is approximately 12 mm. Based on the anatomy of ACL (Girgis et al., 1975) and the study of Payer, C. et al. (Payer et al., 2016) on medical image landmark localization, for both 2D and 3D CNNs, a localization failure case occurred when the distance between the ground-truth location and the predicted location was larger than 10 mm.

3.4 Implementation

The training and evaluation of our pipeline was done on a desktop computer running a 64-bit Linux operating system with

8 V100 SXM3-32GB GPUs and CUDA version 10.2. All machine learning algorithms were implemented in PyTorch with Python 3.7, and each CNN was trained individually. The model was validated by a fivefold cross-validation. The data were randomly divided up into 5 non-overlapping groups known as folds and each fold consisted of 17 MRI images. One of those folds was retained as the validation set, and the remaining images were used for training. The average accuracy of all the folds was the overall accuracy of our system.

3.5 Training and evaluation of the fully automated anterior cruciate ligament rupture localization system

The reference standard for training the segmentation network was the image patch segmentation bounded by a manually labeled femoral footprint and tibial footprint performed on the sagittal T2-weighted sequences of all 85 subjects. The labeling of the femoral footprint and tibial footprint areas was performed by an orthopedic fellow (D.D., with 8 years of labeling experience) using the ITK-SNAP program (https://www.itksnap.org/pmwiki/pmwiki.php). The reference standard for training the localization network was the centroid physical coordinate of the rupture region marked on the MRI of the corresponding patient by an orthopedic fellow (D.D.) using the location of the arthroscopic ACL injury as the reference standard.

3.6 Evaluation by clinical readers

To compare the localization accuracy of our pipeline with that of clinical readers, a 3rd-year musculoskeletal clinician [MY (Resident 1)], a 6th-year musculoskeletal clinician [CYW (Resident 2)], and a 6th-year radiologist [ZC (Fellow)] independently reviewed the MR images of all 85 patients. The clinical readers identified the site of the ACL rupture by placing image patches where they believed the ACL rupture occurred on the sagittal T2-weighted MR images using the ITK-SNAP program. Then, the centroid physical coordinates of the manually labeled image patches are calculated and compared with the coordinates predicted by the deep learning-based model to evaluate the localization accuracy and classification performance of the model. All the clinical reviewers had no formal training or calibration courses prior to evaluating the ACL rupture site.

3.7 Statistical analysis

All the statistical analyses were calculated using SPSS (Version 26; IBM Corporation, Armonk, NY, United States). The p values less than 0.05 were considered statistically significant. Euclidean distances (mean value ±standard

TABLE 2 Accuracy and error rate of clinical residents, musculoskeletal radiology fellow, 2D CNNs, and 3D CNNs in localization of ACL ruptures.

	Accuracy* (mm)	Error rate (%)
2D method	4.68 ± 3.92	11 (9/85)
3D method	3.77 ± 2.74	3.5 (3/85)
Resident 1	8.27 ± 4.47[a,b]	31 (28/85)
Resident 2	8.34 ± 3.36[a,b]	40 (34/85)
Fellow	8.00 ± 5.74[a,b]	31 (28/85)
p value	<0.01	

*Euclidean distances (mean value ±standard deviation) used to evaluate the localization accuracy.
[a,b]$p < 0.01$ vs. 2D method group. $p < 0.01$ vs. 3D method group.
ACL, anterior cruciate ligament; CNNs, convolutional neural networks; 2D, two-dimensional; 3D, three-dimensional.

deviation, millimeters) between the ground-truth locations and the predicted locations of the landmarks were used to evaluate the algorithm localization accuracy. The localization error rate was defined as the ratio between the number of failure cases and the total samples. Interobserver agreement between two of the three independent blinded clinical readers was assessed using single-measure intraclass correlation coefficients (ICC) with a two-way random-effects model for absolute agreement. The performance statistics for the classification of ACL rupture were reported for sensitivity, specificity, precision, F1-score, and overall accuracy.

$$Sensitivity = TP/(TP + FN) \quad (1)$$

$$Specificity = TN/(TN + FP) \quad (2)$$

$$Precision = TP/(TP + FP) \quad (3)$$

$$F1 - score = TP/(TP + 0.5 * (FP + FN)) \quad (4)$$

$$Overall\ accuracy = \frac{correct\ classifications}{all\ classifications} \quad (5)$$

where TP, TN, FP, and FN are true positive, true negative, false positive, and false negative, respectively. Also, '*' and '/' represent multiplication and division, respectively.

4 Results

Compared with models proposed by Bien et al. (Bien et al., 2018) and Liu et al. (Liu et al., 2019), the training time for our pipeline was 60 min, and the average time for the ACL rupture localization system to locate and classify the rupture site for one subject was 1.6 s using the trained networks.

Table 2 compares the accuracy and error rates of the proposed pipeline (both the 2D and 3D methods) with those of the clinical readers. The mean localization accuracies were 4.68 ± 3.92 [standard deviation] (mm) for the 2D method, 3.77 ± 2.74 (mm) for the 3D method, 8.27 ± 4.47 (mm) for Resident 1, 8.34 ±

TABLE 3 Intraclass correlation coefficients (ICC) for Interobserver Agreement between the Clinical Readers in Localization of ACL Ruptures.

Reader	Resident 1	Resident 2	Fellow
Resident 1	NA	0.54 (0.37, 0.68)	0.32 (0.12, 0.50)
Resident 2	0.54 (0.37, 0.68)	NA	0.19 (−0.03, 0.38)
Fellow	0.32 (0.12, 0.50)	0.19 (−0.03, 0.38)	NA

Data are ICC values, with 95% confidence intervals in parentheses. NA, not applicable.

TABLE 4 Confusion matrices for the clinical residents, musculoskeletal radiology fellow, 2D CNNs, and 3D CNNs for performance in sides classifying of ACL rupture on the image patches.

Predict truth	Femoral side	Middle	Tibial side
Resident1			
femoral side	8	0	0
middle	30	30	4
tibial side	5	5	3
Resident2			
femoral side	1	0	0
middle	40	32	4
tibial side	1	3	3
Fellow			
femoral side	32	10	3
middle	6	13	1
tibial side	5	12	3
2D CNNs			
femoral side	28	10	1
middle	13	23	5
tibial side	2	2	1
3D CNNs			
femoral side	37	9	0
middle	6	25	2
tibial side	0	1	5

ACL, anterior cruciate ligament; CNNs, convolutional neural networks; 2D, two-dimensional; 3D, three-dimensional.

3.36 (mm) for Resident 2, and 8.00 ± 5.74 (mm) for Fellow. There was no significant difference in ACL rupture location performance between the 3D and 2D CNNs or among the clinical readers (Accuracy, $p < 0.01$). The error rates of the 2D and 3D CNNs were 11% (9/85) and 3.5% (3/85), respectively. In comparison, the error rates of the clinical readers ranged between 31% (28/85) and 40% (34/85). Table 3 shows the ICC values for interobserver agreement between the clinical readers in the localization of ACL ruptures on the same image patches. There was poor to moderate interobserver agreement between the clinical readers, with ICC values between 0.19 and 0.54.

TABLE 5 Sensitivity, specificity, precision, F1-score, and overall accuracy for clinical residents, musculoskeletal radiology fellow, 2D CNNs, and 3D CNNs for performance in sides classifying of ACL rupture on the image patches.

	Position class	Sensitivity	Specificity	Precision	F1-score	Overall accuracy
3D CNNs	Femoral side	0.86	0.79	0.80	0.83	0.79
	Middle	0.71	0.84	0.76	0.74	
	Tibial side	0.71	0.99	0.83	0.77	
2D CNNs	Femoral side	0.65	0.74	0.72	0.68	0.61
	Middle	0.66	0.64	0.56	0.61	
	Tibial side	0.14	0.95	0.2	0.17	
Resident 1	Femoral side	0.19	1	1	0.31	0.48
	Middle	0.86	0.32	0.47	0.61	
	Tibial side	0.43	0.87	0.23	0.3	
Resident 2	Femoral side	0.02	1	1	0.05	0.42
	Middle	0.91	0.10	0.42	0.58	
	Tibial side	0.43	0.95	0.43	0.43	
Fellow	Femoral side	0.74	0.69	0.71	0.73	0.56
	Middle	0.37	0.86	0.65	0.47	
	Tibial side	0.43	0.78	0.15	0.22	

ACL, anterior cruciate ligament; CNNs, convolutional neural networks; 2D, two-dimensional; 3D, three-dimensional.
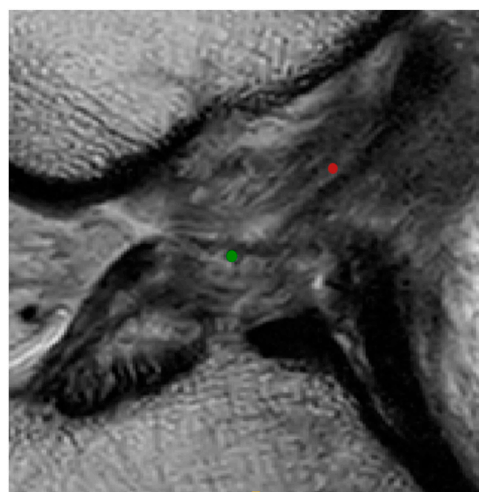
FIGURE 4
Sagittal views of the cropped MR image, mislocalization and false classification. The predicted rupture point is marked by **red** circle, while the true rupture point is **green**. The deep learning pipeline outputs incorrect localization results due to the Euclidean distance between the true and predicted rupture point locations being greater than 10 mm, which exceeds the maximum error threshold we set. A mislocalization resulted in a false classification. The true part of the rupture is the middle side, but the prediction is femoral side.

Tables 4, 5 show the confusion matrices and sensitivity and also the specificity, precision, F1-score, and overall system accuracy values for the clinical readers, and also the 2D and 3D CNNs for evaluating the side classification performance on ACL ruptures on the image patches in all 85 MR datasets. The confusion matrix results for the ACL injury classification corresponding to each evaluator in Table 4 show that the 3D CNNs had the highest performance on ACL rupture classifications. As shown in Table 5, both models performed better than the clinical readers in describing the location of ACL ruptures. The 3D CNNs performed best among the five evaluators in classifying the femoral side (sensitivity of 0.86 and specificity of 0.79), middle side (sensitivity of 0.71 and specificity of 0.84), and tibial side ACL rupture (sensitivity of 0.71 and specificity of 0.99). While the overall accuracy of
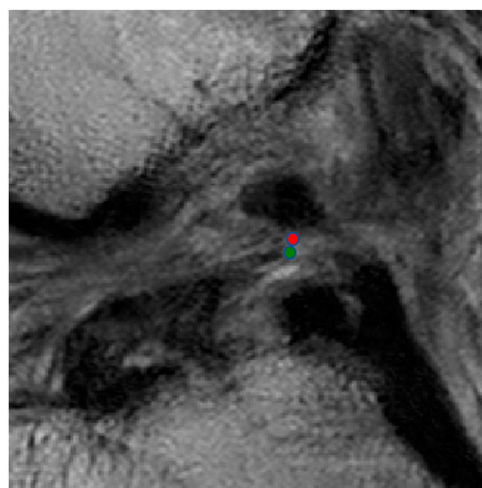
FIGURE 5
Sagittal views of the cropped MR image, correct localization and classification. The predicted rupture point is marked by **red** circle, while the true rupture point is **green**. The model predicted a correct localization, and the system shows a correct classification (the middle side).

clinical readers ranged between 0.42 and 0.56, the overall accuracy of the ACL localization system for the 3D and 2D CNNs was 0.79 and 0.61, respectively.

Figure 4 displays sagittal views of the cropped knee MR image, which were processed by the deep learning model for mislocalization and false classification. The true part of the rupture is on the middle side but the model outputs a classification result on the femoral side. The deep learning pipeline outputs incorrect localization results due to the Euclidean distance between the true and predicted rupture point locations being greater than 10 mm, which exceeds the maximum error threshold we set. Based on our model, the results of ACL rupture classification are directly related to the accuracy of its rupture localization, and incorrect localization leads to incorrect classification.

Figure 5 shows that the predicted rupture point location is very close to the true rupture point location and the Euclidean distance between them is within the set error range. The deep learning model is able to correctly locate the ACL rupture point and therefore outputs the correct classification.

5 Discussion

Our study describes a fully automated ACL rupture localization system utilizing a segmentation network adapted from 3D U-Net (Cicek et al., 2016) for approximately narrowing the specific areas that contain an ACL. This is followed by a second landmark detection network based on the YOLOF (for the 2D model) and 3D full resolution nnU-Net (Isensee et al., 2021) (for the 3D model) with several modifications to localize the ACL rupture within the

cropping patches that contain the ACL rupture region of interest according to the coordinate. The 3D CNNs achieved the highest performance among all the models and clinicians, with a localization accuracy reaching 3.77 ± 2.74 (mm). The error rate and the overall system accuracy were 3.5% (3/85) and 79%, respectively. In addition, the 3D CNNs performed best among the five evaluators in classifying the femoral side (F1-score: 0.83), middle side (F1-score: 0.74), and tibial side ACL rupture (F1-score: 0.77).

Previous work using deep learning methods has been limited to detecting the presence or absence of ACL ruptures or triaging the lesion severity of ACL injuries on knee MR images. Bien et al. (Bien et al., 2018) made predictions from three series types of knee MRIs to train different MRNets with a pretrained AlexNet, and the experimental results showed a 0.911 AUC, 0.968 specificity, and 0.759 sensitivity for ACL tears. Namiri et al. (Namiri et al., 2020) created a deep learning model to predict four lesion severities for the ACL, used V-Net to segment the knee and determined the ACL boundaries of the original input MRI. Then, the cropped images were tested on the 2D and 3D CNNs, which detected reconstructed, fully torn, partially torn and intact ACLs. The 2D and 3D CNNs achieved high overall accuracies of 92% and 89%, respectively. Most recently, Awan et al. (Javed Awan et al., 2021) trained a customized ResNet-14 architecture utlizing class balancing and data augmentation, which performed at an average accuracy of 92% for three classes. The results showed that the AUC was 0.980 for healthy ACLs, 0.970 for partially torn ACLs and 0.999 for fully torn ACLs. In contrast to the work described above, our pipeline has many advantages. Our pipeline localizes and classifies ACL ruptures on knee MR images, which can help clinicians roughly determine whether a patient has a potential for ACL repair based on the results of ACL injury classification. Based on the ACL injury treatment algorithm proposed by Van der List et al.

(van der List and DiFelice, 2016; van der List et al., 2017), we believe that proximal ACL injuries (femoral side) have the potential for ACL repair surgery whereas ACL reconstruction surgery is recommended for injuries near the middle and tibial sides. In addition, our localization system is not influenced by human factors. The interobserver agreement between clinicians in our study did not perform very well (ICC range between 0.19 and 0.54), which may be due to inexperience, distraction, and different interpretations of MRI by clinicians with different specialties. Our pipeline avoids these problems by using arthroscopy as a reference standard and labeling the location of the ACL injury on the corresponding MR images. Furthermore, both CNNs and clinical readers localized ACL rupture within a set threshold (10 mm), but CNNs performed better than clinicians in localization (CNNs/clinicians: 3.77–4.68 mm/8.00–8.34 mm). With accurate localization of ACL injuries, our system also allows the surgeon to adjust the range of ACL injury classification to suit the actual situation.

Our study had several limitations. First, our dataset has a small sample size which only allows for the process of data cross-validation, and more data are needed to verify the reliability of our system. Second, proton density-weighted MR sequences are considered to be commonly used to evaluate knee injuries. MR data in our study are sagittal T2-weighted and coronal T1–weighted MR sequences, and more sequences need to be added to train the localization system to make the results more reliable. In addition, given the fair interobserver agreement among clinicians, we need more experienced clinicians to join the evaluators to calculate ACL injury localization accuracy and classification reliability. Finally, we can include the negative control group in which there is no ACL rupture in the development of the deep learning pipeline, which may be of greater translational and applied value to clinical scenarios.

6 Conclusion

In conclusion, our pipeline was found to be more accurate in locating and classifying ACL ruptures (femoral side, middle, and tibial side) than clinicians with varying levels of experience, which may help clinicians determine whether an ACL injured patient has the potential for ACL repair based on the classification results.

Data availability statement

The raw data supporting the conclusion of this article will be made available by the authors, without undue reservation.

Ethics statement

The studies involving human participants were reviewed and approved by the Ethics Committee Northeast and Central Switzerland 2018-01410. Written informed consent to participate in this study was provided by the participants' legal guardian/next of kin. Written informed consent was obtained from the individual(s), and minor(s)' legal guardian/next of kin, for the publication of any potentially identifiable images or data included in this article.

Author contributions

Guarantors of integrity of entire study, CQ, HY, and XL; study concepts/study design or data acquisition or data analysis/interpretation, all authors; manuscript drafting or manuscript revision for important intellectual content, all authors; manuscript final version approval, all authors; agrees to ensure any questions related to the work are appropriately resolved, all authors; literature research, CQ, HY, CW, JZ, and XL; clinical studies, CQ, HY, CyW, MY, ZC, DD, and XL; experimental studies, CQ, HY, KY, and JZ; statistical analysis, CQ, HY, CW, and XL; and manuscript editing, CQ, HY, CyW, KL, T-YT, and XL.

Funding

Conflict of interest

The authors declare that the research was conducted in the absence of any commercial or financial relationships that could be construed as a potential conflict of interest.

Publisher's note

All claims expressed in this article are solely those of the authors and do not necessarily represent those of their affiliated organizations, or those of the publisher, the editors and the reviewers. Any product that may be evaluated in this article, or claim that may be made by its manufacturer, is not guaranteed or endorsed by the publisher.

Supplementary material

The Supplementary Material for this article can be found online at: https://www.frontiersin.org/articles/10.3389/fbioe.2022.1024527/full#supplementary-material

References

Aga, C., Wilson, K. J., Johansen, S., Dornan, G., La Prade, R. F., and Engebretsen, L. (2017). Tunnel widening in single- versus double-bundle anterior cruciate ligament reconstructed knees. *Knee Surg. Sports Traumatol. Arthrosc.* 25 (4), 1316–1327. doi:10.1007/s00167-016-4204-0

Ahmad, S. S., Schreiner, A. J., Hirschmann, M. T., Schröter, S., Döbele, S., Ahrend, M. D., et al. (2019). Dynamic intraligamentary stabilization for ACL repair: A systematic review. *Knee Surg. Sports Traumatol. Arthrosc.* 27 (1), 13–20. doi:10.1007/s00167-018-5301-z

Astuto, B., Flament, I., K Namiri, N., Shah, R., Bharadwaj, U., M Link, T., et al. (2021). Automatic deep learning-assisted detection and grading of abnormalities in knee MRI studies. *Radiol. Artif. Intell.* 3 (3), e200165. doi:10.1148/ryai.2021200165

Awan, M. J., Rahim, M. S. M., Salim, N., Rehman, A., Nobanee, H., and Shabir, H. (2021). Improved deep convolutional neural network to classify osteoarthritis from anterior cruciate ligament tear using magnetic resonance imaging. *J. Pers. Med.* 11 (11), 1163. doi:10.3390/jpm11111163

Bien, N., Rajpurkar, P., Ball, R. L., Irvin, J., Park, A., Jones, E., et al. (2018). Deep-learning-assisted diagnosis for knee magnetic resonance imaging: Development and retrospective validation of MRNet. *PLoS Med.* 15 (11), e1002699. doi:10.1371/journal.pmed.1002699

Caballo, M., Pangallo, D. R., Mann, R. M., and Sechopoulos, I. (2020). Deep learning-based segmentation of breast masses in dedicated breast CT imaging: Radiomic feature stability between radiologists and artificial intelligence. *Comput. Biol. Med.* 118, 103629. doi:10.1016/j.compbiomed.2020.103629

Çiçek, Ö., Abdulkadir, A., Lienkamp, S. S., Brox, T., and Ronneberger, O. (2016). 3D U-net: Learning dense volumetric segmentation from sparse annotation. *Med Image Comput Comput Assist Interv.* 424–432. Springer.

DiFelice, G. S., and van der List, J. P. (2018). Clinical outcomes of arthroscopic primary repair of proximal anterior cruciate ligament tears are maintained at mid-term follow-up. *Arthrosc. J. Arthrosc. Relat. Surg.* 34 (4), 1085–1093. doi:10.1016/j.arthro.2017.10.028

Feagin, J. A., Jr., and Curl, W. W. (1976). Isolated tear of the anterior cruciate ligament: 5-year follow-up study. *Am. J. Sports Med.* 4 (3), 95–100. doi:10.1177/036354657600400301

Flannery, S. W., Kiapour, A. M., Edgar, D. J., Murray, M. M., Beveridge, J. E., and Fleming, B. C. (2022). A transfer learning approach for automatic segmentation of the surgically treated anterior cruciate ligament. *J. Orthop. Res.* 40 (1), 277–284. doi:10.1002/jor.24984

Flannery, S. W., Kiapour, A. M., Edgar, D. J., Murray, M. M., and Fleming, B. C. (2021). Automated magnetic resonance image segmentation of the anterior cruciate ligament. *J. Orthop. Res.* 39 (4), 831–840. doi:10.1002/jor.24926

Girgis, F. G., Marshall, J. L., and Monajem, A. (1975). The cruciate ligaments of the knee joint. Anatomical, functional and experimental analysis. *Clin. Orthop. Relat. Res.* 106, 216–231. doi:10.1097/00003086-197501000-00033

Heusdens, C. H. W. (2021). ACL repair: A game changer or will history repeat itself? A critical appraisal. *J. Clin. Med.* 10 (5), 912. doi:10.3390/jcm10050912

Hoogeslag, R. A. G., Brouwer, R. W., Boer, B. C., de Vries, A. J., and Huis In 't Veld, R. (2019). Acute anterior cruciate ligament rupture: Repair or reconstruction? Two-year results of a randomized controlled clinical trial. *Am. J. Sports Med.* 47 (3), 567–577. doi:10.1177/0363546519825878

Isensee, F., Jaeger, P. F., Kohl, S. A. A., Petersen, J., and Maier-Hein, K. H. (2021). nnU-Net: a self-configuring method for deep learning-based biomedical image segmentation. *Nat. Methods* 18 (2), 203–211. doi:10.1038/s41592-020-01008-z

Janani, G., Suresh, P., Prakash, A., Parthiban, J., Anand, K., and Arumugam, S. (2020). Anterior knee pain in ACL reconstruction with BPTB graft - is it a myth? Comparative outcome analysis with hamstring graft in 1, 250 patients. *J. Orthop.* 22, 408–413. doi:10.1016/j.jor.2020.09.015

Javed Awan, M., Mohd Rahim, M. S., Salim, N., Mohammed, M. A., Garcia-Zapirain, B., and Abdulkareem, K. H. (2021). Efficient detection of knee anterior cruciate ligament from magnetic resonance imaging using deep learning approach. *Diagnostics* 11 (1), 105. doi:10.3390/diagnostics11010105

Kraeutler, M. J., Welton, K. L., McCarty, E. C., and Bravman, J. T. (2017). Revision anterior cruciate ligament reconstruction. *J. Bone Jt. Surg.* 99 (19), 1689–1696. doi:10.2106/jbjs.17.00412

Li, Z. (2022). Efficacy of repair for ACL injury: A meta-analysis of randomized controlled trials. *Int. J. Sports Med.* [online ahead of print] doi:10.1055/a-1755-4925

Lin, T.-Y., Goyal, P., Girshick, R., He, K., and Dollar, P. (2020). Focal loss for dense object detection. *IEEE Trans. Pattern Anal. Mach. Intell.* 42 (2), 318–327. doi:10.1109/tpami.2018.2858826

Lindström, M., Strandberg, S., Wredmark, T., Felländer-Tsai, L., and Henriksson, M. (2013). Functional and muscle morphometric effects of ACL reconstruction. A prospective CT study with 1 year follow-up. *Scand. J. Med. Sci. Sports* 23 (4), 431–442. doi:10.1111/j.1600-0838.2011.01417.x

Litjens, G., Kooi, T., Bejnordi, B. E., Setio, A. A. A., Ciompi, F., Ghafoorian, M., et al. (2017). A survey on deep learning in medical image analysis. *Med. Image Anal.* 42, 60–88. doi:10.1016/j.media.2017.07.005

Liu, F., Guan, B., Zhou, Z., Samsonov, A., Rosas, H., Lian, K., et al. (2019). Fully automated diagnosis of anterior cruciate ligament tears on knee mr images by using deep learning. *Radiol. Artif. Intell.* 1 (3), 180091. doi:10.1148/ryai.2019180091

Mahapatra, P., Horriat, S., and Anand, B. S. (2018). Anterior cruciate ligament repair - past, present and future. *J. Exp. Orthop.* 5 (1), 20. doi:10.1186/s40634-018-0136-6

Mehier, C., Ract, I., Metten, M. A., Najihi, N., and Guillin, R. (2022). Primary anterior cruciate ligament repair: Magnetic resonance imaging characterisation of reparable lesions and correlation with arthroscopy. *Eur. Radiol.* 32 (1), 582–592. doi:10.1007/s00330-021-08155-7

Murray, M. M., Fleming, B. C., Badger, G. J., Freiberger, C., Henderson, R., Barnett, S., et al. (2020). Bridge-enhanced anterior cruciate ligament repair is not inferior to autograft anterior cruciate ligament reconstruction at 2 Years: Results of a prospective randomized clinical trial. *Am. J. Sports Med.* 48 (6), 1305–1315. doi:10.1177/0363546520913532

Namiri, N. K., Flament, I., Astuto, B., Shah, R., Tibrewala, R., Caliva, F., et al. (2020). Deep learning for hierarchical severity staging of anterior cruciate ligament injuries from mri. *Radiol. Artif. Intell.* 1 (4), e190207–e190208. doi:10.1148/ryai.2020190207

Odgaard, F., Tuxoe, J., Joergensen, U., Lange, B., Lausten, G., Brettlau, T., et al. (2002). Clinical decision making in the acutely injured knee based on repeat clinical examination and MRI. *Scand. J. Med. Sci. Sports* 12 (3), 154–162. doi:10.1034/j.1600-0838.2002.00246.x

Payer, C., Stern, D., Bischof, H., and Urschler, M. (2016). "Regressing heatmaps for multiple landmark localization using CNNs," in Proceeding of the International Conference on Medical Image Computing and Computer-Assisted Intervention, 02 October 2016 (New York City: Springer Link), 230–238. doi:10.1007/978-3-319-46723-8_27

Ranjan, R., Patel, V. M., and Chellappa, R. (2019). HyperFace: A deep multi-task learning framework for face detection, landmark localization, pose estimation, and gender recognition. *IEEE Trans. Pattern Anal. Mach. Intell.* 41 (1), 121–135. doi:10.1109/tpami.2017.2781233

Reijman, M., Eggerding, V., van Es, E., van Arkel, E., van den Brand, I., van Linge, J., et al. (2021). Early surgical reconstruction versus rehabilitation with elective delayed reconstruction for patients with anterior cruciate ligament rupture: COMPARE randomised controlled trial. *Bmj* 372, n375. doi:10.1136/bmj.n375

Sherman, M. F., Lieber, L., Bonamo, J. R., Podesta, L., and Reiter, I. (1991). The long-term followup of primary anterior cruciate ligament repair. Defining a rationale for augmentation. *Am. J. Sports Med.* 19 (3), 243–255. doi:10.1177/036354659101900307

Shin, H. C., Roth, H. R., Gao, M., Lu, L., Xu, Z., Nogues, I., et al. (2016). Deep convolutional neural networks for computer-aided detection: CNN architectures, dataset characteristics and transfer learning. *IEEE Trans. Med. Imaging* 35 (5), 1285–1298. doi:10.1109/TMI.2016.2528162

Sim, Y., Chung, M. J., Kotter, E., Yune, S., Kim, M., Do, S., et al. (2020). Deep convolutional neural network-based software improves radiologist detection of malignant lung nodules on chest radiographs. *Radiology* 294 (1), 199–209. doi:10.1148/radiol.2019182465

Spindler, K. P., and Wright, R. W. (2008). Anterior cruciate ligament tear. *N. Engl. J. Med. Overseas. Ed.* 359 (20), 2135–2142. doi:10.1056/NEJMcp0804745

Taylor, D. C., Posner, M., Curl, W. W., and Feagin, J. A. (2009). Isolated tears of the anterior cruciate ligament: Over 30-year follow-up of patients treated with arthrotomy and primary repair. *Am. J. Sports Med.* 37 (1), 65–71. doi:10.1177/0363546508325660

van der List, J. P., and DiFelice, G. S. (2018). Preoperative magnetic resonance imaging predicts eligibility for arthroscopic primary anterior cruciate ligament repair. *Knee Surg. Sports Traumatol. Arthrosc.* 26 (2), 660–671. doi:10.1007/s00167-017-4646-z

van der List, J. P., and DiFelice, G. S. (2016). Preservation of the anterior cruciate ligament: A treatment algorithm based on tear location and tissue quality. *Am. J. Orthop.* 45 (7), E393–E405.

van der List, J. P., and DiFelice, G. S. (2017). Primary repair of the anterior cruciate ligament: A paradigm shift. *Surg.* 15 (3), 161–168. doi:10.1016/j.surge.2016.09.006

van der List, J. P., Mintz, D. N., and DiFelice, G. S. (2017). The location of anterior cruciate ligament tears: A prevalence study using magnetic resonance imaging. *Orthop. J. Sports Med.* 5 (6), 232596711770996. doi:10.1177/2325967117709966

Wang, L. J., Zeng, N., Yan, Z. P., Li, J. T., and Ni, G. X. (2020). Post-traumatic osteoarthritis following ACL injury. *Arthritis Res. Ther.* 22 (1), 57. doi:10.1186/s13075-020-02156-5

Yu, Y., Wang, N., Huang, N., Liu, X., Zheng, Y., Fu, Y., et al. (2021). Determining the invasiveness of ground-glass nodules using a 3D multi-task network. *Eur. Radiol.* 31 (9), 7162–7171. doi:10.1007/s00330-021-07794-0

Check for updates

*CORRESPONDENCE
Xiaoreng Feng,
fengxrsurgeon@163.com
Bin Chen,
chb@smu.edu.cn

Biomechanical comparison of the undercut thread design *versus* conventional buttress thread for the lag screw of the dynamic hip screw system

Fei Liu[1], Xiaoreng Feng[1,2]*, Jianxiong Zheng[1], Frankie Leung[3] and Bin Chen[1]*

[1]Division of Orthopaedics and Traumatology, Department of Orthopaedics, Nanfang Hospital, Southern Medical University, Guangzhou, China, [2]Department of Orthopaedics and Traumatology, Yangjiang People's Hospital, Yangjiang, China, [3]Department of Orthopaedics and Traumatology, Queen Mary Hospital, The University of Hong Kong, Hong Kong, Hong Kong SAR, China

Objective: To compare the fixation stability of the lag screw with a undercut thread design for the dynamic hip screw (DHS) system *versus* the lag screw with the conventional buttress thread.

Methods: The lag screws with the undercut thread (a flat crest feature, a tip-facing undercut feature) and buttress thread were both manufactured. Fixation stability was investigated using cyclic compressive biomechanical testing on custom osteoporotic femoral head sawbone. The forces required for the same vertical displacement in the two types of lag screw were collected to evaluate the resistance to migration. Varus angle was measured on X-ray images to assess the ability in preventing varus collapse. Finite element analysis (FEA) was performed to analyze the stress and strain distribution at the bone-screw interface of the two types of lag screws.

Results: The biomechanical test demonstrated that the force required to achieve the same vertical displacement of the lag screw with the undercut thread was significantly larger than the lag screw with conventional buttress thread ($p < 0.05$). The average varus angles generated by the undercut and buttress threads were $3.38 \pm 0.51°$ and $5.76 \pm 0.38°$, respectively ($p < 0.05$). The FEA revealed that the region of high-stress concentration in the bone surrounding the undercut thread was smaller than that surrounding the buttress thread.

Conclusion: The proposed DHS system lag screw with the undercut thread had higher migration resistance and superior fixation stability than the lag screw with the conventional buttress thread.

KEYWORDS

lag screw, dynamic hip screw, undercut thread, buttress thread, biomechanical test, finite element analysis

1 Introduction

Hip fractures are commonly encountered and challenging in the elderly population because of their poor bone quality (Veronese and Maggi, 2018; Dobre et al., 2021). Operation is usually necessary for this condition to decrease the complications associated with prolonged bed confinement (Roberts et al., 2015). The dynamic hip screw (DHS), which comprises a lag screw and a sliding plate, is a widely utilized fixation implant for hip fractures, especially for intertrochanteric hip fractures (Matre et al., 2013; Law et al., 2021; Lim et al., 2021). However, fixation failure of DHS is common. In particular, the failure incidence can reach 51.4% in unstable intertrochanteric hip fractures (Memon et al., 2021). Failure patterns include femoral head varus collapse, medialization of distal fragment and screw cut-out of the lag screw, which always result in a revision surgery (Boukebous et al., 2018; Taheriazam and Saeidinia, 2019; Memon et al., 2021).

Although fracture type and surgical techniques are crucial in fixation failure of DHS treatment (Hsu et al., 2016), the configurations of the lag screw are also critical factors; inner diameter, outer diameter, pitch, screw length and thread shape are main configuration parameters for orthopedics screws (Feng et al., 2015; Feng et al., 2016; Gustafson et al., 2019; Kilian et al., 2019; Schliemann et al., 2019). The thread shape is the most important structure, as it can determine the mechanical environment at the bone-screw interface, and influence the biomechanical performance and osseointegration, accordingly (Abuhussein et al., 2010; Alemayehu and Jeng, 2021; Feng et al., 2021; Watanabe et al., 2022). An FEA study found that under the same pullout force, the V-shaped thread and square thread generated less stress than the thin-thread at the bone-screw interface (Geng et al., 2004). The reverse buttress thread also exhibits superior performance in FEA and biomechanical pullout test (Gracco et al., 2012; Oswal et al., 2016). However, another biomechanical study showed that screws with trapezoidal thread had higher pullout strength than screws with reverse buttress thread (Yashwant et al., 2017). At present, the thread shape of the DHS lag screw is standard buttress thread, which was first proposed by Robert Danis in the 1950s and is prevalent among different orthopedics screws. The typical buttress thread has the optimal performance in terms of the resistance of the unidirectional axial pull-out loading force (Ricci et al., 2010). However, the loading forces are multiaxial during the physiological motion in vivo. The failure risk for standard buttress thread screw is high when exposed to multidirectional loading forces (Stahel et al., 2017). A clinical research and finite element analysis (FEA) validated that radial stress affects screw loosening in the plate fixation of long bone fractures more than axial stress (Feng et al., 2019). The major complication of DHS is screw cutout, usually due to lateral migration of the lag screw relative to the femoral head (Taheriazam and Saeidinia, 2019). Our previous researches have demonstrated that the undercut thread design for
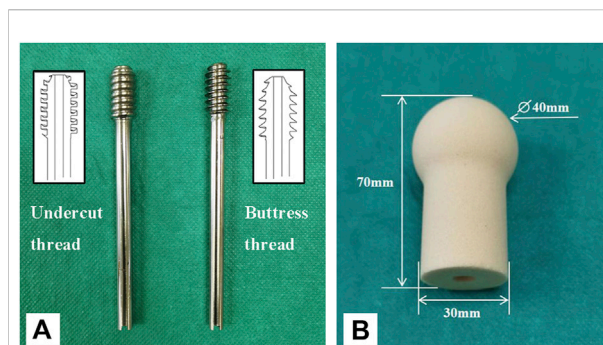
FIGURE 1
The lag screws and surrogate femoral head used in this study. **(A)** A lag screw with the undercut thread (left), and a lag screw with conventional buttress thread (right). **(B)** Surrogate femoral head manufactured from polyurethane foam blocks.

cancellous bone screw exhibited better lateral resistance than the standard buttress cancellous bone screw (Feng et al., 2022a). In addition, compared with the buttress thread, the undercut thread can make the stress distribution of the bone around the thread more uniform, and effectively avoid stress shielding, thus facilitating the process of osseointegration (Feng et al., 2022b).

The purpose of the present study was to evaluate the biomechanical performance of the DHS lag screw with the undercut thread design versus the standard conventional thread pattern (buttress thread) using biomechanical testing on surrogate femoral heads and FEA.
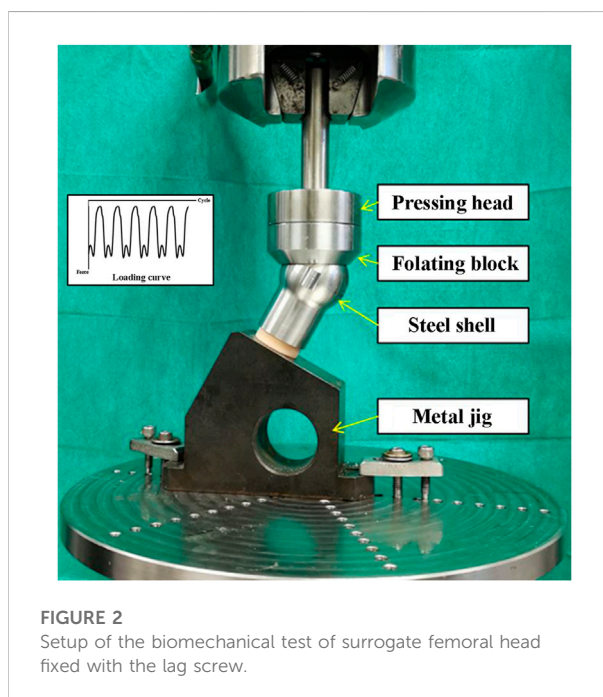
FIGURE 2
Setup of the biomechanical test of surrogate femoral head fixed with the lag screw.
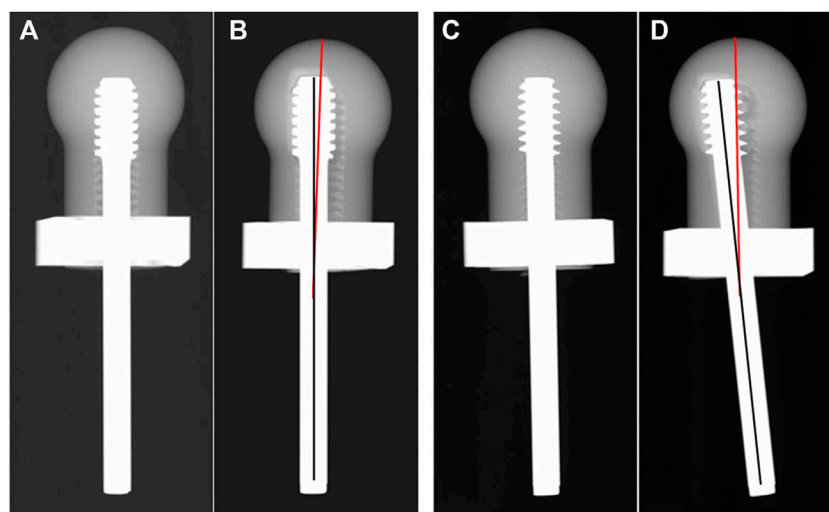
FIGURE 3
Images of X-ray scan pre-test **(A,C)** and post-test **(B,D)**. The solid black line represents the axis of the screw, the solid red line represents the axis of the femoral head.

2 Materials and methods

2.1 Biomechanical test

The DHS lag screws with undercut (n = 5) and buttress threads (n = 5) were manufactured from 316 low carbon vacuum melt stainless steel. Configurations of the screws were all identical except thread shape, including major diameter of 12.88 mm, minor diameter of 7.80 mm, thread pitch of 3.00 mm and screw length of 120 mm. Additionally, the undercut thread had a flat crest of 1.57 mm (Figure 1A).

Solid rigid polyurethane foam blocks with a density of 0.16 g/cm³ (Sawbones 10 PCF; Pacific Research Laboratories, Vashon, Washington, United States) were used to imitate the human osteoporotic cancellous bone (O'Neill et al., 2012). The foam blocks were custom manufactured into the shape of a femoral head (Figure 1B). A pilot hole with the diameter of 8 mm and depth of 55 mm was reamed for each surrogate femoral head. Dimensions of the femoral head are shown in Figure 1B (Lee et al., 2014). A steel shell with a thickness of 2 mm that matched the shape of the femoral head was also custom manufactured (Figure 2). A metal jig was custom manufactured to fix the implant, with a special design slope to simulate the 17° clinical angle of peak walking force vector acting toward the center of the femoral head in the frontal plane (Figure 2) (Bergmann et al., 2016).

Each lag screw was inserted into the pilot hole of the surrogate femoral head using a screwdriver. Digital X-ray images (20 kV, 5 s) were taken to ensure that the screw reached the end of the hole (Figure 3). Then, the femoral head was assembled with the steel shell and fixed into the metal jig. Subsequently, each sample was mounted on the loading cell of an MTS 858 Mini Bionix (MTS Systems Corporation, Eden Prairie, Minnesota, United States) hydraulic loading machine for cyclic loading test (Figure 2). The loading force was applied to the steel shell through a pressing head and a floating block (Figure 2). The cyclic loading program was a double-peak loading curve with the minimum and maximum forces ranging from 100 N to 1000 N, respectively, for the first cycle. The maximum force increased by 0.2 N per cycle at 1 Hz with the minimum force kept at 10% of the maximum force. Continuous loading was applied until the vertical displacement of 7 mm was reached. After loading, a digital X-ray image was taken for each sample in the anterior-posterior (AP) view.

The load required to reach the axial displacement of 1, 2, 3, 4, 5, 6 and 7 mm was collected, respectively. The varus angle, which was defined as the angle between the axis of the lag screw and the central line of the femoral head after loading, was measured on the X-ray image in the AP view (Figure 3).

2.2 Finite element analysis

FEA is an engineering tool for structural analysis and has been widely used to evaluate the stress distribution of bones and implants. FEA can reveal detailed information, such as stress and strain distributions, that can be difficult or impossible to measure in laboratory biomechanical tests. The FEA models in this study were established to simulate the scenario of a human in a
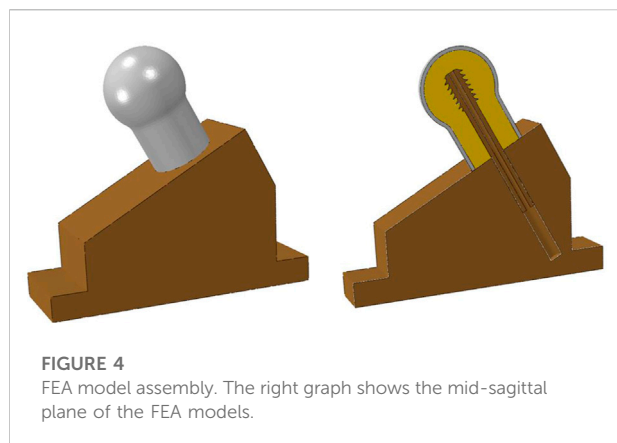
FIGURE 4
FEA model assembly. The right graph shows the mid-sagittal plane of the FEA models.

FIGURE 5
Results of the biomechanical test. **(A)** Force required to reach the vertical displacement of 1, 2, 3, 4, 5, 6, and 7 mm. **(B)** Varus angle generated post-test by the two types of lag screws. **, $p <$ 0.01; ***, $p <$ 0.001.

TABLE 1 Material properties for the FEA models used in this study.

Material	Young's modulus, MPa	Poisson's ratio
Cancellous bone	260	0.29
Cortical bone	2600	0.3
Screw	200000	0.3

stationary standing position. The FEA 3D models included the two kinds of lag screws with different thread shape, the femoral head of the cancellous bone and the metal jig, which possessed the same dimensions as described previously in the biomechanical test section. The 3D model of cortical bone was designed as a shell with a thickness of 2 mm wrapped around the surface of the femoral head cancellous bone. The assembly of the 3D models is shown in Figure 4.

The 3D finite element models were created for each geometry using ABAQUS software suite (6.13/CAE; Simulia, Providence, Rhode Island, United States). The metal jig was defined as a rigid body. The material properties of the cancellous bone, cortical bone, and screw are summarized in Table 1 (Benli et al., 2008; Saba, 2012; Lee et al., 2016). The material properties were all defined as homogeneous, isotropic and linear elastic (Feng et al., 2022a). The cancellous bone and screw were simulated as osteoporotic cancellous bone and stainless steel, respectively (Benli et al., 2008; Oftadeh et al., 2015; Lee et al., 2016). Bone-screw contact interfaces were defined as sliding interactions with a Coulomb friction coefficient of 0.3 (MacLeod et al., 2012). Bone-metal jig and screw-mental jig contact interfaces were defined as frictionless sliding interactions (Afferrante and Ciavarella, 2006). Cortical bone was tied with cancellous bone (Fu et al., 2022). A constant load of 250N was applied straight down on the femoral head with the bottom of the metal jig fixed (Ching et al., 2020).

Since the stress distribution and strain distribution in the bone were the focus of this study, the bone was modeled using quadratic tetrahedral elements, while the screws and metal jig were modeled using linear tetrahedral elements. The approximate number of elements used in the cancellous bone, cortical bone, screw, and metal jig were 760,000, 120,000, 190,000, and 1,280,000, respectively. All bone models incorporated mesh refinement at the bone-screw interface. The size of the element edge near the screw hole was 0.02 mm. A mesh convergence study was performed to determine the appropriate mesh size for each part of the models based on their effect on the maximum Von Mises stress. The maximum Von Mises stress of the undercut thread model changed by 0.97%, when the number of elements in the bone was doubled. Therefore, the number of elements mentioned previously was considered suitable for the analysis of the FEA models used in this study.
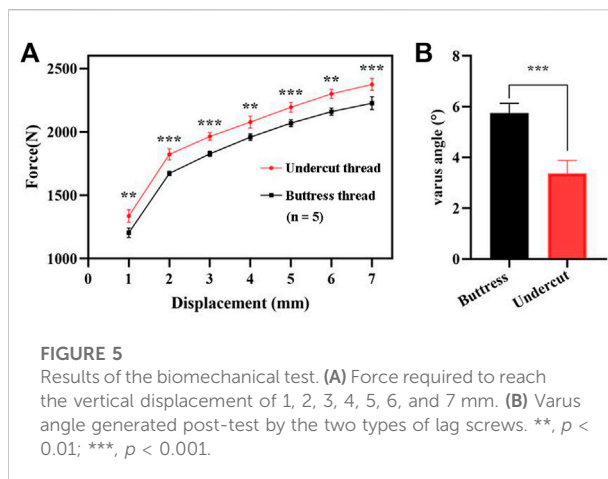
To assess the effect of the undercut thread and the buttress thread on the bone, the maximum Von Mises stress, the maximum principal strain, and the minimum principal strain were evaluated for cancellous bone surrounding the bone-screw interface for the two FEA models in the mid-sagittal plane. In addition, the volume of the bone around the screw thread at the bone-screw interface, when the Von Mises stress exceeded a set threshold, was calculated for both FEA models.

3 Data and statistical analysis

The varus angle, and the load required to reach the axial displacement of 1, 2, 3, 4, 5, 6 and 7 mm were expressed as means and standard deviations (SD). An independent sample t test was used to compare differences between the two studied groups and $p < 0.05$ was considered statistically significant. All statistical analyses were conducted using SPSS (IBM SPSS Statistics for Windows, IBM Corp, Armonk, NY, Version 19.0).

FIGURE 6
FEA results of the two models. **(A,B)** The Von Mises stress distribution of the cancellous bone in the mid-sagittal plane associated with the buttress thread and undercut thread, respectively. **(C)** The volume of bone with Von Mises stress >0.45 MPa.
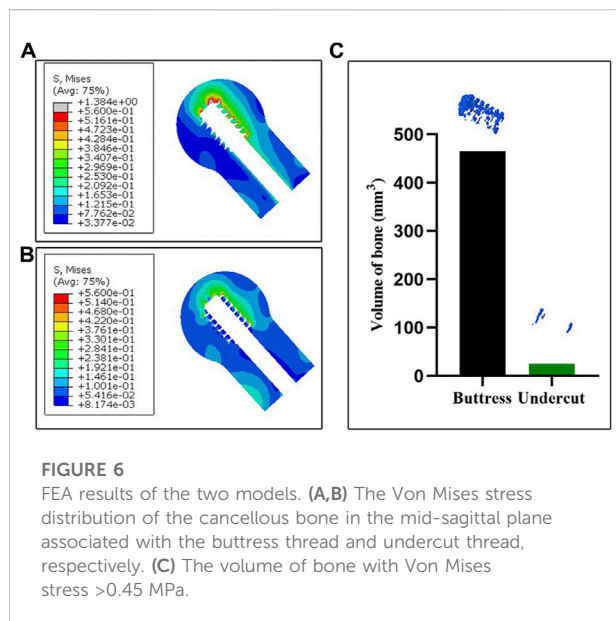
4 Results

4.1 Biomechanical test

The mean load required to reach the axial displacement of 1, 2, 3, 4, 5, 6, and 7 mm for the proposed lag screw with undercut thread was 1,336.50 ± 49.58 N, 1882.67 ± 44.53 N, 1964.87 ± 29.63 N, 2078.55 ± 47.69 N, 2194.86 ± 39.32 N, 2300.47 ± 36.47 N, and 2375.29 ± 46.29 N, respectively. The corresponding mean load for the lag screw with buttress head was 1205.17 ± 38.25 N, 1672.07 ± 18.08 N, 1827.16 ± 20.05 N, 1959.64 ± 25.70 N, 2070.35 ± 27.25 N, 2161.02 ± 28.37 N, and 2227.88 ± 50.91 N, respectively (Figure 5A). The mean varus angles of the undercut and buttress thread lag screws were 3.38 ± 0.51° and 5.76 ± 0.38°, respectively (Figure 5B).

4.2 Finite element analysis

The Von Mises stress distribution of the cancellous bone for the two FEA models in the mid-sagittal plane is illustrated in Figures 6A,B. The maximum Von Mises stresses of the undercut thread model and buttress thread models were 0.56 MPa and 1.38 MPa, respectively. Stress concentrations were observed at the superior screw-bone interface for both models. However, the area and value of the stress concentration of the undercut thread model were smaller than in buttress thread model. A threshold was defined as the 80% of the maximum Von Mises stress of the undercut thread model, which was 0.45 MPa. The volumes of the bone with Von Mises stress >0.45 MPa of the undercut thread model and buttress thread model were 25.63 mm³ and 465.30 mm³, respectively (Figure 6C).

The maximum principal strain distribution of the cancellous bone in the mid-sagittal plane of the two femoral head models reveals the tensile strain distribution (Figure 7). The region of the tensile strain distribution concentration was observed at the superior screw-bone interface for both models. The area and value of the tensile strain distribution concentration of the undercut thread model were smaller than in the buttress thread model.

The minimum principal strain distribution of the cancellous bone in the mid-sagittal plane of the two femoral head models reveals the compressive strain distribution (Figure 7). The region of the compressive strain distribution concentration was also observed at the superior screw-bone interface for both models. The area of compressive strain distribution of the buttress thread model was larger compared to the undercut thread model.

5 Discussion

The results of the biomechanical test showed the proposed the undercut thread produced a higher load and a smaller varus angle when loaded to the same vertical displacement as the conventional buttress thread (Figure 5), which demonstrated the superiority of the resistance to migration of the proposed DHS lag screw with the undercut thread compared to the conventional buttress thread under the simulated physiological loading pattern. FEA revealed that the undercut thread can reduce the stress and strain of the cancellous bone at the bone-screw interface (Figures 6, 7). These results show that the undercut thread can potentially reduce the failure incidence of the DHS when treating hip fractures.

Although the biggest advantage of the buttress thread is the resistance to axial pullout forces (Ryu et al., 2014; Mosavar et al., 2015), bones *in vivo* need to withstand complex forces in multiple directions during physiological activities. A clinical investigation combined with FEA simulation demonstrated that axial stress was not the main reason for screw loosening (Feng et al., 2019). In this study, screw loosening was observed using X-ray images, which showed that the screw closest to the fracture line was most prone to loosening. FEA simulation indicated the radial stress, rather than the axial stress, produced more volume of bone destruction, which induced bone resorption and in turn led to screw loosening. The buttress thread design screw can produce microfractures at the bone-screw interface, as it is more likely to stripping (Stahel et al., 2017). Previous studies have validated that the undercut thread can effectively reduce stress concentration and stress shielding and that it possesses superior fixation stability in both lateral and torsional loading (Feng et al., 2022a; Feng et al., 2022b). In the present study, the undercut thread exhibited higher resistance to migration, compared to the buttress thread, in the biomechanical test simulated physiological load of the hip joint. FEA results suggested that the reason for this phenomenon could be the undercut thread that can reduce the Von Mises stress at the bone-screw surface. The
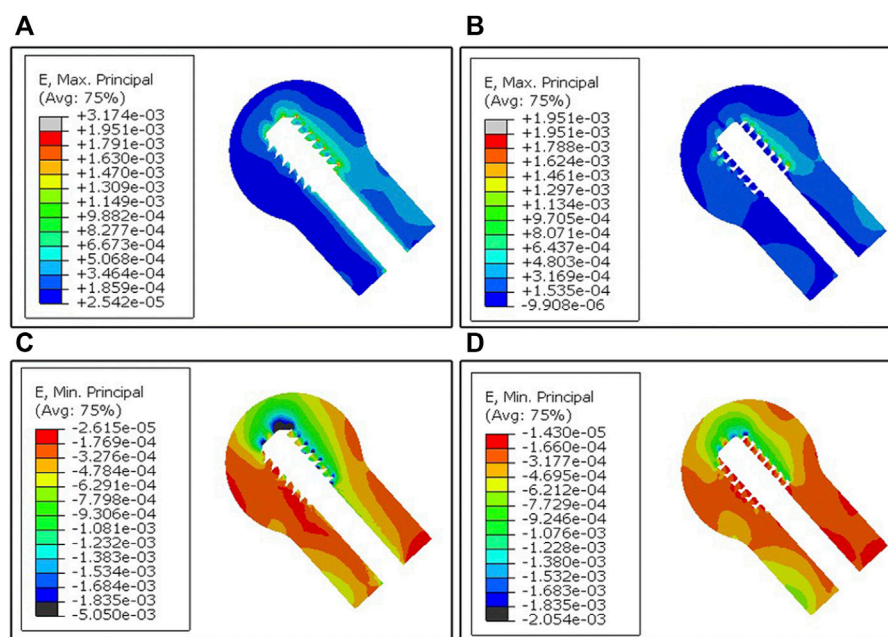
FIGURE 7
FEA results of the two models. **(A,B)** The maximum principal strain distribution of the cancellous bone in the mid-sagittal plane generated from the buttress thread and undercut thread, respectively. **(C,D)** The minimum principal strain distribution of the cancellous bone in the mid-sagittal plane generated from the buttress thread and undercut thread, respectively.

peak Von Mises stress was 1.38 MPa for the buttress thread, whereas for the undercut thread, it was 0.56 MPa. The volume of the bone with stress higher than 0.45 MPa of the buttress thread model was larger than that of the undercut thread model, which meant that less bone destruction would occur surrounding the undercut thread. The flat crest of the undercut thread increased the lateral surface area of the thread meant that larger force was needed to achieve the same displacement as the buttress thread. This is the theoretical reason for the lower bone-screw interface stress of the undercut thread. In other words, the fixation construct with the undercut thread lag screw had greater stiffness and was stabler than the buttress thread under cyclic loading.

Varus collapse of the femoral head is the most common failure of DHS, often accompanied with cut-out of the lag screw through the femoral head, which usually requires revision surgery treatment, like total hip arthroplasty (Chen et al., 2017; Taheriazam and Saeidinia, 2019). In this study, the degree of varus collapse can be represented by the varus angle. In the case of the undercut thread, the mean varus angle after the biomechanical test was $3.38° \pm 0.51°$, which was significantly smaller than for the buttress thread with $5.76° \pm 0.38°$. The results demonstrated the undercut thread could effectively reduce the incidence of the varus collapse and cut-out of the lag screw for DHS treatment. Larger varus angles can result in greater deformation of the surrounding cancellous bone at the bone-screw interface. Consequently, increased volume of bone destruction and resorption is produced. This was revealed by the features of the post-

test X-ray images and FEA simulation. Compared with the undercut thread, X-ray images showed that more cancellous bone was stripped by the buttress thread. The FEA simulation revealed that the maximum and minimum principal strain was larger at the bone-screw interface of the buttress thread than in the undercut thread. In other words, the undercut thread can reduce the microfracture occurrence in the cancellous bone at the bone-screw interface and thus lower the incidence of varus collapse.

Loads applied to the bone-screw interface can produce three types of forces on the surrounding bone tissue, including compressive, tensile and shear forces (Misch and Abbas, 2008). Bone tissue is more resistant to compression than tension (Oftadeh et al., 2015; Morgan et al., 2018). Compressive force is the most beneficial to bone tissue as it can increase bone density and its strength (Bolind et al., 2005). On the other hand, shear force could impair the mechanical properties of the trabecular bone (Wang and Niebur, 2006; Misch and Abbas, 2008). Different thread shapes have a significant effect on the distribution and proportion of these three types of forces (Abuhussein et al., 2010). Conceptually, the flat crest of undercut thread can reduce the shear stress and increase the proportion of compressive stress compared to the buttress thread, when subjected to lateral loads. Therefore, the mechanical environment at the bone-screw interface by the undercut thread design is favorable to bone resorption reduction and osseointegration improvement. However, this structure increases the lateral area of the thread, which may cause difficulty in screwing in. Therefore, in the

clinical scenario, the screw with this thread may need a self-tapping structure.

Limitations exist in this study. Polyurethane foam of the Sawbones synthetic bone is a homogeneous material and cannot accurately reflect the reality in which cancellous bone is highly heterogeneous *in vivo*. Thus, conclusions based on results of the biomechanical test on artificial bone should be cautious. The models used were not an intact femur, so the conclusions may not represent the real clinical situation. Therefore, biomechanical testing on the cadaveric specimen should be conducted to validate the conclusions of this study in the future.

6 Conclusion

Overall, the lag screw of dynamic hip screw with the undercut thread had higher resistance to migration than the lag screw with conventional buttress thread. Biomechanical testing demonstrated that the lag screw with the undercut thread required a higher force to reach the same displacement as the lag screw with the buttress thread. Furthermore, the varus angle generated by the undercut thread was much smaller. Finite element analysis revealed that the Von Mises stress, the maximum and minimum principal strain at the bone-screw interface around the undercut thread were lower. The undercut thread can effectively relieve the high-stress concentration compared with the buttress thread.

Data availability statement

The raw data supporting the conclusion of this article will be made available by the authors, without undue reservation.

Author contributions

BC and XF were responsible for the design of the study. FL were responsible for biomechanical test and writing the manuscript. JZ and FL performed the FEA and statistical analyses. All authors have read and approved the final manuscript.

Funding

Conflict of interest

The authors declare that the research was conducted in the absence of any commercial or financial relationships that could be construed as a potential conflict of interest.

Publisher's note

All claims expressed in this article are solely those of the authors and do not necessarily represent those of their affiliated organizations, or those of the publisher, the editors and the reviewers. Any product that may be evaluated in this article, or claim that may be made by its manufacturer, is not guaranteed or endorsed by the publisher.

References

Abuhussein, H., Pagni, G., Rebaudi, A., and Wang, H. -L. (2010). The effect of thread pattern upon implant osseointegration. *Clin. Oral Implants Res.* 21 (2), 129–136. doi:10.1111/j.1600-0501.2009.01800.x

Afferrante, L., and Ciavarella, M. (2006). Frictionless" and "frictional" ThermoElastic dynamic instability (TEDI) of sliding contacts. *J. Mech. Phys. Solids* 54 (11), 2330–2353. doi:10.1016/j.jmps.2006.06.008

Alemayehu, D. -B., and Jeng, Y. -R. (2021). Three-Dimensional finite element investigation into effects of implant thread design and loading rate on stress distribution in dental implants and anisotropic bone. *Materials* 14 (22), 6974. doi:10.3390/ma14226974

Benli, S., Aksoy, S., Havitcioğlu, H., and Kucuk, M. (2008). Evaluation of bone plate with low-stiffness material in terms of stress distribution. *J. Biomech.* 41 (15), 3229–3235. doi:10.1016/j.jbiomech.2008.08.003

Bergmann, G., Bender, A., Dymke, J., Duda, G., and Damm, P. (2016). Standardized loads acting in hip implants. *PLoS One* 11 (5), e0155612. doi:10.1371/journal.pone.0155612

Bolind, P. K., Johansson, C. B., Becker, W., Langer, L., Sevetz, E. B., Jr, and Albrektsson, T. O. (2005). A descriptive study on retrieved non-threaded and threaded implant designs. *Clin. Oral Implants Res.* 16 (4), 447–455. doi:10.1111/j.1600-0501.2005.01129.x

Boukebous, B., Guillon, P., Vandenbussche, E., and Rousseau, M. A. (2018). Correlation between femoral offset loss and dynamic hip screw cut-out

complications after pertrochanteric fractures: A case-control study. *Eur. J. Orthop. Surg. Traumatol.* 28 (7), 1321–1326. doi:10.1007/s00590-018-2204-0

Chen, C. -Y., Huang, S. -W., Sun, J. -S., Lin, S. -Y., Yu, C. -S., Pan, H. -P., et al. (2017). Wing-augmentation reduces femoral head cutting out of dynamic hip screw. *Med. Eng. Phys.* 44, 73–78. doi:10.1016/j.medengphy.2017.02.015

Ching, M., Gee, A., Balso, C. D., Lawendy, A., Schemitsch, E., Zdero, R., et al. (2020). Biomechanical consequences of nail insertion point and anterior cortical perforation for antegrade femoral nailing. *Biomed. Res. Int.* 2020, 1–10. doi:10.1155/2020/5878607

Dobre, R., Niculescu, D. A., Cirstoiu, C., Popescu, G., and Poiana, C. (2021). Osteoporotic hip fracture incidence rates in the main urban area of Romania. *Acta Endocrinol. (Copenh).* 17 (1), 60–67. doi:10.4183/aeb.2021.60

Feng, X., Fang, J., Lin, C., Zhang, S., Lei, W., Li, Y., et al. (2015). Axial perspective to find the largest intraosseous space available for percutaneous screw fixation of fractures of the acetabular anterior column. *Int. J. Comput. Assist. Radiol. Surg.* 10 (8), 1347–1353. doi:10.1007/s11548-015-1149-6

Feng, X., Lin, G., Fang, C. X., Lu, W. W., Chen, B., and Leung, F. K. L. (2019). Bone resorption triggered by high radial stress: The mechanism of screw loosening in plate fixation of long bone fractures. *J. Orthop. Res.* 37 (7), 1498–1507. doi:10.1002/jor.24286

Feng, X., Qi, W., Fang, C. X., Lu, W. W., Leung, F. K. L., and Chen, B. (2021). Can barb thread design improve the pullout strength of bone screws? *Bone Jt. Res.* 10 (2), 105–112. doi:10.1302/2046-3758.102.BJR-2020-0072.R2

Feng, X., Zhang, S., Liang, H., Chen, B., and Leung, F. (2022b). Development and initial validation of a novel undercut thread design for locking screws. *Injury* 53 (7), 2533–2540. doi:10.1016/j.injury.2022.02.048

Feng, X., Zhang, S., Luo, Q., Fang, J., Lin, C., Leung, F., et al. (2016). Definition of a safe zone for antegrade lag screw fixation of fracture of posterior column of the acetabulum by 3D technology. *Injury* 47 (3), 702–706. doi:10.1016/j.injury.2016.01.026

Feng, X., Zhang, S., Luo, Z., Liang, H., Chen, B., and Leung, F. (2022a). Development and initial validation of a novel thread design for nonlocking cancellous screws. *J. Orthop. Res.* doi:10.1002/jor.25305

Fu, G., Zhong, G., Yang, Z., Cheng, S., Ma, L., and Zhang, Y. (2022). Two cannulated screws provide sufficient biomechanical strength for prophylactic fixation in adult patients with an aggressive benign femoral neck lesion. *Front. Bioeng. Biotechnol.* 10, 891338. doi:10.3389/fbioe.2022.891338

Geng, J. P., Ma, Q. S., Xu, W., Tan, K. B., and Liu, G. R. (2004). Finite element analysis of four thread-form configurations in a stepped screw implant. *J. Oral Rehabil.* 31 (3), 233–239. doi:10.1046/j.0305-182X.2003.01213.x

Gracco, A., Giagnorio, C., Incerti, P. S., Alessandri, B. G., and Siciliani, G. (2012). Effects of thread shape on the pullout strength of miniscrews. *Am. J. Orthod. Dentofac. Orthop.* 142 (2), 186–190. doi:10.1016/j.ajodo.2012.03.023

Gustafson, P. A., Veenstra, J. M., Bearden, C. R., and Jastifer, J. R. (2019). The effect of pitch variation and diameter variation on screw pullout. *Foot Ankle Spec.* 12 (3), 258–263. doi:10.1177/1938640018789999

Hsu, C. -E., Huang, K. -C., Lin, T. -C., Tong, K. -M., Lee, M. -H., and Chiu, Y. -C. (2016). Integrated risk scoring model for predicting dynamic hip screw treatment outcome of intertrochanteric fracture. *Injury* 47 (11), 2501–2506. doi:10.1016/j.injury.2016.09.012

Kilian, M., Simkovic, P., Zamborsky, R., Skoda, A., and Labas, P. (2019). What are the ideal screw lengths in volar locking plate fixation for distal radius fractures? *Bratisl. Lek. Listy* 120 (7), 505–509. doi:10.4149/BLL_2019_080

Law, G. W., Wong, Y. R., Gardner, A., and Ng, Y. H. (2021). Intramedullary nailing confers an increased risk of medial migration compared to dynamic hip screw fixation in unstable intertrochanteric hip fractures. *Injury* 52 (11), 3440–3445. doi:10.1016/j.injury.2021.01.011

Lee, C. H., Shih, C. M., Huang, K. C., Chen, K. H., Hung, L. K., and Su, K. C. (2016). Biomechanical analysis of implanted clavicle hook plates with different implant depths and materials in the acromioclavicular joint: A finite element analysis study. *Artif. Organs* 40 (11), 1062–1070. doi:10.1111/aor.12679

Lee, C. K., Kwan, M. K., Merican, A. M., Ng, W. M., Saw, L. B., Teh, K. K., et al. (2014). Femoral head diameter in the Malaysian population. *Singap. Med. J.* 55 (8), 436–438. doi:10.11622/smedj.2014103

Lim, E. J., Shon, H. -C., Cho, J. -W., Oh, J. -K., Kim, J., and Kim, C. -H. (2021). Dynamic hip screw versus cannulated cancellous screw in pauwels type II or type III femoral neck fracture: A systematic review and meta-analysis. *J. Pers. Med.* 11 (10), 1017. doi:10.3390/jpm11101017

MacLeod, A. R., Pankaj, P., and Simpson, A. H. (2012). Does screw-bone interface modelling matter in finite element analyses? *J. Biomech.* 45 (9), 1712–1716. doi:10.1016/j.jbiomech.2012.04.008

Matre, K., Havelin, L. I., Gjertsen, J. -E., Espehaug, B., and Fevang, J. M. (2013). Intramedullary nails result in more reoperations than sliding hip screws in two-part intertrochanteric fractures. *Clin. Orthop. Relat. Res.* 471 (4), 1379–1386. doi:10.1007/s11999-012-2728-2

Memon, K., Siddiqui, A. M., Khan, Z. A., and Zahoor, A. (2021). Dynamic hip screw fixation vs. Proximal femur nail for unstable per-trochanteric fractures: A comparative analysis of outcomes and complications. *J. Ayub Med. Coll. Abbottabad.* 33 (1), 34–38.

Misch, C. E., and Abbas, H. A. (2008). *Contemporary implant dentistry.* 3rd. St. Louis: Mosby, 1061.

Morgan, E. F., Unnikrisnan, G. U., and Hussein, A. I. (2018). Bone mechanical properties in healthy and diseased states. *Annu. Rev. Biomed. Eng.* 20, 119–143. doi:10.1146/annurev-bioeng-062117-121139

Mosavar, A., Ziaei, A., and Kadkhodaei, M. (2015). The effect of implant thread design on stress distribution in anisotropic bone with different osseointegration conditions: A finite element analysis. *Int. J. Oral Maxillofac. Implants* 30 (6), 1317–1326. doi:10.11607/jomi.4091

O'Neill, F., Condon, F., McGloughlin, T., Lenehan, B., Coffey, C., and Walsh, M. (2012). Validity of synthetic bone as a substitute for osteoporotic cadaveric femoral heads in mechanical testing: A biomechanical study. *Bone Jt. Res.* 1 (4), 50–55. doi:10.1302/2046-3758.14.2000044

Oftadeh, R., Perez-Viloria, M., Villa-Camacho, J. C., Vaziri, A., and Nazarian, A. (2015). Biomechanics and mechanobiology of trabecular bone: A review. *J. Biomech. Eng.* 137 (1), 0108021–01080215. doi:10.1115/1.4029176

Oswal, M. M., Amasi, U. N., Oswal, M. S., and Bhagat, A. S. (2016). Influence of three different implant thread designs on stress distribution: A three-dimensional finite element analysis. *J. Indian Prosthodont. Soc.* 16 (4), 359–365. doi:10.4103/0972-4052.191283

Ricci, W. M., Tornetta, P. R., Petteys, T., Gerlach, D., Cartner, J., Walker, Z., et al. (2010). A comparison of screw insertion torque and pullout strength. *J. Orthop. Trauma* 24 (6), 374–378. doi:10.1097/BOT.0b013e3181c4a655

Roberts, K. C., Brox, W. T., Jevsevar, D. S., and Sevarino, K. (2015). Management of hip fractures in the elderly. *J. Am. Acad. Orthop. Surg.* 23 (2), 131–137. doi:10.5435/JAAOS-D-14-00432

Ryu, H. S., Namgung, C., Lee, J. H., and Lim, Y. J. (2014). The influence of thread geometry on implant osseointegration under immediate loading: A literature review. *J. Adv. Prosthodont.* 6 (6), 547–554. doi:10.4047/jap.2014.6.6.547

Saba, L. (2012). *Computed tomography: Clinical applications.* Norderstedt, Germany: BoD–Books on Demand.

Schliemann, B., Risse, N., Frank, A., Müller, M., Michel, P., Raschke, M. J., et al. (2019). Screws with larger core diameter and lower thread pitch increase the stability of locked plating in osteoporotic proximal humeral fractures. *Clin. Biomech. (Bristol, Avon.* 63, 21–26. doi:10.1016/j.clinbiomech.2019.02.006

Stahel, P. F., Alfonso, N. A., Henderson, C., and Baldini, T. (2017). Introducing the "Bone-Screw-Fastener" for improved screw fixation in orthopedic surgery: A revolutionary paradigm shift? *Patient Saf. Surg.* 11, 6. doi:10.1186/s13037-017-0121-5

Taheriazam, A., and Saeidinia, A. (2019). <p>Salvage of failed dynamic hip screw fixation of intertrochanteric fractures</p>. *Orthop. Res. Rev.* 11, 93–98. doi:10.2147/ORR.S215240

Veronese, N., and Maggi, S. (2018). Epidemiology and social costs of hip fracture. *Injury* 49 (8), 1458–1460. doi:10.1016/j.injury.2018.04.015

Watanabe, K., Mitchell, B., Sakamaki, T., Hirai, Y., Kim, D. G., Deguchi, T., et al. (2022). Mechanical stability of orthodontic miniscrew depends on a thread shape. *J. Dent. Sci.* 17 (3), 1244–1252. doi:10.1016/j.jds.2021.11.010

Wang, X., and Niebur, G. L. (2006). Microdamage propagation in trabecular bone due to changes in loading mode. *J. Biomech.* 39 (5), 781–790. doi:10.1016/j.jbiomech.2005.02.007

Yashwant, A. V., Dilip, S., Krishnaraj, R., and Ravi, K. (2017). Does change in thread shape influence the pull out strength of Mini implants? An *in vitro* study. *J. Clin. Diagn. Res.* 11 (5), ZC17–ZC20. doi:10.7860/JCDR/2017/25774.9808

Multi-planar instability, laxity and reduced knee flexion during the support phase of walking are determinants of return to sports

Tianping Zhou[1†], Yihong Xu[1†], Lan Zhou[2], Siya Wang[2], Shaobai Wang[2]* and Weidong Xu[1]*

[1]Department of Joint Surgery and Sports Medicine, Changhai Hospital Affiliated to Navy Medical University, Shanghai, China, [2]Key Laboratory of Exercise and Health Sciences of Ministry of Education, Shanghai University of Sport, Shanghai, China

Background: After anterior cruciate ligament reconstruction, some patients are not recommended to return to high-level physical activity because they fail to pass return-to-sports tests. The kinematic difference between these patients and those who pass the return-to-sports tests is unclear.

Methods: Eighty-two patients who received anatomic single-bundle anterior cruciate ligament (ACL) reconstruction for unilateral ACL injury underwent return-to-sport tests during a hospital visit at a minimum of 9 months (9−11 months) of follow-up. Fifteen patients who passed the return-to-sports tests (RTS group) and fifteen patients who did not (NRTS group) were randomly selected to perform a treadmill walk under dual-fluoroscopic imaging system surveillance for a 6 degrees of freedom kinematic evaluation.

Results: Of the 82 patients, 53 passed the return-to-sports tests 9 months after surgery, with a return-to-sports rate of 64.6%. In the stance phase, the NRTS group had a larger anterior tibial translation (1.00 $\pm$ 0.03 mm vs. 0.76 $\pm$ 0.03 mm, p = 0.001), a larger lateral tibial movement (1.61 $\pm$ 0.05 mm vs. 0.77 $\pm$ 0.05 mm, p < 0.001), a larger distal tibial displacement (−3.09 $\pm$ 0.05 mm vs. −2.69 $\pm$ 0.05 mm, p < 0.001), a smaller knee flexion angle (6.72 $\pm$ 0.07° vs. 8.34 $\pm$ 0.07°, p < 0.001), a larger varus angle (−0.40 $\pm$ 0.03°VS. -0.01 $\pm$ 0.03°, p < 0.001) and a larger external rotation angle (1.80 $\pm$ 0.05° vs. 1.77 $\pm$ 0.05°, p < 0.001) than the RTS group. The maximum anterior tibial translation of the NRTS group is also larger than that of the RTS group (3.64 $\pm$ 0.42 mm vs. 3.03 $\pm$ 0.59 mm, p = 0.003).

Conclusion: Compared with patients passing RTS tests, those who fail to pass show significant anterior, lateral, and rotational instability; knee laxity; and reduced flexion angle of the knee in the support phase during walking, which may be the possible factors hindering a return to sports.

Introduction

Anterior cruciate ligament (ACL) reconstruction is the main treatment for an anterior cruciate ligament injury to restore knee stability and, eventual, a return to sports (Kohn et al., 2020). Return to sports (RTS) is often defined as a return to the same level, intensity, and frequency of exercise as those before the injury (Meredith et al., 2020). Whether patients are suitable for returning to sports is usually determined by their performance on the RTS tests. However, under the current RTS criteria, the recent return-to-sports rate in most studies are unsatisfactory, ranging from 15.5% to 64% (Lefevre et al., 2017; Rahardja et al., 2021; Webster et al., 2022). In addition, with the lack of adequate kinematic studies, there is a considerable debate about the value of RTS tests in identifying patients who are at higher risk of reinjury (Gokeler et al., 2022; Hurley et al., 2022). Therefore, studying the kinematic differences between patients who pass the RTS tests and those who fail at 9 months after ACL reconstruction will be of great significance for us to deeply understand the kinematic mechanism of return to sports after ACL reconstruction and the value of RTS tests. The hypothesis in this study was that, compared with the RTS group, the NRTS group would show significant differences in knee kinematics during walking 9 months after ACL reconstruction.

The purpose of the present study was to compare the kinematic differences of the knee joint in the support phase during the level walking process between a return-to-sports (RTS) group and a nonreturn-to-sports (NRTS) group 9 months after ACL reconstruction with the high-speed dual-plane fluoroscopic imaging system (DFIS). The DFIS is a new motion-capture system that can accurately measure the spatial position of the knee joint during movement based on the projections of the bone structure of the knee joint in two different directions under X-ray. The system has been verified by the previous literature and is considered an accurate kinematics measurement equipment with displacement and angle measurement errors do not exceed $0.1°$ and 0.1 mm (Li et al., 2004; Zhu and Li, 2012).

Methods

Study design

This study is an observational follow-up study that was approved by the ethics committee of the institution (CHEC 2020097). All patients signed written informed consent forms when they were included in the study. From May 2020 to March 2021, a total of 87 patients who were diagnosed with primary anterior cruciate ligament rupture at Changhai hospital and underwent arthroscopic autologous hamstring tendon single-bundle anterior cruciate ligament reconstruction were included in this study (Figure 1). The purpose of ACL

reconstruction was to restore ACL biomechanical function and knee stability which may be the determinants of a return to sports. Based on the parameters of the DFIS and relevant researches, the cumulative radiation dose received by a patient in this study was about 5 mGy, which not exceeded the dose of a typical chest CT scan and shall be considered as safe (Biswas et al., 2009; Xiao et al., 2021).

Inclusion and exclusion criteria

The inclusion and exclusion criteria were as follows: 1) adult (over 18 years old) male or female patients; 2) diagnosis of ACL rupture under arthroscopy; 3) anatomical single-bundle reconstruction of the ACL with hamstring tendon; and 4) willingness to complete 1 year of regular follow-up. The exclusion criteria were as follows: 1) other severe knee injuries (i.e., collateral ligament, posterior cruciate ligament); 2) ACL reconstruction with other graft types (bone-patellar-tendon-bone, artificial ligament, etc.) and surgical techniques; 3) history of severe lower extremity trauma that may affect knee motion (posterior cruciate ligament injury, collateral ligaments injuries, etc.); and unwillness to participate in the trial or to complete the follow-up.

Surgery technique and postoperative management

In this study, the anterior cruciate ligament injury was first determined under arthroscopy and the combined meniscus injury was treated with meniscus suture technique. Then the hamstring tendon was harvested and braided into six strands. With the anteromedial approach, the tibial and femoral tunnels were drilled at the ACL tibial and femoral footprints respectively. The remnant tissue of both sides was preserved in the operation. The femoral and tibial ends of the graft were fixed with Endobutton and Intrafix screws respectively. Finally, range of motion of the knee joint, graft tension and graft impingement were checked under arthroscopy. ACL reconstruction of all patients were performed by the same senior doctor (Dr. Xu).

All the patients were treated with the standard rehabilitation mode as reported (Badawy et al., 2022). During the first 2 weeks after the operation, patients were asked to perform exercises including straight leg raises, ankle pumps, passive/active knee flexion, extension, and hip adduction to control the inflammatory response (swelling, pain, etc.); restore the partial range of motion of the knee joint (full extension–90° flexion); restore the patella range of motion; and improve the quadriceps femoris. During 3–5 weeks after the operation, rehabilitation measures such as moving up and downstairs and standing on one leg were used to restore the normal range of motion and normal gait of the knee joint. Patients were allowed for running

and jumping 3 months after operation while noncontact sports at 6 months. All the patients were followed up at 2 weeks, 1 month, 3 months, and 6 months after the operation and were given rehabilitation guidance. Return-to-sports and knee kinematics assessments were performed 9 months postoperatively.

Return-to-sports criteria and tests

According to the Panther consensus in 2020, return-to-sports criteria should include the postoperative time, a subjective score, an objective assessment of knee function, and a psychological readiness assessment (Meredith et al., 2020). On this basis, this study referred to related research and determined the following RTS criteria (Webster and Hewett, 2019). Patients who meet all of the following criteria are considered to pass the RTS tests.

(1) Postoperative time ≥9 months;
(2) Limb symmetry index (LSI) > 90% in three hop tests (single; triple; triple crossover);
(3) IKDC2000 subjective scale >90 points (Rossi et al., 2002);
(4) Anterior cruciate ligament return-to-sports after injury scale (ACL-RSI)>56 points (Webster et al., 2008).

All patients were asked to complete the IKDC2000 and ACL-RSI questionnaires according to their actual situation at the 9-month postoperative outpatient follow-up. All patients were tested with Lachman's test and a pivot-shift test by senior professional physicians as previously reported (Sokal et al., 2022). The patients were fully informed of the relevant rules and requirements when conducting the hop test. Subjects decide whether to participate in this test according to their knee joint function recovery. If the subject gave up or dared not take the test because of poor knee recovery, the test result was considered unqualified (LSI <90%). The hop tests were performed as described by Barber and Noyes et al. (Barber et al., 1990; Noyes et al., 1991).

Kinematic evaluation

Based on the RTS test results, 15 patients from both those who passed the RTS tests (RTS group) and those who failed (NRTS group) were randomly selected for further kinematic examination. CT (Siemens, Germany) images (slice thickness 0.6 mm; resolution 512 × 512pixels) of the operated knee of all patients were acquired. The CT images were imported into 3D modelling software (Amira 6.7; Thermo Fisher Scientific), and the 3D model of the knee joint and the corresponding coordinate systems were established using methods described in previous studies (Rao et al., 2020; Rao et al., 2021). In order to establish the tibial coordinate system, two circles on the tibial plateau plane
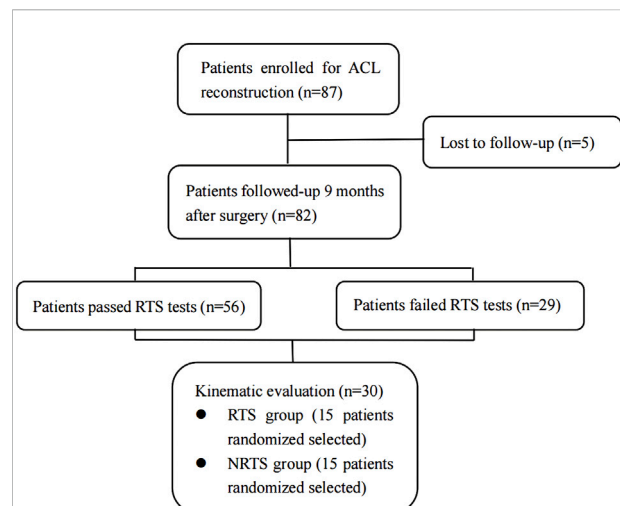
FIGURE 1
CONSORT (Consolidated Standards of Reporting Trials) flow diagram for kinematic evaluation. ACL, anterior cruciate ligament; ACLR, anterior cruciate ligament reconstruction; RTS, return-to-sports; NRTS, non-return-to-sports.
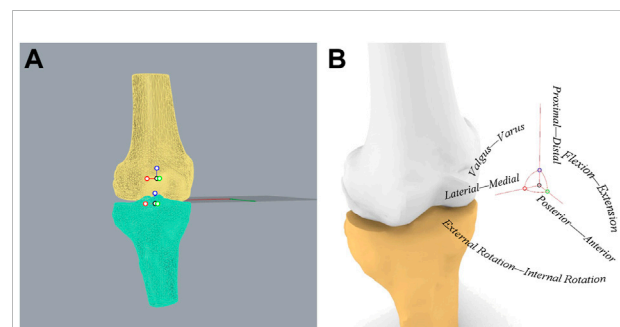
FIGURE 2
Establishment of knee joint coordinate system. **(A)** Coordinate systems established in the femur and tibia. **(B)** The relationship between the knee joint coordinate system and the kinematics of six degrees of freedom.

which were tangent to the edges of the medial tibial plateau and the lateral tibial plateau were found respectively. The straight line through the center of both circles was set as the X-axis [medial (−) and lateral (+) axis], and the straight line parallel to the long axis of the tibia through the origin of the coordinate system was set as the Z-axis [proximal (+) and distal (−) axis]. A plane was established by the X-axis and the Z-axis, and the straight line perpendicular to the plane through the origin of the coordinate system was set as the Y-axis [anterior (+) and posterior (−) axis]. Then the femoral coordinate system was established, and the transepicondylar axis (TEA) which connected the most prominent points of the medial and lateral epicondyles was set as the X-axis [medial (−) and lateral (+) axis]. The

FIGURE 3
Acquisition of kinematic images of the knee joint. **(A)** Walking on a treadmill at 1 m/s. **(B)** Kinematic images of the knee joint acquired simultaneously in both directions.

FIGURE 4
Kinematic measurement of six degrees of freedom of the knee joint. **(A)** Mechanism of the dual-plane fluoroscopic imaging system for measuring knee kinematic indicators. **(B)** Registration of 3-dimension model of knee joint with kinematic images.

midpoint of the TEA was set as the coordinate origin of the femoral coordinate system, and the line passing through this point and parallel to the long axis of the femur was set as the Z-axis [proximal (+) and distal (−) axis]. A plane was determined based on the X-axis and Z-axis, and the straight line passing through the origin of the femur coordinate and perpendicular to the plane was set as the Y-axis [anterior (+) and posterior (−) axis] (Figure 2).

In this study, a high-speed dual-plane fluoroscopy system (DFIS) (Shanghai Yidong Medical Technology Co., Ltd., Shanghai, China) was used to collect kinematic images of the knee joint. The preliminary positions of the X-ray transmitter and the receiver were adjusted according to the position of the treadmill to ensure that the images during the entire exercise process could be presented on the receiver from two different directions. The specific operation and use of DFIS were as described in previous studies (Li et al., 2004; Rao et al., 2020). Finally, the X-ray transmitter was adjusted to 60kV and 10 mA to achieve the best shooting effect. The DFIS was adjusted to continuous pulse mode, the exposure time was adjusted to 1/1000 s, and the sampling frequency was adjusted to 200 frames/second.

A suitable plantar pressure-sensing insole was placed on the subject's sole pad. Subjects were asked to perform 3 min of adaptive activity on a treadmill before initiation of the sampling. When the sampling officially started, the patients put on a protective lead vest and a protective lead scarf for radiation protection. The patients were asked to stand on the treadmill, and the treadmill speed was slowly adjusted to 1 m/s. After the patients adapted, the images of knee joint motion during a complete gait cycle during flat walking were collected according to the pressure changes of the sole pressure insole (Figure 3).

Among all the images of the support phase of the gait cycle, the biplane images of the corresponding time points were selected in turn at intervals of 10% of the total time of the support phase. After the selected images and the 3D model of the femur and tibia were imported into MATLAB (R2018a;
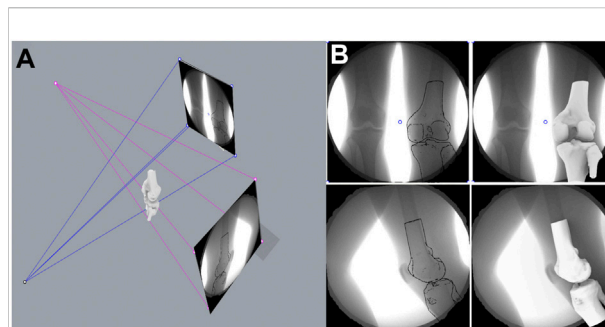
MathWorks), the spatial position of the femur and tibia model were adjusted to fit the outlines in images from both directions. Finally, the relative positional relationship between the tibia and the femur was calculated (the displacement and rotation angle on the X, Y, and Z axes) (Figure 4).

Statistical analysis

SPSS 22.0 (IBM SPSS Statistics, United States) software was used for statistical analysis in this experiment. The count data conforming to the normal distribution were expressed as the mean ± standard deviation, and the measurement data were expressed as frequency. For measurement data such as age, height, BMI, and time from surgery, two independent samples t tests or Mann-Whitney U tests were selected according to their normality and homogeneity of variance. Count data were tested by the chi-square test or Fisher's exact test Table 1. The repeated measures analysis of variance statistical method was used to compare the kinematic indices of the six DOF kinematics of the support phase period of the knee joint between the RTS group and the NRTS group. A p-value of <0.05 was considered to be significant. A post hoc power analysis indicated that 15 subjects would provide over 95% power to detect the kinematics changes (shown in Table 2).

Results

Patient and clinical characteristics

Of the 87 patients initially enrolled, 82 completed the 9-month follow-up and return-to-sports tests. Of all the patients who were followed-up, 53 passed the RTS tests, and 29 failed due to failures in one or more test items. Fifteen people were randomly selected from the RTS patients and NRTS patients

TABLE 1 Patients and clinical characteristics.

	NRTS group (n = 15)	RTS group (n = 15)	*p*-value
Age (yrs)	27.60 ± 6.05	27.47 ± 6.06	0.952
Mass (kg)	175.60 ± 3.31	175.73 ± 4.32	0.925
Body height (cm)	74.27 ± 8.65	73.53 ± 6.52	0.795
Body mass index (kg/m^2)	24.09 ± 2.75	23.81 ± 1.91	0.743
Time from surgery (mo)	9.50 ± 0.37	9.43 ± 0.52	0.471
Male/Female	11/4	13/2	0.651
Right/Left	10/5	11/4	0.996
Meniscus injury (Yes/No)	12/3	11/4	0.951
Lachman test			0.475
Normal	12	14	
Grade 1+	2	1	
Grade 2+	1	0	
Grade 3+	0	0	
Pivot-shift test grade			0.505
Normal	11	13	
Grade 1+	3	2	
Grade 2+	1	0	
Grade 3+	0	0	

for kinematic evaluation. Among them, 13 males and two females were included in the NRTS group, including 10 right knees and five left knees, and their ages ranged from 22 to 49 years old. A total of 13 males and two females were included in the RTS group, including 11 right knees and four left knees, ranging in age from 21 to 47 years old. There was no significant difference in age, height, weight, BMI, gender composition, or distribution of left and right knee joints between the NRTS group and the RTS group ($p > 0.05$). The clinical characteristics of the two groups of patients are shown in.

Kinematic evaluation of the knee

Anterior-posterior translation. The mean anterior tibial translation (ATT) in the NRTS group was greater than that in the RTS group throughout the stance cycle (1.00 ± 0.03 mm vs. 0.76 ± 0.03 mm, $p = 0.001$) (Table 2). Pairwise comparisons showed that the anteroposterior position of the tibia relative to the femur was different between the two groups at 0%, 20%, 50%, 60%, 70%, 80%, and 100% of the support phase cycle. At 0% of the support phase, the ATT in the two groups was the smallest, and the ATT in the NRTS group was smaller than that in the RTS group (−2.79 mm ± 0.15 vs. −2.21 ± 0.15 mm, $p = 0.01$). At 30% of the support phase, the ATT in the two groups was greatest, and the ATT of the NRTS group was greater at this time (3.64 ± 0.42 mm vs. 3.03 ± 0.59 mm, $p = 0.003$) (Figure 5).

Medial-lateral translation. The mean lateral tibial translation of the NRTS group was greater than that of the RTS group during

the whole stance cycle (1.61 ± 0.05 mm vs. 0.77 ± 0.05 mm, $p < 0.001$). Pairwise comparisons showed that the medial and lateral positions of the tibia relative to the femur differed between the two groups at 0%, 10%, 20%, 30%, 40%, 60%, 80%, and 90% of the support phase cycle. At 80% of the support phase, the lateral tibial translation in the two groups was smallest and the tibia in the NRTS group was more lateral than that in the RTS group (−0.59 ± 0.42 mm vs. −1.94 ± 0.43 mm, $p < 0.001$). At 100% of the support phase, the tibia in the two groups was located at the outermost position relative to the femur, and there was no significant difference in the medial and lateral positions of the tibia relative to the femur between the two groups (3.05 ± 0.71 mm vs. 2.96 ± 0.69 mm, $p = 0.729$).

Proximal-distal translation. The tibial movement downwards relative to the femur in the NRTS group during the support phase period was greater than that in the RTS group (−3.09 ± 0.05 mm vs. −2.67 ± 0.05 mm, $p < 0.001$). Pairwise comparisons showed that there was a difference in the up-and-down displacement of the tibia relative to the femur between the two groups at 0%, 80%, and 100% of the support phase cycle. At 0% of the support phase, the downwards displacement of the tibia relative to the femur was the greatest in both groups, at which time the tibia in the NRTS group had a greater downwards displacement than the RTS group (−6.34 ± 0.77 mm vs. −4.37 ± 0.73 mm, $p < 0.001$). At 50% of the support phase, the downwards displacement of the tibia relative to the femur in the two groups was the smallest, and there was no significant difference in the medial and lateral positions of the tibia relative to the femur between the two groups (−1.74 ± 0.37 mm vs. −1.70 ± 0.37 mm, $p = 0.763$).

TABLE 2 Comparison of knee kinematics between those who passed the return-to-sports test and those who failed 9 months after ACL reconstruction.[a] The maximum valgus angle was at 100% stance phase in the NRTS group while 0% in the RTS group. NRTS, not return-to-sports; RTS, return-to-sports; CI, confidence interval; SD, standard deviation; AVG, average value; Max, maximum value; Min, minimum value; A-P, anterior-posterior; L-M, lateral-medial; P-D, proximal-distal; F-E, flexion-extension; Valg-Var, valgus-varus; Er-Ir, external rotation-internal rotation.

| | | Stance phase (%) | NRTS group | | | | RTS group | | | | p-value |
| | | | 95%CI | | | | 95%CI | | | | |
			Mean	SD	Lower	Upper	Mean	SD	Lower	Upper	
A-P (mm)	AVG	\	1.00	0.03	0.93	1.07	0.76	0.03	0.70	0.83	<0.001
	Max	30	3.64	0.42	3.37	3.91	3.03	0.59	2.71	3.34	0.003
	Min	0	−2.79	0.59	−3.09	−2.48	−2.21	0.58	−2.52	−1.90	0.01
L-M(mm)	AVG	\	1.61	0.05	1.51	1.71	0.77	0.05	0.67	0.87	<0.001
	Max	100	3.05	0.71	2.68	3.42	2.96	0.69	2.59	3.33	0.729
	Min	80	−0.59	0.42	−0.81	−0.36	−1.94	0.43	−2.17	−1.72	<0.001
P-D (mm)	AVG	\	−3.09	0.05	−3.18	−2.99	−2.69	0.05	−2.79	−2.59	<0.001
	Max	50	−1.74	0.37	−1.93	−1.54	−1.70	0.37	−1.89	−1.50	0.763
	Min	0	−6.34	0.77	−6.73	−5.94	−4.37	0.73	−4.76	−3.97	<0.001
F-E (°)	AVG	\	6.72	0.07	6.57	6.86	8.34	0.07	8.20	8.49	<0.001
	Max	100	21.39	1.54	20.56	22.21	23.74	1.56	22.92	24.56	<0.001
	Min	80	0.18	0.08	0.13	0.22	0.13	0.08	0.08	0.17	0.084
Valg-Var (°)	AVG	\	−0.40	0.03	−0.45	−0.34	−0.01	0.03	−0.06	0.05	<0.001
	Max	100/0	0.68	0.37	0.49	0.87	0.84	0.33	0.66	1.01	0.656
	Min	70	−2.36	0.65	−2.67	−2.04	−2.11	0.54	−2.42	−1.79	0.262
Er-Ir (°)	AVG	\	1.80	0.05	1.69	1.91	1.77	0.05	1.66	1.88	<0.001
	Max	100	7.52	1.05	6.98	8.05	7.46	0.99	6.92	7.99	0.871
	Min	0	−2.77	0.57	−3.06	−2.47	−2.13	0.55	−2.42	−1.83	0.004

Flexion-extension. The mean knee flexion angle (KFA) of the NRTS group was lower than that of the RTS group during the stance phase (6.72 ± 0.07° vs. 8.34 ± 0.07°, $p < 0.001$). Pairwise comparisons showed that there were significant differences in KFA between the two groups at 10%, 20%, 30%, 40%, 50%, 70%, and 100% of the stance cycle. At 80% of the stance phase, the KFA of the two groups was the smallest, but there was no significant difference between the two groups (0.13 ± 0.08° vs. 0.18 ± 0.08°, $p = 0.084$). At 100% of the support phase, the KFA of the two groups was the largest, and the KFA of the RTS group was significantly greater than that of the NRTS group (23.74 ± 1.56° vs. 21.39 ± 1.54°, $p < 0.001$).

Varus-valgus. The mean varus angle of the knee in the NRTS group was larger than that in the RTS group in the whole stance phase (−0.40 ± 0.03° vs. −0.01 ± 0.03°, $p < 0.001$). The pairwise comparison results showed that there were significant differences in the valgus and varus angles of the knee between the two groups at 0%, 10%, 60%, 80%, and 90% of the stance cycle. At 70% of the support phase, the knee varus angle of the two groups was the largest, but there was no significant difference in the knee varus angle between the two groups (−2.11 ± 0.54° vs. −2.36 ± 0.65°, $p = 0.262$).

Internal-external rotation. The average external rotation angle (ERA) of the knee in the NRTS group was greater than that in the RTS group during the stance phase cycle (1.80 ± 0.05° vs. 1.77 ± 0.05°, $p < 0.001$). The pairwise comparison results showed that there were significant differences in the internal and external rotation angles of the knee joint between the two groups at 0%, 20%, 50%, and 60% of the stance phase cycle. At 0% of the stance phase, the internal rotation angle (IRA) of the knee joint in both groups was the largest, and the IRA of the NRTS group was significantly larger than that of the RTS group (−2.77 ± 0.57° vs. −2.13 ± 0.55°, $p = 0.004$). At 100% of the support phase, the ERA of the knee was the largest in the two groups, and there was no significant difference in the ERA between the two groups (7.52 ± 1.05° vs. 7.46 ± 0.99°, $p = 0.871$).

Discussion

The aim of this study was to compare the kinematic differences of the knee joint in the support phase during the level walking process between a return-to-sports (RTS) group and a nonreturn-to-sports (NRTS) group 9 months after ACL
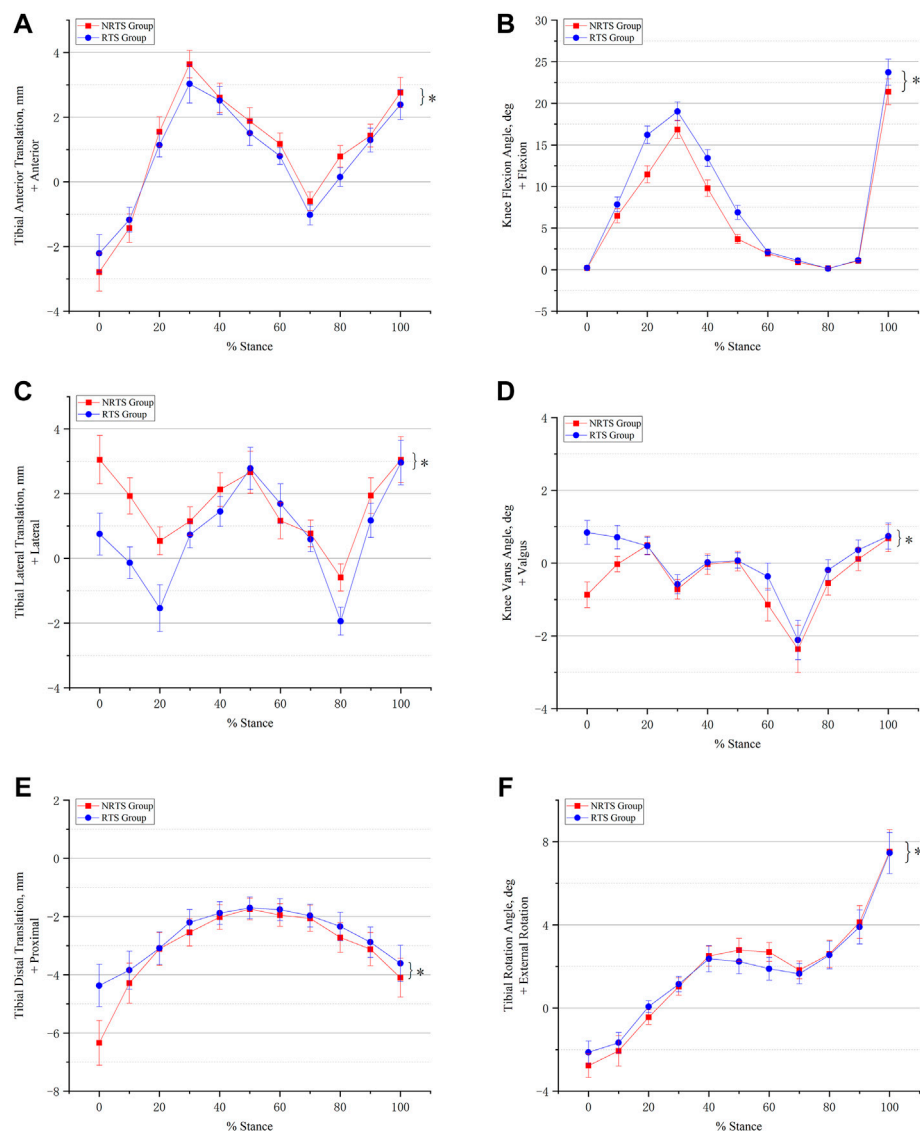
FIGURE 5
Comparison of six-degree-of-freedom knee kinematics during walking between those who passed the return-to-sports test and those who failed 9 months after ACL reconstruction. **(A)** Anterior-posterior translation. **(B)** Knee flexion and extension. **(C)** Medial-lateral translation. **(D)** Varus-valgus movement. **(E)** Proximal-distal translation. **(F)** External-internal rotation. * Significant difference between groups. NRTS, not return-to-sports; RTS, return-to-sports.

reconstruction. This study found that, compared with the RTS group, the NRTS group had significant differences in 6-DOF knee kinematics during walking. First, the mean and maximum anterior tibial displacement in the NRTS group were greater than those in the RTS group during the stance phase (1.00 ± 0.03 mm vs. 0.76 ± 0.03 mm, $p = 0.001$; 3.64 ± 0.42 mm vs. 3.03 ± 0.59 mm, $p = 0.003$). This result suggests that patients who do not return to sports after ACL reconstruction have instability in the anterior-posterior direction of the knee. In fact, the anteroposterior stability of the knee joint is closely related to the function of the ACL (Wang et al., 2021). Li C et al. found that there was more

anterior tibial translation in ACL-deficient knees than in healthy control knees during gait (Li et al., 2022). Anterior tibial translation was greatly reduced after ACL reconstruction (Gao and Zheng, 2010). Currently, the relationship between anterior knee stability and return-to-sports after ACL reconstruction is still being explored (Keizer et al., 2021; Kamada et al., 2022). Faleide et al. measured the anterior tibial translation of the knee joint with KT-1000 and found that it was one of the RTS factors (Faleide et al., 2021). Some studies also found that the anterior stability of the knee joint after ACL reconstruction is closely related to the functional performance (Andrä et al., 2021).

Therefore, the restoration of anterior stability of the knee joint after ACL reconstruction is of great significance for the recovery of knee joint function and even the return to sports.

In addition, NRTS patients have significant lateral and rotational instability with larger mean lateral tibial translation (1.61 ± 0.05 mm vs. 0.77 ± 0.05 mm, $p < 0.001$) and average external rotation angles ($1.80 \pm 0.05°$ vs. $1.77 \pm 0.05°$, $p < 0.001$). These knee instabilities manifestations have been widely reported in activities such as walking and single-leg hopping after ACL reconstruction (Hofbauer et al., 2014; Shabani et al., 2015). This study found that lateral and rotational instability of the knee is more severe in patients who did not pass RTS tests after ACL reconstruction. In addition, this study found an increased tibial-femoral distance in NRTS patients, especially in the early and late stages of the support phase (-6.34 ± 0.77 mm vs. -4.37 ± 0.73 mm, $p < 0.001$; -4.10 ± 0.67 mm vs. -3.61 ± 0.62 mm, $p = 0.046$). According to previous studies (Liu et al., 2018), an increased tibial-femoral distance can reduce the tibiofemoral contact area and ultimately influence knee rotation and lateral instability. Therefore, the lateral and rotational instability of the knee joint after ACL reconstruction is an important problem. This study found that there was an increased tibiofemoral distance and lateral and rotational instability of the knee in NRTS patients, which needs further investigation.

During the stance phase, there was a decrease in knee flexion in the NRTS group compared with the RTS group ($6.72 \pm 0.07°$ vs. $8.34 \pm 0.07°$, $p < 0.001$). Reduction of the knee flexion angle after ACL reconstruction is a common problem and has been reported in many studies (Goetschius et al., 2018). This study found that the reduction in flexion angle during walking was more obvious in NRTS patients. There has been some progress in the study of decreased knee flexion angles after ACL reconstruction. Blackburn et al. (Blackburn et al., 2019) found that abnormal coactivation of the quadriceps and hamstrings was associated with a decrease in knee flexion during the stance phase. The abnormal joint action of the quadriceps femoris and hamstrings during the support phase makes the knee joint more "stiff", which is manifested as a decrease in the flexion angle at each moment and a decrease in the overall range of flexion and extension. In addition, it has been reported that a decrease in the knee flexion angle during the support phase is also related to the occurrence and development of osteoarthritis (Pamukoff et al., 2018). To clearly determine the relationship between a reduced knee flexion angle and RTS, more research is needed in the future.

Finally, this study still has the following shortcomings. Due to the workload, it did not accurately calculate the relative position of the tibiofemoral joint in each frame of images during the stance phase, because this takes a lot of time. Therefore, this study refers to the practice of similar previous investigations; that is, the images at every 10% point in the support phase cycle are selected for calculation (Zhang et al., 2021). Since walking is a continuous process, these time points can already well describe the kinematic changes in the whole process. Therefore, we believe that this will not have a significant impact on the conclusions of the experiment, as has been confirmed in the previous literature.

Conclusion

There are still 35.6% of patients who fail the return-to-sport tests and are not allowed to return to sports 9 months after ACL reconstruction. Compared with those who pass the RTS tests, patients who do not pass show significant anterior, lateral, and rotational instability; knee laxity; and reduced flexion angle of the knee during the support phase during walking. Therefore, the current RTS tests are good at identifying patients with abnormal knee kinematics. The causes and mechanisms of abnormal kinematic performance in patients who fail RTS tests after ACL reconstruction remain to be further studied.

Data availability statement

The raw data supporting the conclusions of this article will be made available by the authors, without undue reservation.

Ethics statement

The studies involving human participants were reviewed and approved by Changhai Hospital Medical Ethics Committee (CHEC2020097). The patients/participants provided their written informed consent to participate in this study.

Author contributions

Conceptualization: WX, TZ, and SW; Methodology: TZ, YX, SW, and LZ; Formal analysis and investigation: TZ, YX, LZ, SW, and YX; Writing—original draft preparation: TZ and YX; Writing—review and editing: TZ, SW, and WX; Funding acquisition: YX and WX; Resources: SW and WX; Supervision: SW and WX.

Funding

Conflict of interest

The authors declare that the research was conducted in the absence of any commercial or financial relationships that could be construed as a potential conflict of interest.

Publisher's note

All claims expressed in this article are solely those of the authors and do not necessarily represent those of their affiliated organizations, or those of the publisher, the editors and the reviewers. Any product that may be evaluated in this article, or claim that may be made by its manufacturer, is not guaranteed or endorsed by the publisher.

References

Andrä, K., Kayaalp, E., Prill, R., Irlenbusch, L., Liesaus, E., Trommer, T., et al. (2021). Joint effusion, anteroposterior stability, muscle strength and degree of patellofemoral osteoarthritis significantly impact outcome following revision ACL reconstruction. *J. Exp. Orthop.* 8, 70. doi:10.1186/s40634-021-00370-x

Badawy, C. R., Jan, K., Beck, E. C., Fleet, N., Taylor, J., Ford, K., et al. (2022). Contemporary principles for postoperative rehabilitation and return to sport for athletes undergoing anterior cruciate ligament reconstruction. *Arthrosc. Sports Med. Rehabil.* 4, e103–e113. doi:10.1016/j.asmr.2021.11.002

Barber, S. D., Noyes, F. R., Mangine, R. E., Mccloskey, J. W., and Hartman, W. (1990). Quantitative assessment of functional limitations in normal and anterior cruciate ligament-deficient knees. *Clin. Orthop. Relat. Res.* 255, 204–214. doi:10.1097/00003086-199006000-00028

Biswas, D., Bible, J. E., Bohan, M., Simpson, A. K., Whang, P. G., and Grauer, J. N. (2009). Radiation exposure from musculoskeletal computerized tomographic scans. *J. Bone Jt. Surgery-American Volume* 91, 1882–1889. doi:10.2106/jbjs.h.01199

Blackburn, T., Pietrosimone, B., Goodwin, J. S., Johnston, C., and Spang, J. T. (2019). Co-activation during gait following anterior cruciate ligament reconstruction. *Clin. Biomech. (Bristol, Avon.* 67, 153–159. doi:10.1016/j.clinbiomech.2019.05.010

Faleide, A. G. H., Magnussen, L. H., Bogen, B. E., Strand, T., Mo, I. F., Vervaat, W., et al. (2021). Association between psychological readiness and knee laxity and their predictive value for return to sport in patients with anterior cruciate ligament reconstruction. *Am. J. Sports Med.* 49, 2599–2606. doi:10.1177/03635465211021831

Gao, B., and Zheng, N. N. (2010). Alterations in three-dimensional joint kinematics of anterior cruciate ligament-deficient and -reconstructed knees during walking. *Clin. Biomech. (Bristol, Avon.* 25, 222–229. doi:10.1016/j.clinbiomech.2009.11.006

Goetschius, J., Hertel, J., Saliba, S. A., Brockmeier, S. F., and Hart, J. M. (2018). Gait Biomechanics in anterior cruciate ligament-reconstructed knees at different time frames postsurgery. *Med. Sci. Sports Exerc.* 50, 2209–2216. doi:10.1249/mss.0000000000001693

Gokeler, A., Dingenen, B., and Hewett, T. E. (2022). Rehabilitation and return to sport testing after anterior cruciate ligament reconstruction: Where are we in 2022? *Arthrosc. Sports Med. Rehabil.* 4, e77–e82. doi:10.1016/j.asmr.2021.10.025

Gupta, R., Singhal, A., Malhotra, A., Soni, A., Masih, G. D., and Raghav, M. (2020). Predictors for anterior cruciate ligament (ACL) Re-injury after successful primary ACL reconstruction (ACLR). *Malays. Orthop. J.* 14, 50–56. doi:10.5704/moj.2011.009

Hofbauer, M., Thorhauer, E. D., Abebe, E., Bey, M., and Tashman, S. (2014). Altered tibiofemoral kinematics in the affected knee and compensatory changes in the contralateral knee after anterior cruciate ligament reconstruction. *Am. J. Sports Med.* 42, 2715–2721. doi:10.1177/0363546514549444

Hurley, E. T., Mojica, E. S., Haskel, J. D., Mannino, B. J., Alaia, M., Strauss, E. J., et al. (2022). Return to play testing following anterior cruciate reconstruction - a systematic review & meta-analysis. *Knee* 34, 134–140. doi:10.1016/j.knee.2021.11.010

Kamada, K., Matsushita, T., Nagai, K., Hoshino, Y., Araki, D., Kanzaki, N., et al. (2022). Risk factors of residual pivot-shift after anatomic double-bundle anterior cruciate ligament reconstruction. *Arch. Orthop. Trauma Surg.* doi:10.1007/s00402-022-04428-y

Keizer, M. N. J., Otten, E., Beijersbergen, C. M. I., Brouwer, R. W., and Hijmans, J. M. (2021). Copers and noncopers use different landing techniques to limit anterior tibial translation after anterior cruciate ligament reconstruction. *Orthop. J. Sports Med.* 9, 232596712199806. doi:10.1177/2325967121998061

Korakakis, V., Kotsifaki, A., Korakaki, A., Karanasios, S., and Whiteley, R. (2021). Current perspectives and clinical practice of physiotherapists on assessment, rehabilitation, and return to sport criteria after anterior cruciate ligament injury and reconstruction. An online survey of 538 physiotherapists. *Phys. Ther. Sport* 52, 103–114. doi:10.1016/j.ptsp.2021.08.012

Lefevre, N., Klouche, S., Mirouse, G., Herman, S., Gerometta, A., and Bohu, Y. (2017). Return to sport after primary and revision anterior cruciate ligament reconstruction: A prospective comparative study of 552 patients from the fast cohort. *Am. J. Sports Med.* 45, 34–41. doi:10.1177/0363546516660075

Li, C., Lin, Y., Kernkamp, W. A., Xia, H., and Lin, Z. (2022). Effect of time after injury on tibiofemoral joint kinematics in anterior cruciate ligament-deficient knees during gait. *Orthop. J. Sports Med.* 10, 232596712211101. doi:10.1177/23259671221110160

Li, G., Wuerz, T. H., and Defrate, L. E. (2004). Feasibility of using orthogonal fluoroscopic images to measure *in vivo* joint kinematics. *J. Biomech. Eng.* 126, 313–318. doi:10.1115/1.1691448

Liu, C., Wang, Y., Li, Z., Li, J., Zhang, H., Fu, Y., et al. (2018). Tibiofemoral joint contact area and stress after single-bundle anterior cruciate ligament reconstruction with transtibial versus anteromedial portal drilling techniques. *J. Orthop. Surg. Res.* 13, 247. doi:10.1186/s13018-018-0956-1

Mahood, C., Perry, M., Gallagher, P., and Sole, G. (2020). Chaos and confusion with confidence: Managing fear of Re-Injury after anterior cruciate ligament reconstruction. *Phys. Ther. Sport* 45, 145–154. doi:10.1016/j.ptsp.2020.07.002

Meredith, S. J., Rauer, T., Chmielewski, T. L., Fink, C., Diermeier, T., Rothrauff, B. B., et al. (2020). Return to sport after anterior cruciate ligament injury: Panther symposium ACL injury return to sport consensus group. *Knee Surg. Sports Traumatol. Arthrosc.* 28, 2403–2414. doi:10.1007/s00167-020-06009-1

Noyes, F. R., Barber, S. D., and Mangine, R. E. (1991). Abnormal lower limb symmetry determined by function hop tests after anterior cruciate ligament rupture. *Am. J. Sports Med.* 19, 513–518. doi:10.1177/036354659101900518

Pamukoff, D. N., Montgomery, M. M., Holmes, S. C., Moffit, T. J., Garcia, S. A., and Vakula, M. N. (2018). Association between gait mechanics and ultrasonographic measures of femoral cartilage thickness in individuals with ACL reconstruction. *Gait Posture* 65, 221–227. doi:10.1016/j.gaitpost.2018.07.174

Rahardja, R., Love, H., Clatworthy, M. G., Monk, A. P., and Young, S. W. (2021). Higher rate of return to preinjury activity levels after anterior cruciate ligament reconstruction with a bone-patellar tendon-bone versus hamstring tendon autograft in high-activity patients: Results from the New Zealand ACL registry. *Am. J. Sports Med.* 49, 3488–3494. doi:10.1177/03635465211044142

Randsborg, P. H., Cepeda, N., Adamec, D., Rodeo, S. A., Ranawat, A., and Pearle, A. D. (2022). Patient-reported outcome, return to sport, and revision rates 7-9 Years after anterior cruciate ligament reconstruction: Results from a cohort of 2042 patients. *Am. J. Sports Med.* 50, 423–432. doi:10.1177/03635465211060333

Rao, Z., Zhou, C., Kernkamp, W. A., Foster, T. E., Bedair, H. S., and Li, G. (2020). *In vivo* kinematics and ligamentous function of the knee during weight-bearing flexion: An investigation on mid-range flexion of the knee. *Knee Surg. Sports Traumatol. Arthrosc.* 28, 797–805. doi:10.1007/s00167-019-05499-y

Rao, Z., Zhou, C., Zhang, Q., Kernkamp, W. A., Wang, J., Cheng, L., et al. (2021). There are isoheight points that measure constant femoral condyle heights along the knee flexion path. *Knee Surg. Sports Traumatol. Arthrosc.* 29, 600–607. doi:10.1007/s00167-020-05990-x

Rossi, M. J., Lubowitz, J. H., and Guttmann, D. (2002). Development and validation of the international knee documentation committee subjective knee form. *Am. J. Sports Med.* 30, 152. doi:10.1177/03635465020300011301

Shabani, B., Bytyqi, D., Lustig, S., Cheze, L., Bytyqi, C., and Neyret, P. (2015). Gait knee kinematics after ACL reconstruction: 3D assessment. *Int. Orthop.* 39, 1187–1193. doi:10.1007/s00264-014-2643-0

Sokal, P. A., Norris, R., Maddox, T. W., and Oldershaw, R. A. (2022). The diagnostic accuracy of clinical tests for anterior cruciate ligament tears are comparable but the lachman test has been previously overestimated: A systematic review and meta-analysis. *Knee Surg. Sports Traumatol. Arthrosc.* 30, 3287–3303. doi:10.1007/s00167-022-06898-4

Van Melick, N., Van Cingel, R. E., Brooijmans, F., Neeter, C., Van Tienen, T., Hullegie, W., et al. (2016). Evidence-based clinical practice update: Practice guidelines for anterior cruciate ligament rehabilitation based on a systematic review and multidisciplinary consensus. *Br. J. Sports Med.* 50, 1506–1515. doi:10.1136/bjsports-2015-095898

Wang, M., Lin, Z., Wang, W., Chen, L., Xia, H., Zhang, Y., et al. (2021). Kinematic alterations after anterior cruciate ligament reconstruction via transtibial techniques with medial meniscal repair versus partial medial meniscectomy. *Am. J. Sports Med.* 49, 3293–3301. doi:10.1177/03635465211033982

Webster, K. E., Feller, J. A., and Lambros, C. (2008). Development and preliminary validation of a scale to measure the psychological impact of returning to sport following anterior cruciate ligament reconstruction surgery. *Phys. Ther. Sport* 9, 9–15. doi:10.1016/j.ptsp.2007.09.003

Webster, K. E., and Hewett, T. E. (2019). What is the evidence for and validity of return-to-sport testing after anterior cruciate ligament reconstruction surgery? A systematic review and meta-analysis. *Sports Med.* 49, 917–929. doi:10.1007/s40279-019-01093-x

Webster, K. E., Klemm, H. J., and Feller, J. A. (2022). Rates and determinants of returning to Australian rules football in male nonprofessional athletes after anterior

cruciate ligament reconstruction. *Orthop. J. Sports Med.* 10, 232596712210749. doi:10.1177/23259671221074999

Xiao, Y., Ling, M., Liang, Z., Ding, J., Zhan, S., Hu, H., et al. (2021). Dual fluoroscopic imaging and CT-based finite element modelling to estimate forces and stresses of grafts in anatomical single-bundle ACL reconstruction with different femoral tunnels. *Int. J. Comput. Assist. Radiol. Surg.* 16, 495–504. doi:10.1007/s11548-021-02307-2

Zhang, L., Fan, S., Ye, J., Jiang, X., and Cai, B. (2021). Gender differences in knee kinematics during weight-bearing knee flexion for patients with arthrofibrosis after anterior cruciate ligament reconstruction. *J. Orthop. Surg. Res.* 16, 573. doi:10.1186/s13018-021-02729-3

Zhu, Z., and Li, G. (2012). An automatic 2D-3D image matching method for reproducing spatial knee joint positions using single or dual fluoroscopic images. *Comput. Methods Biomech. Biomed. Engin.* 15, 1245–1256. doi:10.1080/10255842.2011.597387

Design of personalized scoliosis braces based on differentiable biomechanics—Synthetic study

Kateryna Kardash, Christos Koutras and Miguel A. Otaduy*

Department of Computer Science, Universidad Rey Juan Carlos, Madrid, Spain

This work describes a computational methodology for the design of braces for adolescent idiopathic scoliosis. The proposed methodology relies on a personalized simulation model of the patient's trunk, and automatically searches for the brace geometry that optimizes the trade-off between clinical improvement and patient comfort. To do this, we introduce a formulation of differentiable biomechanics of the patient's trunk, the brace, and their interaction. We design a simulation model that is differentiable with respect to both the deformation state and the brace design parameters, and we show how this differentiable model is used for the efficient update of brace design parameters within a numerical optimization algorithm. To evaluate the proposed methodology, we have obtained trunk models with personalized geometry for five patients of adolescent idiopathic scoliosis, and we have designed Boston-type braces. In a simulation setting, the designed braces improve clinical metrics by 45% on average, under acceptable comfort conditions. In the future, the methodology can be extended beyond synthetic validation, and tested with physical braces on the actual patients.

1 Introduction

Scoliosis is a clinical condition marked mostly by a lateral curvature of the spine. Moderate cases of adolescent idiopathic scoliosis (AIS) are typically treated through conservative methods (Karimi and Rabczuk, 2018), which try to naturally correct scoliosis during the growth of the patients. A common conservative treatment is to use orthotic brace structures (Negrini et al., 2022) that transmit forces to the spine and try to correct the existing deformities (Kuroki, 2018; Kaelin, 2020). Such scoliosis braces are designed in a variety of shapes and procedures, but most design methods rely to date on physical experimentation and prototyping. Even though computational strategies have been studied to some extent (Cobetto et al., 2016; Vergari et al., 2016), they are typically limited to evaluating design iterations. The design decisions on the braces are not made by intelligent computer programs; they are instead made by clinical experts, using information from simulation models.

In our work, we try to answer if brace design can be further automated, devising an intelligent computer program that can automatically explore the design space of a brace, and select optimal design parameters. The development of such a brace design solution faces two important research challenges. First, it requires a personalized biomechanical model of brace-trunk interaction. Using this biomechanical model, it is possible to predict trunk deformations as a function of changes to the brace design. This simulation is key for computer evaluation of design metrics, such as a clinical objective and a comfort objective. Second, the biomechanical model must be embedded within a numerical optimization solver, which will automatically search for brace design parameters. State-of-the-art optimization methods use gradients to efficiently and robustly search for optimal parameters; therefore, the biomechanics formulation must allow for the computation of gradients with respect to design parameters.

In this work, we propose a differentiable biomechanics model for the optimization of scoliosis brace designs. By formulating biomechanics simulation as a differentiable function, we can embed the simulation model within advanced optimization procedures, and automatically achieve effective brace designs, with flexible definition of design goal metrics.

The first major component of our approach, presented in Section 3, is a predictive model of the passive biomechanics of the trunk. We put the focus on modeling biomechanics elements that affect the deformation of the thoracolumbar spine under forces produced by a scoliosis brace. To this end, we largely rely on previous work for the development of the trunk model (Koutras et al., 2021) and personalization of its geometry (Koutras et al., 2022) (mechanical personalization is left as future work).

The second major component of our approach, presented in Section 4, is an optimization algorithm that relies on differentiable biomechanics. We show that differentiable biomechanics can be efficiently formulated by implicitly linearizing the equilibrium constraints of a biomechanics simulation engine, and we provide insight into the design of all elements of the biomechanics model to ensure efficient and robust differentiation.

We have tested our personalized brace design approach on a cohort of 5 (potential) patients of AIS. For each patient, we personalize the trunk model, initialize a Boston brace design (Périé et al., 2003), and then optimize this design using the differentiable biomechanics formulation. The results of our experiments show that a fully automated algorithm manages to reduce Cobb angle by an average of 7.8°, while keeping brace forces within a comfortable range of 220 N. To date, we have limited our experiments to a synthetic study, considering only simulated brace-trunk interactions. Our work demonstrates the feasibility of the approach, but real-world application requires further iterating other aspects of the brace design, as well as validating the clinical and comfort objectives before letting actual patients wear the resulting braces.

2 Related work

2.1 Trunk modeling and parameter estimation

Designing a personalized biomechanical model entails two tasks: fitting the morphology and connections of anatomical elements to those of the patient, and parameterizing the mechanical models to match the response of the patient's body. Biomechanical modeling of the spine has received a lot of attention, with popular approaches largely divided into two categories. One category follows the Finite Element Method (FEM, please see (Wang et al., 2014) for a survey of methods); the other category uses a simpler but more efficient solution based on multi-body models.

In terms of FEM models, many approaches have been developed for the lumbar (Xu et al., 2017; Finley et al., 2018; Dong et al., 2020), thoracic (Aroeira et al., 2017; Aroeira et al., 2018) or the cervical spine (Lasswell et al., 2017). Furthermore, Dicko et al., (2015) developed a hybrid lumbar spine model containing rigid bodies, FEM and contact mechanics, while Clin et al., (2011) developed a novel method to include gravitational forces in an FE model. While these methods are potentially accurate, they require careful estimation of model parameters for personalized design applications.

FE models of the trunk have been coupled to brace models and patient geometry for personalized brace design in the context of AIS (Gignac et al., 2000; Liao et al., 2007; Nie et al., 2009). Some studies include the evaluation of the effectiveness of these techniques on large cohorts of patients (Cobetto et al., 2017; Vergari et al., 2020; Guy et al., 2021).

In terms of multi-body models, de Zee et al., (2007) made a generic detailed rigid-body model of the lumbar spine. Bayoglu et al., (2019) developed a multi-body muscoloskeletal model of the human spine in order to study the spinal loads. Raabe and Chaudhari, (2016) investigated the jogging biomechanics using a full-body spine model developed in OpenSim, an open-source musculoskeletal simulation software. Le Navéaux et al., (2016) developed biomechanical models based on multi-body dynamics to analyze the effects of implant density and distribution on curve correction and the resulting forces on the vertebrae. Ignasiak et al., 2016 predicted the dynamic spinal loading using a multi-body thoracolumbar spine model with articulated rib cage.

In the category of multi-body models, a strong effort has been devoted to finding accurate simplifications of the models and designing parameter estimation techniques. In our design and parameterization of a spine-and-trunk model, we borrow insight and design choices from this collection of work.

Panjabi et al., (1994) studied the mechanical behavior of the human lumbar and lumbosacral spine as shown by three dimensional load-displacement curves. Panjabi et al., (1976) estimated the rotational stiffness coefficients of the thoracic spine from experiments. Bisschop et al., (2012) and Panjabi

et al., (1976) found the translational stiffness coefficients of the thoracic spine through experimental studies. Moroney et al., (1988) estimated the load displacement properties of the cervical spine from experiments. Andriacchi et al., (1974) estimated the stiffness coefficients of the elastic properties of the rib cage through simulations. Wilke et al., (2017) examined the flexibility of every thoracic spinal segment in an *in vitro* experiment. Liebsch et al., (2017); Liebsch et al., (2019) investigated the kinematic and stiffness properties of the thoracic spine and the rib cage through experimental studies.

Moreover, many studies tried to estimate the mechanical parameters of the soft tissue in the human's body. Choi and Zheng, (2005) estimated Young's modulus and Poisson's ratio of soft tissue from indentation using two different-sized indentors in a finite element analysis. Song et al., (2006) studied the elasticity of the living abdominal wall in laparoscopic surgery. Hostettler et al., (2010) measured the Bulk modulus and volume variation of the liver and the kidneys *in vivo*. McKee et al., (2011) compared the reported values of Young's modulus obtained from indentation and tensile deformations of soft biological tissues.

2.2 Optimization-based shape design

As mentioned earlier, some works have considered computational optimization of scoliosis braces leveraging simulation models of brace-trunk interaction (Gignac et al., 2000; Liao et al., 2007; Nie et al., 2009). These works suffer strong limitations though. On one hand, the biomechanics models they use are limited, e.g., some limit brace interaction to point forces applied on the skin surface (Gignac et al., 2000). On the other hand, the optimization solvers require complex simulation of trunk biomechanics for every small optimization step, which turns into large inefficiencies.

The computational approach explored in this work considers tight connection between the optimization formulation and the biomechanics engine, to design efficient search methods. This approach is popular in the fields of parameter estimation and computational fabrication, and it relies on implicit differentiation of the biomechanics model. For instance, the work of Miguel et al., (2012) used implicit differentiation of a cloth model to execute efficient parameter estimation of cloth simulation models, and the works of Pérez et al., (2015); Pérez et al., (2017) used implicit differentiation of rod meshes to explore shape designs later produced through 3D printing. Recently, differentiable simulation methodologies have also seen success in robotics. The applications include the optimization of control policies (Du et al., 2021; Murthy et al., 2021), or even the design of sensor networks (Tapia et al., 2020).

It is important to note that computational optimization methods have been explored for various objects, very different from braces, but the methodologies could be applicable. Montes et al., (2020) recently developed a design method for tight clothing that considers design and comfort metrics, and accounts for simulation models of both clothing and the body. Zhao et al., (2021) recently developed a similar method to design supporting surfaces for the human body, accounting for metrics that optimize ergonomics.

3 Trunk and brace simulation model

In this section, we describe the biomechanical model of the torso, the model and parameterization of the brace, and the interaction between both. We put all these elements together in a biomechanics simulation engine that, given a brace geometry as input, outputs the deformation of the trunk and the forces between trunk and brace. We borrow the biomechanical model of the trunk from the work of Koutras et al., (2021), and we refer to their publication for details.

In the definition of the biomechanical model of the trunk and brace, we seek a formulation that can be differentiated, to be efficiently embedded within a design optimization approach. To this end, we model all biomechanical components using smooth energy potentials.

3.1 Biomechanical model of the trunk

The purpose of the trunk simulation model is to predict the deformation of the spine under the action of a scoliosis brace. To this end, we characterize the trunk as a multi-body system, consisting of articulated rigid bodies to model the skeleton, and surrounding soft tissue to model the skin, muscles and organs. In particular, and following the rationale of (Koutras et al., 2021), we consider the trunk model passive, without muscle activation. While the exact instantaneous trunk deformation depends on the instantaneous muscle activity, we consider a passive trunk model as an approximate average of muscle activity conditions.

We group all degrees of freedom (DoFs) of the trunk in a large vector $\mathbf{x}_{\text{trunk}}$. This vector includes: 1) translation and rotation of all bones in the trunk skeleton (the rotation is parameterized using incremental axis angle (Taylor and Kriegman, 1994)); and 2) nodes of a tetrahedral mesh of the soft tissue. The trunk skeleton includes the bones relevant for predicting the deformation of the lumbar and thoracic spine, which are: all lumbar and thoracic vertebrae, the sternum, the rib cage, and the pelvis. The soft-tissue mesh is constructed from the surface of the trunk between neck and waist, and clipped at the shoulders. We provide as input this
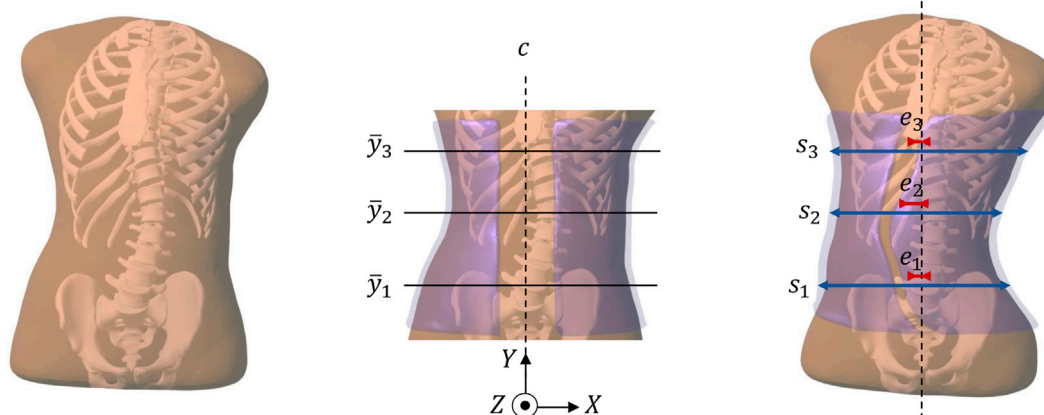
FIGURE 1
This figure summarizes the pipeline of our computational brace design methodology. From left to right: (i) Starting from radiographs of a patient, we obtain a personalized simulation model of the trunk (including the spine, the rib cage, and the surrounding soft tissue). (ii) We initialize a brace geometry (in semi-transparent purple) by trimming and slightly offsetting the patient´s skin. In this initial brace geometry, we identify the frontal center line c, and three heights $\bar{y}_1, \bar{y}_2, \bar{y}_3$ where we focus the contact forces between brace and trunk. (iii) We automatically optimize the eccentricity e and horizontal scale s at the three heights. As a result, the brace deforms the full trunk, and produces a correction of the spine curvature.

surface as a triangle mesh, together with sample points on the surfaces of the bones, and we produce a conformal tetrahedral mesh (Si, 2015). Introducing mesh nodes on the surfaces of bones facilitates the coupling between skeleton and soft tissue. We rigidly couple these nodes to the bones, and we remove them from the DoF vector $\mathbf{x}_{\text{trunk}}$.

The mechanics of the trunk are modeled as a sum of energy terms parameterized by the DoFs $\mathbf{x}_{\text{trunk}}$. The energy terms include compliant joint models between skeletal bones W_{joints} ($\mathbf{x}_{\text{trunk}}$), and the soft-tissue internal energy W_{tissue} ($\mathbf{x}_{\text{trunk}}$). We describe the joint energies W_{joints} as 6-DoF joints between pairs of bones, acting on both their translation and rotation. By tuning the stiffness of each constraint axis, we effectively model different types of joints and their anisotropy. We describe the soft-tissue energy W_{trunk} using a Neo-Hookean strain energy density model, integrated on the volume of the tetrahedral mesh using a finite-element formulation. As mentioned above, we refer to (Koutras et al., 2021) for details on the biomechanical model of the trunk, such as the definition of the energy terms.

In our study, we use the trunk model to simulate the biomechanical response of different subjects suffering from AIS. To adapt the model to each subject, we start from a template geometry corresponding to a healthy (non-scoliotic) adolescent female, and then we apply the morphing method in (Koutras et al., 2022), using as input low-dose radiographs of the subjects. Full personalization would also require estimating subject-specific mechanical parameters, but in this synthetic study we limit ourselves to the default mechanical parameters listed in (Koutras et al., 2021).

3.2 Model and parameterization of the brace

There are many different types of scoliosis braces. Designing a computational solution that explores the different brace types is a complex task, as the design space is not continuous. Therefore, for our solution we focus on one particular type of brace, specifically the classic Boston brace (Périé et al., 2003), which concentrates brace-trunk forces on three locations. One of these locations corresponds to the location of peak curvature in the spine, and the other two locations are above and below, to produce counteracting forces and a net torque that rotates the spine in a corrective direction. Note that more modern variants of the Boston brace consider also other design principles, but we leave such extensions for future work.

We describe the geometry of the Boston brace as a parametric surface $\mathcal{S}(\mathbf{p})$, which depends on a set of design parameters $\mathbf{p}$. Figure 1 shows how we model and parameterize the brace geometry. We start by initializing a reference geometry $\bar{S}$, by copying the geometry of the trunk surface, clipped at the waist and under the armpits. This clipped surface covers the scoliotic portion of the spine. Computer optimization of the brace shape requires a compact parameterization of its geometry. There are many possible approaches to define this parameterization, such as the use of control points and spline surface definitions. In our prototype solution, we rely heavily on the 3-point design methodology of Boston braces, and we parameterize the brace based on X-axis scale s and eccentricity e with respect to the X-axis center line c at three different heights. Our choice of design parameters is aimed at maximizing impact on the lateral flexion

of the spine; however, since the trunk is modeled fully in 3D and the axial rotation of the spine is not constrained, the brace will also produce the physically expected axial rotation. To mimic the 3-point methodology, we pick the height of the maximum spine curvature, and two heights above and below this location. We linearly interpolate scale and eccentricity values along the height of the brace. Formally, given an initial brace point $(\bar{x}, \bar{y}, \bar{z}) \in \bar{\mathcal{S}}$, the design transformation returns a point $(x = s(\bar{y}) \cdot (\bar{x} - c) + c + e(\bar{y}), \quad y = \bar{y}, \quad z = \bar{z})$.

In addition to the design transformation, the initial shape of the brace is transformed to provide pressure on the trunk, and thus forces on the spine that produce an incremental correction. This produces the actual brace surface $\mathcal{S}(\bar{\mathcal{S}}, \mathbf{p}, \mathbf{x}_{\text{brace}})$, which depends on the initial brace geometry $\bar{\mathcal{S}}$, the design parameters $\mathbf{p}$, and some brace transformation DoFs $\mathbf{x}_{\text{brace}}$. Following common designs of Boston braces, we split the brace surface vertically in two-halves. Each of these halves is modeled mechanically as a rigid body, i.e., we ignore the deformation of the brace. On the back of the brace, we connect the two-halves using a vertical hinge joint. With the rigid transformation of one-half of the brace, and the angle of the hinge joint, we define the DoFs of the brace $\mathbf{x}_{\text{brace}}$ in the simulation. On the front of the brace, we connect the two-halves using a strap. This strap has zero rest-length and a stiffness k_{strap}. Then, given strap connections x_{left} and x_{right}, the strap is modeled mechanically as a simple spring with energy

$$W_{\text{strap}} = \frac{1}{2} k_{\text{strap}} \|x_{\text{left}}(\mathbf{x}_{\text{brace}}) - x_{\text{right}}(\mathbf{x}_{\text{brace}})\|^2. \tag{1}$$

3.3 Contact and regularization

To model the interaction between the brace and the trunk, we use a potential-based contact model. An alternative would be to solve contact with hard constraints, but the differentiation of hard constraints is considerably more expensive (Liang et al., 2019). Among potential-based contact models, some recent methods propose highly nonlinear potentials to strongly enforce non-penetration (Li et al., 2020). However, we opt for a quadratic potential to improve the convergence of the design optimization solver.

Given a deformation of the trunk defined by its DoFs x_{trunk}, we define a distance field of its surface, $\phi_{\text{trunk}}(x, \mathbf{x}_{\text{trunk}})$, $x \in \mathbb{R}^3$. The distance is positive outside the trunk and negative inside. Based on this distance field, we define a potential energy that penalizes interpenetration between the brace surface $\mathcal{S}$ and the trunk:

$$W_{\text{contact}} = \int_{\bar{\mathcal{S}}} \frac{1}{2} k_{\text{contact}} \, \text{neg}(\phi_{\text{trunk}}(\mathcal{S}(\bar{\mathcal{S}}, \mathbf{p}, \mathbf{x}_{\text{brace}}), \mathbf{x}_{\text{trunk}}))^2 \, d\bar{\mathcal{S}},$$
$$\text{neg}(r) = \min(r, 0). \tag{2}$$

We approximate the integral through finite-element integration on the triangular surface elements of the brace surface $\bar{\mathcal{S}}$.

In our contact model, we do not account for friction between the brace and the trunk. Friction indeed exists in the real world when the trunk moves, but it is always possible to adjust the brace and let skin relax to remove such friction. Therefore, we are interested in modeling frictionless interaction.

This said, friction plays another important role in simulation, as it ensures that the trunk cannot slip through the brace. We replace this effect with a small regularization term that tries to maintain the brace in place, by penalizing the norm of the brace DoFs.

$$W_{\text{reg}} = \frac{1}{2} k_{\text{reg}} \|\mathbf{x}_{\text{brace}}\|^2. \tag{3}$$

3.4 Simulation engine

Based on the various energy terms defined in the previous sections, the total energy of the trunk-brace system can be computed as:

$$W = W_{\text{joints}} + W_{\text{tissue}} + W_{\text{strap}} + W_{\text{contact}} + W_{\text{reg}}. \tag{4}$$

Given a set of brace design parameters $\mathbf{p}$, we wish to predict the deformation of the trunk produced by the brace. We do this by solving a static equilibrium problem. For convenience, we concatenate all DoFs in one large vector $\mathbf{x} = (\mathbf{x}_{\text{brace}}, \mathbf{x}_{\text{trunk}})$. Then, we can express the computation of the trunk and brace configuration as the following minimization of the total energy:

$$\mathbf{x}(\mathbf{p}) = \arg\min_{\mathbf{x}} W(\mathbf{p}, \mathbf{x}). \tag{5}$$

At the configuration of minimum energy, the biomechanics satisfy static equilibrium, i.e., zero net energy gradient or zero net force everywhere in the brace-trunk system:

$$-\frac{\partial W(\mathbf{p}, \mathbf{x})^T}{\partial \mathbf{x}} = \mathbf{f}(\mathbf{p}, \mathbf{x}) = 0. \tag{6}$$

Note that the forces on the DoFs, $\mathbf{f}$, are simply the (negative) gradient of the energy. Static equilibrium is a direct consequence of the optimality conditions of the optimization. We can also regard these optimality conditions as *biomechanics constraints*.

To solve the optimization (Eq. 5), we use Newton's method with line search (Nocedal and Wright, 2006). On every Newton iteration, we compute the Jacobian of the forces, i.e., the (negative) energy Hessian, $\frac{\partial \mathbf{f}}{\partial \mathbf{x}} = -\frac{\partial^2 W}{\partial \mathbf{x}^2}$, we solve a linear system for the change in the DoFs, and we take a safe step that minimizes the energy. Our biomechanics model is implemented in C++ in SOFA (Faure et al., 2012), which allows to implement energies, forces, and force Jacobians in a flexible and efficient way. However, we have built the Newton solver on Python, with bindings to the SOFA model.

4 Brace optimization

In this section, we describe the formulation of an optimization problem for brace design. We start with the formulation of a design objective function, and we continue with efficient computation of the objective gradient using our differentiable biomechanics formulation.

4.1 Design optimization problem

To guide the change of the brace shape, we need a merit function that quantifies the impact on the spine from a clinical standpoint. In our approach, we use the Cobb angle (Safari et al., 2019) to characterize the severity of scoliosis. More complex, multi-objective merit functions are left for future work, but are briefly discussed in Section 6. The Cobb angle measures the largest angle between the superior end plate of a vertebra and the inferior end plate of some other vertebra, thus characterizing the maximum bending of the spine. The Cobb angle $\Psi(\mathbf{x}_{\text{trunk}})$ can be computed from the DoFs of the vertebrae embedded in $\mathbf{x}_{\text{trunk}}$. Then, our clinical merit function is:

$$\mathcal{L}_{\text{Cobb}} = \left(\frac{\Psi(\mathbf{x}_{\text{trunk}})}{\Psi(\mathbf{x}_{\text{trunk},0})} \right)^2. \tag{7}$$

Note that the metric is normalized by the initial Cobb angle $\Psi(\mathbf{x}_{\text{trunk},0}$, to simplify weighing of the metric across subjects.

However, optimizing the Cobb angle might produce braces that are uncomfortable or even impossible to wear. Therefore, we also add the total force applied by the brace on the trunk as a comfort function, penalizing designs that would be too uncomfortable. We obtain per-point forces by differentiating the penalty potential in (Eq. 2), we compute its squared norm, and we integrate the result over the surface of the brace:

$$\mathcal{L}_{\text{contact}} = \int_{\bar{\mathcal{S}}} k_{\text{contact}}^2 \, \text{neg}(\phi_{\text{trunk}}(\mathcal{S}(\bar{\mathcal{S}}, \mathbf{p}, \mathbf{x}_{\text{brace}}), \mathbf{x}_{\text{trunk}}))^2 \, d\bar{\mathcal{S}}$$
$$= 2 \, k_{\text{contact}} W_{\text{contact}}. \tag{8}$$

Adding the clinical metric (Eq. 7) and the comfort metric (Eq. 8), we obtain the full objective function of the brace design problem:

$$\mathcal{L} = \mathcal{L}_{\text{Cobb}} + \lambda \, \mathcal{L}_{\text{contact}}, \tag{9}$$

where λ is the relative weight of the two components of the objective function. A proper weight adjustment λ of the clinical and comfort metrics produces designs that are both effective and comfortable to wear. We consider a Cobb angle of 75% as a sufficient objective, and a force of 250 N as a reasonable contact force. Then, a value of $\lambda = 9e^{-6}$ assigns equal weight to both the clinical and comfort metrics.

4.2 Optimization algorithm

Given the brace design objective $\mathcal{L}$ in (Eq. 9), the biomechanics energy W in (Eq. 4), the DoFs of the trunk and the brace $\mathbf{x}$, and the parameterization of the brace geometry $\mathbf{p}$, the computation of the brace design can formally be expressed as finding the brace parameters that minimize the design objective, subject to biomechanical constraints:

$$\mathbf{p} = \arg\min_{\mathbf{p}} \mathcal{L}(\mathbf{p}, \mathbf{x}), \quad \text{s.t. } \mathbf{f}(\mathbf{p}, \mathbf{x}) = 0. \tag{10}$$

We rely on numerical optimization methods to automatically search for brace geometries that produce optimal designs. In our implementation, we choose the bounded L-BFGS optimization algorithm (Nocedal and Wright, 2006), as it offers a good balance between speed and convergence. L-BFGS requires the evaluation of the gradient of the objective function with respect to the design parameters, i.e., $\frac{\partial \mathcal{L}}{\partial \mathbf{p}}$.

The challenge in the evaluation of this gradient is that a change of design parameters $\mathbf{p}$ affects the DoFs $\mathbf{x}$ in a complex way, through the equilibrium condition (Eq. 6). Due to this complexity, a common approach to evaluate $\frac{\partial \mathcal{L}}{\partial \mathbf{p}}$ is to use finite differences. This approach requires solving the static equilibrium condition for an incremental change to each of the design parameters. Therefore, it can be formally expressed as:

$$\frac{\partial \mathcal{L}}{\partial \mathbf{p}_i} = \frac{\mathcal{L}(\mathbf{p} + \varepsilon \, \mathbf{e}_i, \, \text{argmin}_{\mathbf{x}} W(\mathbf{p} + \varepsilon \, \mathbf{e}_i, \mathbf{x})) - \mathcal{L}(\mathbf{p}, \, \text{arg min}_{\mathbf{x}} W(\mathbf{p}, \mathbf{x}))}{\varepsilon}, \tag{11}$$

where $\mathbf{e}_i$ is a unit vector in the direction of the ith parameter, and ε is a small value. For small parameter sets, finite-differences may be computationally effective, but their cost grows linearly with the number of design parameters, and they soon become the bottleneck of the optimization.

4.3 Differentiable biomechanics

Instead of using finite differences, we leverage our differentiable biomechanics formulation to compute the gradient of DoFs with respect to design parameters, $\frac{\partial \mathbf{x}}{\partial \mathbf{p}}$, and use this to evaluate the gradient of the objective function.

With the definition of the objective function (Eq. 9), we note that the clinical metric $\mathcal{L}_{\text{Cobb}}$ depends only on the DoFs $\mathbf{x}$, while the comfort metric $\mathcal{L}_{\text{contact}}$ depends on the DoFs but also directly on the brace design parameters $\mathbf{p}$. Then, the full objective gradient can be written as:

$$\frac{\partial \mathcal{L}}{\partial \mathbf{p}} = \lambda \, \frac{\partial \mathcal{L}_{\text{contact}}}{\partial \mathbf{p}} + \left(\frac{\partial \mathcal{L}_{\text{Cobb}}}{\partial \mathbf{x}} + \lambda \, \frac{\partial \mathcal{L}_{\text{contact}}}{\partial \mathbf{x}} \right) \frac{\partial \mathbf{x}}{\partial \mathbf{p}}. \tag{12}$$

Thanks to the implicit function theorem (IFT), the biomechanics equilibrium constraints (Eq. 6) must be satisfied

for small changes to the DoFs and the design parameters. Then, we can differentiate those constraints to obtain:

$$\frac{\partial \mathbf{f}}{\partial \mathbf{p}} + \frac{\partial \mathbf{f}}{\partial \mathbf{x}} \frac{\partial \mathbf{x}}{\partial \mathbf{p}} = 0 \quad \rightarrow \quad \frac{\partial \mathbf{x}}{\partial \mathbf{p}} = -\frac{\partial \mathbf{f}}{\partial \mathbf{x}}^{-1} \frac{\partial \mathbf{f}}{\partial \mathbf{p}}. \tag{13}$$

IFT provides an implicit definition of the Jacobian of the DoFs with respect to design parameters, such that the equilibrium constraints remain satisfied.

We leverage this Jacobian to differentiate the objective (Eq. 9) analytically, and substitute it in (Eq. 12) to obtain:

$$\frac{\partial \mathcal{L}}{\partial \mathbf{p}} = \lambda \frac{\partial \mathcal{L}_{\text{contact}}}{\partial \mathbf{p}} - \left(\frac{\partial \mathcal{L}_{\text{Cobb}}}{\partial \mathbf{x}} + \lambda \frac{\partial \mathcal{L}_{\text{contact}}}{\partial \mathbf{x}} \right) \frac{\partial \mathbf{f}}{\partial \mathbf{x}}^{-1} \frac{\partial \mathbf{f}}{\partial \mathbf{p}}. \tag{14}$$

The evaluation of the gradient (Eq. 14) requires substituting the implicit derivative (Eq. 13). In practice, however, this is done using the adjoint method:

$$\frac{\partial \mathcal{L}}{\partial \mathbf{p}} = \lambda \frac{\partial \mathcal{L}_{\text{contact}}}{\partial \mathbf{p}} - \mathbf{u}^T \frac{\partial \mathbf{f}}{\partial \mathbf{p}},$$

$$\text{with } \frac{\partial \mathbf{f}}{\partial \mathbf{x}} \mathbf{u} = \left(\frac{\partial \mathcal{L}_{\text{Cobb}}}{\partial \mathbf{x}} + \lambda \frac{\partial \mathcal{L}_{\text{contact}}}{\partial \mathbf{x}} \right)^T. \tag{15}$$

On each step of L-BFGS, given a new tentative set of brace parameters $\mathbf{p}$, we solve the static equilibrium (Eq. 5) to obtain the trunk and brace DoFs. Then, we solve for the adjoint $\mathbf{u}$ in (Eq. 15), and we evaluate the full objective gradient.

4.4 Implementation details

Our optimization is built in Python, using the L-BFGS solver in scipy. As mentioned in Section 3.4, we use SOFA for the biomechanics, and then we build the full gradient in Python and we feed it to the L-BFGS solver. By defining smooth biomechanics functions with respect to both DoFs $\mathbf{x}$ and design parameters $\mathbf{p}$, we can efficiently evaluate the objective gradient $\frac{\partial \mathcal{L}}{\partial \mathbf{p}}$. Next, we provide some details about the computation of the derivative terms in (Eq. 15).

The Jacobian of forces $\frac{\partial \mathbf{f}}{\partial \mathbf{x}}$ is already used by the Newton-type solver of biomechanics simulation (see Section 3.4), and it requires all energy terms to be twice-differentiable. This condition is the default for most energy terms, including W_{joints}, W_{tissue}, W_{strap}, and our ad-hoc term W_{reg}. In Section 3.3, we also pay special care to design a twice-differentiable contact model W_{contact}.

The gradient of the comfort metric with respect to the DoFs can be obtained trivially from the contact forces. From (Eq. 8), we derive that $\frac{\partial \mathcal{L}_{\text{contact}}}{\partial \mathbf{x}} = 2 k_{\text{contact}} \frac{\partial W_{\text{contact}}}{\partial \mathbf{x}} = -2 k_{\text{contact}} \mathbf{f}_{\text{contact}}$.

The gradient of the comfort metric with respect to the brace parameters does not differ much from the contact forces. It can be computed as $\frac{\partial \mathcal{L}_{\text{contact}}}{\partial \mathbf{p}} = 2 k_{\text{contact}} \int_{\bar{\mathcal{S}}} \frac{\partial W_{\text{contact}}}{\partial S} \frac{\partial S}{\partial \mathbf{p}} d\bar{\mathcal{S}}$. $\frac{\partial W_{\text{contact}}}{\partial S}$ represents per-point contact forces on the brace, which are then multiplied through the chain rule by the gradient of the

transformed brace with respect to the design parameters, $\frac{\partial S}{\partial \mathbf{p}}$. This last gradient can be easily obtained from the definition of the brace parameterization in Section 3.2.

The most complex term is probably the Jacobian of forces with respect to brace parameters, $\frac{\partial \mathbf{f}}{\partial \mathbf{p}}$. The forces affected directly by the parameters are the contact forces (on both the brace and the trunk) and the strap forces. Similar to the derivation of $\frac{\partial \mathcal{L}_{\text{contact}}}{\partial \mathbf{p}}$ above, the Jacobian of contact forces can be obtained as the chain rule of per-surface-point force Jacobians and the gradient of the transformed brace surface with respect to design parameters, i.e., $\frac{\partial \mathbf{f}_{\text{contact}}}{\partial \mathbf{p}} = \int_{\bar{\mathcal{S}}} \frac{\partial \mathbf{f}_{\text{contact}}}{\partial S} \frac{\partial S}{\partial \mathbf{p}} d\bar{\mathcal{S}}$. The Jacobian of the strap force, $\frac{\partial \mathbf{f}_{\text{strap}}}{\partial \mathbf{p}}$, is simple, as it just involves two points on the surface of the brace, as shown in (Eq. 1).

The last necessary term is the gradient of the clinical metric with respect to the DoFs, $\frac{\partial \mathcal{L}_{\text{Cobb}}}{\partial \mathbf{x}}$. To this end, within each iteration of the optimization, we consider that the vertebrae defining the Cobb angle do not change. Then, the expression of Cobb angle becomes a smooth and differentiable formula.

The IFT applied in (Eq. 13) to implicitly define the derivative of DoFs with respect to design parameters is only valid when the biomechanics constraints (Eq. 6) are satisfied. For this reason, the static equilibrium is solved on each L-BFGS iteration. We have experimented with the accuracy required by the static equilibrium solve, which in turn affects the accuracy of $\frac{\partial \mathbf{x}}{\partial \mathbf{p}}$. We have concluded that a threshold of 1 mN is necessary to this end. However, this does not affect performance much. We have observed that, in practice, the solver leverages the expected quadratic convergence of Newton's method once the residual is small.

5 Experiments

This section describes the cases that were evaluated in our study. We start with a description of the patient data, and then we provide an analysis of performance of the brace design methodology. As discussed in the introduction, to date we have limited our experiments to a synthetic study, and we evaluate the performance of brace designs only on simulation models of the patients.

5.1 Test cohort

The proposed computational brace design method was applied to a cohort of five female potential AIS patients, ranging from 10 to 13 years old, with an average height of 163.6 cm (±11 cm). The subjects were selected because they had to be screened for scoliosis based on previous diagnosis or examination, but subject #2 was not considered an AIS patient after all, and subject #3 would not require brace treatment in clinical practice. As discussed in the definition of the clinical metric in Section 4.1, in our study we use the Cobb angle metric

TABLE 1 Features of the subjects evaluated in our study. The table indicates the severity of the main spine curve (i.e., the Cobb angle) of each subject, as well as the size of the simulation meshes used in our optimization algorithm.

Subject ID	Gender	Age	Height (cm)	Cobb angle (deg)	Soft-tissue tets	Surface tris
1	female	10	157	28.9	12737	682
2	female	11	179	5.5	11781	596
3	female	13	168	13.5	14144	566
4	female	11	150	22.8	8644	548
5	female	13	164	16.5	13459	598
avg (± std dev)	—	11.6 ± 1.3	163.6 ± 11.0	17.4 ± 8.9	12153 ± 2148	598 ± 51

(Safari et al., 2019) to characterize the severity of scoliosis, as it is the standard clinical metric for this purpose. The average Cobb angle measured on the subjects was 17.4° (±8.9°).

In order to proceed with the study, all patients provided oral and written consent according to national Danish guidelines and the Helsinki Declaration, and with approval of the local ethics committee at University Hospital of Hvidovre (No H-17034237). For each subject, we captured biplanar radiographs of the trunk, as they are readily available as part of the regular check-up of scoliotic patients, using a DelftDI D2RS system with fluoroscopic exposure (Wong et al., 2021). Then, we followed the procedure in (Koutras et al., 2022) to morph a template trunk geometry and obtain personalized trunk biomechanical models. Table 1 provides the individual patient data, as well as the complexity of the simulation models, characterized by the number of triangles of the surface mesh (which dominates the cost of contact computations) and the number of tetrahedra of the soft-tissue mesh (which dominates the cost of deformation computations).

5.2 Brace optimization results

Figure 2 illustrates the result of brace optimization for each subject evaluated in the study. The figure shows the trunk geometry and the brace geometry before and after the computational optimization. As evidenced in the images, the optimization algorithm automatically finds brace designs that push on the rib cage at the appropriate location to induce a correction of the spine curvature.

Table 2 compares the Cobb angle before and after applying the scoliosis brace to each of the subjects. Note that we refer to the in-brace correction of Cobb angle; our work has no way of predicting the correction of Cobb angle after brace removal, as this temporal process is not handled by our simulation model. On average, the Cobb angle was reduced by 7.8° (±4.9°), which amounts to a reduction of 45.4% ± 18.9%. Moreover, thanks to the comfort metric described in Section 4.1, this reduction in

Cobb angle was achieved under average contact forces of 185.8 N (±29.8 N). None of the subjects reached the limit of 250 N in contact force, indicating a good balance of the clinical and comfort metrics in (Eq. 9). An average reduction of 7.8° in Cobb angle may be considered low with respect to the reduction achieved by real-world braces (in particular in the case of subject #3), and we consider two reasons behind this limitation: 1) The degrees of freedom of our computational braces are currently far fewer than those of real braces; 2) The comfort metric may be too conservative. Both limitations are avenues for further improvement, but they do not challenge the overall methodology.

Finally, Table 3 summarizes the computational performance of our proposed optimization algorithm. Thanks to differentiable biomechanics and the efficient computation of gradients, the optimizations take 16.4 min on average (±7.3 min). This is in contrast to the average of 94.1 min required by state-of-the-art optimization using finite-difference gradients. The average speed-up across subjects is of 9.2×. This number is particularly affected by the performance of subject #4, for whom the finite-difference version suffered considerably worse convergence. Even removing this outlier case, the average speed-up across subjects is of 4.5×. In our current parameterization of the brace, described in Section 3.2, we use just 6 parameters. With a larger number of parameters, the speed-up of our differentiable biomechanics formulation would be even higher, as the computation of gradients is insensitive to the number of parameters.

6 Discussion

In this paper, we have presented a computational method to design personalized scoliosis Boston braces. The main novelty of the proposed method is to leverage differentiable biomechanics to enable efficient use of numerical optimization methods. Differentiable biomechanics formulates static equilibrium equations as constraints, and evaluates the relationship between deformation state and design variables through
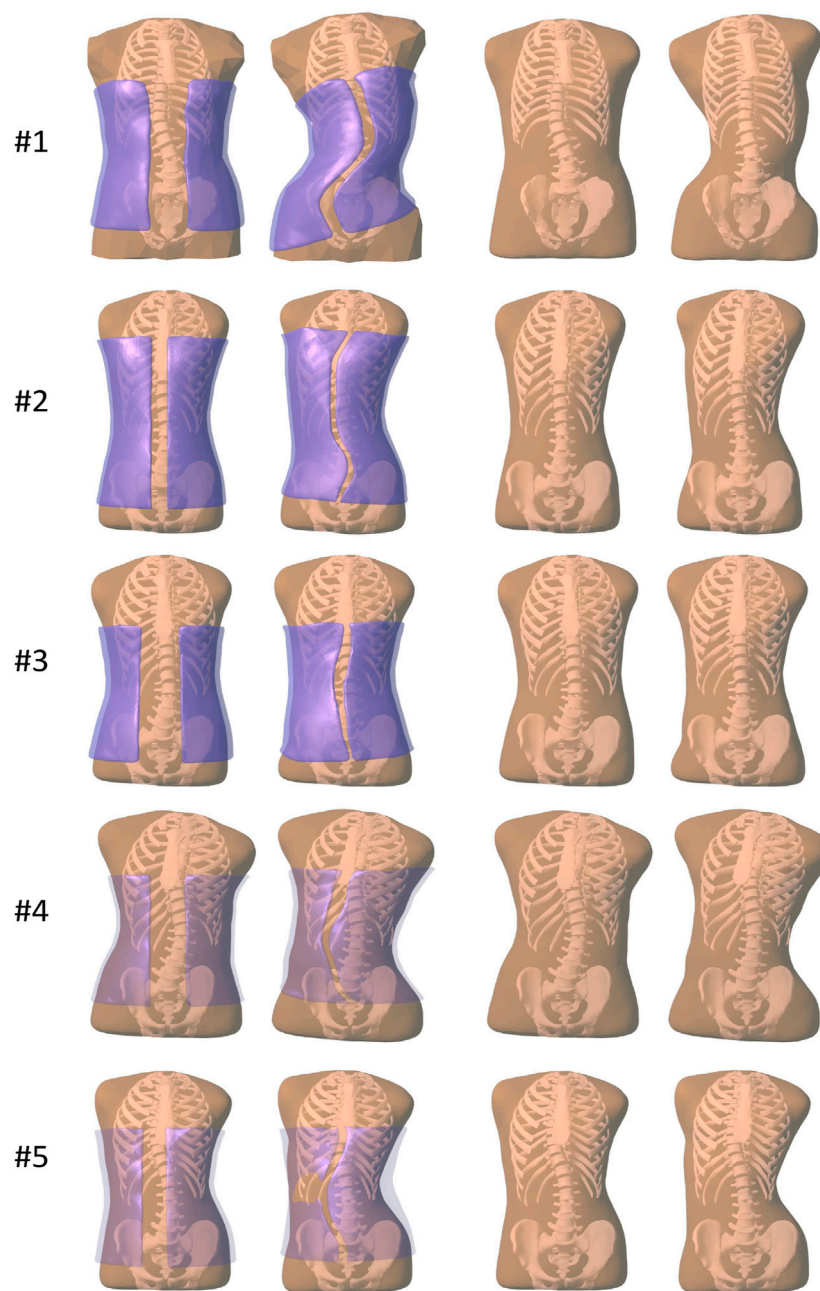
FIGURE 2
Images of all the subjects evaluated in our study. From left to right, (i) before brace optimization, with the initial brace geometry shown semi-transparent purple, (ii) after brace optimization, with the final brace geometry shown semi-transparent purple, (iii) before brace optimization, just the initial trunk geometry, (iv) after brace optimization, showing the deformed trunk geometry.

implicit differentiation. This relationship is then used within the numerical optimization algorithm to quickly advance toward optimal brace design parameters. We have shown that the differentiable biomechanics formulation provides a large speed-up over state-of-the-art numerical optimization approaches. And this already large speed-up can even increase

as the versatility of brace designs grows with more complex parameterizations.

We have demonstrated the use of differentiable biomechanics to design personalized scoliosis braces for five different potential AIS patients. The overall methodology combines personalized trunk simulation models with the differentiable-biomechanics technical

TABLE 2 Quantitative results achieved by optimization-based brace design on each of the test subjects. The table lists the reduction in Cobb angle (in degrees and in percentage of the initial angle), as well as the total force on the subject's trunk as a measure of comfort.

Subject ID	Cobb before (deg)	Cobb after (deg)	Reduction (deg)	% Reduction	Force (N)
1	28.9	15.7	13.2	45.6	210
2	5.5	2.0	3.5	63.7	152
3	13.5	11.7	1.8	13.8	187
4	22.8	11.8	11.4	50.0	220
5	16.5	7.6	8.9	54.0	160
avg (± std dev)	17.4 ± 8.9	9.7 ± 5.2	7.8 ± 4.9	45.4 ± 18.9	185.8 ± 29.9

TABLE 3 Performance of our method, using differentiable biomechanics, compared with state-of-the-art optimization using finite differences (FD) for the computation of gradients. All timings are measured in minutes. We report the number of steps of each optimization, the total time, the time per step, the total speed-up, and the speed-up per step.

Subject ID	Ours			FD			Speed-up	
	Steps	Time	Time/Step	Steps	Time	Time/Step	Total	Per step
1	9	14.3	1.59	14	89.6	6.40	6.3×	4.0×
2	21	16.6	0.79	22	75.6	3.43	4.6×	4.3×
3	17	23.2	1.36	16	67.3	4.20	2.9×	3.1×
4	25	5.2	0.21	29	142.9	4.93	27.4×	23.6×
5	20	22.8	1.14	24	96.4	4.0	4.3×	3.5×
Avg	18.4	16.4	1.02	21.0	94.4	4.60	912×	7.7×

contribution. Altogether, we demonstrate that it is possible to design scoliosis braces following a fully computational methodology. The braces balance a clinical metric and a comfort metric, ensuring that they are both effective and practical.

Our study and evaluation are to date limited to synthetic experiments. While the input data belong to real (potential) AIS patients, we have not fabricated and physically tested the brace designs. The contribution of our work is to demonstrate that a computational design methodology is feasible and efficient, but further work is necessary before actual braces are physically tested on real patients. One of the elements that requires further study is the design of the comfort metric. Our current metric considers the total force on the body surface, but this metric is not proven to be suitable or sufficient. Therefore, our work should be complemented with a specific analysis on comfort metrics for scoliosis braces. Another element that requires further study is the accuracy of the overall computational approach, as well as the sensitivity of its various elements. The different computational elements (i.e., the model geometry, the mechanical model, the model parameters, or the weight of the clinical vs comfort metrics) introduce error in the estimated Cobb angle and contact forces. It is necessary to understand the degree of

possible error, and thus design a tolerance on the contact forces computed in the simulation. Once the computational model is fully validated, it will be necessary to execute a clinical study concentrated on patient-reported outcome measures, including treatment acceptance and compliance.

In addition to the work necessary for bringing the method to practice, our methodology could also see some improvements on the technical choices. Some of the possible extensions include a richer parameterization of the brace geometry (e.g., using spline surfaces with control points), or personalization of the mechanical parameters of the trunk model. Regarding this last extension, using personalized vs default parameters poses a trade-off between complexity and accuracy. While designing a personalized model would indeed increase accuracy, it is interesting to understand the error produced in practice by a default model.

To conclude, our work has been applied so far only to one type of scoliosis brace, the Boston-type brace, and considering only Cobb angle as clinical metric. It would be interesting to address other types of braces, which would require a different geometric design and a different parameterization. For practical cases, the optimization methodology may even search among different brace types, and find the one that is most convenient for each patient. However, the

challenge is two-fold. First, more complex braces require more modeling effort; but this can always be approached by progressively including brace elements of higher impact. Second, some of the design parameters define a continuous parametric space, which can be explored by our current numerical optimization method, but others may define discontinuous or discrete spaces, which require different optimization methods. For instance, optimizing the expansion chambers of Chêneau braces might require topology optimization methods. It would also be interesting to address richer clinical metrics, which are accounted for in the design of braces in practice. One example is the addition of a sagittal-plane metric on top of our current frontal-plane-only metric (e.g., sagittal-plane isostatic balance as a function of lumbopelvic incidence). Our overall approach can be extended to include more advanced multi-objective clinical metrics. For such extension to be possible without critical changes to the overall methodology, the new metrics must be computed from the geometry available in the trunk model, and they must be (locally) continuous and differentiable.

Data availability statement

The data analyzed in this study is subject to the following licenses/restrictions: The dataset was obtained in the context of the MSCA Rainbow project, and use is limited to research within that project. Requests to access these datasets should be directed to miguel.otaduy@urjc.es.

Ethics statement

The studies involving human participants were reviewed and approved by University Hospital of Hvidovre. Written informed consent to participate in this study was provided by the participants' legal guardian/next of kin.

Author contributions

KK led the development of the models, implementation of the methods, and testing and evaluation of results. CK contributed to the development of the model and the obtention of the input data. MO contributed to the design of the methodology, evaluation of results and writing of the paper. All authors reviewed and agreed to the final manuscript.

References

Conflict of interest

The authors declare that the research was conducted in the absence of any commercial or financial relationships that could be construed as a potential conflict of interest.

Publisher's note

All claims expressed in this article are solely those of the authors and do not necessarily represent those of their affiliated organizations, or those of the publisher, the editors and the reviewers. Any product that may be evaluated in this article, or claim that may be made by its manufacturer, is not guaranteed or endorsed by the publisher.

Author disclaimer

This paper only contains the author's views and the Research Executive Agency and the Commission are not responsible for any use that may be made of the information it contains.

Supplementary material

The Supplementary Material for this article can be found online at: https://www.frontiersin.org/articles/10.3389/fbioe.2022.1014365/full#supplementary-material

Andriacchi, T., Schultz, A., Belytschko, T., Galante, J., and Galante, J. (1974). A model for studies of mechanical interactions between the human spine and rib cage. *J. Biomechanics* 7, 497–507. doi:10.1016/0021-9290(74)90084-0

Aroeira, R. M. C., Pertence, A. E. d. M., Kemmoku, D. T., and Greco, M. (2017). Three-dimensional geometric model of the middle segment of the thoracic spine based on graphical images for finite element analysis. *Res. Biomed. Eng.* 33, 97–104. doi:10.1590/2446-4740.08916

Aroeira, R. M. C., Pertence, A. E. M., Kemmoku, D. T., and Greco, M. (2018). The effect of hypokyphosis on the biomechanical behavior of the adolescent thoracic spine. *J. Braz. Soc. Mech. Sci. Eng.* 40, 128. doi:10.1007/s40430-018-1061-4

Bayoglu, R., Galibarov, P. E., Verdonschot, N., Koopman, B., and Homminga, J. (2019). Twente spine model: A thorough investigation of the spinal loads in a complete and coherent musculoskeletal model of the human spine. *Med. Eng. Phys.* 68, 35–45. doi:10.1016/j.medengphy.2019.03.015

Bisschop, A., Mullender, M. G., Kingma, I., Jiya, T. U., van der Veen, A. J., Roos, J. C., et al. (2012). The impact of bone mineral density and disc degeneration on shear strength and stiffness of the lumbar spine following laminectomy. *Eur. Spine J.* 21, 530–536. doi:10.1007/s00586-011-1968-2

Choi, A., and Zheng, Y. (2005). Estimation of young's modulus and Poisson's ratio of soft tissue from indentation using two different-sized indentors: Finite element analysis of the finite deformation effect. *Med. Biol. Eng. Comput.* 43, 258–264. doi:10.1007/bf02345964

Clin, J., Aubin, C.-É., Lalonde, N., Parent, S., and Labelle, H. (2011). A new method to include the gravitational forces in a finite element model of the scoliotic spine. *Med. Biol. Eng. Comput.* 49, 967–977. doi:10.1007/s11517-011-0793-4

Cobetto, N., Aubin, C.-É., Parent, S., Barchi, S., Turgeon, I., and Labelle, H. (2017). 3d correction of ais in braces designed using cad/cam and fem: A randomized controlled trial. *Scoliosis Spinal Disord.* 12, 24–28. doi:10.1186/s13013-017-0128-9

Cobetto, N., Aubin, C. E., Parent, S., Clin, J., Barchi, S., Turgeon, I., et al. (2016). Effectiveness of braces designed using computer-aided design and manufacturing (CAD/CAM) and finite element simulation compared to CAD/CAM only for the conservative treatment of adolescent idiopathic scoliosis: A prospective randomized controlled trial. *Eur. Spine J.* 25, 3056–3064. doi:10.1007/s00586-016-4434-3

de Zee, M., Hansen, L., Wong, C., Rasmussen, J., and Simonsen, E. B. (2007). A generic detailed rigid-body lumbar spine model. *J. Biomechanics* 40, 1219–1227. doi:10.1016/j.jbiomech.2006.05.030

Dicko, A. H., Tong-Yette, N., Gilles, B., Faure, F., and Palombi, O. (2015). Construction and validation of a hybrid lumbar spine model for the fast evaluation of intradiscal pressure and mobility. *Int. J. Med. Health Sci.* 9 (2). 139–150.

Dong, E., Shi, L., Kang, J., Li, D., Liu, B., Guo, Z., et al. (2020). Biomechanical characterization of vertebral body replacement *in situ*: Effects of different fixation strategies. *Comput. Methods Programs Biomed.* 197, 105741. doi:10.1016/j.cmpb.2020.105741

Du, T., Wu, K., Ma, P., Wah, S., Spielberg, A., Rus, D., et al. (2021). Diffpd: Differentiable projective dynamics. *ACM Trans. Graph.* 41, 1–21. doi:10.1145/3490168

Faure, F., Duriez, C., Delingette, H., Allard, J., Gilles, B., Marchesseau, S., et al. (2012). "Sofa: A multi-model framework for interactive physical simulation," in *Soft tissue biomechanical modeling for computer assisted surgery*. Editor Y. Payan (Springer), 11, 283–321. of Studies in Mechanobiology, Tissue Engineering and Biomaterials. doi:10.1007/8415_2012_125

Finley, S. M., Brodke, D. S., Spina, N. T., DeDen, C. A., and Ellis, B. J. (2018). Febio finite element models of the human lumbar spine. *Comput. methods biomechanics Biomed. Eng.* 21, 444–452. doi:10.1080/10255842.2018.1478967

Gignac, D., Aubin, C.-É., Dansereau, J., and Labelle, H. (2000). Optimization method for 3d bracing correction of scoliosis using a finite element model. *Eur. spine J.* 9, 185–190. doi:10.1007/s005860000135

Guy, A., Labelle, H., Barchi, S., Audet-Duchesne, E., Cobetto, N., Parent, S., et al. (2021). Braces designed using cad/cam combined or not with finite element modeling lead to effective treatment and quality of life after 2 years: A randomized controlled trial. *Spine* 46, 9–16. doi:10.1097/brs.0000000000003705

Hostettler, A., George, D., Rémond, Y., Nicolau, S. A., Soler, L., and Marescaux, J. (2010). Bulk modulus and volume variation measurement of the liver and the kidneys *in vivo* using abdominal kinetics during free breathing. *Comput. methods programs Biomed.* 100, 149–157. doi:10.1016/j.cmpb.2010.03.003

Ignasiak, D., Dendorfer, S., and Ferguson, S. J. (2016). Thoracolumbar spine model with articulated rib cage for the prediction of dynamic spinal loading. *J. Biomechanics* 49, 959–966. doi:10.1016/j.jbiomech.2015.10.010

Kaelin, A. J. (2020). Adolescent idiopathic scoliosis: Indications for bracing and conservative treatments. *Ann. Transl. Med.* 8, 28. doi:10.21037/atm.2019.09.69

Karimi, M., and Rabczuk, T. (2018). Scoliosis conservative treatment: A review of literature. *J. Craniovertebr. Junction Spine* 9, 3–8. doi:10.4103/jcvjs.JCVJS_39_17

Koutras, C., Pérez, J., Kardash, K., and Otaduy, M. A. (2021). A study of the sensitivity of biomechanical models of the spine for scoliosis brace design. *Comput. Methods Programs Biomed.* 207, 106125. doi:10.1016/j.cmpb.2021.106125

Koutras, C., Shayestehpour, H., Pérez, J., Wong, C., Rasmussen, J., Tournier, M., et al. (2022). Biomechanical morphing for personalized fitting of scoliotic torso skeleton models. *Front. Bioeng. Biotechnol.* 10, 945461. doi:10.3389/fbioe.2022.945461

Kuroki, H. (2018). Brace treatment for adolescent idiopathic scoliosis. *J. Clin. Med.* 7, 136. doi:10.3390/jcm7060136

Lasswell, T. L., Cronin, D. S., Medley, J. B., and Rasoulinejad, P. (2017). Incorporating ligament laxity in a finite element model for the upper cervical spine. *Spine J.* 17, 1755–1764. doi:10.1016/j.spinee.2017.06.040

Le Navéaux, F., Larson, A. N., Labelle, H., Wang, X., and Aubin, C.-É. (2016). How does implant distribution affect 3d correction and bone-screw forces in thoracic adolescent idiopathic scoliosis spinal instrumentation? *Clin. Biomech.* 39, 25–31. doi:10.1016/j.clinbiomech.2016.09.002

Li, M., Ferguson, Z., Schneider, T., Langlois, T., Zorin, D., Panozzo, D., et al. (2020). Incremental potential contact: Intersection-and inversion-free, large-deformation dynamics. *ACM Trans. Graph.* 39. doi:10.1145/3386569.3392425

Liang, J., Lin, M., and Koltun, V. (2019). "Differentiable cloth simulation for inverse problems," in *Advances in neural information processing systems*. Editors H. Wallach, H. Larochelle, A. Beygelzimer, F. d' Alché-Buc, E. Fox, and R. Garnett (Vancouver: Curran Associates, Inc.), 32.

Liao, Y.-C., Feng, C.-K., Tsai, M.-W., Chen, C.-S., Cheng, C.-K., and Ou, Y.-C. (2007). Shape modification of the boston brace using a finite-element method with topology optimization. *Spine* 32, 3014–3019. doi:10.1097/brs.0b013e31815cda9c

Liebsch, C., Graf, N., Appelt, K., and Wilke, H.-J. (2017). The rib cage stabilizes the human thoracic spine: An *in vitro* study using stepwise reduction of rib cage structures. *PLoS One* 12, e0178733. doi:10.1371/journal.pone.0178733

Liebsch, C., Graf, N., and Wilke, H.-J. (2019). *In vitro* analysis of kinematics and elastostatics of the human rib cage during thoracic spinal movement for the validation of numerical models. *J. biomechanics* 94, 147–157. doi:10.1016/j.jbiomech.2019.07.041

McKee, C. T., Last, J. A., Russell, P., and Murphy, C. J. (2011). Indentation versus tensile measurements of young's modulus for soft biological tissues. *Tissue Eng. Part B Rev.* 17, 155–164. doi:10.1089/ten.teb.2010.0520

Miguel, E., Bradley, D., Thomaszewski, B., Bickel, B., Matusik, W., Otaduy, M. A., et al. (2012). Data-driven estimation of cloth simulation models. *Comput. Graph. Forum* 31, 519–528. doi:10.1111/j.1467-8659.2012.03031.x

Montes, J., Thomaszewski, B., Mudur, S., and Popa, T. (2020). Computational design of skintight clothing. *ACM Trans. Graph.* 39. doi:10.1145/3386569.3392477

Moroney, S. P., Schultz, A. B., Miller, J. A., and Andersson, G. B. (1988). Load-displacement properties of lower cervical spine motion segments. *J. biomechanics* 21, 769–779. doi:10.1016/0021-9290(88)90285-0

Murthy, J. K., Macklin, M., Golemo, F., Voleti, V., Petrini, L., Weiss, M., et al. (2021). "gradsim: Differentiable simulation for system identification and visuomotor control," in *International conference on learning representations*.

Negrini, S., Aulisa, A., Cerny, P., de Mauroy, J., McAviney, J., Mills, A., et al. (2022). The classification of scoliosis braces developed by sosort with srs, ispo, and posna and approved by esprm. *Eur. Spine J.* 31, 980–989. Publisher Copyright: © 2022, The Author(s). doi:10.1007/s00586-022-07131-z

Nie, W.-Z., Ye, M., Liu, Z.-D., and Wang, C.-T. (2009). The patient-specific brace design and biomechanical analysis of adolescent idiopathic scoliosis. *J. Biomech. Eng.* 131, 041007. doi:10.1115/1.3049843

Nocedal, J., and Wright, S. J. (2006). *Numerical optimization*. 2e edn. New York, NY, USA: Springer.

Panjabi, M. M., Brand, R. A., Jr, and White, A. A., III (1976). Three-dimensional flexibility and stiffness properties of the human thoracic spine. *J. biomechanics* 9, 185–192. doi:10.1016/0021-9290(76)90003-8

Panjabi, M. M., Oxland, T., Yamamoto, I., and Crisco, J. J. (1994). Mechanical behavior of the human lumbar and lumbosacral spine as shown by three-dimensional load-displacement curves. *J. Bone Jt. Surg.* 76, 413–424. doi:10.2106/00004623-199403000-00012

Pérez, J., Otaduy, M. A., and Thomaszewski, B. (2017). Computational design and automated fabrication of Kirchhoff-plateau surfaces. *ACM Trans. Graph.* 36, 1–12. doi:10.1145/3072959.3073695

Pérez, J., Thomaszewski, B., Coros, S., Bickel, B., Canabal, J. A., Sumner, R., et al. (2015). Design and fabrication of flexible rod meshes. *ACM Trans. Graph.* 34, 1–12. doi:10.1145/2766998

Périé, D., Aubin, C., Petit, Y., Beauséjour, M., Dansereau, J., and Labelle, H. (2003). Boston brace correction in idiopathic scoliosis: A biomechanical study. *Spine* 28, 1672–1677. doi:10.1097/01.brs.0000083165.93936.6d

Raabe, M. E., and Chaudhari, A. M. (2016). An investigation of jogging biomechanics using the full-body lumbar spine model: Model development and validation. *J. biomechanics* 49, 1238–1243. doi:10.1016/j.jbiomech.2016.02.046

Safari, A., Parsaei, H., Zamani, A., and Pourabbas, B. (2019). A semi-automatic algorithm for estimating cobb angle. *J. Biomed. Phys. Eng.* 9, 317–326. doi:10.31661/jbpe.v9i3jun.730

Si, H. (2015). Tetgen, a delaunay-based quality tetrahedral mesh generator. *ACM Trans. Math. Softw.* 41, 1–36. doi:10.1145/2629697

Song, C., Alijani, A., Frank, T., Hanna, G., and Cuschieri, A. (2006). Elasticity of the living abdominal wall in laparoscopic surgery. *J. biomechanics* 39, 587–591. doi:10.1016/j.jbiomech.2004.12.019

Tapia, J., Knoop, E., Mutný, M., Otaduy, M. A., and Bächer, M. (2020). Makesense: Automated sensor design for proprioceptive soft robots. *Soft Robot.* 7, 332–345. doi:10.1089/soro.2018.0162

Taylor, C. J., and Kriegman, D. J. (1994). *Minimization on the lie group SO(3) and related manifolds. Tech. Rep.*. Yale University.

Vergari, C., Chen, Z., Robichon, L., Courtois, I., Ebermeyer, E., Vialle, R., et al. (2020). Towards a predictive simulation of brace action in adolescent idiopathic scoliosis. *Comput. Methods Biomechanics Biomed. Eng.* 24, 874–882. 1–8. doi:10.1080/10255842.2020.1856373

Vergari, C., Courtois, I., Ebermeyer, E., Bouloussa, H., Vialle, R., and Skalli, W. (2016). Experimental validation of a patient-specific model of orthotic action in adolescent idiopathic scoliosis. *Eur. Spine J.* 25, 3049–3055. doi:10.1007/s00586-016-4511-7

Wang, W., Baran, G. R., Betz, R. R., Samdani, A. F., Pahys, J. M., and Cahill, P. J. (2014). The use of finite element models to assist understanding and treatment for scoliosis: A review paper. *Spine Deform.* 2, 10–27. doi:10.1016/j.jspd.2013.09.007

Wilke, H.-J., Herkommer, A., Werner, K., and Liebsch, C. (2017). *In vitro* analysis of the segmental flexibility of the thoracic spine. *PLoS One* 12, e0177823. doi:10.1371/journal.pone.0177823

Wong, C., Adriansen, J., Jeppsen, J., and Balslev-Clausen, A. (2021). Intervariability in radiographic parameters and general evaluation of a low-dose fluoroscopic technique in patients with idiopathic scoliosis. *Acta Radiol. Open* 10, 205846012110432. doi:10.1177/20584601211043258

Xu, M., Yang, J., Lieberman, I. H., and Haddas, R. (2017). Lumbar spine finite element model for healthy subjects: Development and validation. *Comput. methods biomechanics Biomed. Eng.* 20, 1–15. doi:10.1080/10255842.2016.1193596

Zhao, D., Li, Y., Langlois, T., Chaudhuri, S., and Barbic, J. (2021). Ergoboss: Ergonomic optimization of body-supporting surfaces. *IEEE Trans. Vis. Comput. Graph.* 1, 1. doi:10.1109/TVCG.2021.3112127

Biomechanical effects of individualized artificial titanium alloy lamina implantation after laminectomy: A finite element analysis

Xuqiang Gong†, Aobo Zhang, Qing Han†, Yang Wang, Yang Liu, Jianhang Jiao, Jing Yue, Hao Chen, Wangwang Luo, Jincheng Wang* and Minfei Wu*

Department of Orthopedics, The Second Hospital of Jilin University, Changchun, China

Background and objectives: Laminectomy is a common surgical procedure in spine surgery. However, disruption of the posterior ligamentous complex of the spine may lead to a range of postoperative complications. Artificial lamina as a kind of bionic implant can well restore the posterior spinal structure. In this study, an individualized artificial titanium alloy lamina was designed to reconstruct the posterior spinal structure after laminectomy and explored its biomechanical effects, which could provide a theoretical basis for the clinical application of the artificial lamina.

Methods: Three finite element models were constructed, namely the nonlinear and non-homogeneous intact model of the whole lumbar spine, the lumbar decompression alone surgical model, and the artificial lamina implantation surgical model. The range of motion, intradiscal pressure, and annulus fibrosus peak stress were compared between the three models at the surgical and adjacent segments. The stresses of the artificial lamina and fixation screws were also analyzed for the four movement states.

Results: Compared with the intact model, the lumbar decompression alone surgical model showed an increase in range of motion, intradiscal pressure, and annulus fibrosus peak stresses at the surgical segment and adjacent segments under all conditions. The artificial lamina implantation surgical model showed an increase in these measurements only in flexion, increasing by 7.5%−22.5%, 7.6%−17.9%, and 6.4%−19.3%, respectively, over the intact model, while there was little difference under other conditions. The peak stresses in both the screw and the artificial lamina were highest in axial rotation, i. e. 46.53 MPa and 53.84 MPa, respectively. Screw stresses were concentrated on the connection between the screw and the artificial lamina, and artificial lamina stresses were concentrated on the spinous root, around the screw hole, and the contact with the vertebral body.

Conclusion: An individualized artificial titanium alloy lamina can effectively reduce the range of motion, intradiscal pressure, and annulus fibrosus stress at the surgical segment and adjacent segments. The application of artificial lamina

could better preserve the biomechanical properties of the intact lumbar spine and reduce the risk of adjacent segmental disease.

Introduction

Posterior lumbar laminectomy alone is the traditional surgical method for the treatment of symptomatic lumbar spinal stenosis and intraspinal tumors, which allows sufficient decompression and tumor resection by removing the posterior spinal structures (Hamawandi et al., 2019; Wang et al., 2020). However, laminectomy might cause epidural fibrous tissue proliferation in the lamina defect area, thereby developing new compression and increasing the difficulty of revision surgery (Avellanal et al., 2014). More importantly, it is well documented that laminectomy can lead to changes in the biomechanics of the lumbar spine, resulting in lumbar instability (Kim et al., 2015; Veisari and Haghpanahi, 2021). All of these factors may result in the development of failed back surgery syndrome (FBSS) after lumbar spine surgery (Sebaaly et al., 2018).

A large number of researchers have dedicated themselves to developing a vertebral plate replacement to restore the posterior spinal structure to prevent FBSS, and the artificial lamina, as a bionic implant, is well suited to achieve this purpose (Li et al., 2020). Nevertheless, there are few studies on the artificial lamina, especially in biomechanics. Liu et al. (2021) designed an individualized artificial lamina of PEEK material and performed biomechanical analysis to demonstrate the role of the artificial lamina in reconstructing the posterior structure of the lumbar spine and reducing the incidence of postoperative complications in the lumbar spine. However, the PEEK is a biologically inert material that is not conducive to osseointegration (Ma and Tang, 2014). On the contrary, titanium alloy materials have good biocompatibility and are currently the best bio metallic materials and the material of choice for bone implants (Lv et al., 2015; Jing et al., 2020). While to the best of our knowledge, biomechanical analysis of individualized artificial titanium alloy lamina has not been reported.

Therefore, an individualized artificial titanium alloy lamina was designed and biomechanical analysis was performed using the finite element method in this study. Finite element analysis (FEA) can realistically simulate the surgical procedure and the biomechanical effects of the prosthesis on the body (Finley et al., 2018). A three-dimensional nonlinear inhomogeneous finite element model of L1-L5 was developed and two surgical procedures were simulated, including lumbar laminectomy decompression alone (DA) and laminectomy followed by artificial lamina implantation (ALI). By evaluating the biomechanical differences between the three models, we explored the biomechanical properties of the artificial titanium

alloy lamina implanted after laminectomy and expected to provide a theoretical basis for further clinical applications of the artificial lamina.

Materials and methods

FE modeling of the lumbar spine

A three-dimensional nonlinear inhomogeneous FE model of L1-L5 was created based on computed tomography (CT) images of a healthy young male (Figure 1C). The CT images of a participant were obtained at intervals of 0.625 mm (Dual Source CT; Siemens, Munich, Germany). Mimics 21.0 (Materialise, Inc., Leuven, Belgium) was provided to reconstruct the geometric structure of the L1–L5. Initial smoothing and model repair with 3-Matic 13.0 (Materialise, Inc., Leuven, Belgium) and creation of discs, endplates, and facet joints (Figure 1A). These models were then imported into Hypermesh 16.0 (Altair Engineering, Troy, Michigan, United States) for meshing. The vertebral body was divided into a tetrahedral mesh. The intervertebral disc, endplates, and facet joints were divided into a hexahedral mesh. The thickness of the endplate is 0.8 mm, and the thickness of the facet joints is 0.2 mm (Kim et al., 2014). The vertebral body was assigned non-homogeneous values based on CT gray values in Mimics 21.0 software (Materialize, Leuven, Belgium) (Figure 1B) (Rho et al., 1995; Rana et al., 2020). Both the fluid-like behavior of the nucleus pulposus and the hyperelastic properties of the annulus matrix were modeled using the isotropic, incompressible, hyperelastic Mooney-Rivlin formulation (Schmidt et al., 2007). Annulus fibers consist of tension-only truss elements embedded into the annulus matrix, and the fiber stiffness gradually increases from inside to outside (Kim et al., 2014). The anterior longitudinal ligament, posterior longitudinal ligament, intertransverse ligament, ligamentum flavum, capsular ligament, interspinous ligament, and supraspinous ligament were modeled by using tension-only truss elements (Kim et al., 2014; Guo and Fan, 2018; Rana et al., 2020). The files of all models were imported into Abaqus (version 6.14; SIMULIA Inc.) in inp format. Facet joints were approximated by frictionless contact surfaces, and other contact surfaces are defined as Tie (Kim et al., 2014). Finally, nonlinear analysis is carried out in FEA software Abaqus (version 6.14; SIMULIA Inc.). Material properties of tissues of the lumbar spine model were extracted from the literature (Table1).
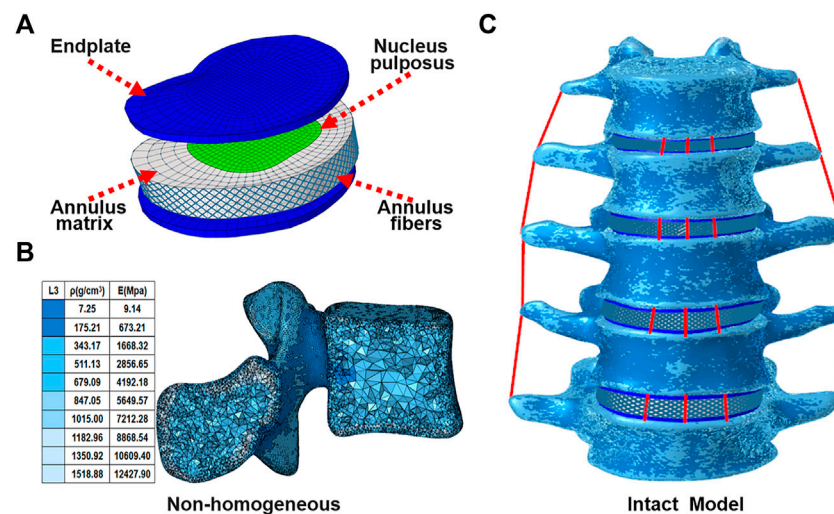
FIGURE 1
FE model of the lumbar spine:**(A)** Disc and endplate,**(B)** Vertebral body,**(C)** L1-L5.

Design of an individualized artificial titanium alloy lamina

The artificial lamina designed in this study is a bionic implant with a shape similar to the *in situ* vertebral plate to ensure successful decompression surgery. The L3 vertebral plate was removed during the laminectomy procedure, and the removed vertebral plate was trimmed, including thinning of the vertebral plate at the root of the spinous process to reduce mass, perforating the posterior spinous process to preserve the posterior ligament to reconstruct the posterior structure, and increasing the ventral curvature of the vertebral plate to expand the volume of the spinal canal so as to provide space for decompression. Finally, the modified lamina served as a template, and the lateral fixation structure was added to its posterior side, with the added lateral fixation structure conforming exactly to the posterior surface of the vertebral body. Holes were punched in the lateral lamina for screw fixation. The length and diameter of the screws were 20 mm and 4.5 mm, respectively. All the above-mentioned operations were performed on a 3-Matic 13.0 (Materialize, Leuven, Belgium). As a result, a complete model of the artificial lamina was obtained, as shown in Figure 2. The artificial lamina and fixation screws were made of Ti6Al4V.

FE model of the surgical procedure

A total of two surgical approaches were simulated and contrasted in this study, namely the lumbar decompression alone surgical model (DA) (Figure 3B) and the artificial lamina implantation surgical model (ALI) (Figure 3C). For the DA surgical model, it was simulated by removing the medial portion of the L3 vertebral body, the supraspinous ligament, the interspinous ligament, and the ligamentum flavum, while preserving the facet joints on both sides. For the ALI surgical model, artificial lamina was implanted in the laminectomy area and the supraspinous ligaments and interspinous ligaments were reconstructed. The material properties of the above devices are shown in Table 1.

Boundary and loading conditions

For all FE models, the lower surface of the L5 vertebrae was constrained. the FE model loading process consisted of two steps. In the first step, a vertical axial preload of 500 N was applied to the upper surface of L1 as a representation of the upper body weight and muscle forces. In the second step, a 10 N-m moment was applied to the top center of the L1 vertebral body to simulate four movements of flexion, extension, lateral bending, and axial rotation for clinical prediction (Biswas et al., 2018; Song et al., 2021).

Results

Model validation

To validate the intact lumbar FE model, the intersegmental ROMs (L1/2, L2/3, L3/4, and L4/5) were compared with previous FE models and *in vitro* experimental results (Panjabi et al., 1994; Umale et al., 2020; Leszczynski et al., 2022) by applying incremental moments of up to 10 N-m at 2.5 N-m intervals to

TABLE 1 Material properties of the model.

Component	Young modulus (MPa)	Cross-section (mm^2)	Poisson's ratio	Element type	References
Vertebrae (L1-L5)	$\rho = 47 + 1.112*HU$ $E = 0.63\rho^{1.35}$		0.3	C3D4	Rho et al. (1995); Rana et al. (2020)
Disc					
Nucleus pulposus	Mooney-Rivlin: c10 = 0.12, c01 = 0.03			C3D8	Schmidt et al. (2007)
Annulus matrix	Mooney-Rivlin: c10 = 0.18, c01 = 0.045			C3D8	Schmidt et al. (2007)
Annulus fibers	360–550		0.3	T3D2	Kim et al. (2014)
Endplate	4,000		0.3	C3D8	Kim et al. (2014)
Facet	23.8		0.4	C3D8	Kim et al. (2014)
Ligament					Kim et al. (2014); Rana et al. (2020)
Anterior longitudinal	7.8 (<12%) 20 (>12%)	63.7		T3D2	
Posterior longitudinal	10 (<11%) 20 (>11%)	20		T3D2	
Ligamentum flavum	15 (<6.2%) 19.5 (>6.2%)	40		T3D2	
Capsular	7.5 (<25%) 32.9 (>25%)	30		T3D2	
Interspinous	10 (<14%) 11.6 (>14%)	40		T3D2	
Supraspinous	8.0 (<20%) 15 (>20%)	30		T3D2	
Intertransverse	10 (<18%) 58.7 (>18%)	1.8		T3D2	
Implants					Kim et al. (2014)
Artificial lamina, screws (Ti6Al4V)	110,000		0.3	C3D4	

the upper surface of L1 for flexion, extension, lateral bending, and axial rotation tests (Figure 4). In addition, the total ROM was compared with previous data in the literature (Rohlmann et al., 2001; Umale et al., 2020) by applying pure moments of 3.75N-m, 7.5N-m, and 7.5N-m moment combined with 280N preload on the upper surface of L1, respectively (Figure 5). After validation, the intersegmental ROM and total ROM of the intact lumbar FE model were consistent with previous literature, indicating that the L1-L5 intact FE model established in this study is valid and applicable for further clinical and experimental studies.

Range of motion

The equations should be inserted in editable format from the equation editor. The ROM of all models in the L2/3, L3/4, and L4/5 segments are presented in Table 2. At the surgical segment (L3/4), the DA model showed the largest increase over the intact model in the flexion condition, followed by extension and axial rotation, which increased the least in lateral bending. The ROM increased by 52.5%, 10.3%, 2.5%, and 20.0% in the four conditions, respectively. In contrast, the ALI model had little effect on ROM, which increased only by 22.5% in flexion compared to the intact model, while remaining virtually unchanged in the other conditions.

At the adjacent segments (L2/3 and L4/5), no significant changes were observed in the DA model under lateral bending and axial rotation conditions. Whereas, the DA model increased by 6%–15% and 14.3%–23% in the cranial adjacent segment (L2/3) and caudal adjacent segment (L4/5) under lateral bending and axial rotation conditions, respectively. On the contrary, the ALI model showed a small change in ROM in the adjacent segment with a magnitude of less than 9.4%.
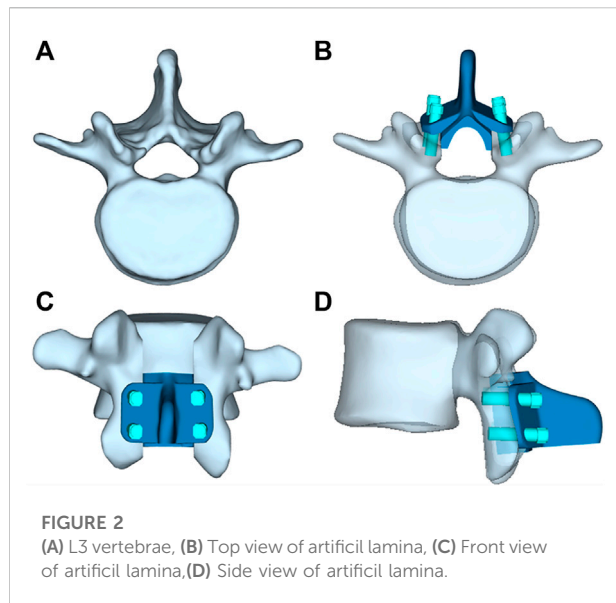
FIGURE 2
(A) L3 vertebrae, **(B)** Top view of artificil lamina, **(C)** Front view of artificil lamina,**(D)** Side view of artificil lamina.
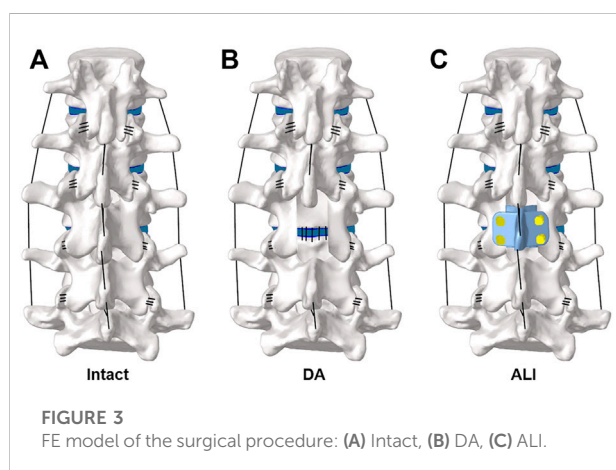

FIGURE 3
FE model of the surgical procedure: **(A)** Intact, **(B)** DA, **(C)** ALI.

Intradiscal pressure and maximum Von Mises stress of the annulus fibrosus

Table 3 shows the IDP and maximum Von Mises stress of the annulus fibrosus at the surgical and adjacent segments. The study indicated that the IDP and annulus fibrosus peak stress of the DA model increased at the surgical segment for all conditions. The increase was most pronounced in flexion, with 53.5% and 57.4% percent, respectively. Under other conditions, the IDP and annulus fibrosus stress peak increased by 0.4%–11.8% and 5.7%–8.9%, respectively. However, the ALI model increased the IDP and annulus fibrosis peak stress by 17.9% and 19.3% over the intact model only in flexion, while the change in all other conditions was less than 7.8%.

The changes in the IDP and annulus fibrosus peak stress for the DA model at adjacent segments were similar to those of the surgical segments, i.e., the increase was most obvious in flexion,

followed by extension, lateral bending, and axial rotation. In flexion, the IDP and annulus fibrosus peak stress increased by 46.7%–49% and 21.6%–44.3% at cranial adjacent segments and caudal adjacent segments, respectively.

Compared to the intact model, the ALI model showed no apparent changes in IDP and annulus fibrosus peak stress in all motion conditions, with changes ranging from 0.2% to 11% and 0.1–10.2%, respectively.

As shown in Figure 6, the disc stresses are mainly concentrated on the edges of the disc under different motion conditions. In flexion and extension, the stresses were concentrated on the anterior and posterior sides of the disc. Similarly, in lateral bending, there was an obvious stress concentration on the compressed side of the disc and a tendency to decrease gradually toward the center of the disc. In axial rotation, the disc stress was concentrated on the lateral anterior side in the direction of axial rotation.

Von Mises stress in the artificial lamina and screws

Figure 7 shows the stress peak for screws and artificial laminas under different conditions. The peak stresses of the screws were 12.0 MPa, 21.3 MPa, 8.3 MPa, and 46.53 MPa in flexion, extension, lateral bending, and axial rotation, respectively, while the peak stresses of the artificial lamina were 19.6 MPa, 33.9 MPa, 17.8 MPa, and 53.84 MPa, respectively. In addition, the stress distributions of the screws and artificial lamina are shown in Figure 8. Under different conditions, the stresses of the fixed screws are mainly concentrated at the connection between the screws and the artificial lamina. The stresses in the artificial lamina were mainly concentrated at the root of the spinous process, around the screw hole, and at contact with the vertebral body. Moreover, there was an obvious stress concentration under the spinous process during flexion due to the stretching effect of the ligaments.

Discussion

The artificial lamina can reconstruct the posterior ligamentous complex (PLC) after laminectomy to restore lumbar stability and provide a good mechanical barrier against epidural fibrous tissue proliferation, thereby reducing the incidence of FBSS (Lv et al., 2013; Li et al., 2020; Liu et al., 2021). However, a satisfactory match between the artificial lamina and the posterior spinal structure as well as the choice of artificial lamina material is crucial to restoring the function of the posterior spinal structure. Individualized reverse engineering methods are applied to build artificial lamina that can perfectly match posterior spinal structures with complex morphology.

FIGURE 4
Comparison of the intersegmental ROM between the present intact model and the outcomes of previous publications under pure moments of 2.5N-m,5N-m,7.5n-m, and 10N-m conditions at **(A)** L1-2, **(B)** L2-3, **(C)** L3-4, and **(D)** L4-5. Error bars represent standard deviation.
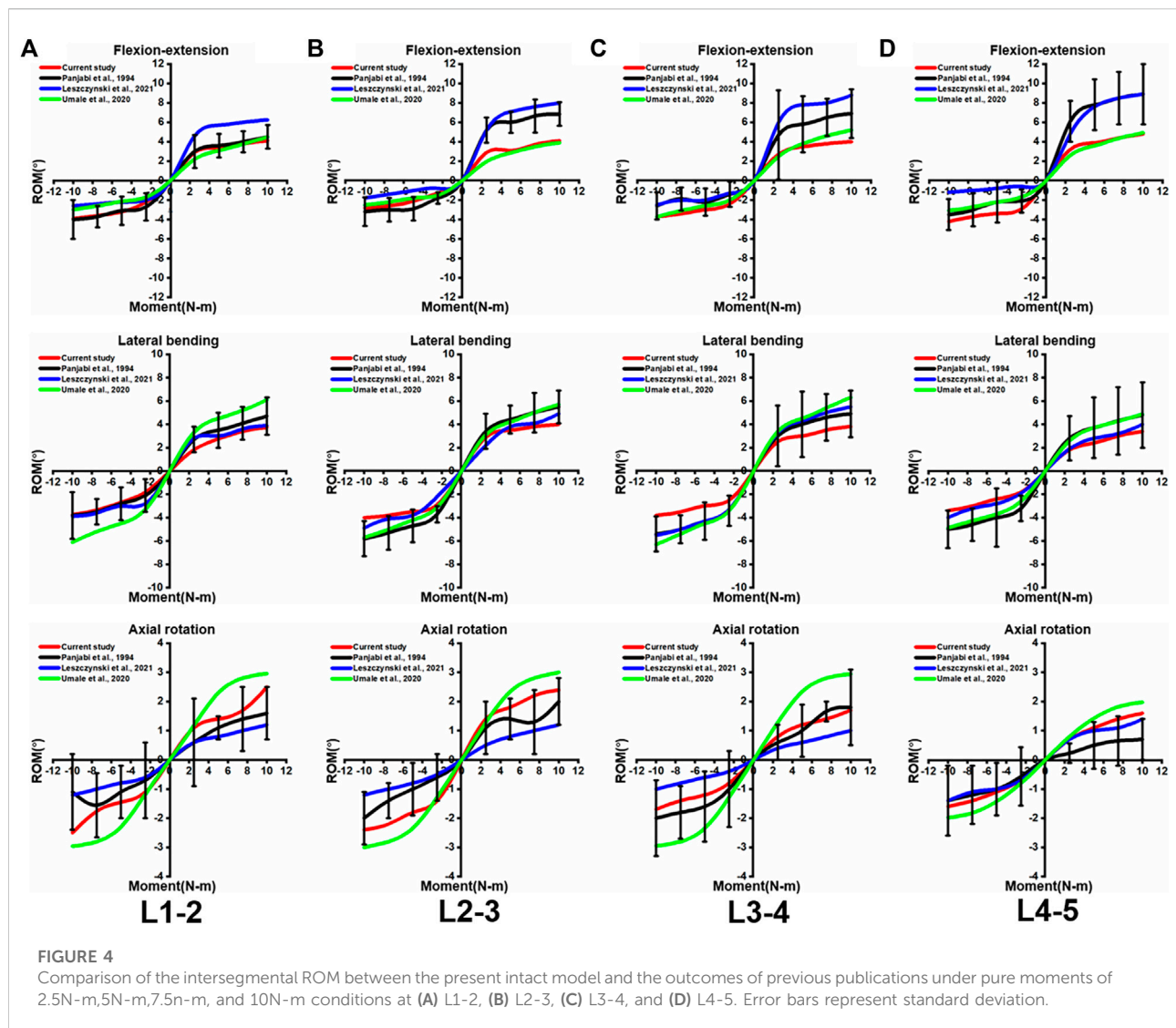
Titanium alloy material is the best substrate material for 3D printing of orthopedic implants because of its good mechanical strength and biocompatibility (Lv et al., 2015; Jing et al., 2020). Therefore, an individualized artificial titanium alloy lamina may be the best option to repair the defective area of the vertebral plate after laminectomy.

In this study, an individualized artificial titanium alloy lamina was designed based on lamina reimplantation and the ALI model was simulated like lamina reimplantation. Lamina reimplantation has previously been shown in studies to achieve good clinical results with reconstructed PLC (Li et al., 2019). A nonlinear inhomogeneous FE model of the whole lumbar spine was developed and simulated for both DA and ALI procedures to evaluate the biomechanical effects of the implanted artificial lamina. Briefly, the artificial lamina is implanted after laminectomy with preservation of the supraspinous and interspinous ligaments and then fixed with short screws to

reduce the difficulty of the surgical procedure. At the same time, the supraspinous and interspinous ligaments are secured to the artificial lamina with silk threads. The lateral flanks of our artificial lamina fit closely to the residual bone surface, adequately filling the bone defect area and ensuring sufficient decompression space by increasing its ventral curvature. Then FEA was performed to measure the relevant indicators, including ROM, IDP, and annulus fibrosus peak stress at the surgical segment and adjacent segments.

The traditional laminectomy usually requires sacrificing the PLC to achieve the surgical purpose. However, PLC has a significant stabilizing effect on the spine and can restrict hyperflexion of the spine (Solomonow et al., 1998; Wu et al., 2018). As shown in our findings, the ROM of both the surgical and adjacent segments increased after laminectomy. In particular, the increase in ROM at the surgical level was most pronounced in flexion and axial rotation, with increases of 52.5%
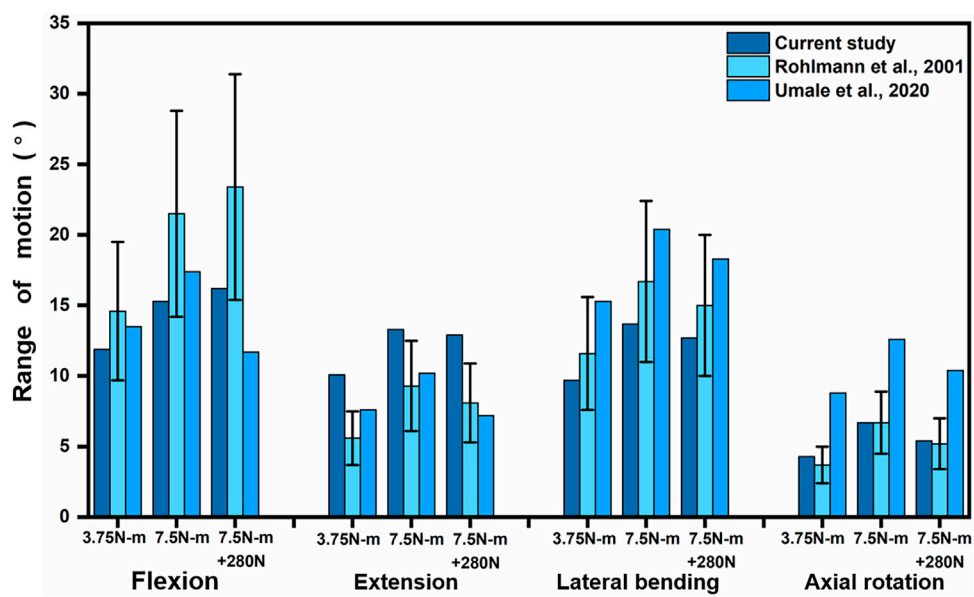
FIGURE 5
Comparison of L1-L5 total ROM between the present model and the results of previous publications under pure moments of 3.75N-m and 7.5N-m as well as 7.5N-m moments combined with 280N preload conditions at Flexion, extension, lateral bending, and axial rotation. Error bars represent standard deviation.

TABLE 2 ROM of the surgical segment and adjacent segment (°).

		Flexion	Extension	Later bending	Axial rotation
Intact	L2/3	4.0	3.2	4.1	2.7
	L3/4	4.0	3.9	4.0	2.0
	L4/5	4.9	4.4	3.5	1.8
DA	L2/3	3.4	3.4	4.1	2.7
	L3/4	6.1	4.3	4.1	2.4
	L4/5	5.6	4.5	3.5	1.8
ALI	L2/3	4.3	2.9	4.1	2.8
	L3/4	4.9	3.7	4.0	2.0
	L4/5	5.3	4.4	3.5	1.9

and 20%, respectively, which is consistent with the findings of Kim et al. (2015). Therefore, patients who were subjected to laminectomy should avoid hyperflexion and excessive axial rotation. Compared to the intact model, the ALI model increased the ROM of the surgical level in flexion by only 22.5%, and the rest of the conditions had a little change in ROM by 5%. In addition, compared with the DA model, the ROM at the surgical level of the ALI model was reduced by approximately 30% and 20% in flexion and axial rotation, respectively. It is because the ALI model restores the posterior tension band of the lumbar spine and reconstructs the PLC structure, in which the lamina is resistant to axial rotation and the

posterior tension band is resistant to flexion. The study showed that preserving the posterior tension band structure is beneficial for improving lumbar symptoms, reducing the incidence of complications, and providing early recovery of function (Xue et al., 2022). Interestingly, Gillespie and Dickey, (2004) found through their study that the contribution of the ligamentum flavum to resist flexion was 24.7%. In the present study, the ROM of the ALI model in flexion was still increased after PLC reconstruction, which might be attributed to ligamentum flavum failure to reconstruct. However, it was generally found that the ALI model had less effect on ROM, which highlights the ability of the artificial lamina to not only

TABLE 3 Intradiscal pressure and maximum Von Mises stress of the annulus fibrosus (MPa).

		Flexion		Extension		Lateral bending		Axial rotation	
		IDP	Annulus fibrosus stress	IDP	Annulus fibrosus stress	IDP	Annulus fibrosus stress	IDP	Annulus fibrosus stress
Intact	L2/3	0.429	1.181	0.473	1.714	0.570	1.335	0.308	0.658
	L3/4	0.385	1.157	0.570	2.108	0.514	1.667	0.277	0.665
	L4/5	0.409	0.982	0.570	1.335	0.456	1.572	0.216	0.707
DA	L2/3	0.639	1.704	0.529	1.811	0.584	1.376	0.313	0.677
	L3/4	0.591	1.821	0.586	2.163	0.591	1.816	0.278	0.713
	L4/5	0.469	1.194	0.584	1.376	0.468	1.618	0.218	0.721
ALI	L2/3	0.476	1.257	0.440	1.580	0.571	1.334	0.307	0.655
	L3/4	0.454	1.380	0.563	2.088	0.512	1.651	0.274	0.651
	L4/5	0.440	1.082	0.571	1.334	0.456	1.571	0.216	0.706

reconstruct the stability of the spine but also to preserve the original ROM of the spine.

In this study, the IDP and the annulus fibrosus stresses were increased in both the surgical segment and the adjacent segment after laminectomy, especially in flexion. Compared with the intact model, the IDP and annulus fibrosus stresses at the surgical segment and the adjacent segments increased by 21.6%–53.5% in the DA model in flexion, while only 6.4%–19.3% in the ALI model. The IDP and annulus fibrosus stresses were also slightly greater in the DA model than in the ALI model under other conditions. This may be due to the fact that when the PLC is damaged, the posterior spinal structures lose their resistance to compressive forces and most of the compressive forces are transferred to the intervertebral disc (Merter et al., 2019). A spinous osteotomy study showed that preserving the PLC can reduce disc stresses in the decompressed segment (Li et al., 2017). Huang et al. (2016) found that preservation of the PLC in posterior lumbar interbody fusion surgery was effective in preventing the incidence of adjacent segmental disease (ASD). Furthermore, another study also found that laminectomy alone also caused ASD (Bydon et al., 2016). As shown in our results, increased IDP and annulus fibrosus stress at adjacent segments after laminectomy probably resulted in it. Therefore, we could deduce that artificial lamina is helpful to prevent ASD and reduce disc stress in the decompressed segment by restoring posterior spinal structures. The ligamentum flavum can create a resistance effect in flexion to reduce stresses in the anterior part of the disc (Merter et al., 2019), so the IDP and annulus fibrosus stresses of the ALI model are increased in flexion. Our results also confirm that the posterior

spinal structures have a greater influence on disc stress values and a smaller influence on disc stress distribution, which is consistent with the description by Zander et al. (2003).

The stress distribution of the artificial lamina is gradually dispersed along with the spinal roots. The maximum stress occurs in axial rotation and is mainly concentrated on the contact surface between the artificial lamina and the vertebral body. The stresses on the fixation screws were also greatest in axial rotation and were mainly concentrated on the contact between the screws and the artificial lamina. This suggests that the lamina produces greater resistance stresses in axial rotation, which is consistent with the findings reported by Liu et al. (2021). Besides, a titanium plate fixation with lamina reimplantation found that restoration of the posterior spinal structures maintained resistance to axial rotation and maintained spinal stability (Nong et al., 2015). Another interesting phenomenon is that a significant stress concentration occurs in flexion at the artificial lamina-ligamentous junction, while not in other conditions, which is determined by the characteristic of the ligament being subjected to only tension and not pressure. Therefore, excessive flexion should be avoided after the implantation of the artificial lamina.

In conclusion, the artificial lamina can decrease ROM, IDP, and annulus fibrosus stresses at the surgical segment and adjacent segments by reconstructing PLC, which demonstrates biomechanically the role of artificial titanium lamina in stabilizing the lumbar spine and reducing ASD.

There are still some limitations in this study. In the study of Elmasry et al. (2017); Elmasry et al. (2018), the intervertebral disc
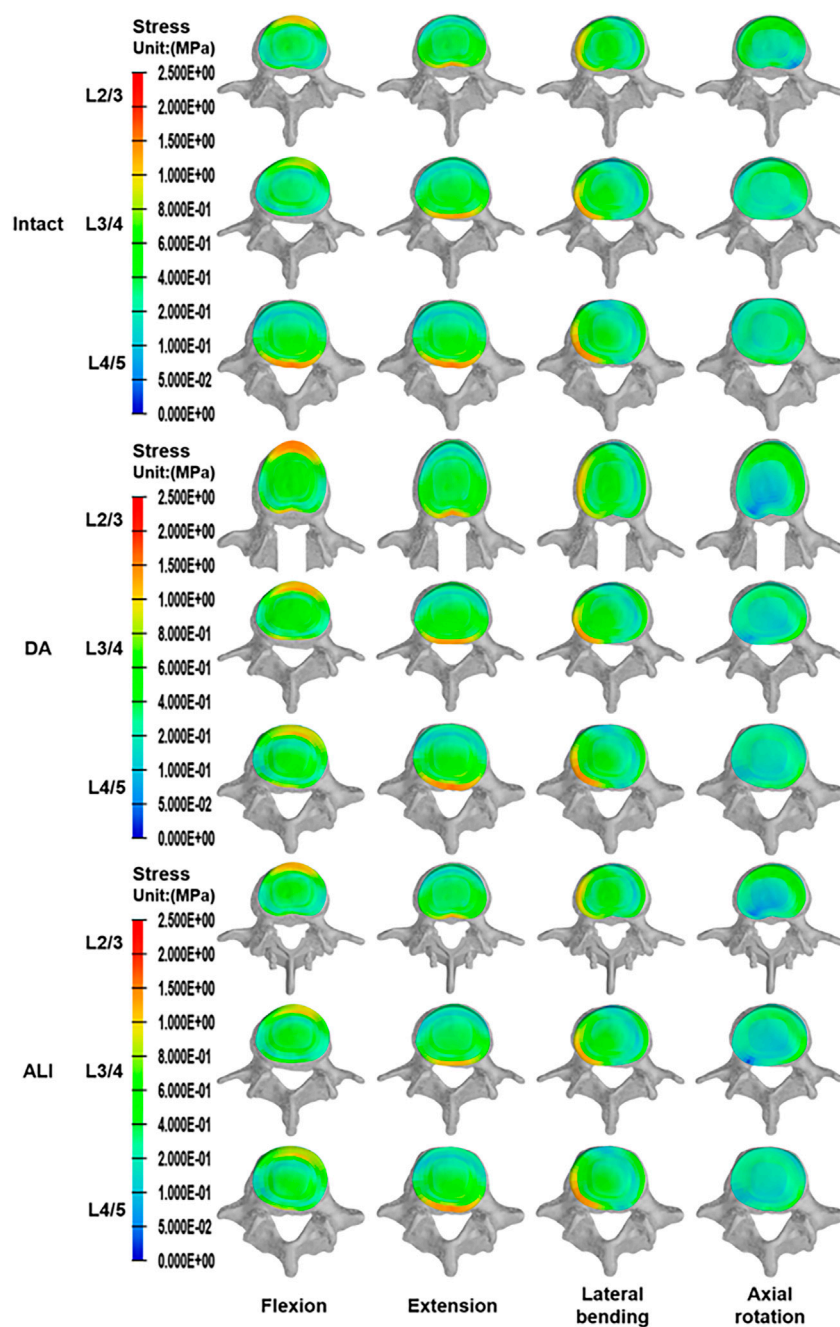
FIGURE 6
The distribution of disc stress at the surgical segment and adjacent segments.

was defined as poroelastic material, consisting of a solid phase embedded in a fluid media, which is more in line with the real disc material properties, whereas in the present experiments the disc was only defined as a simple hyperelastic material, so the modeling approach needs further refinement. Since the elastic modulus of titanium alloy is 9.2 times higher than cortical bone, the stress shielding phenomenon and stress concentration are

inevitable. Topology optimization techniques can effectively decrease the modulus of elasticity of the prosthesis to avoid stress shielding (Bartolomeu et al., 2020). Therefore, the manufacture of topologically optimized individualized artificial lamina for clinical treatment is a better choice. In addition, the experiment still needs further animal or in vitro-related experiments to validate.
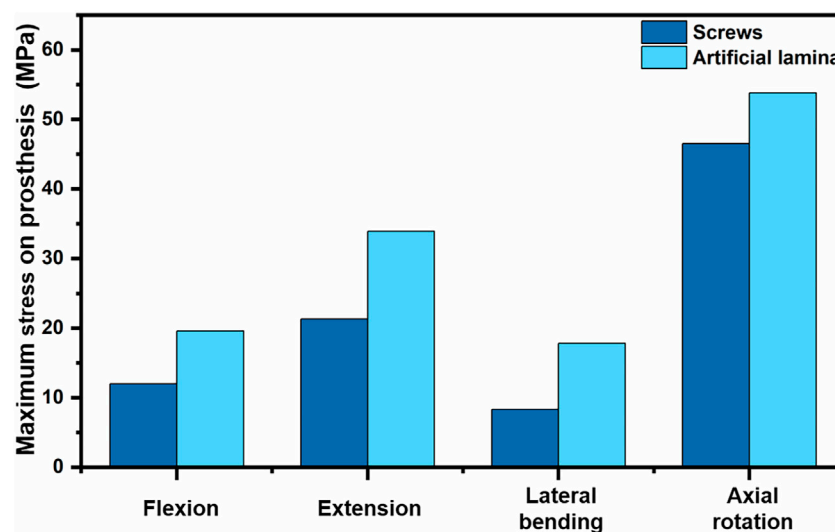
FIGURE 7
Stresses in the screws and artificial lamina.
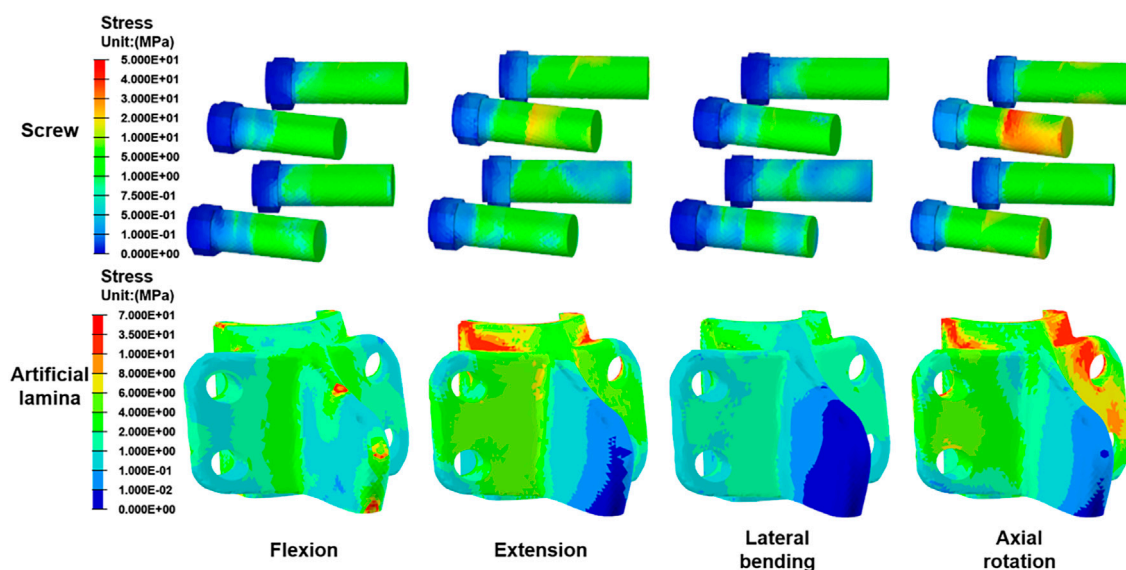
FIGURE 8
The stress distribution of screws and artificial lamina in all conditions.

Conclusion

Compared with the DA model, the ALI model reduces ROM, IDP, and annulus fibrosus stresses at the surgical segment and adjacent segments. The ALI model better preserves the biomechanical properties of the intact lumbar spine. It is biomechanically demonstrated that the artificial lamina has

the potential advantage of reducing the risk of ASD. However, there is still a degree of hypermobility and increased disc stress in flexion after artificial lamina implantation, so patients undergoing artificial lamina implantation should avoid excessive flexion that could cause secondary injury. These findings are expected to provide a theoretical basis for the further clinical application of the artificial lamina.

Data availability statement

The original contributions presented in the study are included in the article/supplementary material, further inquiries can be directed to the corresponding authors.

Ethics statement

The studies involving human participants were reviewed and approved by the Ethics Committee of the Second Hospital of Jilin University. The patients/participants provided their written informed consent to participate in this study.

Author contributions

XG: experimental design and writing—original manuscript preparation; AZ: data organization and software operation; QH: reviewing, and editing; YW and YL: drawing; JJ and JY: table making; HC: data analysis; WL: supervision and validation; JW and MW: supervision, conceptualization and funding acquisition.

Funding

Conflict of interest

The authors declare that the research was conducted in the absence of any commercial or financial relationships that could be construed as a potential conflict of interest.

Publisher's note

All claims expressed in this article are solely those of the authors and do not necessarily represent those of their affiliated organizations, or those of the publisher, the editors and the reviewers. Any product that may be evaluated in this article, or claim that may be made by its manufacturer, is not guaranteed or endorsed by the publisher.

References

Avellanal, M., Diaz-Reganon, G., Orts, A., and Soto, S. (2014). One-year results of an algorithmic approach to managing failed back surgery syndrome. *Pain Res. Manag.* 19 (6), 313–316. doi:10.1155/2014/474510

Bartolomeu, F., Dourado, N., Pereira, F., Alves, N., Miranda, G., and Silva, F. S. (2020). Additive manufactured porous biomaterials targeting orthopedic implants: A suitable combination of mechanical, physical and topological properties. *Mater. Sci. Eng. C* 107, 110342. doi:10.1016/j.msec.2019.110342

Biswas, J. K., Rana, M., Majumder, S., Karmakar, S. K., and Roychowdhury, A. (2018). Effect of two-level pedicle-screw fixation with different rod materials on lumbar spine: A finite element study. *J. Orthop. Sci.* 23 (2), 258–265. doi:10.1016/j.jos.2017.10.009

Bydon, M., Macki, M., De la Garza-Ramos, R., McGovern, K., Sciubba, D. M., Wolinsky, J. P., et al. (2016). Incidence of adjacent segment disease requiring reoperation after lumbar laminectomy without fusion: A study of 398 patients. *Neurosurgery* 78 (2), 192–199. doi:10.1227/NEU.0000000000001007

Elmasry, S., Asfour, S., and Travascio, F. (2017). Effectiveness of pedicle screw inclusion at the fracture level in short-segment fixation constructs for the treatment of thoracolumbar burst fractures: A computational biomechanics analysis. *Comput. Methods Biomech. Biomed. Engin.* 20 (13), 1412–1420. doi:10.1080/10255842.2017.1366995

Elmasry, S. S., Asfour, S. S., and Travascio, F. (2018). Finite element study to evaluate the biomechanical performance of the spine after augmenting percutaneous pedicle screw fixation with kyphoplasty in the treatment of burst fractures. *J. Biomech. Eng.* 140 (6). doi:10.1115/1.4039174

Finley, S. M., Brodke, D. S., Spina, N. T., DeDen, C. A., and Ellis, B. J. (2018). FEBio finite element models of the human lumbar spine. *Comput. Methods Biomechanics Biomed. Eng.* 21 (6), 444–452. doi:10.1080/10255842.2018.1478967

Gillespie, K. A., and Dickey, J. P. (2004). Biomechanical role of lumbar spine ligaments in flexion and extension: Determination using a parallel linkage robot and a porcine model. *Spine* 29 (11), 1208–1216. doi:10.1097/00007632-200406010-00010

Guo, L. X., and Fan, W. (2018). Dynamic response of the lumbar spine to whole-body vibration under a compressive follower preload. *Spine* 43 (3), E143–E153. doi:10.1097/BRS.0000000000002247

Hamawandi, S. A., SulaimanII, and Al-Humairi, A. K. (2019). Microdecompression versus open laminectomy and posterior stabilization for multilevel lumbar spine stenosis: A randomized controlled trial. *Pain Res. Manag.* 2019, 1–6. doi:10.1155/2019/7214129

Huang, Y. P., Du, C. F., Cheng, C. K., Zhong, Z. C., Chen, X. W., Wu, G., et al. (2016). Preserving posterior complex can prevent adjacent segment disease following posterior lumbar interbody fusion surgeries: A finite element analysis. *Plos One* 11 (11), e0166452. doi:10.1371/journal.pone.0166452

Jing, Z. H., Zhang, T., Xiu, P., Cai, H., Wei, Q. G., Fan, D. Y., et al. (2020). Functionalization of 3D-printed titanium alloy orthopedic implants: A literature review. *Biomed. Mat.* 15 (5), 052003. doi:10.1088/1748-605X/ab9078

Kim, H. J., Chun, H. J., Kang, K. T., Lee, H. M., Chang, B. S., Lee, C. K., et al. (2015). Finite element analysis for comparison of spinous process osteotomies

technique with conventional laminectomy as lumbar decompression procedure. *Yonsei Med. J.* 56 (1), 146–153. doi:10.3349/ymj.2015.56.1.146

Kim, H. J., Kang, K. T., Chang, B. S., Lee, C. K., Kim, J. W., and Yeom, J. S. (2014). Biomechanical analysis of fusion segment rigidity upon stress at both the fusion and adjacent segments: A comparison between unilateral and bilateral pedicle screw fixation. *Yonsei Med. J.* 55 (5), 1386–1394. doi:10.3349/ymj.2014.55.5.1386

Leszczynski, A., Meyer, F., Charles, Y. P., Deck, C., and Willinger, R. (2022). Development of a flexible instrumented lumbar spine finite element model and comparison with *in-vitro* experiments. *Comput. Methods Biomech. Biomed. Engin.* 25 (2), 221–237. doi:10.1080/10255842.2021.1948021

Li, J. W., Li, S. B., Liu, X. Y., Wei, F. X., Wang, X. S., Fang, G. J., et al. (2020). Individualized artificial titanium alloy spinal lamina with 3D printing technology. *Mat. express* 10 (5), 648–656. doi:10.1166/mex.2020.1678

Li, Q. Y., Kim, H. J., Son, J., Kang, K. T., Chang, B. S., Lee, C. K., et al. (2017). Biomechanical analysis of lumbar decompression surgery in relation to degenerative changes in the lumbar spine - validated finite element analysis. *Comput. Biol. Med.* 89, 512–519. doi:10.1016/j.compbiomed.2017.09.003

Li, Y., Wang, H., Cui, W., Zhou, P., Li, C., Xiao, W., et al. (2019). Treatment of benign tumors in thoracic spinal canal by modified replanting posterior ligament complex applying piezoelectric osteotomy. *Zhongguo xiu fu chong jian wai ke za zhi* 33 (8), 991–995. doi:10.7507/1002-1892.201811126

Liu, L., Ma, H. Y., Yuan, Q. L., Zhao, X. M., Lou, X. X., and Zhang, Y. G. (2021). Biomechanical effects of reconstruction of the posterior structures after laminectomy with an individualized poly-ether-ether-ketone (PEEK) artificial lamina. *J. Biomater. Appl.* 35 (10), 1327–1336. doi:10.1177/0885328220981191

Lv, C. L., Zhou, Z. J., Song, Y. M., Liu, L. M., Liu, H., Gong, Q., et al. (2013). Novel biodegradable lamina for lamina repair and reconstruction. *Spine J.* 13 (12), 1912–1920. doi:10.1016/j.spinee.2013.06.055

Lv, J., Jia, Z. J., Li, J., Wang, Y. N., Yang, J., Xiu, P., et al. (2015). Electron beam melting fabrication of porous Ti6Al4V scaffolds: Cytocompatibility and osteogenesis. *Adv. Eng. Mat.* 17 (9), 1391–1398. doi:10.1002/adem.201400508

Ma, R., and Tang, T. T. (2014). Current strategies to improve the bioactivity of PEEK. *Int. J. Mol. Sci.* 15 (4), 5426–5445. doi:10.3390/ijms15045426

Merter, A., Karaca, M. O., and Yazar, T. (2019). Biomechanical effects of sequential resection of the posterior ligamentous complex on intradiscal pressure and resistance to compression forces. *Acta Orthop. Traumatologica Turcica* 53 (6), 502–506. doi:10.1016/j.aott.2019.08.016

Nong, L. M., Zhou, D., Xu, N. W., Du, R., and Jiang, X. J. (2015). Lamina replacement with titanium plate fixation improves spinal stability after total lumbar laminectomy. *Comput. Methods Biomechanics Biomed. Eng.* 18 (16), 1753–1759. doi:10.1080/10255842.2014.953491

Panjabi, M. M., Oxland, T. R., Yamamoto, I., and Crisco, J. J. (1994). Mechanical behavior of the human lumbar and lumbosacral spine as shown by three-dimensional load-displacement curves. *J. Bone Jt. Surg.* 76 (3), 413–424. doi:10.2106/00004623-199403000-00012

Rana, M., Roy, S., Biswas, P., Biswas, S. K., and Biswas, J. K. (2020). Design and development of a novel expanding flexible rod device (frd) for stability in the lumbar spine: A finite-element study. *Int. J. Artif. Organs* 43 (12), 803–810. doi:10.1177/0391398820917390

Rho, J. Y., Hobatho, M. C., and Ashman, R. B. (1995). Relations of mechanical properties to density and CT numbers in human bone. *Med. Eng. Phys.* 17 (5), 347–355. doi:10.1016/1350-4533(95)97314-F

Rohlmann, A., Neller, S., Claes, L., Bergmann, G., and Wilke, H. J. (2001). Influence of a follower load on intradiscal pressure and intersegmental rotation of the lumbar spine. *Spine (Phila Pa 1976)* 26 (24), E557–E561. doi:10.1097/00007632-200112150-00014

Schmidt, H., Kettler, A., Heuer, F., Simon, U., Claes, L., and Wilke, H. J. (2007). Intradiscal pressure, shear strain, and fiber strain in the intervertebral disc under combined loading. *Spine* 32 (7), 748–755. doi:10.1097/01.brs.0000259059.90430.c2

Sebaaly, A., Lahoud, M. J., Rizkallah, M., Kreichati, G., and Kharrat, K. (2018). Etiology, evaluation, and treatment of failed back surgery syndrome. *Asian Spine J.* 12 (3), 574–585. doi:10.4184/asj.2018.12.3.574

Solomonow, M., Zhou, B. H., Harris, M., Lu, Y., and Baratta, R. V. (1998). The ligamento-muscular stabilizing system of the spine. *Spine* 23 (23), 2552–2562. doi:10.1097/00007632-199812010-00010

Song, M., Sun, K., Li, Z., Zong, J., Tian, X., Ma, K., et al. (2021). Stress distribution of different lumbar posterior pedicle screw insertion techniques: A combination study of finite element analysis and biomechanical test. *Sci. Rep.* 11 (1), 12968. doi:10.1038/s41598-021-90686-6

Umale, S., Yoganandan, N., and Kurpad, S. N. (2020). Development and validation of osteoligamentous lumbar spine under complex loading conditions: A step towards patient-specific modeling. *J. Mech. Behav. Biomed. Mat.* 110, 103898. doi:10.1016/j.jmbbm.2020.103898

Veisari, S. F., and Haghpanahi, M. (2021). Implications of different types of decompression spinal stenosis surgical procedures on the biomechanics of lumbar spine. *J. Med. Biol. Eng.* 41 (1), 71–76. doi:10.1007/s40846-020-00580-1

Wang, Z. C., Li, S. Z., Sun, Y. L., Yin, C. Q., Wang, Y. L., Wang, J., et al. (2020). Application of laminoplasty combined withARCHPlate in the treatment of lumbar intraspinal tumors. *Orthop. Surg.* 12 (6), 1589–1596. doi:10.1111/os.12758

Wu, C. C., Jin, H. M., Yan, Y. Z., Chen, J., Wang, K., Wang, J. L., et al. (2018). Biomechanical role of the thoracolumbar ligaments of the posterior ligamentous complex. A finite element study. *World Neurosurg.* 112, E125–E133. doi:10.1016/j.wneu.2017.12.171

Xue, Y., Li, S., Wang, Y., Zhang, H., Cheng, L., Wu, Y., et al. (2022). Unilateral modified posterior lumbar interbody fusion combined with contralateral lamina fenestration treating severe lumbarspinal stenosis: A retrospective clinical study. *Surg. Innov.*, 0(0), 1–11. doi:10.1177/15533506221096016

Zander, T., Rohlmann, A., Klockner, C., and Bergmann, G. (2003). Influence of graded facetectomy and laminectomy on spinal biomechanics. *Eur. Spine J.* 12 (4), 427–434. doi:10.1007/s00586-003-0540-0

Check for updates

Elucidation of target implant orientations with the safety range of hip rotation with adduction or abduction during squatting: Simulation based on *in vivo* replaced hip kinematics

Satoru Harada[1], Satoshi Hamai[1,2]*, Satoru Ikebe[3],
Daisuke Hara[1,4], Hidehiko Higaki[5], Hirotaka Gondo[5],
Shinya Kawahara[1], Kyohei Shiomoto[1], Tetsunari Harada[1] and
Yasuharu Nakashima[1]

[1]Department of Orthopaedic Surgery, Graduate School of Medical Sciences, Kyushu University,
Higashi-ku, Fukuoka, Japan, [2]Department of Medical-Engineering Collaboration for Healthy
Longevity, Kyushu University, Higashi-ku, Fukuoka, Japan, [3]Department of Creative Engineering,
National Institute of Technology, Kitakyushu College, Kitakyushu, Fukuoka, Japan, [4]Department of
Artificial Joints and Biomaterials, Faculty of Medical Science, , Kyushu University, Higashi-ku, Fukuoka,
Japan, [5]Department of Birobotics, Faculty of Engineering, Kyushu Sangyo University, Higashi-ku,
Fukuoka, Japan

Objectives: The study aimed to elucidate target cup orientation and stem anteversions to avoid impingement between the liner and stem neck even at hip rotation with adduction during the deeply flexed posture.

Methods: A computer simulation analysis was performed on 32 total hip arthroplasty patients applying patient-specific orientation of the components and *in vivo* hip kinematics obtained from three-dimensional analysis of the squatting motion. The anterior/posterior liner-to-neck distance and impingement were evaluated based on a virtual change in internal/external rotation (0°–60°) and adduction/abduction (0°–20°) at actual maximum flexion/extension during squatting. Cutoff values of cup orientations, stem anteversion, and combined anteversion to avoid liner-to-neck impingements were determined.

Results: The anterior liner-to-neck distance decreased as internal rotation or adduction increased, and the posterior liner-to-neck distance decreased as external rotation or adduction increased. Negative correlations were found between anterior/posterior liner-to-neck distances at maximum flexion/extension and internal/external rotation. Anterior/posterior liner-to-neck impingements were observed in 6/18 hips (18/56%) at 45° internal/external rotation with 20° adduction. The range of target cup anteversion, stem anteversion, and combined anteversion to avoid both anterior and posterior liner-to-neck impingements during squatting were 15°–18°, 19°–34°, and 41°–56°, respectively.

Conclusion: Simulated hip rotations caused prosthetic impingement during squatting. Surgeons could gain valuable insights into target cup orientations and stem anteversion based on postoperative simulations during the deeply flexed posture.

Introduction

Total hip arthroplasty (THA) is recognized as an effective surgical treatment for end-stage osteoarthritis (OA) of the hip joint, osteonecrosis of the femoral head (ONFH), and other severe hip diseases to eliminate pain and improve hip function and patient activity with a high level of patient satisfaction (Berry et al., 2002; Ethgen et al., 2004; Mont et al., 2015; Hamai et al., 2016; Hara et al., 2018; Shiomoto et al., 2019). Nevertheless, dislocation after THA remains a major cause of revision despite innovations in prostheses and surgical techniques (Nakashima et al., 2014; Saiz et al., 2019; Shoji et al., 2020; Harada et al., 2021). The revision rate for THA patients with the 32-mm head due to dislocation was 0.60–0.72% at 6-year follow-up (Zijlstra et al., 2017; Hoskins et al., 2022). Even prosthetic impingement between the liner and stem neck (liner-to-neck impingement) is a risk factor for dislocation and accelerated wear and linear fractures, which affect the longevity of implants (Marchetti et al., 2011; Miki et al., 2013).

Squatting is a routine activity in many cultures and requires a greater range of motion of the hip joint (Sugano et al., 2012; Cheatham et al., 2018). Previous reports suggest that *in vivo* squatting kinematics offer no danger of impingement or subsequent dislocation after THA due to sufficient distance between the liner and stem neck (liner-to-neck distance); however, an unintentional internally rotated and adducted posture and lower cup anteversion still remain at risks for posterior dislocation (Harada et al., 2022a). During further analyses in the latter study, simulated unintentional hip rotation was performed without potential disadvantages for dislocation to define impingement-free implant alignment with a safety range of hip rotation. Although there have been several studies on target component orientations simulating impingement using preoperative computed tomography (CT) data (Murphy et al., 2018; Shoji et al., 2020; Vigdorchik et al., 2020), they may not reflect the actual limb position during movement due to a lack of *in vivo* data.

The purpose of the present study, therefore, was to assess the liner-to-neck distance during squatting by changing internal/external rotation and adduction/abduction under a more realistic simulation, which incorporated patient-specific component placements and actual kinematics. In particular, the following question was addressed: What are the target orientations of the components to achieve no liner-to-neck impingement even in an unintentional "dislocation-prone" posture during squatting?

Materials and methods

Participants

Between February 2011 and December 2015, a total of 543 patients underwent cementless THA at a single university hospital. Of these, 499 satisfied the following inclusion criteria: 1) alive at the time of the survey, 2) > 1 year since the last surgery, 3) evaluation by a surgeon <1 year, 4) no revision surgery, and 5) no severe dementia or unrelated physical disorder. The survey questionnaire was mailed to all patients, of which 328 patients completed it. The original question investigated the ease of squatting, which was surveyed with four options: 1) yes, "easily possible," 2) yes, "possible with some support," 3) no, "impossible," and 4) no, "have not tried" (Harada et al., 2022a). The subjects were recruited randomly for the study from 211 patients who answered "easily possible" and "possible with some support." All patients gave informed consent for their data to be included in this institutional review board (IRB number 30–91) approved study. Eligible patients

TABLE 1 Demographic and radiographic data.

Hips, n = 32; patients, n = 30

Age at surgery[a], y	62.9 ± 9.3 (47–84)
Sex (male; female), hips	14; 18
Body mass index[a], kg/m²	22.8 ± 3.2 (17.7–32.2)
Diagnosis (OA; ONFH), hips	27; 5
Follow-up[a], y	7.4 ± 1.9 (5.4–8.9)
Preoperative Harris hip score[a], points	48.5 ± 13.2 (27–81)
Postoperative Harris hip score[a], points	95.6 ± 3.6 (90–100)
Cup size (48; 50; 52; 54 mm), hips	17; 5; 7; 3
Stem size (#10; 11; 12; 13; 14), hips	6; 3; 12; 9; 2
Prosthetic head diameter (32 mm)	32
Cup inclination[a], degree	38.1 ± 5.8 (27–48)
Cup anteversion[a], degree	16.4 ± 6.0 (4–32)
Stem anteversion[a], degree	33.6 ± 11.4 (7–60)

OA, osteoarthrosis; ONFH, osteonecrosis of the femoral head.
[a]Values are given as the mean ± standard deviations with the range in parentheses.
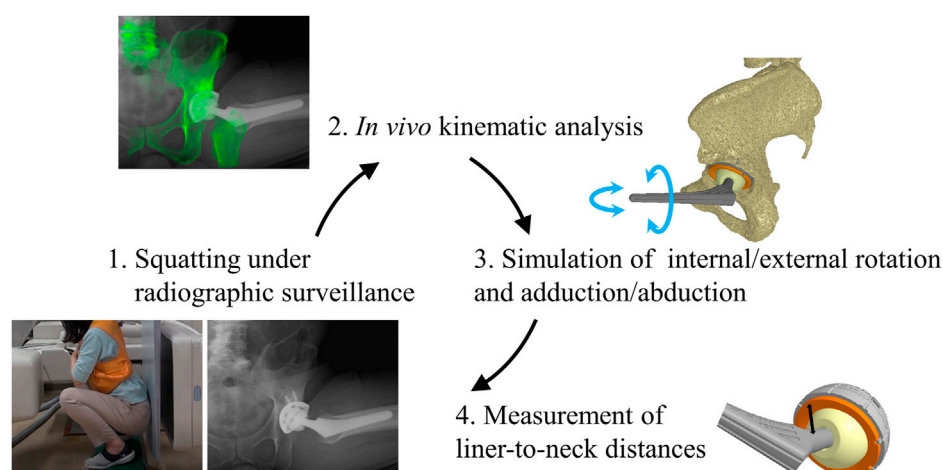
FIGURE 1
Schema represents the concept of this study. (1) Patients who had undergone total hip arthroplasty stood from a squat position with their heels down, and their hip motions were captured using a flat-panel X-ray detector. (2) The digitally reconstructed radiographs (DRRs) from computed tomography slices were matched to the actual radiographic images to analyze *in vivo* kinematic data [13]. (3) Computer simulations of the hip internal/external rotation and adduction/abduction were performed using *in vivo* implant placement and kinematic data to examine prosthetic impingement at maximum hip flexion and extension during squatting. (4) The minimum distances between the liner and stem neck (liner-to-neck distances) were measured based on three dimensionally (3D) reconstructed images to define an impingement-free implant alignment.

underwent cementless THA as a surgical treatment for severe OA and ONFH between 2011 and 2015 and met the following inclusion criteria: 1) no neuromuscular disorders; 2) no previous surgery of the analyzed hip; 3) no previous surgery or symptoms of other joints or the spine; 4) non-inflammatory arthritis; and 5) use of a 32-mm head during THA. This study consisted of 32 hips in 30 patients including 27 hips in 25 OA patients and 5 hips in 5 ONFH patients (Table 1). There were no cases of dislocation among the patients in this study.

Implants

A cementless hemispherical press-fit cup, straight metaphyseal fit stem, and a highly cross-linked ultra-high molecular weight polyethylene liner (AMS and PerFix HA; Aeonian; Kyocera, Kyoto, Japan) were used. The stem-neck angle was 130°. All materials of the femoral heads were alumina ceramic, and all head sizes were 32 mm. The head-neck ratio was 3.56, being the ratio of a 32-mm head to a 9-mm neck diameter.

Surgical technique

Surgery was performed using a standard posterolateral approach with the lateral decubitus position and combined anteversion (CA) technique (Jolles et al., 2002; Dorr et al., 2009). The femur was prepared first so that femoral anteversion was known before cup

placement (Murray, 1993; Dorr et al., 2009; Nakashima et al., 2014). Anteversion of the final broach was measured as the angle between the lower leg's axis and the trial stem's axis by flexing the knee and placing the tibia in a vertical position using a manual goniometer. Cup anteversion was then adjusted using a manual manufacturer's cup inserter with a goniometer, according to the stem anteversion, so that CA ranged from 40° to 60° (Jolles et al., 2002; Nakashima et al., 2014). 45° internal rotation with 20° adduction and 60° internal rotation without adduction are the index positions to check THA posterior stability intraoperatively.

Orientation of components

Orientation of the acetabular cup and femoral stem was evaluated using postoperative CT (Table 1). Cup inclination was measured as the angle of abduction using the inter-teardrop line as the baseline (radiographic inclination). Cup anteversion was measured as the angle of anteversion in the sagittal plane (radiographic anteversion) (Murray, 1993). Femoral anteversion was measured as the angle of anteversion between the prosthetic femoral neck and the posterior condylar line. The sum of the cup and stem anteversions was used to determine CA (Nakashima et al., 2014).

Hip kinematics

Patients who had undergone THA stood from a squatting position with their heels down under radiographic surveillance,

TABLE 2 Hip adduction/abduction and internal/external angles at maximum hip flexion and extension during squatting.

Parameter	Maximum hip flexion	Maximum hip extension
Hip flexion/extension[a], degree (flexion +, extension −)	80.7 ± 12.3 (60.6–114.2)	1.6 ± 8.4 (−13.0–20.7)
Hip adduction/abduction[a], degree (abduction +, adduction −)	7.3 ± 5.4 (1.1–17.7)	3.6 ± 3.1 (−4.5–1.4)
Hip internal/external hip rotation[a], degree (internal +, external −)	−22.7 ± 11.4 (−40.6–2.2)	-10.0 ± 6.5 (−28.7–1.2)

Some of the analysis data have been reported in the previous study (Harada et al., 2022a).
[a]Values are given as the mean ± standard deviations with the range in parentheses.

FIGURE 2
Schema represents the simulation of hip internal/external rotation and abduction/adduction based on *in vivo* implant placement and hip flexion/extension during squatting. The internal rotation and adduction at maximum hip flexion were changed from 0° to 60° in 15° increases **(A)** and from −20° to 20° in 10° increases **(B)**, respectively. The external rotation and adduction at maximum hip extension were changed from 0° to 60° in 15° increases **(C)** and from −20° to 20° in 10° increases **(D)**, respectively.

and dynamic hip kinematics were analyzed using density-based, image-matching techniques, as described previously (Figure 1) (Harada et al., 2022a: Hara et al., 2016a; Shiomoto et al., 2019). The squatting position was performed by bending the hip, knee, and ankle joints to descend to the maximum attainable depth. Some of the analysis data have been reported in a previous study (Harada et al., 2022a). Continuous radiographic images during squatting were recorded (Ultimax-i flat-panel X-ray detector [FPD] multipurpose system; Canon, Tochigi, Japan) with a field view of 420 mm × 420 mm, resolution of 0.274 mm × 0.274 mm/pixel, a pulse width of 0.02 s, 80 kV and 360 mA, and a frame rate of 3.5 frames/s. Each patient underwent computed tomography (CT; Aquilion; a 1-mm thickness spanning from the superior edge of the pelvis to Canon) with a 512 × 512 image matrix, a 0.35 × 0.35-pixel dim, and below the knee joint line. This method generated digitally reconstructed radiographs (DRRs) from CT and components' data, matched the DRRs to the actual radiographs, and calculated the pelvis/acetabular cup and femur/stem orientations (Table 2). The coordinate system of the pelvis was based on the anterior pelvic plane. The center of the acetabular cup was defined as the origin of the coordinate system of the acetabular cup. The coordinate system of the femur was based on the center of the femoral head and the transepicondylar axis, which was defined as the line from the medial to lateral femoral epicondyles (Yoshioka et al., 1987). Hip movement was determined using the Cardan/Euler angle system in the x-y-z order (flexion/extension, adduction/abduction, and internal rotation/external rotation) (Hara et al., 2014). To analyze the orientation of the stem relative to the acetabular cup, local coordinate systems were constructed for each implant to track implant movements. The root mean square errors for bone/implant movement were 0.36/0.43 mm for in-plane translation, 0.37/0.48 mm for out-of-plane translation, and 0.48°/0.52° for rotation (Hara et al., 2014; Hara et al., 2016b).
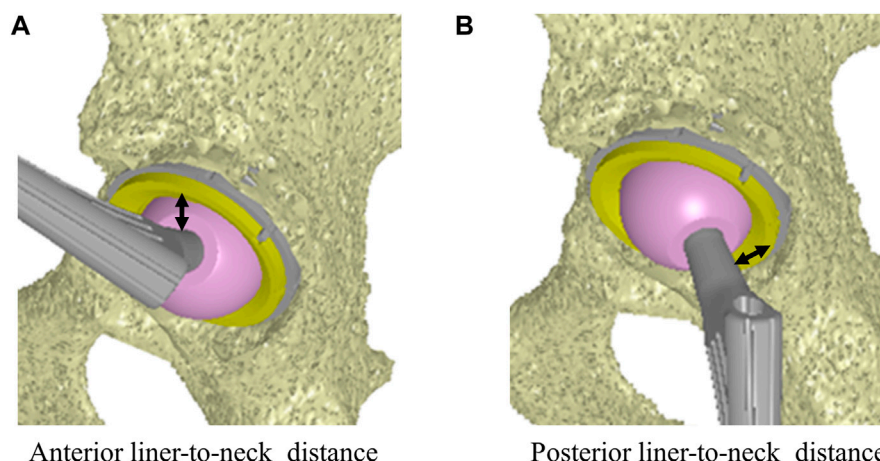
FIGURE 3
Minimum distance on the anterior side to the stem at the maximum hip flexion as the anterior liner-to-neck distance **(A)**. Minimum distance on the posterior side to the stem at the maximum hip extension as the posterior liner-to-neck distance **(B)**.

Simulation analysis

Computer simulations were performed using a custom-made software program (Komiyama et al., 2019; Shiomoto et al., 2021) based on *in vivo* data, including patient-specific component placements and kinematics during squatting, to examine liner-to-neck impingement (Figure 1). 1) Internal rotation and adduction/abduction at actual maximum flexion and 2) external rotation and adduction/abduction at actual maximum extension were changed virtually, increasing the angles from 0° to 60° in 15° increases and from −20° to 20° in 10° increases, respectively (Figure 2). The minimum distance between the polyethylene liner and stem neck was measured on the anterior side at maximum hip flexion as the anterior liner-to-neck distance, and the minimum distance on the posterior side at the maximum hip extension as the posterior liner-to-neck distance at each setting was measured using a computer-aided design software program (CATIA V5; Dassault Systèmes, Vélizy-Villacoublay, France) (Hara et al., 2014; Shiomoto et al., 2019; Harada et al., 2022a); the presence or absence of liner-to-neck impingement (Tanino et al., 2008) was also examined (Figure 3). Cup inclination and anteversion, stem anteversion, and CA to avoid anterior impingement at 45° internal rotation with 20° adduction at maximum flexion and posterior impingement at 45° external rotation with 20° adduction at maximum extension, and 60° internal rotation at maximum flexion and posterior impingement at 60° external rotation at maximum extension were examined using receiver operating characteristic (ROC) curves (Shiomoto et al., 2021). All hips were simulated with a flat liner to eliminate the effect of the liner type and the position of the elevated wall.

Statistical analysis

Statistical analyses were performed by JMP software v.14.0 (SAS Institute, Cary, NC, United States). Correlation between the liner-to-neck distance and internal/external rotation was analyzed using Pearson's correlation coefficient and linear regression. The cup inclination, cup and stem anteversions, and CA were compared between hips with and without liner-to-neck impingement using Student's *t*-test and Wilcoxon rank-sum test for normally distributed variables and non-normally distributed variables, respectively. ROC curves were created to calculate the cutoff values of cup inclination, cup and stem anteversions, and CA for anterior/posterior liner-to-neck impingements at 45° internal/external rotation with 20° adduction and at 60° internal/external rotation without adduction. Statistical significance was set as $p < 0.05$. To detect a 14° difference in combined anteversion between liner-to-neck impingement and non-impingement, with a standard deviation of 14°, alpha of 5%, and power of 80%, a sample size of 32 hips was needed in this study (Shiomoto et al., 2021).

Results

Liner-to-neck distances and impingements

The anterior liner-to-neck distance decreased as internal rotation or adduction increased, and the posterior liner-to-neck distance decreased as external rotation or adduction increased, respectively. Negative correlations between anterior liner-to-neck distances at maximum flexion and internal rotation
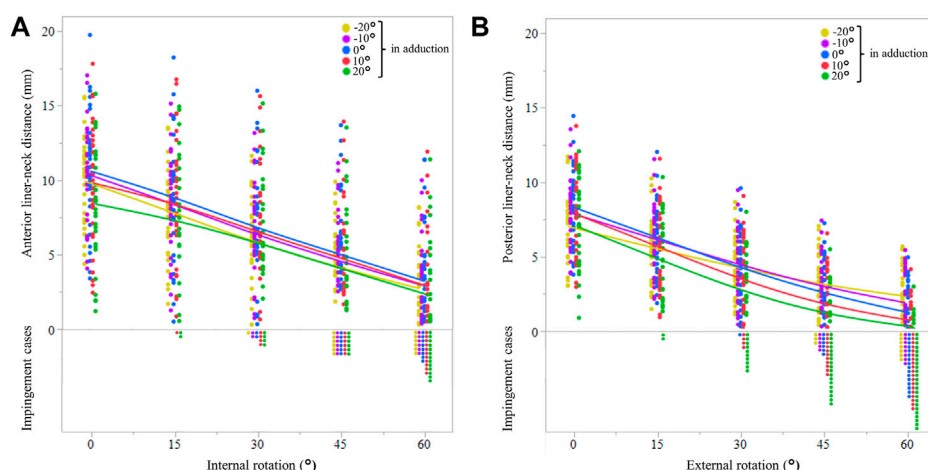
FIGURE 4
Anterior liner-to-neck distances are based on the simulated internal rotation and adduction at maximum hip flexion **(A)**. Yellow, violet, blue, red, and green solid lines represent average values of −20°, −10°, 0°, 10°, and 20° in adduction, respectively. The dots show the actual values for each patient in each simulation. The posterior liner-to-neck distances are based on the simulated external rotation and adduction at maximum hip extension **(B)**. Yellow, violet, blue, red, and green solid lines represent average values of −20°, −10°, 0°, 10°, and 20° in adduction, respectively. The dots show the actual values for each patient in each simulation.

were found ($p < 0.05$, Figure 4). The rate of anterior liner-to-neck impingement increased as internal rotation or adduction increased. Anterior liner-to-neck impingements were observed in some cases from 15° internal rotation with 20° adduction/abduction. Similarly, negative correlations between the posterior liner-to-neck distance at maximum extension and external rotation were found ($p < 0.05$, Figure 4). The rate of posterior liner-to-neck impingement at maximum extension increased as external rotation or increased adduction. Posterior liner-to-neck impingements were observed in some cases from 15° external rotation with 20° adduction/abduction. Angles of 10° and 20° adduction significantly decreased both anterior and posterior liner-to-neck distances at 60° rotation compared to 0°, 10°, and 20° abduction ($p < 0.01$, Figure 4).

In a 45° internal rotation with 20° adduction, the cup and stem anteversions, and CA with anterior liner-to-neck impingement ($n = 6$ [18%], $15.8 \pm 11.3°$, $16.7 \pm 11.3°$, and $32.6 \pm 14.0°$, respectively) were significantly lower than those without impingement ($n = 26$ [82%], $22.1 \pm 8.4°$, $37.8 \pm 7.7°$, and $56.5 \pm 14.2°$, respectively; $p < 0.05$). Meanwhile, in 45° external rotation with 20° adduction, the cup and stem anteversions, and CA with posterior liner-to-neck impingement ($n = 18$ [56%], $23.4 \pm 7.7°$, $36.7 \pm 13.5°$, and $60.2 \pm 13.2°$, respectively) were significantly higher than those without impingement ($n = 14$ [44%], $19.5 \pm 10.0°$, $29.5 \pm 15.7°$, and $48.7 \pm 18.4°$, respectively; $p < 0.05$). In a 60° internal rotation with 0° adduction/abduction, the cup and stem anteversions, and CA with anterior liner-to-neck impingement [($n = 8$ 25%, $16.3 \pm 10.8°$, $16.3 \pm 9.8°$, and $32.6 \pm 12.1°$, respectively)] were significantly lower than those without impingement [($n =$

24 75%, $22.5 \pm 8.2°$, $35.9 \pm 12.8°$, and $58.5 \pm 12.8°$, respectively; $p < 0.05$)]. Meanwhile, in a 60° external rotation with 0° adduction/abduction, the cup and stem anteversions, and CA with posterior liner-to-neck impingement [($n = 16$ 50%, $24.5 \pm 8.0°$, $37.0 \pm 14.7°$, and $61.6 \pm 13.2°$, respectively)] were significantly higher than those without impingement [($n = 16$ 50%, $17.3 \pm 9.0°$, $25.0 \pm 12.5°$, and $42.4 \pm 14.7°$, respectively; $p < 0.05$)]. Two hips (6%) demonstrated both anterior and posterior liner-to-neck impingements at 60° rotation with 0° adduction/abduction.

Cutoff values of the cup and stem anteversions and combined anteversion

Based on ROC curve analyses, the cutoff values of the cup inclination, cup and stem anteversions, and CA for anterior liner-to-neck impingement at 45° internal rotation with 20° adduction were 45.1°, 14.5°, 18.6°, and 41.3°, respectively (Figure 5). Based on ROC curve analyses, the cutoff values of the cup inclination, cup and stem anteversions, and CA for anterior liner-to-neck impingement at 60° internal rotation with 0° adduction were 45.1°, 14.5°, 19.6°, and 41.3°, respectively (Figure 6). The cutoff values of the cup inclination, cup and stem anteversions, and CA for posterior liner-to-neck impingement at 45° external rotation with 20° adduction were 36.8°, 17.6°, 34.0°, and 56.2°, respectively (Figure 5). The cutoff values of the cup inclination, cup and stem anteversions, and CA for posterior liner-to-neck impingement at 60° external rotation with 0° adduction were 36.8°, 18.1°, 35.6°, and 58.7°, respectively (Figure 6). Angles of 60° internal/external
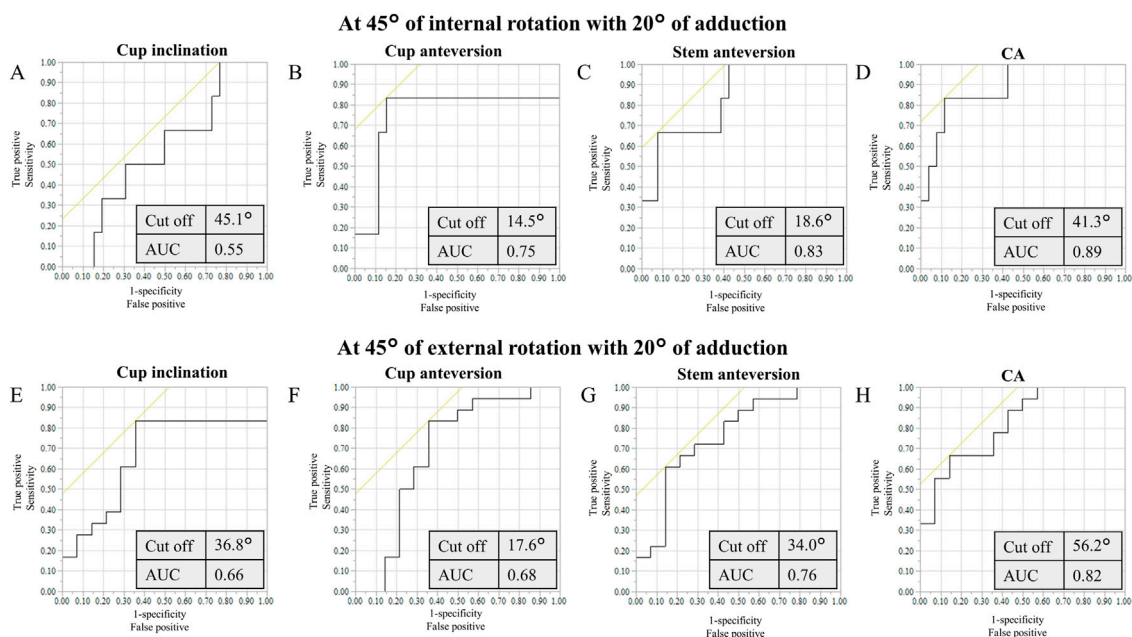
FIGURE 5

ROC curves of the cup inclination **(A)**, cup anteversion **(B)**, stem anteversion **(C)**, and CA **(D)** to prevent from anterior impingement at maximum hip flexion with simulated 45° internal rotation and 20° adduction. ROC curves of the cup inclination **(E)**, cup anteversion **(F)**, stem anteversion **(G)**, and CA **(H)** to prevent from posterior impingement at maximum hip extension with simulated 45° external rotation and 20° adduction, ROC: receiver operating characteristic, CA: combined anteversion, AUC: area under the curve.
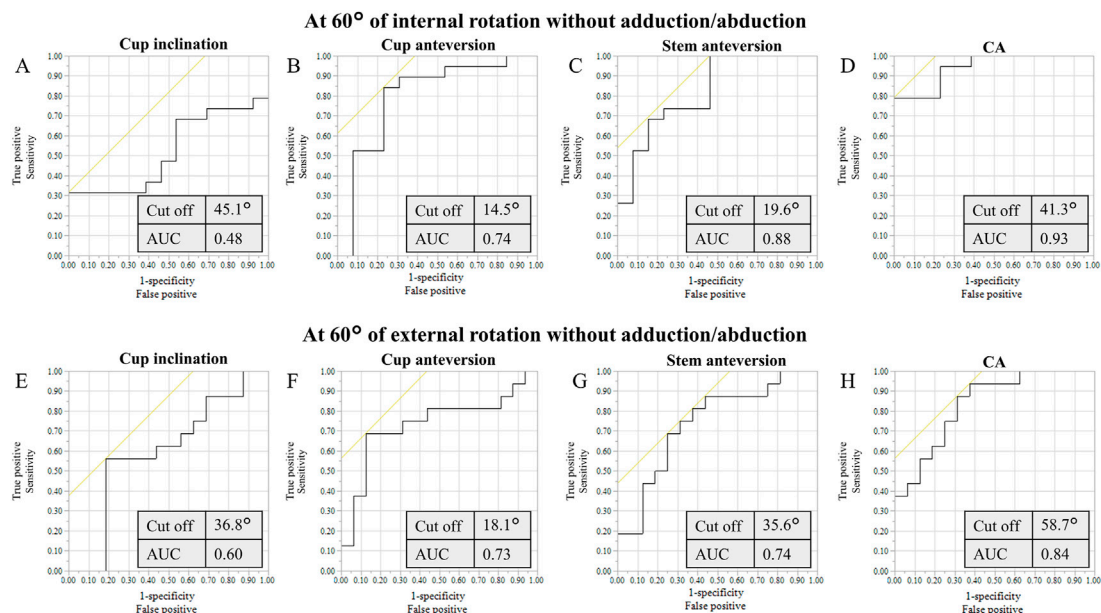
FIGURE 6

ROC curves of the cup inclination **(A)**, cup anteversion **(B)**, stem anteversion **(C)**, and CA **(D)** to prevent from anterior impingement at maximum hip flexion with simulated 60° internal rotation and 0° adduction. ROC curves of the cup inclination **(E)**, cup anteversion **(F)**, stem anteversion **(G)**, and CA **(H)** to prevent from posterior impingement at maximum hip extension with simulated 60° external rotation and 0° adduction.

rotation with 10° and 20° adduction showed no significant cutoff values to avoid neither anterior nor posterior liner-to-neck impingements.

Discussion

This is the first study to assess target orientations of components to avoid liner-to-neck impingements based on *in vivo* replaced hip kinematics during squatting. At the actual maximum hip flexion, the anterior liner-to-neck distance significantly decreased as simulated internal rotation or adduction increased. Consequently, anterior liner-to-neck impingements were observed in some cases from 15° or more of internal rotation with 20° adduction. Also, at the actual maximum hip extension, the posterior liner-to-neck distance significantly decreased as simulated external rotation or adduction increased. Consequently, posterior liner-to-neck impingements were observed in some cases from 15° or more of external rotation with 20° adduction. The ranges of the cup and stem anteversions, and CA to achieve neither anterior impingement at maximum hip extension with simulated 45° external rotation and 20° adduction nor posterior impingement at maximum hip flexion with simulated 45° internal rotation and 20° adduction during squatting were 15°–18°, 19°–34°, and 41°–56°, respectively. Using CA could provide a larger range than a separate cup and stem anteversion.

Examining target implant orientations based on postoperative CT data with patient-specific kinematics could mimic the post-THA clinical scenario more closely, guiding the revision of surgical techniques (Harada et al., 2022b). Komiyama et al. reported that a higher vertical center of rotation results in a longer distance between the impingement site and a lower range of flexion and internal rotation (Komiyama et al., 2016). Also, Shoji et al. determined the influence of the stem design on a range of motion (ROM) by using preoperative CT data and simulation software (Shoji et al., 2020). However, previous studies simulating impingement using preoperative CT data in a supine position do not reflect patient-specific *in vivo* kinematics during weight-bearing conditions (Murphy et al., 2018; Shoji et al., 2020; Vigdorchik et al., 2020). This study utilized patients' specific component position and pelvic tilt during actual deep flexion movements for simulation (Shiomoto et al., 2020; Shiomoto et al., 2021). It has been previously reported that the cutoff values for cup anteversion and combined anteversion to avoid impingement at 60° rotation during chair-rising were 12°–25° and 38°–62°, respectively. However, for kinematics of the hip joint that requires a greater ROM, such as squatting, the target cup position may be more limited to avoid impingement. Squatting is an important function for many daily activities all over the world, as well as a basic movement for strengthening lower limb muscles (Hemmerich et al., 2006; Tang et al., 2014; Cheatham et al., 2018). THA should meet the higher demands of patients and

society with regard to functional outcomes (Snijders et al., 2021). Koyanagi et al. (2011) reported that no prosthetic impingement was observed during squatting in an *in vivo* study, suggesting that unexpected postures other than daily activities may lead to dislocation. The maximum hip flexion during squatting was reported to average on 86° (Snijders et al., 2021), which was equivalent to the results of this study: 81°. A previous study also demonstrated that *in vivo* squatting kinematics seem to be safe against impingement and subsequent dislocation (Harada et al., 2022a), but unintentional hip rotation remains a risk. Furthermore, there is widespread interest in improving the impingement-free ROM of the hip after THA. Previous studies have reported that the required ROM for daily activities is 30°–45° of internal/external rotation in hip flexion/extension (Hemmerich et al., 2006; Miki et al., 2007; Nadzadi et al., 2003; Pedersen et al., 2005; Sugano et al., 2012; Yamamura et al., 2007). The target cup anteversion and CA required to avoid impingement at 45° rotation with 20° adduction during squatting were 15°–18° and 41°–56°, respectively, which is significantly lower than that during chair-rising (Shiomoto et al., 2021).

For cup inclination and anteversion, our results were lower than Lewinnek's safe zone (cup inclination: 40° ± 10°, anteversion: 15° ± 10°) (Lewinnek et al., 1978). Indeed, there have been several reports of dislocations even within Lewinnek's safe zone (Danoff et al., 2016; Dorr and Callaghan, 2019; Elkins et al., 2015; Tiberi et al., 2015). Widmer and Zurfluh recently reported the target cup anteversion as 20°–28° and CA as 37° (Widmer and Zurfluh, 2004). Hisatome and Doi reported the ideal range of cup anteversion as 15°–35° and the target CA as 42° based on a mathematical formula (Hisatome and Doi, 2011). As previously mentioned, Shiomoto et al. reported that the target cup anteversion and CA were 12°–25° and 38°–62°, respectively (Komiyama et al., 2019; Shiomoto et al., 2021). In the present study, the ranges of cup anteversion and CA to achieve neither anterior nor posterior impingement during squatting were 15°–18° and 41°–56°, respectively. Compared with the reported safe zones, a relatively narrow safety zone was revealed in this study. An optimal implant alignment to prevent prosthetic impingement exists with a sufficient safety margin of hip rotation during squatting. Hips without anterior/posterior liner-to-neck impingement showed significantly higher/lower cup anteversion and CA than those with impingement. These results were comparable with previous studies (Sato et al., 2013; Hara et al., 2014; Harada et al., 2021). As an extreme limb position, the target cup anteversion and CA that achieve no prosthetic impingement at 60° rotation with 10° or 20° adduction did not exist after THA. These data may be beneficial for advising patients after THA regarding postoperative squatting activities in daily life.

Both cup and stem anteversion showed significant relationships with the liner-to-neck distance and postoperative potential ROM (Shiomoto et al., 2021; Harada et al., 2022a). Stem anteversion has been reported to have a strong correlation with preoperative native anteversion when inserting a straight metaphyseal fit stem (Hirata et al., 2014; Park et al., 2015). In hips with excessively low or high

amounts of femoral anteversion, changeable neck or cone-type stems may be useful options, by adjusting femoral anteversion to achieve the target CA (Matsushita et al., 2010; Howie et al., 2012). Computer-assisted surgeries such as navigation or robot-assisted systems have been reported as useful tools to verify and achieve the precise orientation of components (Hazratwala et al., 2020; Rhee et al., 2019).

The present study has several limitations. First, only a single component design was analyzed: a hemispherical press-fit cup and a straight metaphyseal fit stem. However, the design was similar to many other components currently available. Second, the simulation was performed with all hips unified to flat liners. Previous studies reported that an elevated liner had a significant effect on posterior impingement, and the results may be different in hips with an elevated liner (Shiomoto et al., 2019). Third, this study excluded a 28-mm head and included only one ball diameter: a 32-mm head (Harada et al., 2022a). Although this study is not directly applicable to THA with a head size larger than 32 mm, our results can still be useful because larger heads increase the impingement-free arc of hip motion (Malik et al., 2009). Fourth, this study did not include hip kinematics in patients with symptomatic lumbar disease. Fifth, we could not find any significant difference ($p > 0.05$) in implant orientations or hip kinematics in a deep squatting position between males and females probably due to a limited number of patients. Further investigation will be necessary to understand a gender-specific safe zone or a patient-specific safe zone in patients with a flat back deformity and/or stiff spine. Sixth, soft tissue has not been considered a limitation to the range of motion before impingement. Seventh, all hip replacements were performed using a standard posterolateral approach. Different approaches could create different postoperative soft tissue environments and hip joint kinematics. Eighth, only one activity rising from a squatting position was considered, and a specific recommendation for target orientations of components in this study could not be adapted to the other activities, such as leg cross, stooping, pivoting, and lunging. Target orientations of components need to be a compromise to satisfy the disparate requirements of different activities (Nadzadi et al., 2003; Pryce et al., 2022).

In conclusion, simulated unintentional hip rotations caused anterior/posterior prosthetic impingement during squatting. The target cup and stem anteversions and CA to avoid prosthetic impingement at 45° internal/external hip rotation with 20° adduction during squatting ranged from 15° to 18°, from 19° to 34°, and from 41° to 56°, respectively. Surgeons could gain valuable insights into target component orientations based on postoperative simulations during the deeply flexed posture.

Data availability statement

The original contributions presented in the study are included in the article/supplementary material; further inquiries can be directed to the corresponding author.

Ethics statement

The studies involving human participants were reviewed and approved by the Kyushu University Institutional Review Board (IRB number 30–91). The patients/participants provided their written informed consent to participate in this study.

Author contributions

SHR, SHM, and DH designed the study and drafted the manuscript. SHM, SI, HH, HG, SK, KS, TH, and YN collected the data. All authors contributed to data analysis, revised the manuscript for important intellectual content, and approved the final submitted manuscript.

Funding

Acknowledgments

Conflict of interest

The authors declare that the research was conducted in the absence of any commercial or financial relationships that could be construed as a potential conflict of interest.

Publisher's note

All claims expressed in this article are solely those of the authors and do not necessarily represent those of their affiliated organizations, or those of the publisher, the editors, and the reviewers. Any product that may be evaluated in this article, or claim that may be made by its manufacturer, is not guaranteed or endorsed by the publisher.

References

Berry, D. J., Harmsen, W. S., Cabanela, M. E., and Morrey, B. F. (2002). Twenty-five-year survivor-ship of two thousand consecutive primary charnley total hip replacements: Factors affecting survivorship of acetabular and femoral components. *J. Bone Jt. Surgery-American Volume* 84, 171–177. doi:10.2106/00004623-200202000-00002

Cheatham, S. W., Stull, K. R., Fantigrassi, M., and Ian, M. (2018). Hip musculoskeletal conditions and associated factors that influence squat performance: A systematic review. *J. Sport Rehabil.* 27, 263–273. doi:10.1123/jsr.2016-0246

Danoff, J. R., Bobman, J. T., Cunn, G., Murtaugh, T., Gorroochurn, P., Geller, J. A., et al. (2016). Redefining the acetabular component safe zone for posterior approach total hip arthroplasty. *J. Arthroplasty* 31, 506–511. doi:10.1016/j.arth.2015.09.010

Dorr, L. D., and Callaghan, J. J. (2019). Death of the Lewinnek "safe zone". *J. Arthroplasty* 34, 1–2. doi:10.1016/j.arth.2018.10.035

Dorr, L. D., Malik, A., Dastane, M., and Wan, Z. (2009). Combined anteversion technique for total hip arthroplasty. *Clin. Orthop. Relat. Res.* 467 (1), 119–127. doi:10.1007/s11999-008-0598-4

Elkins, J. M., Callaghan, J. J., and Brown, T. D. (2015). The 2014 frank stinchfield award: The 'landing zone' for wear and stability in total hip arthroplasty is smaller than we thought: A computational analysis. *Clin. Orthop. Relat. Res.* 473, 441–452. doi:10.1007/s11999-014-3818-0

Ethgen, O., Bruyère, O., Richy, F., Dardennes, C., and Reginster, J. Y. (2004). Health-related quality of life in total hip and total knee arthroplasty: A qualitative and systematic review of the literature. *J. Bone Jt. Surg.* 86, 963–974. doi:10.2106/00004623-200405000-00012

Hamai, S., Nakashima, Y., Mashima, N., Yamamoto, T., Kamada, T., Motomura, G., et al. (2016). Comparison of 10-year clinical wear of annealed and remelted highly cross-linked polyethylene: A propensity-matched cohort study. *J. Mech. Behav. Biomed. Mat.* 59, 99–107. doi:10.1016/j.jmbbm.2015.12.022

Hara, D., Hamai, S., Komiyama, K., Motomura, G., Shiomoto, K., and Nakashima, Y. (2018). Sports participation in patients after total hip arthroplasty vs periacetabular osteotomy: A propensity score-matched asian cohort study. *J. Arthroplasty* 33, 423–430. doi:10.1016/j.arth.2017.08.035

Hara, D., Nakashima, Y., Hamai, S., Higaki, G., Ikebe, S., Shimoto, T., et al. (2016b). Dynamic hip kinematics during the golf swing after total hip arthroplasty. *Am. J. Sports Med.* 44, 1801–1809. doi:10.1177/0363546516637179

Hara, D., Nakashima, Y., Hamai, S., Higaki, H., Ikebe, S., Shimoto, T., et al. (2016a). Dynamic hip kinematics in patients with hip osteoarthritis during weight-bearing activities. *Clin. Biomech. (Bristol, Avon.* 32, 150–156. doi:10.1016/j.clinbiomech.2015.11.019

Hara, D., Nakashima, Y., Hamai, S., Higaki, H., Ikebe, S., Shimoto, T., et al. (2014). Kinematic analysis of healthy hips during weight-bearing activities by 3D-to-2D model-to-image registration technique. *Biomed. Res. Int.* 457573, 1–8. doi:10.1155/2014/457573

Harada, S., Hamai, S., Gondo, H., Shiomoto, K., Komiyama, K., Hara, D., et al. (2022a). Squatting after total hip arthroplasty: Patient-reported outcomes and *in vivo* three-dimensional kinematic study. *J. Arthroplasty* 37, 734–741. doi:10.1016/j.arth.2021.12.028

Harada, S., Hamai, S., Motomura, G., Ikemura, S., Fujii, M., Kawahara, S., et al. (2022b). Evaluation of optimal implant alignment in total hip arthroplasty based on postoperative range of motion simulation. *Clin. Biomech. (Bristol, Avon.* 92, 105555. doi:10.1016/j.clinbiomech.2021.105555

Harada, S., Hamai, S., Shiomoto, K., Hara, D., Fujii, M., Ikemura, S., et al. (2021). Patient-reported outcomes after primary or revision total hip arthroplasty: A propensity score-matched asian cohort study. *PLoS One* 16, e0252112. doi:10.1371/journal.pone.0252112

Hazratwala, K., Brereton, S. G., Grant, A., and Dlaska, C. E. (2020). Computer-assisted technologies in arthroplasty: Navigating your way today. *JBJS Rev.* 8, e0157–e0158. doi:10.2106/JBJS.RVW.19.00157

Hemmerich, A., Brown, H., Smith, S., Marthandam, S. S. K., and Wyss, U. P. (2006). Hip, knee, and ankle kinematics of high range of motion activities of daily living. *J. Orthop. Res.* 24, 770–781. doi:10.1002/jor.20114

Hirata, M., Nakashima, Y., Itokawa, T., Ohishi, M., Sato, T., Hara, D., et al. (2014). Influencing factors for the increased stem version compared to the native femur in cementless total hip arthroplasty. *Int. Orthop.* 38, 1341–1346. doi:10.1007/s00264-014-2289-y

Hisatome, T., and Doi, H. (2011). Theoretically optimum position of the prosthesis in total hip arthroplasty to fulfill the severe range of motion criteria due to neck impingement. *J. Orthop. Sci.* 16 (2), 229–237. doi:10.1007/s00776-011-0039-1

Hoskins, W., Corfield, S., Lorimer, M., Peng, Y., Bingham, R., Graves, S. E., et al. (2022). Is the revision rate for femoral neck fracture lower for total hip arthroplasty than for hemiarthroplasty? A comparison of registry data for contemporary surgical options. *J. Bone Jt. Surg.* 104 (17), 1530–1541. doi:10.2106/JBJS.21.01256

Howie, D. W., Holubowycz, O. T., Middleton, R., Allen, B., Brumby, S., Chehade, M., et al. (2012). Large femoral heads decrease the incidence of dislocation after total hip arthroplasty: A randomized controlled trial. *J. Bone Jt. Surg.* 94, 1095–1102. doi:10.2106/JBJS.K.00570

Jolles, B. M., Zangger, P., and Leyvraz, P. F. (2002). Factors predisposing to dislocation after primary total hip arthroplasty: A multivariate analysis. *J. Arthroplasty* 17 (3), 282–288. doi:10.1054/arth.2002.30286

Komiyama, K., Hamai, S., Ikebe, S., Yoshimoto, K., Higaki, H., Hara, D., et al. (2019). *In vivo* kinematic analysis of replaced hip during stationary cycling and computer simulation of optimal cup positioning against prosthetic impingement. *Clin. Biomech. (Bristol, Avon.* 68, 175–181. doi:10.1016/j.clinbiomech.2019.05.035

Komiyama, K., Nakashima, Y., Hirata, M., Hara, D., Kohno, Y., and Iwamoto, Y. (2016). Does high hip center decrease range of motion in total hip arthroplasty? A computer simulation study. *J. Arthroplasty* 31 (6), 2342–2347. doi:10.1016/j.arth.2016.03.014

Koyanagi, J., Sakai, T., Yamazaki, T., Watanabe, T., Akiyama, K., Sugano, N., et al. (2011). *In vivo* kinematic analysis of squatting after total hip arthroplasty. *Clin. Biomech. (Bristol, Avon.* 26 (5), 477–483. doi:10.1016/j.clinbiomech.2010.11.006

Lewinnek, G. E., Lewis, J. L., Tarr, R., Compere, C. L., and Zimmerman, J. R. (1978). Dislocations after total hip-replacement arthroplasties. *J. Bone Jt. Surg.* 60 (2), 217–220. doi:10.2106/00004623-197860020-00014

Malik, A., Dorr, L. D., and Long, W. T. (2009). Impingement as a mechanism of dissociation of a metasul metal-on-metal liner. *J. Arthroplasty* 24, 323.e13–323.e16. doi:10.1016/j.arth.2008.05.023

Marchetti, E., Krantz, N., Berton, C., Bocquet, D., Fouilleron, N., Migaud, H., et al. (2011). Component impingement in total hip arthroplasty: Frequency and risk factors. A continuous retrieval analysis series of 416 cup. *Orthop. Traumatology Surg. Res.* 97, 127–133. doi:10.1016/j.otsr.2010.12.004

Matsushita, A., Nakashima, Y., Fujii, M., Sato, T., and Iwamoto, Y. (2010). Modular necks improve the range of hip motion in cases with excessively anteverted or retroverted femurs in THA. *Clin. Orthop. Relat. Res.* 468, 3342–3347. doi:10.1007/s11999-010-1385-6

Miki, H., Sugano, N., Yonenobu, K., Tsuda, K., Hattori, M., and Suzuki, N. (2013). Detecting cause of dislocation after total hip arthroplasty by patient-specific four-dimensional motion analysis. *Clin. Biomech. (Bristol, Avon.* 28, 182–186. doi:10.1016/j.clinbiomech.2012.11.009

Miki, H., Yamanashi, W., Nishii, T., Sato, Y., Yoshikawa, H., and Sugano, N. (2007). Anatomic hip range of motion after implantation during total hip arthroplasty as measured by a navigation system. *J. Arthroplasty* 22 (7), 946–952. doi:10.1016/j.arth.2007.02.004

Mont, M. A., Cherian, J. J., Sierra, R. J., Jones, L. C., and Lieberman, J. R. (2015). Nontraumatic osteonecrosis of the femoral head: Where do we stand today? A ten-year update. *J. Bone Jt. Surg.* 97 (19), 1604–1627. doi:10.2106/JBJS.O.00071

Murphy, W. S., Yun, H. H., Hayden, B., Kowal, J. H., and Murphy, S. B. (2018). The safe zone range for cup anteversion is narrower than for inclination in THA. *Clin. Orthop. Relat. Res.* 476, 325–335. doi:10.1007/s11999.0000000000000051

Murray, D. W. (1993). The definition and measurement of acetabular orientation. *J. Bone Jt. Surg. Br. volume* 75 (2), 228–232. doi:10.1302/0301-620X.75B2.8444942

Nadzadi, M. E., Pedersen, D. R., Yack, H. J., Callaghan, J. J., and Brown, T. D. (2003). Kinematics, kinetics, and finite element analysis of commonplace maneuvers at risk for total hip dislocation. *J. Biomech.* 36 (4), 577–591. doi:10.1016/s0021-9290(02)00232-4

Nakashima, Y., Hirata, M., Akiyama, M., Itokawa, T., Yamamoto, T., Motomura, G., et al. (2014). Combined anteversion technique reduced the dislocation in cementless total hip arthroplasty. *Int. Orthop.* 38, 27–32. doi:10.1007/s00264-013-2091-2

Park, K. K., Tsai, T. Y., Dimitriou, D., and Kwon, Y. M. (2015). Utility of preoperative femoral neck geometry in predicting femoral stem anteversion. *J. Arthroplasty* 30, 1079–1084. doi:10.1016/j.arth.2015.01.016

Pedersen, D. R., Callaghan, J. J., and Brown, T. D. (2005). Activity-dependence of the "safe zone" for impingement versus dislocation avoidance. *Med. Eng. Phys.* 27 (4), 323–328. doi:10.1016/j.medengphy.2004.09.004

Pryce, G. M., Sabu, B., Al-Hajjar, M., Wilcox, R. K., Thompson, J., Isaac, G. H., et al. (2022). Impingement in total hip arthroplasty: A geometric model. *Proc. Inst. Mech. Eng. H.* 236 (4), 504–514. doi:10.1177/09544119211069472

Rhee, S. J., Kim, H. J., Lee, C. R., Kim, C. W., Gwak, H. C., and Kim, J. H. (2019). A comparison of long-term outcomes of computer-navigated and conventional total knee arthroplasty: A meta-analysis of randomized controlled trials. *J. Bone Jt. Surg.* 101, 1875–1885. doi:10.2106/JBJS.19.00257

Saiz, A. M., Lum, Z. C., and Pereira, G. C. (2019). Etiology, evaluation, and management of dislocation after primary total hip arthroplasty. *JBJS Rev.* 7, e7–e11. doi:10.2106/JBJS.RVW.18.00165

Sato, T., Nakashima, Y., Matsushita, A., Fujii, M., and Iwamoto, Y. (2013). Effects of posterior pelvic tilt on anterior instability in total hip arthroplasty: A parametric experimental modeling evaluation. *Clin. Biomech. (Bristol, Avon.* 28, 178–181. doi:10.1016/j.clinbiomech.2012.12.011

Shiomoto, K., Hamai, S., Hara, D., Higaki, H., Gondo, H., Wang, Y., et al. (2019). *In vivo* kinematics, component alignment and hardware variables influence on the liner-to-neck clearance during chair-rising after total hip arthroplasty. *J. Orthop. Sci.* 25 (3), 452–459. doi:10.1016/j.jos.2019.05.012

Shiomoto, K., Hamai, S., Ikebe, S., Higaki, Hara D., Gondo, H., et al. (2021). Computer simulation based on *in vivo* kinematics of a replaced hip during chair-rising for elucidating target cup and stem positioning with a safety range of hip rotation. *Clin. Biomech.* 20 (91), 105537. doi:10.1016/j.clinbiomech.2021.105537

Shiomoto, K., Hamai, S., Motomura, G., Ikemura, S., Fujii, M., and Nakashima, Y. (2020). Influencing factors for joint perception after total hip arthroplasty: Asian cohort study. *J. Arthroplasty* 35 (5), 1307–1314. doi:10.1016/j.arth.2019.12.039

Shoji, T., Ota, Y., Saka, H., Murakami, H., Takahashi, W., Yamasaki, T., et al. (2020). Factors affecting impingement and dislocation after total hip arthroplasty – computer simulation analysis. *Clin. Biomech. (Bristol, Avon.* 80, 105151. doi:10.1016/j.clinbiomech.2020.105151

Snijders, T. E., Schlösser, T. P. C., van Straalen, M., Castelein, R. M., Stevenson, R. P., Weinans, H., et al. (2021). The effect of postural pelvic dynamics on the three-dimensional orientation of the acetabular cup in THA

is patient specific. *Clin. Orthop. Relat. Res.* 479 (3), 561–571. doi:10.1097/CORR.0000000000001489

Sugano, N., Tsuda, K., Miki, H., Takao, M., Suzuki, N., and Nakamura, N. (2012). Dynamic measurements of hip movement in deep bending activities after total hip arthroplasty using a 4-dimensional motion analysis system. *J. Arthroplasty* 27 (8), 1562–1568. doi:10.1016/j.arth.2012.01.029

Tang, H., Du, H., Tang, Q., Yang, D., Dhao, H., and Zhou, Y. (2014). Chinese patients' satisfaction with total hip arthroplasty: What is important and dissatisfactory? *J. Arthroplasty* 29, 2245–2250. doi:10.1016/j.arth.2013.12.032

Tanino, H., Ito, H., Harman, M. K., Matsuno, T., Hodge, W. A., and Banks, S. A. (2008). An *in vivo* model for intraoperative assessment of impingement and dislocation in total hip arthroplasty. *J. Arthroplasty* 23 (5), 714–720. doi:10.1016/j.arth.2007.07.004

Tiberi, J. V., Antoci, V., Malchau, H., Rubash, H. E., Freiberg, A. A., and Kwon, Y. M. (2015). What is the fate of total hip Arthroplasty (THA) acetabular component orientation when evaluated in the standing position? *J. Arthroplasty* 30, 1555–1560. doi:10.1016/j.arth.2015.03.025

Vigdorchik, J. M., Sharma, A. K., Madurawe, C. S., Elbuluk, A. M., Baré, J. V., and Pierrepont, J. W. (2020). Does prosthetic or bony impingement occur more often in total hip arthroplasty: A dynamic preoperative analysis. *J. Arthroplasty* 35 (9), 2501–2506. doi:10.1016/j.arth.2020.05.009

Widmer, K. H., and Zurfluh, B. (2004). Compliant positioning of total hip components for optimal range of motion. *J. Orthop. Res.* 22 (4), 815–821. doi:10.1016/j.orthres.2003.11.001

Yamamura, M., Miki, H., Nakamura, N., Murai, M., Yoshikawa, H., and Sugano, N. (2007). Open-configuration MRI study of femoro-acetabular impingement. *J. Orthop. Res.* 25, 1582–1588. doi:10.1002/jor.20448

Yoshioka, Y., Siu, D., and Cooke, T, D. (1987). The anatomy and functional axes of the femur. *J. Bone Jt. Surg.* 69, 873–880. doi:10.2106/00004623-198769060-00012

Zijlstra, W. P., De Hartog, B., Van Steenbergen, L. N., Scheurs, B. W., and Nelissen, R. G. H. H. (2017). Effect of femoral head size and surgical approach on risk of revision for dislocation after total hip arthroplasty. *Acta Orthop.* 88 (4), 395–401. doi:10.1080/17453674.2017.1317515

Check for updates

*CORRESPONDENCE
Tao Ji,
jitaomd@163.com
Wei Guo,
bonetumor@163.com

†These authors have contributed equally
to this work and share senior authorship

Novel axial compressive endoprosthesis ACE can enhance metaphyseal fixation and facilitate osseointegration: A biomechanical study

Siyi Huang[1,2], Tao Ji[1,2]*[†], Xiaodong Tang[1,2] and Wei Guo[1,2]*[†]

[1]Musculoskeletal Tumor Center, Peking University People's Hospital, Beijing, China, [2]Key Laboratory for Musculoskeletal Tumor of Beijing, Beijing, China

Background: Metaphyseal fixation for endoprosthetic reconstruction after bone tumor resection is difficult due to the short residual bone length and reverse funnel shape of the metaphysis. In the current study, 3D-printed axial compressive endoprosthesis (ACE) with a short stem and intramedullary axial compressive mechanism is proposed to improve metaphyseal fixation. The rationales of ACE are that 1) intramedullary axial compress enhances the stability of endoprosthesis and facilitates bone ingrowth at the osteotomy site; 2) 3D printed porous metallic surface at osteotomy surface and stem allows bone ingrowth to achieve osseointegration.

Methods: A biomechanical study was performed to explore the initial stability using Sawbones. A diaphysis and metaphyseal segmental defect were created and four fixation structures were simulated: 1) ACE; 2) ACE + lateral plate; 3) stem prosthesis + unilateral plate; 4) stem prosthesis + bilateral plates. Bending and torsional stiffness were determined with a material testing machine. The relationship between the torque of the compression nut and the axial compression force of the bone-implant surface was measured using a round gasket load sensor.

Results: ACE + lateral plate was the stiffest in the bending test (sagittal 324.3 ± 110.8 N/mm, coronal 307.7 ± 8.7 N/mm). ACE + lateral plate and stem prosthesis + bilateral plates had the highest torsional stiffness (10.9 ± 1.3 Nm/° and 10.7 ± 0.2 Nm/° respectively). The bending stiffness of ACE was equivalent to stem prosthesis + bilateral plates (sagittal 196 ± 10 N/mm vs. 200 ± 7 N/mm, coronal 197 ± 14 N/mm vs. 209 ± 3 N/mm), but the torsional stiffness of ACE was inferior to stem prosthesis + bilateral plates (6.1 ± 1.3 Nm/° vs. 10.7 ± 0.2 Nm/°). Stem prosthesis + unilateral plate was the least stiff both in bending and torsion. The relationship between torque (T/Nm) and axial pressure (F/N) was $F = 233.5T$.

Conclusion: The axial compressive design of ACE enhances primary stability and facilitates osseointegration, which provides an alternative option of metaphyseal fixation for endoprosthetic reconstruction.

1 Introduction

Thanks to advances in imaging, chemotherapy and multidisciplinary treatment, the long-term survival of patients with primary malignant bone tumors has seen a significant increase in recent decades, and is now approaching 80% (SEER Cancer Statistics Review (CSR), 1975–2017). Limb-salvage surgery is now achievable in most extremity tumors (Ferrari et al., 2012). For malignant bone tumors involving metaphysis or diaphysis of long bones, joint-preserving surgery is a feasible choice (Panagopoulos et al., 2017). The reconstruction options are allografts, devitalized autografts, vascularized fibular grafts, or combined with allograft and segmental endoprosthesis (Panagopoulos et al., 2017).

Endoprosthetic reconstruction has the advantages of early weight-bearing, rapid rehabilitation, and satisfying function, however, the long-term survival is unsatisfactory with a high rate of structural failure and implant loosening (Ruggieri et al., 2011; Sewell et al., 2011; Benevenia et al., 2016). Metaphyseal fixation is frequently encountered at one or both ends of joint-preserving surgery, which is challenging due to the short remaining bone segment and reverse funnel shape of the metaphysis. The short remaining bone segment results in insufficient bone/cement or bone/implant interface (Qu et al., 2015), and the reverse funnel shape of metaphysis means the stem was surrounded by less solid cancellous bone (Coathup et al., 2000), which all lead to an increased risk of aseptic loosening.

A variety of attempts have been made to reduce the aseptic loosening rate and improve metaphyseal fixation stability. Extracortical plates (Cobb et al., 2005; Stevenson et al., 2017), cross-pin (Bernthal et al., 2019), and interlocking screws (Streitburger et al., 2020) are applied to enhance stability. A hydroxyapatite-coated collar is used in cemented stem fixation to prevent wear particles from entering the medullary cavity (Cobb et al., 2005; Stevenson et al., 2017). A 3D-printed stem with a porous structure is designed to achieve long-term osseointegration (Wang et al., 2021). However, there is still no well-established optimal technique for metaphyseal fixation.

A novel device 3D printed axial compressive endoprosthesis (ACE) with a short stem and the axial compressive mechanism is proposed by the senior author (Ji T) to improve metaphyseal fixation. The design rationales of ACE are that 1) intramedullary axial compression enhances initial stability of endoprosthesis and facilitates bone ingrowth at the bone-implant interface; 2) 3D printed porous metallic surface at osteotomy surface and stem allows bone ingrowth to achieve osseointegration.

In this study, metaphyseal fixation stability is compared between ACE and regular stem prostheses from an *in vitro* biomechanical test.
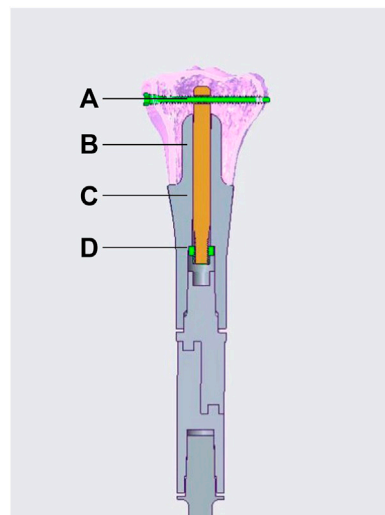

FIGURE 1
Schematic diagram of an ACE. **(A)** transverse interlocking screw, **(B)** axis rod, **(C)** stem, **(D)** compression nut. The set screw is not illustrated in the diagram.
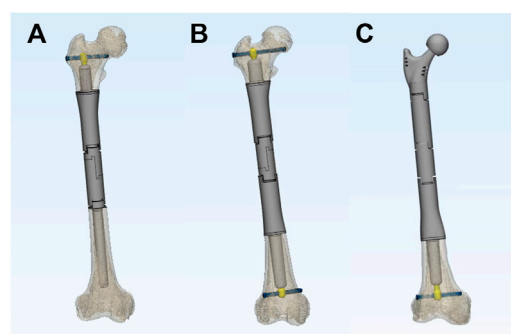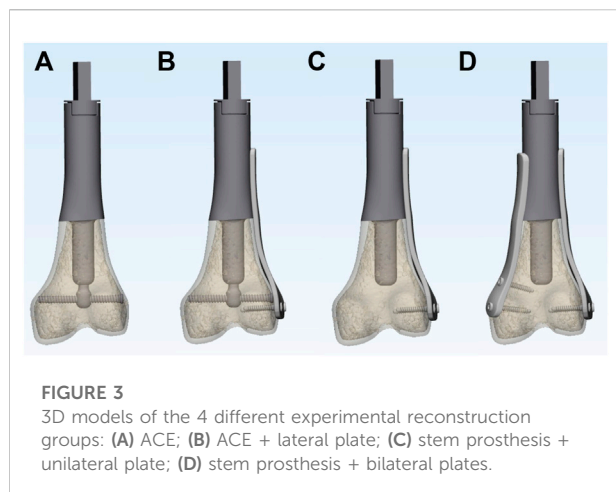

FIGURE 2
The versatility of ACE. ACE can be combined with a regular cement/press-fit stem **(A)**, double-ACE **(B)**, or an endoprosthesis with joint **(C)** for different ranges of bone defects.

FIGURE 3
3D models of the 4 different experimental reconstruction groups: **(A)** ACE; **(B)** ACE + lateral plate; **(C)** stem prosthesis + unilateral plate; **(D)** stem prosthesis + bilateral plates.

2 Materials and methods

2.1 Design and fabrication of ACE

The ACE is custom fabricated, based on the patients' specific CT and MRI data. It is composed of five parts, stem, axis rod, transverse interlocking screw, compression nut, and set screw (Figure 1). The length and diameter of the stem are determined by the medullar geometry of the bone stump. The bone-contact surface of the stem is a layer of porous metallic structure created by 3D printing, allowing bone ingrowth. The other end of the stem is a taper structure that can be connected with regular modular megaprostheses. It can be assembled into different types on the other end providing flexible reconstruction solutions, a regular cement/press-fit stem, another ACE, or an endoprosthesis with a joint based on the length of residual bone on the other end (Figure 2). The stem of ACE is hollow and an axis rod (diameter, 8–10 mm) passes through the center of the stem. A 6.5-mm transverse interlocking screw is placed through the end of the axis rod within the metaphyseal bone. The other end of the axis rod is threaded with a compression nut. When the compression nut is tightened, the interface between ACE and bone is compressed and the ACE is fixed to the bone stump. There is a groove on the axis rod. The set screw can be fixed on the groove through the endoprosthesis to prevent the axis rod from rotating relative to the stem. A lateral plate can be screw fixed to the prosthesis to provide additional stability, mainly for anti-rotation purposes. The ACE is fabricated by 3D printing with Ti6Al4V alloy using the electron beam melting technique (ARCAM Q10plus, Molndal, Sweden).

2.2 Biomechanical testing

2.2.1 Study groups and instrumentation

Fourth-generation bone composite models (Sawbones, Pacific Research Laboratories, Vashon, WA, United States)

were selected instead of cadaveric bones as composite models simulate accurately the biomechanical behavior of human bones (Gardner et al., 2010; Elfar et al., 2014), avoiding the disadvantages of variety in geometry, strength and bone density. In total, 25 adult femur specimens (#3403–105) were used for the biomechanical study.

To simulate typical metaphyseal fixation, all composite models of the femur were marked and cut to create identical defects. The osteotomy was planned at 9 cm from the joint surface of the femoral condyle and perpendicular to the long axis of the femur. The bone defects were then reconstructed using four different options: 1) ACE; 2) ACE + unilateral plate; 3) stem prosthesis + unilateral plate; 4) stem prosthesis + bilateral plates (Figure 3). Each group had 6 specimens. The stem of ACE in this study was 5 cm in length and 17 mm in diameter. The surface of the stem featured a layer of metallic porous structure with 2 mm thickness. The compression nut was tightened to 5 Nm for compressive fixation. The same stem of ACE was used for the stem prosthesis reconstruction, and the compressive structure was removed. The medial and lateral plates were fixed to the prosthesis. Each plate stabilized the bone with two locking screws.

2.2.2 Stiffness testing

An Instron E10000 materials testing machine (Instron, Canton, MA, United States) was used to conduct the testing. Bending stiffness was determined in the sagittal plane (anterior cortex in tension) and coronal plane (lateral cortex in tension). The femur was held horizontally and the proximal end of the endoprosthesis was fixed in a vice (Figure 4). A load was applied to the apex of the anterior aspect of the femoral condyle and the lateral aspect of the femoral condyle for sagittal and coronal plane stiffness test, respectively. Mechanical loading was applied using a displacement control mode. A preload of 50 N was applied to stabilize the construct, calibrated, and then followed by 5 load cycles (Sakellariou et al., 2012). The data of the last three cycles were collected for analysis. The maximum displacement was set as 1 mm. The goal was to perform non-destructive testing and ensure that the specimens remained in the linear elastic portion of the load-displacement curve (Talbot et al., 2008). Load (N) versus displacement (mm) curves were generated directly from the load cell in the actuator. The slope of the ascending linear portion was used to compute the bending stiffness (N/mm) by linear regression.

In a torsional test, the construct was secured vertically with two ends (Figure 4). The rotation axis was aligned with the long axis of the construct. A preload of 1 Nm was applied to stabilize the construct, zeroed, and then followed by 5 load cycles. The data from the last three cycles were collected for analysis. One degree of torsion was set as a limit for non-destructive testing. Load (Nm) versus angle (degrees) curves
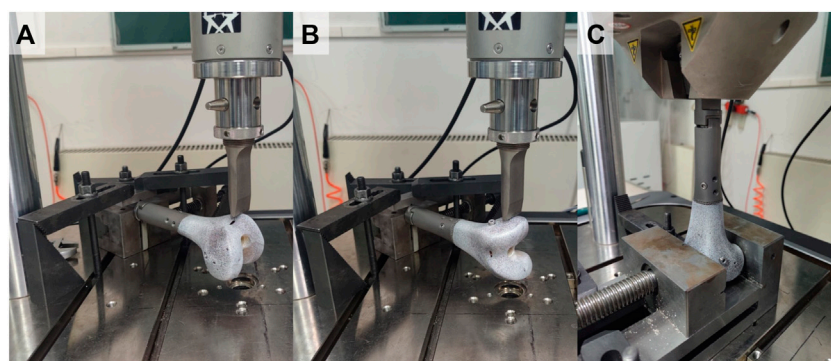
FIGURE 4
Test set-up: **(A)** sagittal bending test, **(B)** coronal bending test, **(C)** torsional test.

were generated directly from the load cell in the actuator. The slope of the ascending linear portion was used to calculate the torsional stiffnesses (Nm/degree).

The loading was sequential following the same pattern for all specimens that were tested; the composite sawbones models were tested first for sagittal bending, then for coronal bending, and finally for torsion. After each cycle of loading the specimens were examined for implant loosening, the presence of cracks as well as the need for additional tightened of the screws.

2.2.3 Torque—Axial compression force relationship test

The relationship between axis torque and axial compression force at the interface of bone-implant was measured using a gasket load sensor (JHBM-4-DZQ-500KG, Bengbu Jinnuo, Anhui, China). An ACE with a 6 cm-length and 20 mm-diameter stems was manufactured to allow the load sensor assembled. The torque of the compression nut was measured using a torque wrench (WWM-10, Wenzhou Weidu Electronics, Zhejiang, China). During the compression process, compression force (N) versus torque (Nm) was recorded. The experiment was repeated 6 times. Linear regression was used to calculate the relationship between the torque of the compression nut and axial compression force.

2.3 Statistical analysis

Statistical analyses were performed with SPSS software (version 20.0, Chicago, IL, United States). One-way analysis of variance (ANOVA) was used to test for any significant differences between the mean values of sagittal bending stiffness, coronal bending stiffness, and torsional stiffness of four different reconstructions. Levene's test was used to assess variance homogeneity. If there was no significant difference

between the variances of these sets of data, a post hoc Tukey test was used, or a post hoc Tamhane's T2 test was used. The threshold for statistical significance was set at $p = 0.05$.

3 Results

3.1 Stiffness test

All specimens were loaded within linear elastic region at subyield level. There were no events of implant or bone composite model failures observed. No implant or screw loosening was detected after each mode of loading. No tightening of screws was needed.

The mean stiffness and standard deviation (SD) for sagittal bending, coronal bending, and torsion for each reconstruction are listed in Table 1. One-way analysis of variance (ANOVA) showed a statistically significant difference in each set of data. Specifically, the F ratio of sagittal bending stiffness was 336.8 ($p < 0.001$), of coronal bending stiffness 273.0 ($p < 0.001$), and of torsional stiffness 134.7 ($p < 0.001$). Levene's test showed that the variances for sagittal bending stiffness and coronal bending stiffness were equal ($p = 0.682$ and $p = 0.058$, respectively), while the variances for torsional stiffness were not equal ($p = 0.001$).

A post hoc comparison of groups was performed in sagittal bending stiffness and coronal bending stiffness using the Tukey multiple comparison procedure. Sagittal and coronal bending stiffness were statistically significantly higher for the ACE + lateral plate group compared to the other three groups ($p < 0.001$) (Figure 5). Sagittal and coronal bending stiffness were statistically significantly higher for the ACE and stem prosthesis + bilateral plates comparing to the stem prosthesis + unilateral plate ($p < 0.01$ in coronal bending, ACE versus stem prosthesis + unilateral plate, $p < 0.001$ in other three comparisons). No significant differences were found between ACE and stem prosthesis + bilateral plate in sagittal or coronal bending stiffness.

TABLE 1 The mean stiffness and standard deviation for sagittal bending, coronal bending, and torsion for each reconstruction.

	ACE		ACE + lateral plate		stem prosthesis + unilateral plate		stem prosthesis + bilateral plates	
	Mean	SD	Mean	SD	Mean	SD	Mean	SD
sagittal bending (N/mm)	196.3	10.2	324.3	10.8	164.1	9.3	199.6	7.1
coronal bending (N/mm)	197.4	13.7	307.7	8.7	179.7	4.1	209.3	3.1
axial torsion (Nm/Degree)	6.13	1.28	10.94	1.28	1.78	0.13	10.67	0.21

FIGURE 5
Comparison of bending and torsional stiffness of four reconstruction groups. **$p < 0.01$, ***$p < 0.001$.

FIGURE 6
Compression force−Torque relationship. (A) Test set-up: A- ACE, B- gasket load sensor, C- Sawbones, (B) Relationship between torque and axial force.
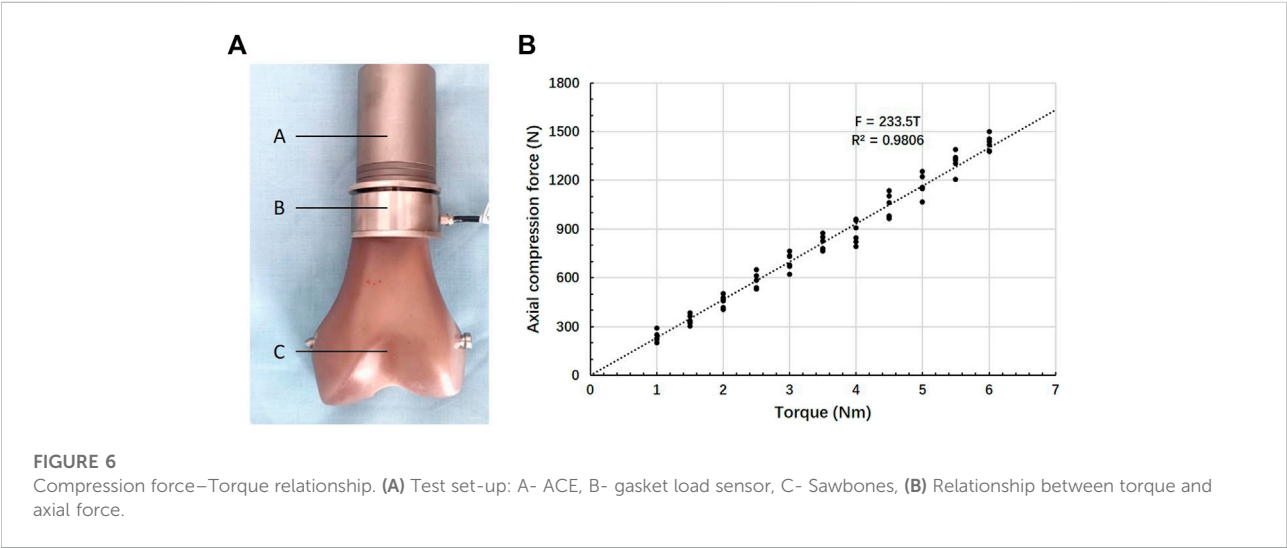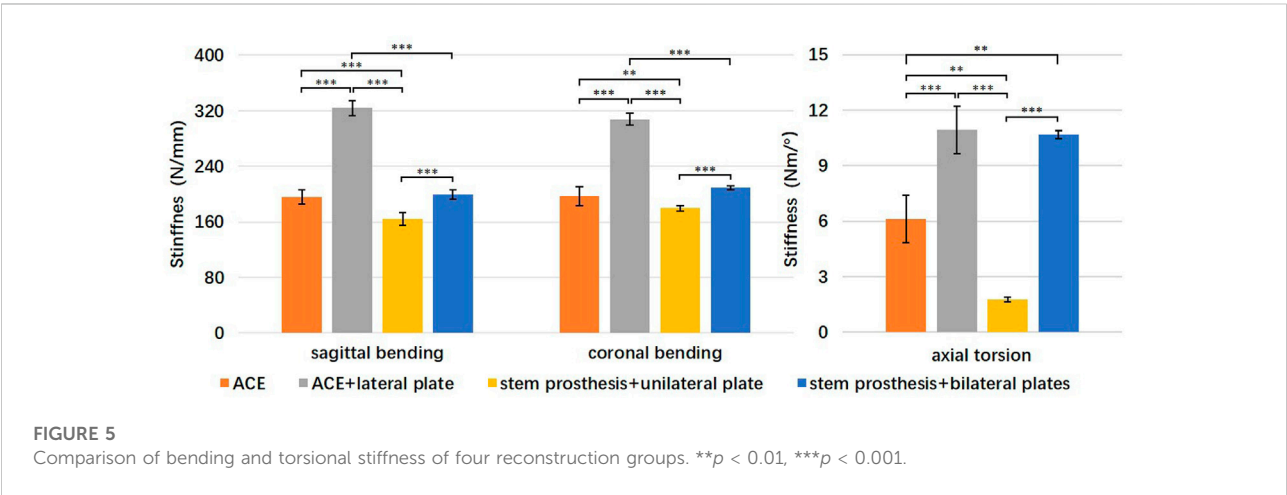
A post hoc comparison of groups was performed in torsional stiffness using Tamhane's T2 test. Torsional stiffness was statistically significantly higher for the ACE + lateral plate and stem prosthesis + bilateral plates compared to the ACE and stem prosthesis + unilateral plate ($p < 0.01$ in ACE versus stem prosthesis + bilateral plate, $p < 0.001$ in the other three comparisons). Torsional stiffness was statistically significantly higher for the ACE compared to the stem prosthesis + unilateral

plate ($p < 0.01$). No significant differences were found between ACE + lateral plate and stem prosthesis + bilateral plates in torsional stiffness.

3.2 Axial compression force–Torque relationship test

The fitted regression equation of torque (T/Nm) and axial pressure (F/N) was as follows: F = 233.5T (Figure 6). The Pearson correlation coefficient was 0.9806. The axially compressive force of the bone-implant surface was 1,167.5 N when the torque of the compression nut was 5 Nm.

4 Discussion

Metaphyseal fixation of endoprosthesis reconstruction after segmental bone removal is usually difficult due to the short remaining bone segment and reverse funnel shape of the metaphysis. Traditional stems rely on a certain length of the stem being placed into a tubular bone for fixation. The reduced bone/cement or bone/implant interface (Qu et al., 2015) and relatively weak cancellous bone (Coathup et al., 2000) at metaphysis make both cemented stem and press-fit stem under an increased risk of aseptic loosening.

4.1 Efforts to improve metaphysis fixation

Efforts to improve metaphysis fixation can be summarized into two categories. One is auxiliary fixation structure to enhance reconstruction, the other is a surface modification to achieve osseointegration (Bini et al., 2000; Dieckmann et al., 2014; Stevenson et al., 2017; Bernthal et al., 2019; Wang et al., 2021).

Stevenson et al. (2017) reported that HA (hydroxyapatite) coated extra-cortical plates increased the survivorship of short-cemented-stemmed endoprostheses. In their study, the average length of the intramedullary stem was 33 mm. The follow-up results of 37 patients showed that no implants with extra-cortical plate osseointegration suffered loosening at a mean of 8.5 years, while three of ten (30%) without osseointegration suffered aseptic loosening at a mean of 7.7 years. Bernthal et al. (2019) reported the long-term outcomes of a cross-pin fixation construct designed to minimize rotational stress and subsequent aseptic loosening. The median follow-up of 56 implants was 132 months. Five implants (9%) were revised for aseptic loosening. However, three implants had a fatigue fracture of the stem through cross-pin holes in the endoprostheses. Dieckmann et al. (2014) reported a short-stem reconstruction with screw fixation in the femoral neck to avoid rotation and enhance primary rotation stability. Two aseptic loosenings were noted in a total of 15 patients during the mean

follow-up period of 37 months. Wang et al. (2021) reported a 3D-printed custom-made ultra-short stem with a porous structure for metaphysis fixation. Cross-pins were used to enhance stability. One of 15 patients experienced aseptic loosening which was managed with immobilization and bisphosphonates infusion at a median follow-up of 42 months. All implants were well osseointegrated at the final follow-up.

The Compress prosthesis offered a new coupling system. It has a porous–coated titanium surface with a conical section mounted transversely to the axis of the bone. The implant is compressed against the host bone with Belleville spring washers tightened by a bolt over an intramedullary traction bar (Bini et al., 2000). The aim of the Compress prosthesis was to prevent bone resorption by allowing stress sharing by the implant and the bone, and provide a stable bone-prosthesis interface suitable for early weight bearing and long-term osseointegration. The aseptic loosening rate was 9.7% at 10 years (Healey et al., 2013). The conical spindle rather than an intramedullary stem was used in the Compress prosthesis. A compression force from 400 lbs to 800 lbs was applied to the osteotomy surface according to the cortical thickness (Parlee et al., 2020). A cortical thickness of less than 2.5 mm was a contraindication of this device. The Compress prosthesis required approximately 8 cm of resected bone at the distal femur, 13 cm at the proximal femur, 15 cm at the proximal tibia, and 12 cm at the proximal humerus (Parlee et al., 2020). The requirement of cortical thickness and resected bone length limited its application in metaphyseal fixation.

4.2 Superior stability of ACE

In the biomechanical testing, the ACE reconstruction had higher bending stiffness than the stem prosthesis + unilateral plate. The ACE + lateral plate had the highest bending stiffness among the four reconstructions. The interface between ACE and bone was compressed, which not only increased maximum static friction between bone and metal prosthesis but also prevented the pulling out of the tension side under bending force. The traditional stem relies on the press fit technique to provide friction, but the reverse funnel shape of metaphysis makes it not able to achieve press fitting.

The ACE reconstruction was superior to the stem prosthesis + unilateral plate on torsional stiffness while was inferior to the stem prosthesis + bilateral plate. The ACE + unilateral plate had similar torsional stiffness with the stem prosthesis + bilateral plate. The compression between ACE and bone increased friction. The transverse interlocking screw also enhanced the torsional stiffness. However, the screw hole on the axis rod was not threaded. There was a slight relative rotation between the axis rod and the transverse interlocking screw under torsion.

The above findings indicated that the intramedullary axial compress system was more stable than traditional stem plus plate

fixation. The lateral plate fixed to the ACE provided additional initial stability, especially torsional stability.

The torque of the compression nut is set to 4 Nm and 5 Nm during surgery depending on the cortical thickness and quality of cancellous bone. The corresponding axial compressive force is 934 N and 1,167.5 N according to our test. The compressing force is from 400lbs (1778 N) to 800lbs (3555 N) in the Compress prosthesis. It is reasonable that the compression force is lower in the ACE than the Compress prosthesis, considering the thinner cortical bone at metaphysis than diaphysis.

4.3 Limitations

The present study had several limitations. Sawbones were used in the biomechanical experiments, which reflected the biomechanical properties of the early postoperative period, but not after bone ingrowth. Future research could carry animal studies to further investigate the effect of osseointegration on the mechanical properties of metaphyseal fixation. Only distal femoral metaphyseal fixation was evaluated in biomechanical experiments. We believe that the results can be applied to other long bone metaphyses, but further experimental verification is needed.

4.4 Conclusion

The axial compressive design of ACE enhances primary stability and has facilitated osseointegration, which provides an alternative option of metaphyseal fixation for endoprosthetic reconstruction.

Data availability statement

The raw data supporting the conclusion of this article will be made available by the authors, without undue reservation.

Author contributions

Conception and design of study: TJ and WG. Acquisition of data: SH and TJ. Analysis and/or interpretation of data: SH and TJ. Drafting the manuscript: SH and TJ. Revising the manuscript critically for important intellectual content: TJ, XT, and WG.

Conflict of interest

The authors declare that the research was conducted in the absence of any commercial or financial relationships that could be construed as a potential conflict of interest.

Publisher's note

All claims expressed in this article are solely those of the authors and do not necessarily represent those of their affiliated organizations, or those of the publisher, the editors and the reviewers. Any product that may be evaluated in this article, or claim that may be made by its manufacturer, is not guaranteed or endorsed by the publisher.

References

Benevenia, J., Kirchner, R., Patterson, F., Beebe, K., Wirtz, D. C., Rivero, S., et al. (2016). Outcomes of a modular intercalary endoprosthesis as treatment for segmental defects of the femur, tibia, and humerus. *Clin. Orthop. Relat. Res.* 474 (2), 539–548. doi:10.1007/s11999-015-4588-z

Bernthal, N. M., Upfill-Brown, A., Burke, Z. D. C., Ishmael, C. R., Hsiue, P., Hori, K., et al. (2019). Long-term follow-up of custom cross-pin fixation of 56 tumour endoprosthesis stems: A single-institution experience. *bone & Jt. J.* 101 (6), 724–731. doi:10.1302/0301-620X.101B6.BJJ-2018-0993.R1

Bini, S. A., Johnston, J. O., and Martin, D. L. (2000). Compliant prestress fixation in tumor prostheses: Interface retrieval data. *Orthopedics* 23 (7), 707–712. doi:10.3928/0147-7447-20000701-18

Coathup, M. J., Cobb, J. P., Walker, P. S., and Blunn, G. W. (2000). Plate fixation of prostheses after segmental resection for bone tumours. *J. Orthop. Res.* 18 (6), 865–872. doi:10.1002/jor.1100180604

Cobb, J. P., Ashwood, N., Robbins, G., Witt, J. D., Unwin, P. S., and Blunn, G. (2005). Triplate fixation: A new technique in limb-salvage surgery. *J. Bone Jt. Surg. Br* 87 (4), 534–539. doi:10.1302/0301-620X.87B4.14967

Dieckmann, R., Henrichs, M. P., Gosheger, G., Holl, S., Hardes, J., and Streitburger, A. (2014). Short-stem reconstruction for megaendoprostheses in case of an ultrashort proximal femur. *BMC Musculoskelet. Disord.* 15, 190. doi:10.1186/1471-2474-15-190

Elfar, J., Menorca, R. M., Reed, J. D., and Stanbury, S. (2014). Composite bone models in orthopaedic surgery research and education. *J. Am. Acad. Orthop. Surg.* 22 (2), 111–120. doi:10.5435/JAAOS-22-02-111

Ferrari, S., Ruggieri, P., Cefalo, G., Tamburini, A., Capanna, R., Fagioli, F., et al. (2012). Neoadjuvant chemotherapy with methotrexate, cisplatin, and doxorubicin with or without ifosfamide in nonmetastatic osteosarcoma of the extremity: An Italian sarcoma group trial ISG/OS-1. *J. Clin. Oncol.* 30 (17), 2112–2118. doi:10.1200/jco.2011.38.4420

Gardner, M. P., Chong, A. C., Pollock, A. G., and Wooley, P. H. (2010). Mechanical evaluation of large-size fourth-generation composite femur and tibia models. *Ann. Biomed. Eng.* 38 (3), 613–620. doi:10.1007/s10439-009-9887-7

Healey, J. H., Morris, C. D., Athanasian, E. A., and Boland, P. J. (2013). Compress knee arthroplasty has 80% 10-year survivorship and novel forms of bone failure. *Clin. Orthop. Relat. Res.* 471 (3), 774–783. doi:10.1007/s11999-012-2635-6

Panagopoulos, G. N., Mavrogenis, A. F., Mauffrey, C., Lesenský, J., Angelini, A., Megaloikonomos, P. D., et al. (2017). Intercalary reconstructions after bone tumor resections: A review of treatments. *Eur. J. Orthop. Surg. Traumatol.* 27 (6), 737–746. doi:10.1007/s00590-017-1985-x

Parlee, L., Kagan, R., Doung, Y. C., Hayden, J. B., and Gundle, K. R. (2020). Compressive osseointegration for endoprosthetic reconstruction. *Orthop. Rev.* 12 (3), 8646. doi:10.4081/or.2020.8646

Qu, H., Guo, W., Yang, R., Tang, X., Yan, T., Li, D., et al. (2015). Cortical strut bone grafting and long-stem endoprosthetic reconstruction following massive bone tumour resection in the lower limb. *Bone Jt. J.* 97 (4), 544–549. doi:10.1302/0301-620X.97B4.34695

Ruggieri, P., Mavrogenis, A. F., Bianchi, G., Sakellariou, V. I., Mercuri, M., and Papagelopoulos, P. J. (2011). Outcome of the intramedullary diaphyseal segmental defect fixation system for bone tumors. *J. Surg. Oncol. (Tallinn).* 104 (1), 83–90. doi:10.1002/jso.21893

Sakellariou, V. I., Mavrogenis, A. F., Babis, G. C., Soucacos, P. N., Magnissalis, E. A., and Papagelopoulos, P. J. (2012). Comparison of four reconstructive methods for diaphyseal defects of the humerus after tumor resection. *J. Appl. Biomech.* 28 (5), 568–578. doi:10.1123/jab.28.5.568

Sewell, M. D., Hanna, S. A., McGrath, A., Aston, W. J., Blunn, G. W., Pollock, R. C., et al. (2011). Intercalary diaphyseal endoprosthetic reconstruction for malignant tibial bone tumours. *J. Bone Jt. Surg. Br* 93 (8), 1111–1117. doi:10.1302/0301-620x.93b8.25750

Stevenson, J. D., Wigley, C., Burton, H., Ghezelayagh, S., Morris, G., Evans, S., et al. (2017). Minimising aseptic loosening in extreme bone resections: Custom-made tumour endoprostheses with short medullary stems and extra-cortical plates. *Bone Jt. J.* 99 (12), 1689–1695. doi:10.1302/0301-620X.99B12.BJJ-2017-0213.R1

Streitburger, A., Hardes, J., Nottrott, M., and Guder, W. K. (2020). Reconstruction survival of segmental megaendoprostheses: A retrospective analysis of 28 patients treated for intercalary bone defects after musculoskeletal tumor resections. *Arch. Orthop. Trauma Surg.* 142 (1), 41–56. doi:10.1007/s00402-020-03583-4

Talbot, M., Zdero, R., Garneau, D., Cole, P. A., and Schemitsch, E. H. (2008). Fixation of long bone segmental defects: A biomechanical study. *Injury* 39 (2), 181–186. doi:10.1016/j.injury.2007.08.026

Wang, J., An, J., Lu, M., Zhang, Y., Lin, J., Luo, Y., et al. (2021). Is three-dimensional-printed custom-made ultra-short stem with a porous structure an acceptable reconstructive alternative in peri-knee metaphysis for the tumorous bone defect? *World J. Surg. Oncol.* 19 (1), 235. doi:10.1186/s12957-021-02355-7

Biomechanical consequences of cement discoplasty: An *in vitro* study on thoraco-lumbar human spines

Chloé Techens[1,2,3], Sara Montanari[1], Ferenc Bereczki[2,4], Peter Endre Eltes[2,3]*, Aron Lazary[2,3] and Luca Cristofolini[1]

[1]Department of Industrial Engineering, School of Engineering and Architecture, Alma Mater Studiorum—Università di Bologna, Bologna, Italy, [2]In Silico Biomechanics Laboratory, National Center for Spinal Disorders, Buda Health Center, Budapest, Hungary, [3]Department of Spinal Surgery, Department of Orthopaedics, Semmelweis University, Budapest, Hungary, [4]School of PhD Studies, Semmelweis University, Budapest, Hungary

With the ageing of the population, there is an increasing need for minimally invasive spine surgeries to relieve pain and improve quality of life. Percutaneous Cement Discoplasty is a minimally invasive technique to treat advanced disc degeneration, including vacuum phenomenon. The present study aimed to develop an *in vitro* model of percutaneous cement discoplasty to investigate its consequences on the spine biomechanics in comparison with the degenerated condition. Human spinal segments (n = 27) were tested at 50% body weight in flexion and extension. Posterior disc height, range of motion, segment stiffness, and strains were measured using Digital Image Correlation. The cement distribution was also studied on CT scans. As main result, percutaneous cement discoplasty restored the posterior disc height by 41% for flexion and 35% for extension. Range of motion was significantly reduced only in flexion by 27%, and stiffness increased accordingly. The injected cement volume was 4.56 $\pm$ 1.78 ml (mean $\pm$ SD). Some specimens (n = 7) exhibited cement perforation of one endplate. The thickness of the cement mass moderately correlated with the posterior disc height and range of motion with different trends for flexions vs. extension. Finally, extreme strains on the discs were reduced by percutaneous cement discoplasty, with modified patterns of the distribution. To conclude, this study supported clinical observations in term of recovered disc height close to the foramen, while percutaneous cement discoplasty helped stabilize the spine in flexion and did not increase the risk of tissue damage in the annulus.

1 Introduction

The ageing of the global population due to increasing life expectancy (Fuster, 2017) results in the changing epidemiology of disease and spinal disorders (Fehlings et al., 2015). In the ageing spine, the intervertebral disc degeneration (IDD) leads to biomechanical and structural changes of the spine (Kirnaz et al., 2022). The terminal disc degeneration is characterized by total disorganization of the intervertebral tissue, and complete resorption of the nucleus pulposus causing in many cases: this condition is often referred to as "vacuum phenomenon" in the clinical context (Knutsson, 1942; Samuel, 1948; Morishita, et al., 2008). IDD-related structural changes lead to biomechanical malfunctions (Inoue and Espinoza Orías, 2011), such as segmental instability. Surgical treatment possibilities of segmental instability in elderly patients are limited (Fehlings et al., 2015). Minimally invasive surgical (MIS) procedures are the preferred options (Yue et al., 2010). Percutaneous cement discoplasty (PCD) is a MIS procedure, where the vacuum space in the intervertebral disc is filled with percutaneously injected acrylic cement. The PCD procedure is expected to provide a segmental stabilizing effect and indirect decompression of the neuronal elements (Varga et al., 2015; Sola et al., 2018; Kiss et al., 2019). Initially PCD was biomechanically investigated on cervical discs (Roosen, 1982; Wilke, et al., 2000). However, PCD as low-back-pain treatment has only been evaluated in terms of patient outcome by clinical studies (Varga et al., 2015; Kiss et al., 2019; Camino Willhuber et al., 2020). Recently, *in vivo* models of PCD have been developed on porcine and ovine specimens (Techens et al., 2020; Ghandour et al., 2022) proposing promising methods for the experimental evaluation of the surgery biomechanics. In addition, PCD has started to be investigated *in silico*, bringing complementary data on the spine stability and load sharing. A numerical study assessed the impact of injected cement volume and reduction of the nerve root stress following PCD (Jia, et al., 2022). Another study compared the effect of friction at the cement-endplate interface on the disc tissue stress (Li et al., 2022). If PCD appeared efficient to relieve patient's pain, biomechanics of the human spine following the surgery remain largely unknown and require supplementary investigations (Techens et al., 2022). Combining more experimental and numerical studies would help expanding the research on PCD and improve the surgical technique. This study aims at investigating the consequences of percutaneous cement discoplasty on the biomechanics of the human spine with respect to the pre-operative degenerated condition. Therefore, the first objective was to develop a reliable *in vitro* model of percutaneous cement discoplasty. This was then used to evaluate the *in vitro* biomechanical behaviour of the treated segment. The core objective of this study was monitoring the biomechanical effects of PCD and identifying the potential links between PCD and the biomechanical outcomes in order to assess the benefits and detect potential detrimental effects. In particular, we hypothesized that PCD would increase the disc height in the posterior region with respect to the degenerated condition. We furthermore hypothesized that PCD would impact the intervertebral kinematics. Finally, we conjectured that, as a side effect, PCD could possibly represent a challenge for the surrounding tissue since the cement mass stiffness differs from the nucleus pulposus. We also hypothesized that the cement volume and its distribution inside the disc would impact on the biomechanical behaviour of the treated functional spinal unit (FSU).

2 Materials and methods

2.1 Compliance with ethical standards

This study was performed in line with the principles of the Declaration of Helsinki. Approval was granted by the Bioethics Committee of the University of Bologna (Prot. 76497, 1 June 2018). The cadaveric spines were obtained through two institutions: an international donation program (International Institute for the Advancement of Medicine) and the hospital of the NCSD after ethical approval of both entities.

2.2 Overview of the study

PCD is the ultimate treatment for polymorbid patients. This surgery does not aim to completely restore the conditions of a healthy spine, but to mechanically act on the disc foramen to relieve the pain. Thus, this study aimed to assess whether PCD would recover the disc height and impact the intervertebral kinematics in comparison with degenerated discs. The overall workflow is presented in this section; additional technical explanations are detailed in Supplementary Material S1 File. Functional spinal units (FSUs) were prepared for testing (Figure 1). They were biomechanically tested non-destructively after simulating disc degeneration. Then percutaneous cement discoplasty was simulated. The specimens were re-tested under the same loading conditions. Kinematics and strains were measured using digital image correlation (DIC).

2.3 Cadaveric specimens

For this study, 27 FSUs were extracted from 15 Caucasian lumbar spines (9 males/6 females) aged 35 to 86 years old. Death was unrelated to a spine disease. Based on computed tomography (CT) scan images, specimens with fractures or bridged osteophytes were excluded from the study by a clinician. Only specimens presenting intact endplates were selected. The selection did not consider the degree of disc degeneration. All
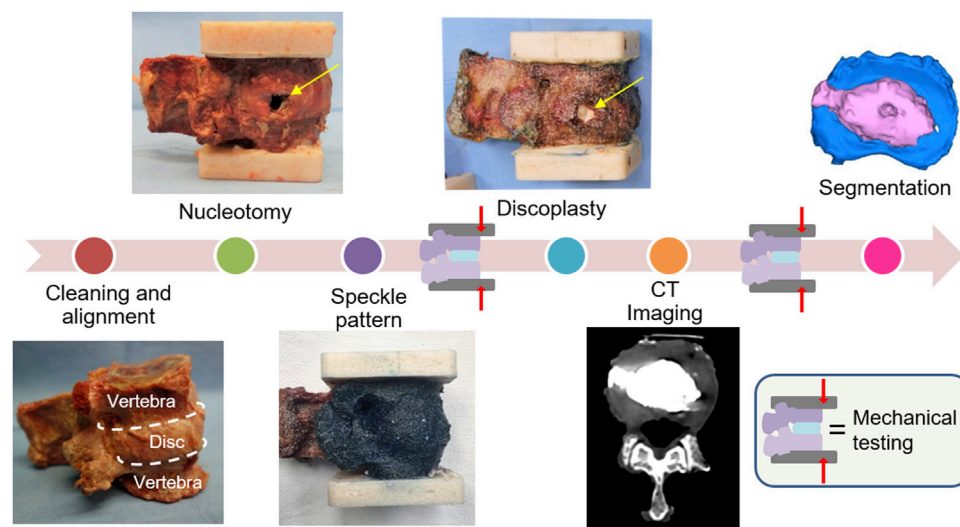
FIGURE 1
Experimental workflow of the study. The specimens were prepared with a high-contrast speckle pattern to allow measuring displacements and strains under load with digital image correlations. Each specimen underwent biomechanical testing (under the same loading conditions) after nucleotomy and after simulated percutaneous cement discoplasty. The cement injected was investigated on CT images.

soft tissues were carefully removed from the segment preserving the anterior (ALL), supraspinous and posterior ligaments, the facet joints, and the intervertebral disc (IVD) to keep the natural kinematics of the segment (Behrsin and Briggs, 1988; Palanca et al., 2020). As muscles were removed from the spine segments, rigor mortis did not affect the tests. Each segment disc was horizontally aligned, using a six-degree-of-freedom clamp; both segment extremities were embedded with acrylic cement. Specimens were stored at −28°C between cleaning and testing phases, and were thawed in physiological solution at room temperature prior to each test phase; hydration was granted during preparation and testing spraying the specimens (Tan and Uppuganti, 2012).

2.4 Surgical procedure

2.4.1 Nucleotomy

PCD is recommended for advanced degeneration of the disc, when a vacuum is observed instead of the nucleus pulposus (NP), inducing a negative pressure within the disc (Varga et al., 2015; Sola et al., 2018). As donor specimens with a vacuum disc are complicated to obtain, a similar disc degeneration state was artificially created by manually emptying the disc. This degenerated disc simulation has been previously developed on animal specimens (Moissonnier et al., 2014; Techens et al., 2020) to provide the anatomical vacuum characteristics needed for PCD using a substitutive method. A rectangular incision as high as the disc and 5–8 mm wide was performed with a scalpel blade

in the annulus fibrosus on the lateral side (Figure 1), preferably on the side showing irregularities (small osteophytes, wrinkled tissues). Although it differed from the clinical posterior approach used for PCD, lateral fenestration was chosen in consideration of the loading directions as it avoided damaging the disc and ligaments in the posterior region. The nucleus pulposus was extracted through the excision and the cartilaginous endplates were shaved by scratching the cartilage off by a spine surgeon.

As the incision of the annulus fibrosus (AF) was suspected to critically affect the biomechanics of the remaining annulus, a separate methodological study was performed on eight additional specimens to quantify the consequences of this preparation (Supplementary Material S2 File). Briefly, only NP removal significantly impacted the PDH. AF incision did not significantly impact the posterior disc height nor the biomechanics.

2.4.2 Cement discoplasty

After being tested in a simulated degenerated condition, the specimens were treated with a highly radiopaque acrylic cement (Mendec Spine; Tecres, Sommacampagna, Italy, containing 30% $BaSo_4$). Acrylic cement is known to be biocompatible and so commonly used in other spine surgeries such as vertebroplasty. The cement was prepared as clinically recommended (Sola et al., 2018), mixing the component at room temperature, and waiting a few minutes to obtain the desired viscosity. It was injected inside of the disc through the incision performed during nucleotomy until the cement would fill the cavity (Figure 1). Because the empty IVD was no longer stretched, the disc height

FIGURE 2
Workflow for the detection of the bony endplates and cement mass to visualize and assess the distribution of the cement in the intervertebral space, and to measure the cement thickness.
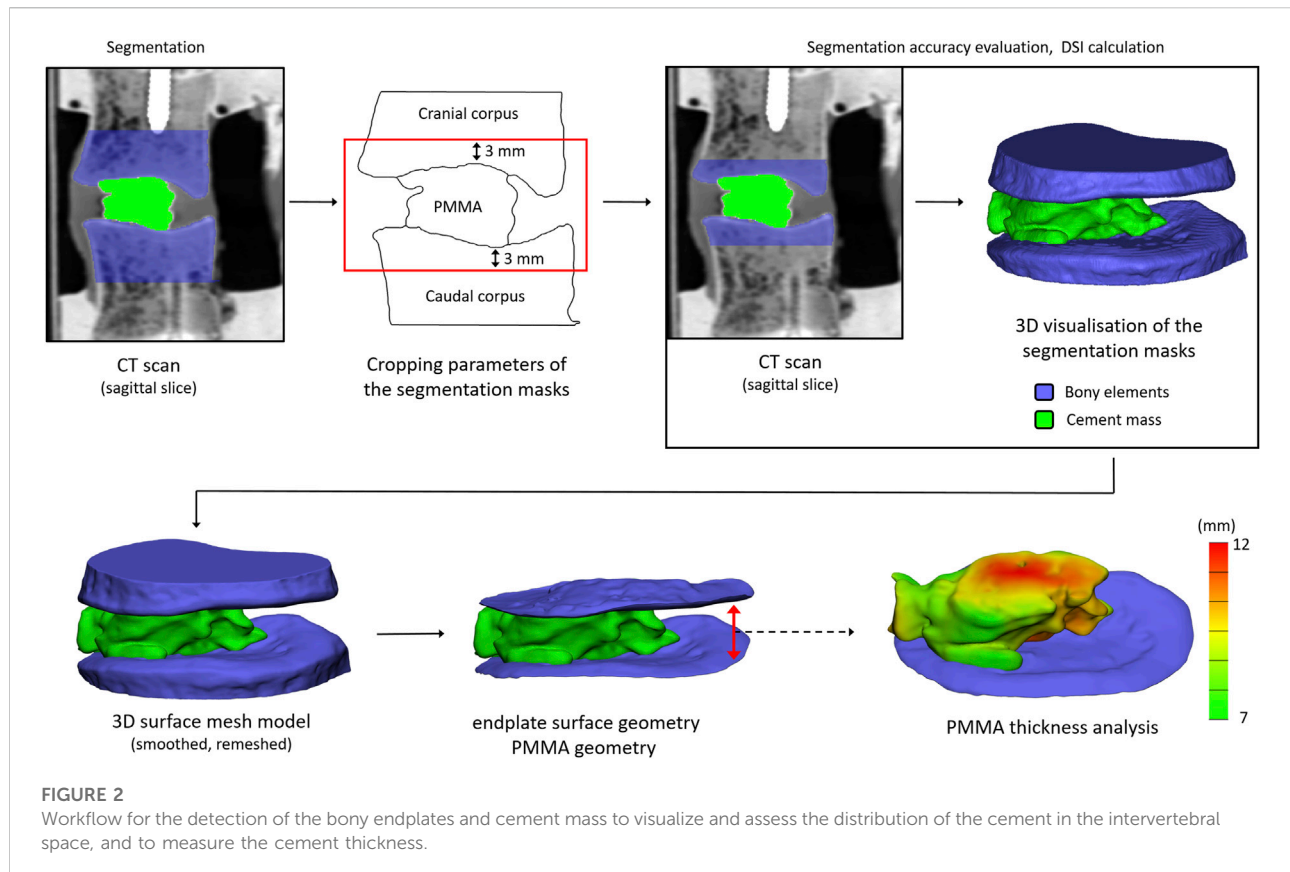
was manually kept constant during the injection to avoid an underestimation of the cement volume. The stretch was released once the cement started hardening, to avoid cement leakage through the annulus incision. CT imaging and cement geometry visualization.

In order to study the cement distribution inside of the disc, the specimens were scanned after PCD with a clinical computed tomography scanner (Aquilion ONE, Toshiba) with 220 mA, 120 kV, 0.3 mm slice thickness, 0.214 mm pixel size. The vertebrae and the cement mass were segmented with an image analysis software (Mimics Innovation Suite-v23.0, Materialise, Leuven, Belgium) on the CT slices using thresholding algorithm. Because of the extremity pots used for mechanical testing, the *in vitro* vertebrae were uniformly cropped at 3 mm from the deepest part of the endplate curvature to achieve a region of interest common to all specimens. (Figure 2). All segmentations were performed by two independent operators (C.T and F.B). Segmentation repeatability was measured with Dice Similarity Index (DSI) (Eltes et al., 2020).

The segmented masks were automatically converted into 3D surface meshes, and smoothed (iterations: 6, smooth factor: 0.7, with shrinkage compensation). The geometries were imported and measured (3-Matic 14.0, Mimics Innovation Suite v23.0). The vertebrae and bone cement geometries were first uniformly

re-meshed (target triangle edge length: 0.3 mm, surface contour preservation, bad edges removing, split edge factor: 0.2). The endplate surfaces were manually selected. The cement thickness was defined between the two-endplate surface planes, and was measured with the Midplane Thickness Analysis module of 3-Matic.

2.5 Biomechanical testing

The scope of our work was to test if discoplasty can provide relief by increasing the foramen space with respect to the degenerated conditions. *In vivo*, one of the most concerning loading scenarios for nerve compression within the foramen is related to a combination of an axial load and motions in a sagittal plane. For this reason, the specimens were mechanically tested in flexion and extension using a uniaxial testing machine (Mod. 8032, Instron, United Kingdom). For these motions, spinal specimens are usually tested under pure moments, even if it was found less physiological for damaged or treated segments in comparison with axial loadings (Wilke et al., 2001). Thus, one pot was rigidly fixed to the top of the testing machine. In order not to constrain the relative motion of the two vertebrae and avoid buckling, the caudal vertebra was loaded through a spherical joint
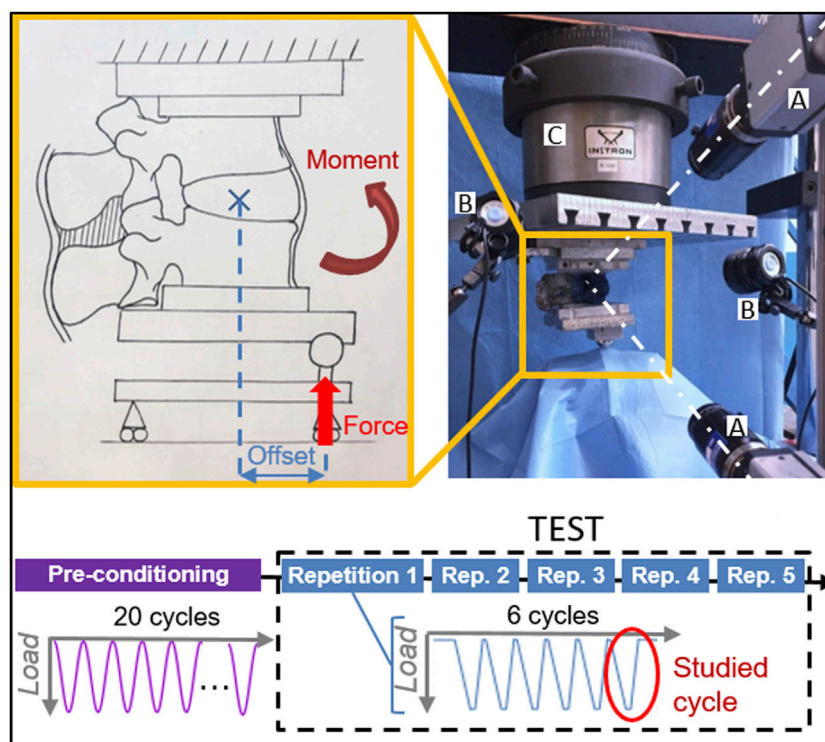
FIGURE 3
Testing protocol with the experimental setup of the test in flexion and composition of the test sequence. Two cameras (A) targeted the specimen, which was illuminated by high-intensity LEDs (B). The force applied by the testing machine (C) was delivered with an offset, resulting in a combination of a force and a moment.

moving along a low-friction rail (Figure 3). This set-up allowed to reach the full load in a relatively fast loading, comparable to the speed one can expect in living subjects (file wp4_130109_1_17 from database OrthoLoad (Bergmann, 2008)).

For each specimen, a force of 50% of the respective Body Weight (BW) of the respective donor, representing the upper body above the lumbar vertebra, was applied with an anterior (posterior) offset, generating a combination of compression and flexion (extension) (Table 1). To have an anatomical definition of the offsets, the lever arms were measured with respect to the centre of the disc on CT images. As the segments are more flexible in flexion, the assigned offset was smaller (35% of the antero-posterior length of the disc) compared to extension (70% of the length) to ensure a similar bending moment was applied in both directions. A reduced load, as close as possible to 50% BW, was applied to some specimens which exhibited a large mobility after nucleotomy, to prevent the endplates from coming in contact and possibly being damaged under the initially planned load (Table 1). Because the loading conditions integrated the body anatomy, the resulting moment would vary between specimens, with a standard deviation of 1.15 Nm in flexion and 2.31 Nm in extension.

The loading ramp lasted 1.0 s; the maximum loading was held for 0.3 s, then the specimen was unloaded. Each test consisted of 6 loading cycles, where the last one was analysed in detail (Figure 3). Three cycles are sufficient for minimizing the effect of the viscous component in the response in another study (Cottrell et al., 2006), the subsequent cycles being nearly identical in term of loads and displacements. Each 6-cycle test was repeated five times to assess the repeatability. Before being tested, each specimen was pre-conditioned applying the test load as a sinusoid at 0.5 Hz for 20 cycles. The specimens were tested in nucleotomy and cement discoplasty conditions for both directions of loading. The applied load and the actuator displacement were recorded by an independent datalogger (PXI, Labview, National Instruments, Austin Texas, US) at 500 Hz.

During each test, the 3-dimensional displacements and strain distribution of the specimen surface were tracked using a Digital Image Correlation (DIC) system. This technique requires a high-contrast speckle pattern on both the vertebrae and the intervertebral disc (Figure 1). First, the segment was stained with a methylene blue solution to create a dark background without impacting the properties of the tissues (Lionello, et al., 2014). The white pattern was then sprayed with a water-based

TABLE 1 Donors' data and testing parameters for flexion and extension.

Specimen	Sex-age	Lumbar level	Offset (mm)		Axial displacement variation (mm)		Testing load (N)	
			Flexion	Extension	Flexion	Extension	Flexion	Extension
P01	M-68	T12-L1	12.3	24.5	−0.59	−1.35	402	
		L4-L5	14.6	29.3	−0.49	−0.35	402	
P02	M-79	L2-L3	15.1	30.1	–	−0.61	–	387
P03	M-53	L2-L3	13.1	26.3	−1.40	−0.73	402	
		L4-L5	13.6	27.2	−2.21	−0.15	402	
P04	F-35	T12-L1	10.4	20.8	−0.37	−0.21	309	
		L2-L3	10.7	21.5	−3.20	−0.43	309	
		L4-L5	11.0	22.1	–	−0.34	–	309
P05	F-68	T12-L1	9.1	18.2	−2.06	−0.84	396*	
P06	M-59	L2-L3	10.9	21.8	0.49	−0.02	326*	
		L4-L5	11.6	23.2	0.59	−0.52	140*	326*
P07	F-78	L1-L2	12.9	25.8	−0.46	−0.09	348	
		L3-L4	13.4	26.9	1.05	−0.69	348	
P08	M-79	L1-L2	12.8	25.7	−2.02	−1.34	456	
		L3-L4	14.8	29.5	−1.22	−0.68	456	
P09	F-86	L1-L2	13.6	27.2	−1.17	−0.56	265*	
		L3-L4	15.8	31.5	−0.92	−0.61	265*	
P10	M-71	L1-L2	11.9	23.7	−1.98	−0.38	343	
		L3-L4	13.3	26.5	–	−0.40	–	343
P11	M-68	L2-L3	12.6	25.3	−0.44	−0.11	319	
		L4-L5	13.2	26.3	−1.51	−0.01	319	
P12	F-80	L3-L4	13.9	27.9	−0.63	−0.42	378	
P13	M-64	L1-L2	12.8	25.6	−1.62	−0.09	417	
		L4-L5	14.9	29.8	−4.31	0.09	417	
P14	M-73	L3-L4	16.6	33.1	−2.12	−0.57	515	
P15	F-74	L1-L2	12.3	24.6	−1.65	−1.01	412	
		L4-L5	15.4	30.7	−1.16	0.24	412	

*Reduced load to avoid damages.

TABLE 2 Material and parameters of the DIC system.

Material	Acquisition	Images post-processing
2 cameras: 5 megapixels, 2440 × 2050 pixels, 8-bit. 26° between the cameras	Software: Instra 4D, v.4.3.1, dantec dynamics	Facet size: 35 pixels
35 mm lenses: Apo-Xenoplan 1.8/35, Schneider-Kreuznach, Bad-Kreuznach, Germany	Calibration: Al4-BMB-9 × 9, dantec dynamics	Grid spacing: 11 pixels
Lights: cold-light LEDs	Field of view: 60 mm × 100 mm Pixel size: 0.04 mm	Filtering: local 7 × 7 pixels kernel

acrylic paint, following a procedure optimized elsewhere (Lionello, et al., 2014; Palanca, et al., 2015). Four white dots were manually added along the endplates to accurately identify the disc cranial and caudal borders from the images. To measure the displacements and the deformations over the specimen surface, a 3D-DIC system (Q400, Dantec Dynamics,

Skovlunde, Denmark) was optimized (Palanca, et al., 2015) (Table 2) and used (Figure 3). Image acquisition was performed in lateral view with the cameras pointing to the neuroforamen. Images were recorded at 15 Hz from the unloaded condition (reference frame, no load applied) to the end of the sixth cycle. In order to synchronize the DIC images

with the testing machine data, the axial translation of the mobile vertebra, corresponding to the actuator motion, was derived from the images. The PXI load-displacement and axial translation curves were then temporally aligned by automatically identifying the peaks and valleys of the cycles.

2.6 Data analysis

All measurements were compared for each specimen and each loading configuration (flexion, extension) between the two conditions: nucleotomy (NUCL), and percutaneous cement discoplasty (PCD). Since PCD aims to assess the changes of the height of neuroforamen, the posterior disc height (PDH) was measured at the peak load as the cranial-caudal distance between endplates close to the neuroforamen (Supplementary Material S1 File).

The motions (translations and rotations) of each vertebra were computed from DIC images (Morosato, et al., 2019; Techens et al., 2020). The range of motion (ROM) was defined as the relative angle between the vertebrae in the sagittal plane between the peak load and unloaded conditions. Laxity (LZ) and elastic zones (EZ) were identified from load-displacement curves (Supplementary Material S1 File) as respectively the region of large mobility and no loading, and the region where tissue stretched. The transition point defined the limit between the two zones and the elastic stiffness was evaluated on the EZ (M. L. Tanaka et al., 2011).

The maximum and minimum true principal strains (ε_1, ε_2) over the vertebrae and IVD were measured at the peak load. Their median over the disc surface were computed, as well as their extreme values (defined as the 95%-percentile, to avoid local measurement artifacts).

All the computations were performed with dedicated Matlab scripts (MathWorks Inc., Natick, MA, United States). To overcome the inter-specimen variability, the parameters measured after cement discoplasty were normalized to the nucleotomy condition of the respective specimen.

2.7 Statistical analysis

Shapiro-Wilk tests were applied to all parameter distributions to assess their normality ($\alpha = 0.05$). Depending on the normality assessment, comparisons between nucleotomy and discoplasty were made for ROM, stiffness, height, and the strain median with either a non-parametric Wilcoxon's test or a paired t-test. Influence of the spine level on the results was assessed with a one-way ANOVA. Finally, correlations between the cement distribution and the biomechanical parameters were evaluated with Spearman's rank correlation coefficient using

SPSS Statistics 25.0 (IBM Corp., Armonk, NY, United States) with $p = 0.05$. The interpretation of the correlation strength was based on Evans' classification (Evans, 1996) ($\rho < 0.20$ is very weak, 0.20 to 0.39 is weak, 0.40 to 0.59 is moderate, 0.60 to 0.79 is strong and 0.80 or greater is a very strong correlation).

3 Results

The different indicators were normalized between NUCL and simulated PCD for each specimen and each direction of loading. Main trends are reported here, the detailed parameter values are found in Supplementary Material S1 File.

Two specimens were excluded in flexion: for one, the posterior process broke but the specimen was unaffected in extension; a third specimen broke during the test. One specimen had a DIC-correlated area too small and was only used to measure the stiffness.

3.1 Posterior disc height

The posterior disc height (PDH) was measured from DIC correlations for flexion ($n = 24$) and extension ($n = 27$). The specimens exhibited a PDH increase of 41% ± 46% (mean ± SD) in flexion (paired t-test, $p < 0.001$) and 35% ± 38% in extension ($p < 0.001$). In particular, the largest increase of PDH in both flexion and extension were respectively measured at the L3-L4 level whereas the smallest increase happened at T12-L1 (extension) and L2-L3 levels (flexion) (Figure 4). However, spine level did not significantly impact PDH (ANOVA; $p = 0.69$ in flexion, $p = 0.65$ in extension).

3.2 Range of motion

The range of motion (ROM) was derived from DIC correlations in flexion ($n = 24$) and extension ($n = 27$). Discoplasty decreased the ROM by 27% ± 27% (mean ± SD) in flexion (paired t-test, $p < 0.001$) and decreased it by 9% ± 96% in extension ($p = 0.33$). The different spine levels exhibited different trends in flexion with a mean ROM drop about 40% for segments between T12 and L2, whereas the low lumbar spine showed a smaller decrease about 20% (ANOVA, $p = 0.66$) (Figure 4). Conversely, similar ROM was measured in extension, independent of the spinal segment ($p = 0.56$).

3.3 Stiffness

The specimens showed different behaviours according to the loading configuration and disc condition (Figure 5). After
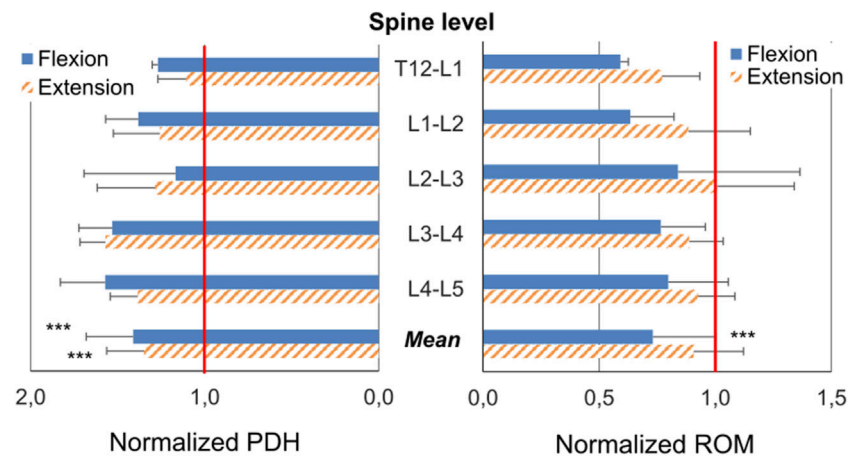
FIGURE 4
Changes (Mean ± SD) of the posterior disc height (PDH) and of the Range of Motion (ROM) caused by cement discoplasty at the different spine levels and as an average of all levels. The PDH and ROM after discoplasty were normalized with respect to the value before discoplasty: a normalized value of 1.00 indicates no change; a value greater (smaller) than 1.00 indicates that the respective magnitude was increased (decreased) due to discoplasty. First quartile, median and third quartile are represented by lines. Mean is indicated by the cross and min and max values by the whiskers. Statistical significance (paired t-test, $p < 0.001$) is designated by ***.
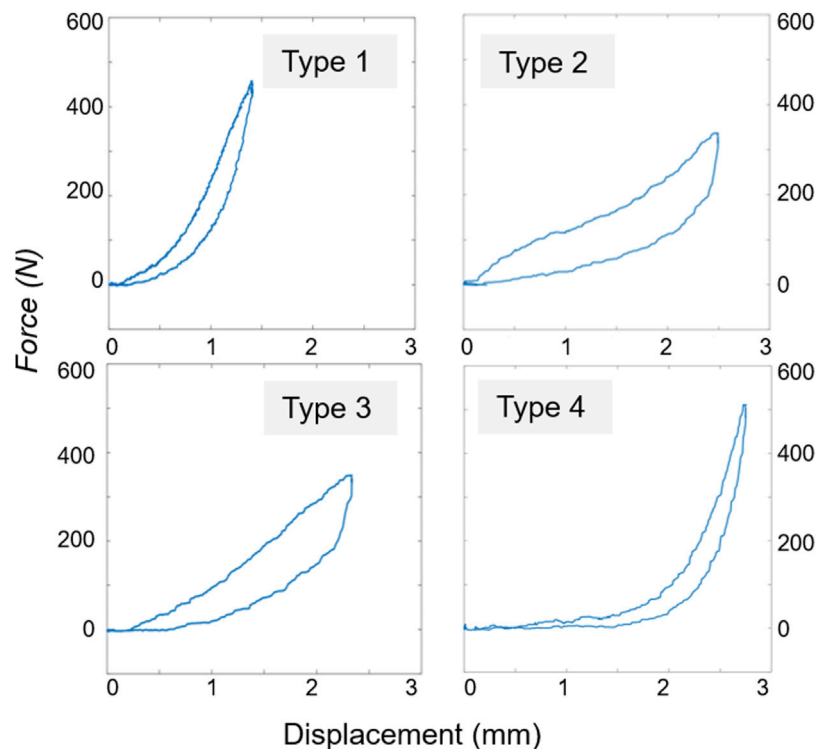
FIGURE 5
Typical load-displacement curves found for the 27 specimens depending on the testing conditions (disc condition, motion) resulting in 104 tests. Type 1: the majority of the tests (79/104) was described with an exponential toe region, and linear elastic part which were fitted following Tanaka et al., 2011 model. Type 2: S-shaped was followed by 2/27 specimens in nucleotomy flexion and 7/27 in cement discoplasty flexion. Type 3: 1/27 specimens in nucleotomy extension, 1/27 in cement discoplasty extension, and 4/27 in discoplasty flexion followed a flat toe region and linear elastic region. Type 4: L-shaped was followed by 10/27 specimens in nucleotomy extension.
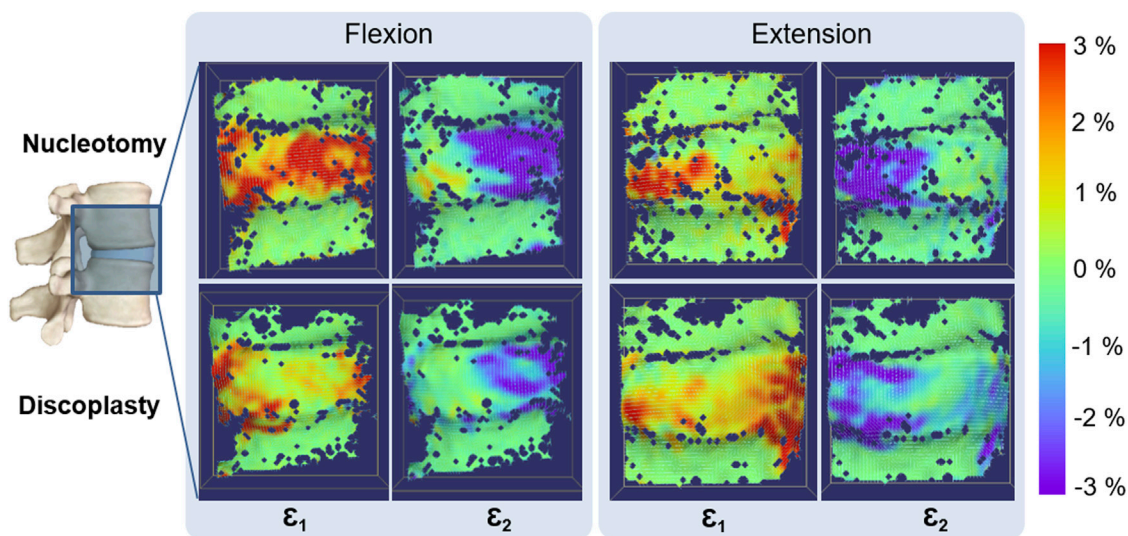
FIGURE 6
Typical distribution of Maximum (ε_1) and Minimum (ε_2) True Principal strains on the specimen surface in flexion and extension. The dark blue spots on the specimen surface correspond to the areas where the DIC algorithm could not correlate, in particular along the endplates. Only the disc underwent large strains.

nucleotomy, in flexion load-displacement was described by an exponential curve for the LZ and a linear curve for the EZ in equivalent proportion. In extension, the loading phase showed a flat linear LZ associated with a sharper transition to the linear EZ. After PCD, different behaviours were observed in flexion. Some specimens exhibited an S-shaped load-displacement curve, others a very short LZ followed by a linear EZ. The rest displayed the usual exponential-linear shape already observed after nucleotomy. In extension, specimens followed an exponential-linear behaviour too.

The elastic stiffness, transition load and displacement were estimated by fitting the load-displacement curves (Supplementary Material S1 File: Supplementary Table S1_1, Supplementary Figure S1_2). In flexion, mean transition displacement was reduced by 38% from nucleotomy to cement discoplasty (paired t-test, $p < 0.001$) while transition load was unaffected ($p = 0.28$). In extension, both parameters respectively dropped by 28% and 16% (paired t-test, $p < 0.001$). For both loading configurations, the LZ was larger after PCD. Finally, discoplasty increased the mean elastic stiffness at peak load by 37% (one sample t-test, $p < 0.01$) in flexion but decreased it by 7% ($p = 0.07$) in extension.

When sorting the results by spine level, differences were more pronounced in flexion: the high lumbar spine showed a shorter LZ with very low variability between specimens. Similarly, the variability between specimens was smaller for high levels in flexion. Conversely, in extension, results showed similar trends for all the spine levels.

3.4 Strain

The mean true strains were derived between specimens (Supplementary Material S1 File: Supplementary Table S1_1, Supplementary Figure S1_3). In flexion, the maximum strain after discoplasty was 12% (paired t-test, $p < 0.05$) smaller than after nucleotomy and the minimum strain 40% higher (Wilcoxon test, $p < 0.01$). In extension both strains were reduced by discoplasty by 12% (Wilcoxon test, $p < 0.05$) and 14% (paired t-test, $p < 0.01$). These changes of the median value after PCD were associated with a reduction of the extreme strain values, and a shrinkage of the highly strained regions. Discoplasty was associated with a migration of the maximum strains towards the endplates, while minimum strains were located at the disc mid-height (Figure 6). In nucleotomy, in the compressive side of the disc the maximum (tensile) principal strains were directed circumferentially and the minimum (compressive) ones axially. After discoplasty, in the compressive part of the disc the minimum principal strains were directed axially and in the stretched part, the maximum strains were directed circumferential. We also analyzed the number of specimens in which strains exceeded 5%, 10% and 15%. The number of specimens showing high strain values was smaller after PCD (Supplementary Material S1 File: Supplementary Figure S1_4). After discoplasty, the strains did not exceed 10% except in flexion where the number of specimens exhibiting maximum strains exceeding 10% increased. Finally, the most extreme maximum and minimum strains values measured among all specimens were respectively 13.6% and −22.9% regardless the disc condition.

TABLE 3 Summary of the cement distribution analysis for each specimen. The cement thickness between the endplates was measured axially.

Specimen	Level	Cement geometry		Cement thickness				Caudal endplate	Cranial endplate
		Surface (cm²)	Volume (cm³)	Min (mm)	Max (mm)	Mean (mm)	SD (mm)	Total surface (cm²)	Total surface (cm²)
P01	T12-L1	18.94	4.18	4.6	9.3	7.4	0.9	15.25	14.98
	L4-L5	21.77	4.12	5.6	13.5	9.5	1.8	13.99	13.98
P02	L2-L3	35.12	7.89	6.5	14.0	10.1	1.6	22.56	21.86
P03	L2-L3	23.72	5.05	6.2	14.3	9.3	1.4	17.82	18.44
	L4-L5	21.67	5.27	6.8	15.0	10.5	1.5	19.90	18.13
P04	T12-L1	11.81	2.14	6.0	10.1	8.4	0.8	12.45	12.08
	L2-L3	16.61	3.40	7.4	12.3	9.6	1.0	13.97	13.79
	L4-L5	13.49	2.02	6.5	12.6	10.5	1.4	13.35	14.00
P05	T12-L1	12.93	2.34	3.4	11.1	6.6	1.3	8.48	9.44
P06	L2-L3	11.49	2.49	5.8	16.9	8.9	1.7	10.89	11.02
	L4-L5	15.35	3.18	4.3	13.8	8.0	1.6	12.14	12.67
P07	L1-L2	21.84	2.86	7.5	19.8	10.8	2.4	21.66	16.58
	L3-L4	20.03	5.07	7.1	16.0	10.6	1.3	16.34	15.56
P08	L1-L2	26.84	7.04	3.8	16.8	9.0	2.3	17.86	18.55
	L3-L4	22.38	3.88	5.3	12.2	9.8	1.6	20.25	19.94
P09	L1-L2	26.12	6.02	4.6	13.8	9.3	1.5	18.81	18.36
	L3-L4	38.70	8.89	5.2	17.2	9.9	1.7	19.72	21.35
P10	L1-L2	24.28	5.51	4.8	15.7	9.9	1.8	15.26	14.77
	L3-L4	24.74	5.44	6.6	18.3	11.6	2.0	16.01	15.98
P11	L2-L3	16.07	3.36	6.4	11.6	9.7	1.3	15.37	15.20
	L4-L5	17.03	3.31	7.1	13.1	10.4	1.3	14.32	14.92
P12	L3-L4	20.14	3.52	2.4	11.9	8.5	2.2	18.12	17.99
P13	L1-L2	22.95	5.69	7.3	15.9	10.9	1.5	15.53	14.89
	L4-L5	27.29	5.15	9.3	16.6	13.2	1.3	16.00	16.05
P14	L3-L4	30.31	7.15	4.3	14.3	9.3	1.8	21.52	20.83
P15	L1-L2	16.51	3.57	5.7	13.9	9.5	1.3	14.25	14.67
	L4-L5	19.40	4.42	3.7	14.8	8.8	2.2	18.25	18.67
	Mean	**21.39**	**4.56**			**9.6**		**16.30**	**16.10**
	(SD)	**(6.65)**	**(1.78)**			**(1.3)**		**(3.44)**	**(3.10)**

The bold values are indicated to be Mean and Sd.

3.5 Visualization of the cement geometry and thickness measurement

The inter-operator DSI for the cement and the vertebrae were 0.98 ± 0.02 and 0.97 ± 0.01 (mean ± SD) respectively, indicating a high repeatability. For consistency, the cement distribution over the caudal vertebral endplate in the intervertebral space was visually assessed in the same view for all specimens (Supplementary Material S1 File: Supplementary Figures S1_5,S1_6). In most cases, the cement distributions mimicked the nucleus shape with an average volume of 4.56 ± 1.78 ml (mean ± SD). Surfaces of both endplates and the injected cement were also measured (Table 3). Seven specimens exhibited leakage of cement into at least one vertebral body in different proportions (Supplementary Material S1 File: Supplementary Figure S1_7). The cranial-caudal thickness of the cement was 9.62 ± 1.30 mm (mean ± SD among specimens, Table 3) with larger values for specimens with perforation of the endplate (Supplementary Material S1 File: Supplementary Figure S1_6).
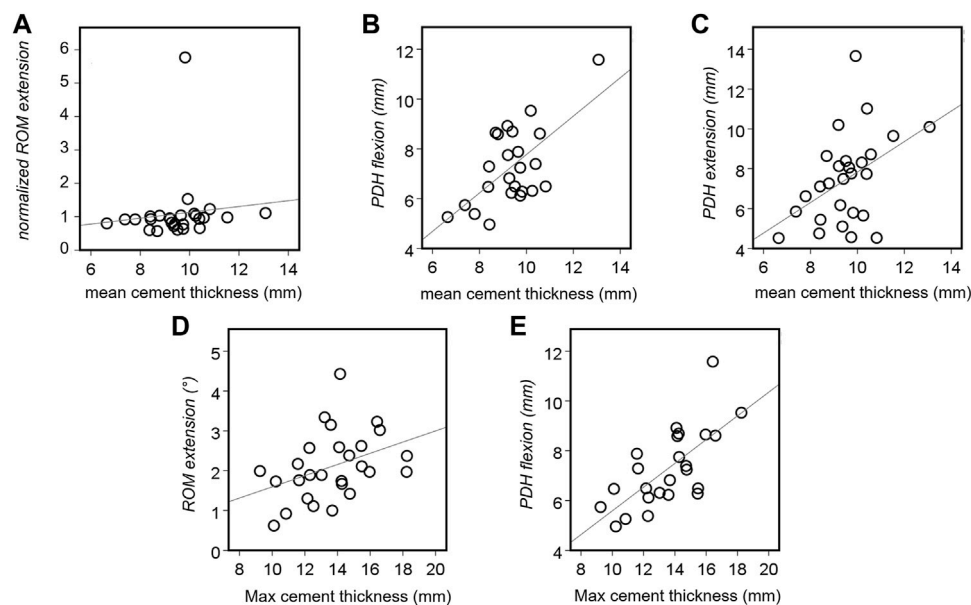
FIGURE 7
Statistically significant associations between the cement thickness and the biomechanical parameters of the tested specimens. Correlations were found for the ROM in extension ((**A**): $p = 0.037$ and (**D**): $p = 0.032$), the PDH in extension ((**B**): $p = 0.048$) and flexion ((**C**): $p = 0.034$ and (**E**): $p < 0.001$).

3.6 Correlation between cement geometry and biomechanical parameters

Relationships between cement distribution and biomechanical parameters were investigated for each direction of loading (Figure 7). The mean cement thickness positively and moderately correlated with PDH after discoplasty in both extension and flexion (Spearman's coefficient $\rho = 0.410$, $p = 0.034$, C and $\rho = 0.407$, $p = 0.048$, B). It also moderately affected the normalized ROM in extension ($\rho = 0.432$, $p = 0.037$, A). Similarly, the maximum cement thickness strongly affected PDH in flexion ($\rho = 0.663$, $p < 0.001$, E) and showed a moderate positive correlation with the absolute ROM in extension ($\rho = 0.413$, $p = 0.032$, D). Relations with other parameters were not significant.

4 Discussion

This study assessed the biomechanical consequences of PCD on the spine kinematics and on the strain distribution. To investigate the effects of PCD on the intervertebral range of motion and stiffness, and on the strain distribution, 27 FSUs were prepared with a simulated disc lesion, and then treated with cement discoplasty. Simulated discoplasty was found to significantly increase the intervertebral height in the posterior region both when flexion and extension were applied.

Discoplasty also impacted the segment kinematics, significantly reducing the flexibility in flexion. This was associated with a

shortening of the laxity zone and an increase of the elastic stiffness. The difference of load-displacement behaviours after nucleotomy and after discoplasty were caused by the combination of the action of the elements of the intervertebral joint. In flexion, facet capsules and posterior ligaments were shown to transmit the load (Tencer, et al., 1982). Different from nucleotomy condition, where the vertebrae are free to rotate until the posterior elements stretch (exponential + linear behaviour), the presence of cement already spaced the facets and pre-stretched the posterior ligaments. This resulted in an immediate loading of the facet capsules followed by the posterior ligaments explaining the two load increases of the S-shape.

Conversely, the cement mass did not affect the mobility in extension. It only impacted the beginning of the segment motion, shortening the laxity zone: during extension, the motion of the vertebrae, "rolling" on the cement, is only constrained by the contact of the posterior elements independently to the presence of cement. Discoplasty also modified the load-displacement behaviour. Following nucleotomy, the intervertebral joint only transmitted the load after the facets contact, resulting on a suddenly stiffening behaviour (L-shape). Discoplasty smoothed this behaviour, probably restoring part of the role of the joint elements. A study suggested that anterior longitudinal ligament had a limited effect on load-resistance in extension attributing it to the bulk compression in the posterior of disc (Tencer, et al., 1982 Ahmed and Burke, 1982).

Discoplasty also reduced the disc tissue deformation: in average, both the maximum and the minimum strain were

lower than after nucleotomy. After nucleotomy a large bulging was induced in the disc under load in particular on the compressed side of the disc, leading to both high tensile and compressive strains in the same location at mid-height. Conversely, once the disc height was restored by PCD, the anatomical elements retrieved their functions in the spine motion, with tensile strains located on the ALL in extension and in the posterior disc in flexion. The distribution of compressive strains became more defined after PCD, with concentrations along the endplates. The largest values of strain found on the surface were reduced after discoplasty. Comparing the corresponding stretches, discoplasty induced values within the same range as estimated strains *in vivo* (Long et al., 2016). Thus, discoplasty did not seem to present a risk of damage for AF outer tissues.

The injected cement was largely distributed in the disc space. In some cases, the injection process resulted in perforation of the endplates, due to degenerative lesions or deterioration caused by the nucleotomy. Cement perforation of the endplates is a clinically known phenomenon which does not represent a contraindication to PCD (only leakages into the spinal canal are represent a relevant clinical complication, and must be treated accordingly (Varga et al., 2015; Sola et al., 2018; Willhuber et al., 2019)). Cement geometry directly impacted PDH and ROM. The thicker the cement, the higher PDH for both directions of loading. The thickness also induced a significant positive moderate correlation with the ROM in extension as a consequence of a larger PDH. Indeed, extension motion is restricted by the contact of the facets. A high PDH spaced the cranial and caudal facets giving a wider range of mobility in extension.

As presented in clinical studies, PCD aims to recovering the healthy disc height and neuroforamen section by creating a cement spacer between the vertebral bodies. This study supported clinical observations (Varga et al., 2015; Sola et al., 2018; Kiss et al., 2019), presenting a significant increase of PDH under bending, which is a more critical loading scenario with a reduced foramen than in *in vivo* measurements made in supine/prone position. In addition, a clear reduction of the stress in the nerve root after surgery was numerically reported compared to the degenerated case (Jia, et al., 2022).

Percutaneous cement discoplasty application to lumbar spine is a recent surgical technique. The only paper about *in vitro* biomechanical testing which can be found in literature was performed on porcine lumbar discs (Techens et al., 2020). Different from the present human study, that preliminary porcine study did not report any significant change of ROM nor stiffness after PCD, but reported similar changes in the strain distribution concluding that discoplasty procedure tends to restore the deformation state of a healthy disc. The difference between the present findings and the previous study probably relates to the difference between human and porcine in terms of NP and AF, and anatomy of the facets. The ROMs measured at

peak load were in the same range as others *in vitro* studies on human spines (Markolf, 1972; Posner et al., 1982; Janevic, et al., 1991; Spenciner et al., 2006; Heuer et al., 2007; Heuer, et al., 2008; Zirbel et al., 2013; Amin et al., 2016). Other studies on the effect of nucleotomy demonstrated that the absence of NP reduced segmental rotational stability, significantly increasing the ROM (Johannessen et al., 2006; Wilke et al., 2006; Heuer et al., 2007; Russo et al., 2017). Only Eysel *et al.* found a drop of ROM for both motions (Eysel et al., 1999). Heuer *et al.* presented the strain map of intact IVDs, exhibiting similar distributions with the strain measured in this present study after PCD (Heuer, et al., 2008). Experimental results could also be put in perspective with *in silico* study findings. Li *et al.* showed that PCD reduced the maximum stresses in the annulus tissue for both flexion and extension in comparison to intact disc (Li et al., 2022), supporting the conclusion drawn here from the strain map. They also reported an increase of stress in the endplates for both directions of motion, in particular below the disc. Such asymmetry did not clearly appear in the experimental strain distribution, neither in another numerical study (Jia, et al., 2022).

In parallel, clinical studies investigated the surgical procedure. The *in vivo* cement masses presented by Eltes *et al.* (Eltes et al., 2021) almost filled the disc volume. In our case, donors were relatively old, but still had a very strong annular structure. Removing it to only have the outer layer like in advanced degeneration with vacuum was very difficult considering that the nucleus was removed by a spine surgeon using standard surgical tools. Then, the cement volumes injected in our study entirely fit the nucleus space with values close to the range of 3–5 ml clinically reported (Varga et al., 2015). Finally, one should highlight the lack of bone cement extrusion through the AF defect at the end of testing. Indeed, extrusion of the filling material is a major concern in the research of NP regeneration techniques, particularly when the AF is damaged to allow the material insertion (Wilke et al., 2006). Therefore, PCD does not require AF repair.

One limitation relates to the simplified loading conditions applied. FSUs *in vitro* are usually subject to pure bending moments (Wilke, et al., 1998) sometimes coupled with a compressive preload (Janevic, et al., 1991; Gardner-Morse and Stokes, 2003; Zirbel et al., 2013). The setup used in this study applied an eccentric compressive load which induced the bending, as in other spine studies (Adams and Dolan, 1996; Flamme et al., 2006; McNally, et al., 2012). Although the pivot point does not remain stationary during the motion, the lever arm variation during the tests was evaluated by DIC in term of relative translation of the vertebra. This resulted in a change of the bending moment between nucleotomy and discoplasty conditions of 3.2% ± 2.8% (mean ± SD) in flexion and 1.1% ± 1.0% in extension, making the loading conditions comparable.

Due to the diverse degeneration states of the donors' intervertebral discs and the limited number of available specimens,

nucleotomy was required to establish a common condition allowing possible repetition of the study. For that, fenestration in the AF was needed, which can be suspected to compromise the biomechanics of the FSU. The impact of fenestration on the segment stability was assessed in a dedicated experiment (Supplementary Material S2 File). The PDH, ROM, stiffness and strain distribution were checked. Fenestration of the AF did not significantly perturb the disc behaviour in comparison to the nucleus extraction/removal. Nucleotomy only significantly reduced the disc height. Lateral bending was not investigated because the position of the defect would have prevented the test of both bending directions.

5 Conclusion

This study was the first to investigate the impact of cement discoplasty on the biomechanics and kinematics using *in vitro* human lumbar spines. Because *in vitro* testing only tries to model the *in vivo* conditions, the clinical integration of the result absolute values is limited. However, general assumptions can be drawn from the comparative data and integrated into clinics.

- The cement filled the empty discs and *in vitro* distributions had similar volume and thickness as clinically observed.
- The posterior disc height was increased after discoplasty with respect to the nucleotomy condition: the cement mass acted like a spacer, supporting clinical observations.
- Stability of the segment was greater in flexion after discoplasty: the range of motion was significantly reduced, and the elastic stiffness increased.
- No indication of risks of mechanical damage on the outer disc was observed after discoplasty: the distribution of strain on the disc showed a clear decrease of large disc deformations.
- The cement geometry, in particular cement thickness, directly influenced the posterior disc height, and impacted the range of motion in extension only.

Data availability statement

The datasets generated for this study can be found in the Figshare repository "Biomechanical consequences of cement discoplasty: An *in vitro* study on thoraco-lumbar human spines" https://doi.org/10.6084/m9.figshare.19145255, https://doi.org/10.6084/m9.figshare.19145411, https://doi.org/10.6084/m9.figshare.19145075, https://doi.org/10.6084/m9.figshare.19145213, https://doi.org/10.6084/m9.figshare.19145231, https://doi.org/10.6084/m9.figshare.19145372, https://doi.org/10.6084/m9.figshare.19145363, https://doi.org/10.6084/m9.figshare.19145348, https://doi.org/10.6084/m9.figshare.19145378.

Author contributions

The study was suggested by LC, PEE, and AL. The test protocol was defined by LC, PEE, and AL. The tests and the analysis of the results were performed by CT, SM, and FB. The manuscript writing was handled by CT, SM, and LC. The manuscript was corrected by FB, AL, and PEE. All authors contributed to the article and approved the submitted version.

Funding

Acknowledgments

Conflict of interest

The authors declare that the research was conducted in the absence of any commercial or financial relationships that could be construed as a potential conflict of interest.

Publisher's note

All claims expressed in this article are solely those of the authors and do not necessarily represent those of their affiliated organizations, or those of the publisher, the editors and the reviewers. Any product that may be evaluated in this article, or claim that may be made by its manufacturer, is not guaranteed or endorsed by the publisher.

Supplementary material

The Supplementary Material for this article can be found online at: https://www.frontiersin.org/articles/10.3389/fbioe.2022.1040695/full#supplementary-material

References

Adams, M., and Dolan, P. (1996). Time-dependent changes in the lumbar spine's resistance to bending. *Clin. Biomech.* 11 (4), 194–200. doi:10.1016/0268-0033(96)00002-2

Amin, D. B., Sommerfeld, D., Lawless, I. M., Stanley, R. M., Ding, B., and Costi, J. J. (2016). Effect of degeneration on the six degree of freedom mechanical properties of human lumbar spine segments. *J. Orthop. Res.* 34 (8), 1399–1409. doi:10.1002/jor.23334

Behrsin, J. F., and Briggs, C. A. (1988). Ligaments of the lumbar spine: A review. *Surg. Radiol. Anat.* 10 (3), 211–219. doi:10.1007/BF02115239

Bergmann, G. (2008). Charité Universitaetsmedizin Berlin. OrthoLoad [Preprint].

Camino Willhuber, G., Kido, G., Pereira Duarte, M., Estefan, M., Bendersky, M., Bassani, J., et al. (2020). Percutaneous cement discoplasty for the treatment of advanced degenerative disc conditions: A case series analysis. *Glob. Spine J.* 10 (6), 729–734. doi:10.1177/2192568219873885

Cottrell, J. M., van der Meulen, M. C. H., Lane, J. M., and Myers, E. R. (2006). Assessing the stiffness of spinal fusion in animal models. *HSS Jrnl.* 2 (1), 12–18. doi:10.1007/s11420-005-5123-7

Eltes, P. E., Kiss, L., Bartos, M., Gyorgy, Z. M., Csakany, T., Bereczki, F., et al. (2020). Geometrical accuracy evaluation of an affordable 3D printing technology for spine physical models. *J. Clin. Neurosci.* 72, 438–446. doi:10.1016/j.jocn.2019.12.027

Eltes, P. E., Kiss, L., Bereczki, F., Szoverfi, Z., Techens, C., Jakab, G., et al. (2021). A novel three-dimensional volumetric method to measure indirect decompression after percutaneous cement discoplasty. *J. Orthop. Transl.* 28, 131–139. doi:10.1016/j.jot.2021.02.003

Evans, J. D. (1996). *Straightforward statistics for the behavioral sciences*. Pacific Grove: Brooks/Cole Pub. Co.

Eysel, P., Rompe, J. D., Schoenmayr, R., and Zoellner, J. (1999). Biomechanical behaviour of a prosthetic lumbar nucleus. *Acta Neurochir.* 141 (10), 1083–1087. doi:10.1007/s007010050486

Fehlings, M. G., Tetreault, L., Nater, A., Choma, T., Harrop, J., Mroz, T., et al. (2015). The aging of the global population: The changing epidemiology of disease and spinal disorders. *Neurosurgery* 77, S1–S5. doi:10.1227/NEU.0000000000000953

Flamme, C. H., von der Heide, N., Heymann, C., and Hurschler, C. (2006). Primary stability of anterior lumbar stabilization: Interdependence of implant type and endplate retention or removal. *Eur. Spine J.* 15 (6), 807–818. doi:10.1007/s00586-005-0993-4

Fuster, V. (2017). Changing demographics: A new approach to global health care due to the aging population. *J. Am. Coll. Cardiol.* 69 (24), 3002–3005. doi:10.1016/j.jacc.2017.05.013

Gardner-Morse, M. G., and Stokes, I. A. (2003). Physiological axial compressive preloads increase motion segment stiffness, linearity and hysteresis in all six degrees of freedom for small displacements about the neutral posture. *J. Orthop. Res.* 21 (3), 547–552. doi:10.1016/S0736-0266(02)00199-7

Ghandour, S., Pazarlis, K., Lewin, S., Isaksson, P., Forsth, P., and Persson, C. (2022). An *ex-vivo* model for the biomechanical assessment of cement discoplasty. *Front. Bioeng. Biotechnol.* 10, 939717. doi:10.3389/fbioe.2022.939717

Heuer, F., Schmidt, H., Klezl, Z., Claes, L., and Wilke, H. J. (2007). Stepwise reduction of functional spinal structures increase range of motion and change lordosis angle. *J. Biomechanics* 40 (2), 271–280. doi:10.1016/j.jbiomech.2006.01.007

Heuer, F., Schmidt, H., and Wilke, H.-J. (2008). Stepwise reduction of functional spinal structures increase disc bulge and surface strains. *J. Biomechanics* 41 (9), 1953–1960. doi:10.1016/j.jbiomech.2008.03.023

Inoue, N., and Espinoza Orías, A. A. (2011). Biomechanics of intervertebral disk degeneration. *Orthop. Clin. N. Am.* 42 (4), 487–499. doi:10.1016/j.ocl.2011.07.001

Janevic, J., Ashton-Miller, J. A., and Schultz, A. B. (1991)., Large compressive preloads decrease lumbar motion segment flexibility. 9. Official Publication of the Orthopaedic Research Society, 228–236. doi:10.1002/jor.1100090211*J. Orthop. Res.*2

Jia, H., Xu, B., and Qi, X. (2022). Biomechanical evaluation of percutaneous cement discoplasty by finite element analysis. *BMC Musculoskelet. Disord.* 23 (1), 594. doi:10.1186/s12891-022-05508-1

Johannessen, W., Cloyd, J. M., O'Connell, G. D., Vresilovic, E. J., and Elliott, D. M. (2006). Trans-endplate nucleotomy increases deformation and creep response in axial loading. *Ann. Biomed. Eng.* 34 (4), 687–696. doi:10.1007/s10439-005-9070-8

Kirnaz, S., Capadona, C., Wong, T., Goldberg, J. L., Medary, B., Sommer, F., et al. (2022). Fundamentals of intervertebral disc degeneration. *World Neurosurg.* 157, 264–273. doi:10.1016/j.wneu.2021.09.066

Kiss, L., Varga, P. P., Szoverfi, Z., Jakab, G., Eltes, P. E., and Lazary, A. (2019). Indirect foraminal decompression and improvement in the lumbar alignment after percutaneous cement discoplasty. *Eur. Spine J.* 28 (6), 1441–1447. doi:10.1007/s00586-019-05966-7

Knutsson, F. (1942). The vacuum phenomenon in the intervertebral discs. *Acta Radiol.* 23 (2), 173–179. doi:10.1177/028418514202300207

Li, S., Xu, B., Liu, Y., Zhang, J., Xu, G., Shao, P., et al. (2022). Biomechanical evaluation of spinal column after percutaneous cement discoplasty: A finite element analysis. *Orthop. Surg.* 14 (8), 1853–1863. doi:10.1111/os.13314

Lionello, G., Sirieix, C., and Baleani, M. (2014). An effective procedure to create a speckle pattern on biological soft tissue for digital image correlation measurements. *J. Mech. Behav. Biomed. Mater.* 39, 1–8. doi:10.1016/j.jmbbm.2014.07.007

Long, R. G., Torre, O. M., Hom, W. W., Assael, D. J., and Iatridis, J. C. (2016). Design requirements for annulus fibrosus repair: Review of forces, displacements, and material properties of the intervertebral disk and a summary of candidate hydrogels for repair. *J. Biomech. Eng.* 138 (2), 021007. doi:10.1115/1.4032353

Markolf, K. L. (1972). Deformation of the thoracolumbar intervertebral joints in response to external loads: A biomechanical study using autopsy material. *J. Bone Jt. Surg.* 54 (3), 511–533. doi:10.2106/00004623-197254030-00005

McNally, D., Naylor, J., and Johnson, S. (2012). An *in vitro* biomechanical comparison of Cadisc™-L with natural lumbar discs in axial compression and sagittal flexion. *Eur. Spine J.* 21 (5), 612–617. doi:10.1007/s00586-012-2249-4

Moissonnier, P., Fitzpatrick, D., and Bernard, F. (2014). Radiography and biomechanics of sixth and seventh cervical vertebrae segments after disc fenestration and after insertion of an intervertebral body spacer. *Vet. Comp. Orthop. Traumatol.* 27 (1), 54–61. doi:10.3415/VCOT-11-11-0159

Morishita, K., Kasai, Y., and Uchida, A. (2008). Clinical symptoms of patients with intervertebral vacuum phenomenon. *Neurologist* 14 (1), 37–39. doi:10.1097/NRL.0b013e3180dc9992

Morosato, F., Traina, F., and Cristofolini, L. (2019). Effect of different motor tasks on hip cup primary stability and on the strains in the periacetabular bone: An *in vitro* study. *Clin. Biomech.* 70, 137–145. doi:10.1016/j.clinbiomech.2019.08.005

Palanca, M., Brugo, T. M., and Cristofolini, L. (2015). Use of digital image correlation to investigate the biomechanics of the vertebra. *J. Mech. Med. Biol.* 15 (02), 1540004. doi:10.1142/S0219519415400047

Palanca, M., Ruspi, M. L., Cristofolini, L., Liebsch, C., Villa, T., Brayda-Bruno, M., et al. (2020). The strain distribution in the lumbar anterior longitudinal ligament is affected by the loading condition and bony features: An *in vitro* full-field analysis. *PloS One* 15 (1), e0227210. doi:10.1371/journal.pone.0227210

Palanca, M., Tozzi, G., and Cristofolini, L. (2015). The use of digital image correlation in the biomechanical area: A review. *Int. Biomech.* 3, 1–21. doi:10.1080/23335432.2015.1117395

Posner, I., White, A. A., Edwards, W. T., and Hayes, W. C. (1982). A biomechanical analysis of the clinical stability of the lumbar and lumbosacral spine. *Spine* 7 (4), 374–389. doi:10.1097/00007632-198207000-00008

Roosen, K. (1982). Bone cement as replacement material of cervical disks. *Fortschr. Med.* 100 (45), 2120–2126.

Russo, F., Hartman, R. A., Bell, K. M., Vo, N., Sowa, G. A., Kang, J. D., et al. (2017). Biomechanical evaluation of transpedicular nucleotomy with intact annulus fibrosus. *SPINE* 42 (4), E193–E201. doi:10.1097/BRS.0000000000001762

Samuel, E. (1948). Vacuum intervertebral discs. *Br. J. Radiol.* 21 (247), 337–339. doi:10.1259/0007-1285-21-247-337

Sola, C., Camino Willhuber, G., Kido, G., Pereira Duarte, M., Bendersky, M., Mereles, M., et al. (2018). Percutaneous cement discoplasty for the treatment of advanced degenerative disk disease in elderly patients. *Eur. Spine J.* 30 (8), 2200–2208. doi:10.1007/s00586-018-5547-7

Spenciner, D., Greene, D., Paiva, J., Palumbo, M., and Crisco, J. (2006). The multidirectional bending properties of the human lumbar intervertebral disc. *Spine J.* 6 (3), 248–257. doi:10.1016/j.spinee.2005.08.020

Tan, J. S., and Uppuganti, S. (2012). Cumulative multiple freeze-thaw cycles and testing does not affect subsequent within-day variation in intervertebral flexibility of human cadaveric lumbosacral spine. *SPINE* 37 (20), E1238–E1242. doi:10.1097/BRS.0b013e31826111a3

Tanaka, M. L., Weisenbach, C. A., Carl Miller, M., and Kuxhaus, L. (2011). A continuous method to compute model parameters for soft biological materials. *J. Biomech. Eng.* 133, 074502. doi:10.1115/1.4004412

Techens, C., Eltes, P E, Lazary, A, and Cristofolini, L (2022). Critical review of the state-of-the-art on lumbar percutaneous cement discoplasty. *Frontiers in Surgery* 9, 902831. doi:10.3389/fsurg.2022.902831

Techens, C., Palanca, M., Eltes, P. E., Lazary, A., and Cristofolini, L. (2020). Testing the impact of discoplasty on the biomechanics of the intervertebral disc with simulated degeneration: An *in vitro* study. *Med. Eng. Phys.* 84, 51–59. doi:10.1016/j.medengphy.2020.07.024

Tencer, A. F., Ahmed, A. M., and Burke, D. L. (1982). Some static mechanical properties of the lumbar intervertebral joint, intact and injured. *J. Biomech. Eng.* 104 (3), 193–201. doi:10.1115/1.3138348

Varga, P. P., Jakab, G., Bors, I., Lazary, A., and Szoverfi, Z. (2015). Experiences with PMMA cement as a stand-alone vertebral spacer. *Orthopade* 44 (1), 1–8. doi:10.1007/s00132-014-3060-1

Wilke, H.-J., Heuer, F., Neidlinger-Wilke, C., and Claes, L. (2006). Is a collagen scaffold for a tissue engineered nucleus replacement capable of restoring disc height and stability in an animal model? *Eur. Spine J.* 15 (3), 433–438. doi:10.1007/s00586-006-0177-x

Wilke, H.-J., Kettler, A., and Claes, L. (2000). Primary stabilizing effect of interbody fusion devices for the cervical spine: An *in vitro* comparison between three different cage types and bone cement. *Eur. Spine J.* 9 (5), 410–416. doi:10.1007/s005860000168

Wilke, H.-J., Rohlmann, A., Neller, S., Schulthei, M., Bergmann, G., Graichen, F., et al. (2001). Is it possible to simulate physiologic loading conditions by applying pure moments?: A comparison of: *In vivo*: And: *In vitro*: Load components in an internal fixator. *Spine* 26 (6), 636–642. doi:10.1097/00007632-200103150-00014

Wilke, H.-J., Wenger, K., and Claes, L. (1998). Testing criteria for spinal implants: Recommendations for the standardization of *in vitro* stability testing of spinal implants. *Eur. Spine J.* 7 (2), 148–154. doi:10.1007/s005860050045

Willhuber, G. C., Kido, G., Pereria Duarte, M, Estefan, M, Bendersky, M, Bassani, J,, et al. (2019) 'Percutaneous cement discoplasty for the treatment of advanced degenerative disc conditions: A case series analysis'. *global spine journal* 10 (6), 729–734. doi:10.1177/2192568219873885

Yue, J., Guyer, R., Johnson, J. P., Khoo, L., and Hochschuler, S. (2010). *The Comprehensive treatment of the aging spine - 1st edition - minimally invasive and advanced techniques*. Netherlands: Elsevier.

Zirbel, S. A., Stolworthy, D. K., Howell, L. L., and Bowden, A. E. (2013). Intervertebral disc degeneration alters lumbar spine segmental stiffness in all modes of loading under a compressive follower load. *Spine J.* 13 (9), 1134–1147. doi:10.1016/j.spinee.2013.02.010

Check for updates

Biomechanical comparison of pedicle screw fixation strength among three different screw trajectories using single vertebrae and one-level functional spinal unit

Ching-Lung Tai[1,2], Weng-Pin Chen[3], Mu-Yi Liu[1], Yun-Da Li[1,2], Tsung-Ting Tsai[2], Po-Liang Lai[2] and Ming-Kai Hsieh[2]*

[1]Department of Biomedical Engineering, Chang Gung University, Taoyuan, Taiwan, [2]Department of Orthopaedic Surgery, Spine Section, Bone and Joint Research Center, Chang Gung Memorial Hospital and Chang Gung University College of Medicine, Taoyuan, Taiwan, [3]Department of Mechanical Engineering, National Taipei University of Technology, Taipei, Taiwan

Three key factors are responsible for the biomechanical performance of pedicle screw fixation: screw mechanical characteristics, bone quality and insertion techniques. To the best of the authors' knowledge, no study has directly compared the biomechanical performance among three trajectories, i.e., the traditional trajectory (TT), modified trajectory (MT) and cortical bone trajectory (CBT), in a porcine model. This study compared the pullout strength and insertion torque of three trajectory methods in single vertebrae, the pullout strength and fixation stiffness including flexion, extension, and lateral bending in a one-level instrumented functional spinal unit (FSU) that mimics the *in vivo* configuration were clarified. A total of 18 single vertebrae and 18 FSUs were randomly assigned into three screw insertion methods ($n = 6$ in each trajectory group). In the TT group, the screw converged from its entry point, passed completely inside the pedicle, was parallel to the superior endplate, was located in the superior third of the vertebral body and reached to at least the anterior third of the vertebral body. In the MT group, the convergent angle was similar to that of the TT method but directed caudally to the anterior inferior margin of the vertebral body. The results of insertion torque and pullout strength in single vertebrae were analyzed; in addition, the stiffness and pullout strength in the one-level FSU were also investigated. This study demonstrated that, in single vertebrae, the insertion torque was significantly higher in CBT groups than in TT and MT groups ($p < 0.05$). The maximal pullout strength was significantly higher in MT groups than in TT and CBT groups ($p < 0.05$). There was no significant difference in stiffness in the three motions among all groups. The maximal pullout strength in FSUs of MT and CBT groups were significantly higher than the TT groups ($p < 0.05$). We concluded that either MT or CBT provides better biomechanical performance than TT in single vertebrae or FSUs. The lack of significance of stiffness in FSUs among three methods suggested that MT or CBT could be a reasonable alternative to TT if the traditional trajectory was not feasible.

1 Introduction

Pedicle screw fixation for lumbar spinal segments has been described for a variety of surgical indications including scoliosis, deformity, fracture, infection or tumors (Wang et al., 2014; Tschugg et al., 2017; Fan et al., 2018; Chan et al., 2020; Perna et al., 2022). Immediate stability of pedicle screw-rod instrumentation provides the benefit of a quicker and reliable fusion mass and finally reaches permanent stability (Wang et al., 2019; Zhao et al., 2019; He et al., 2020). Several factors affect the fixation stability of a pedicle screw, including the screw shape, diameter, length, thread type/shape, pitch width, outer/inner core difference and bone mineral density (Liu et al., 2020; Hsieh et al., 2021a). In addition to the morphometric characteristics of the pedicle screw, the trajectory of the screw also has a strong influence on fixation strength (Lehman et al., 2003; Phan et al., 2015; Delgado-Fernandez et al., 2017; Jarvers et al., 2021). Currently, three methods for the insertion of pedicle screws are widely used in the lumbar spine. First, in the traditional trajectory (TT), the screw converges from its entry point, passes completely inside the pedicle, and reaches at least the anterior third of the vertebral body (Youssef et al., 1999; Lehman et al., 2003; Phan et al., 2015; Wadhwa et al., 2015; Delgado-Fernandez et al., 2017; Jarvers et al., 2021). In the sagittal plane, traditional screws should be located in the superior third of the vertebral body and parallel to the superior endplate (Lehman and Kuklo, 2003; Suk et al., 2005). Second, the modified trajectory (MT) has a convergent angle similar to that of the TT but directed caudally to the anterior inferior margin of the vertebral body without penetrating the inferior endplate (Lehman et al., 2003; Lehman and Kuklo, 2003; Wadhwa et al., 2015). Anatomically, longer-sized screws could be used in MT, which is supposed to purchase more bone than the traditional method (Hsieh et al., 2019; Hsieh et al., 2020). Third, cortical bone trajectory screws (CBT), starting medially from the pars inter-articularis and following a cranio-lateral direction through the pedicle with the objective of maximizing thread contact with cortical bone, have been proven to have similar clinical outcomes and better operative parameters, such as shorter incision length, quicker operative time, and less blood loss, than TTs in posterior lumbar interbody fusion surgery (Perez-Orribo et al., 2013; Lee et al., 2015; Oshino et al., 2015). However, inconsistent biomechanical results among different trajectories come from using different bone densities, different species of cadaveric specimens (Perez-Orribo et al., 2013; Lee et al., 2015; Oshino et al., 2015; Delgado-Fernandez et al., 2017), various finite element models (Matsukawa et al., 2017; Molinari et al., 2021), uncontrolled cephalad angles of CBT screws (Perez-Orribo et al., 2013; Oshino et al., 2015), and undefined MT axes (Lehman et al., 2003; Lehman and Kuklo, 2003). Studies to date have been predominantly based on single screw fixation stability, which may not be the actual clinical representation of implant failure (Lehman et al., 2003; Lehman and Kuklo, 2003; Delgado-Fernandez et al., 2017; Jarvers et al., 2021). To the best of our knowledge, no study has directly compared the biomechanical performance among these three trajectories in single vertebrae and one-level functional spinal units (FSUs) in a porcine model.

The purpose of the present study was to compare the pullout strength and insertion torque of three trajectory methods in single vertebrae; moreover, the pullout strength and fixation stiffness including flexion, extension, and lateral bending in one-level instrumented FSUs that mimicked the *in vivo* configuration were clarified to recommend further clinical use.

2 Materials and methods

This study was approved by the committee of Ministry of Science and Technology, Taiwan (MOST 109-2221-E-182-006-MY2). All specimens were purchased from commercial meat market (Yahsen Frozen Foods Co., Taiwan) and were exempted from filing an Institutional Animal Care and Use Committees (IACUCs) protocol for the use of dead animal-derived bone.

2.1 Specimen preparation and implantation

A total of 18 single vertebrae and 18 FSUs were used in the study, with L1-6 fresh-frozen lumbar vertebrae harvested from mature pigs (weight 100–110 kg). All animals were healthy before harvesting and never exposed to any drugs or treatments that could affect the bone mineral density. All the specimens were separated into individual vertebrae or FSUs after being stripped of the surrounding musculature, ligaments, and periosteum. All specimens were stored at -20°C until the day of testing and thawed for 24 h before implantation. A pilot hole was drilled using a 2.5 mm "twist" metric drill bit attached to a Dremel 4000 rotary tool that was mounted on a Dremel WorkStation Model 220–01. The pilot hole of the TT group was at the junction of the transverse process and facet joint. Drilling was determined using lateral fluoroscopy, and the direction was parallel to the superior endplate and medial to produce a converging appearance. The pilot track was followed with a 2.5 mm standard straight pedicle drill to a depth of 40 mm. Cylindrical coarse-thread screws with a size of 6.0 mm × 45 mm were inserted until the final thread was engaged in the lateral

FIGURE 1
Photograph showing three types of pedicle screws used in TT, MT, and CBT trajectories (from left to right). The dimensions (diameter × length) of the TT, MT and CBT screws were 6.0 mm × 45 mm, 6.0 mm × 50 mm and 6.0 mm × 35 mm, respectively. The screw pitches of the TT, MT and CBT screws were 3.0 mm, 3.0 mm and 1.5 mm, respectively. All screws had identical thread depths of 1.2 mm.

facet cortex. In the MT group, the pilot hole was at the superior edge of the superior articular process, and the pilot track was followed with a 2.5 mm standard straight pedicle drill to a depth of 45 mm toward the anterior inferior edge of the vertebral body under lateral fluoroscopy. Cylindrical coarse-thread screws with a size of 6.0 mm × 50 mm were inserted in this group. In the CBT group, the pilot hole in the pars inter-articularis was created using a 2.5 mm drill bit and followed a 25° caudal and 25° lateral trajectory to a pilot tract of 30 mm (Matsukawa et al., 2013). Cylindrical fine-thread screws with a size of 6.0 mm × 35 mm (Figure 1) were inserted in this group. In the 18 FSUs, polyaxial screws (Baui Biotech, Co., Taipei, Taiwan) were chosen and randomly implanted into each pedicle of the vertebrae by an experienced surgeon. Six FSUs in each trajectory group were implanted according to methods in single vertebra with paired segmental pedicle screws (diameter × length of 6.0 mm × 45 mm in the TT group, 6.0 mm × 50 mm in the MT group and 6.0 mm × 35 mm in the CBT group), and 5.5 mm diameter titanium rods were used to connect the pedicle screws in all three

groups. Axial and sagittal views were examined *via* X-ray imaging for all specimens prior to the biomechanical test to confirm an appropriate screw trajectory and insertion depth in single vertebrae (Figure 2) and FSUs (Figure 3). The specimens were also examined thoroughly to rule out any fractures or defects caused by screw insertion.

2.2 Biomechanical testing

In single vertebrae, the maximal insertion torque was measured with an electronic torque wrench (OLY 921/6NB, New Taipei City, Taiwan) in the last thread of screw insertion. Each of the 18 single instrumented vertebrae was embedded in acrylate resin (#20–3568; Buehler, Lake Bluff, IL, United States) to allow clamping during the screw pullout test. The method for the screw pullout test was identical to that used in our previous study (Hsieh et al., 2019; Hsieh et al., 2020). Each prepared specimen was secured to a custom-made grip mounted on the platform of the testing machine (Bionix 810; MTS Systems Corp., MN, United States) to conduct axial pullout tests of the screws (Figure 4). The screw head was fixed to one end of an adapter having an inner thread that matched the outer thread of the screw head. The other end of the adapter was then clamped to the upper wedge grip of the MTS testing machine. The adapter equipped with a universal joint ensuring vertical pullout alignment during pullout test. The potted specimen was secured on a lower custom-made grip capable of x-y plane translation and rotation to achieve the coaxial alignment of the pedicle screw with the pullout arm. After the specimens were mounted, pullout force was applied at a constant crosshead rate of 5 mm/min. During the pullout test, the relation between the applied force and displacement was simultaneously recorded in 0.1 mm increments until failure. The peak force recorded was defined as the ultimate pullout strength for comparison.

In the FSUs, the specimens were mounted for flexion, extension, and lateral bending using an axial MTS testing machine (Bionix 858, MTS Corp., MN, United States) (Tai et al., 2008; Hsieh et al., 2021b). The superior segment was embedded in acrylic resin (#20–3568; Buehler, Lake Bluff, IL, United States) and constrained by the upper clamp with an adjustable moment arm, whereas the inferior segment, embedded in acrylic resin, was constrained by the lower clamp (Figure 5). This experimental setup resulted in a compressive preload of 20 N due to the weight of the upper fixation acrylic resin. Each FSUs was non-destructively tested in three sequential modes: flexion, extension, and lateral bending. The clamp was designed with a pin that rotated horizontally across the upper plate, and the pin was perpendicular to the motion plane of the specimen. The horizontal pin and vertical motion path of the specimen resulted in a *3-D* configuration that ensured that the specimen moved vertically as the spinal construct was flexed, extended or laterally bent. The position of the horizontal pin was adjusted to
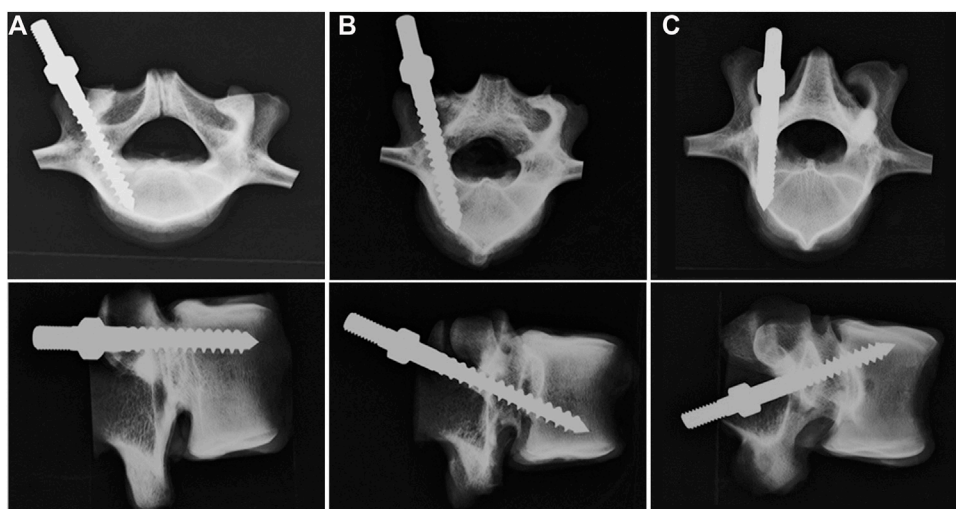
FIGURE 2
Axial (upper) and sagittal (lower) X-ray images of the vertebrae after the insertion of screws with **(A)** TT, **(B)** MT, and **(C)** CBT trajectories. In the axial view, the pedicle screws in the TT and MT groups were convergently inserted into the vertebral body, whereas in the CBT group, the screw was inserted divergently toward the lateral cortex. In the sagittal view, the screw in the TT group was parallel to the superior endplate; in the MT group, the screw was inserted toward the anterior inferior edge of the vertebral body with proper depth. In the CBT group, the screw was placed 25° caudally toward the superior endplate. No fractures or lateral wall breach were detected in either view.
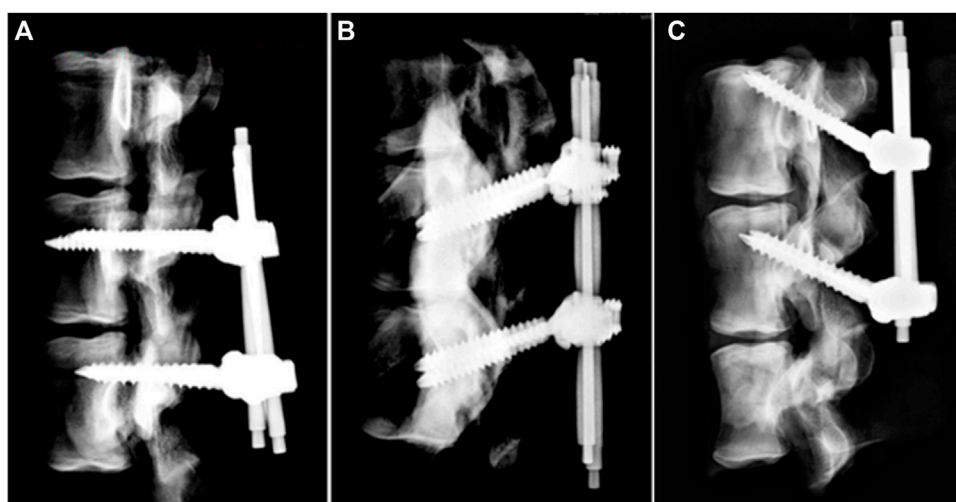
FIGURE 3
X-ray images of the FSU constructs after assembly of the screw and rod. **(A)** TT, **(B)** MT, and **(C)** CBT. Pedicle screws in each trajectory group of FSUs were implanted according to methods in single vertebra with paired segmental pedicle screws (diameter × length of 6.0 mm × 45 mm in the TT group, 6.0 mm × 50 mm in the MT group and 6.0 mm × 35 mm in the CBT group) and 5.5 mm diameter titanium rods were used to connect the pedicle screws in all three groups.

set the moment arm to 120 mm, and an increasing compressive force up to 70 N was applied to the horizontal pin across the upper plate. Therefore, the resultant applied moment was 8,400 N-mm, which remains within the viscoelastic range (Karakaşli et al., 2013; Karakaşli et al., 2014). During testing, the displacement data associated with the applied moment were recorded simultaneously. The FSU stiffnesses in flexion, extension, and lateral bending were defined as the applied
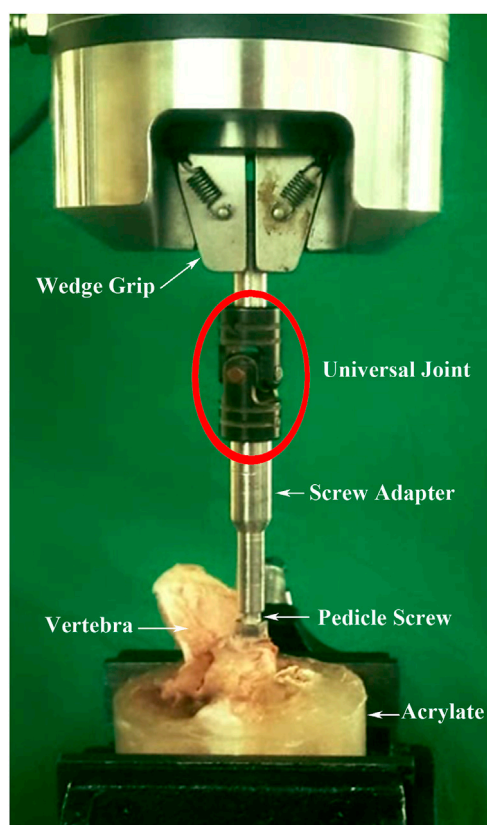
FIGURE 4
Experimental setup of the screw pullout test of the single vertebrae. The screw head was fixed to one end of an adapter having an inner thread that matched the outer thread of the screw head. The other end of the adapter was then clamped to the upper wedge grip of the MTS testing machine. The adapter equipped with a universal joint ensuring vertical pullout alignment during the pullout test.

moment divided by the value of displacement at the latest stage for all three loading modes.

Following the stiffness test, the FSUs were re-embedded into acrylate resin to allow clamping during the construct pullout test (Bionix 810; MTS Systems Corp., MN, United States). A custom-made turnbuckle fixture was used to attach the actuator to the rod (Figure 6). The pedicle screw-rod construct was tested in tension at a rate of 5 mm/min. Load and displacement data were collected at 1.6 Hz. During the pullout test, the relation between the applied force and displacement was simultaneously recorded in 0.1 mm increments until failure. The peak force recorded was defined as the maximal pullout strength for comparison.

2.3 Statistical analysis

To evaluate the biomechanical performance of the three trajectory groups in each model, the magnitudes of insertional

torque and ultimate pullout force of single vertebrae and stiffness and ultimate pullout force of FSUs were statistically compared. All of the measurements are expressed as the mean ± standard deviation (SD). Statistical software (SPSS for Windows version 12.0, SPSS, Inc., Chicago, IL) was used to analyze the biomechanical performance of all groups in the two models. ANOVA with *post hoc* analyses was performed to evaluate the differences among groups. Differences were considered to be significant at $p < 0.05$.

3 Results

3.1 Specimen characterization

An appropriate screw trajectory and insertional depth were confirmed using axial and sagittal X-ray imaging prior to biomechanical testing (Figures 2, 3). In the axial view, the pedicle screws in the TT and MT groups were convergently inserted into the vertebral body, whereas in the CBT group, the screw was inserted divergently toward the lateral cortex. In the sagittal view, the screw in the TT group was parallel to the superior endplate; in the MT group, the screw was inserted toward the anterior inferior edge of the vertebral body with proper depth. In the CBT group, the screw was placed 25° caudally toward the superior endplate. No fractures or lateral wall breach were detected in either view.

3.2 Biomechanical performance

In single vertebrae, the insertion torques of the TT, MT and CBT groups were 2.64 ± 0.64, 3.18 ± 0.87, and 3.71 ± 1.05 Nm, respectively (Figure 7). The insertion torque was significantly higher in the CBT group than in the TT and MT groups. There was no significant difference in insertion torque between the TT and MT groups. The maximal pullout strengths of the TT, MT and CBT groups were 1,143.75 ± 181.41, 1,324.69 ± 154.37, and 1,051.61 ± 303.12 N, respectively (Figure 8). The maximal pullout strength was significantly higher in the MT group than in the TT and CBT groups. There was no significant difference in pullout strength between the TT and CBT groups.

In the FSU groups, the stiffnesses of flexion, extension and lateral bending were 1962.9 ± 417.4, 2,307.6 ± 512.1 and 1,847.9 ± 306.9 N-mm/mm in the TT groups, 2,234.7 ± 694.1, 2,558.7 ± 467.6 and 1,344.9 ± 491.9 N-mm/mm in the MT groups and 2,518.4 ± 561.5, 1,968.7 ± 824.5 and 1,675.7 ± 282.1 N-mm/mm in the CBT groups (Figure 9). There was no significant difference in stiffness in the three motions among all groups. The maximal pullout strengths in the FSUs of the TT, MT and CBT groups were 2,511.7 ± 309.2, 3,755.1 ± 711.4, and 3,512.2 ± 519.9 N, respectively (Figure 10). The values in the MT and CBT groups

FIGURE 5
Schematic drawings (upper) and photographs showing the experimental setup for **(A)** flexion, **(B)** extension, and **(C)** lateral bending of the FSU constructs. The tests were performed on a biaxial (axial and rotation) MTS machine. A maximal 8,400 N-mm moment generated through the axial movement of the MTS actuator was applied to the spine specimen to achieve flexion, extension and lateral bending motions.
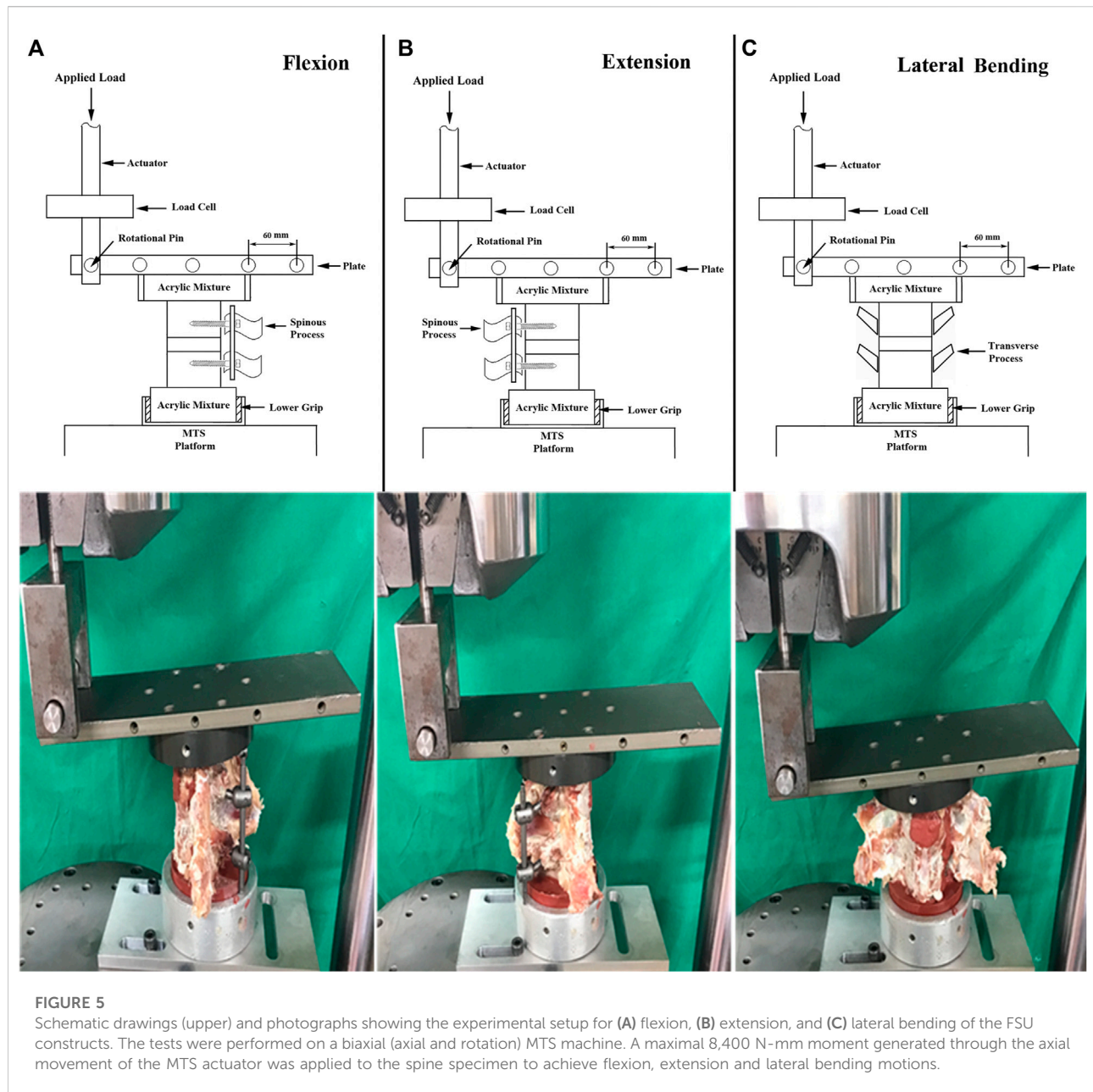
were significantly higher than those in the TT groups. There was no significant difference between the MT and CBT groups.

4 Discussion

The aim of this study was to compare the pullout strength and insertion torque of three trajectory methods (TT, MT, CBT) in porcine vertebrae. In single vertebrae, we found the insertion torque was significantly higher in CBT groups than in TT and MT groups ($p < 0.05$). However, the maximal pullout strength was significantly higher in MT groups than in TT and CBT

groups ($p < 0.05$). In functional spinal units (FSUs), no significant difference was found in stiffness in the three motions among all groups. The maximal pullout strength in FSUs of MT and CBT groups were significantly higher than the TT groups ($p < 0.05$). Our results demonstrated that either MT or CBT provided better biomechanical performance than TT in single vertebrae or FSUs.

There are three different screw trajectory techniques of the lumbar spine at present. However, there is still no clear consensus regarding the optimal screw trajectory in single vertebrae and functional spine units (Lehman et al., 2003; Phan et al., 2015; Delgado-Fernandez et al., 2017; Hsieh et al., 2021a). Three key
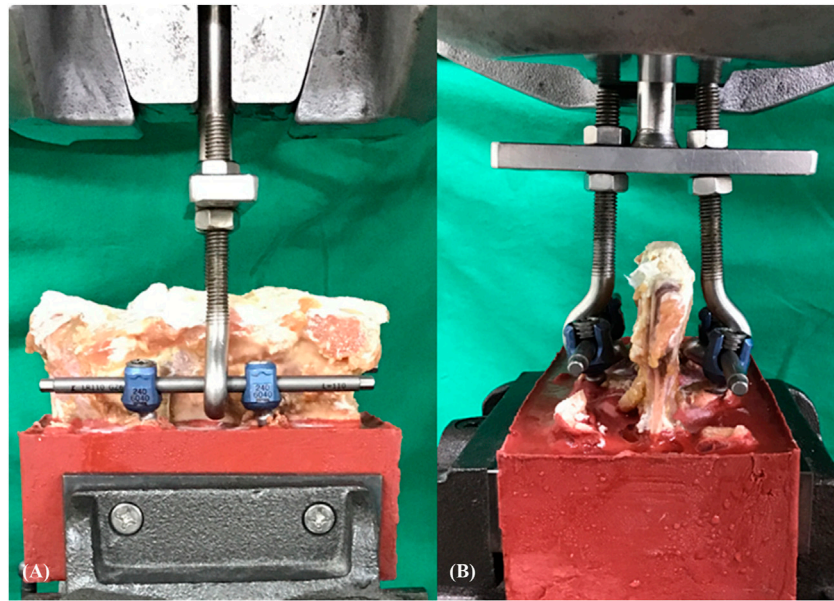
FIGURE 6
Experimental setup of the screw pullout test of FSU constructs. **(A)** Sagittal view and **(B)** axial view. A custom-made turnbuckle fixture was used to attach the actuator to the rod.
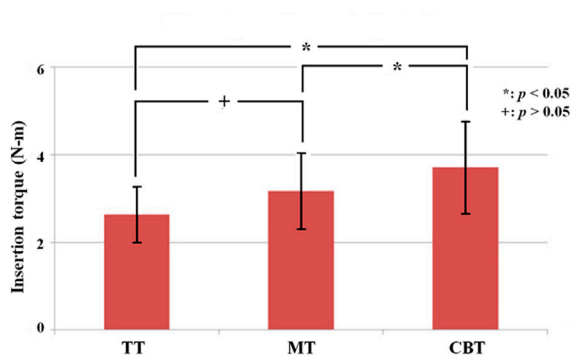
FIGURE 7
Mean maximal insertion torque of pedicle screws for a single vertebra treated with TT, MT and CBT trajectories. The insertion torque was significantly higher in the CBT group than in the TT and MT groups. Significant difference was not observed between the TT and MT groups.
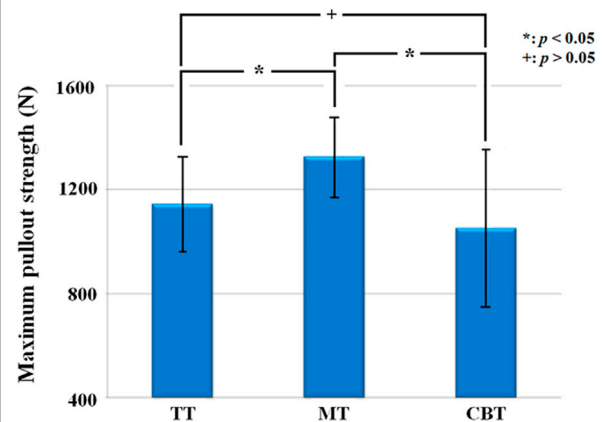
FIGURE 8
Mean maximum pullout strength of pedicle screws for a single vertebra treated with TT, MT and CBT trajectories. The maximum pullout strength was significantly higher in the MT group than in the TT and CBT groups. Significant difference was not observed between the TT and CBT groups.

factors are responsible for the biomechanical performance of pedicle screw fixation: screw mechanical characteristics, bone quality and implantation techniques (Shen et al., 2019; Matsukawa et al., 2021; Qiu et al., 2022). In our study, bone quality, pilot methods and screw morphometric data, including thread type/shape and outer/inner diameter, were controlled; only the lengths of the three methods were

different because of the anatomical characteristics (Lehman et al., 2003; Phan et al., 2015; Delgado-Fernandez et al., 2017; Hsieh et al., 2021a). Newcomb, et al. comparing varying pedicle screw orientations in the axial and sagittal planes on non-idealized finite element vertebrae found that

FIGURE 9
Mean flexion, extension and lateral bending stiffnesses of FSU constructs treated with TT, MT and CBT trajectories. Significant differences were not observed among the groups in the flexion, extension and lateral bending motions ($p > 0.05$).

FIGURE 10
Mean maximum pullout strength of pedicle screws for FSU constructs treated with TT, MT and CBT trajectories. The values in the MT and CBT groups were significantly higher than those in the TT group. There was no significant difference between MT and CBT groups.

cadaveric thoracic vertebrae, various bone density specimens, screws of the same size and uncontrolled anatomical trajectory angles seem clinically impractical. To reveal the true clinical condition without interference by the anterior cortex, the MT tract was longer than the TT tract, so we chose an incremental 5 mm of screw length in the MT groups. The maximal pullout strength was significantly higher in the MT groups than in the TT groups, but there was no significance in insertion torque due to the greater amount of cancellous bone purchased in our study (Hsieh et al., 2020). Varghese, et al. compared the effect of various insertion angles on the pull-out strength in single screw and two screw-rod configurations in normal and osteoporotic polyurethane foam models (Varghese et al., 2017; Varghese et al., 2018a; Varghese et al., 2018b). The pull-out value decreased by 52% from insertion angles of 0°–30° in the single screw configuration. In the two screw-rod configuration, the pull-out strength was maximum for relative lower insertion angles of 10°–15°. The phenomenon was conflict with our study which significantly higher pullout strength was found in higher insertional angle group (MT groups). In our study, for the pullout test using single vertebrae, the screw head was fixed to a custom-made adapter equipped with a universal joint to ensure the long axis of the screw was coaxial with the movement of the testing machine actuator. The experimental setup was different with the above studies (Krishnan et al., 2016; Varghese et al., 2017; Varghese et al., 2018a; Varghese et al., 2018b). In the biomechanical performance of FSUs, motion stiffness of flexion, extension and lateral bending was used instead of direct pullout test from construct rod. Studies retrospectively analyzed the anatomical location of acute thoracolumbar vertebral fractures and found that the fracture rate of the superior endplate is much higher than that of the inferior endplate (Che-Nordin et al., 2018; Wang et al., 2020). Our biomechanical results suggested that MT screws are not only superior in pullout strength but also potentially decrease future upper instrumented fractures.

CBT involves a medial-to-lateral and a caudo-cephalad direction from the pars interarticularis with the objective of maximizing thread contact with the higher-density cortex. The fixation mechanism was totally different with the TT or MT group, so we chose a shorter-sized and fine threads screws as commonly used screws in the clinic. The insertion torque was significantly higher in the CBT groups than in the TT and MT groups, which may be due to the fine threads cortex fixation (Matsukawa et al., 2013; Oshino et al., 2015); however, there was no significant difference in maximal pullout strength, this may attributed to the shorter fixation length of screws in CBT. In a 124-patients prospective randomized controlled trial comparing CBT and TT fixation method for osteoporotic single-level lumbar fusion showed significantly better post-operative lumbar stability in the CBT group (Ding et al., 2022). Both the pullout strength

angulations in both the sagittal and axial planes affected stresses on the cortical and cancellous bones and the screw (Newcomb et al., 2017). Pedicle screws placed laterally in the axial plane and superiorly in the sagittal plane reduce the risk of screw loosening and screw breakage. The result implied better biomechanical performance in TT than MT method which is different from our study. Uncontrolled specimens using vertebrae from seven human cadaveric spines and assessment using maximal and cumulative stress on the screw and bone made drastic conclusions. A biomechanical study compared traditional *versus* anatomical trajectory techniques and concluded that the traditional technique results in a 39% increase in maximum insertion torque and a 27% increase in pullout strength compared to the anatomic technique (Lehman et al., 2003). However,

and insertion torque showed higher values in the CBT group than in the TT group when using a diseased osteoporotic spine to highlight the fine threads effect in the CBT groups (Santoni et al., 2009; Baluch et al., 2014; Matsukawa et al., 2014; Matsukawa et al., 2015a; Matsukawa et al., 2015b).

In our stiffness test of FSUs, the horizontal pin and vertical motion path of the specimen resulted in a *3-D* configuration that ensured that the specimen moved vertically as the spinal construct was flexed, extended or laterally bent, which excluded other biomechanical interfering factors during setting up. To the best of our knowledge, no study has evaluated FSUs and compared intervertebral stability among the three trajectory methods. Our biomechanical comparison between TT and CBT corresponded to other studies (Perez-Orribo et al., 2013; Oshino et al., 2015). Perez-Orribo et al. (Perez-Orribo et al., 2013) found that CBT demonstrated equivalent stiffness to TT in bending tests of human cadaveric lumbar FSUs with presence of interbody fusion. Oshino et al. (Oshino et al., 2015) also mentioned the same phenomenon in deer lumbar FSUs.

In our present study, a higher pullout strength of FSUs was exhibited in the MT and CBT groups than in the TT group without significant differences in stiffness, indicating that the longer screws in the MT group and larger cortical contact in the CBT group increased the efficacy of the screw. However, the lack of significant differences in stiffness among the three groups may be due to different spinal mobility between quadrupeds and humans (Hart et al., 2006; Cornaz et al., 2021) and multiple anatomical confounding factors, including facet joints, disco-vertebral joints and interspinous ligaments (Putzer et al., 2016; Bashkuev et al., 2018).

The limitations of this study include the following: first, porcine spines were used as specimens, and different geometries or density distributions of vertebrae might affect the generalizability of our results to human patients (Schomberg et al., 2016; Miranpuri et al., 2018). CT scans found that similar vertebral body height, shape of the end-plates, shape of the spinal canal, and pedicle size between human and porcine spine (Busscher et al., 2010). The size of both superior and inferior endplates increased more caudally in the human spine but less increased in porcine spine, which indicate the vertebral width in human was larger than porcine. More purchase of CBT screws would be expected in human spine which implied the significantly higher value of insertion torque would be achieved in the CBT group than in the TT and MT groups in single human vertebrae; and the maximal pullout strength could be corresponding to the insertional torque. Second, screws of more sizes and different geometries including cannulated, conical, or dual threaded pedicle screws should be performed to obtain a more conclusive result. Third, the limited number of specimens might increase the variability of the data and reduce the statistical reliability. Finally, the lack of significance in motion among the three methods implies that intervertebral stiffness could be affected not only by pullout strength but also by more functional spinal units, which should be performed for further clinical application.

5 Conclusion

The *in vitro* biomechanical study provides insight into the fact that MT can provide a higher pullout strength and CBT can provide a higher insertion torque in single vertebrae. In FSUs, the higher pullout strength found in the MT and CBT groups corresponded to the single vertebrae. The lack of significance of stiffness in one-level FSUs among the three methods suggested that MT and CBT could both be reasonable alternatives to TT if the traditional tract was not feasible.

Data availability statement

The original contributions presented in the study are included in the article/Supplementary Material, further inquiries can be directed to the corresponding author.

Ethics statement

This study was approved by the committee of Ministry of Science and Technology, Taiwan (MOST 109-2221-E-182-006-MY2). All specimens were purchased from commercial meat market (Yahsen Frozen Foods Co., Taiwan) and were exempted from filing an Institutional Animal Care and Use Committees (IACUCs) protocol for the use of dead animal-derived bone.

Author contributions

All authors have made substantial contributions to the conception and design of the study, analysis and interpretation of data, preparing the manuscript, and also attest to the validity and legitimacy of the data and its interpretation, and approved it for publication.

Acknowledgments

Conflict of interest

The authors declare that the research was conducted in the absence of any commercial or financial relationships that could be construed as a potential conflict of interest.

Publisher's note

All claims expressed in this article are solely those of the authors and do not necessarily represent those of their affiliated organizations, or those of the publisher, the editors and the reviewers. Any product that may be evaluated in this article, or claim that may be made by its manufacturer, is not guaranteed or endorsed by the publisher.

References

Baluch, D. A., Patel, A. A., Lullo, B., Havey, R. M., Voronov, L. I., Nguyen, N. L., et al. (2014). Effect of physiological loads on cortical and traditional pedicle screw fixation. *Spine* 39 (22), E1297–E1302. doi:10.1097/BRS.0000000000000553

Bashkuev, M., Reitmaier, S., and Schmidt, H. (2018). Effect of disc degeneration on the mechanical behavior of the human lumbar spine: A probabilistic finite element study. *Spine J.* 18 (10), 1910–1920. doi:10.1016/j.spinee.2018.05.046

Busscher, I., Ploegmakers, J. J. W., Verkerke, G. J., and Veldhuizen, A. G. (2010). Comparative anatomical dimensions of the complete human and porcine spine. *Eur. Spine J.* 19 (7), 1104–1114. doi:10.1007/s00586-010-1326-9

Chan, A., Parent, E., Wong, J., Narvacan, K., San, C., and Lou, E. (2020). Does image guidance decrease pedicle screw-related complications in surgical treatment of adolescent idiopathic scoliosis: A systematic review update and meta-analysis. *Eur. Spine J.* 29 (4), 694–716. doi:10.1007/S00586-019-06219-3

Che-Nordin, N., Deng, M., Griffith, J. F., Leung, J. C. S., Kwok, A. W. L., Zhu, Y. Q., et al. (2018). Prevalent osteoporotic vertebral fractures more likely involve the upper endplate than the lower endplate and even more so in males. *Ann. Transl. Med.* 6 (22), 442. doi:10.21037/atm.2018.10.61

Cornaz, F., Widmer, J., Snedeker, J. G., Spirig, J. M., and Farshad, M. (2021). Cross-links in posterior pedicle screw-rod instrumentation of the spine: A systematic review on mechanical, biomechanical, numerical and clinical studies. *Eur. Spine J.* 30 (1), 34–49. doi:10.1007/s00586-020-06597-z

Delgado-Fernandez, J., García-Pallero, M. Á., Blasco, G., Pulido-Rivas, P., and Sola, R. G. (2017). Review of cortical bone trajectory: Evidence of a New technique. *Asian Spine J.* 11 (5), 817–831. doi:10.4184/asj.2017.11.5.817

Ding, H., Hai, Y., Liu, Y., Guan, L., Pan, A., Zhang, X., et al. (2022). Cortical trajectory fixation versus traditional pedicle-screw fixation in the treatment of lumbar degenerative patients with osteoporosis: A prospective randomized controlled trial. *Clin. Interv. Aging* 17, 175–184. doi:10.2147/CIA.S349533

Fan, Y., Du, J. P., Liu, J. J., Zhang, J. N., Liu, S. C., and Hao, D. J. (2018). Radiological and clinical differences among three assisted technologies in pedicle screw fixation of adult degenerative scoliosis. *Sci. Rep.* 8, 890. doi:10.1038/s41598-017-19054-7

Hart, R., Hettwer, W., Liu, Q., and Prem, S. (2006). Mechanical stiffness of segmental versus nonsegmental pedicle screw constructs: The effect of cross-links. *Spine* 31 (2), E35–E38. doi:10.1097/01.BRS.0000194835.89010.22

He, W., He, D., Sun, Y., Xing, Y., Liu, M., Wen, J., et al. (2020). Quantitative analysis of paraspinal muscle atrophy after oblique lateral interbody fusion alone vs. combined with percutaneous pedicle screw fixation in patients with spondylolisthesis. *BMC Musculoskelet. Disord.* 21 (1), 30. doi:10.1186/S12891-020-3051-9

Hsieh, M. K., Li, Y. D., Liu, M. Y., Lin, C. X., Tsai, T. T., Lai, P. L., et al. (2021). Biomechanical comparison of fixation stability among various pedicle screw geometries: Effects of screw outer/inner projection shape and thread profile. *Appl. Sci. (Basel).* 11 (21), 9901. doi:10.3390/APP11219901

Hsieh, M. K., Liu, M. Y., Chen, J. K., Tsai, T. T., Lai, P. L., Niu, C. C., et al. (2019). Biomechanical study of the fixation stability of broken pedicle screws and subsequent strategies. *PLoS One* 14 (6), e0219189. doi:10.1371/journal.pone.0219189

Hsieh, M. K., Liu, M. Y., Chen, J. K., Tsai, T. T., Lai, P. L., Niu, C. C., et al. (2020). Use of longer sized screws is a salvage method for broken pedicles in osteoporotic vertebrae. *Sci. Rep.* 2020 (1), 10441. doi:10.1038/s41598-020-67489-2

Hsieh, M. K., Liu, M. Y., Tsai, T. T., Lai, P. L., and Tai, C. L. (2021). Biomechanical comparison of different numbers and configurations of cross-links in long-segment spinal fixation-an experimental study in a porcine model. *Glob. Spine J.*, 2192568221990646. doi:10.1177/2192568221990646

Jarvers, J. S., Schleifenbaum, S., Pfeifle, C., Oefner, C., Edel, M., von der Hoh, N., et al. (2021). Comparison of three different screw trajectories in osteoporotic vertebrae: A biomechanical investigation. *BMC Musculoskelet. Disord.* 22 (1), 418–511. doi:10.1186/s12891-021-04254-0

Karakaşli, A., Çeçen, B., Erduran, M., Taylan, O., Hapa, O., and Havitcioğlu, H. (2014). Rigid fixation of the lumbar spine alters the motion and mechanical stability at the adjacent segment level. *Jt. Dis. Relat. Surg.* 25 (1), 42–46. doi:10.5606/EHC.2014.09

Karakaşli, A., Yildiz, D. V., Kumtepe, E., Kizmazoğlu, C., and Havitçioğlu, H. (2013). Biomechanical comparison of intact lumbar lamb spine and endoscopic discectomized lamb spine. *Jt. Dis. Relat. Surg.* 24 (1), 33–38. doi:10.5606/EHC.2013.08

Krishnan, V., Varghese, V., and Kumar, G. S. (2016). Comparative analysis of effect of density, insertion angle and reinsertion on pull-out strength of single and two pedicle screw constructs using synthetic bone model. *Asian Spine J.* 10 (3), 414. doi:10.4184/ASJ.2016.10.3.414

Lee, G. W., Son, J. H., Ahn, M. W., Kim, H. J., and Yeom, J. S. (2015). The comparison of pedicle screw and cortical screw in posterior lumbar interbody fusion: A prospective randomized noninferiority trial. *Spine J.* 15 (7), 1519–1526. doi:10.1016/J.SPINEE.2015.02.038

Lehman, R. A., and Kuklo, T. R. (2003). Use of the anatomic trajectory for thoracic pedicle screw salvage after failure/violation using the straight-forward technique: A biomechanical analysis. *Spine* 28 (18), 2072–2077. doi:10.1097/01.brs.0000084628.37133.ba

Lehman, R. A., Polly, D. W., Kuklo, T. R., Cunningham, B., Kirk, K. L., and Belmont, P. J. (2003). Straight-forward versus anatomic trajectory technique of thoracic pedicle screw fixation: A biomechanical analysis. *Spine* 28 (18), 2058–2065. doi:10.1097/01.BRS.0000087743.57439.4F

Liu, M. Y., Tsai, T. T., Lai, P. L., Hsieh, M. K., Chen, L. H., and Tai, C. L. (2020). Biomechanical comparison of pedicle screw fixation strength in synthetic bones: Effects of screw shape, core/thread profile and cement augmentation. *PLoS One* 15 (2), e0229328. doi:10.1371/journal.pone.0229328

Matsukawa, K., Taguchi, E., Yato, Y., Imabayashi, H., Hosogane, N., Asazuma, T., et al. (2015). Evaluation of the fixation strength of pedicle screws using cortical bone trajectory: What is the ideal trajectory for optimal fixation? *Spine* 40 (15), E873–E878. doi:10.1097/BRS.0000000000000983

Matsukawa, K., Yato, Y., Hynes, R. A., Imabayashi, H., Hosogane, N., Yoshihara, Y., et al. (2017). Comparison of pedicle screw fixation strength among different transpedicular trajectories: A finite element study. *Clin. spine Surg.* 30 (7), 301–307. doi:10.1097/BSD.0000000000000258

Matsukawa, K., Yato, Y., Imabayashi, H., Hosogane, N., Asazuma, T., and Nemoto, K. (2015). Biomechanical evaluation of the fixation strength of lumbar pedicle screws using cortical bone trajectory: A finite element study. *J. Neurosurg. Spine* 23 (4), 471–478. doi:10.3171/2015.1.SPINE141103

Matsukawa, K., Yato, Y., and Imabayashi, H. (2021). Impact of screw diameter and length on pedicle screw fixation strength in osteoporotic vertebrae: A finite element analysis. *Asian Spine J.* 15 (5), 566–574. doi:10.31616/ASJ.2020.0353

Matsukawa, K., Yato, Y., Kato, T., Imabayashi, H., Asazuma, T., and Nemoto, K. (2014). *In vivo* analysis of insertional torque during pedicle screwing using cortical bone trajectory technique. *Spine* 39 (4), E240–E245. doi:10.1097/BRS.0000000000000116

Matsukawa, K., Yato, Y., Nemoto, O., Imabayashi, H., Asazuma, T., and Nemoto, K. (2013). Morphometric measurement of cortical bone trajectory for lumbar pedicle screw insertion using computed tomography. *J. Spinal Disord. Tech.* 26 (6), E248–E253. doi:10.1097/BSD.0B013E318288AC39

Miranpuri, G. S., Schomberg, D. T., Stan, P., Chopra, A., Buttar, S., Wood, A., et al. (2018). Comparative morphometry of the Wisconsin miniature Swine<TM> thoracic spine for modeling human spine in translational spinal cord injury research. *Ann. Neurosci.* 25 (4), 210–218. doi:10.1159/000488022

Molinari, L., Falcinelli, C., Gizzi, A., and DiMartino, A. (2021). Effect of pedicle screw angles on the fracture risk of the human vertebra: A patient-specific computational model. *J. Mech. Behav. Biomed. Mat.* 116, 104359. doi:10.1016/J.JMBBM.2021.104359

Newcomb, A. G. U. S., Baek, S., Kelly, B. P., and Crawford, N. R. (2017). Effect of screw position on load transfer in lumbar pedicle screws: A non-idealized finite element analysis. *Comput. Methods Biomech. Biomed. Engin.* 20 (2), 182–192. doi:10.1080/10255842.2016.1209187

Oshino, H., Sakakibara, T., Inaba, T., Yoshikawa, T., Kato, T., and Kasai, Y. (2015). A biomechanical comparison between cortical bone trajectory fixation and pedicle screw fixation. *J. Orthop. Surg. Res.* 10 (1), 125. doi:10.1186/S13018-015-0270-0

Perez-Orribo, L., Kalb, S., Reyes, P. M., Chang, S. W., and Crawford, N. R. (2013). Biomechanics of lumbar cortical screw-rod fixation versus pedicle screw-rod fixation with and without interbody support. *Spine* 38 (8), 635–641. doi:10.1097/BRS.0B013E318279A95E

Perna, A., Smakaj, A., Vitiello, R., Velluto, C., Proietti, L., Tamburrelli, F. C., et al. (2022). Posterior percutaneous pedicle screws fixation versus open surgical instrumented fusion for thoraco-lumbar spinal metastases palliative management: A systematic review and meta-analysis. *Front. Oncol.* 0, 884928. doi:10.3389/FONC.2022.884928

Phan, K., Hogan, J., Maharaj, M., and Mobbs, R. J. (2015). Cortical bone trajectory for lumbar pedicle screw placement: A review of published reports. *Orthop. Surg.* 7 (3), 213–221. doi:10.1111/os.12185

Putzer, M., Auer, S., Malpica, W., Suess, F., and Dendorfer, S. (2016). A numerical study to determine the effect of ligament stiffness on kinematics of the lumbar spine during flexion. *BMC Musculoskelet. Disord.* 17 (1), 95–97. doi:10.1186/s12891-016-0942-x

Qiu, L., Niu, F., Wu, Z., Zhang, W., Chen, F., Tan, J., et al. (2022). Comparative outcomes of cortical bone trajectory screw fixation and traditional pedicle screws in lumbar fusion: A meta-analysis. *World Neurosurg. x.* 164, e436–e445. doi:10.1016/j.wneu.2022.04.129

Santoni, B. G., Hynes, R. A., McGilvray, K. C., Rodriguez-Canessa, G., Lyons, A., Henson, M., et al. (2009). Cortical bone trajectory for lumbar pedicle screws. *Spine J.* 9 (5), 366–373. doi:10.1016/J.SPINEE.2008.07.008

Schomberg, D. T., Tellez, A., Meudt, J. J., Brady, D. A., Dillon, K. N., Arowolo, F. K., et al. (2016). Miniature swine for preclinical modeling of complexities of human disease for translational scientific discovery and accelerated development of therapies and medical devices. *Toxicol. Pathol.* 44 (3), 299–314. doi:10.1177/0192623315618292

Shen, F., Kim, H. J., Kang, K. T., and Yeom, J. S. (2019). Comparison of the pullout strength of pedicle screws according to the thread design for various degrees of bone quality. *Appl. Sci. (Basel).* 9 (8), 1525. doi:10.3390/APP9081525

Suk, S. I., Lee, S. M., Chung, E. R., Kim, J. H., and Kim, S. S. (2005). Selective thoracic fusion with segmental pedicle screw fixation in the treatment of thoracic idiopathic scoliosis: More than 5-year follow-up. *Spine* 30 (14), 1602–1609. doi:10.1097/01.BRS.0000169452.50705.61

Tai, C. L., Hsieh, P. H., Chen, W. P., Chen, L. H., Chen, W. J., and Lai, P. L. (2008). Biomechanical comparison of lumbar spine instability between laminectomy and

bilateral laminotomy for spinal stenosis syndrome - an experimental study in porcine model. *BMC Musculoskelet. Disord.* 9, 84. doi:10.1186/1471-2474-9-84

Tschugg, A., Hartmann, S., Lener, S., Rietzler, A., Sabrina, N., and Thomé, C. (2017). Minimally invasive spine surgery in lumbar spondylodiscitis: A retrospective single-center analysis of 67 cases. *Eur. Spine J.* 26 (12), 3141–3146. doi:10.1007/s00586-017-5180-x

Varghese, V., Krishnan, V., and Kumar, G. S. (2018). Evaluating pedicle-screw instrumentation using decision-tree analysis based on pullout strength. *Asian Spine J.* 12 (4), 611–621. doi:10.31616/ASJ.2018.12.4.611

Varghese, V., Krishnan, V., and Kumar, G. S. (2018). Testing pullout strength of pedicle screw using synthetic bone models: Is a bilayer foam model a better representation of vertebra? *Asian Spine J.* 12 (23), 398–406. doi:10.4184/asj.2018.12.3.398

Varghese, V., Saravana Kumar, G., and Krishnan, V. (2017). Effect of various factors on pull out strength of pedicle screw in normal and osteoporotic cancellous bone models. *Med. Eng. Phys.* 40, 28–38. doi:10.1016/J.MEDENGPHY.2016.11.012

Wadhwa, R. K., Thakur, J. D., Khan, I. S., James, J., Ahmed, O., Zhang, S., et al. (2015). Adjustment of suboptimally placed lumbar pedicle screws decreases pullout strength and alters biomechanics of the construct: A pilot cadaveric study. *World Neurosurg. x.* 83 (3), 368–375. doi:10.1016/J.WNEU.2014.04.065

Wang, J., He, X., and Sun, T. (2019). Comparative clinical efficacy and safety of cortical bone trajectory screw fixation and traditional pedicle screw fixation in posterior lumbar fusion: A systematic review and meta-analysis. *Eur. Spine J.* 28 (7), 1678–1689. doi:10.1007/S00586-019-05999-Y

Wang, L., Li, J., Wang, H., Yang, Q., Lv, D., Zhang, W., et al. (2014). Posterior short segment pedicle screw fixation and TLIF for the treatment of unstable thoracolumbar/lumbar fracture. *BMC Musculoskelet. Disord.* 15 (1), 40–11. doi:10.1186/1471-2474-15-40

Wang, X., Xu, F., Fu, Y., Chen, H., Gao, X., and Huang, Q. (2020). Traumatic vertebral fractures involve the anterior end plate more than the posterior end plate: A retrospective study. *Med. Baltim.* 99 (34), e21572. doi:10.1097/MD.0000000000021572

Youssef, J. A., McKinley, T. O., Yerby, S. A., and McLain, R. F. (1999). Characteristics of pedicle screw loading. Effect of sagittal insertion angle on intrapedicular bending moments. *Spine* 24 (11), 1077–1081. doi:10.1097/00007632-199906010-00006

Zhao, Y., Yang, S., and Ding, W. (2019). Unilateral versus bilateral pedicle screw fixation in lumbar fusion: A systematic review of overlapping meta-analyses. *PLoS One* 14 (12), e0226848. doi:10.1371/JOURNAL.PONE.0226848

The efficacy of femoral augmentation for hip fracture prevention using ceramic-based cements: A preliminary experimentally-driven finite element investigation

Anita Fung[1]*, Ingmar Fleps[2], Peter A. Cripton[3,4], Pierre Guy[4,5], Stephen J. Ferguson[1] and Benedikt Helgason[1]

[1]Laboratory for Orthopaedic Technology, Institute for Biomechanics, Department of Health Sciences and Technology, ETH Zürich, Zürich, Switzerland, [2]Orthopaedic and Developmental Biomechanics Laboratory, Department of Mechanical Engineering, Boston University, Boston, MA, United States, [3]Orthopaedic and Injury Biomechanics Group, School of Biomedical Engineering and Departments of Mechanical Engineering and Orthopaedics, University of British Columbia, Vancouver, BC, Canada, [4]Centre for Hip Health and Mobility, University of British Columbia, Vancouver, BC, Canada, [5]Division of Orthopaedic Trauma, Department of Orthopaedics, University of British Columbia, Vancouver, BC, Canada

Femoral fractures due to sideways falls continue to be a major cause of concern for the elderly. Existing approaches for the prevention of these injuries have limited efficacy. Prophylactic femoral augmentation systems, particularly those involving the injection of ceramic-based bone cements, are gaining more attention as a potential alternative preventative approach. We evaluated the mechanical effectiveness of three variations of a bone cement injection pattern (basic ellipsoid, hollow ellipsoid, small ellipsoid) utilizing finite element simulations of sideways fall impacts. The basic augmentation pattern was tested with both high- and low-strength ceramic-based cements. The cement patterns were added to the finite element models (FEMs) of five cadaveric femurs, which were then subject to simulated sideways falls at seven impact velocities ranging from 1.0 m/s to 4.0 m/s. Peak impact forces and peak acetabular forces were examined, and failure was evaluated using a strain-based criterion. We found that the basic HA ellipsoid provided the highest increases in both the force at the acetabulum of the impacted femur ("acetabular force", 55.0% ± 22.0%) and at the force plate ("impact force", 37.4% ± 15.8%). Changing the cement to a weaker material, brushite, resulted in reduced strengthening of the femur (45.2% ± 19.4% acetabular and 30.4% ± 13.0% impact). Using a hollow version of the ellipsoid appeared to have no effect on the fracture outcome and only a minor effect on the other metrics (54.1% ± 22.3% acetabular force increase and 35.3% ± 16.0% impact force increase). However, when the outer two layers of the ellipsoid were removed (small ellipsoid), the force increases that were achieved were only 9.8% ± 5.5% acetabular force and 8.2% ± 4.1% impact force. These results demonstrate the importance of supporting the femoral neck cortex to prevent femoral fractures in a sideways fall, and provide plausible options for prophylactic femoral augmentation. As this is a preliminary study, the surgical technique, the possible effects of trabecular bone damage during the augmentation process, and the effect on the blood supply to the femoral head must be assessed further.

1 Introduction

Hip fractures in the elderly are associated with high socio-economic costs. By 2025, 810,000 fractures are expected to occur in the EU and cost 25.3 billion euros per year in direct medical costs (Hernlund et al., 2013). Hip fractures are associated with high morbidity and mortality rates (Fierens and Broos, 2006) and occur, in the vast majority of cases, due to sideways falls (Parkkari et al., 1999). At 6 months after a hip fracture, only 15% of survivors can walk across a room unaided (Marottoli et al., 1992). Furthermore, patients who have already sustained a hip fracture are more predisposed to having a second hip fracture (Sobolev et al., 2015), which often require more healthcare resources than the first hip fracture (Guy et al., 2017) and longer periods of immobilization (Ekström et al., 2009).

Existing treatments to prevent hip fractures include the use of pharmacological interventions to strengthen the femur and hip protectors which protect the femurs, but both have limited efficacy (Body et al., 2011; Järvinen et al., 2015). Cement-based interventions for the prophylactic augmentation of the proximal femur could overcome these limitations but require extensive evaluation to confirm that they would be safe, effective, durable and could be effectively introduced using surgical techniques that are safe for this patient population. The evaluation of the mechanical efficacy of polymer and ceramic cement-based femoral augmentations have been performed on cadavers (Heini et al., 2004; Beckmann et al., 2007; Sutter et al., 2010b; Sutter et al., 2010a; Beckmann et al., 2011; Fliri et al., 2013; Basafa et al., 2015; Stroncek et al., 2019). One of the main drawbacks of these important previous studies is in the method in which the strength of each femur is measured. In each study, each femur is loaded to fracture in order to measure its strength. These experiments measure the femoral strength without evaluating whether the subject-specific loads experienced during a sideways fall would actually surpass the femoral strength. It is also unclear how this method of measuring strength increases relative to unaugmented control femurs relates to a reduction in fracture risk because it does not take into account the subject-specific loading and fall probabilities (Parkkari et al., 1999; Choi et al., 2015). Additionally, it has been previously shown that the surrounding structures, such as the pelvis and soft tissue, absorb most of the impact energy in a sideways fall, and only 5%–10% of the energy is absorbed by the femur itself (Robinovitch et al., 1995; Laing and Robinovitch, 2010; Fleps et al., 2018a; 2019a). Furthermore, femoral augmentation might not only change femoral strength, but also toughness (i.e. energy absorbed prior to fracture). The increase in toughness alone could lead to reduced fracture risk. However, this reduction in risk can only be demonstrated by considering the impact force and energy due to a particular fall, which can result in impacts that do not fracture the femur. It follows that less than 5% of falls result in fractures (Nevitt et al., 1989; Hayes et al., 1996; Nachreiner et al., 2007). Without an estimate of the applied impact loading under consideration, a decrease in fracture risk due to an increase in toughness is challenging to quantify.

In order to address these shortcomings of the testing methods, a dynamic inertia-driven sideways fall simulator (Fleps et al., 2018b) has been developed, which includes the femurs, pelvis, and soft tissue surrogate. Advantages of the test setup include the use of subject-specific loading and the direct identification of fractures caused by sideways falls. Finite element models (FEMs) of the fall simulator have also been developed and validated, where they accurately predicted the fracture outcome in 10 of 11 specimens (Fleps et al., 2019b).

A previously-published *in silico* study using the FEMs of the novel sideways fall simulator (Fung et al., 2022) evaluated the mechanical efficacy of implants and found that although the implants increased the force sustained by the femur in a sideways fall prior to fracture, the femur still fractured at the highest impact velocities (3.1 m/s or higher). The results showed that the implants were not providing sufficient support to the weaker areas of the femur, such as at the femoral neck cortex, which is where the fractures typically initiate (de Bakker et al., 2009). The use of bone cements in these weaker areas could overcome these deficiencies because cements allow for the flexibility in both positioning and shaping. These attributes are useful for applications that require the direct support of the femoral neck cortex in three dimensions, such as for the prophylactic femoral augmentation under discussion here. In addition, the injection of relatively large volumes of ceramic-based bone cement is less concerning than for PMMA injections because of their good biocompatibility and absence of exothermic reactions that could damage tissue. Furthermore, the clinical feasibility of injections with large volumes into the proximal femur has previously been demonstrated (Howe et al., 2019; Stroncek et al., 2019).

Therefore, the aim of this study was to evaluate the strengthening effect of a ceramic-based bone cement pattern used for prophylactic femoral augmentation using FEMs of the novel fall simulator (Fleps et al., 2019b). The hypotheses for this study were: a) the augmented femurs would fracture for fewer of the simulated impacts and sustain a higher peak force in the inertia-driven simulations, b) changing the material of the bone cement would have a minor effect on the fracture outcome and peak forces, and c) making the cement pattern hollow would have a minor effect on the fracture outcome and peak forces.

2 Materials and methods

2.1 Baseline FEMs

The five specimens (1 female, 4 males) used in this analysis were previously described in another study (Fung et al., 2022), and are a subset of eleven specimens (6 females, 5 males) that were tested using an inverted-pendulum sideways fall simulator (Fleps et al., 2019a). The five specimens had exhibited femoral fractures in the fall simulator experiments and were thus identified as candidates that could benefit from prophylactic femoral augmentation. Therefore, the validated unaugmented FEMs for the five specimens were used as the controls in the present study.
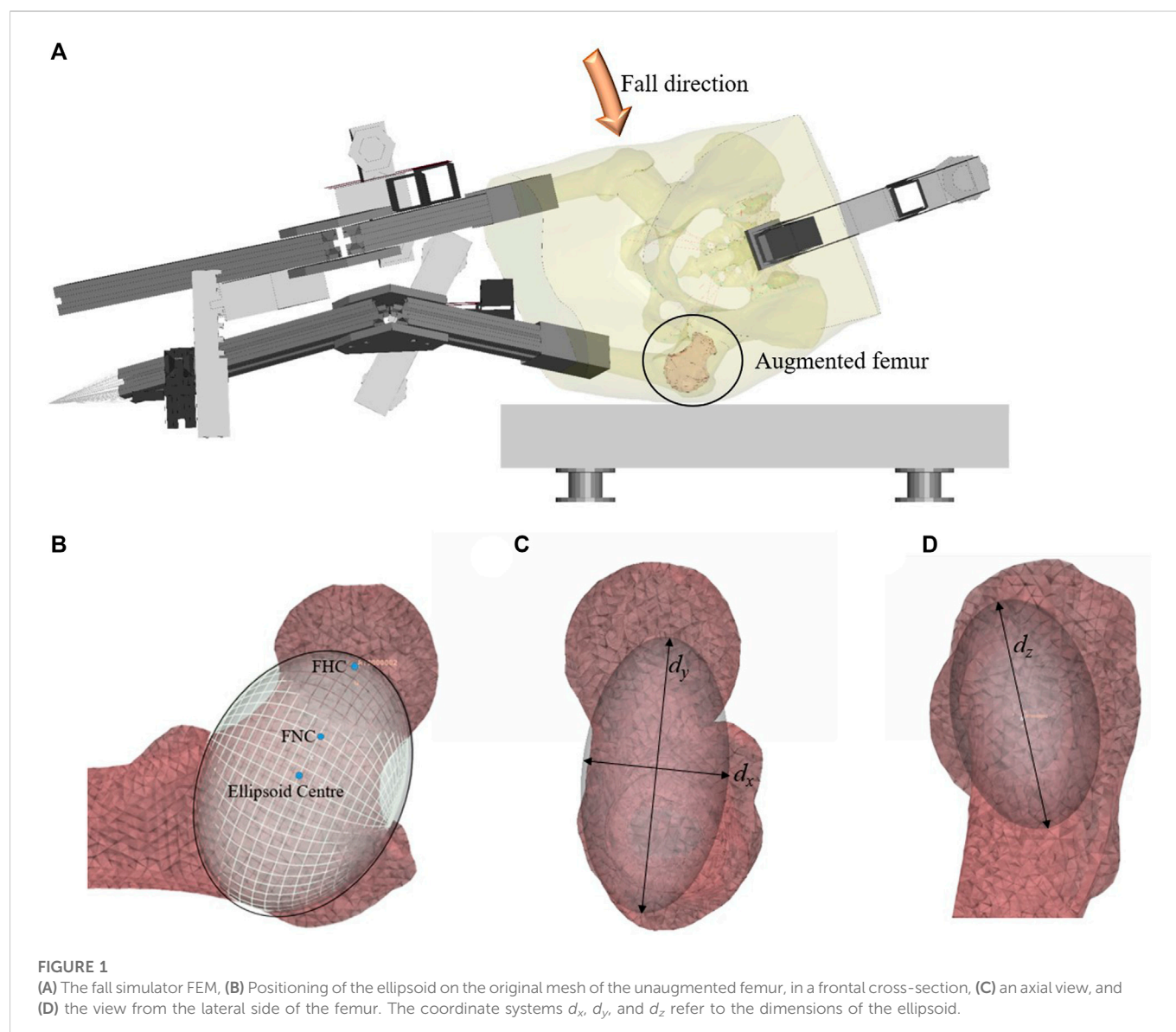
FIGURE 1
(A) The fall simulator FEM, **(B)** Positioning of the ellipsoid on the original mesh of the unaugmented femur, in a frontal cross-section, **(C)** an axial view, and **(D)** the view from the lateral side of the femur. The coordinate systems d_x, d_y, and d_z refer to the dimensions of the ellipsoid.

To construct the FEMs (Figure 1A), the geometries of each specimen's pelvis and femurs were obtained using clinical-resolution CT scans (120 kVp, 200 mAs, voxel size: 0.78 mm × 0.78 mm × 0.3 mm). Descriptions of the lower limb geometry, soft tissue surrogate, cartilage, ligaments, and contact conditions have been previously published (Fleps et al., 2018a). Commercial FEM pre-processing software (Ansa 17.1.0, Beta CAE Systems, Switzerland) and solvers (LS-Dyna, Livermore, United States) were used to build the models.

2.2 Femoral augmentation

The cement augmentation pattern that was chosen for this study was determined by the positioning of an ellipsoid (Figures 1B–D) which provides a repeatable way to determine the placement of the bone cement. This pattern was informed by previous work which showed that the greater trochanter and femoral neck were susceptible to fracture during a sideways fall (Fleps et al., 2019a). In practice, this

pattern would require the removal of the marrow and trabecular bone enclosed by the ellipsoid, followed by the filling of the cavity with bone cement.

For the FEMs, the cement augmentation pattern was created by placing an ellipsoid on the mesh of the unaugmented left femur. The long axis of the ellipsoid (d_y) was aligned with the femoral neck axis and extended from the femoral head centre (FHC) to 5 mm beyond the cortex on the lateral side of the femur. The femoral neck axis was defined as the line extending from the femoral neck centre (FNC) to the FHC, with both points defined using the algorithm described in a previous publication (Enns-Bray et al., 2019). The dimension d_x of the ellipsoid was 1.5 times the width of the femoral neck at the FNC, and the dimension d_z of the ellipsoid was twice the width of the femoral neck at the FNC. The final ellipsoid shape and volume were adapted to the fit the intramedullary space at the femoral neck using the endosteal contour of the femur neck cortex of each specimen as its limit. This created the basic ellipsoid (Figure 2A). The dimensions and volumes of the constructed ellipsoids for each specimen are shown in Table 1.

FIGURE 2
Planar cut views of **(A)** the basic ellipsoid cement pattern, **(B)** the hollow ellipsoid pattern, and **(C)** the small ellipsoid pattern.

TABLE 1 Femoral neck width and the dimensions and volume of the construction ellipsoid for each specimen. The dimensions d_x, d_y, and d_z are illustrated in **Figure 1.**

	H1389	H1397	H1399	H1401	H1406	Mean	SD
Femoral neck width at FNC (mm)	25.4	29.7	28.1	27.6	27.6	27.7	1.4
d_x (mm)	38.2	44.6	42.1	41.3	41.4	41.5	2.1
d_y (mm)	74.6	84.0	86.5	80.2	80.9	81.2	4.0
d_z (mm)	50.9	59.4	56.2	55.1	55.2	55.4	2.8
Volume (cm³)	75.8	116.6	107.3	95.6	96.9	98.4	13.7

TABLE 2 Cement volume of the cement ellipsoid patterns for each specimen.

	H1389	H1397	H1399	H1401	H1406	Mean	SD
Basic Ellipsoid (mL)	43.3	55.1	54.2	53.2	56.1	52.4	4.7
Hollow Ellipsoid (mL)	31.9	47.1	46.9	44.6	46.0	43.3	5.8
Small Ellipsoid (mL)	11.4	8.0	7.4	8.7	10.1	9.1	1.5

TABLE 3 Cement volume of the cement ellipsoid patterns for the cement volume sub-study.

	H1389	H1397	H1399	H1401	H1406	Mean	SD
Basic Ellipsoid (mL)	44.4	68.8	57.8	57.2	71.3	59.9	10.8
Hollow Ellipsoid (mL)	18.2	33.4	24.9	21.8	27.4	25.1	5.7
Small Ellipsoid (mL)	26.2	35.5	32.8	35.4	43.9	34.8	6.4

To assign the cement properties, elements with nodes on the surface of the femur, as well as elements with an apparent density greater than 1.4 g/cm³ (Enns-Bray et al., 2018) were excluded for the identification of elements within the cement volume. The remaining elements inside the ellipsoid were assigned the mechanical properties of the bone cement (Figure 2A), either hydroxyapatite (HA) or brushite, as described in the Material Models section below. In order to determine the influence of bridging between different parts of the femoral cortex, additional injection patterns were developed that only included the two outermost layers of the identified elements for the cement assignment (hollow ellipsoid) in Figure 2B and a pattern that excluded the two outermost layers (small

ellipsoid) in Figure 2C. The hollow ellipsoid uses a smaller volume of the augmentation material compared to the original pattern but still bridges between all parts of the femoral cortex, while the smaller filled ellipsoid does not connect to the femoral cortex directly. The volumes of the cement for the different ellipsoid patterns for each specimen are shown in Table 2.

Table 2 reveals the potential confounding factor of the bone cement volume, as the cement volume of the hollow ellipsoid pattern exceeds the volume of the small ellipsoid pattern across all specimens. Therefore, a sub-study was done on all specimens to examine whether having a hollow ellipsoid with a lower cement volume than the small ellipsoid would affect

FIGURE 3
Material model implemented in the FEM for the hydroxyapatite cement. Inset figure **(A)** is a magnification of the elastic region of the curve, while inset figure **(B)** shows the curve at higher compressive strains.
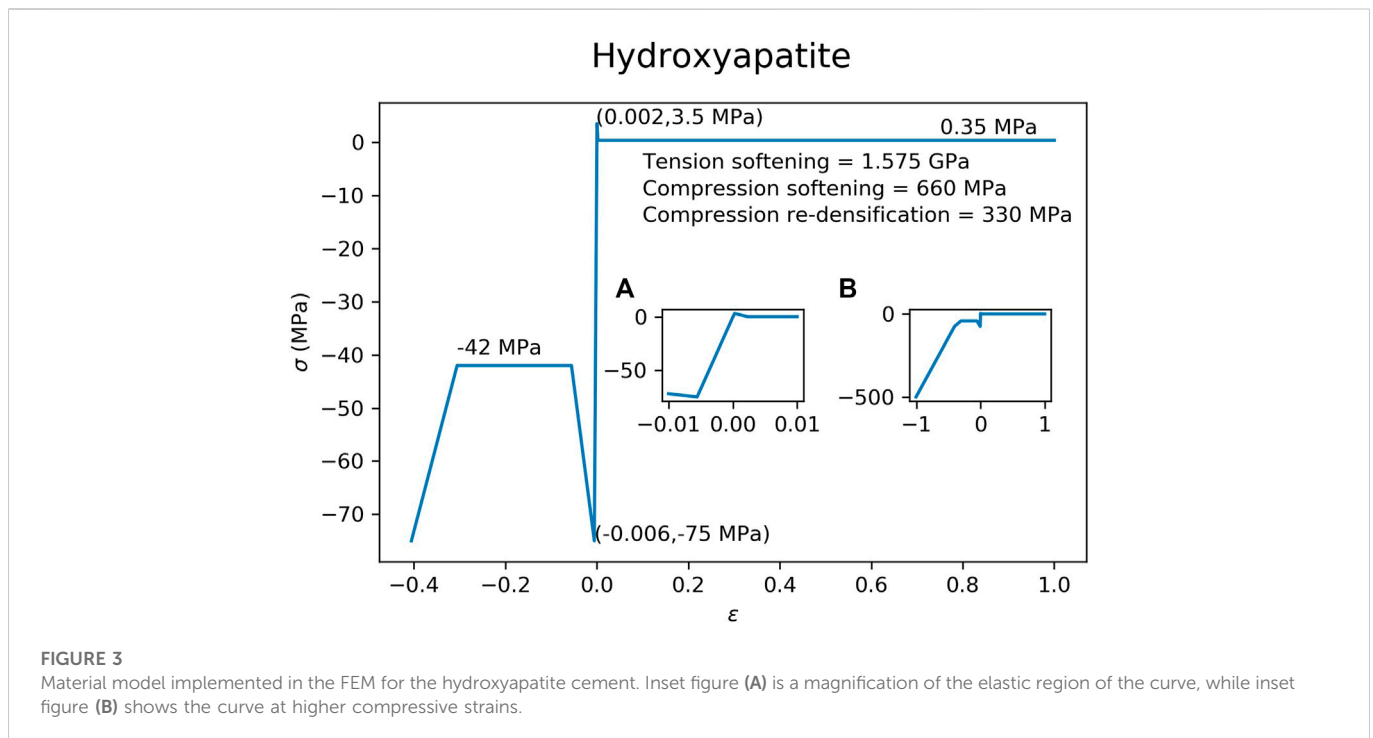
the relative mechanical efficacy of the cement injection patterns. This sub-study required reducing the mesh size of the femur to 2 mm instead of 3 mm. The cement volumes in the sub-study are listed in Table 3.

2.3 Simulated sideways falls

The FEM and corresponding experiment has been described previously (Fleps et al., 2018a). In short, the model consists of an inertia-driven sideways fall simulator that rotates around the foot point and falls onto a force plate. The fall simulator comprises of a metal leg assembly with a cadaveric pelvis and proximal femur construction embedded in a soft tissue surrogate. The input velocities in the present study are the same as those used previously (Fung et al., 2022), and range between 1.0 m/s and 4.0 m/s. The input velocity for all simulations in the cement volume sub-study was 3.1 m/s, which was the same impact velocity for the original lab experiments using this inertia-driven fall model (Fleps et al., 2019a). The evaluated outputs of the FEMs include the impact force at the force plate, the force at the acetabulum of the impacted femur, and the fracture outcome of the specimen. Details of these outputs are described in Section 2.6.

2.4 Material models

The material mapping strategy for the bone tissue used in the present study has been described previously (Enns-Bray et al., 2018). Briefly, elements were assigned to 500 equally-spaced stiffness values between 0.01 GPa and 22 GPa. As in the previous models (Fung et al., 2022), the pelvis and contralateral femur was assigned strain rate dependent linear material properties, while the impacted femur had strain rate dependent non-linear material properties with tension-compression asymmetry. This was done to avoid having pelvic fractures as a confounding

factor in the results. The femoral head shells described in the previous study (Fung et al., 2022) were also used in the present study.

The material properties of the hydroxyapatite (Figure 3) and brushite (Figure 4) used in the FEM simulations were based on experimental test results (Charrière et al., 2001). A material model with tension-compression asymmetry (LS-DYNA, MAT 124) was implemented for both cement materials. After yielding, the compressive stress of the hydroxyapatite was decreased to 56.0% of the compressive strength (Figure 3), which corresponds to the reported porosity of 44.0% of the hydroxyapatite (Charrière et al., 2001). In a similar manner, the compressive stress of the brushite cement was decreased to 62.8% of its compressive strength (Figure 4), which corresponds to its porosity of 37.2% (Charrière et al., 2001). Densification was assumed for an additional 30% strain in compression for both cements. A similar implementation has already been used to successfully predict bone cement in cranial implant simulations (Lewin et al., 2020). FEMs using the HA properties were used for all three types of ellipsoids. The brushite material was used on only the basic ellipsoid pattern.

2.5 Cement-bone interface sensitivity analysis

The contact between the cement and the bone was modelled as fully tied under the assumption that a bond would be made (Tamimi et al., 2009; Draenert et al., 2013) through direct apposition and some interdigitation of remaining cancellous bone and cement. In the FEMs, this was modelled with the elements of the cement sharing nodes with the elements of the bone. To test the sensitivity of the cement-bone interface conditions, a worst-case frictionless interface test was run on the hydroxyapatite basic ellipsoid models at 3.1 m/s for all specimens. For the models with the frictionless cement-bone interface, a 0.01 mm gap was created between the cement elements and the bone elements to allow for movement of the cement.
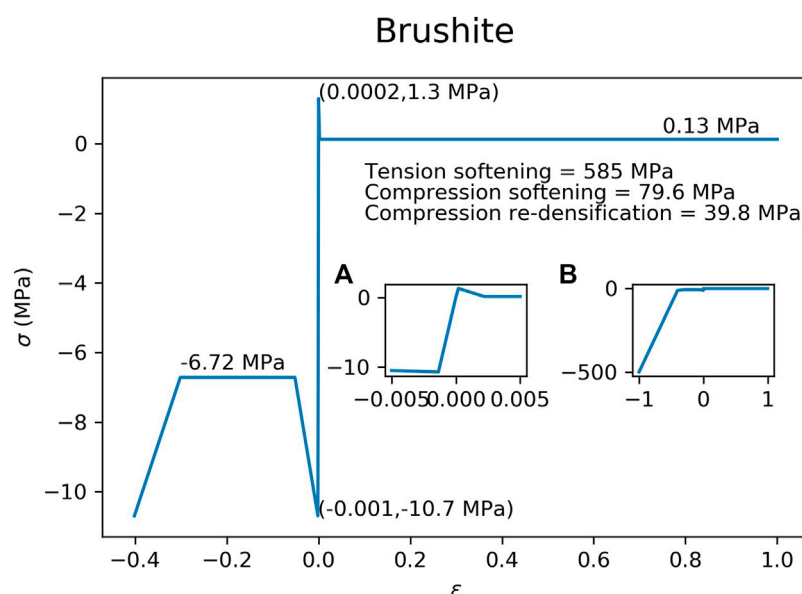
FIGURE 4
Material model implemented in the FEM for the brushite cement. Inset figure **(A)** is a magnification of the elastic region of the curve, while inset figure **(B)** shows the curve at higher compressive strains.

2.6 Data processing

We calculated peak impact forces and peak acetabular forces (Fung et al., 2022). In addition, failure was evaluated using a strain-based criterion. Briefly, peak forces were estimated using virtual transducers at the acetabulum ("acetabular force") and the surface of the force plate ("impact force"). Acetabular forces could be compared to the forces applied in femur-only studies (Beckmann et al., 2007; Sutter et al., 2010a; Stroncek et al., 2019), and the impact forces could be compared to experiments and simulations done on the sideways fall simulator (Fleps et al., 2019a; Fung et al., 2022).

The fragility ratio (FR) was also calculated by finding the ratio between the peak forces in the elastic simulation (FEMs$_{lin}$) and corresponding non-linear simulation (FEMs$_{non-lin}$). The maximum fragility ratio that a femur reaches before fracturing indicates how much the femur is relying on its ductility and toughness in the non-linear part of the loading curve. We used strain-based criteria to determine bone failure. The first and third principal engineering strains (LS-Dyna history variables #18 and #20) at 2 ms past the peak impact force were used to determine femoral fracture. The trabecular bone strain thresholds were 1.4% in tension and −2.0% in compression, while the cortical bone strain thresholds were 2.8% in tension and −5.9% in compression (Grassi et al., 2021). Bone failure was classified in three groups "no fracture", a "trochanteric fracture", and a "femoral neck fracture" (Fung et al., 2022).

3 Results

3.1 Peak forces and fragility ratios

The peak acetabular force increases across all specimens and impact velocities in which the femurs had fractured, were on average 55.0% (SD = 22.0%) for the basic HA ellipsoid, 45.2% (SD = 19.4%) for the basic brushite ellipsoid, 9.8% (SD = 5.5%) for the small HA ellipsoid, and 54.1% (SD = 22.3%) for the hollow HA ellipsoid. The peak impact force increases were 37.4% (SD = 15.8%) for the basic HA ellipsoid, 30.4% (SD = 13.0%) for the basic brushite ellipsoid, 8.2% (SD = 4.1%) for the small HA ellipsoid, and 35.3% (SD = 16.0%) for the hollow HA ellipsoid.

The results for the fragility ratios (Table 4) were also consistent with those for the peak forces as expected. No common fragility ratio threshold across specimens and augmentation conditions was apparent for the fragility ratios calculated with the acetabular force or the impact forces.

3.2 Effect of bone cement material

The graphs on Figure 5 show that changing the cement material of the augmentation results in only small changes in the peak acetabular forces. In 4 of the 5 specimens, there was less than 5% difference between the peak forces of the HA ellipsoid augmentation and the brushite ellipsoid augmentation for any given specimen at any impact velocity. For higher impact velocities, the percent differences increased to a maximum of 13.2% for peak acetabular forces, and a maximum of 9.9% for peak impact forces.

3.3 Effect of bone cement pattern

In the cement volume sub-study, the basic ellipsoid augmentation FEM and the hollow ellipsoid FEM reached similar peak acetabular and impact forces (within 1.8% difference). Relative to the peak forces of the basic ellipsoid FEM, the peak acetabular force of the small

TABLE 4 Acetabular force fragility ratios. Green cells represent models exhibiting no femoral fractures, yellow cells represent fractures at the greater trochanter, and red cells represent femoral neck fractures as shown in (Fung et al., 2022).

a) Impact speed and corresponding acetabular force fragility ratio for specimen H1389.

H1389	1.0 m/s	1.5 m/s	2.0 m/s	2.5 m/s	3.1 m/s	3.5 m/s	4.0 m/s
Unaugmented	1.0	1.1	1.6	2.0	2.4	2.7	3.0
HA ellipsoid	1.0	1.1	1.3	1.3	1.3	1.5	1.6
Brushite ellipsoid	1.0	1.1	1.3	1.4	1.5	1.6	1.8
HA small ellipsoid	1.0	1.2	1.5	1.9	2.3	2.5	2.8
HA hollow ellipsoid	1.0	1.1	1.3	1.3	1.3	1.5	1.6

b) Impact speed and corresponding acetabular force fragility ratio for specimen H1397.

H1397	1.0 m/s	1.5 m/s	2.0 m/s	2.5 m/s	3.1 m/s	3.5 m/s	4.0 m/s
Unaugmented	1.0	1.0	1.1	1.2	1.3	1.4	1.6
HA ellipsoid	1.0	1.0	1.1	1.1	1.2	1.2	1.3
Brushite ellipsoid	1.0	1.0	1.1	1.1	1.2	1.2	1.3
HA small ellipsoid	1.0	1.0	1.1	1.2	1.3	1.4	1.5
HA hollow ellipsoid	1.0	1.0	1.1	1.1	1.2	1.2	1.2

c) Impact speed and corresponding acetabular force fragility ratio for specimen H1399.

H1399	1.0 m/s	1.5 m/s	2.0 m/s	2.5 m/s	3.1 m/s	3.5 m/s	4.0 m/s
Unaugmented	1.1	1.2	1.3	1.5	1.7	1.9	2.1
HA ellipsoid	1.1	1.2	1.2	1.3	1.3	1.3	1.3
Brushite ellipsoid	1.1	1.2	1.2	1.3	1.3	1.3	1.3
HA small ellipsoid	1.1	1.2	1.2	1.4	1.5	1.7	1.9
HA hollow ellipsoid	1.1	1.2	1.2	1.3	1.3	1.3	1.3

d) Impact speed and corresponding acetabular force fragility ratio for specimen H1401.

H1401	1.0 m/s	1.5 m/s	2.0 m/s	2.5 m/s	3.1 m/s	3.5 m/s	4.0 m/s
Unaugmented	1.0	1.0	1.2	1.4	1.7	1.8	2.0
HA ellipsoid	1.0	1.0	1.1	1.1	1.2	1.2	1.2
Brushite ellipsoid	1.0	1.0	1.1	1.1	1.2	1.2	1.2
HA small ellipsoid	1.0	1.0	1.2	1.3	1.5	1.6	1.7
HA hollow ellipsoid	1.0	1.0	1.1	1.1	1.2	1.2	1.2

e) Impact speed and corresponding acetabular force fragility ratio for specimen H1406.

H1406	1.0 m/s	1.5 m/s	2.0 m/s	2.5 m/s	3.1 m/s	3.5 m/s	4.0 m/s
Unaugmented	1.0	1.1	1.2	1.4	1.7	1.9	2.1
HA ellipsoid	1.0	1.1	1.1	1.2	1.3	1.3	1.6
Brushite ellipsoid	1.0	1.1	1.1	1.2	1.2	1.3	1.5
HA small ellipsoid	1.0	1.1	1.1	1.2	1.5	1.7	1.9
HA hollow ellipsoid	1.0	1.1	1.1	1.2	1.3	1.4	1.6

ellipsoid FEM was on average 10.9% lower, and the peak impact force was on average 9.0% lower.

Figure 6 shows that changing the size of the cement ellipsoid has a greater effect than making the cement pattern hollow. For all five specimens, both the peak acetabular forces and the peak impact forces were drastically reduced by reducing the size of the ellipsoid. However, the differences in the peak forces remain relatively unchanged if the ellipsoid is hollowed.
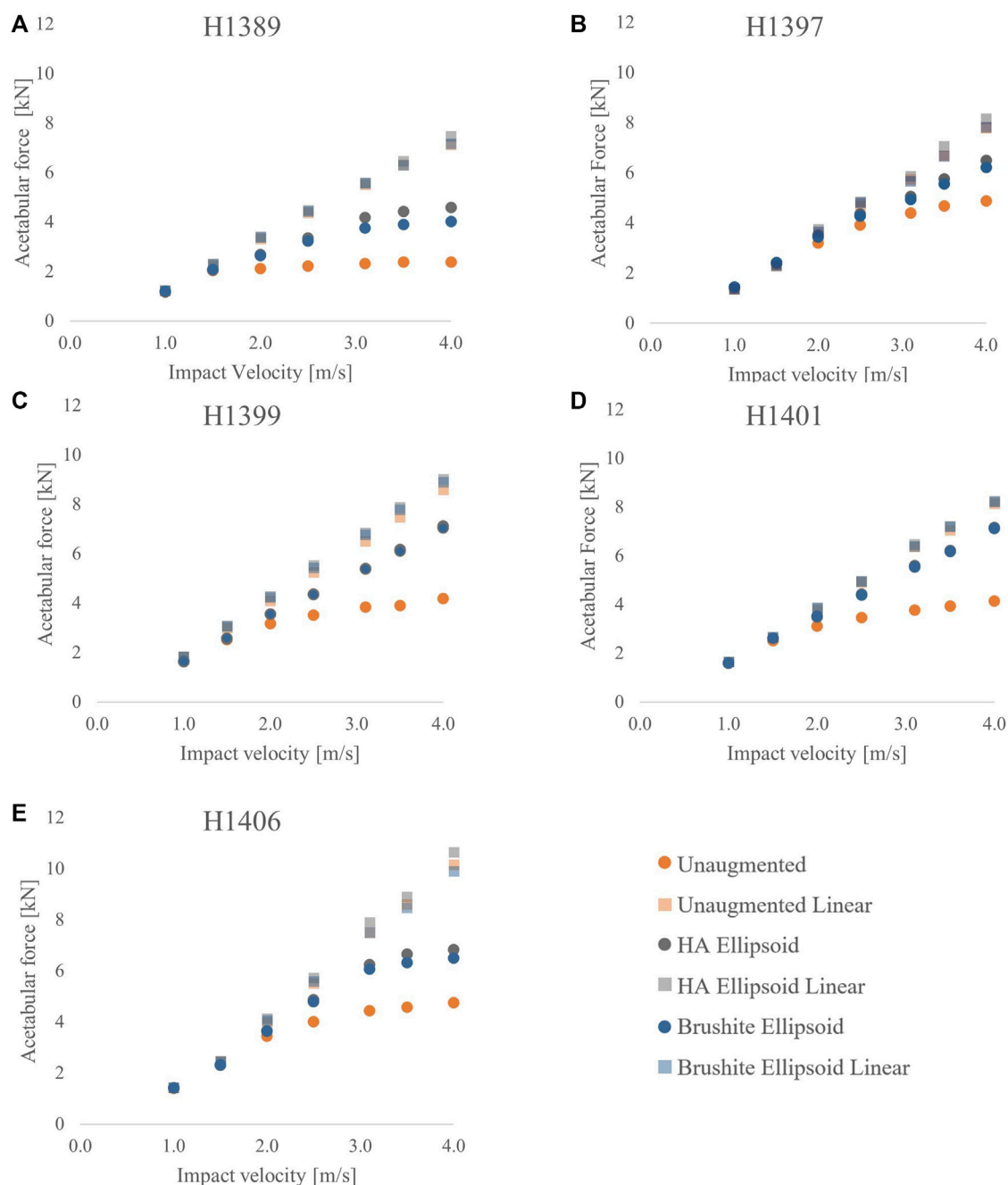
FIGURE 5
Acetabular force vs. impact velocity for the unaugmented, HA ellipsoid, and brushite ellipsoid pattern FEMs for each specimen: **(A)** H1389, **(B)** H1397, **(C)** H1399, **(D)** H1401, and **(E)** H1406.

3.4 Fracture outcomes

Out of 35 non-linear simulations for each augmentation condition, femoral neck fractures appeared in 22 unaugmented femurs, 5 femurs augmented with the basic HA ellipsoid, 10 femurs augmented with the basic brushite ellipsoid, 17 femurs augmented with the small HA ellipsoid, and 5 femurs augmented with the HA hollow ellipsoid.

The breakdown of the fractured specimens by impact velocity and augmentation condition is shown in Figure 7. The predicted fracture outcome for the specimens augmented with the basic HA ellipsoid improved in all specimens at velocities up to 3.5 m/s. At 4.0 m/s, the femoral neck fractures for several specimens shifted to the trochanteric region. The first femoral neck fracture appeared at an impact velocity that was at least 0.5 m/s higher than in the unaugmented femur for all specimens. Changing the material of the cement to brushite had changed the fracture outcomes for 3 of the 5 specimens, reducing the impact velocity at which the first femoral neck fracture occurred. Reducing the size of the ellipsoid also resulted in slightly worse fracture outcomes than with the basic ellipsoid, but using a hollow ellipsoid did not change the fracture outcomes.
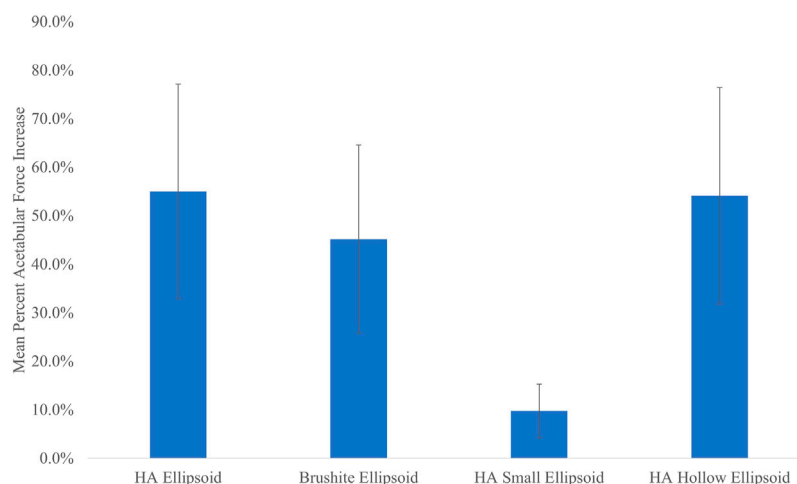
FIGURE 6
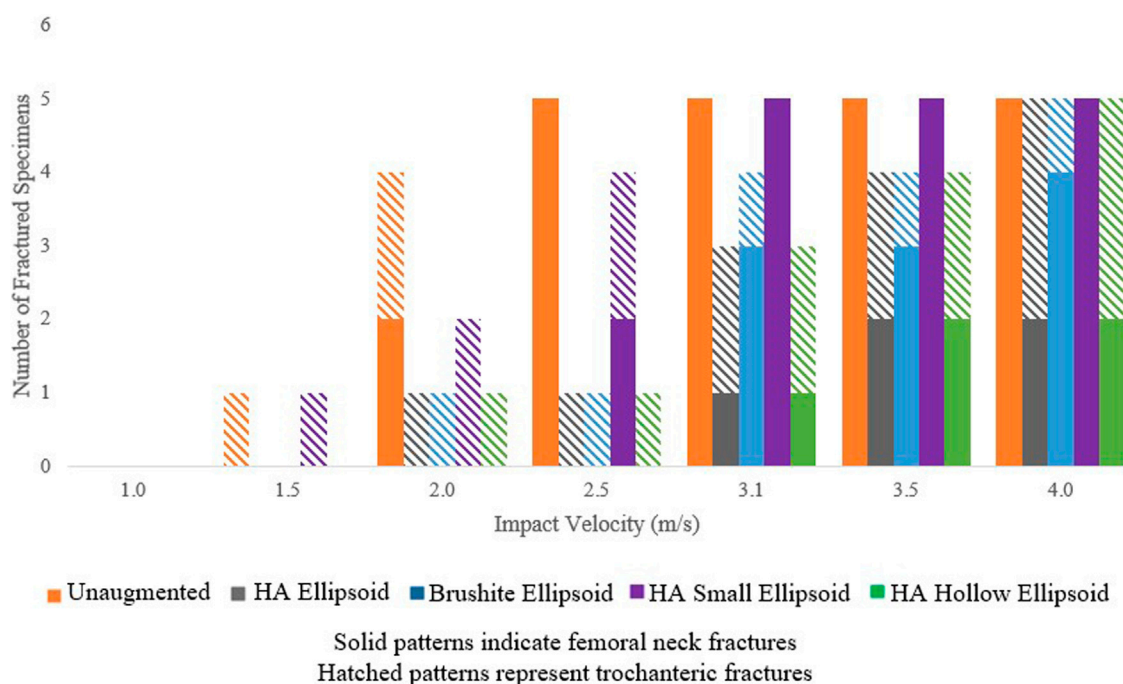Mean percent acetabular force increase vs. cement pattern. Error bars indicate standard deviation.

FIGURE 7
Number of fractured specimens vs. impact velocity as grouped by the type of fracture and augmentation pattern.

3.5 Effect of cement-bone interface conditions

The peak acetabular forces (Figure 8) of the basic HA ellipsoid FEMs at an impact velocity of 3.1 m/s and a frictionless cement-bone interface were on average 17.0% lower than the corresponding FEMs with the fully-bonded cement-bone interface. Of the five specimens, only H1399 had a worse fracture outcome with the frictionless cement-bone interface. On average, the acetabular force increase of the femurs augmented with the frictionless basic HA ellipsoid relative to the unaugmented FEMs was 19.5%. This is compared to 44.8% for the fully bonded basic HA ellipsoid augmentation at an impact velocity of 3.1 m/s.

Accordingly, the peak impact forces of the frictionless cement-bone interface FEMs were 13.2% lower than the corresponding FEMs with the fully-bonded interface. The average impact force increase of the frictionless interface FEMs were 13.8% relative to the unaugmented FEMs. This is compared to 31.4% for the FEM with the fully-bonded interface.
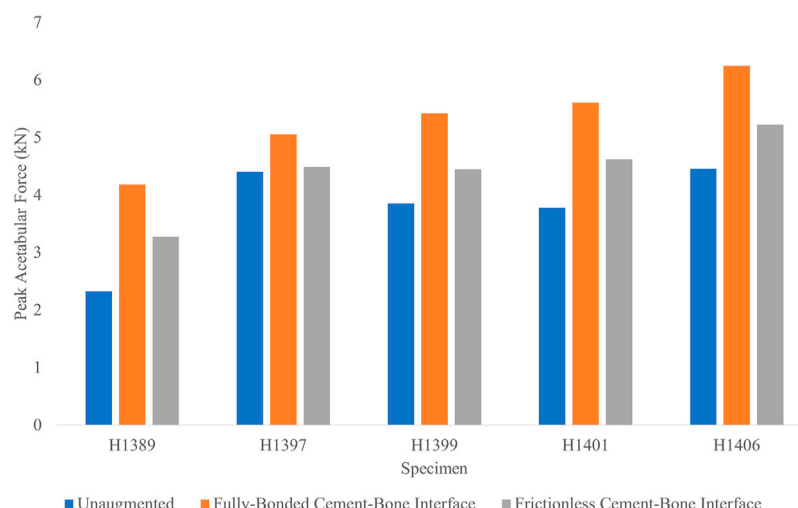
FIGURE 8
Peak acetabular forces for each specimen in the cement-bone interface sensitivity analysis.

4 Discussion

The aim of this study was to evaluate the mechanical efficacy of a ceramic-based bone cement augmentation pattern using FEMs of a dynamic inertia-driven sideways fall simulator. The results showed that the acetabular force increases were the highest with the HA ellipsoid pattern and the hollow ellipsoid pattern, followed by the brushite ellipsoid pattern and the small ellipsoid pattern. Changing the cement to a weaker material reduced the peak forces and increased the number of fractures. Decreasing the size of the ellipsoid had a greater effect than making the cement pattern hollow. Having a weaker interface between the bone and the cement led to lower peak forces, but the augmented FEMs with a weaker cement-bone interface still had higher peak forces than the corresponding unaugmented femurs.

All specimens exhibited fractures at the highest velocity of 4.0 m/s, but the augmentation appears to shift some fractures from the femoral neck to the trochanteric region (Figure 7). In a clinical setting, a trochanteric fracture would be a better outcome than a fracture at the neck or at the trochanter, as they are most often minimally displaced or non-displaced and do not require surgery.

In this study, the maximum impact speed at which most of the augmented femurs did not fracture was 3.5 m/s, which was with the basic HA ellipsoid, the basic brushite ellipsoid, and the hollow HA ellipsoid. Comparing these values to the impact speeds reported in real-life falls (Choi et al., 2015), which had a mean of 2.14 m/s (SD = 0.63), this suggests that the augmentation could prevent femoral fractures at impact speeds with a maximum of two standard deviations above the mean impact speed.

In the present study, the increase in force that the femurs could support for the basic HA and brushite ellipsoid patterns were similar to the strength increases in some femur-only tests using femurs augmented in similar PMMA patterns (Beckmann et al., 2007; Sutter et al., 2010a). However, there was one study (Heini et al., 2004) which reported a strength increase for a PMMA-augmented femur which was substantially higher than the acetabular force increases found in the present study.

Compared to experimental studies that examined resorbable ceramic-based cement, the peak acetabular force increases were higher than the strength increases reported previously (Howe et al., 2019; Stroncek et al., 2019). The peak acetabular force increases for the small HA ellipsoid were similar to the values reported in a study using FEMs with cement patterns with similar cement volumes (Kok et al., 2019). These differing results suggest that while the fracture strengths from the previous studies may be correlated to the acetabular peak forces in the present study, the values may not be directly comparable. It is also difficult to compare the present results to those from previous studies because the results might also depend on the fact that the present and previous studies capture the subject dependency of different femurs.

The results of the cement volume sub-study showed that the cement location is more important for femoral augmentation than the injected cement volume. In the sub-study, the cement volume for the hollow ellipsoid was approximately 60% of the volume of the basic ellipsoid, yet the peak forces between the two patterns were within only 1.8%. However, the small ellipsoid pattern, which had a higher cement volume than the hollow ellipsoid pattern, had lower peak forces of approximately 10%. This could be because the basic cement ellipsoid and the hollow ellipsoid support the cortical bone of the femoral neck by being in direct contact with the endosteal side of the cortex. This is in contrast with the implants tested previously (Fung et al., 2022), which had one rod going into the femoral neck. This finding is further supported by the results of the smaller ellipsoid, which did not have any contact with the femoral neck cortex. Removing the contact with the cortical bone had a negative effect on the fracture outcome, and also reduced the percent force increases and increased the fragility ratio. When the basic ellipsoid was made hollow, keeping only the cement elements that were in contact with the femoral neck cortex, the fracture outcomes were not affected, and only minor changes in the fragility ratio and force increases were observed. These results suggest that in order to prevent femoral fractures from sideways falls, it is important to support and thus stiffen or strengthen the cortex of the femoral neck.

Another factor that influences the mechanical efficacy of the bone cement injections is the material properties of the cement. When the

properties of the HA basic ellipsoid were changed to a relatively weaker material, brushite, the fracture outcomes changed for 3 of the 5 specimens, with the femurs augmented with brushite failing at lower impact velocities. However, using the brushite ellipsoid still had improved fracture outcomes over the unaugmented femur and the femurs augmented by the implants tested in the previous study (Fung et al., 2022). These results demonstrate that for the best augmentation outcomes, it is also important to select a cement with strong tensile and compressive properties.

The results of the sensitivity test of the cement-bone interface conditions show that having no bonding between the cement and bone would decrease the peak acetabular forces by almost 17%. However, the increase of the peak acetabular forces of almost 20% relative to the unaugmented femurs shows that an augmentation with a weak cement-bone interface could still increase the load-bearing capacity of the femur.

In order to implement the cement ellipsoid in a femur, it is necessary to remove the cancellous bone occupying the space of the ellipsoid before injecting the cement. Table 2 shows that for the basic ellipsoid pattern, an average of over 50 mL of cement is required, which corresponds to an average of more than 50 mL of bone and marrow to be removed. One advantage of using ceramic-based cements instead of polymer cements such as PMMA is that these large volumes of cement could be injected without having temperature changes due to exothermic curing as a concern. Although the hollow ellipsoid provides an alternative for reducing the volume of cement without compromising the fracture outcome or mechanical strengthening effects, the pattern may be difficult to implement in practice.

Another practical consideration is the suitability of the cements for femoral augmentation. Although the two cements tested in this study have appropriate mechanical properties, both have shortfalls in either the injectability or the resorbability of the cement. Hydroxyapatite has a relatively slow resorption rate but is not injectable, while brushite is injectable but resorbs in 24 weeks (Charrière et al., 2001; Oberle et al., 2005). Although non-resorbable cements such as calcium aluminium phosphate are currently used in biomedical applications (Medri et al., 2011), the material properties are not well-described in the literature. Thus, further investigation into the development of fully non-resorbable ceramic-based cements with the appropriate mechanical properties would be recommended.

The present study has the limitation of having only one female specimen due to the fracture outcomes of the original validation study with the full set of specimens (Fleps et al., 2019a). Future studies should include more female specimens due to the higher likelihood of femoral fractures in females (Schuit et al., 2004; Haleem et al., 2008). Additionally, there is the limitation of a low overall number of specimens. It is possible that there are femurs that are not represented in this study in which it is very difficult to prevent fractures. Nevertheless, the results show that even in those cases, the load bearing capacity of the femurs will be improved with the augmentation, and the fragility ratio will be decreased, which shows that the femur is strengthened by the augmentation. Limitations of the FEMs are described in another study (Fleps et al., 2019b). They include the lack of an upper body, and homogeneity of the soft tissue, and the rigid attachment of masses in the leg assembly. An assumption that was made in the present study was the full osseointegration between the cement and the bone. This assumption was made because both HA and brushite cement have been shown to have good osseointegration,

which provides instantaneous strength to the bone (Schliephake et al., 1991; Tamimi et al., 2009). Another limitation is the lack of experimental validation data for specimens augmented with cement tested using the novel fall simulator that the FEM is based on. Therefore, it is important that this study is followed up with an experimental validation study.

5 Conclusion

In summary, we found that a hydroxyapatite bone cement ellipsoid in contact with the endosteal side of the femoral neck cortex was able to prevent femoral fractures in finite element models of five cadaveric specimens for up to two standard deviations above the mean impact speed (Choi et al., 2015). The augmentation increased the peak forces supported by the femurs and decreased the fragility ratios. Changing the cement to a weaker material, brushite, reduced the impact speed at which the first femoral fracture appeared, but was still effective at preventing some femoral fractures. Making the ellipsoid hollow had no effect on the fracture outcomes, but reducing the size of the ellipsoid to remove contact with the cortex decreased the effectiveness of the augmentation. The results suggest that ceramic-based cements could be a viable option for prophylactic femoral augmentation for hip fracture prevention. Experimental validation of the augmented femur FEMs and further development of the cements and surgical techniques are recommended to optimize the treatment.

Data availability statement

The raw data supporting the conclusion of this article will be made available by the authors, without undue reservation.

Author contributions

AF, IF, and BH contributed to conception and design of the study. AF carried out the study, performed the analysis, and wrote the first draft of the manuscript. BH, PC, PG, and SF provided supervision of the project. BH acquired funding for the project. All authors contributed to the manuscript revision, read, and approved the submitted version.

Funding

Conflict of interest

The authors declare that the research was conducted in the absence of any commercial or financial relationships that could be construed as a potential conflict of interest.

Publisher's note

All claims expressed in this article are solely those of the authors and do not necessarily represent those of their affiliated organizations, or those of the publisher, the editors and the reviewers. Any product that may be evaluated in this article, or claim that may be made by its manufacturer, is not guaranteed or endorsed by the publisher.

References

Basafa, E., Murphy, R. J., Otake, Y., Kutzer, M. D., Belkoff, S. M., Mears, S. C., et al. (2015). Subject-specific planning of femoroplasty: An experimental verification study. *J. Biomech.* 48, 59–64. doi:10.1016/j.jbiomech.2014.11.002

Beckmann, J., Ferguson, S. J., Gebauer, M., Luering, C., Gasser, B., and Heini, P. (2007). Femoroplasty - augmentation of the proximal femur with a composite bone cement-feasibility, biomechanical properties and osteosynthesis potential. *Med. Eng. Phys.* 29, 755–764. doi:10.1016/j.medengphy.2006.08.006

Beckmann, J., Springorum, R., Vettorazzi, E., Bachmeier, S., Lüring, C., Tingart, M., et al. (2011). Fracture prevention by femoroplasty-cement augmentation of the proximal femur. *J. Orthop. Res.* 29, 1753–1758. doi:10.1002/jor.21410

Body, J. J., Bergmann, P., Boonen, S., Boutsen, Y., Bruyere, O., Devogelaer, J. P., et al. (2011). Non-pharmacological management of osteoporosis: A consensus of the Belgian bone club. *Osteoporos. Int.* 22, 2769–2788. doi:10.1007/s00198-011-1545-x

Charrière, E., Terrazzoni, S., Pittet, C., Mordasini, P., Dutoit, M., Lemaître, J., et al. (2001). Mechanical characterization of brushite and hydroxyapatite cements. *Biomaterials* 22, 2937–2945. doi:10.1016/S0142-9612(01)00041-2

Choi, W. J., Wakeling, J. M., and Robinovitch, S. N. (2015). Kinematic analysis of video-captured falls experienced by older adults in long-term care. *J. Biomech.* 48, 911–920. doi:10.1016/j.jbiomech.2015.02.025

de Bakker, P. M., Manske, S. L., Ebacher, V., Oxland, T. R., Cripton, P. A., and Guy, P. (2009). During sideways falls proximal femur fractures initiate in the superolateral cortex: Evidence from high-speed video of simulated fractures. *J. Biomech.* 42, 1917–1925. doi:10.1016/j.jbiomech.2009.05.001

Draenert, M., Draenert, A., and Draenert, K. (2013). Osseointegration of hydroxyapatite and remodeling-resorption of tricalciumphosphate ceramics. *Microsc. Res. Tech.* 76, 370–380. doi:10.1002/jemt.22176

Ekström, W., Miedel, R., Ponzer, S., Hedström, M., Samnegård, E., and Tidermark, J. (2009). Quality of life after a stable trochanteric fracture-A prospective cohort study on 148 patients. *J. Orthop. Trauma* 23, 39–44. doi:10.1097/BOT.0b013e318191f5e4

Enns-Bray, W. S., Bahaloo, H., Fleps, I., Ariza, O., Gilchrist, S., Widmer, R., et al. (2018). Material mapping strategy to improve the predicted response of the proximal femur to a sideways fall impact. *J. Mech. Behav. Biomed. Mater.* 78, 196–205. doi:10.1016/j.jmbbm.2017.10.033

Enns-Bray, W. S., Bahaloo, H., Fleps, I., Pauchard, Y., Taghizadeh, E., Sigurdsson, S., et al. (2019). Biofidelic finite element models for accurately classifying hip fracture in a retrospective clinical study of elderly women from the AGES Reykjavik cohort. *Bone* 120, 25–37. doi:10.1016/j.bone.2018.09.014

Fierens, J., and Broos, P. L. O. (2006). Quality of life after hip fracture surgery in the elderly. *Acta Chir. belg.* 106, 393–396. doi:10.1080/00015458.2006.11679913

Fleps, I., Enns-Bray, W. S., Guy, P., Ferguson, S. J., Cripton, P. A., and Helgason, B. (2018a). On the internal reaction forces, energy absorption, and fracture in the hip during simulated sideways fall impact. *PLoS One* 13, 02009522–e201018. doi:10.1371/journal.pone.0200952

Fleps, I., Fung, A., Guy, P., Ferguson, S. J., Helgason, B., and Cripton, P. A. (2019a). Subject-specific *ex vivo* simulations for hip fracture risk assessment in sideways falls. *Bone* 125, 36–45. doi:10.1016/j.bone.2019.05.004

Fleps, I., Guy, P., Ferguson, S. J., Cripton, P. A., and Helgason, B. (2019b). Explicit finite element models accurately predict subject-specific and velocity-dependent kinetics of sideways fall impact. *J. Bone Min. Res.* 34, 1837–1850. doi:10.1002/jbmr.3804

Fleps, I., Vuille, M., Melnyk, A., Ferguson, S. J., Guy, P., Helgason, B., et al. (2018b). A novel sideways fall simulator to study hip fractures *ex vivo*. *PLoS One* 13, 02010966–e201115. doi:10.1371/journal.pone.0201096

Fliri, L., Sermon, A., Wähnert, D., Schmoelz, W., Blauth, M., and Windolf, M. (2013). Limited V-shaped cement augmentation of the proximal femur to prevent secondary hip fractures. *J. Biomater. Appl.* 28, 136–143. doi:10.1177/0885328212443274

Fung, A., Fleps, I., Cripton, P. A., Guy, P., Ferguson, S. J., and Helgason, B. (2022). Prophylactic augmentation implants in the proximal femur for hip fracture prevention: An *in silico* investigation of simulated sideways fall impacts. *J. Mech. Behav. Biomed. Mater.* 126, 104957–105016. doi:10.1016/j.jmbbm.2021.104957

Grassi, L., Fleps, I., Sahlstedt, H., Väänänen, S. P., Ferguson, S. J., Isaksson, H., et al. (2021). Validation of 3D finite element models from simulated DXA images for biofidelic simulations of sideways fall impact to the hip. *Bone* 142, 115678. doi:10.1016/j.bone.2020.115678

Guy, P., Sobolev, B., Sheehan, K. J., Kuramoto, L., and Lefaivre, K. A. (2017). The burden of second hip fractures: Provincial surgical hospitalizations over 15 years. *Can. J. Surg.* 60, 101–107. doi:10.1503/cjs.008616

Haleem, S., Lutchman, L., Mayahi, R., Grice, J. E., and Parker, M. J. (2008). Mortality following hip fracture: Trends and geographical variations over the last 40 years. *Injury* 39, 1157–1163. doi:10.1016/j.injury.2008.03.022

Hayes, W. C., Myers, E. R., Robinovitch, S. N., Van Den Kroonenberg, A., Courtney, A. C., and McMahon, T. A. (1996). Etiology and prevention of age-related hip fractures. *Bone* 18, S77–S86. doi:10.1016/8756-3282(95)00383-5

Heini, P. F., Franz, T., Fankhauser, C., Gasser, B., and Ganz, R. (2004). Femoroplasty-augmentation of mechanical properties in the osteoporotic proximal femur: A biomechanical investigation of PMMA reinforcement in cadaver bones. *Clin. Biomech.* 19, 506–512. doi:10.1016/j.clinbiomech.2004.01.014

Hernlund, E., Svedbom, A., Ivergård, M., Compston, J., Cooper, C., Stenmark, J., et al. (2013). Osteoporosis in the European union: Medical management, epidemiology and economic burden: A report prepared in collaboration with the international osteoporosis foundation (IOF) and the European federation of pharmaceutical industry associations (efpia). *Arch. Osteoporos.* 8, 136. doi:10.1007/s11657-013-0136-1

Howe, J. G., Hill, R. S., Stroncek, J. D., Shaul, J. L., Favell, D., Cheng, R. R., et al. (2019). Treatment of bone loss in proximal femurs of postmenopausal osteoporotic women with AGN1 local osteo-enhancement procedure (LOEP) increases hip bone mineral density and hip strength: A long-term prospective cohort study. *Osteoporos. Int.* 31, 921–929. doi:10.1007/s00198-019-05230-0

Jansen, J., Ooms, E., Verdonschot, N., and Wolke, J. (2005). Injectable calcium phosphate cement for bone repair and implant fixation. *Orthop. Clin. North Am.* 36, 89–95. doi:10.1016/j.ocl.2004.06.014

Järvinen, T. L. N., Michaëlsson, K., Jokihaara, J., Collins, G. S., Perry, T. L., Mintzes, B., et al. (2015). Overdiagnosis of bone fragility in the quest to prevent hip fracture warrant our current approach. *BMJ* 350, 1–7. doi:10.1136/bmj.h2088

Kok, J., Širka, A., Grassi, L., Raina, D. B., Tarasevičius, Š., Tägil, M., et al. (2019). Fracture strength of the proximal femur injected with a calcium sulfate/hydroxyapatite bone substitute. *Clin. Biomech.* 63, 172–178. doi:10.1016/j.clinbiomech.2019.03.008

Laing, A. C., and Robinovitch, S. N. (2010). Characterizing the effective stiffness of the pelvis during sideways falls on the hip. *J. Biomech.* 43, 1898–1904. doi:10.1016/j.jbiomech.2010.03.025

Lewin, S., Fleps, I., Neuhaus, D., Öhman-Mägi, C., Ferguson, S. J., Persson, C., et al. (2020). Implicit and explicit finite element models predict the mechanical response of calcium phosphate-titanium cranial implantsfinite element models predict the mechanical response of calcium phosphate-titanium cranial implants. *J. Mech. Behav. Biomed. Mater.* 112, 104085–104110. doi:10.1016/j.jmbbm.2020.104085

Marottoli, R. A., Berkman, L. F., and Cooney, L. M. (1992). Decline in physical function following hip fracture. *J. Am. Geriatr. Soc.* 40, 861–866. doi:10.1111/j.1532-5415.1992.tb01980.x

Medri, V., Mazzocchi, M., and Bellosi, A. (2011). Doped calcium-aluminium-phosphate cements for biomedical applications. *J. Mater. Sci. Mater. Med.* 22, 229–236. doi:10.1007/s10856-010-4205-3

Nachreiner, N. M., Findorff, M. J., Wyman, J. F., and McCarthy, T. C. (2007). Circumstances and consequences of falls in community-dwelling older women. *J. Women's Heal* 16, 1437–1446. doi:10.1089/jwh.2006.0245

Nevitt, M. C., Cummings, S. R., Kidd, S., and Black, D. (1989). Risk factors for recurrent nonsyncopal falls: A prospective study. *JAMA J. Am. Med. Assoc.* 261, 2663–2668. doi:10.1001/jama.1989.03420180087036

Oberle, A., Theiss, F., Bohner, M., Müller, J., Kästner, S. B., Frei, C., et al. (2005). Untersuchungen über den klinischen Einsatz von Brushite-und Hydroxylapatit-Zement beim Schaf. *Schweiz. Arch. Tierheilkd.* 147, 482–490. doi:10.1024/0036-7281.147.11.482

Parkkari, J., Kannus, P., Palvanen, M., Natri, A., Vainio, J., Aho, H., et al. (1999). Majority of hip fractures occur as a result of a fall and impact on the greater trochanter of the femur: A prospective controlled hip fracture study with 206 consecutive patients. *Calcif. Tissue Int.* 65, 183–187. doi:10.1007/s002239900679

Robinovitch, S. N., McMahon, T. A., and Hayes, W. C. (1995). Force attenuation in trochanteric soft tissues during impact from a fall. *J. Orthop. Res.* 13, 956–962. doi:10.1002/jor.1100130621

Schliephake, H., Neukam, F. W., and Klosa, D. (1991). Influence of pore dimensions on bone ingrowth into porous hydroxylapatite blocks used as bone graft substitutes. *Int. J. Oral Maxillofac. Surg.* 20, 53–58. doi:10.1016/S0901-5027(05)80698-8

Schuit, S. C. E., Van Der Klift, M., Weel, A. E. A. M., De Laet, C. E. D. H., Burger, H., Seeman, E., et al. (2004). Fracture incidence and association with bone mineral density in elderly men and women: The Rotterdam Study. *Bone* 34, 195–202. doi:10.1016/j.bone.2003.10.001

Sobolev, B., Sheehan, K. J., Kuramoto, L., and Guy, P. (2015). Risk of second hip fracture persists for years after initial trauma. *Bone* 75, 72–76. doi:10.1016/j.bone.2015.02.003

Stroncek, J. D., Shaul, J. L., Favell, D., Hill, R. S., Huber, B. M., Howe, J. G., et al. (2019). *In vitro* injection of osteoporotic cadaveric femurs with a triphasic calcium-based implant confers immediate biomechanical integrity. *J. Orthop. Res.* 37, 908–915. doi:10.1002/jor.24239

Sutter, E. G., Mears, S. C., and Belkoff, S. M. (2010a). A biomechanical evaluation of femoroplasty under simulated fall conditions. *J. Orthop. Trauma* 24, 95–99. doi:10.1097/BOT.0b013e3181b5c0c6

Sutter, E. G., Wall, S. J., Mears, S. C., and Belkoff, S. M. (2010b). The effect of cement placement on augmentation of the osteoporotic proximal femur. *Geriatr. Orthop. Surg. Rehabil.* 1, 22–26. doi:10.1177/2151458510378406

Tamimi, F., Torres, J., Lopez-Cabarcos, E., Bassett, D. C., Habibovic, P., Luceron, E., et al. (2009). Minimally invasive maxillofacial vertical bone augmentation using brushite based cements. *Biomaterials* 30, 208–216. doi:10.1016/j.biomaterials.2008.09.032

Frontiers in Bioengineering and Biotechnology

*CORRESPONDENCE
Richard J. van Arkel,
✉ r.vanarkel@imperial.ac.uk

†PRESENT ADDRESS
Nupur Kohli,
Biomedical Engineering Department,
Khalifa University, Abu Dhabi, United Arab
Emirates

‡These authors contributed equally to the
article and share first authorship

Bioreactor analyses of tissue ingrowth, ongrowth and remodelling around implants: An alternative to live animal testing

Nupur Kohli[1†‡], Konstantinos Theodoridis[1‡], Thomas A. G. Hall[1], Inigo Sanz-Pena[1], David C. A. Gaboriau[2] and Richard J. van Arkel[1*]

[1]Biomechanics Group, Department of Mechanical Engineering, Imperial College London, London, United Kingdom, [2]FILM, National Heart & Lung Institute, Imperial College London, London, United Kingdom

Introduction: Preclinical assessment of bone remodelling onto, into or around novel implant technologies is underpinned by a large live animal testing burden. The aim of this study was to explore whether a lab-based bioreactor model could provide similar insight.

Method: Twelve *ex vivo* trabecular bone cylinders were extracted from porcine femora and were implanted with additively manufactured stochastic porous titanium implants. Half were cultured dynamically, in a bioreactor with continuous fluid flow and daily cyclic loading, and half in static well plates. Tissue ongrowth, ingrowth and remodelling around the implants were evaluated with imaging and mechanical testing.

Results: For both culture conditions, scanning electron microscopy (SEM) revealed bone ongrowth; widefield, backscatter SEM, micro computed tomography scanning, and histology revealed mineralisation inside the implant pores; and histology revealed woven bone formation and bone resorption around the implant. The imaging evidence of this tissue ongrowth, ingrowth and remodelling around the implant was greater for the dynamically cultured samples, and the mechanical testing revealed that the dynamically cultured samples had approximately three times greater push-through fixation strength ($p < 0.05$).

Discussion: *Ex vivo* bone models enable the analysis of tissue remodelling onto, into and around porous implants in the lab. While static culture conditions exhibited some characteristics of bony adaptation to implantation, simulating physiological conditions with a bioreactor led to an accelerated response.

1 Introduction

Secure implant fixation in bone is necessary for a successful outcome for a wide range of surgical procedures, including arthroplasty, spine fusion, fracture fixation, and dental implants, impacting millions of patients worldwide each year (Pabinger et al., 2015; Abbott et al., 2017; Pabinger et al., 2018; Borgström et al., 2020). The field is rife with
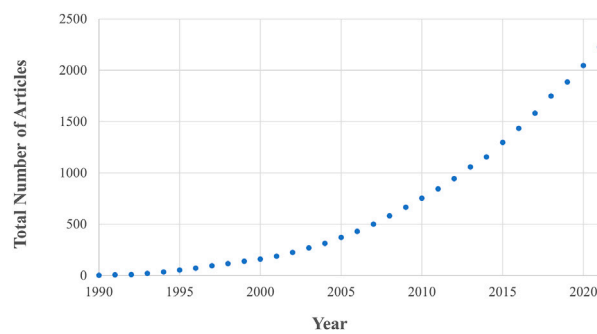
FIGURE 1
The number of *in vivo* animal studies published in the field of implant fixation as a function of publication year. Both the total number of articles and rate of publication is increasing. These data are the result of a Web of Science database search (17th August 2022) for: implant AND {fixation OR cementless OR osseointegration OR osteointegration OR [bone AND ("in-growth" OR "ingrowth" OR "in growth" OR "ongrowth" OR "on-growth" OR "on growth")]} AND (porcine OR pig OR ovine OR sheep OR murine OR mouse OR mice OR rat OR bovine OR cow OR canine OR dog OR equine OR horse OR animal) AND ("*in vivo*" OR "*in-vivo*") NOT review.

innovation, including new implant technologies such as additively manufactured porous structures (Brogini et al., 2021; Munford et al., 2022) nano coatings (Bai et al., 2021) and biophysical stimulation (Soares dos Santos et al., 2016; de Sousa et al., 2021), as well as novel approaches to design (van Arkel et al., 2018; Wang et al., 2021) and innovation in surgical technique (Doyle et al., 2019; Doyle et al., 2020).

Fundamental to the success of new implant fixation technology is whether it drives favourable bone remodelling into, onto and around the implant. This remodelling process is driven by the interactions of three bone cell types, osteoblast, osteoclasts, and osteocytes, and is affected by the mechanical loading environment in addition to implant, patient, and surgical factors (Kohli et al., 2018). This complex interaction between different cell types, bone morphology and loading means that preclinical testing of new technology relies of on live animal testing. *In vivo* animal research has rapidly gained traction since the 1990s and is now considered a gold standard in the field, leading to an ever-increasing animal burden. Currently, ~200 articles are published every year in the field of implant fixation alone (Figure 1) with >60 animals experimented on per paper (Öztürk and Ersan, 2020).

Ex vivo models of implant fixation could be a route to reduce this burden: many consider this to be replacement as the 3Rs principle (Replacement-Reduction-Refinement) is associated with live animal research. But even if not considered replacement, the approach still contributes greatly to reduction and refinement by enabling multiple samples to be obtained for each animal sacrificed, reuse of material that might otherwise be wasted, and by refining the protocol to eliminate all experimentation on the animal while it is living. There is even scope to use human tissue by utilising waste from routine surgical procedures, such as femoral heads resected during hip arthroplasty (Swarup et al., 2018; Styczynska-Soczka et al., 2021).

Early research has demonstrated that *ex vivo* bone can grow and adapt to mechanical loading in a bioreactor setup (Jones et al., 2003; Davies et al., 2006; David et al., 2008; Vivanco et al., 2013; Birmingham et al., 2015; Birmingham et al., 2016). More recent research has demonstrated material and cell transfer to an implant surface (Dua et al., 2021; Zankovic et al., 2021) and that is possible to maintain viability in samples as large as human femoral heads (Swarup et al., 2018; Styczynska-Soczka et al., 2021), but it is still not clear if the *ex vivo* bone can be used to explore the early stages of implant bone ingrowth into porous implants. Nor is it clear if the full remodelling pathways of bone are active. For example, osteoclasts survive for ~2 weeks (Owen and Reilly, 2018), and so if new cells do not differentiate, one would expect a bias for growth driven by osteoblast activity in experiments lasting 3 weeks or more. Given that bone growth is considered the favourable outcome for new technologies, a meaningful preclinical test must also allow for the possibility of bone resorption.

The aim of this research is to analyse whether *ex vivo* bone models can be used to assess bone remodelling into, onto and around new implant fixation technology. Porous stochastic titanium scaffolds were used as an example implant technology given the large research interest in these structures for arthroplasty implants (Ghouse et al., 2019; Reznikov et al., 2019; Dion et al., 2020; Brogini et al., 2021; Munford et al., 2022), and two culture conditions were explored to understand the effects of research design on *ex vivo* bone remodelling and implant bony ingrowth.

2 Materials and methods

2.1 Bone sample preparation

The research was registered annually in accordance with the host institution's policy for use of animals in research, with all tissue sourced as a waste product from pigs that were sacrificed for unrelated reasons. Twelve femoral trabecular bone cores were obtained from healthy large white pigs (~70 kg, Royal Veterinary College, UK), within 4h *post-mortem*. Briefly, hind limbs were transported on ice to the lab immediately following sacrifice. The limbs were transected at the mid-femur and mid-tibia and dissected free of soft tissue while preserving the knee capsule. The knee was moved into a sterile hood and placed in a container filled with 70% ethanol for 15 min, followed by a wash in
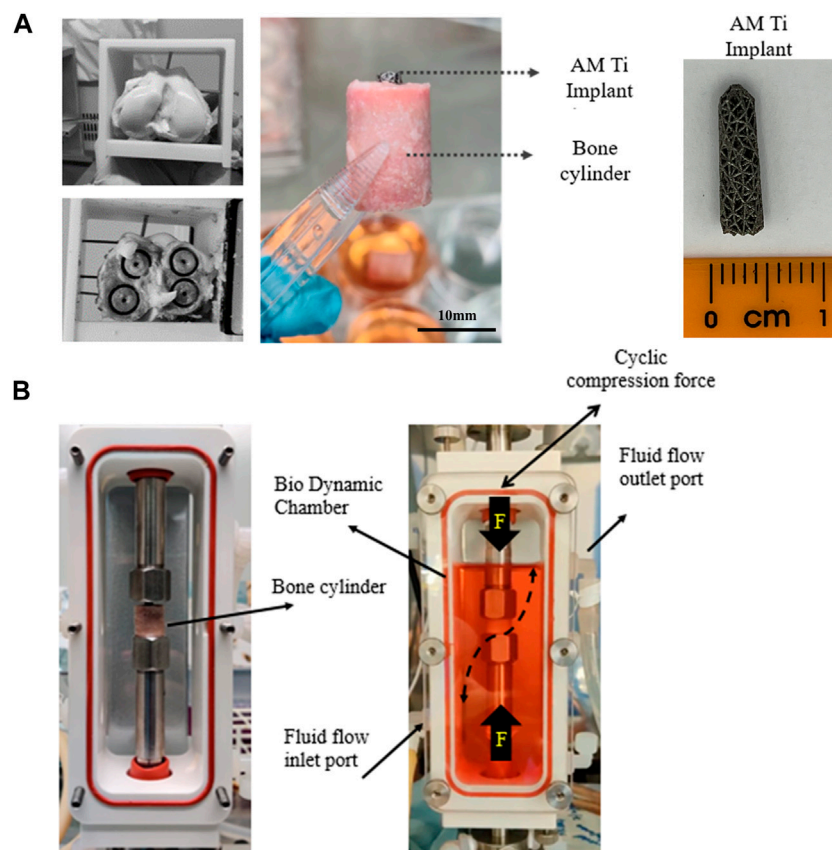
FIGURE 2
(A) Extraction of 4 trabecular bone cores from porcine femoral condyles and preparation for implantation with a tapered porous titanium peg. **(B)** For dynamic culture, the implanted bone cores were fixed within the biodynamic chamber of the bioreactor.

Dulbecco's Phosphate-Buffered Saline (1x DPBS, Thermo Fisher Scientific, United States) containing 5% antimicrobial solution (Penicillin-Streptomycin-Amphotericin B, MP Biomedicals, Gibco™, Thermo Fisher Scientific, United States) for 5 min. The knee capsule was dissected, and the distal femur resected with a sagittal saw to expose the trabecular bone, guided by an autoclaved cutting guide, akin to the distal femoral resection in total knee arthroplasty. A second guided cut was made 16 mm proximal to the first. Bone cylinders (Ø12 mm, height 16 mm, Figure 2A) were then extracted with a diamond hole saw followed by a Ø2.5 mm centred drill to insert the implants and placed in 50 mL tubes containing PBS with 1% antimicrobial solution. All procedures were done at low speed/rpm with constant irrigation of cold sterile phosphate buffered saline (PBS) to reduce heat generation during cutting.

2.2 Implant design and insertion

Tapered stochastic porous titanium implants of base Ø3 mm, taper angle 1.7° and length 13 mm (Figure 2A) were additively manufactured from commercially pure titanium powder (ASTM B348 Grade 2 spherical powder, Ø15-45 µm, Carpenter Additive, United States) using a powder bed fusion

system (AM250, Renishaw, UK). The layer thickness was set to 50 µm and laser parameters were controlled in accordance with previous research (Ghouse et al., 2017; van Arkel et al., 2018), which characterized the properties of the stochastic porous structure used: apparent modulus 600 MPa, yield strength 8 MPa and 90% porosity (van Arkel et al., 2018). The implants were removed from the substrate, rinsed, cleaned ultrasonically, autoclave sterilised, and then press fitted into to the centre-drilled holes of the bone cylinders, leaving ~2 mm of the top of the implant exposed. The implanted cylinders were transferred into 6-well tissue culture plates containing 10 mL of pre-warmed (37°C) culture medium, consisting of Dulbecco's Modified Eagle's Medium (DMEM/F-12, HEPES, Gibco™, Thermo Fisher Scientific, United States), 10% Fetal Bovine Serum (FBS, Gibco™, Thermo Fisher Scientific, United States) and 1% antimicrobial solution. The bone cylinders were incubated overnight (37°C, 21% O_2, and 5% CO_2) prior to bioreactor setup.

2.3 Culture conditions

The implanted bone cylinders were divided into static (n = 6) and dynamic (n = 6) groups; the former used as controls.

2.3.1 Static culture

Static samples were placed in a 6-well plate with fresh culture medium and cultured for 21 days. The media were changed at least every 3 days. To assess mineralising bone surfaces, fluorochrome labels were added to the media on day 7 (Calcein, Sigma-Aldrich) and 14 (Alizarin Red, Sigma-Aldrich), both at a concentration of 50 μg/mL and replaced with fresh media after 24 h.

2.3.2 Dynamic culture

Dynamic samples were placed within a perfusion bioreactor (Figure 2B, Electroforce Biodynamic 5100, TA Instruments, Waters, UK). Chambers were filled with 150 mL of culture medium and connected to a reservoir filled with a further 100 mL of culture medium *via* platinum-cured silicone tubing and a peristaltic pump (Masterflex, Cole-Parmer, UK). Fluid flow was induced by circulating the media at a continuous rate of 8 mL/min.

Cyclic compressive loading was applied to the exposed top of the implant to model *in vivo* loading of press-fit pegs during daily activity, e.g., for femoral (Berahmani et al., 2015) or glenoid (Geraldes et al., 2017) arthroplasty components. The resulting axial displacement of the tapered peg into the straight sided drilled hole generates both tensile hoop stress and compressive radial stress in the bone. The loading was applied by the actuator *via* the biodynamic compression platens: implants were preloaded to 5 N, and then 30 μm cyclic compressive displacement (sinusoidal wave) at 1 Hz was applied for 300 cycles/day. The magnitude of the displacement was based on the level of interfacial micromotion consistently associated with osseointegration *in vivo* (Kohli et al., 2021). The resulting force was measured with the machine's load cell and recorded. Fluorochrome labels were added on day 7 and 14 as per the static culture.

2.4 Imaging and mechanical analyses

Post culture, static, and dynamic bone cores were washed with PBS, sliced with a thickness of ~4 mm below the top surface of the bone using a low-speed cutting saw (IsoMet 1000, Buehler, Lake Bluff, IL, US), and fixed in 10% neutral buffered formalin for 24 h. Once fixed, the samples were washed again with PBS and kept in the dark for further analysis. The bulk of the samples (cylinders of ~12 mm height) were used for different imaging analyses and the tops for destructive mechanical testing.

For the imaging analyses, n = 3 dynamic and n = 3 static samples were imaged as cylinders, and 3 of each were resin embedded and sectioned. The latter was achieved by dehydrating samples in graded methylated spirits (50%, 75%, 85%, 95%, and 2% × 100%). Dehydrated samples were immersed in chloroform for 24 h, and then chloroform was switched to methyl methacrylate resin (LR White) for a further 72 h. After resin saturation, an accelerator was added to polymerize and block the specimens at −20°C. The polymethyl methacrylate blocks were sectioned parallel to the axis of the cylindrical implant, using a water-cooled bandsaw (Model 311, Exakt, Ger.). Sections were grinded (Model 400 CS, Exakt, Ger.) and polished to a final thickness of 50 μm/slice. Some of the slices remained unstained for fluorescent imaging, and the rest were further processed for histology.

2.4.1 Widefield fluorescence microscopy

The top surface of the bone cylinder was scanned with a ×5 objective (Axio Observer, ZEISS, Oberkochen, Ger.) using a tile and stitching method (ZEN Pro, ZEISS, Oberkochen, Ger.) (Figure 3A). Wavelengths of $\lambda_{ex}495/\lambda_{em}515$ and $\lambda_{ex}545/\lambda_{em}580$ were set for calcein and alizarin red, respectively.

Bone remodelling activity around the implant was first quantified by measuring calcein fluorescent intensity on the top surface of the cylindrical samples as a measure of total mineral accumulation. We used Fiji/ImageJ (National Institutes of Health (NIH), United States) to calculate the mean intensity in three zones: the full cross-section (zone 1), the outer ring of the bone cores that were damaged during cutting (zone 2) and most exposed to the fluid flow, and an inner ring immediately adjacent to the implant (zone 3) (Figure 3B). Bone labelling found within the porous implant was excluded from this analysis of bone adaptation by designing a circular mask centred on the implant hole and removing all stained areas within that circle.

The top surfaces of the cylindrical samples were also used to measure the mineralizing surface (MS) as a percentage of the bone surface (BS) in regions where both fluorochrome stains were detected. Stained surfaces were annotated in QuPath (Bankhead et al., 2017), and the day 7 surface was divided from the day 14 surface (Figure 4BI).

Unstained resin-embedded sections were also analysed with fluorescent microscopy. From each section, bone labelling was quantified. The mineral apposition rate (μm/day) was evaluated on the sides of the bone cylinder by finding the mean distance between both labels (Figure 4B. III) divided by 7 (the time interval between the administration).

2.4.2 Scanning electron microscopy

Morphology distribution of new bone tissue formation was observed by visualizing the surface of explanted porous implants with Scanning Electron Microscopy (SEM). Samples were fixed with 4% v/v glutaraldehyde, rinsed with PBS, and then dehydrated in increasing concentrations of ethanol series (30%–100% v/v). The samples were dried, sputter coated with a 15 nm layer of chromium, and observed under SEM-EDS (Mira, TESCAN, Cz.) at an accelerating voltage of 15 kV. Resin embedded sections were also visualized under SEM to assess tissue formation and distribution within the porous architecture of the implant using the Back Scatter Electron (BSE) technique.

2.4.3 Micro-computed tomography

Samples were dehydrated in series of ethanol (25%, 50%, 75%), for 2.5 h per ethanol concentration and immersed in Phosphotungstic acid hydrate solution for 24 h to facilitate high contrast X-ray visualization. This solution comprised of 1% (w/v) Phosphotungstic acid (PTA, Sigma-Aldrich, UK), water solution (30 mL), all mixed with 70 mL absolute ethanol, to make 0.3% PTA in 70% ethanol (Metscher, 2009). Micro-CT scans (Xradia 510 Versa, ZEISS, Ger.) were acquired at a Zeiss at a voltage of 140 kV and 70 μA, without a filter and full rotation of 360°. The pixel size was set to 4.11 μm. All micro-CT scans were re-assembled as Z-stacks in Icy (De Chaumont et al., 2012). All Z-stacks were then converted for segmentation using Imaris software (Bitplane, Zurich, Switz.). The volume of the segmented tissue and titanium construct
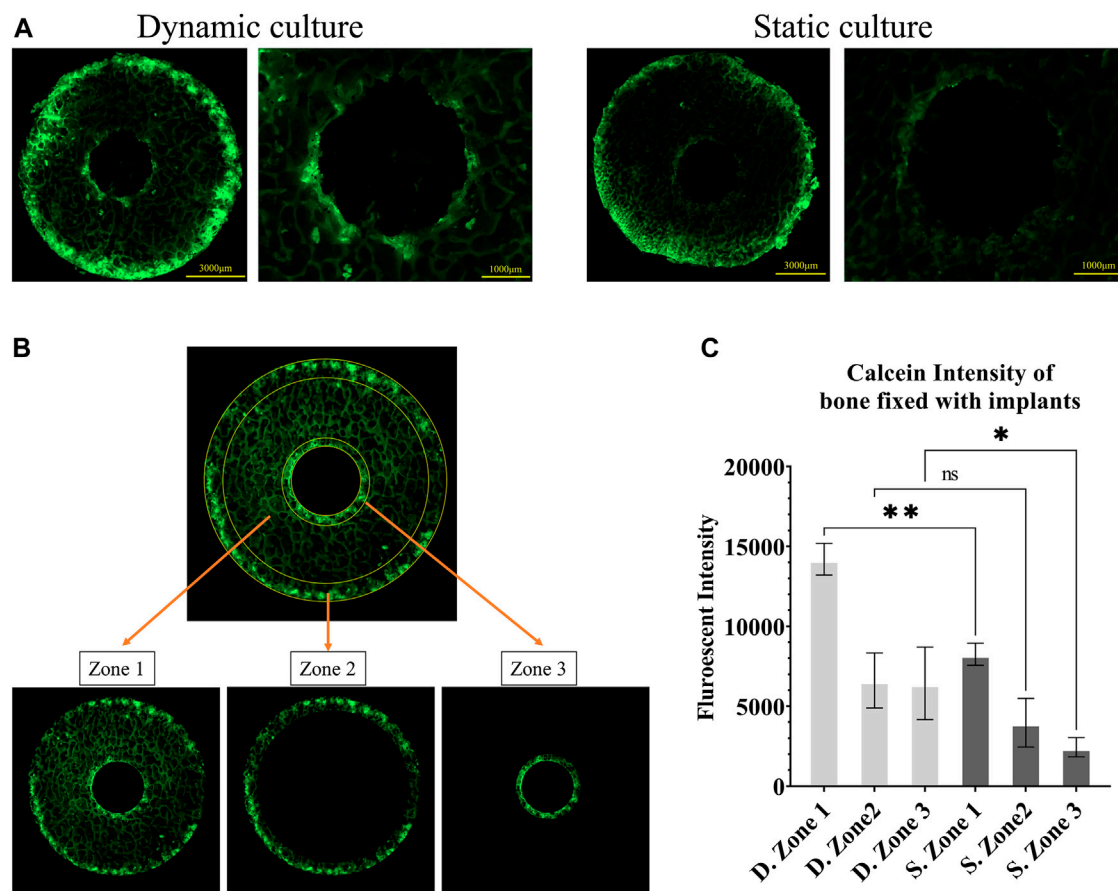
FIGURE 3
Fluorescent images of calcein administered on the seventh day **(A)** Representative images from static and dynamic cultures showing the top surfaces of the bone cylinders, assessed with widefield microscopy at λex495/λem515. **(B)** The three regions of interest that were quantitively analysed: zone 1, the whole bone cylinder, zone 2, the outer bone perimeter, and zone 3, the bone adjacent to the implant. **(C)** Analysis of calcein fluorescent intensity, showing mineralisation accumulation, comparing these 3 zones in static and dynamic culture samples. Values are means of n = 3 (±SD); *p <0.05, **p <0.01, ***p <0.001.

were calculated as to the truncated cone. Newly formed tissue was expressed as a percentage of the pore void, and 3D rendered images of the scanned specimens were created to represent the total tissue distribution.

2.4.4 Histology

Resin-embedded sections were stained with toluidine blue and paragon stain for histological analyses. The cross-sectional slides of the bone tissue and the implant were digitised at ×5 objective and stitched using the tile method of the ZEN Pro software.

2.4.5 Mechanical analysis

The characteristic loading times, T_{load}, for the cyclic loading applied in the dynamic culture were calculated in accordance with the method established by Scheiner et al. (2016):

$$T_{load} = \frac{|Q|}{|\dot{Q}|}$$

where Q is the force measured by the load cell.

Post testing, the mechanical strength of the bone-implant interface was measured with push-through testing in a material-testing machine

(Model 5565, Instron, UK). The top sections of the bone cylinders (height ~4 mm) were placed on a compression platen with a central Ø8 mm hole (Figure 8A). A top compression platen of less than Ø3 mm (smaller than the implant) was brought into contact with the exposed implant (~2 mm), before compressing the implant at a displacement rate of 1 mm/s. Force–displacement data were recorded, and the fixation strength was calculated by dividing the load at the first peak by the implant-bone contact area (a truncated cone).

2.5 Statistical analysis

GraphPad Prism software (version 9.4.0; GraphPad Software, San Diego, CA, United States) was used for the statistical analysis. Multiple comparisons between groups were performed using one-way ANOVA, followed by *post hoc* Tukey's test. Differences between means were considered statistically significant when p) < 0.05 (∗), $p < 0.01$ (∗∗), $p < 0.001$ (∗∗∗). Data were presented as mean ± SD for N = 3 biological replicates for imaging analyses and N ≥ 5 for mechanical testing.
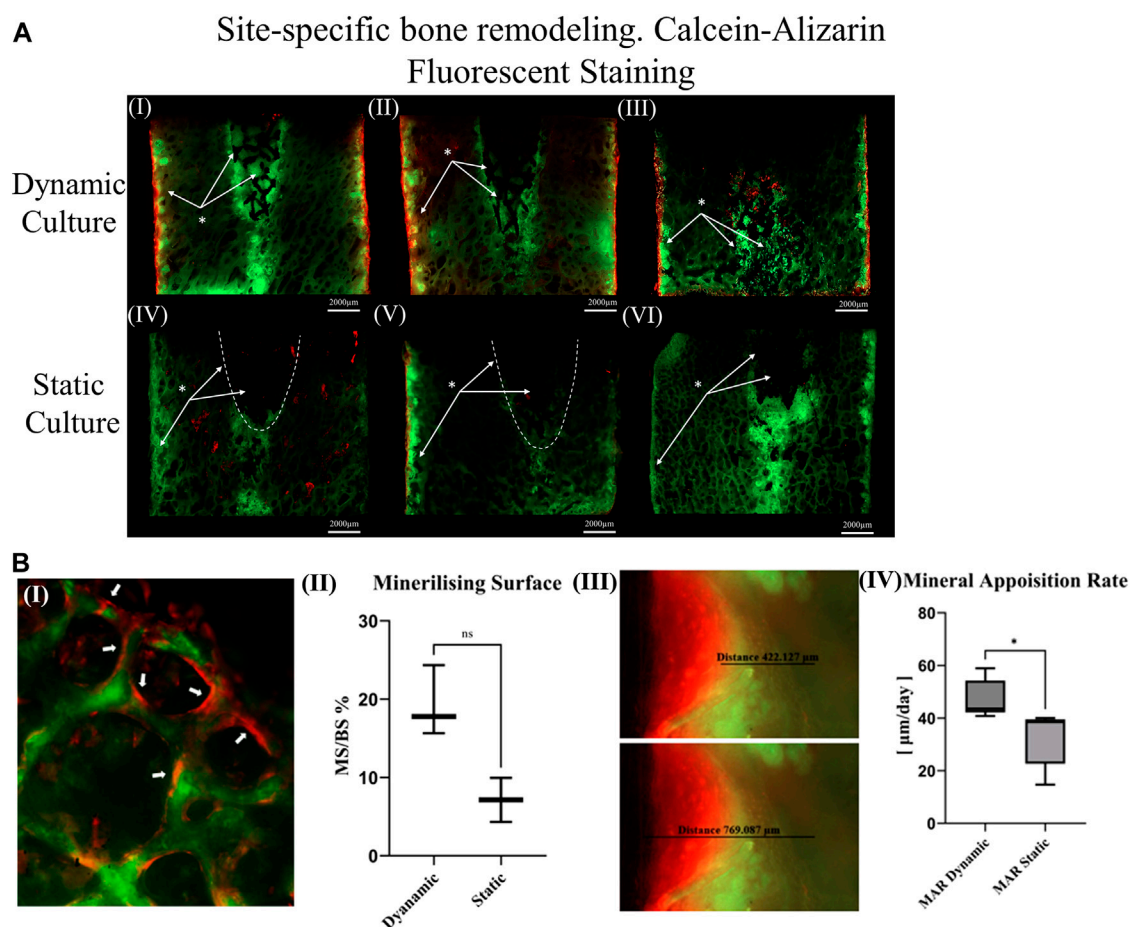
FIGURE 4
(A) Thinned sections (50 μm/slice) of the bone cylinders stained with calcein on the seventh day and Alizarin red on the 14th day for three dynamic culture replicates (I-III) and three static culture replicates (IV-VI) **(B)** Representative images from dynamic samples. (B.I) Mineralizing surfaces (MS) evaluated from the bone struts found on the outer perimeter of the bone cylinders on the top surfaces. (B.II) Measurements of the MS/BS expressed in percentage. (B.III) Mineral apposition rate found on the sides of the bone cylinders (thinned sections) and (B. IV) mean distance of both labels divided by seven expressed in μm/day. Values are means of n = 3 ($\pm$SD); *p <0.05.

3 Results

3.1 Bone formation labelling—widefield analysis

Calcium mineralisation was detected when assessing the top surfaces of the cylindrical samples. Day 7 fluorochrome intensity was affected by the culture conditions (Figures 3A, B). Mean intensity across the full cross section was 172% greater for the dynamic samples compared to the static controls (p = 0.003, Figure 3C). When examining only the bone adjacent to the implant, the intensity was found to be 264% greater for the dynamic samples (p = 0.045, Figure 3C). Additionally, mineralised surfaces, stained with Alizarin red after 14 days of culture, were observed on the outer edges of the bone cylinders. Increased mineralised surface at the circumference of top surfaces for the dynamic samples was observed but did not reach statistical significance (p = 0.055, Figure 4B. I, II).

Sectioned images revealed calcium deposits within the porous implants for dynamically cultured samples, with less stain found within statically cultured implants (Figure 4A). Some calcium deposits were also observed in the intact bone below the implant's push-in direction for both culture conditions. Mineralised surfaces stained with Alizarin red after 14 days of culture, were only observed to the outer edges of the bone cylinders and not inside the porous implants, consistent with the observations made from the cylindrical images. Analysis of these mineralising surfaces in the sectioned surfaces revelated that mineral apposition rate was 45% greater for the dynamic samples (p < 0.05).

3.2 Macroscopic characteristics and bone ongrowth—SEM analysis

Images from the thinned cross-sectional slides of dynamic samples revealed the most backscatter signal within the implant's
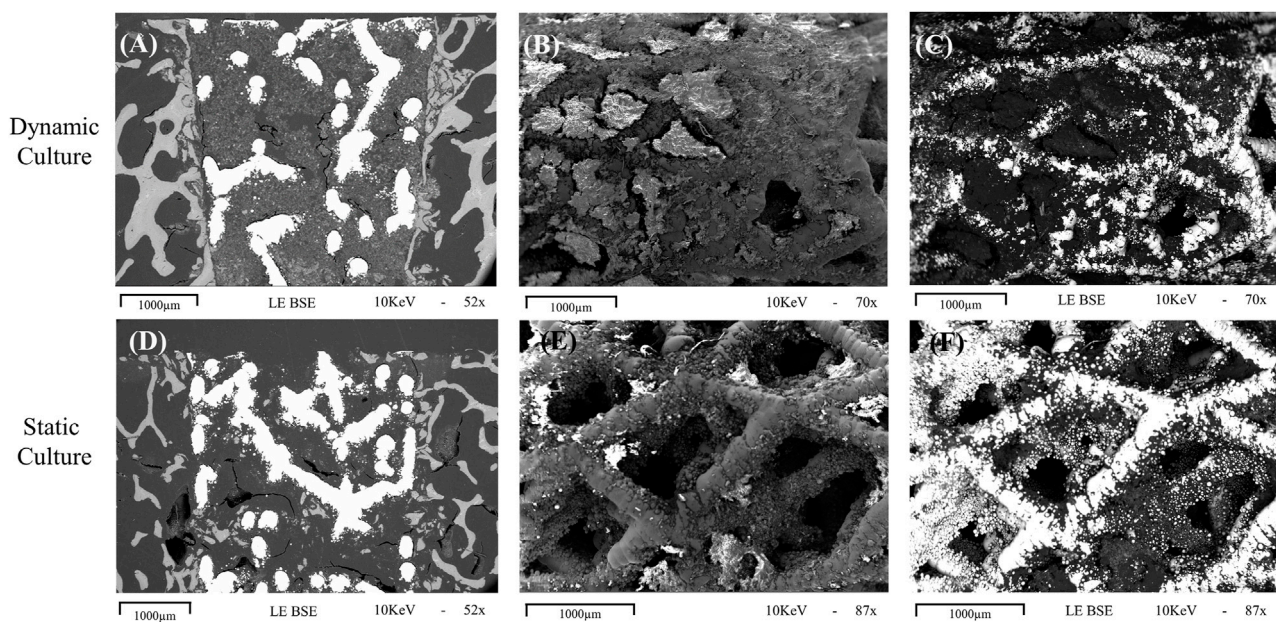
FIGURE 5
Representative images obtained with scanning electron microscopy for dynamic (top row, **(A-C)** and static (bottom row, **D-F**) cultures **(A, D)** Cross sections of the implant *in situ*, taken with the BSE technique showing evidence of mineralisation within the implant pores, with more seen in the sample taken from dynamic culture. **(B, C)** macroscopic images taken with standard and BSE methods, respectively, showing the outer cylindrical surface of an explanted implant with abundant tissue formation on the surface and within the pores. **(E, F)** standard and BSE images of the outer surface of an explanted statically cultured implant also showing tissue formation on the surface, albeit less than that seen for the dynamic culture. 1000 µm scalebars are shown.
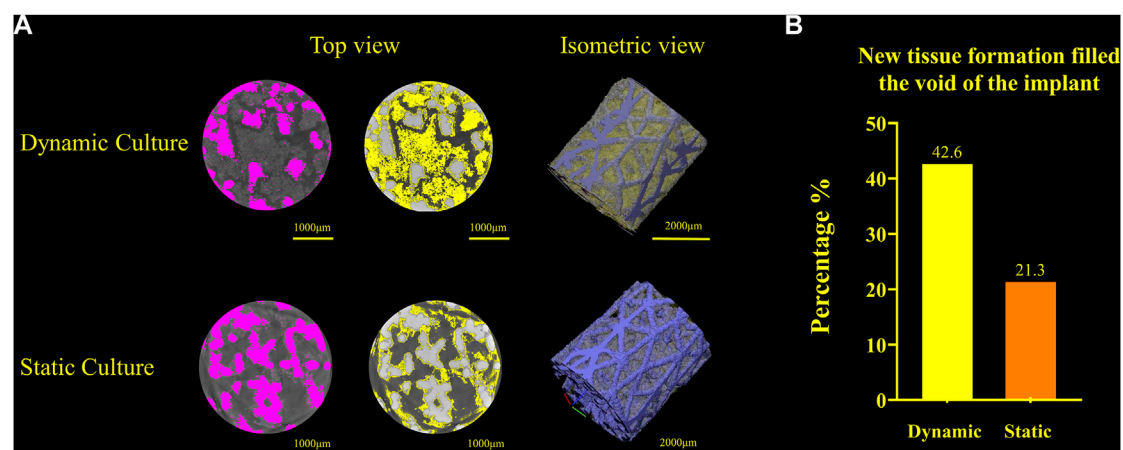
FIGURE 6
(A) Titanium implant micro-CT scans and 3D volume renderings for the dynamic culture (top) and the static culture (bottom) showing the segmented implant (pink, left), tissue (yellow, middle) and 3D render (titanium blue, tissue yellow, right). **(B)** Twice as much tissue volume, as a percentage of the void space, was detected for the dynamic culture condition.

pore network (Figure 5A), indicative of the newly formed mineralized tissue. Some back-scatter signal was also detected within the pore network of the implant or at the bone-implant interface in static samples (Figure 5D).

For the explanted cylindrical implants, the surfaces and the first layers of the porous structure inside pores were visible in the SEM (Figure 5). For the dynamic samples large amounts of extracellular matrix was detected on the struts of the scaffolds, and inside the pores, bridging them with a newly formed tissue network (Figures 5B, C). The static culture also led to tissue formation in some pores, but not yet enough to develop abundant tissue formation on or within the pore network (Figures 5E, F).
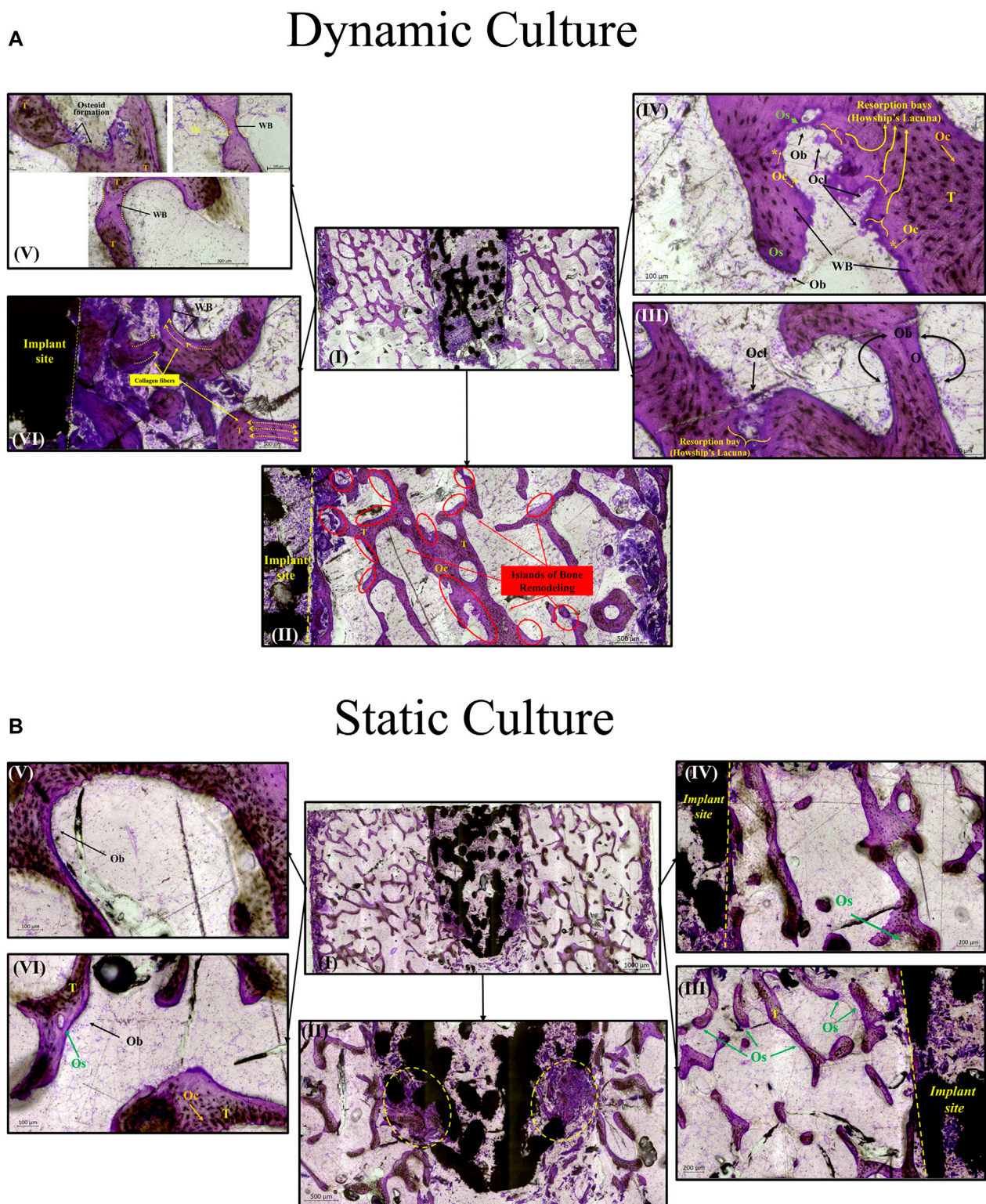
FIGURE 7
Transverse tissue sections stained with Paragon—Toluidine blue **(A)** *Ex-vivo* cancellous bone cultured for 21 Days within bioreactor (I) Cross section of the bone cylinder, (II) representative areas next to the implant fixation showing the newly formed bone tissue islands (red circles) on the existing trabeculae struts (T), (III) bone remodelling produced from osteoblasts (Ob) lining on both sides of the trabeculae, and bone resorption by osteoclasts (Ocl) occupying small depressions on the bone surface (Howship's lacunae), (IV) areas of new osteoid formation (Os), woven bone (WB), bone resorption activity (Howship's lacunae) and some newly formed Osteocytes (Oc*) together with mature osteocytes (Oc), (V) existing trabeculae struts with formation of new osteoid (Os) and woven bone formation bridging trabeculae struts with newly formed Osteocytes (Oc*) trapped inside, (VI) woven bone formation near the implant site with collagen fibers situated parallel in sheets and oriented opposite to the mechanical force acting on the sample. **(B)** Static culture for 21 Days (I) Cross section of the bone cylinders, (II) conical edge of the peg with circles highlighting mixed bone tissue (old mineralized bone and new connective tissue reformation), (III) left side and (IV) right side of bone next to the implant showing minor islands of osteoid (Os) formation, (V) and (VI) areas away from the implant with osteoblasts (Ob) forming new osteoid (Os). Scalebars are shown within the pictures.

I (%)	II (%)	III (%)	IV (%)
17 ± 11	60 ± 13	20 ± 16	3 ± 5

EDS analysis revealed the presence of both calcium and phosphorus in this on-grown tissue.

3.3 Evaluation of tissue formation within the pores—Micro-CT analysis

Newly formed tissue was identified inside the porous structure with micro-CT for both culture conditions (Figure 6). The new tissue formation for the dynamic culture condition was twice that of the static culture, filling half the void space within the porous titanium implant.

3.4 Site specific bone remodelling—histology

For the dynamic samples, numerous osteoid formation seams and woven bone islands were observed (Figure 7A. I, II). Dense connective tissue formation was observed next to the implant, full of collagen (blue/pale blue). Formation of connective tissue, distributed within the pore network of the peg, was also noted. Osteoblasts with recognizable large, round nuclei and abundant basophilic cytoplasm that had deposited new osteoid (dark pink) on peri-implant bone surfaces, as well as deeper into the bone tissue (Figure 7A. III, IV, VI). Additionally, osteoclasts usually with four to seven nuclei, were observed, actively forming resorption bays and Howship's lacunae (Figure 7A. III, IV). Active osteoblasts depositing new osteoid on trabeculae were also found, while other areas of mineralized bone struts had been bridged with new woven bone matrix (Figure 7A. V). Some of these osteoblasts were detected entrapped inside their own secreted bone matrix, differentiating to osteocytes (yellow asterisk, Figure 7A. IV, V). Collagen fibres situated parallel to each other like pillars, directing upwards and opposite to the compression force applied on the dynamically cultured samples, were observed in remodelling bone tissue close to the implant (Figure 7A. VI).

For static samples, osteoid seams were also observed (Figure 7B. I, III and IV). For these samples, connective tissue was formed predominantly at the tip of the implant where it was mixed with old bone tissue, (Figure 7B. II). Close to implant's outer region, less area with new osteoid matrix formation was visible, and even less in the whole bone trabeculae network (Figure 7B. III, IV, V and VI).

3.5 Mechanical results

The characteristic loading times for the dynamic cultures was mostly of a short duration, with T_{load} typically less than a second (Table 1).

Push through mechanical testing was not possible for one sample, meaning that N = 6 dynamic and N = 5 static samples were tested. Dynamic samples were found to have 3x greater push-through fixation strength ($p = 0.046$, Figure 8B).

4 Discussion

The most important finding of this study is that the *ex vivo* model can be used to examine the early stages of tissue ingrowth
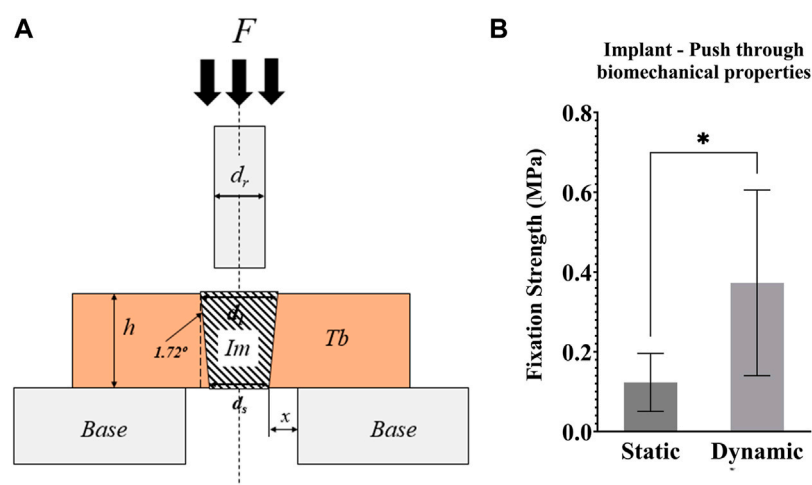
FIGURE 8
(A) Schematic representation of the push-through mechanical testing. Compression testing of all samples was performed after 21 days of culture. F = force applied to the implant with a compression platen; Im = implant; Tb = trabecular bone; h = height of the Tb; Base = support of the bone cylinder; x = clearance of hole in the support base; ds = small implant diameter; dl = large implant diameter; dr = push-through rod diameter < dl **(B)** Graph of the push-through fixation strength (MPa) comparing static and dynamic samples. *p <0.05, **p <0.01.

(Figures 4–7), bone ongrowth (Figure 5) and bone remodelling (Figures 3, 4, 7) around porous implants. The use of a bioreactor with more physiological conditions (mechanical loading and fluid flow) led to greater bone remodelling around the implant and mineralised tissue formation within the implant. The bioreactor is inherently controllable and so could enable more repeatable preclinical tests, with scope to evaluate new technology under the exact same conditions allowing for more direct comparisons between novel, state-of-the-art and established implant fixation technologies.

The fluorescent intensity analysis found differences for the whole bone cross-section and in the bone adjacent to the implant (that was most mechanically stressed), however, the intensity analysis of the outer circumference of the bone (most exposed to fluid flow) did not reach statistical significance. This difference at the bone implant interface between static and dynamic samples was apparent along the length of the implant. This suggests that the daily cyclic mechanical loading applied to the implant had an important effect on the day 7 remodelling in our *ex vivo* model of implant fixation. Interestingly, the initial press-fit implantation in our study also affected early bone remodelling: the cross-sectional fluorescent imaging revealed day 7 calcium deposits directly below the implant in both the static and dynamic cultures. This finding that the mechanical loading has an important effect agrees with Birmingham et al. who analysed the effects of mechanical loading and fluid shear on trabecular remodelling and concluded that bone strain was likely the overall driving mechanical signal for new bone formation (Birmingham et al., 2016). Osteocytes have been measured to be the most mechanosensitive bone cells (Klein-Nulend et al., 1995). Two mechanisms have been proposed through which osteocytes could sense the strain that arises during physiological loading: fluid flow through the canaliculi, or pressurisation of the lacunar pores (Gardinier et al., 2010; Scheiner et al., 2016; Wittkowske et al., 2016; Estermann and Scheiner, 2018). For longer characteristic loading times (>8 s), fluid flow through the canaliculi could occur (Gardinier et al., 2010); however in this *ex vivo* study, only a small portion of the recorded loading times were of a such a duration (Table 1). Rather, the characteristic loading times in this experiment were much shorter, typically <1 s, indicating that lacunar pore pressurisation was likely to be the driver of osteocyte activity (Scheiner et al., 2016). The distribution of the characteristic loading times (Table 1) were physiological, similar to that experienced at the knee while ascending stairs and at the hip during gait (Scheiner et al., 2016).

The SEM analysis revealed many tissue deposits onto the surface of dynamically cultured samples (Figure 5). The tissue formed on the porous implants was visually similar to tissue-engineered woven bone grown on titanium *in vitro* from cultured osteoblasts (Chen et al., 2010), and the EDX analysis confirmed the presence of calcium and phosphorus. Previous *ex vivo* research utilising SEM analyses also found that application of cyclic loading plus fluid flow in a bioreactor led to increased extracellular matrix transfer to an implant surface indicative of the early stages of implant bone ongrowth (Dua et al., 2021). In their study, the amount of matrix was highest after 7 weeks of culture. Our static culture led to visually similar level of matrix after 3 weeks, with even more observed in the dynamic model. This may be a result of the amount of mechanical stress induced in the bone because of the press-fit fixation, but it

could also be a result of the different pore sizes and surface topography of the stochastic porous implant used in our study leading to an increased rate of bone ongrowth.

Woven bone formation was observed in the trabecular network and mineralisation was detected inside the dynamically cultured implants (Figure 7). Bone remodelling and tissue maturation *in vivo* occurs over a period of months (Kohli et al., 2018), rather than days, and hence a longer-term culture would be required to assess the extent to which tissue ingrowth can remodel to a fully osseointegrated implant. After 6 weeks *in vivo* in an ovine femoral condyle model, a similarly designed, but larger diameter, stochastic porous implant had 11% bone ingrowth, with the outer porous struts encased in woven bone (Ghouse et al., 2019). A rat model of commercially pure titanium implants found that after 1 week, the implant-bone interface was characterized by fibrous tissue, at 2 weeks, there was little evidence of bone-implant contact, with the appearance of fragments with fibrous layers adjacent to the implant, like that observed in our model, and by 4 weeks, bone-implant contact had nearly trebled, with newly formed woven bone attached to the implant (Zhang et al., 2010). The remodelling pathway observed in our model appears like the early stages observed *in vivo* but at a slower rate. A similar observation was also made by others (Dua et al., 2021) The dynamic culture led to more remodelling, refinement of the fluid flow and loading conditions may thus allow for the rate of remodelling to be accelerated further.

Ex vivo models simulate blood supply with fluid flow but do not currently model angiogenesis which is required for remodelling *in vivo* (Kohli et al., 2018). Thus, the model may be best applied to narrow the design space and screen how new technology influences the bone remodelling pathway before final proof-of-concept in an *in vivo* model. Adoption of *ex vivo* models for early research (technology readiness levels 1–4) would still have a tangible ethical impact and financial impact (the cost of the protocol is one to two orders of magnitude lower than that of a large animal model). The level of control enabled will also facilitate comparison across research centres and years. Cell viability assessment for the *ex vivo* bone was found to be more challenging than for cell culturing experiments: the common microscopy approach (Calcein AM and Ethidium Homodimer with confocal microscopy) was less effective as the dye did not penetrate most of the cells, preventing accurate quantitative analysis. This was likely a consequence of the abundant bone extracellular matrix that is inherent to *ex vivo* bone covering the cells. Others have previously reported live/dead images, but did not include quantitative analyses (Dua et al., 2021). Qualitatively, they described fewer dead cells after 7 weeks of dynamic culture. Early *ex vivo* bone research used *in situ* histochemical analysis to demonstrate that 60% of osteocytes are viable after 3 weeks in loaded samples (David et al., 2008). Cell metabolic activity measurements could also provide insight into viability, with prior research suggesting no change in viability for *ex vivo* bone from days 4–5 to days 21–22 (Birmingham et al., 2015). Media measurements could also be used to quantify the levels of formation/resorption markers at regular time intervals throughout the experiment, while development of a protocol to enable RT-PCR measurements could provide additional quantitative insight from an end-test analysis. Bone samples

were extracted from both condyles, and bone density and properties may have differed between samples at day zero (Munford et al., 2020). We randomized the location for which static and dynamic samples were obtained to minimise these effects when comparing culture conditions. Further, our imaging analyses of bone remodelling were not dependent on bone density/volume. For our mechanical testing, we chose to test fixation as a push-through test rather than a push-out test to capture the effects of bone remodelling around the tapered implant, in addition to any mechanical bone-implant fixation. A pull-out test could be used in future research to focus purely on the bone-implant fixation strength. Modelling the initial press-fit fixation and the subsequent daily cyclic loading would also be valuable future work to predict the bone stress-strain state for this bioreactor model of implant fixation. Linking these predictions to previous poromicromechanics simulations (Scheiner et al., 2016) would lead to further insight into the stimulus experienced by the osteocytes. Finally, it is possible that the loading could have affected the distribution of the fluorochrome strains even in the absence of active bone formation. This effect is likely to be small as there was good stain penetration throughout the samples in both the dynamic and static samples, and the histology analysis provided complementary evidence of osteoid formation, and the histology and backscatter SEM analyses provided complementary evidence of mineralisation within the implant pores.

In conclusion, *ex vivo* bone models enable the analysis of tissue remodelling onto, into and around implants in the lab. While static culture conditions exhibited some characteristics of bony adaptation to implantation, controlling the fluid flow and mechanical loading environment with a bioreactor to simulate physiological conditions led to an accelerated response.

Data availability statement

The original contributions presented in the study are included in the article/Supplementary Material, further inquiries can be directed to the corresponding author.

Ethics statement

Ethical review and approval was not required for the animal study because there was no experimentation on living animals. The research was registered annually in accordance with the host institution's policy for use of animals in research, with all tissue sourced as a waste product from pigs that were sacrificed for unrelated reasons.

References

Abbott, T. E. F., Fowler, A. J., Dobbs, T. D., Harrison, E. M., Gillies, M. A., and Pearse, R. M. (2017). Frequency of surgical treatment and related hospital procedures in the

Author contributions

Contributor Roles (CRediT): NK Investigation, Methodology, Visualisation, Writing – Original Draft. KT Formal Analysis, Investigation, Methodology, Visualisation, Writing – Original Draft. TH Investigation, Software, Writing – Review and Editing. IS-P Investigation, Methodology, Writing – Review and Editing. DG Methodology, Resources, Writing – Review and Editing. RvA Conceptualisation, Funding Acquisition, Project Administration, Supervision, Writing – Original Draft. NK formal analysis, investigation, methodology, visualization, writing—original draft.

Funding

Acknowledgments

Conflict of interest

The authors declare that the research was conducted in the absence of any commercial or financial relationships that could be construed as a potential conflict of interest.

Publisher's note

UK: a national ecological study using hospital episode statistics. *Br. J. Anaesth.* 119 (2), 249–257. doi:10.1093/bja/aex137

Bai, L., Chen, P., Zhao, Y., Hang, R., Yao, X., Tang, B., et al. (2021). A micro/nano-biomimetic coating on titanium orchestrates osteo/angio-genesis and osteoimmunomodulation for advanced osseointegration. *Biomaterials* 278, 121162. doi:10.1016/j.biomaterials.2021.121162

Bankhead, P., Loughrey, M. B., Fernández, J. A., Dombrowski, Y., McArt, D. G., Dunne, P. D., et al. (2017). QuPath: Open source software for digital pathology image analysis. *Sci. Rep.* 7 (1), 16878. doi:10.1038/s41598-017-17204-5

Berahmani, S., Janssen, D., van Kessel, S., Wolfson, D., de Waal Malefijt, M., Buma, P., et al. (2015). An experimental study to investigate biomechanical aspects of the initial stability of press-fit implants. *J. Mech. Behav. Biomed. Mater.* 42, 177–185. doi:10.1016/j.jmbbm.2014.11.014

Birmingham, E., Kreipke, T. C., Dolan, E. B., Coughlin, T. R., Owens, P., McNamara, L. M., et al. (2015). Mechanical stimulation of bone marrow *in situ* induces bone formation in trabecular explants. *Ann. Biomed. Eng.* 43 (4), 1036–1050. doi:10.1007/s10439-014-1135-0

Birmingham, E., Niebur, G. L., McNamara, L. M., and McHugh, P. E. (2016). An experimental and computational investigation of bone formation in mechanically loaded trabecular bone explants. *Ann. Biomed. Eng.* 44 (4), 1191–1203. doi:10.1007/s10439-015-1378-4

Borgström, F., Karlsson, L., Ortsäter, G., Norton, N., Halbout, P., Cooper, C., et al. (2020). Fragility fractures in europe: burden, management and opportunities. *Arch. Osteoporos.* 15 (1), 59. doi:10.1007/s11657-020-0706-y

Brogini, S., Sartori, M., Giavaresi, G., Cremascoli, P., Alemani, F., Bellini, D., et al. (2021). Osseointegration of additive manufacturing Ti–6Al–4V and Co–Cr–Mo alloys, with and without surface functionalization with hydroxyapatite and type I collagen. *J. Mech. Behav. Biomed. Mater.* 115, 104262. doi:10.1016/j.jmbbm.2020.104262

Chen, J., Birch, M. A., and Bull, S. J. (2010). Nanomechanical characterization of tissue engineered bone grown on titanium alloy *in vitro*. *J. Mater. Sci. Mater. Med.* 21 (1), 277–282. doi:10.1007/s10856-009-3843-9

David, V., Guignandon, A., Martin, A., Malaval, L., Lafage-Proust, M.-H., Rattner, A., et al. (2008). *Ex vivo* bone formation in bovine trabecular bone cultured in a dynamic 3D bioreactor is enhanced by compressive mechanical strain. *Tissue Eng. Part A* 14 (1), 117–126. doi:10.1089/ten.a.2007.0051

Davies, C., Jones, D., Stoddart, M., Koller, K., Smith, E., Archer, C., et al. (2006). Mechanically loaded *ex vivo* bone culture system 'zetos': Systems and culture preparation. *Eur. Cell Mater* 11, 57–75. doi:10.22203/ecm.v011a07

De Chaumont, F., Dallongeville, S., Chenouard, N., Hervé, N., Pop, S., Provoost, T., et al. (2012). Icy: an open bioimage informatics platform for extended reproducible research. *Nat. Methods* 9 (7), 690–696. doi:10.1038/nmeth.2075

de Sousa, B. M., Correia, C. R., Ferreira, J. A., Mano, J. F., Furlani, E. P., Soares dos Santos, M. P., et al. (2021). Capacitive interdigitated system of high osteoinductive/conductive performance for personalized acting-sensing implants. *NPJ Regen. Med.* 6 (1), 80–14. doi:10.1038/s41536-021-00184-6

Dion, C., Yamomo, G., Howard, J., Teeter, M., Willing, R., and Lanting, B. (2020). Revision total knee arthroplasty using a novel 3D printed titanium augment: A biomechanical cadaveric study. *J. Mech. Behav. Biomed. Mater.* 110, 103944. doi:10.1016/j.jmbbm.2020.103944

Doyle, R., van Arkel, R. J., and Jeffers, J. R. T. (2019). Effect of impaction energy on dynamic bone strains, fixation strength, and seating of cementless acetabular cups. *J. Orthop. Res.* 37 (11), 2367–2375. doi:10.1002/jor.24418

Doyle, R., Arkel, R. J. v., Muirhead-Allwood, S., and Jeffers, J. R. T. (2020). Impaction technique influences implant stability in low-density bone model. *Bone Jt. Res.* 9 (7), 386–393. doi:10.1302/2046-3758.97.Bjr-2019-0303.R1

Dua, R., Jones, H., and Noble, P. C. (2021). Evaluation of bone formation on orthopedic implant surfaces using an *ex-vivo* bone bioreactor system. *Sci. Rep.* 11 (1), 22509. doi:10.1038/s41598-021-02070-z

Estermann, S.-J., and Scheiner, S. (2018). Multiscale modeling provides differentiated insights to fluid flow-driven stimulation of bone cellular activities. *Front. Phys.* 6. doi:10.3389/fphy.2018.00076

Gardinier, J. D., Townend, C. W., Jen, K.-P., Wu, Q., Duncan, R. L., and Wang, L. (2010). *In situ* permeability measurement of the mammalian lacunar–canalicular system. *Bone* 46 (4), 1075–1081. doi:10.1016/j.bone.2010.01.371

Geraldes, D. M., Hansen, U., Jeffers, J., and Amis, A. A. (2017). Stability of small pegs for cementless implant fixation. *J. Orthop. Res.* 35 (12), 2765–2772. doi:10.1002/jor.23572

Ghouse, S., Babu, S., van Arkel, R. J., Nai, K., Hooper, P. A., and Jeffers, J. R. T. (2017). The influence of laser parameters and scanning strategies on the mechanical properties of a stochastic porous material. *Mater. Des.* 131, 498–508. doi:10.1016/j.matdes.2017.06.041

Ghouse, S., Reznikov, N., Boughton, O. R., Babu, S., Ng, K. C. G., Blunn, G., et al. (2019). The design and *in vivo* testing of a locally stiffness-matched porous scaffold. *Appl. Mater. Today* 15, 377–388. doi:10.1016/j.apmt.2019.02.017

Jones, D. B., Broeckmann, E., Pohl, T., and Smith, E. L. (2003). Development of a mechanical testing and loading system for trabecular bone studies for long term culture. *Eur. Cell Mater* 5, 48–60. discussion 59-60. doi:10.22203/ecm.v005a05

Klein-Nulend, J., Van Der Plas, A., Semeins, C. M., Ajubi, N. E., Erangos, J. A., Nijweide, P. J., et al. (1995). Sensitivity of osteocytes to biomechanical stress *in vitro*. *FASEB J.* 9 (5), 441–445. doi:10.1096/fasebj.9.5.7896017

Kohli, N., Ho, S., Brown, S. J., Sawadkar, P., Sharma, V., Snow, M., et al. (2018). Bone remodelling *in vitro*: Where are we headed?: -A review on the current understanding of physiological bone remodelling and inflammation and the strategies for testing biomaterials *in vitro*. *Bone* 110, 38–46. doi:10.1016/j.bone.2018.01.015

Kohli, N., Stoddart, J. C., and van Arkel, R. J. (2021). The limit of tolerable micromotion for implant osseointegration: a systematic review. *Sci. Rep.* 11 (1), 10797–10811. doi:10.1038/s41598-021-90142-5

Metscher, B. D. (2009). MicroCT for comparative morphology: Simple staining methods allow high-contrast 3D imaging of diverse non-mineralized animal tissues. *BMC Physiol.* 9 (1), 11. doi:10.1186/1472-6793-9-11

Munford, M. J., Ng, K. G., and Jeffers, J. R. (2020). Mapping the multi-directional mechanical properties of bone in the proximal tibia. *Adv. Funct. Mater.* 30 (46), 2004323. doi:10.1002/adfm.202004323

Munford, M. J., Stoddart, J. C., Liddle, A. D., Cobb, J. P., and Jeffers, J. R. (2022). Total and partial knee arthroplasty implants that maintain native load transfer in the tibia. *Bone Jt. Res.* 11 (2), 91–101. doi:10.1302/2046-3758.112.bjr-2021-0304.r1

Owen, R., and Reilly, G. C. (2018). *In vitro* models of bone remodelling and associated disorders. *Front. Bioeng. Biotechnol.* 6 (134), 134. doi:10.3389/fbioe.2018.00134

Öztürk, A., and Ersan, Ö. (2020). Are the lives of animals well-spent in laboratory science research? A study of orthopaedic animal studies in Turkey. *Clin. Orthop. Relat. Res.* 478 (9), 1965–1970. doi:10.1097/corr.0000000000001335

Pabinger, C., Lothaller, .H., and Geissler, A . (2015). Utilization rates of knee-arthroplasty in OECD countries. *Osteoarthr. Cartil.* 10 (23), 1664–1673. doi:10.1016/j.joca.2015.05.008

Pabinger, C., Lothaller, H., Portner, N., and Geissler, A. (2018). Projections of hip arthroplasty in OECD countries up to 2050. *Hip Int.* 28 (5), 498–506. doi:10.1177/1120700018757940

Reznikov, N., Boughton, O. R., Ghouse, S., Weston, A. E., Collinson, L., Blunn, G. W., et al. (2019). Individual response variations in scaffold-guided bone regeneration are determined by independent strain- and injury-induced mechanisms. *Biomaterials* 194, 183–194. doi:10.1016/j.biomaterials.2018.11.026

Scheiner, S., Pivonka, P., and Hellmich, C. (2016). Poromicromechanics reveals that physiological bone strains induce osteocyte-stimulating lacunar pressure. *Biomechanics Model. Mechanobiol.* 15 (1), 9–28. doi:10.1007/s10237-015-0704-y

Soares dos Santos, M. P., Marote, A., Santos, T., Torrão, J., Ramos, A., Simões, J. A., et al. (2016). New cosurface capacitive stimulators for the development of active osseointegrative implantable devices. *Sci. Rep.* 6 (1), 30231–30315. doi:10.1038/srep30231

Styczynska-Soczka, K., Amin, A. K., Simpson, A. H. W., and Hall, A. C. (2021). Optimization and validation of a human *ex vivo* femoral head model for preclinical cartilage research and regenerative therapies. *Cartilage* 13, 386S–397S. doi:10.1177/1947603520934534

Swarup, A., Weidner, H., Duncan, R., and Nohe, A. (2018). The preservation of bone cell viability in a human femoral head through a perfusion bioreactor. *Materials* 11 (7), 1070. doi:10.3390/ma11071070

van Arkel, R. J., Ghouse, S., Milner, P. E., and Jeffers, J. R. T. (2018). Additive manufactured push-fit implant fixation with screw-strength pull out. *J. Orthop. Res.* 36 (5), 1508–1518. doi:10.1002/jor.23771

Vivanco, J., Garcia, S., Ploeg, H. L., Alvarez, G., Cullen, D., and Smith, E. L. (2013). Apparent elastic modulus of *ex vivo* trabecular bovine bone increases with dynamic loading. *Proc. Instit. Mech. Eng. Part H J. Eng. Med.* 227 (8), 904–912. doi:10.1177/0954411913486855

Wang, L., Gao, Z., Su, Y., Liu, Q., Ge, Y., and Shan, Z. (2021). Osseointegration of a novel dental implant in canine. *Sci. Rep.* 11 (1), 4317–4410. doi:10.1038/s41598-021-83700-4

Wittkowske, C., Reilly, G. C., Lacroix, D., and Perrault, C. M. (2016). *In vitro* bone cell models: impact of fluid shear stress on bone formation. *Front. Bioeng. Biotechnol.* 4, 87. doi:10.3389/fbioe.2016.00087

Zankovic, S., Seidenstuecker, M., Prall, W. C., Loos, J., Maderer, F., Oberle, M., et al. (2021). A method for the evaluation of early osseointegration of implant materials *ex vivo*: Human bone organ model. *Mater. (Basel)* 14 (11), 3001. doi:10.3390/ma14113001

Zhang, L., Ayukawa, Y., LeGeros, R. Z., Matsuya, S., Koyano, K., and Ishikawa, K. (2010). Tissue–response to calcium-bonded titanium surface. *J. Biomed. Mater. Res. Part A* 95A (1), 33–39. doi:10.1002/jbm.a.32763

Medial–lateral translational malalignment of the prosthesis on tibial stress distribution in total knee arthroplasty: A finite element analysis

Zhiqian Zheng†, Yang Liu†, Aobo Zhang, Hao Chen, Qian Wan,
Lei Zhong, Xiaonan Wang, Qing Han* and Jincheng Wang*

Department of Orthopedics, The Second Hospital of Jilin University, Changchun, China

Background: Poor prosthesis alignment during total knee arthroplasty could cause problems such as polyethylene spacer wear, leading to surgical failure and revision surgery. The problems caused by the malalignment of the tibial plateau prosthesis in the medial and lateral planes are unclear. We aimed to investigate the stress distribution and micromotion of the tibia when the tibial plateau prosthesis is translated 1 and 2 mm medially and laterally, respectively, using finite element analysis (FEA).

Method: A non-homogeneous tibia model was created and load conditions when standing on two legs were applied using FEA to simulate the misaligned prosthesis. The stresses, stress distribution, and micromotion of the proximal tibia were analyzed in five positions of the tibial plateau prosthesis: Lateral-2 mm; Lateral-1 mm; Medium; Medial-2 mm; Medial-1 mm.

Result: The maximum stress in the five groups with different misalignments of the platform was 47.29 MPa (Lateral-2 mm). The maximum micromotion among the five groups in different positions was 7.215 μm (Lateral-2 mm).

Conclusion: When placing the tibial plateau prosthesis during total knee arthroplasty, an error of 2 mm or less is acceptable as long as it does not overhang.

1 Introduction

Several studies have shown that total knee arthroplasty (TKA) is an effective and durable treatment for end-stage knee arthritis (Vessely et al., 2006; Guo et al., 2012). The primary goals of TKA include reducing knee pain, re-aligning the femur and tibia, maintaining knee stability, and preserving joint flexibility. Despite the great clinical results of TKA, revision rates remain high due to poorly aligned prosthetic components, resulting in aseptic loosening, instability, and polyethylene wear (Dalury et al., 2013).

To predict and avoid the problems mentioned above and thus improve the prognosis of surgery, the analytical approach (Jin et al., 1995), experimental measurement (Liau et al., 1999) and finite element analysis (Popescu et al., 2019; Dong et al., 2020; Park et al., 2021) (FEA) have been widely used in the field of orthopedics. Matsuda et al. (1999) investigated

the effect of varus tilt on contact stresses in total knee prostheses using electronic pressure sensors; Liau et al. (1999) studied the effect of tibiofemoral joint contact alignment of knee prosthesis using Fuji pressure-sensitive film in an *in vitro* biomechanical test. They also explored the effect of the tibial polyethylene component of the total knee prosthesis on stresses using FEA (Liau et al., 2002). Different misalignment conditions are tested by FEA by simulating angles, friction, and stresses. These findings are applied in preoperative planning to prevent potential TKA failure (Perillo-Marcone and Taylor, 2007; Minh et al., 2013). To our knowledge, there have been few studies examining the effect of medial-lateral translational misalignment of the tibial plateau prosthesis on the tibia.

Inoue et al. (2016) showed that the risk of medial tibial condylar fractures increases with increased tilt of the valgus angle of the tibial prosthesis. If the tibial prosthesis is poorly rotated, firstly, the riser of the polyethylene prosthesis will be worn further and, since the femoral and tibial prostheses are no longer matched in the same position, the soft tissue will be twisted during flexion and extension activities, resulting in a stiff knee (Bedard et al., 2011). Secondly, internal rotation can bring about lateral patellar subluxation and wear of the lateral patellofemoral joint, while external rotation can cause inward patellar trajectory, internal tibial rotation, or a change in gait (Perillo-Marcone et al., 2000; Ishii et al., 2015). Any errors that cause asymmetric loading of the joint, such as misalignment or instability of the prosthesis, could lead to increased wear rates, resulting in surgical failure and revision (Fraser et al., 2015).

We aimed to investigate the stress distribution and micromotion of the tibia when the tibial plateau prosthesis is translated 1 mm and 2 mm medially and laterally, respectively, using FEA. This may contribute to the reduction of TKA revision rates and improved satisfaction of patients after TKA.

2 Materials and methods

2.1 Establishment of a non-homogeneous three-dimensional (3D) tibia model and surgical simulation

Computed tomography (CT) scan data were recorded from a 49-year-old male volunteer. The images were imported into Mimics (v21.0, Materialise, Leuven, Belgium), and the right tibia was rebuilt as a 3D model. This research was approved by the Ethics Committee of the Second Hospital of Jilin University and the volunteer provided informed consent.

The 3D model of the right tibia and the tibial plateau prosthesis (Ai Kang A3)were prepared as STL format files, and the simulated surgery was performed in Magics (v21.0, Materialise, Leuven, Belgium). The posterior slope was set to 5°, and the tibial model was resected in the traditional surgical fashion (Indelli et al., 2016; Maderbacher et al., 2017), by removing the tibia 6 mm below the medial tibial articular surface, perpendicular to the mechanical axis. The application of this study focused on the stress distribution during the interaction of the proximal bone with the platform prosthesis, so the distal tibia was separated from the system to reduce the calculation time.

After installing the tibial plateau prosthesis, the prosthesis was moved medially and laterally by 1 mm and 2 mm, respectively, to

simulate a slippage dislocation. The prosthesis is shown in the middle position, as well as translated 2 mm to the medial and lateral side, in Figure 1.

In the Mimics software, the 3D model of the tibia with inhomogeneous material properties was defined based on the grayscale values of the CT scans. Following previous studies, the material properties of the tibia were determined according to the following equations (Rho et al., 1995):

$$\rho\,(g/m^3) = -13.4 + 1017 \times GV\,(HU) \qquad (1)$$

$$E\,(Pa) = -388.8 + 5925 \times \rho\,(g/m^3) \qquad (2)$$

in which E is the modulus of elasticity, ρ is the bone density, and GV is the gray value of the bone in the CT data. According to other previous studies (Thompson et al., 2016), the Poisson's ratio of the bone was set to 0.3 and the modulus of elasticity of the tibial plateau prosthesis was set to 114,500 MPa with a Poisson's ratio of 0.3. To differentiate, the tibia was divided into ten colored regions, and the material properties are shown in Figure 2.

2.2 Meshing and load setting

All components were imported into Hypermesh (14.0, Altair, Troy, MI) to create triangular meshes with the element type C3D4. The number of elements in the bone and prosthesis are 420,036 and 117,094 respectively. A non-linear friction model with surface-surface contact was established between the superior surface of the tibia and the inferior surface of the prosthesis, and the friction coefficient was set to 0.2 (Li et al., 2019). A static analysis of the tibia was performed under a load condition of 963 N to simulate a two-legged stance (Kutzner et al., 2010). According to a previous study (Lin et al., 2017), the ratio of force between the lateral and medial tibial plateau is 40%:60%, respectively, so the force was divided into 385 N and 578 N and loaded with rigid bar element 3 (Rbe3) to transfer the force uniformly. The inferior surface of the distal tibia was constrained in all directions (Figure 3).

3 Results

3.1 Finite element analysis

3.3.1 Stress

Figure 4 shows the maximum von Mises stress in the tibia for five sets of platforms in different positions. The highest stress peak of 47.29 MPa can be seen when the platform is misaligned by 2 mm to the lateral side, followed by the stress peak of 20.90 MPa when the platform is misaligned by 2 mm to the medial side. The remaining three data groups were not significantly different compared to each other.

The proximal tibia was divided into seven regions to analyze the stress distribution (Figure 5). All cell points in each region were extracted separately and the data was analyzed using SPSS software. Since the data does not obey a normal distribution, the results were analyzed using the Kruskal–Wallis test. According to the stress distribution in the first six regions, the
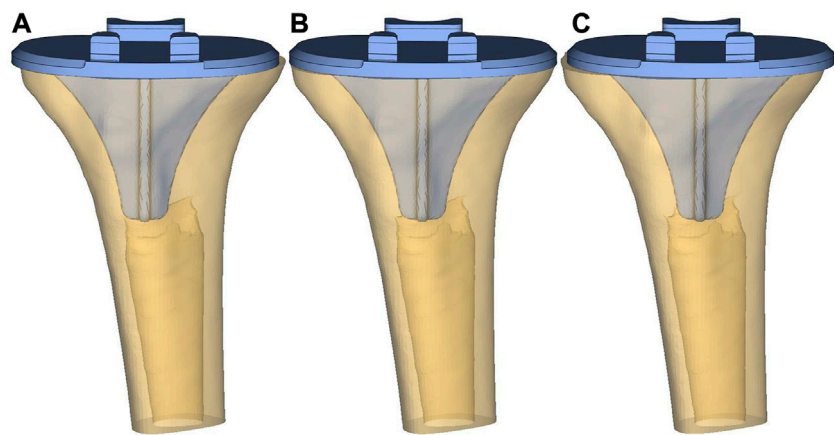
FIGURE 1
Prosthesis in different positions. **(A)** Lateral-2 mm; **(B)** Medium; **(C)** Medial-2 mm.
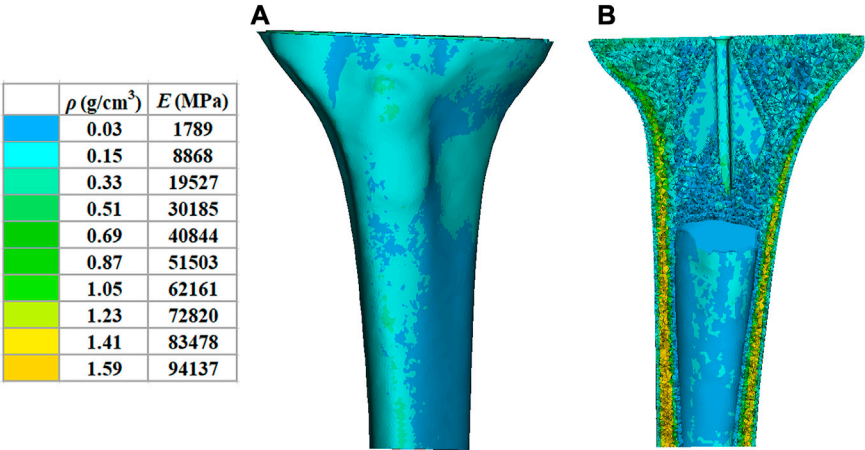
FIGURE 2
Material properties of the inhomogeneous tibia. **(A)** External material properties of the tibia. **(B)** Internal material properties of the tibia. ρ: bone density. **(E)** elastic modulus.

data statistics were obtained as shown in Figure 6. Significant differences were found between the groups except for those labeled $p > 0.05$. The largest median of 1.43 MPa occurred in the case of a 2 mm medial misalignment in the F region, while the smallest median of 0.075 MPa was seen in the B region where the prosthesis was in the middle position. It can be seen that the red part of the high stress was concentrated in the lower part of the proximal tibia which was the G region.

A representative evaluation path was defined for qualitative and quantitative comparison among the different positions of stresses at the region of the tibia plateau. Figure 7 shows stresses along the path defined at the stem cavity border. The major differences along this path pertain to the extreme values at the distance of 25–50 mm. The maximum stress along the defined path occurred in the lateral-2 mm group; the maximum stress in this case was 6.43 MPa. In the same

location, the least stress model represents the medium group, with the maximum value of 1.38 MPa.

3.2 Micromotion

Figure 8 shows the micromotion clouds of one of the groups and Figure 9 demonstrates the micromotion of the five sets of platforms for different misalignment situations. When the platform was misaligned to the lateral side by 2 mm, its micromotion of 7.215 μm was significantly larger than the remaining four groups. Additionally, while the platform was misaligned 2 mm medially, its micromotion of 2.869 μm was the smallest among the five groups. The middle three groups of micromotions are almost half of the first group, respectively. Figure 10 shows the micromotion at different

FIGURE 3
Loads and constraints of the tibia. The distal tibia is constrained completely.

FIGURE 4
Comparison of maximum stresses when five groups of platforms are in different misalignment positions.

FIGURE 5
Distribution of von Mises stress in the proximal tibia. **(A–G)** Seven different regions of stress.
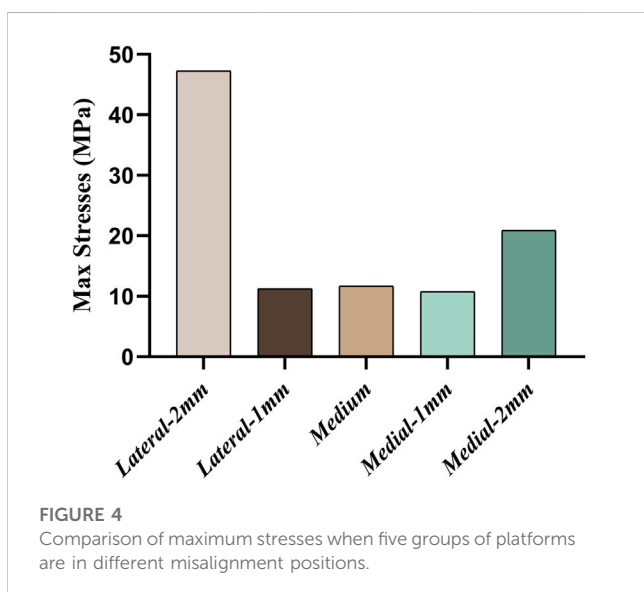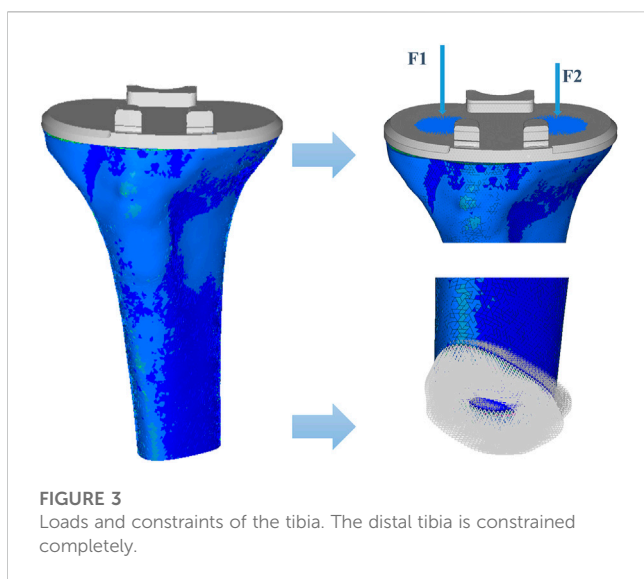
misalignment positions of the plateau and stem. The largest micromotion of 3.854 um occurred on the plateau when the platform was misaligned 1 mm medially.

4 Discussion

Addressing the problems caused by the wear of prostheses in TKA remains a challenge for orthopedic surgeons. In previous studies, varus-valgus, anterior-posterior tilt, and internal and external rotation misalignment of the prosthesis were included (Fraser et al., 2015). However, no studies have been conducted to investigate the medial-lateral translational misalignment of the prosthesis.

FEA is an effective tool to evaluate the mechanical properties of prostheses and bone. The accuracy of the analysis depends on the veracity of the model. In this study, a non-homogeneous 3D tibia model was used, which means that it will be closer to real human bone than a homogeneous bone model, making the results of the study more realistic (Venalainen et al., 2016; Ün and Çalık, 2016). According to Ruggiero et al. (2019) we can learn that the quality of the hexahedral mesh is better than that of the tetrahedral one, especially in the dynamic condition. But based on the static conditions of our study and the fact that we draw the relatively small mesh, the accuracy is guaranteed even if we use the tetrahedral mesh in this study.
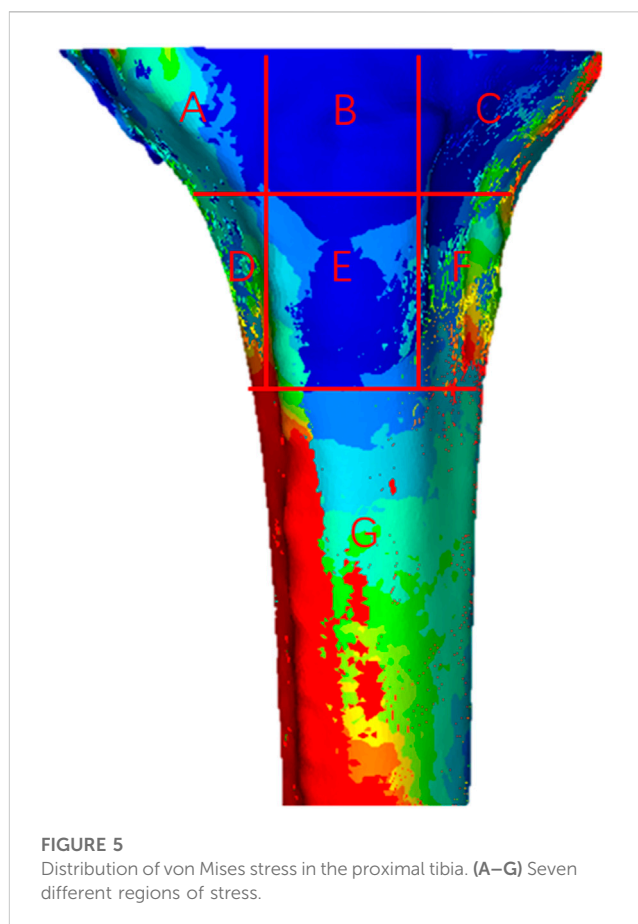
The comparison of the five groups of maximum stresses shows that the maximum stress was 47.29 MPa, which is less than the ultimate stress of 80 MPa in cortical bone (Maslov et al., 2021). This indicates that translational misalignments of 2 mm or less do not result in fractures. As can be seen in Figure 6, the stresses in the A and D regions were high when the platform prosthesis was misaligned to the lateral side, which was in line with our expectations. A similar pattern could be seen in regions C and F, when the tibial plateau prosthesis was transferred medially. Even with these stress concentrations, the stresses were not sufficient to cause significant effects on the proximal tibia (Maslov et al., 2021). Figure 7 demonstrates that, at the stem cavity border, the stresses are concentrated at the rear. Figure 9 shows that the largest micromovement was 7.215 μm, which was much smaller than 28 μm, showing that all five groups could have good bone
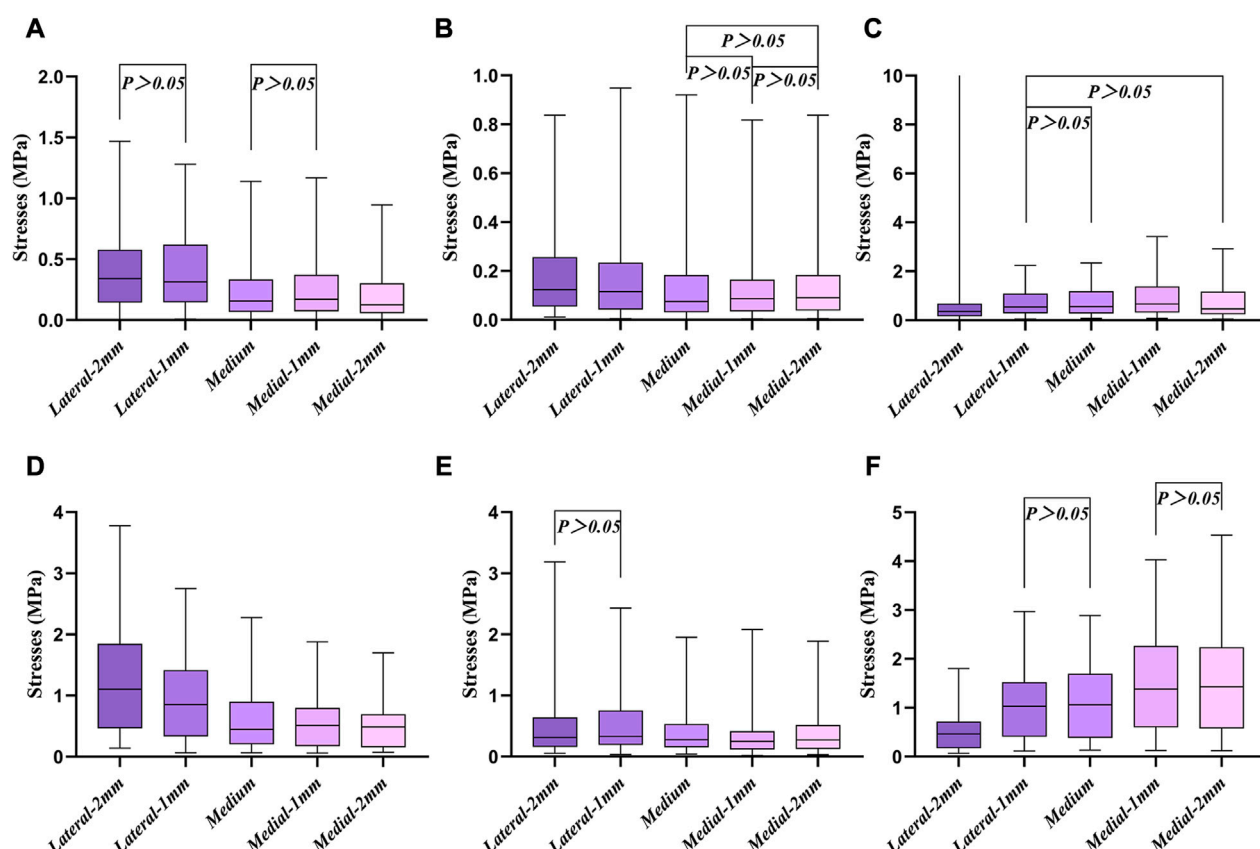
FIGURE 6
Box diagram of the first six different regions. **(A–F)** Six different regions of stress, corresponding to Figure 5, respectively.
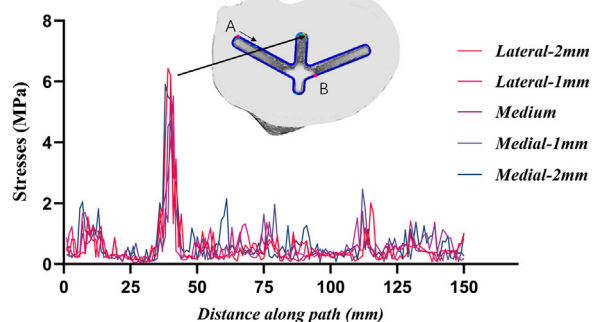
FIGURE 7
Stresses along the border of the stem cavity. Point A is the starting point and point B is the 100 mm position.
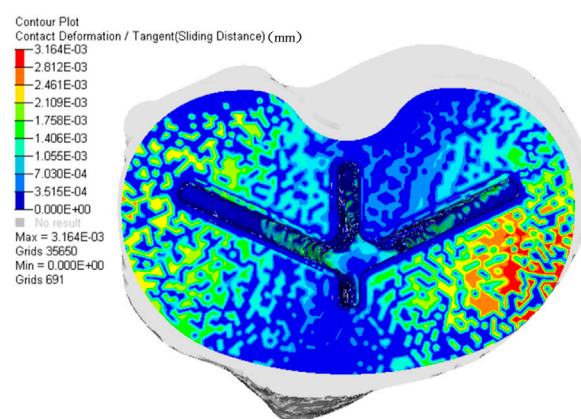
FIGURE 8
Micromotion cloud map when the platform is misaligned 1 mm to the lateral side.

growth in the future (Pilliar et al., 1986; Jasty et al., 1997). From Figure 10 it can be seen that the plateau presents more micromotion than the stem.

In summary, there is no significant effect on the proximal tibia whether the tibial plateau prosthesis is misaligned medially or laterally by 2 mm or 1 mm. However, according to the current study, the tibial plateau prosthesis should be properly aligned on

the tibial surface. A prosthesis overlapping the bony surface will have a negative impact on the surrounding soft tissues, such as the medial and lateral collateral ligaments, and especially upon the popliteal tendon (Bonnin et al., 2017). Dowson and Jin, (1986) showed that in synovial joints, micro-

FIGURE 9
Micromotion at different misalignment positions of the platform.

FIGURE 10
Micromotion at different misalignment positions of the plateau and stem.

conditions such as maximum force in the gait cycle were added in this study. Second, we did not consider the impact on the muscles and ligaments. Third, no synovial lubrication phenomena were considered in this study. Apart from these, Affatato et al. (2019) used *in-vitro* experimental investigation in the study of femoral prosthesis roughness. Such *in-vitro* experiments were not used in our study. In future studies, if the above details are included in the experiments, the results obtained may be more appropriate to clinical settings.

5 Conclusion

FEA of stress distribution and micromotion results showed that misalignment of the tibial plateau prosthesis by 2 or 1 mm medially or laterally during TKA did not significantly negatively affect the stress upon the proximal tibia. However, to prevent postoperative pain and stiffness due to impingement on the surrounding soft tissues and ligaments, it is important to consider and design the most appropriate prosthesis and ensure proper positioning for different patients.

Data availability statement

The raw data supporting the conclusion of this article will be made available by the authors, without undue reservation.

Ethics statement

The studies involving human participants were reviewed and approved by the Ethics committee of The Second Hospital of Jilin University. The patients/participants provided their written informed consent to participate in this study.

Author contributions

ZZ: Investigation, methodology, visualization, writing—original draft, writing—review and editing; YL: Investigation, methodology, supervision, validation, visualization, writing—review and editing; AZ: Software, validation, writing—review and editing. hc: software, validation, writing—review and editing. LZ: Clinical data collection, project administration. xw: clinical data collection, project administration. QW: Clinical data collection. qh: conceptualization, funding acquisition, project administration, resources, supervision, validation, writing—review and editing. JW: Conceptualization, funding acquisition, project administration, resources, supervision, validation.

Conflict of interest

The authors declare that the research was conducted in the absence of any commercial or financial relationships that could be construed as a potential conflict of interest.

elastohydrodynamic action largely smooths the initial roughness of the cartilage surface, which was then considered a form of lubrication responsible for the significant tribological properties of synovial joints. Later, Ruggiero, (2020) reviewed several theories on the natural synovial lubrication phenomenon in human joints that have been proposed over the years. These indicated that the synovial soft tissue was also closely related to friction. In order to achieve basic stability during the postoperative period without the formation of an alignment, the resistance to movement between the bone and the implant is optimized by increasing the friction at the interface. This is necessary because excessive relative movements can inhibit bone growth due to wear and tear of the bone and formation of fibrous tissue at the implant interface, which can lead to loosening and pain (de Vries et al., 2022). Therefore, oversizing or malposition should be avoided when installing a tibial plateau prosthesis during TKA.

This study has some limitations. First, we applied the stress under static conditions, without introducing dynamic factors such as squatting or walking. And no additional loading

Publisher's note

All claims expressed in this article are solely those of the authors and do not necessarily represent those of their affiliated organizations, or those of the publisher, the editors and the reviewers. Any product that may be evaluated in this article, or claim that may be made by its manufacturer, is not guaranteed or endorsed by the publisher.

References

Affatato, S., Merola, M., and Ruggiero, A. (2019). Tribological performances of total knee prostheses: Roughness measurements on medial and lateral compartments of retrieved femoral components. *Measurement* 135, 341–347. doi:10.1016/j.measurement.2018.11.072

Bedard, M., Vince, K. G., Redfern, J., and Collen, S. R. (2011). Internal rotation of the tibial component is frequent in stiff total knee arthroplasty. *Clin. Orthop. Relat. Res.* 469 (8), 2346–2355. doi:10.1007/s11999-011-1889-8

Bonnin, M. P., de Kok, A., Verstraete, M., Van Hoof, T., Van Der Straten, C., Saffarini, M., et al. (2017). Popliteus impingement after TKA may occur with well-sized prostheses. *Knee Surg. Sports Traumatol. Arthrosc.* 25 (6), 1720–1730. doi:10.1007/s00167-016-4330-8

Dalury, D. F., Pomeroy, D. L., Gorab, R. S., and Adams, M. J. (2013). Why are total knee arthroplasties being revised? *J. Arthroplasty* 28 (8), 120–121. doi:10.1016/j.arth.2013.04.051

de Vries, E., Sanchez, E., Janssen, D., Matthews, D., and van der Heide, E. (2022). Predicting friction at the bone - implant interface in cementless total knee arthroplasty. *J. Mech. Behav. Biomed. Mater* 128, 105103. doi:10.1016/j.jmbbm.2022.105103

Dong, Y., Zhang, Z., Dong, W., Hu, G., Wang, B., and Mou, Z. (2020). An optimization method for implantation parameters of individualized TKA tibial prosthesis based on finite element analysis and orthogonal experimental design. *BMC Musculoskelet. Disord.* 21 (1), 165. doi:10.1186/s12891-020-3189-5

Dowson, D., and Jin, Z. M. (1986). Micro-elastohydrodynamic lubrication of synovial joints. *Eng. Med.* 15 (2), 63–65. doi:10.1243/emed_jour_1986_015_019_02

Fraser, J. F., Werner, S., and Jacofsky, D. J. (2015). Wear and loosening in total knee arthroplasty: A quick review. *J. Knee Surg.* 28 (2), 139–144. doi:10.1055/s-0034-1398375

Guo, L., Yang, L., Briard, J. L., Duan, X. J., and Wang, F. Y. (2012). Long-term survival analysis of posterior cruciate-retaining total knee arthroplasty. *Knee Surg. Sports Traumatol. Arthrosc.* 20 (9), 1760–1765. doi:10.1007/s00167-011-1758-8

Indelli, P. F., Graceffa, A., Marcucci, M., and Baldini, A. (2016). Rotational alignment of the tibial component in total knee arthroplasty. *Ann. Transl. Med.* 4 (1), 3. doi:10.3978/j.issn.2305-5839.2015.12.03

Inoue, S., Akagi, M., Asada, S., Mori, S., Zaima, H., and Hashida, M. (2016). The valgus inclination of the tibial component increases the risk of medial tibial condylar fractures in unicompartmental knee arthroplasty. *J. Arthroplasty* 31 (9), 2025–2030. doi:10.1016/j.arth.2016.02.043

Ishii, Y., Noguchi, H., Sato, J., Todoroki, K., and Toyabe, S. (2015). Rotational alignment of tibial components in mobile-bearing TKA: Posterior substituted vs. PCL retaining. *Arch. Orthop. Trauma Surg.* 135 (9), 1299–1305. doi:10.1007/s00402-015-2275-x

Jasty, M., Bragdon, C., Burke, D., O'Connor, D., Lowenstein, J., and Harris, W. H. (1997). *In vivo* skeletal responses to porous-surfaced implants subjected to small induced motions. *J. bone Jt. Surg. Am. volume* 79 (5), 707–714. doi:10.2106/00004623-199705000-00010

Jin, Z. M., Dowson, D., and Fisher, J. (1995). Contact pressure prediction in total knee joint replacements. Part 1: General elasticity solution for elliptical layered contacts. *Proc. Inst. Mech. Eng. H.* 209 (1), 1–8. doi:10.1243/PIME_PROC_1995_209_311_02

Kutzner, I., Heinlein, B., Graichen, F., Bender, A., Rohlmann, A., Halder, A., et al. (2010). Loading of the knee joint during activities of daily living measured *in vivo* in five subjects. *J. Biomech.* 43 (11), 2164–2173. doi:10.1016/j.jbiomech.2010.03.046

Li, Y. R., Gao, Y. H., Yang, C., Ding, L., Zhang, X., Chen, H., et al. (2019). Finite-element analysis of the proximal tibial sclerotic bone and different alignment in total knee arthroplasty. *BMC Musculoskelet. Disord.* 20 (1), 617. doi:10.1186/s12891-019-3008-z

Liau, J. J., Cheng, C. K., Huang, C. H., Lee, Y. M., Chueh, S. C., and Lo, W. H. (1999). The influence of contact alignment of the tibiofemoral joint of the prostheses in *in vitro* biomechanical testing. *Clin. Biomech. (Bristol, Avon)* 14 (10), 717–721. doi:10.1016/s0268-0033(99)00027-3

Liau, J. J., Cheng, C. K., Huang, C. H., and Lo, W. H. (2002). The effect of malalignment on stresses in polyethylene component of total knee prostheses-a finite element analysis. *Clin. Biomech. (Bristol, Avon)* 17 (2), 140–146. doi:10.1016/s0268-0033(01)00109-7

Lin, Y., Ma, L., Zhu, Y., Lin, Z., Yao, Z., Zhang, Y., et al. (2017). Assessment of fracture risk in proximal tibia with tumorous bone defects by a finite element method. *Microsc. Res. Tech.* 80 (9), 975–984. doi:10.1002/jemt.22899

Maderbacher, G., Baier, C., Springorum, H. R., Maderbacher, H., Birkenbach, A. M., Benditz, A., et al. (2017). Impact of axial component alignment in total knee arthroplasty on lower limb rotational alignment: An *in vitro* study. *J. Knee Surg.* 30 (4), 372–377. doi:10.1055/s-0036-1592148

Maslov, L., Borovkov, A., Maslova, I., Soloviev, D., Zhmaylo, M., and Tarasenko, F. (2021). Finite element analysis of customized acetabular implant and bone after pelvic tumour resection throughout the gait cycle. *Mater. (Basel)* 14 (22), 7066. doi:10.3390/ma14227066

Matsuda, S., Whiteside, L. A., and White, S. E. (1999). The effect of varus tilt on contact stresses in total knee arthroplasty: A biomechanical study. *Orthopedics* 22 (3), 303–307. doi:10.3928/0147-7447-19990301-06

Minh, H. L., Park, W. M., Kim, K., Son, S.-W., Lee, S.-H., and Kim, Y. H. (2013). A new patient-specific planning method based on joint contact force balance with soft tissue release in total knee arthroplasty. *Int. J. Precis. Eng. Manuf.* 14 (12), 2193–2199. doi:10.1007/s12541-013-0297-2

Park, H. J., Bae, T. S., Kang, S. B., Baek, H. H., Chang, M. J., and Chang, C. B. (2021). A three-dimensional finite element analysis on the effects of implant materials and designs on periprosthetic tibial bone resorption. *PLoS One* 16 (2), e0246866. doi:10.1371/journal.pone.0246866

Perillo-Marcone, A., and Taylor, M. (2007). Effect of varus/valgus malalignment on bone strains in the proximal tibia after TKR: An explicit finite element study. *J. Biomech. Eng.* 129 (1), 1–11. doi:10.1115/1.2401177

Perillo-Marcone, A., Barrett, D. S., and Taylor, M. (2000). The importance of tibial alignment: Finite element analysis of tibial malalignment. *J. Arthroplasty* 15 (8), 1020–1027. doi:10.1054/arth.2000.17941

Pilliar, R. M., Lee, J. M., and Maniatopoulos, C. (1986). Observations on the effect of movement on bone ingrowth into porous-surfaced implants. *Clin. Orthop. Relat. Res.* 208 (208), 108–113. doi:10.1097/00003086-198607000-00023

Popescu, R., Haritinian, E. G., and Cristea, S. (2019). Relevance of finite element in total knee arthroplasty - literature review. *Chir. (Bucur)* 114 (4), 437–442. doi:10.21614/chirurgia.114.4.437

Rho, J. Y., Hobatho, M. C., and Ashman, R. B. (1995). Relations of mechanical properties to density and CT numbers in human bone. *Med. Eng. Phys.* 17 (5), 347–355. doi:10.1016/1350-4533(95)97314-f

Ruggiero, A., D'Amato, R., and Affatato, S. (2019). Comparison of meshing strategies in THR finite element modelling. *Mater. (Basel)* 12 (14), 2332. doi:10.3390/ma12142332

Ruggiero, A. (2020). Milestones in natural lubrication of synovial joints. *Front. Mech. Eng.* 6. doi:10.3389/fmech.2020.00052

Thompson, S. M., Yohuno, D., Bradley, W. N., and Crocombe, A. D. (2016). Finite element analysis: A comparison of an all-polyethylene tibial implant and its metal-backed equivalent. *Knee Surg. Sports Traumatol. Arthrosc.* 24 (8), 2560–2566. doi:10.1007/s00167-015-3923-y

Ün, K., and Çalık, A. (2016). Relevance of inhomogeneous–anisotropic models of human cortical bone: A tibia study using the finite element method. *Biotechnol. Biotechnol. Equip.* 30 (3), 538–547. doi:10.1080/13102818.2016.1154803

Venalainen, M. S., Mononen, M. E., Vaananen, S. P., Jurvelin, J. S., Toyras, J., Viren, T., et al. (2016). Effect of bone inhomogeneity on tibiofemoral contact mechanics during physiological loading. *J. Biomech.* 49 (7), 1111–1120. doi:10.1016/j.jbiomech.2016.02.033

Vessely, M. B., Whaley, A. L., Harmsen, W. S., Schleck, C. D., and Berry, D. J. (2006). The Chitranjan Ranawat Award: Long-term survivorship and failure modes of 1000 cemented condylar total knee arthroplasties. *Clin. Orthop. Relat. Res.* 452, 28–34. doi:10.1097/01.blo.0000229356.81749.11

Check for updates

Biomechanical comparison of intramedullary nail and plate osteosynthesis for extra-articular proximal tibial fractures with segmental bone defect

Weihang Gao[1,2†], Ke Zhao[1†], Yuanyuan Guo[3], Mao Xie[4], Xiaobo Feng[4], Ping Liu[2], Xin Xie[4]* and Dehao Fu[1]*

[1]Department of Orthopaedics, Shanghai Sixth People's Hospital Affiliated to Shanghai Jiao Tong University School of Medicine, Shanghai, China, [2]Department of Orthopaedics, Liyuan Hospital, Tongji Medical College, Huazhong University of Science and Technology, Wuhan, China, [3]Department of Pharmacy, Liyuan Hospital, Tongji Medical College, Huazhong University of Science and Technology, Wuhan, China, [4]Department of Orthopaedics, Union Hospital, Tongji Medical College, Huazhong University of Science and Technology, Wuhan, China

Purpose: Proximal tibial fractures are common, but the current available internal fixation strategies remain debatable, especially for comminuted fractures. This study aimed to compare the biomechanical stability of three internal fixation strategies for extra-articular comminuted proximal tibial fractures.

Methods: A total of 90 synthetic tibiae models of simulated proximal tibial fractures with segmental bone defects were randomly divided into three groups: Single lateral plating (LP), double plating (DP) and intramedullary nailing (IN). Based on the different number of fixed screws, the above three groups were further divided into nine subgroups and subjected to axial compression, cyclic loading and static torsional testing.

Results: The subgroup of intramedullary nailing with five proximal interlocking screws showed the highest axial stiffness of 384.36 ± 35.00 N/mm. The LP group obtained the lowest axial stiffness performance with a value of 96.59 ± 16.14 N/mm. As expected, the DP group offered significantly greater biomechanical stability than the LP group, with mean static axial stiffness and mean torque increasing by approximately 200% and 50%, respectively. According to static torsional experiments, the maximum torque of the DP subgroup was 3,308.32 ± 286.21 N mm, which outperformed all other groups in terms of torsional characteristics.

Conclusion: Utilizing more than four distal screws did not provide improved biomechanical stability in the LP or DP groups, while a substantial increase in the biomechanical stability of DP was obtained when an additional medial plate was used. For the intramedullary nailing group, increasing the number of proximal interlocking screws could significantly improve biomechanical stability, and the intramedullary nailing with three proximal interlocking screws had similar static and cyclic stiffness as the DP group. The intramedullary nailing with five proximal screws had better axial stability, whereas DP had better torsional stability.

Introduction

Extra-articular proximal tibial fractures, also known as proximal third tibia fractures, account for 5%–11% of all tibial fractures (Court-Brown and McBirnie, 1995; Buckley et al., 2011; Lowe et al., 2011). The management of such fractures is very challenging given the complexity of the proximal tibia's anatomical structure and the high demand for the reduction of major weight-bearing bones (Lembcke et al., 2001; Vestergaard et al., 2020; Shen et al., 2021). When the extra-articular proximal tibia is severely comminuted, a treatment utilizing low mechanical strength may fail to fix fracture sites, leading to looseness and breaking of implants and screws (Gosling et al., 2005; Janssen et al., 2007; Demirtas et al., 2019). In order to reduce failure or other complications, it is necessary to achieve a good reduction and rigid fixation of the comminuted fracture, allowing for early mobilization and functional exercise after surgery (Schütz et al., 2005).

The single lateral plate (LP), double plate (DP) and intramedullary nailing (IN) are the common internal fixation modalities for tibial fractures (Haidukewych et al., 2008; Kandemir et al., 2017), but the literature is inconclusive about what approach is best (Vallier et al., 2011; Lee et al., 2014). Previous finite element simulations showed that DP fixation had the best biomechanical stability compared to IN, and static axial stabilization was proportional to the number of distal screws and the length of the locking plate (Chen et al., 2018). When the distal screws of DP were gradually increased from four to eight, stepwise raise in the biomechanical stability was detected. However, other scholars reached different conclusions, showing that IN was superior to LP and DP fixation techniques in terms of static and cyclic compression properties (Feng et al., 2012; Lee et al., 2014). The inconsistent results may be caused by the different bone materials or parametric experimentation used. Finite element simulations also have their inherent shortcoming, which the materials of the cortical and cancellous bone were both simulated and probably did not reflect the actual conditions. Currently, most of the finite element simulations of bone are limited to static loading conditions, which may not adequately account for complicated loading that may occur in activities, because the dynamic imitation will require considerable computer resources and time (Pakdel et al., 2016; Chen et al., 2018). Biomechanical experiments are a more natural and realistic way to simulate complex physiological conditions, including cyclic loading and torsional testing.

To date, there are no reports regarding the comprehensive and systematic comparison of the biomechanical stability of LP, DP and IN fixation techniques in the literature. The optimal number of distal screws for a locking plate and the proximal interlocking screws for intramedullary nailing have long been debated. To that end, the present study investigated the biomechanical properties of three internal fixation strategies in combination with different numbers of screws using an extra-articular proximal tibial fracture model with segmental bone defects.

Materials and methods

Specimens and study groups

The current study used a total of 90 synthetic composite tibiae (type 1,110. SYNBONE AG, Malans, Switzerland). Three types of implants [locking compression plate for lateral proximal tibia,
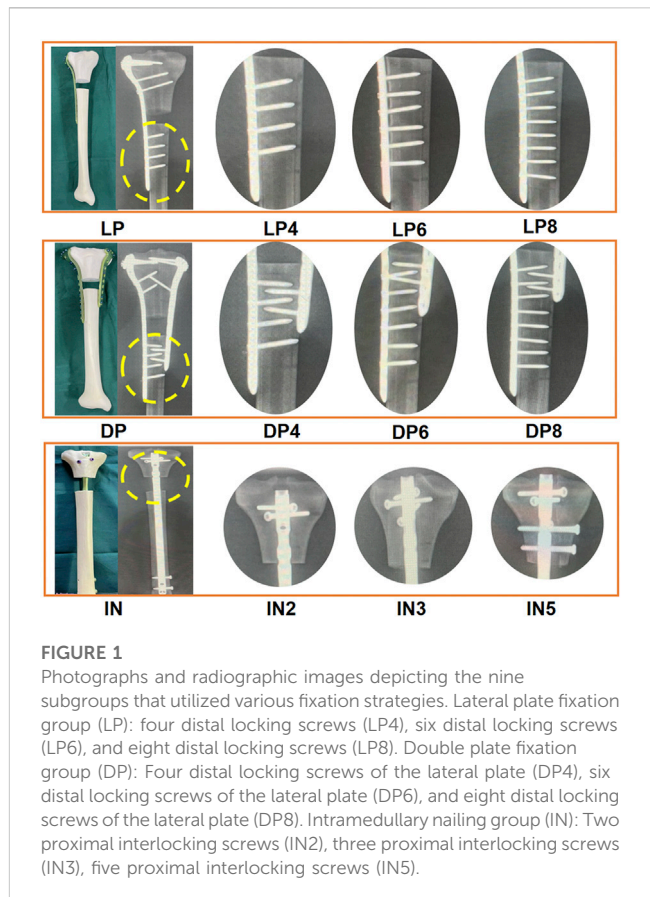
FIGURE 1
Photographs and radiographic images depicting the nine subgroups that utilized various fixation strategies. Lateral plate fixation group (LP): four distal locking screws (LP4), six distal locking screws (LP6), and eight distal locking screws (LP8). Double plate fixation group (DP): Four distal locking screws of the lateral plate (DP4), six distal locking screws of the lateral plate (DP6), and eight distal locking screws of the lateral plate (DP8). Intramedullary nailing group (IN): Two proximal interlocking screws (IN2), three proximal interlocking screws (IN3), five proximal interlocking screws (IN5).

locking compression plate for medial proximal tibia, and intramedullary nail (Double Medical Ltd., Xiamen, China)] were used in the study. Both lateral and medial proximal tibial locking plates were anatomically pre-contoured plates. All nails and plates were made of titanium alloys. An extra-articular proximal tibial segmental bone defect model was established in all specimens by templating cut lines on the synthetic bone at 70 mm and 90 mm from the medial tibial plateau to simulate the comminuted proximal tibial fractures (OTA type 41-A3.3) (Kandemir et al., 2017). A two cm synthetic bone fragment was removed without locking screw implantation in the defective zones (Figure 1). An experienced orthopedic surgeon performed all geometric measurements and established the fracture model. Finally, to rule out any damage resulting from implantation, a radiological examination of all the tibiae was conducted to confirm the exact position of the final implantation.

LP fixation group: The 3.5-mm L-shaped lateral plates with different numbers of distal locking screws were categorized into three subgroups (n = 10). The six proximal locking screws were identical for all three subgroups, with only the number of distal locking screws varying. The LP4 (176 mm in length), LP6 (203 mm in length) and LP8 (228 mm in length) subgroups received four, six and eight distal locking screws, respectively. Distal fixation was achieved by using 26 mm–28 mm bicortical screws.

DP fixation group: Three subgroups were established for models that used the double plate fixation strategy (n = 10). The T-shaped medial plate (135 mm in length) and nine proximal locking screws
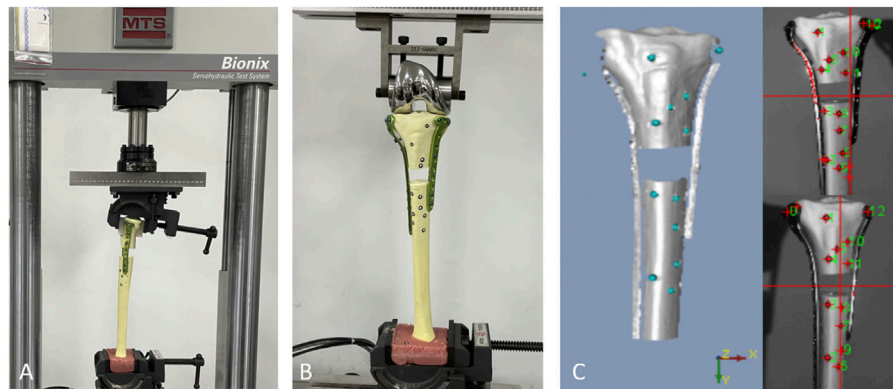
FIGURE 2
A biomechanical machine was used for torsional testing, **(A)** and a 3D-printed mold was used to fix the proximal fragment. **(B)** In the axial compression and cyclic loading test, the load was applied axially through the femoral component of a knee prosthesis. **(C)** The test setup showed the position of the optical measurement system markers.

were identical for all three subgroups, with only the number of distal locking screws differing. The DP4, DP6 and DP8 subgroups received four, six and eight distal locking screws, respectively. Distal fixation was achieved by using 26 mm–28 mm bicortical screws.

IN fixation group: Three subgroups were established for models that utilized intramedullary nailing (320 mm in length, 10 mm in diameter) ($n = 10$). The two distal locking screws were identical for all three subgroups, varying only in the number of proximal interlocking screws. The IN2, IN3 and IN5 groups were fixed using two, three and five proximal interlocking screws, respectively (Figure 1). The size of the screws was 5.0-mm diameter and 50–60 mm in length.

Experimental procedure

The synthetic tibias were potted distally in high-strength resin (Denture Base Materials) and mounted within the loading axis of a material-testing machine (MTS Bionix Servo-hydraulics Test Systems Model 370.02; MTS Systems) using custom-designed alignment fixtures that provided a consistent and repeatable orientation of the repaired tibiae in the loading frame (Figure 2B).

Each subgroup incorporated ten samples; five samples were used for axial compression and static torsional testing, while the other five samples were used for cyclic loading tests. In the axial compression and cyclic loading tests, the load was applied axially through the femoral component of a knee prosthesis. The pre-prepared 3D-printed clamping device was used in the static torsional test to clamp the proximal tibial fragment and facilitate a constant compressive gripping force (Figure 2A). An optoelectrical device with an accuracy of 0.01 mm was used to measure fracture gap movement and fragment displacement (KSCAN-Magic Composite 3D Scanner) (Figure 2C).

Axial compression test: The specimen was loaded with axial loading pressure starting from 0 N to 800 N, with a rate of 50 mm/min. Four load levels with a peak force of up to 200 N, 400 N, 600 N, and 800 N were adapted from previously reported data of the physiological compressive load on an adult knee during a single-limb stance (Ratcliff et al., 2007).

Cyclic loading test: The axial cyclic load was gradually loaded starting from 0 N and finishing at 400 N, at a frequency of 3 Hz for 10,000 cycles (Kandemir et al., 2017; Nie et al., 2020). Displacement was defined as the difference in the crosshead position from the peak of the first cycle to the peak of cycles 2,500, 5,000, 7,500, and 10,000.

Static torsional test: Each specimen was fixed on the mechanical testing machine, and the proximal fragment was able to rotate clockwise with the helical blade as the axis on the plane of the tibial fracture site. A 100 N preload was applied to the tibial plateau to maintain a stable of the tibial axial direction. Then torque was used at a load rate of 2°C/min from 0°C to 5°C.

Statistical analysis

All the data were represented using mean ± SD. Two-way analysis of variance (ANOVA) was used to compare three or more groups, while Student's t-test was used for two groups comparisons. All statistical analyses were performed using SPSS version 23.0 (IBM, Armonk, New York, United States). Graphs were generated using Graphpad Prism 8.0 (Graphpad Software Inc.). A p-value less than 0.05 was considered statistically significant.

Results

Throughout testing (including axial compression, cycle loading and static torsional testing), loading was continued unless implant-bone construction failure (plate loosening or deformation, or screw loosening or breakage) was detected. There were some small displacements during the reduction process, but the actual difference is very small and does not affect the distribution of screws, so the impact on mechanical stability is also negligible. Statistical analysis of axial stiffness, cycling stability and torsional properties under the same conditions found no significant difference

FIGURE 3
The different fixation modalities: lateral plate fixation groups (LP), double plate fixation groups (DP), intramedullary nailing groups (IN) and multiple comparisons. Values represent the mean axial displacements (measured in mm). (ns, no significant difference; *$p < 0.05$; **$p < 0.01$).
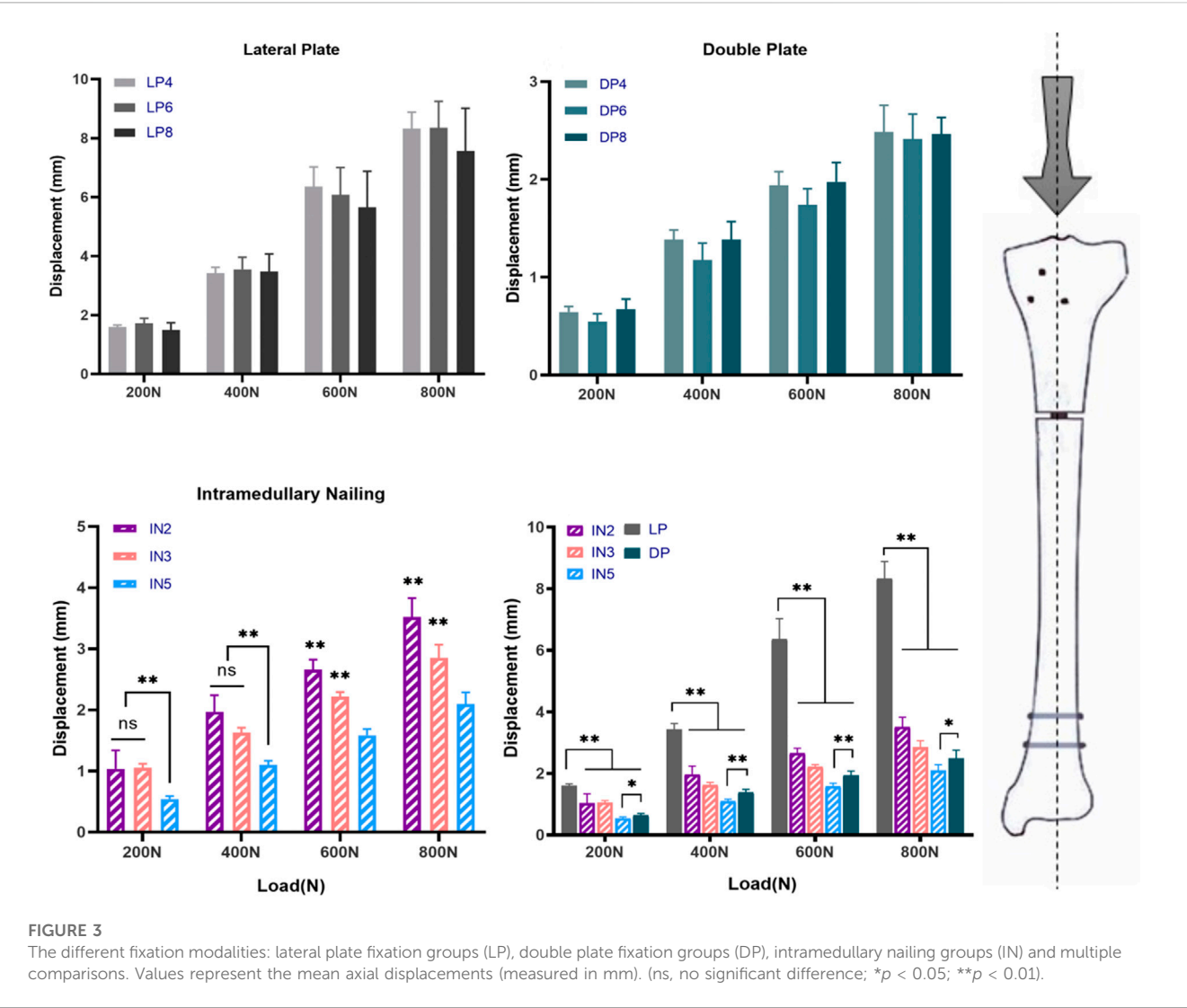
TABLE 1 Mean stiffness in N/mm of each group and standard deviation.

Group		Static loading		Cyclic loading	
		Mean	Median (min to max)	Mean	Median (min to max)
Lateral plate (LP)	LP4	104.33 ± 16.99	98.83 (86.46–130.14)	70.77 ± 2.54	70.99 (67.01–73.93)
	LP6	96.59 ± 16.14	96.92 (73.98–115.44)	71.06 ± 3.55	72.54 (65.03–74.18)
	LP8	108.61 ± 19.39	109.42 (81.79–132.01)	80.53 ± 9.55	77.88 (70.25–93.35)
Double plate (DP)	DP4	328.77 ± 25.35	316.96 (298.94–372.09)	137.10 ± 9.67	135.92 (126.18–152.79)
	DP6	338.39 ± 25.35	336.13 (315.33–380.43)	148.50 ± 11.88	147.71 (136.52–162.60)
	DP8	319.25 ± 30.54	321.67 (277.73–361.34)	141.50 ± 17.53	133.91 (125.47–169.78)
Intramedullary nailing (IN)	IN2	229.01 ± 21.41	217.86 (210.58–261.01)	131.58 ± 15.83	124.61 (116.72–156.68)
	IN3	291.43 ± 23.62	288.18 (268.19–326.04)	163.55 ± 16.81	164.81 (137.79–181.82)
	IN5	384.36 ± 35.00	387.60 (341.88–431.73)	190.19 ± 17.12	186.74 (167.93–213.90)

FIGURE 4
Axial static stiffness (median, range, *n* = 5) and significant differences among groups: lateral plate fixation groups (LP), double plate fixation groups (DP), intramedullary nailing groups (IN). (ns, no significant difference; *p* < 0.05; **p* < 0.01).
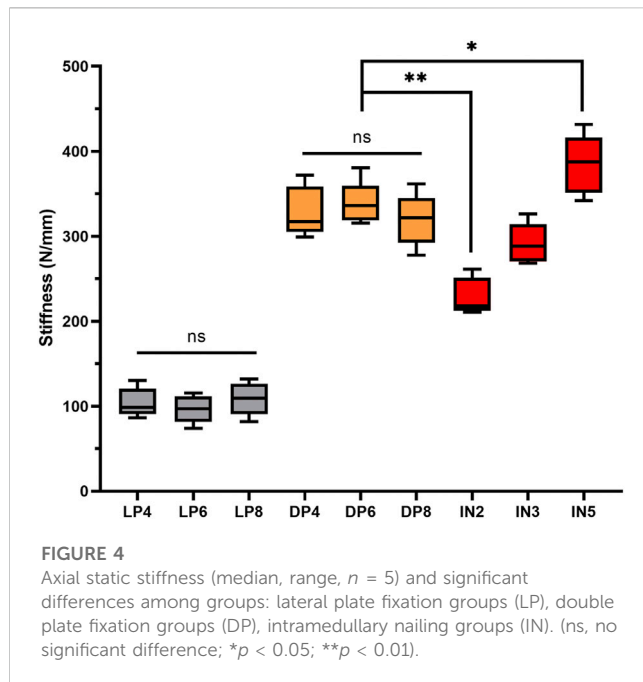
between LP4, LP6 and LP8 subgroups (*p* > 0.05) and between the DP4, DP6 and DP8 subgroups (*p* > 0.05) (Figure 3). As expected, the DP group offered significantly greater biomechanical stability than the LP group, with mean static axial stiffness and mean torque increasing by approximately 200% and 50%, respectively (Table 1). The IN5 subgroup showed the highest axial stiffness of 384.36 ± 35.00 N/mm. The LP group obtained the lowest axial stiffness performance with a value of 96.59 ± 16.14 N/mm. The static axial stiffness values in descending order are as follows: IN5 subgroup > DP group > IN3 subgroup > IN2 subgroup > LP group (Figure 4).

In the cyclic loading test, the displacement of the DP group in each cycle of the nodes was less than that of the IN2 subgroup (*p* > 0.05) but greater than that of the IN5 subgroup (*p* < 0.05). Compared to the LP group, the median stiffness values of the DP group improved by approximately 110%, while the IN5, IN3 and IN2 subgroups increased by around 160%, 120%, and 80%, respectively (Figure 5). In the static torsional test, the maximum torque of the DP subgroup was 3,308.32 ± 286.21 N mm, while that of the IN5 subgroup was 2,836.54 ± 300.84 N mm. Compared to the IN5 subgroup, the torsional characteristics of DP were boosted by more than 15% (Figure 6).

FIGURE 5
The different fixation modalities: lateral plate fixation groups (LP), double plate fixation groups (DP), intramedullary nailing groups (IN) and multiple comparisons. Values represent the mean axial displacement of the proximal tibial fragment after 10,000 cycles under 400 N axial loads. (measured in mm). (ns, no significant difference; *p* < 0.05; **p* < 0.01).
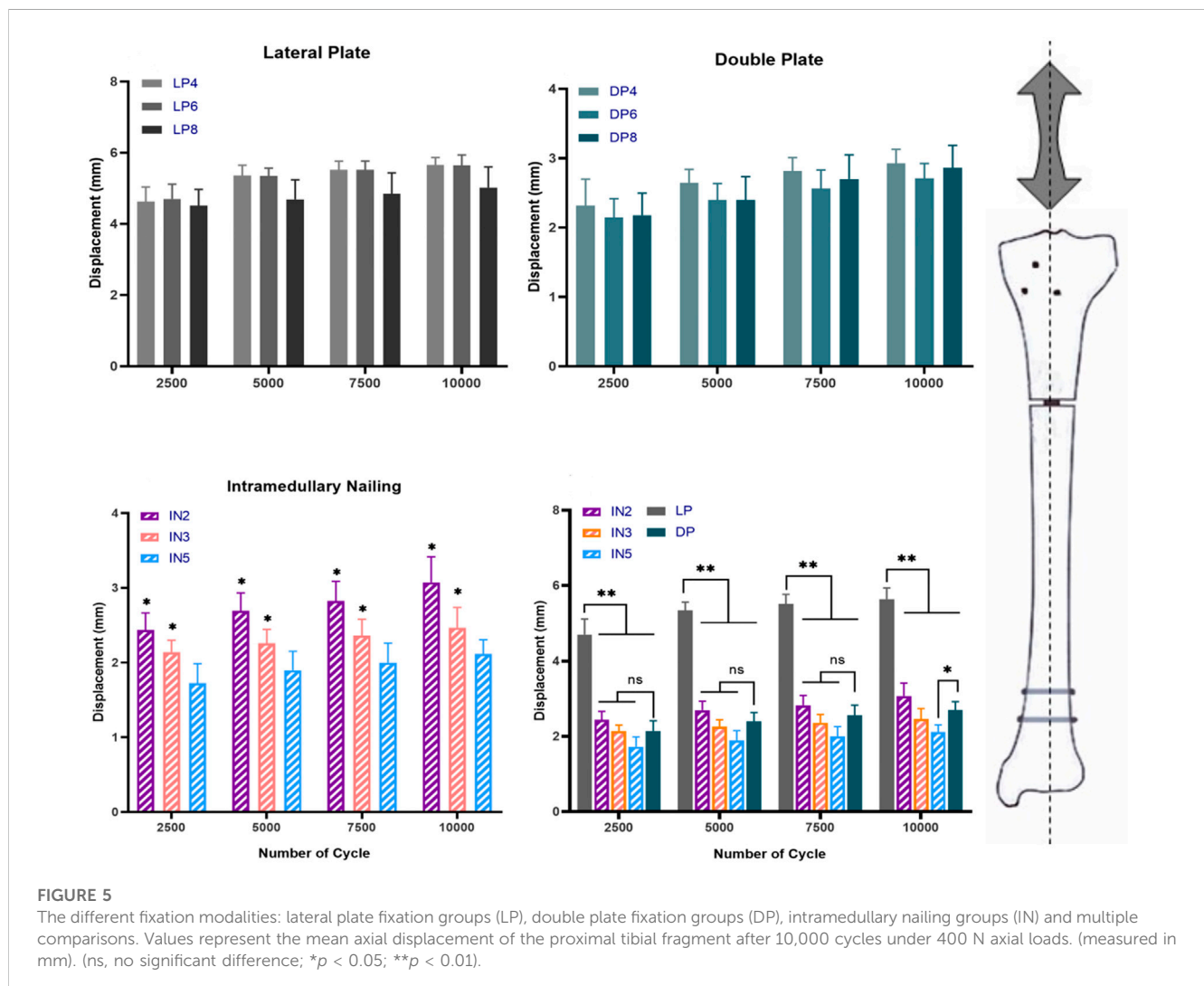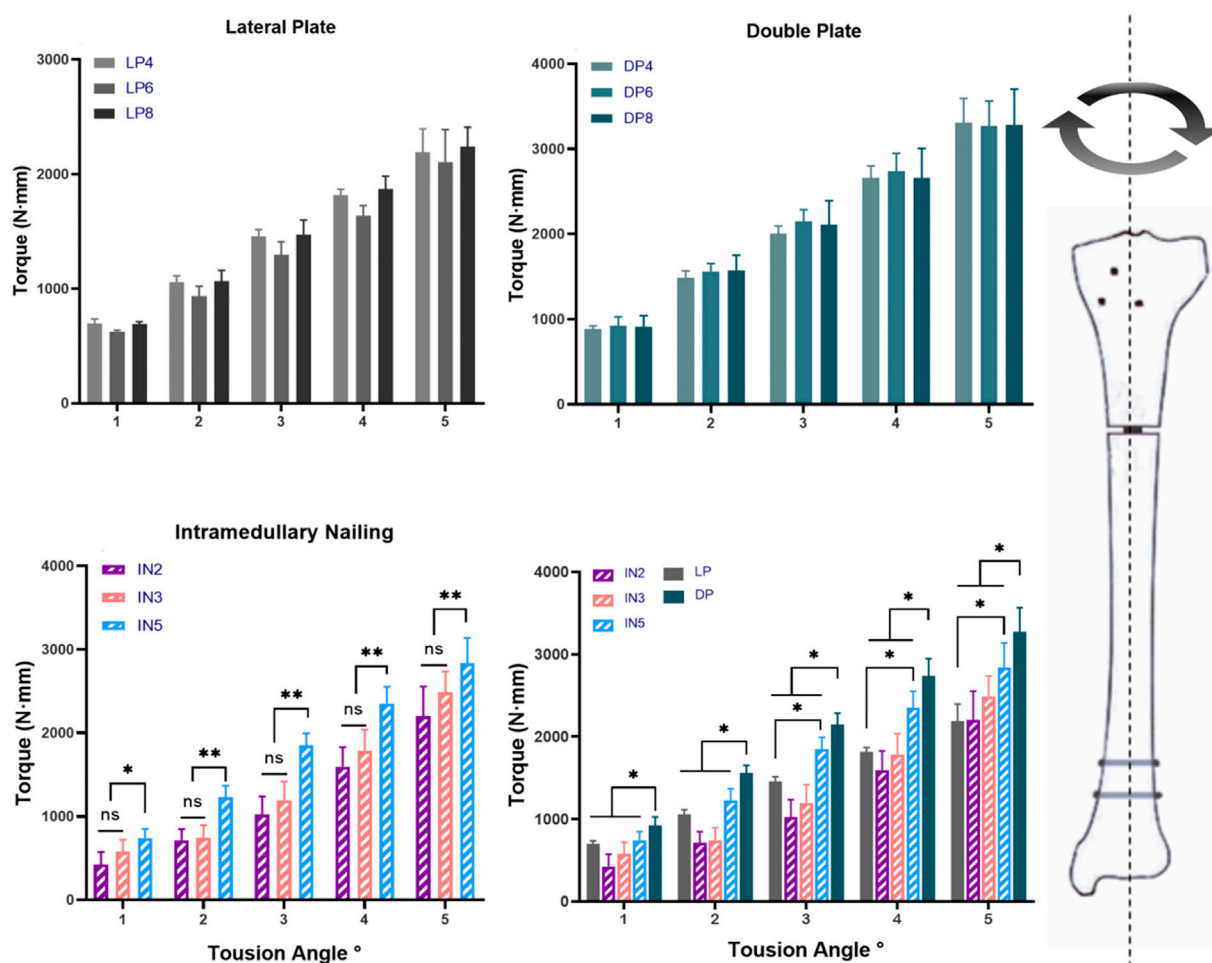
FIGURE 6
Torque and the torsion angle relationship of different models: lateral plate fixation groups (LP), double plate fixation groups (DP), intramedullary nailing groups (IN) and multiple comparisons. (ns, no significant difference; *$p < 0.05$; **$p < 0.01$).

Discussion

The intramedullary nailing and locking plate fixation have offered an alternative to treating proximal tibial fractures (Haidukewych et al., 2008; Kandemir et al., 2017). In recent years, a growing body of research has focused on improving the stability of internal fixation, as well as LP, DP, and IN fixation modalities (Freeman et al., 2011; Kandemir et al., 2017). Although several studies compared the stability of different internal fixations for extra-articular proximal tibial fractures, the conclusions were inconsistent. Some researchers have advocated the use of DP fixation on account of bilateral mechanical advantages, while others have considered LP and IN fixations as minimally invasive options that could provide acceptable biomechanical stability (Feng et al., 2012; Högel et al., 2013; Kandemir et al., 2017). Moreover, the number of screws required, not only for the locking plate but also for the intramedullary nail, is still controversial. Abundant studies have recommended that at least three screws should be inserted on either side of the fracture in each main fragment; adding a fourth screw had little effect on axial stability but could improve torsional stability

(Hertel et al., 2001; Gautier and Sommer, 2003; Cronier et al., 2010). Four screws are commonly used on either side of comminuted fractures in trauma surgery, but it is unclear whether further increasing distal screws would enhance biomechanical stability. Therefore, further comprehensive and systematic experiments with uniformly standardized fracture models and experimental parameters are required to establish a firm conclusion.

Our results showed that biomechanical stability was significantly lower in the LP group compared to the DP and IN groups, which could be explained by the LP belonging to the eccentric load carriers (Mueller et al., 2005). Additionally, our investigation revealed that the mean static stiffness increased about two-fold when a medial assisting plate was added. Similar results obtained from Lee et al. (2014) showed that double plating provided greater biomechanical stability than single-lateral plating, increasing by approximately 17.5%. Moreover, when the number of distal screws exceeded four, no obvious increase of the biomechanical stability was observed. This phenomenon could be explained by stress being concentrated in the region between the fracture gaps and strain being concentrated primarily in the near screw of the fracture line

(Cronier et al., 2010; Chen et al., 2018; Travascio et al., 2021). Taken together, we showed that double plating construct might be superior to LP fixation for treating proximal tibial fractures with segmental defect and no more than four distal locking screws recommended.

According to the present study, the IN5 subgroup had the highest biomechanical stability among the intramedullary nail groups, while the IN2 subgroup displayed the lowest. This would suggest that increasing proximal interlocking screws from two to five would significantly improve biomechanical stability when the intramedullary nail is used to fix tibial proximal fracture. Consistent with a previous report (Hansen et al., 2007; Horn et al., 2009; Gkouvas et al., 2019), the maximum number of proximal interlocking screws in all possible directions should be used to achieve maximum axial stability for intramedullary nailing. The DP group had lower static and cyclic stiffness than the IN5 subgroup, but significantly higher than that of the LP and IN2 groups and was comparable to the IN3 group. This result indicates that at least three proximal interlocking screws are required for IN to achieve the same axial stability as the DP group. Next, the torsional properties of the different internal fixation methods were further investigated in our study, as shown in Figure 6. The results revealed that the DP group showed the highest torsional properties compared to the IN and LP groups. The tibia was not only subjected to axial pressure from the knee joint, but internal and external rotation were also essential movements in routine activities. Double plating with more torsional resistance would provide more stability and safety during torsional movements. In terms of biomechanics, IN and DP fixations primarily provide axial and lateral support, respectively. The IN fixation method provided more axial stiffness for construct stability, whereas DP could handle torsional loads better. Although the IN technique has higher axial stiffness and less soft tissue injury, it could lead to the loss of proximal fragment fixation (Stedtfeld et al., 2004; Vallier et al., 2011). Considering the characteristics of DP fixation, which distributes stress more evenly, it might be more suitable to treat non-osteoporotic young patients who tend to fast recovery and whose bones are biomechanically sturdy. These biomechanical results did not recommend single lateral locking plates as the optimal fixation modality for patients with proximal tibial segmental defect or comminuted fracture due to the weak axial and torsional stability.

Nevertheless, it is undeniable that this study has some inherent limitations. Artificial bone models could not completely simulate the biological changes that occur *in vivo* because the soft tissues around the knee joint and the role of the fibula were not taken into account. Compared with cadaveric *in vitro* studies, the artificial bone models did not account for the physiological variations in density and distribution of force in the human bone.

Conclusion

Our study came to several conclusions based on the above findings. First, using more than four distal screws in the locking plate (LP and DP) did not improve biomechanical stability, which is completely different from the finite element mechanical analysis. Second, the biomechanical stability of IN was improved as the

proximal interlocking screws were increased. At least IN with three proximal interlocking screws is recommended to achieve sufficient stability, which has similar static and cyclic stiffness as the DP group. Third, the single lateral plate displayed relatively low stability and should be used with caution in patients with proximal tibial segmental defect or comminuted fractures. Instead of the DP always providing optimal biomechanical properties as in previous finite element analysis, our results showed better axial stability in IN5 and better torsional stability in DP fixation strategies.

Data availability statement

The original contributions presented in the study are included in the article/Supplementary Material, further inquiries can be directed to the corresponding authors.

Author contributions

WG: Prepared the manuscript draft, performed the experiments, collected the data, and approved the final manuscript. KZ: Collecting and analyzing the data, interpreting the data, writing, editing the manuscript, and approved the final manuscript. YG: Supervised the study, writing, editing the manuscript, and approved the final manuscript. MX: Performed the experiments, collected the data, revised, read, and approved the final manuscript. XF: Supervised the study and prepared the figures, tables, and approved the final manuscript. PL: Performed the specimen preparation, revised, read, and approved the final manuscript. XX: Performed the experiments, collected the data, read, and approve the final manuscript. DF: Conceived the idea, designed the study, and approved the final manuscript.

Conflict of interest

The authors declare that the research was conducted in the absence of any commercial or financial relationships that could be construed as a potential conflict of interest.

Publisher's note

All claims expressed in this article are solely those of the authors and do not necessarily represent those of their affiliated organizations, or those of the publisher, the editors and the reviewers. Any product that may be evaluated in this article, or claim that may be made by its manufacturer, is not guaranteed or endorsed by the publisher.

References

Buckley, R., Mohanty, K., and Malish, D. (2011). Lower limb malrotation following MIPO technique of distal femoral and proximal tibial fractures. *Injury* 42 (2), 194–199. doi:10.1016/j.injury.2010.08.024

Chen, F., Huang, X., Ya, Y., Ma, F., Qian, Z., Shi, J., et al. (2018). Finite element analysis of intramedullary nailing and double locking plate for treating extra-articular proximal tibial fractures. *J. Orthop. Surg. Res.* 13 (1), 12. doi:10.1186/s13018-017-0707-8

Court-Brown, C. M., and McBirnie, J. (1995). The epidemiology of tibial fractures. *J. Bone Jt. Surg. Br.* 77 (3), 417–421. doi:10.1302/0301-620x.77b3.7744927

Cronier, P., Pietu, G., Dujardin, C., Bigorre, N., Ducellier, F., and Gerard, R. (2010). The concept of locking plates. *Orthop. Traumatol. Surg. Res.* doi:10.1016/j.otsr.2010.03.008

Demirtas, A., Azboy, I., Alemdar, C., Gem, M., Ozkul, E., Bulut, M., et al. (2019). Functional outcomes and quality of life in adult ipsilateral femur and tibia fractures. *J. Orthop. Transl.* 16, 53–61. doi:10.1016/j.jot.2018.08.002

Feng, W., Fu, L., Liu, J., Qi, X., Li, D., and Yang, C. (2012). Biomechanical evaluation of various fixation methods for proximal extra-articular tibial fractures. *J. Surg. Res.* 178 (2), 722–727. doi:10.1016/j.jss.2012.04.014

Freeman, A. L., Craig, M. R., and Schmidt, A. H. (2011). Biomechanical comparison of tibial nail stability in a proximal third fracture: Do screw quantity and locked, interlocking screws make a difference? *J. Orthop. Trauma* 25 (6), 333–339. doi:10.1097/BOT.0b013e3181f982e5

Gautier, E., and Sommer, C. (2003). Guidelines for the clinical application of the LCP. *Injury* 34 (2), B63–B76. doi:10.1016/j.injury.2003.09.026

Gkouvas, G., Agathangelidis, F., Nakas, C., David, C., Sagris, D., and Petsatodis, G. (2019). Biomechanical comparison of six intramedullary nails, for the treatment of extra-articular, proximal tibial fractures. *Hippokratia* 23 (2), 58–63.

Gosling, T., Schandelmaier, P., Muller, M., Hankemeier, S., Wagner, M., and Krettek, C. (2005). Single lateral locked screw plating of bicondylar tibial plateau fractures. *Clin. Orthop. Relat. Res.* 439, 207–214. doi:10.1097/00003086-200510000-00036

Haidukewych, G., Sems, S. A., Huebner, D., Horwitz, D., and Levy, B. (2008). Results of polyaxial locked-plate fixation of periarticular fractures of the knee. Surgical technique. *J. Bone Jt. Surg. Am.* 90 (1), 117–134. doi:10.2106/JBJS.G.01086

Hansen, M., Mehler, D., Hessmann, M. H., Blum, J., and Rommens, P. M. (2007). Intramedullary stabilization of extraarticular proximal tibial fractures: A biomechanical comparison of intramedullary and extramedullary implants including a new proximal tibia nail (PTN). *J. Orthop. Trauma* 21 (10), 701–709. doi:10.1097/bot.0b013e31815aba5e

Hertel, R., Eijer, H., Meisser, A., Hauke, C., and Perren, S. M. (2001). Biomechanical and biological considerations relating to the clinical use of the Point Contact-Fixator--evaluation of the device handling test in the treatment of diaphyseal fractures of the radius and/or ulna. *Injury* 32 (2), B10–B14. doi:10.1016/s0020-1383(01)00121-8

Högel, F., Hoffmann, S., Panzer, S., Wimber, J., Bühren, V., and Augat, P. (2013). Biomechanical comparison of intramedullar versus extramedullar stabilization of intra-articular tibial plateau fractures. *Arch. Orthop. Trauma Surg.* 133 (1), 59–64. doi:10.1007/s00402-012-1629-x

Horn, J., Biert, J. H., and Linke, B. (2009). Angle stable interlocking screws improve construct stability of intramedullary nailing of distal tibia fractures: A biomechanical study. *Injury* 40(7):767–771. doi:10.1016/j.injury.2009.01.117

Janssen, K. W., Biert, J., and van Kampen, A. (2007). Treatment of distal tibial fractures: Plate versus nail: A retrospective outcome analysis of matched pairs of patients. *Int. Orthop.* 31 (5), 709–714. doi:10.1007/s00264-006-0237-1

Kandemir, U., Herfat, S., Herzog, M., Viscogliosi, P., and Pekmezci, M. (2017). Fatigue failure in extra-articular proximal tibia fractures: Locking intramedullary nail versus double locking plates-A biomechanical study. *J. Orthop. Trauma* 31 (2), e49–e54. doi:10.1097/BOT.0000000000000729

Lee, S-M., Oh, C-W., Oh, J-K., Kim, J. W., Lee, H. J., Chon, C. S., et al. (2014). Biomechanical analysis of operative methods in the treatment of extra-articular fracture of the proximal tibia. *Clin. Orthop. Surg.* 6 (3), 312–317. doi:10.4055/cios.2014.6.3.312

Lembcke, O., Rüter, A., and Beck, A. (2001). The nail-insertion point in unreamed tibial nailing and its influence on the axial malalignment in proximal tibial fractures. *Arch. Orthop. Trauma Surg.* 121 (4), 197–200. doi:10.1007/s004020000200

Lowe, J. A., Tejwani, N., Yoo, B., and Wolinsky, P. (2011). Surgical techniques for complex proximal tibial fractures. *J. Bone Jt. Surg. Am.* 93 (16), 1548–1559.

Mueller, C. A., Eingartner, C., Schreitmueller, E., Rupp, S., Goldhahn, J., Schuler, F., et al. (2005). Primary stability of various forms of osteosynthesis in the treatment of fractures of the proximal tibia. *J. Bone Jt. Surg. Br.* 87 (3), 426–432. doi:10.1302/0301-620x.87b3.14353

Nie, S., Li, M., Ji, H., Li, Z., Li, W., Zhang, H., et al. (2020). Biomechanical comparison of medial sustainable nail and proximal femoral nail antirotation in the treatment of an unstable intertrochanteric fracture. *Bone Jt. Res.* 9 (12), 840–847. doi:10.1302/2046-3758.912.BJR-2020-0284.R1

Pakdel, A., Fialkov, J., and Whyne, C. M. (2016). High resolution bone material property assignment yields robust subject specific finite element models of complex thin bone structures. *J. biomechanics* 49 (9), 1454–1460. doi:10.1016/j.jbiomech.2016.03.015

Ratcliff, J. R., Werner, F. W., Green, J. K., and Harley, B. J. (2007). Medial buttress versus lateral locked plating in a cadaver medial tibial plateau fracture model. *J. Orthop. Trauma* 21 (7), 444–448. doi:10.1097/bot.0b013e318126bb73

Schütz, M., Müller, M., Regazzoni, P., Hontzsch, D., Krettek, C., Van der Werken, C., et al. (2005). Use of the less invasive stabilization system (LISS) in patients with distal femoral (AO33) fractures: A prospective multicenter study. *Arch. Orthop. Trauma Surg.* 125 (2), 102–108. doi:10.1007/s00402-004-0779-x

Shen, J., Sun, D., Fu, J., Wang, S., Wang, X., and Xie, Z. (2021). Management of surgical site infection post-open reduction and internal fixation for tibial plateau fractures. *Bone Jt. Res.* 10 (7), 380–387. doi:10.1302/2046-3758.107.BJR-2020-0175.R2

Stedtfeld, H-W., Mittlmeier, T., Landgraf, P., and Ewert, A. (2004). The logic and clinical applications of blocking screws. *J. Bone Jt. Surg. Am.* 86-A (2), 17–25. doi:10.2106/00004623-200412002-00004

Travascio, F., Buller, L. T., Milne, E., and Latta, L. (2021). Mechanical performance and implications on bone healing of different screw configurations for plate fixation of diaphyseal tibia fractures: A computational study. *Eur. J. Orthop. Surg. Traumatol.* 31 (1), 121–130. doi:10.1007/s00590-020-02749-5

Vallier, H. A., Cureton, B. A., and Patterson, B. M. (2011). Randomized, prospective comparison of plate versus intramedullary nail fixation for distal tibia shaft fractures. *J. Orthop. Trauma* 25 (12), 736–741. doi:10.1097/BOT.0b013e318213f709

Vestergaard, V., Pedersen, A. B., Tengberg, P. T., Troelsen, A., and Schrøder, H. M. (2020). 20-year trends of distal femoral, patellar, and proximal tibial fractures: A Danish nationwide cohort study of 60,823 patients. *Acta Orthop.* 91 (1), 109–114. doi:10.1080/17453674.2019.1698148

Frontiers | Frontiers in Bioengineering and Biotechnology

Check for updates

Biomechanical comparison of anterior axis–atlanto–occipital transarticular fixation and anterior atlantoaxial transarticular fixation after odontoidectomy: A finite element analysis

Yuzhao Lu[1†], Gai Hang[2†], Yu Feng[2], Bo Chen[3], Shenghui Ma[2],
Yang Wang[1,4]* and Tianhao Xie[5]*

[1]The First Affiliated Hospital of Nanchang University, Nanchang University, Nanchang, Jiangxi, China,
[2]School of Medicine, Wuhan University of Science and Technology, Wuhan, Hubei, China, [3]Ruijin Hospital,
School of Medicine, Shanghai Jiao Tong University, Shanghai, China, [4]Beijing Chaoyang Hospital, Capital
Medical University, Beijing, China, [5]General Hospital of Central Theater Command, Wuhan, Hubei, China

Background: Anterior axis-atlanto-occipital transarticular fixation (AAOF) and anterior atlanto-axial transarticular fixation (AAF) are two common anterior screw fixation techniques after odontoidectomy, but the biomechanical discrepancies between them remain unknown.

Objectives: To investigate the biomechanical properties of craniovertebral junction (CVJ) after odontoidectomy, with AAOF or AAF.

Methods: A validated finite element model of the intact occipital-cervical spine (from occiput to T1) was modified to investigate biomechanical changes, resulting from odontoidectomy, odontoidectomy with AAOF, and odontoidectomy with AAF.

Results: After odontoidectomy, the range of motion (ROM) at C1-C2 increased in all loading directions, and the ROM at the Occiput-C1 elevated by 66.2%, 57.5%, and 41.7% in extension, lateral bending, and torsion, respectively. For fixation models, the ROM at the C1-C2 junction was observably reduced after odontoidectomy with AAOF and odontoidectomy with AAF. In addition, at the Occiput-C1, the ROM of odontoidectomy with AAOF model was notably lower than the normal model in extension (94.9%), flexion (97.6%), lateral bending (91.8%), and torsion (96.4%). But compared with the normal model, in the odontoidectomy with AAF model, the ROM of the Occiput-C1 increased by 52.2%, −0.1%, 92.1%, and 34.2% in extension, lateral bending, and torsion, respectively. Moreover, there were no distinctive differences in the stress at the screw-bone interface or the C2-C3 intervertebral disc between the two fixation systems.

Conclusion: AAOF can maintain CVJ stability at the Occiput-C1 after odontoidectomy, but AAF cannot. Thus, for patients with pre-existing atlanto-

Abbreviations: AAOF, anterior axis-atlanto-occipital transarticular fixation; AAF, anterior atlantoaxial transarticular fixation; CVJ, craniovertebral junction; FEM, finite element model; ROM, range of motion.

occipital joint instability, AAOF is more suitable than AAF in the choice of anterior fixation techniques.

Introduction

Pathological disorders in the craniovertebral junction (CVJ) including non-reducible ventral bony compression, rheumatoid inflammation, tumoral lesions, tubercular diseases, and metabolic-related diseases which usually lead to severe ventral compression (Yang and Gao, 1999; Kerschbaumer et al., 2000; Tubbs et al., 2016). To alleviate the compression of the brain stem or spinal cord, odontoidectomy (transoral or transnasal), is commonly used as an effective decompression approach. However, clinical and *in vitro* studies have indicated that this technique may give rise to progressive craniovertebral instability (Dickman et al., 1992; Dickman et al., 1995).

Posterior fixation is commonly performed as a subsequent operation following odontoidectomy to address CVJ instability (Grob et al., 1992). However, when posterior fixation is unavailable in some clinical cases, anterior fixation technology represented by anterior atlantoaxial transarticular fixation (AAF) has been developed as an alternative (Lu et al., 1998). Compared with posterior fixation, AAF is less likely to damage the vertebral artery and can be performed during odontoidectomy to avoid an additional operation (Sen et al., 2005). Besides, it was demonstrated that AAF was able to efficiently maintain the stability of C1-C2 after odontoidectomy (Magerl and Seemann, 1987). However, the stability at Occiput-C1 was also damaged after odontoidectomy, owing to the destroyed important structures, such as the anterior atlantooccipital membrane, the apical ligament, and the alar ligament which were closely related to the stability of Occiput-C1 (Dickman et al., 1992; Dickman et al., 1995). Moreover, the stability of Occiput-C1 is also crucial for the human body (Dvorak et al., 2003a), especially for patients with instability of Occiput-C1 for the pathology itself.

Anterior axis-atlanto-occipital transarticular fixation (AAOF) is another anterior fixation technique that can retain stability from the occiput to the axis (Dvorak et al., 2003a). Nevertheless, few biomechanical studies have examined whether AAOF can maintain CVJ stability (from the occiput to the axis) after odontoidectomy, and no study has examined the biomechanical difference between AAOF and AAF under odontoidectomy. Thus, our study aimed to investigate the biomechanical properties of AAOF after odontoidectomy and its differences from AAF after odontoidectomy.

Materials and methods

A previously reported nonlinear three-dimensional finite element model (FEM) of a normal whole cervical spine (C0-T1) was used in this study, as shown in Figure 1 (Xie et al., 2021). To validate the intact model, the predicted kinematic results were analyzed and compared with those reported in the literature (Penning, 1978; Penning and Wilmink, 1987; Lind et al., 1989; Panjabi et al., 1998; Ito et al., 2004; Ishii et al., 2006). The validated results of our whole cervical spine were presented in Supplementary Figure S1 (Xie et al., 2021). A CT scan of a healthy volunteer (34 years old, male, height 175 cm, body mass 70 kg) was used to build this finite element model. The detailed values for various materials and properties are the most commonly used values obtained from the literature (Xie et al., 2013; Xie et al., 2021). The material properties are detailed in Supplementary Tables S1–3 (Xie et al., 2021). And informed consent was obtained from the volunteer. The entire study was compliant with the Helsinki Declaration.

Based on the validated cervical spine model, odontoidectomy model, odontoidectomy with AAF model, and odontoidectomy with AAOF model were simulated in this study. The anatomical changes of the three surgical models were constructed according to the real surgical procedures reported in the literature (Figures 2A-I) (Dickman et al., 1995; Lu et al., 1998; Dvorak et al., 2003a; Xie et al., 2021). All models in our study, including the original complete spine model, were analyzed by the finite element software Abaqus 6.12.-1 (SIMULIA Inc, Providence, RI, United States). The selection of mesh type and mesh order in this analysis differs depending on the balance between the computational accuracy and modeling cost. For the bony structure of the cervical spine, C3D4 (linear tetrahedral) and C3D6 (linear trihedral) meshes were used for meshing. For the intervertebral discs, C3D8R (linear hexahedral) with hourglass control was used for modeling. All nodes on the lower surface of the T1 vertebral body were constrained to be fixed in all directions as boundary conditions. The vertebral body and ligaments were connected by shared nodes, and so are the different components of internal fixation. And for the intervertebral disc and the cortical bone, ties were used. A nonlinear surface-to-surface contact was used to simulate the interactions between vertebral joints. Screws are connected to the bones using an embedded setting. The elastic modulus of the medical titanium used for the construction of the AAF and AAOF screws was 110,000 MPa and Poisson's ratio was 0.30 (Rohlmann et al., 2007).

1. The Odontoidectomy model: The C1 anterior arch, C1-C2 anterior longitudinal ligament, anterior atlantooccipital membrane, odontoid, and the ligaments connecting to the odontoid (transverse ligament, alar ligament, apical ligament, and cruciate ligament vertical portion) were removed from the intact C0-T1 model (Dickman et al., 1995).
2. The AAF model (Odontoidectomy with AAF): The anterior atlantoaxial transarticular screw was added to the odontoidectomy model by using Solidworks/UGS software.
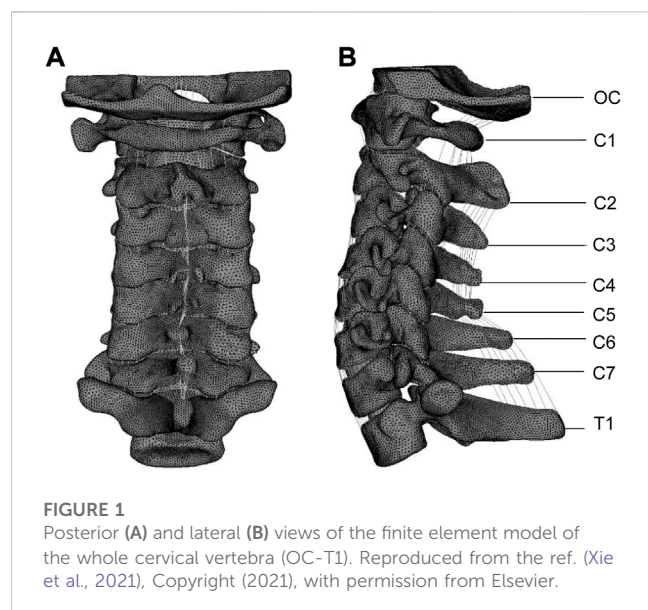
FIGURE 1
Posterior **(A)** and lateral **(B)** views of the finite element model of the whole cervical vertebra (OC-T1). Reproduced from the ref. (Xie et al., 2021), Copyright (2021), with permission from Elsevier.

And the screw insertion point was at the junction of the lateral edge of the C2 vertebral body to 4 mm above the inferior edge of the C2 anterior arch. The screw diameter and length were 3.5 mm and 15 mm, respectively (Lu et al., 1998).

3. The AAOF model (Odontoidectomy with AAOF): The anterior occiput-to-axis screw was drawn using Solidworks/UGS software and added to the odontoidectomy model according to the literature. The caudal of the center of the medial third of the C2 lateral mass articulation was the insertion point for AAOF. From the insertion point, the screw was placed obliquely in an outward, superior, and posterior direction, proceeding through the pivotal vertebral body, atlantoaxial joint, lateral atlantoaxial block, atlantooccipital joint, and successively anchored to the occipital condyle. To avoid injuring the sublingual neural tube and the vertebral artery, the screw was placed with a posterior angle of 25° and an external angle of 15° so that it connected with the posterior third of the occipital condyle. The screw diameter and length were 3.5 mm and 28 mm, respectively (Dvorak et al., 2003a).

Static analysis was conducted by imposing pure moments (sagittal, transverse, and frontal planes) of 1.5 Nm and a 50 N of compressive follower superior on the superior surfaces of occipital bone while the inferior surface of the T1 vertebra was rigidly fixed. ROM (°) values at Occiput-C1 and C1-C2 junctions of the four models including the normal model, odontoidectomy model, AAF model, and AAOF model under extension, flexion, lateral bending, and torsion conditions were measured. Accordingly, the percentage changes (%) of ROM for odontoidectomy model, AAF model, and AAOF model relative to the normal model were calculated ((surgical model-normal model)/normal model) and recorded to one decimal point. Besides, the maximum von Mises stress (MPa) on the implant and C2-C3 disc in the two anterior fixation models under extension, flexion, left bending, right bending, left torsion, and right torsion was also measured. The values of ROM changes and maximum stress mentioned above are shown in the histograms plotted by Prism 8.0 (GraphPad Software, United States).

Results

The ROM of the surgical models

Compared with the normal model, the ROM of odontoidectomy model at the Occiput-C1 junction increased by 66.2%, 57.5%, 41.7%, and −9.8% under loads of extension, lateral bending, torsion, flexion, respectively (Figure 3); the ROM at C1-C2 junction increased by 128.1%, 57.2%, 155.8%, and 32.8% in extension, flexion, lateral bending, and torsion, respectively (Figure 3).

At the C1-C2 junction, there was no significant difference between the two anterior fixation surgical models in the ROM changes (%) compared with the normal model (Figures 3C–F). In the AAF model, the ROM of the C1-C2 junction decreased by 66.1%, 93.8%, 83.5%, and 89.2% in extension, flexion, lateral bending, and torsion, respectively. In the AAOF model, the ROM of the C1-C2 junction decreased by 72.3%, 89.9%, 81.9%, and 91.5% in extension, flexion, lateral bending, and torsion, respectively.

But at the Occiput-C1 junction, the results revealed disparate trends of ROM changes (%) in the two anterior fixation surgical models (Figures 3C–F). In the AAF model, the ROM of the Occiput-C1 junction increased by 52.2%, −0.1%, 92.1%, and 34.2% in extension, flexion, lateral bending, and torsion, respectively. In the AAOF model, the ROM of the Occiput-C1 junction decreased by 94.9%, 97.6%, 91.8%, and 96.4% in extension, flexion, lateral bending, and torsion, respectively.

The maximum von Mises stress on the implant and C2-C3

Figure 4 and Supplementary Figures S2–6 presented the maximum von Mises stress on the screw and C2-C3 of AAF and AAOF models. The maximum stress of AAOF implantation under extension and flexion (170.2 MPa and 175.3MPa, respectively) was greater than that of AAF (164.1 MPa and 165MPa, respectively) (Figure 4 A; Supplementary Figures S2, 3). However, under left bending, right bending left torsion, and right torsion, the maximum stress of AAOF implantation (60.73Mpa, 53.69Mpa, 65.85Mpa, and 53.69Mpa, respectively) was less than that of AAF (75.92Mpa, 81.11Mpa, 98.76Mpa, and 89.78Mpa, respectively) (Figure 4A). There is no obvious difference in the maximum von Mises stresses on the C2-C3 junction in extension, flexion, left bending, right bending, left torsion, and right torsion (<1 MPa) among the AAF model, the AAOF model, and the normal model (Figure 4B; Supplementary Figures S4–6).

Discussion

In this study, a whole cervical spine model established and validated in our previous research (Xie et al., 2021) was used to investigate the biomechanics of surgical models and fixation techniques. Compared with the past studies which only constructed models of the upper cervical segment (Zhang et al., 2016; Chun et al., 2018), this study is more consistent with the integrity of the cervical spine.
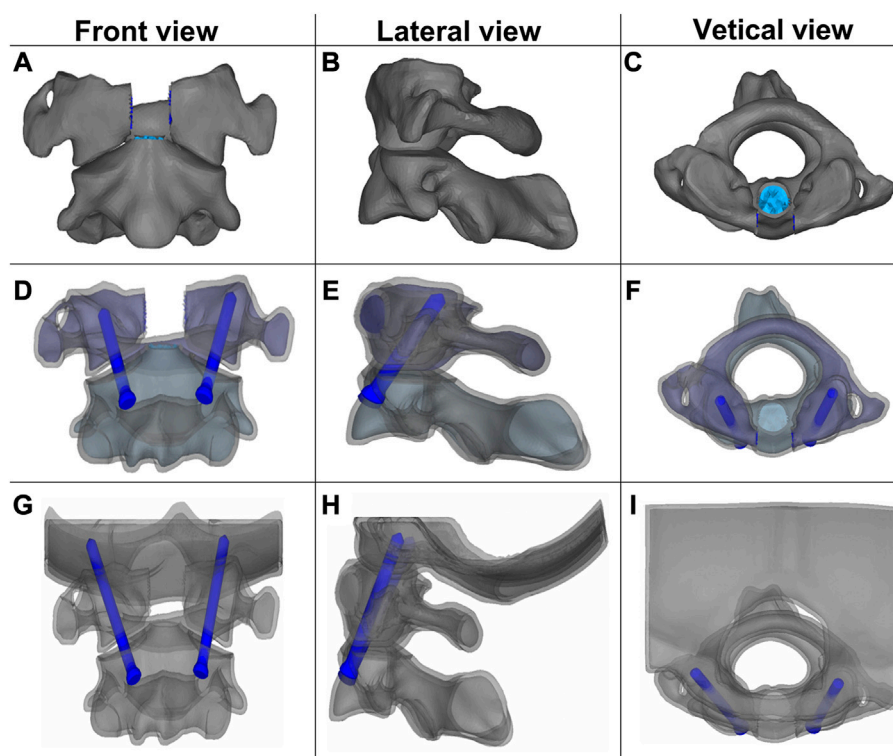
FIGURE 2
Front, lateral, and vertical views of the three surgical finite element models: Odontoidectomy **(A–C)**, AAF **(D–F)**, and AAOF **(G–I)** models. AAOF, anterior axis-atlanto-occipital transarticular fixation; AAF, anterior atlantoaxial transarticular fixation. **(A)** was reproduced from the ref. (Xie et al., 2021), Copyright (2021), with permission from Elsevier.

The stability of CVJ after odontoidectomy

Odontoidectomy was a standard surgical approach for anterior decompression since Kanavel et al. first used it in clinical practice (Kanavel, 1917). Considering the potential complications, the use of this operation is gradually decreasing with the introduction of posterior reduction techniques by Goel et al. (Goel, 2005). However, transoral odontoidectomy is still the first choice when posterior reduction techniques are not available. And Govindasamy et al. think the application scope of transoral odontoidectomy should be broader than the current use (Govindasamy et al., 2020).

The instability of the CVJ is one of the main complications after odontoidectomy. It is reported that more than two-thirds of patients experience significant spinal instability after odontoidectomy (Dickman et al., 1992). This operation may lead to significant biomechanical changes in the CVJ due to the excision of the odontoid process, anterior arch of the atlas, pterygoid ligament, odontoid apex ligament, transverse ligament, and other critical components attached to these bony structures. Dickman et al. found that odontoidectomy led to significant changes in ROM at the C1-C2 junction and load-deformation responses through simulated transoral odontoidectomy in human and baboon cadaveric specimens (Dickman et al., 1995). Our study also showed a similar result as Dickman et al. (Dickman et al., 1995) described and additionally demonstrated the instability of Oc-C1.

The C1-C2 junction is considered the main unstable segment after adenoidectomy (Dickman et al., 1992), and it is usually resolved with atlantoaxial fixation (Chang et al., 2016). However, the resection of the anterior C1 arch, anterior atlanto-occipital membrane, alar ligament, and apical ligament for odontoidectomy is related to instability of the occipital-C1. And in some cases, instability of the occipital-C1 already exists preoperatively, for example, in rheumatoid arthritis patients whose facet capsule ligament of occipital-C1 has been damaged by the primary disease. For these cases whose deformity or instability already exists at OC-C1 before odontoidectomy, the fixation of the occipital-C1 segment may be needed after odontoidectomy.

Fixation techniques after odontoidectomy

Craniocervical fixation techniques have significantly advanced from wiring and cabling to fixation-based rigid segmental approaches in recent years. The development of internal fixation techniques has greatly enhanced the biomechanical stability of the CVJ and provided higher fusion rates. Posterior fixation is currently the most commonly used fixation technique for the instability of CVJ (Takayasu et al., 2016). However, posterior fixation techniques may be limited in special cases including severe thoracic kyphosis, congenital or medical defects of the posterior bony structures, and anomalous vertebral artery anatomy. When posterior fixation is not possible, a transarticular anterior approach fixation can be used as an alternative
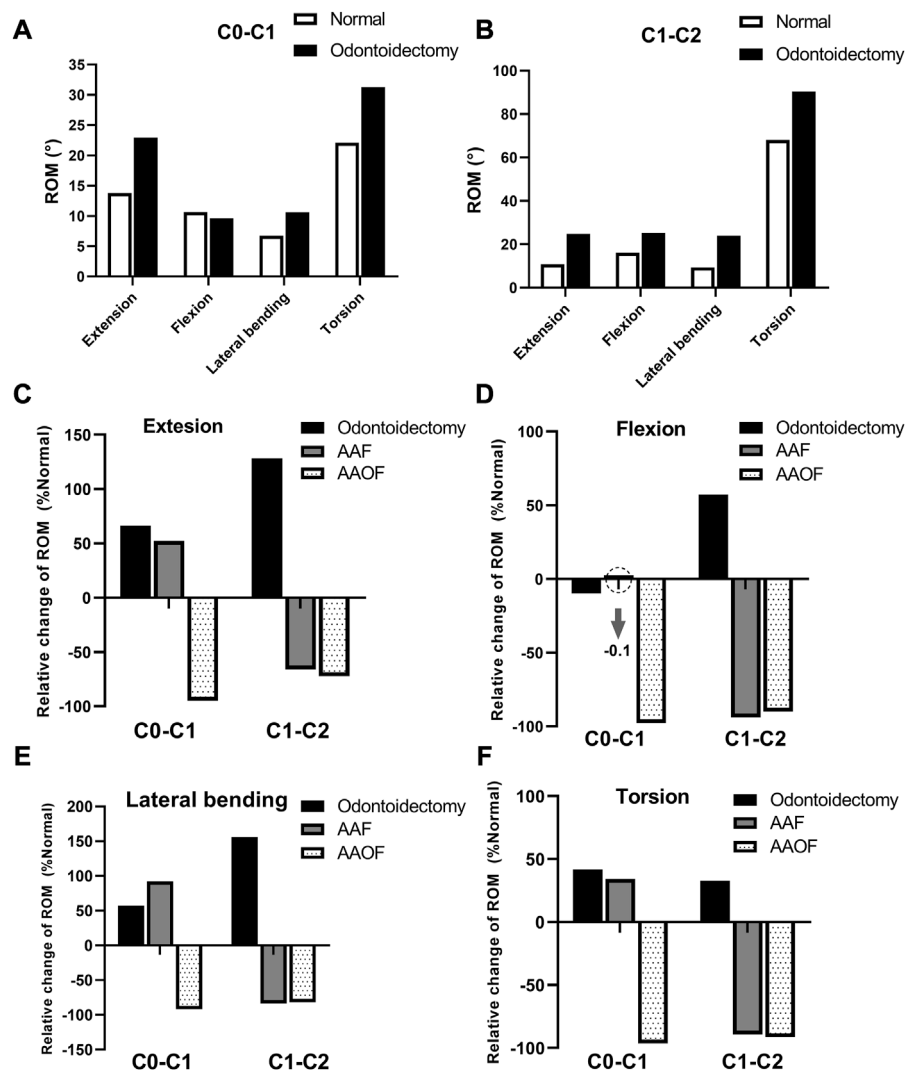
FIGURE 3
The changes of ROM (°) of the three surgical models compared to the normal model at Occiput–C1 and C1-C2 junctions. ROM = range of motion **(A, B)** presented the ROM (°) of odontoidectomy model and normal model at Occiput–C1 and C1-C2 junctions, respectively. And in **(C–F)**, the percentage change of ROMs for the odontoidectomy, AAF, and AAOF models relative to the normal model were shown.

solution. This surgical approach can be performed concurrently with odontoidectomy, which avoids the additional trauma associated with a posterior approach (Dvorak et al., 2003b). In our study, the virtual implantation of AFF screws was performed according to the method described by Lu et al. (Lu et al., 1998), the junction of the lateral edge of the C2 vertebral body to 4 mm above the inferior edge of the C2 anterior arch was chosen for the starting point. In the later studies, other researchers made different improvements in AAF screw placement based on actual anatomy and surgical needs (Reindl et al., 2003; Sen et al., 2005; Wu et al., 2010). AAOF is a less studied technique than AAF, and only a few studies explored this procedure and its biomechanical properties. This technique was first introduced by Dvorak et al. (Dvorak et al., 2003a) in 2003, they performed the AAOF procedure in eight human cervical spine specimens and described the method of screw placement and safe extent. And in a follow up study (Dvorak et al., 2003b), they compared the biomechanical properties of this anterior screw technique with the

traditional posterior fixation technique. After that, a few scholars further explored and improved this surgical method. Wu et al. (Wu et al., 2013) further explored the feasibility of percutaneous AAOF screw implantation and obtained good results in six patients. Moreover, according to the approach described by Dvorak et al., Cai et al. designed an anterior occiput-to-axis locking titanium plate system and explored the biomechanical performance differences between this technique and AAOF using finite element techniques (Cai et al., 2014). Besides rigid internal fixation, bone fusion also plays an important role in long-term postoperative stability (Goel, 2005; Goel et al., 2010). For transarticular screws, the most common method of bone grafting is posterior approach (Magerl and Seemann, 1987). Sasaki et, al (Sasaki et al., 2014) cured a patient with atlantoaxial instability by AAF and conventional posterior approach bone grafting. Dvorak et al. (Dvorak et al., 2003a) also presented in their article that the AAOF technique they invented required concomitant posterior bone grafting to facilitate long-term stable osseous union. However,
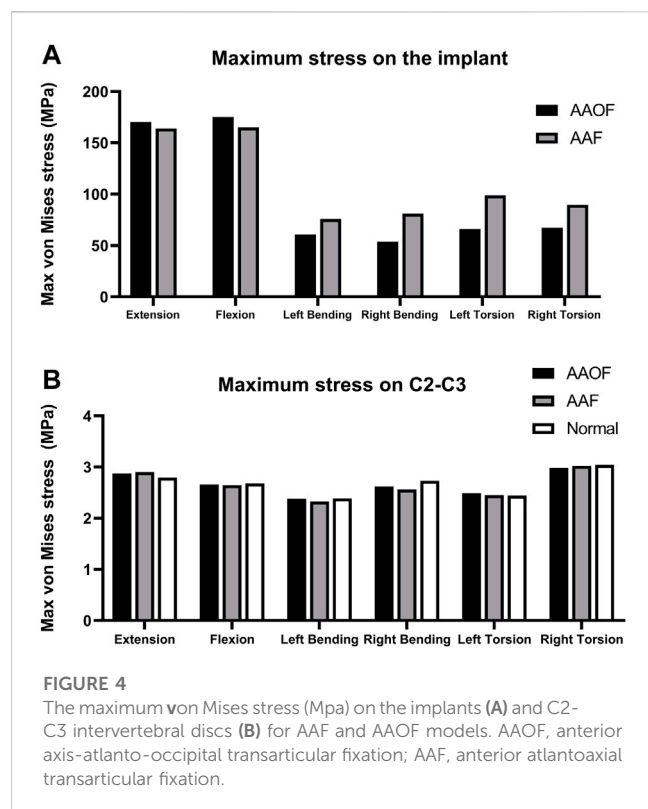
FIGURE 4
The maximum **v**on Mises stress (Mpa) on the implants **(A)** and C2-C3 intervertebral discs **(B)** for AAF and AAOF models. AAOF, anterior axis-atlanto-occipital transarticular fixation; AAF, anterior atlantoaxial transarticular fixation.

Wu et al. (Wu et al., 2013) modified the AAOF procedure, they decorticated the front of the occiput-C2 region and C1/C2 articular process by curette and abrasive drilling after AAOF screws were implanted and then grafted iliac cancellous bone to the front of occiput-C2 region and C1/C2 articular process through the protective tube. In a word, compared with posterior fixation, there is less available experience for anterior fixation techniques, their specific procedure details including the position and length of the screws, and the bone grafting method require further exploration.

Given that internal fixation could provide rigid constructs to promote bony fusion and decrease the need for external immobilization, our study mainly investigated the biomechanical characteristics of internal fixations. In a human cervical spine specimen study, the stability of CVJ after transarticular anterior fixation has been proven to be comparable to that after posterior fixation techniques (Kim et al., 2004). Recently, due to the noninvasive and repeatable characteristics, finite element analysis was widely used to evaluate the biomechanical characteristic of different internal fixation techniques (Chun et al., 2018; Jain and Khan, 2021; Jain and Khan, 2022). However, the differences between anterior and posterior transarticular fixations in the FEM had not been investigated. Thus, we also compared the C1-C2 ROM values of our AAF and AAOF models with that of Chun et al.'s and Kim et al.'s posterior transarticular screws (PTS). The results (Supplementary Table S4) showed that AAF and AAOF models were comparable to PTS models in C1-C2 ROM values under extension + flexion. In addition, slightly larger C1-C2 ROM values were observed in AAF and AAOF than in Chun et al.'s PTS model under lateral bending and torsion. The differences may be due to whole the cervical spine model used in our study, but the

C1-C2 cervical spine for Chun et al.'s study. The mean C1-C2 ROM values of Kim et al.'s PTS screws in sixteen cervical spine specimens were significantly greater than that of AAF, AAOF, and Chun et al.'s PTS FE models. This hints that there are some differences between cadaver and finite element studies.

AAOF and AAF were two classic anterior fixation techniques, and the biomechanical features of AAF after odontoidectomy had been demonstrated (Sen et al., 2005), but few studies had focused on the biomechanical characteristics of AAOF after odontoidectomy. To our knowledge, this is the first study to explore the biomechanical difference between AAF and AAOF after odontoidectomy. In the study, we simulated the biomechanical changes following anterior fixation of AAF and AAOF techniques after odontoidectomy based on a whole cervical spine model (-T1). Our results showed that AAOF and AAF produced similar decreases in ROM at the C1-C2 junction in extension, flexion, lateral bending, and torsion compared with the normal model (Figures 3C–F). Therefore, these two types of anterior fixations have the same effect in maintaining the stability of the C1-C2 segment. However, there were large differences in stability at Occiput-C1 between the AAOF and AAF fixation approaches. Due to additional occipital fixation, the movement of the Occiput-C1 segment can be significantly limited in all four directions after AAOF. In addition, ROM at Occiput-C1 significantly increased after AAF in all directions other than flexion. Therefore, we believe that AAOF is more effective in maintaining Occiput-C1 stability compared to AAF.

In our study, the maximum stress on the implant of AAOF was greater than that of AAF during extension and flexion. However, the differences can be ignored, as they were less than 10% (3.7% and 6.1% for extension and flexion, respectively) (the differences (%) of maximum stress on the implant between AAOF and AAF were calculated as (AAOF-AAF)/AAF). While the maximum stress on the implant of AAOF was significantly smaller than that of AAF during left bending, right bending, left torsion, and right torsion, the percent reductions for AAOF compared to AAF were 20.0%, 33.8%, 33.3%, and 24.9%, respectively. In addition, the maximum stress on the C2-C3 intervertebral disc did not significantly differ among the AAOF model, AAF model, and normal model.

The feasibility and indications of using AAOF

Ideally, the AAOF implantation enters at the caudal of C2 and sequentially crosses the C1 lateral mass towards the occipital condyle (Figures 2G, K, L) (Dvorak et al., 2003a). The sublingual neural tube is located in the anterior-middle third of the occipital condyle and comprises important anatomical structures such as the sublingual nerve, the venous plexus, and the meningeal branch of the ascending pharyngeal artery (Gray et al., 1995). Based on the anatomy of the hypoglossal canal and the occipital condyle, it is relatively safe for the screw tip to be located at the posterolateral third of the occipital condyle. In addition, due to the entry point of AAOF which is far from the vertebroarterial foramen, the anterior approach is less likely to damage the vertebral artery. Given that this surgical procedure probably led to injury to important structures including hypoglossal nerves and vertebral arteries, comprehensive preoperative evaluation of the individual occipitoatlantoaxial joint anatomy preoperatively and intraoperative navigational device are required.

Limitation

Although the material properties of the whole cervical spine model were derived from literature and the whole model had been validated by comparing it with previous results in our recent study. However, some deficiencies exist. Firstly, there is a certain gap between our FEM of the whole spine and the normal human body. The soft tissues such as muscles are ignored in this model, which has a certain influence on the experimental results. Besides, the shortcomings of not taking into account bone fusion in our study may lead to overestimated results in all simulations. The Finite element analysis is a physical approach to analyzing biomechanics, and once the bone fusion is modeled, there will be no mobility between the segments, so we cannot simulate the bone fusion using the finite element method. Thus, the computer-simulated results provided by Finite element analysis can only reflect the immediate postoperative status after internal fixation, rather than long-term stability.

Conclusion

Overall, odontoidectomy can produce instability at the Occiput-C1, while it is not clear that the abnormally increased ROM at the Occiput-C1 requires further fixation. After odontoidectomy, the stability of the Occiput-C1 is primarily maintained by the atlanto-occipital joint. Thus, if the patients have a pre-existing injury to the atlanto-occipital joint before odontoidectomy, Occiput-C1 stability will further deteriorate after the operation. For example, patients with rheumatoid arthritis may have a pre-existing injury to the atlanto-occipital joint (Kandziora et al., 1999). Under these circumstances, the patients will probably require Occiput-C1 fixation, and AAOF is more suitable than AAF for these patients.

Data availability statement

The original contributions presented in the study are included in the article/Supplementary Material, further inquiries can be directed to the corresponding author.

Ethics statement

This study was approved by the Ethics Committee of the Central Theater General Hospital of the Chinese PLA (Wuhan, China). Informed consent was obtained from the the volunteer.

Author contributions

Funding

Acknowledgments

Conflict of interest

The authors declare that the research was conducted in the absence of any commercial or financial relationships that could be construed as a potential conflict of interest.

Publisher's note

All claims expressed in this article are solely those of the authors and do not necessarily represent those of their affiliated organizations, or those of the publisher, the editors and the reviewers. Any product that may be evaluated in this article, or claim that may be made by its manufacturer, is not guaranteed or endorsed by the publisher.

Supplementary material

The Supplementary Material for this article can be found online at: https://www.frontiersin.org/articles/10.3389/fbioe.2023.1067049/full#supplementary-material

References

Cai, X., Yu, Y., Liu, Z., Zhang, M., and Huang, W. (2014). Three-dimensional finite element analysis of occipitocervical fixation using an anterior occiput-to-axis locking plate system: A pilot study. *Spine J.* 14 (8), 1399–1409. doi:10.1016/j.spinee.2013.08.025

Chang, P. Y., Yen, Y. S., Wu, J. C., Chang, H. K., Fay, L. Y., Tu, T. H., et al. (2016). The importance of atlantoaxial fixation after odontoidectomy. *J. Neurosurg. Spine* 24 (2), 300–308. doi:10.3171/2015.5.SPINE141249

Chun, D. H., Kim, K. N., Yi, S., Shin, D. A., and Ha, Y. (2018). Biomechanical comparison of four different atlantoaxial posterior fixation constructs in adults: A finite element study. *Spine* 43 (15), E891–E897. doi:10.1097/BRS.0000000000002584

Dickman, C. A., Crawford, N. R., Brantley, A. G., and Sonntag, V. K. (1995). Biomechanical effects of transoral odontoidectomy. *Neurosurgery* 36 (6), 1146–1153. doi:10.1227/00006123-199506000-00013

Dickman, C. A., Locantro, J., and Fessler, R. G. (1992). The influence of transoral odontoid resection on stability of the craniovertebral junction. *J. Neurosurg.* 77 (4), 525–530. doi:10.3171/jns.1992.77.4.0525

Dvorak, M. F., Fisher, C., Boyd, M., Johnson, M., Greenhow, R., and Oxland, T. R. (2003a). Anterior occiput-to-axis screw fixation: Part I: A case report, description of a new technique, and anatomical feasibility analysis. *Spine* 28 (3), E54–E60. doi:10.1097/01.BRS.0000042237.97483.7B

Dvorak, M. F., Sekeramayi, F., Zhu, Q., Hoekema, J., Fisher, C., Boyd, M., et al. (2003b). Anterior occiput to axis screw fixation: Part II: A biomechanical comparison with posterior fixation techniques. *Spine* 28 (3), 239–245. doi:10.1097/01.BRS.0000042229.38716.8D

Goel, A. (2005). Progressive basilar invagination after transoral odontoidectomy: Treatment by atlantoaxial facet distraction and craniovertebral realignment. *Spine* 30 (18), E551–E555. doi:10.1097/01.brs.0000179414.64741.7b

Goel, A., Shah, A., and Gupta, S. R. (2010). Craniovertebral instability due to degenerative osteoarthritis of the atlantoaxial joints: Analysis of the management of 108 cases. *J. Neurosurg. Spine* 12 (6), 592–601. doi:10.3171/2009.12.SPINE0999

Govindasamy, R., Preethish-Kumar, V., Gopal, S., and Rudrappa, S. (2020). Is transoral surgery still a relevant procedure in atlantoaxial instability? *Int. J. Spine Surg.* 14 (5), 657–664. doi:10.14444/7096

Gray, H., Bannister, L., and Berry, M. (1995). *Gray's Anatomy: The anatomical basis of medicine and surgery*. 38th ed. Edinburgh: Churchill Livingstone, 443–452.

Grob, D., Crisco, J., 3rd, Panjabi, M. M., Wang, P., and Dvorak, J. (1992). Biomechanical evaluation of four different posterior atlantoaxial fixation techniques. *Spine* 17 (5), 480–490. doi:10.1097/00007632-199205000-00003

Ishii, T., Mukai, Y., Hosono, N., Sakaura, H., Fujii, R., Nakajima, Y., et al. (2006). Kinematics of the cervical spine in lateral bending: *In vivo*: Three-dimensional analysis. *Spine* 31 (2), 155–160. doi:10.1097/01.brs.0000195173.47334.1f

Ito, S., Ivancic, P. C., Panjabi, M. M., and Cunningham, B. W. (2004). Soft tissue injury threshold during simulated whiplash: A biomechanical investigation. *Spine* 29 (9), 979–987. doi:10.1097/00007632-200405010-00006

Jain, P., and Khan, M. R. (2022). Comparison of novel stabilisation device with various stabilisation approaches: A finite element based biomechanical analysis. *Int. J. Artif. Organs* 45 (5), 514–522. doi:10.1177/03913988221088334

Jain, P., and Khan, M. R. (2021). Selection of suitable pedicle screw for degenerated cortical and cancellous bone of human lumbar spine: A finite element study. *Int. J. Artif. organs* 44 (5), 361–366. doi:10.1177/0391398820964483

Kanavel, A. (1917). Bullet located between the atlas and the base of the skull: Technique of removal through the mouth. *Surg. Clin. Chic.* 1, 361–366.

Kandziora, F., Mittlmeier, T., and Kerschbaumer, F. (1999). Stage-related surgery for cervical spine instability in rheumatoid arthritis. *Eur. Spine J.* 8 (5), 371–381. doi:10.1007/s005860050190

Kerschbaumer, F., Kandziora, F., Klein, C., Mittlmeier, T., and Starker, M. (2000). Transoral decompression, anterior plate fixation, and posterior wire fusion for irreducible atlantoaxial kyphosis in rheumatoid arthritis. *Spine* 25 (20), 2708–2715. doi:10.1097/00007632-200010150-00029

Kim, S. M., Lim, T. J., Paterno, J., Hwang, T. J., Lee, K. W., Balabhadra, R. S., et al. (2004). Biomechanical comparison of anterior and posterior stabilization methods in atlantoaxial instability. *J. Neurosurg. Spine* 100 (3), 277–283. doi:10.3171/spi.2004.100.3.0277

Lind, B., Sihlbom, H., Nordwall, A., and Malchau, H. (1989). Normal range of motion of the cervical spine. *Archives Phys. Med. rehabilitation* 70 (9), 692–695.

Lu, J., Ebraheim, N. A., Yang, H., Heck, B. E., and Yeasting, R. A. (1998). Anatomic considerations of anterior transarticular screw fixation for atlantoaxial instability. *Spine* 23 (11), 1229–1235. doi:10.1097/00007632-199806010-00011

Magerl, F., and Seemann, P. S. (1987). "Stable posterior fusion of the atlas and axis by transarticular screw fixation," in *Cervical spine I* (Vienna: Springer), 322–327. doi:10.1007/978-3-7091-8882-8_59

Panjabi, M., Nibu, K., and Cholewicki, J. (1998). Whiplash injuries and the potential for mechanical instability. *Eur. Spine J.* 7 (6), 484–492. doi:10.1007/s005860050112

Penning, L. (1978). Normal movements of the cervical spine. *Am. J. Roentgenol.* 130 (2), 317–326. doi:10.2214/ajr.130.2.317

Penning, L., and Wilmink, J. (1987). Rotation of the cervical spine. A CT study in normal subjects. *Spine* 12 (8), 732–738. doi:10.1097/00007632-198710000-00003

Reindl, R., Sen, M., and Aebi, M. (2003). Anterior instrumentation for traumatic C1-C2 instability. *Spine (Phila Pa 1976)* 28 (17), E329–E333. doi:10.1097/01.BRS.0000083328.27907.3B

Rohlmann, A., Burra, N. K., Zander, T., and Bergmann, G. (2007). Comparison of the effects of bilateral posterior dynamic and rigid fixation devices on the loads in the lumbar spine: A finite element analysis. *Eur. Spine J.* 16 (8), 1223–1231. doi:10.1007/s00586-006-0292-8

Sasaki, M., Matsumoto, K., Tsuruzono, K., Yoshimura, K., Shibano, K., and Yonenobu, K. (2014). Anterior transarticular screw fixation as a conventional operation for rigid stabilization. *Surg. Neurol. Int.* 5 (15), S544–S547. doi:10.4103/2152-7806.148032

Sen, M. K., Steffen, T., Beckman, L., Tsantrizos, A., Reindl, R., and Aebi, M. (2005). Atlantoaxial fusion using anterior transarticular screw fixation of C1–C2: Technical innovation and biomechanical study. *Eur. Spine J.* 14 (5), 512–518. doi:10.1007/s00586-004-0823-0

Takayasu, M., Aoyama, M., Joko, M., and Takeuchi, M. (2016). Surgical Intervention for instability of the craniovertebral junction. *Neurol. medico-chirurgica* 56, 2015–0342. doi:10.2176/nmc.ra.2015-0342

Tubbs, R. S., Demerdash, A., Rizk, E., Chapman, J. R., and Oskouian, R. J. (2016). Complications of transoral and transnasal odontoidectomy: A comprehensive review. *Child's Nerv. Syst.* 32(1), 55–59. doi:10.1007/s00381-015-2864-6

Wu, A. M., Chi, Y. L., Weng, W., Xu, H. Z., Wang, X. Y., and Ni, W. F. (2013). Percutaneous anterior occiput-to-axis screw fixation: Technique aspects and case series. *Spine J.* 13 (11), 1538–1543. doi:10.1016/j.spinee.2013.05.056

Wu, Y. S., Chi, Y. L., Wang, X. Y., Xu, H. Z., Lin, Y., Mao, F. M., et al. (2010). Microendoscopic anterior approach for irreducible atlantoaxial dislocation: Surgical techniques and preliminary results. *J. Spinal Disord. Tech.* 23 (2), 113–120. doi:10.1097/BSD.0b013e3181988bf5

Xie, T., Feng, Y., Chen, B., and Ma, L. (2021). Biomechanical evaluation of the craniovertebral junction after odontoidectomy with anterior C1 arch preservation: A finite element study. *Clin. Neurology Neurosurg.* 211, 2–5. doi:10.1016/j.clineuro.2021.106987

Xie, T., Qian, J., Lu, Y., Chen, B., Jiang, Y., and Luo, C. (2013). Biomechanical comparison of laminectomy, hemilaminectomy and a new minimally invasive approach in the surgical treatment of multilevel cervical intradural tumour: A finite element analysis. *Eur. Spine J.* 22 (12), 2719–2730. doi:10.1007/s00586-013-2992-1

Yang, S. Y., and Gao, Y. Z. (1999). Clinical results of the transoral operation for lesions of the craniovertebral junction and its abnormalities. *Surg. Neurol.* 51 (1), 16–20. doi:10.1016/S0090-3019(97)00501-6

Zhang, B., Liu, H., Cai, X., Wang, Z., Xu, F., Liu, X., et al. (2016). Biomechanical comparison of modified TARP technique versus modified Goel technique for the treatment of basilar invagination: A finite element analysis. *Spine* 41 (8), E459–E466. doi:10.1097/BRS.0000000000001297

Computed tomography Osteoabsorptiometry: Review of bone density, mechanical strength of material and clinical application

Guanghua Xu [1,2,3†], Qiuyuan Wang [4†], Zhiqiang Li [5] and Tingrui Wu [1]*

[1]Orthopedic Center, Affiliated Hospital of Guangdong Medical University, Zhanjiang, China, [2]Guangdong Engineering Research Center for Translation of Medical 3D Printing Application, Guangdong Provincial Key Laboratory of Medical Biomechanics, National Key Discipline of Human Anatomy, School of Basic Medical Sciences, Southern Medical University, Guangzhou, China, [3]Institute of Sport and Exercise Medicine, North University of China, Taiyuan, China, [4]Graduate School of Beijing University of Chinese Medicine, Beijing, China, [5]School of Physical Education, North University of China, Taiyuan, China

Computed Tomography (CT) imaging is an effective non-invasive examination. It is widely used in the diagnosis of fractures, arthritis, tumor, and some anatomical characteristics of patients. The density value (Hounsfield unit, HU) of a material in computed tomography can be the same for materials with varying elemental compositions. This value depends on the mass density of the material and the degree of X-ray attenuation. Computed Tomography Osteoabsorptiometry (CTOAM) imaging technology is developed on the basis of CT imaging technology. By applying pseudo-color image processing to the articular surface, it is used to analyze the distribution of bone mineralization under the articular cartilage, evaluate the position of prosthesis implantation, track the progression of osteoarthritis, and determine the joint injury prognosis. Furthermore, this technique was combined with indentation testing to discuss the relationship between the high bone density area of the articular surface, the mechanical strength of the bone, and the anchorage stability of the implant, in addition to the study of the relationship between mechanical strength and bone density. This narrative study discusses the pre- and postoperative evaluation of medical device implantation position, orthopedic surgery, and the clinical treatment of bone injury and degeneration. It also discusses the research status of CTOAM technology in image post-processing engineering and the relationship between bone material and mechanical strength.

1 Introduction

Bone is an organ with active metabolism, which is constantly reshaped throughout life. Bone remodeling involves the removal of mineralized bone by osteoclasts, the formation of bone matrix by osteoblasts, and then the formation of mineralization. The reconstruction cycle includes three consecutive stages: absorption, conversion and post formation (HADJIDAKIS and ANDROULAKIS, 2006). Bone remodeling is to adjust the bone structure to meet the changing mechanical needs, repair minor damage in the bone matrix, and prevent the accumulation of old bone. Therefore, the bone turnover sequence needs to be strictly controlled by the body. If the body has serious abnormal
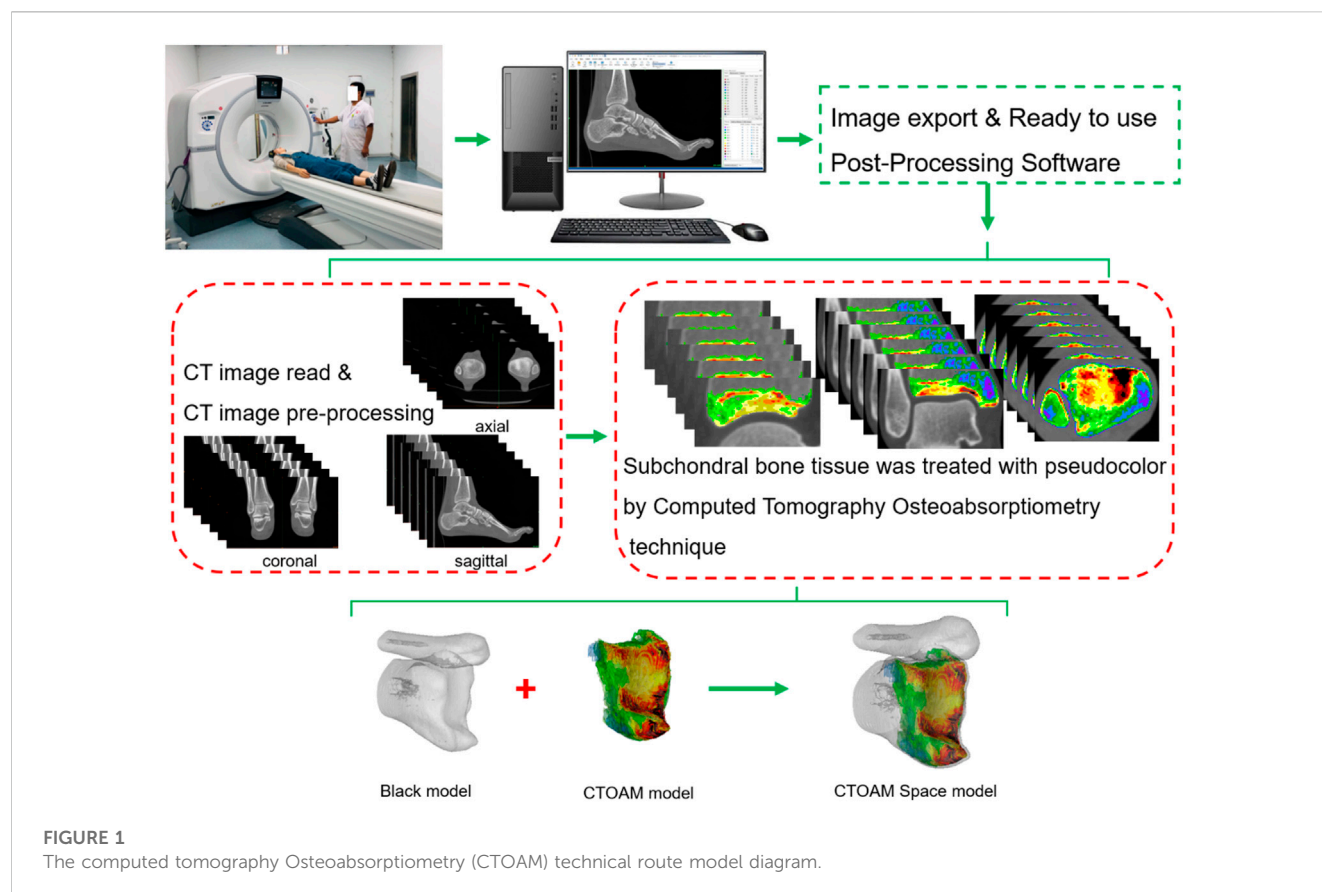
FIGURE 1
The computed tomography Osteoabsorptiometry (CTOAM) technical route model diagram.

bone absorption or bone remodeling imbalance, there would be rapid bone loss and bone growth in the body, especially for the rehabilitation of patients after joint orthopedic surgery, the probability of osteoporosis and fracture.

Computed tomography (CT) is a cross-sectional 2D image and 3D reconstruction model method based on the photoelectric signal conversion formed by the absorption and attenuation effect between X-ray photons and human tissue, and formed by a post-processing system. The attenuation value (HU) corresponding to bone tissue is converted to the equivalent value of bone tissue by calibrating the mold body with hydroxyapatite ceramic and special analysis software. CT has been widely used for diagnosis in clinical practice. It is believed that fracture risk is affected by changes in the structure of specific bone sites, including the different functional roles of cortical bone and trabecular bone, which proves that the efforts to analyze these entities alone are reasonable (Kemp et al., 2014).

The computed tomography Osteoabsorptiometry (CTOAM) technology is a CT image processing technology that uses the absorption attenuation effect between X-ray photons and human bone tissue to form a topographic map of bone tissue specificity with different densities. It was invented by Muller Gerbl et al. in the early 1989s (Müller-Gerbl et al., 1989). According to Wolff's law, bones adapt to functional needs through remodeling, which can also reflect the distribution of resultant forces acting on the bone. This method does not focus on the quantitative calculation of absolute value. The key of this method is to present the difference in relative density on the surface and inside the joint. Due to its relatively greater stiffness

and strength than the covered articular cartilage, the subchondral bone absorbs most of the mechanical force transmitted by the double joint joints and provides mechanical support for the covered articular cartilage (Layton et al., 1988; Madry, 2010). Compared with the relatively slow articular cartilage turnover rate, subchondral bone undergoes faster modeling and remodeling in response to changes in the mechanical environment (Goldring and Bianchi, 2012). By verifying the CT bone mineral density information obtained from anatomical specimens and comparing it with the X-ray bone mineral density information, it was found that the results of bone mineral density between the information of CT and X-ray image were highly similar, and a joint density distribution map was generated in the joint image (in Figure 1.) (Muller-Gerbl et al., 1990a; Muller-Gerbl et al., 1990b). Different from the bone mineral density measurement method in DXA for osteoporosis diagnosis, when using CT for bone mineral density measurement, repeatable results can only be obtained on the subchondral bone plate or dense bone due to various radiological effects (partial volume effect and beam hardening effect). The long-term mechanical stress transmitted in the joint can stimulate the adaptive changes in bone matrix density and mineral salt content in the growth process, which can show the load history, distribution patterns of the subchondral bone density, the place of load areas, and joint sports patterns of articular subchondral bone. Studies have found that mechanical stress acting on the joints can lead to remodeling changes in the subchondral bone of the joint (Oettmeier et al., 1992). The CTOAM was originally used to evaluate the prognosis of osteoarthritis before and after

TABLE 1 CTOAM technique evaluate the value of stress abnormal in the different subchondral bone distribution.

Author/year	Name of disease	Positions	CT type	Layer thickness	Number of patients	Age of patients (yrs)	Preoperative evaluate	Postoperative follow-up	References
Lochmuller et al., 1997	unilateral supraspinatus outlet syndrome	Acromion	Picker 1,200	4 mm	Male: 5 Female: 4	52.8 ± 3.3	1. The density maximum is always located at the lateral edge of the acromion, but only 1 case did not detect other maximums	—	Lochmuller et al. (1997)
							2. The dorso-medial acromion has a submaximal, and occasionally the lateral maximum extends to the ventral side of the acromion (types C and D)		
							3. The mineralization types of the affected side and the healthy side were the same in 6 cases, and the mineralization types were different in 3 cases		
							4. The D-type mineralization pattern appears to be related to the hook-like shape of the lower surface of the acromion		
Anetzberger et al., 2002	Tear of the Supraspinatus	Glenoid	Siemens CT	2 mm	Normal: 67 rupture of the supraspinatus muscle: 43	Normal: 71 ± 14 rupture of the supraspinatus muscle: 84 ± 11	1. Among the normal specimens, the anterior and posterior glenoid of the shoulder joint have the highest density	—	Anetzberger et al. (2002)
							2. In some cases, a maximum can be seen in the third area, located in the center area (17%) or antero-inferior area (4%)		
							3. At the site of supraspinatus tendon tear, the third density maximum often occurs in the center of the glenoid (42%)		
Harada et al., 2018	symptomatic rotator cuff tear	Glenoid	Light Speed ultra 16	0.6 mm	32 Male: 19 Female: 13	67.6 ± 8.0	1. The HU in the central area of the glenoid on the affected side was significantly lower than that on the unaffected side	—	Harada et al. (2018)
							2. The HU in the central area of the affected side was significantly lower in patients with larger rotator cuff tears or sub-rotator cuff tendon tears		

TABLE 1 (*Continued*) CTOAM technique evaluate the value of stress abnormal in the different subchondral bone distribution.

Author/year	Name of disease	Positions	CT type	Layer thickness	Number of patients	Age of patients (yrs)	Preoperative evaluate	Postoperative follow-up	References
Simon et al., 2015	total shoulder arthroplasty subjects with eccentric and concentric wear	Glenoid	GE Lightspeed QZ/i helical scanner	1.25 mm	42	eccentric glenoid wear (65.6 ± 2.4); concentric glenoid wear (66.5 ± 1.6)	1. The SBD of patients with concentric wear type and eccentric wear type was significantly different between different levels 2. In the concentric glenoid, the SBD was evenly distributed, with a higher degree of mineralization in the central region, while lower in the posterior, anterior and superior regions 3. The distribution of SBD in the eccentric group is uneven, and the mineralization is the largest in the rear part, followed by the lower part	—	Simon et al. (2015)
Deml et al., 2016	chronic posttraumatic shoulder instability; J-shaped bone graft	Glenoid	GE Discovery 750 HD	0.625 mm	14	21–44; mean age, 26.6	On preoperative CT scans, 13 (92.9%) patients had a different mineralization pattern than the contralateral shoulder region distribution	Eleven patients (78.6%) showed a uniform distribution of mineralization on both sides after J-shaped bone grafting. The mineralized type C1 type was similar preoperatively and postoperatively in 1 patient. The mineralization distribution of the 3 patients was different before and after surgery	Deml et al. (2016)
Matsui et al., 2018	osteochondritis dissecans (OCD)	Radial head	Unknown	1 mm	54	13.1 ± 1.7	1. The percentage of anteromedial, posteromedial and anterolateral high-density areas of the radial head fovea was significantly higher than that of the posterolateral area 2. The location and size of the lesion and a history of excessive valgus stress are associated with an imbalance in the fovea of the radial head	—	Matsui et al. (2018)
Hasegawa et al., 2020	Ulnar impaction syndrome; ulnar shortening osteotomy	wrist	Unknow	1 mm	Male: 1 Female: 9	Unknown	Severe pain in 5 wrist joints and moderate pain in 5 wrist joints; hyperdense areas of subchondral bone were seen on the distal surface of the ulna	No pain in 3 wrist joints and mild pain in 7 wrist joints; no hyperdense area on the distal surface of the ulna; no significant change in the location of the hyperdense area in the distal radius	Hasegawa et al. (2020)
Hontani et al., 2021	Ulnar impaction syndrome; ulnar shortening osteotomy	distal radioulnar joint	Unknow	1 mm	15	; (Mean age; 47.3)	In L-type, the HDA% in the D area of the sigmoid notch was significantly larger than that in other areas. In type C, the HDA% in the D-V area of the sigmoid notch was significantly larger than that in the dorsal area (D-D and P-D)	The postoperative %HDA in the P-V area of patients with type C was significantly larger than that in the D-D area and tended to be larger than the other two areas (D-V and P-D)	Hontani et al. (2021)

TABLE 1 (*Continued*) CTOAM technique evaluate the value of stress abnormal in the different subchondral bone distribution.

Author/ year	Name of disease	Positions	CT type	Layer thickness	Number of patients	Age of patients (yrs)	Preoperative evaluate	Postoperative follow-up	References
Poilliot et al., 2021	sacroiliac joint dysfunction; Sacroiliac joint arthrodesis	Sacroiliac Joint	conventional CT	0.7–5 mm	18; Male: 9 Female: 9	Mean age; 45 ± 14	The superior zone of the ilium showed significantly higher mineralization values than the corresponding zone of the sacrum	At 3 postoperative follow-ups (≥6 months, ≥12 months, and ≥24 months), a higher degree of mineralization was found to the upper iliac region; Mineral levels all increased in the postoperative state; with regard to the iliac side, there was no significant increase in HU values in any of the subregions at 6, 12, and 24 months	Poilliot et al. (2021)
Iwasaki et al., 2021	medial compartment OA in proximal tibia; high tibial osteotomy	proximal tibia	high-resolution helical CT scanner	1 mm	16	15–30	1. The %HDA of the M2 and M3 regions on the surface of the tibial plateau was significantly higher than that of the control group 2. The %HDA of all 4 subregions of the lateral ventricle of the OA patients was significantly lower than that of the control group	1. The medial ratio was significantly reduced to 75.1% ($p = 0.035$ compared to preoperative value); 2. In the medial compartment, HDA increased in the outermost regions of the 4 subregions after HTO, but decreased in the 3 medial subregions	Iwasaki et al. (2021)
Miura et al., 2022	anterior cruciate ligament injury	posteromedial region of the proximal tibia	high-resolution helical CT scanner	1 mm	20	<35	1. The HDA% of the posteromedial region of the ACL deletion group was 7% higher than that of the control group 2. The HDA% in the anteromedial region of the ACL deletion group was 6% lower than that of the control group 3. In the ACL-deficient group and the control group, there was no significant difference in HDA% between the medial and lateral areas	—	Miura et al. (2022)
Kameda et al., 2021	Medial Open-Wedge High Tibial Osteotomy	Patellofemoral Joint	CT Highspeed Advantage	1 mm	17; Male: 5 Female: 12	Mean age; 54.8	1. The HDA% of the medial notch of the femur is significantly higher than the lateral notch and lateral trochlea of the femur 2. The medial portion of the lateral facet of the patella is significantly higher than the medial facet of the patella	1. Significantly increased HDA% in the lateral notch and lateral trochlea of the femur and in the medial portion of the lateral facet of the patella; 2. Significant decrease in %HDA in the medial trochlea of the femur and the lateral portion of the lateral facet of the patella	Kameda et al. (2021)
Matsubara et al., 2022	Knee OA; Medial Opening-Wedge and Lateral Closing-Wedge High Tibial Osteotomy	Distal Tibia	high-resolution helical CT scanner	1 mm	41; Controls:11; OWHTO:18; CWHTO:12	Mean age; Controls: 26; OWHTO: 60.5; CWHTO: 59.1	There was no significant difference in the percentage of HDA in each region of the distal tibia articular surface between the three groups	After OWHTO, area A was significantly increased, and area D was significantly decreased; after CWHTO, area A was significantly decreased, and area C was significantly increased	Matsubara et al. (2022)

orthopedic surgery. It has also been used for studying the characteristics of the bone and joint in special working groups influenced by extra mechanical stress, such as athletes, physical workers, etc. The stress distribution and stress loading history *in vivo* joints can also be presented through this non-invasive diagnostic technique (von Eisenhart-Rothe et al., 1997; Eckstein et al., 1995a; Eckstein et al., 1995b).

This narrative study discusses the pre- and postoperative evaluation of medical device implantation position, orthopedic surgery, and the clinical treatment of bone injury and degeneration. It also discusses the research status of CTOAM technology in image post-processing engineering and the relationship between bone material and mechanical strength.

2 Technical background

The computed tomography Osteoabsorptiometry (CTOAM) technology is a CT image processing technology that uses the absorption attenuation effect between X-ray photons and human bone tissue to form a topographic map of bone tissue specificity with different densities. According to Wolff's law, bones adapt to functional needs through remodeling, which can also reflect the distribution of resultant forces acting on the bone. This method does not focus on the quantitative calculation of absolute value. The core of this method is to present the difference in relative density on the surface and inside the joint. The long-term mechanical stress transmitted in the joint can stimulate the adaptive changes in bone matrix density and mineral salt content in the growth process, which can show the load history of articular subchondral bone under long-term stress. Studies have found that mechanical stress acting on the joints can lead to remodeling changes in the subchondral bone of the joint (Oettmeier et al., 1992). The non-uniformity of remodeling sites in the joint mainly depends on the initial geometry of the joint surface, the degree of stress load, the main stress sites and the length of loading history.

3 Post-processing applications

The maximum density projection is drawn by extracting the highest signal intensity of each point on the subchondral plate on the projection line. This is a process of converting and compressing a series of voxels on the projection line of a three-dimensional object into a representative pixel in a two-dimensional density map. The reconstructed image is displayed as a gray-scale image, but in fact, there is information about the signal intensity in the saved image. Through Hounsfield unit (HU), that is, the attenuation coefficient used in CT. For better observation, the topographic maps of various densities in CT images are pseudo colored. Finally, the pseudo color topographic map is used for data statistical analysis. As HU is the attenuation coefficient calibrated according to water rather than absolute value, the data difference generated by HU may show different result data according to the difference in CT scanner KV parameters, CT scanner brand, algorithm or inspection conditions, resulting in the lack of repeatability of image measurement data. Of course, under same condition, this error may be reduced to a certain

extent as all subjects use the same CT scanner and the same scanning parameters for shooting, measurement and evaluation (Eckstein et al., 1995a; Eckstein et al., 1995b; Rhee and Baek, 2012). Therefore, CTOAM is a kind of image processing and measurement technology with repeatability and high sensitivity.

4 Correlation between bone density and mechanical strength

Currently, DXA is used as the primary means to assess bone density and establish a diagnosis of osteoporosis, but it is limited to a two-dimensional assessment. In qCT, however, there is a similar situation in which the absolute value of the density of a region of interest in a specific plane is measured. By measuring BMD from a single plane, DXA and qCT only enable clinicians to obtain a broad understanding of bone mass but cannot provide density distribution data for specific regions of interest. On the other hand, although most 3D techniques measure absolute BMD values in specific regions, including cortical and cancellous bone, the density distribution difference of the region of interest, particularly the density distribution of subchondral bone, can be captured by CT-OAM as a 3D imaging approach.

qCT is a methodology for assessing bone density utilizing phantom quantitative technique. Although CT and qCT use the same X-ray absorption-attenuation technique to evaluate bone density, qCT and CT can expose patients to higher levels of ionizing radiation than DXA. Second, in the clinical diagnosis process, the preoperative assessment of patients often adopts X-ray examination to CT testing. If a specific clinical need exists, clinicians will investigate DXA or qCT. Furthermore, qCT is commonly employed in scientific research, whereas DXA is commonly used for clinical bone density evaluation. As a result, CTOAM imaging data can be collected from preoperative CT imaging tests, sparing patients from further dedicated DXA or qCT scans and accompanying radiation, lowering medical expenditures.

Typically, CT examines the absolute value of bone mineral density in a specific region (ROI) of the body, such as cortical bone and cancellous bone, to assess whether the ROI has reached the indication of osteoporosis. However, in other cases, such as bone grafting, osteotomy and correction, prosthesis implantation, loosening and displacement, a single qCT and DXA diagnosis may not be enough to determine the prognosis developments after surgery. CTOAM, as a reproducible and extremely sensitive CT image post-processing technology, may monitor the distribution of bone tissue with varied densities in the joint surface and assist doctors in choosing the suitable anchor for the prosthesis location. In humans, current studies should focus on the relationship between subchondral bone density and mechanical strength of each articular surface. Emphasis should be given to matching the position of the articular surface's local high-density area with the position of high mechanical strength to improve the prosthesis's anchoring stability after implantation. Non-etheless, osteoporotic patients are more likely to experience subsidence, displacement, screw loosening, and iatrogenic fractures during and after spine, shoulder, hip, and knee arthroplasty. It has been demonstrated to some extent that the quality of articular subchondral bone influences the curative impact

of surgery. As a result, prior to prosthesis implantation, the density distribution on the articular surfaces should be examined to reduce the risk of revision and secondary surgery. Simultaneously, the device industry should consider models relating to the mechanical strength and bone density distribution of each joint in the human body, in order to provide an assessment reference for relevant prosthesis design and manufacturing engineers as well as clinical orthopaedic surgeons.

In the early days, some scholars combined the subchondral bone mineral density of the articular surface measured by CTOAM technology with the results of articular surface indentation experiments to determine whether there was a correlation between the two. Mühlhofer et al. confirmed the CTOAM and indentation studies early on to see if the two correlate. The study's findings revealed that the distal tibia's local maximum density values were not equally distributed and were concentrated in the medial and central areas. The findings of the CTOAM study and the indentation test were similar in that high density values were associated with high mechanical strength; low density values with low mechanical strength. A correlation study found a 0.74–0.97 coefficient of determination link (R^2) between density data and mechanical strength at each measurement point. The Pearson correlation coefficient was 0.86–0.98 ($p = 0.05$) (Mühlhofer et al., 2009). This study suggested that the ankle endoprosthesis could be anchored not only in the cancellous bone, but also in the subchondral bone, particularly in the distal medial and central regions of the tibia where high-density areas are concentrated, to reduce loosening caused by the prosthesis's anchoring quality.

Kraljevi et al. discovered that 28 cases of unilateral shoulder glenoid had bicentric high-density distribution, and 4 cases had single-center high-density distribution. The strength test findings revealed that the high mechanical strength area was found in the core of the glenoid's high-density area (double center and single center). The linear correlation between high-density areas and mechanical strength was 0.62–0.96 ($p < 0.02$), and the coefficient of determination (R^2) was 0.39–0.91, all of which were statistically significant (Kraljević et al., 2011). Zumstein et al. discovered that the subchondral bone of the articular surface of the humeral head had a high-density distribution in the center (single-center pattern) and anterior-posterior region (double-center pattern), and the distribution of high mechanical strength regions was similar. The median force is 175 N, but the inter-individual variance is substantial, ranging from 10 to 930 N (25%–75% interquartile range, 137–236 N). There is a substantial link between the degree of mineralization and mechanical strength ($p < 0.01$), the correlation coefficient is 0.59–0.96, and the determination coefficient is 0.35–0.93 (Zumstein et al., 2012). Hoechel et al. discovered that the hyperdense area of the acetabular fossa occurred in the anterosuperior region, whereas the hyperdense area of the articular surface of the femoral head appeared in the anterosuperior or posterosuperior region. The findings of the acetabular fossa and femoral head indentation test were comparable to the results of CTOAM postprocessing, however there were still inter-individual variances. High mechanical strength areas were found in the acetabular fossa's anterosuperior region and the femoral head's region above the fovea. High mechanical strength was substantially linked with high density

regions of the acetabulum and femoral head (SBP correlation coefficients ranged from 0.77 to 0.97 for FL and 0.97 to 0.96 for CF) (Hoechel et al., 2013). Several researchers have discovered a link between the density distribution and mechanical strength of the talar dome (Leumann et al., 2015), cervical vertebral body (Hara et al., 2021), and upper and lower cervical endplate (Orías et al., 2021). Yet, we are aware that, while there is a strong association between the two in this sort of research, a quantitative comparison of bone density and mechanical strength is unachievable. It should be noted that the distribution of subchondral bone density, rather than direct stress measurement, is the direct consequence of CTOAM image measurement. As a result, it may be used as an indirect inference technique for stress changes. The reasoned conclusions, on the other hand, should be referred to and regarded with caution, and realistic biomechanical and clinical examinations are required to validate them.

5 Clinical application research

5.1 Review on orthopedic surgery

CTOAM technology can evaluate the intra-articular stress change by observing the density changes in bone tissues around the joint. It can be used as a low-cost radiological method imaging research technology for long-term follow-up after surgery (Table 1). For spine and lower limb joint, the stress distribution analyzed by CTOAM technology can reflect the status of degeneration. For no weight-bearing joints like the shoulder, elbow, wrist, the stress distribution can help to estimate the influence of pre- and post-operative, working environment, gender, activity level and movement, ligaments and tendons. Commonly, the changes in bone mineral density only occur 6–12 months after the serious changes in mechanical load.

5.1.1 Upper limb joint

Rotator cuff injury is a common disease in sports medicine. Clinicians usually pay more attention to the decrease of shoulder function and the soft tissue repair, but concern less to the abnormal stress distribution on the subchondral bone of the cavities glenoidal is. Some authors observed the mineralization of the lower shoulder peak bottom in patients with unilateral subacromial impingement syndrome. They measured the distribution of subchondral bone density at the lower acromion, found that the subacromial bone density of the patients with subacromial impingement syndrome did not increase, which indicated that the increase of subacromial pressure did not induce the increase of subacromial bone mineral density (Lochmuller et al., 1997). It is speculated that the reason for decreasing subacromial mineralization in subacromial impingement syndrome is the decrease of shoulder joint motion due to shoulder joint disease, which is mainly manifested in the obstruction of shoulder joint abduction and the increase of pain level. As a non-weight-bearing joint, the stress distribution change of the shoulder may be connected with the joint instability caused by the shape of the acromion (Neer classification system), surrounding osteophyte, tendon and ligament injury. The rotator cuff muscle group can balance the intra-articular stress of the shoulder. In the condition of rotator cuff injury, especially the supraspinatus injury,

TABLE 2 Evaluation of stress distribution in subchondral bone of athletes in different sports by CTOAM technique.

Author/ year	Positions	CT type	Layer thickness	Number of patients	Sports project	Age of patients (yrs)	Evaluate results	References
Mochizuki et al., 2005	Glenoid	Lemage Light speed QX/I	2.5 mm	28; Male: 26 Female: 2	Baseball: 25 (pitchers: 18 fielders: 7) handball: 2; volleyball: 1	range, 15–65	1. There were significant differences in mean scores between the two groups in almost all areas except the anterior superior area, the posterior superior area, and the central area	Mochizuki et al. (2005)
							2. In the anterior glenoid area of the shoulder, the average score of the shoulder throwing group was 0.77 points higher than the average score of the control group	
							3. In the anterior inferior glenoid region, the shoulder throwing group was on average 0.68 points higher than the control group	
							4. In the posterior inferior glenoid area of the shoulder joint, the throwing shoulder group was on average 1.06 points higher than the control group	
							5. The DMSB scores of the anterior, anterior inferior, posterior inferior and posterior areas of the shoulder throwing group were significantly higher than those of the control group	
Shimizu et al., 2012	Glenoid	high-resolution helical CT scanner	1 mm	30; male: 30	control group: 10; fielder group:10; pitcher group:10	mean age; control: 22; fielder group: 21; pitcher group: 19	1. A bicentric density distribution pattern across the articular fossa was found in baseball players	Shimizu et al. (2012)
							2. All fielders and pitchers showed greater proportions and a wider distribution of high-density areas in the anterior and posterior glenoid regions compared to controls	
							3. The percentage of high-density area in the total joint socket in the fielder group and the pitcher group was greater than that in the control group	
							4. In the field group, the %HDA of the anterior inferior, posterior inferior and anterior superior glenoid of the shoulder joint was higher than that of the control group	
							5. In the pitchers, the %HDA in the anterior inferior and posterior superior glenoid regions was higher than that in the control group	
							6. The external rotation rate of the shoulder joint of baseball players is greater than that of the control group	

TABLE 2 (*Continued*) Evaluation of stress distribution in subchondral bone of athletes in different sports by CTOAM technique.

Author/year	Positions	CT type	Layer thickness	Number of patients	Sports project	Age of patients (yrs)	Evaluate results	References
Numaguchi et al., 2021	Glenohumeral Joint	high-resolution helical CT scanner	1 mm	50; male: 50	Baseball, fielders; 11; collegiate pitchers: 12; professional fielders: 15; professional pitchers: 12	mean age, collegiate fielders: 20.3; collegiate pitchers: 21.2; professional fielders: 27.5; professional pitchers: 24.4	1. The stress distribution pattern on the articular surface of the dominant side and the non-dominant side of the collegiate pitchers group was different	Numaguchi et al. (2021)
							2. Also different between the two university groups and the professional pitchers group	
							3. The average HU of the non-dominant side and the dominant side in the collegiate pitchers group was significantly greater than that of the non-dominant side	
							4. On the dominant side, the average HU of the dominant side of both the collegiate pitchers group and the professional pitchers group is greater than the non-dominant side of the professional pitchers group	
Kawasaki et al., 2013	Glenoid	Aquilion CXL	0.5 mm	42; male:42	rugby players:25 (forwards: 10; backs:15) control: 17	mean age, rugby: 21.3; control: 26.2	1. The HU value of the 7th region of the shoulder glenoid of the rugby players is higher than that of the control group	Kawasaki et al. (2013)
							2. The instability of the shoulder joint affected the distribution of HU values in the two groups, and the HU value of the unstable shoulder moved to the lower part of the glenoid of the shoulder	
Momma et al., 2020	Shoulder Joint	Unknow	1 mm	22; male: 22	gymnast group: 12; control: 10	mean age, Gymnast group: 19.4; Control: 20.2	1. There was no significant change in the mean density or distribution pattern of subchondral bone on the dominant and non-dominant sides of gymnasts	Momma et al. (2020)
							2. The stress distribution pattern of the shoulder joint surface of the gymnast and the control group is different	
							3. In gymnasts, areas of high density appear in the posterior-superior region of the articular surface of the humeral head and the anterior-superior and/or posterior-superior regions of the glenoid	
							4. Gymnasts have higher average bone mineral density than control group	
Momma et al., 2019	Wrist	Unknow	Unknow	31; male: 31	gymnast group: 16; control: 15	Unknow	1. In the control group, %HDA was mainly located in lunate fossa and scaphoid fossa	Momma et al. (2019)

TABLE 2 (*Continued*) Evaluation of stress distribution in subchondral bone of athletes in different sports by CTOAM technique.

Author/ year	Positions	CT type	Layer thickness	Number of patients	Sports project	Age of patients (yrs)	Evaluate results	References
							2. In the gymnast group, %HDA is mainly distributed in the dorsal part of the scaphoid fossa, palmar part of the scaphoid fossa and the scaphoid area	
							3 The %HDA values of DSF, PSF and S in the gymnast group were higher than those in the control group	
Momma et al., 2011	Elbow Joint	high-resolution helical CT scanner	1 mm	30, male: 30	Baseball, fielders; 10; pitchers: 10; control: 10	Mean age, Fielders: 20.5; Pitchers: 19; Control: 22.3	1. The area of maximum density for all subjects was located posterior to the distal humeral trochlea	Momma et al. (2011)
							2. The maximum density area of the distal trochlear of the pitcher group was higher than that of the control group	
							3. The pitcher group showed the largest density area distribution in the anterior part of the capitulum	
Momma et al., 2012	Elbow Joint	high-resolution helical CT scanner	1 mm	30, male: 30	Baseball, fielders; 10; pitchers: 10; control: 10	Mean age, Fielders: 21; Pitchers: 19; Control: 22	1. In all subjects, the area of greatest density was located posterior to the trochlea notch	Momma et al. (2012)
							2. Compared with the control group, the %HDA of the trochlea notch in the baseball group was significantly increased	
							3. The largest dense area of the pitcher group is also clearly distributed in the front of the radial head	
Funakoshi et al	Elbow Joint	Unknow	1 mm	30, male: 31	Symptomless Baseball player: 12; UCL insufficiency Baseball player: 12; Control: 7	Symptomless Baseball player: 21.2; UCL insufficiency Baseball player: 19.7; Control: 20.7	1. The high-density areas of the asymptomatic group and the symptomatic group were located in the anterolateral and posteromedial parts of the distal humerus, and the posteromedial parts of the radial head and ulna	Funakoshi et al. (2016)
							2. The high-density areas of the anterior and posteromedial regions of the distal humerus, the radial head and the posteromedial region of the ulna in the baseball group were higher than those in the control group	
							3. In the symptomatic group, the percentage of hyperdense areas in the anterolateral region of the distal humerus and the anterolateral region of the ulna was	

(Continued on following page)

175

TABLE 2 (*Continued*) Evaluation of stress distribution in subchondral bone of athletes in different sports by CTOAM technique.

Author/ year	Positions	CT type	Layer thickness	Number of patients	Sports project	Age of patients (yrs)	Evaluate results	References
							significantly higher than in the asymptomatic group	
Momma et al	Elbow Joint	Unknow	1 mm	40, male: 40	Baseball, collegiate pitchers: 15; professional pitchers: 13; Control group: 12	Baseball, collegiate pitchers: 20.8; professional pitchers: 23.4; Control group: 22.1	1. The %HDA of the academic and professional groups is located anterior to the capitulum, posterior to the trochlear, and radial head	Momma et al. (2018)
							2. The %HDA of the anterior part of the humeral head, the posterior part of the trochlear, the radial head and the olecranon in the professional group was significantly higher than that in the university group	
Nishida et al	Patellofemoral Joint	high-resolution helical CT scanner	1 mm	40	Baseball, collegiate fielders:10; collegiate pitchers: 10; collegiate soccer:10; control: 10	Baseball, collegiate fielders:21; collegiate pitchers: 19; collegiate soccer: 23; control: 23	The pitcher and fielders groups developed areas of low density proximal to the lateral pulley, while %HDA was seen at the lateral notch, medial notch, and distal end of the medial pulley	Nishida et al. (2012)
Shiota et al	Ankle	Unkown	1 mm	20, male: 20	Control: 10; soccer: 10	Control: 22.9; soccer: 21.6	1. The distribution of HAD can be seen in the distal tibia, proximal talus and distal fibula of football players	Shiota et al. (2020)
							2. The percentage HDA of the ankle joint surface of football players was higher than that of the control group	
Xu et al	Ankle	GE high-resolution helical CT scanner	0.62 mm	20, male:20	Control: 10; taekwondo players: 10	Control: 20.80 ± 0.92; taekwondo players: 21.10 ± 0.88	1. In taekwondo athletes, the percentage of bone tissue volume in the distal tibia and talus with high and medium BMD was significantly higher than that in the control group	Xu et al. (2022)
							2. Taekwondo athletes have high density distribution in the medial area of distal tibia and talus dome	

the balanced state will break, resulting in poor stability of the shoulder. The compensatory load of the deltoid muscle increased, as the deltoid muscle independently undertaken the shoulder abduction function which was originally joint-maintained by the supraspinatus muscle and deltoid muscle. Some authors have found that the bone mineral density distribution of patients with supraspinatus tears gradually changes from the normal single or dual center mode (anterior upper and posterior upper) to the posterior center and anterior upper center connection mode or three center modes (Anetzberger et al., 2002). The degree and location of supraspinatus muscle injury also determine the balance ability of the supraspinatus muscle and the degree of displacement of the humeral head. This study reported for the first time that the high-density area (HDA) of the glenoid of the shoulder was transferred due to the imbalance of stress distribution in the shoulder joint caused by the tear of the supraspinatus muscle.

The change of glenoid bone mineral density in shoulder arthroplasty (SA) is also a noteworthy research topic. Harada et al. performed CT scanning of bilateral shoulder joints in 32 patients with arthroscopic repair of unilateral rotator cuff tear, and evaluated the distribution of bone mineralization under the shoulder glenoid. They found that the bone mineralization density in the central area of the shoulder glenoid on the affected side was significantly lower than that of the healthy side. In terms of the effect of the size of rotator cuff tear on the degree of bone mineralization, it was found that patients with large area rotator cuff tear had significantly lowered bone mineralization density in the central region of the affected side (Harada et al., 2018). This indicates that the rotator cuff tear of the affected shoulder may reduce the stress load and area distribution in the central area of the glenoid of the shoulder, and the patients who present this kind of distribution usually suffer from a large area rotator cuff tear. In addition, it is also noted that considering that the patients are middle-aged and elderly people. Because the aggregation from the tear and aging of rotator cuff may also lead to an important factor of abnormal stress distribution in the glenoid of the shoulder (Harada et al., 2018).

Total shoulder arthroplasty (TSA) has different wear patterns, which are related to the depth of the replacement joint inserted into the articular surface, the basic bone mass around the prosthesis and the prosthesis type. Some studies used CTOAM technology to observe the distribution of subchondral bone density (SBD) in the glenoid of patients with shoulder osteoarthritis treated with TSA. It was found that there are significant differences in subchondral bone density (SBD) between patients with concentric wear patterns and eccentric wear types. In the concentric shoulder glenoid, SBD distribution is relatively uniform, the mineralization degree in the central area is higher and that in other areas is lower. In the eccentric shoulder glenoid, SBD is unevenly distributed, and the area with highest mineralization degree located in the posterior glenoid, followed by the inferior glenoid (Simon et al., 2015).

Shoulder dislocation is also a common sports injury. Recurrent shoulder dislocation usually involves bone defect of the glenoid. The J-shaped bone transplantation is a classical procedure for treating this case, which fill the defective edge of the glenoid to restore the its normal shape. Deml et al. performed clinical observation and CTOAM measurement on 14 patients with J-shaped bone grafting before and after the operation to evaluate the process of

bone reconstruction. In the subsequent postoperative follow-up, they found t 85.7% of patients had an equal distribution of subchondral mineralization in both articular processes (Deml et al., 2016). This study indicated that the postoperative shoulder glenoid adapted to the new intra-articular stress load, resulting in anatomical and mechanical fusion between the bone tissue and bone grafts at the transplantation site, the stress distribution also gradually normalized. According to Wolff's law, the bone tissue structure can be preserved in the area with sufficient strain. In the low strain region, bone tissue absorbs with time, and the strength and structure of bone tissue decrease. For the shoulder joint, rotator cuff tear not only reduces the stability of the shoulder joint, but also alienates the normal intra-articular stress distribution.

Elbow osteochondritis (OCD) is a common sports injury in adolescent patients. By identifying the abnormal stress distribution of their parts according to imaging classification with the help of CTOAM technology, clinicians can evaluate the pathological status more accurately. Matsui et al. evaluated the elbow of adolescent OCD dissecans with CTOAM images, and explored the relationship between radiologic classification and elbow stress distribution. They found that the percentage of the anterior medial fovea of the radial head, posterior medial and anterior lateral high-density areas were higher than that of posterior lateral areas, the location and size of osteochondritis of the radial head and the history of excessive valgus stress stimulation were correlated with the stress imbalance in the central depression of the radial head (Matsui et al., 2018). Preoperative imaging is helpful for identification of the abnormal stress pattern of the radial head. Especially if the distribution of high-density areas on the outside of the radial head and exfoliative chondritis of the humerus with disorder of the medial epicondyle of the humerus are observed, the risk of late radial humeral arthritis should be considered. Therefore, this study also supported the correlation between the history of excessive valgus stress in the elbow joint and the high-stress distribution in the fovea of the radial head to a certain extent, and illustrated the overloaded stress on the articular surface may reflect the abnormal stress pattern in the radial head joint.

Ulnar impact syndrome (UIS) is defined as painful compression of the ulnar carpal osteofascial compartment due to pathological ulnar variation. This difference may be congenital or acquired, in most cases, it is caused by malunion of distal radius fractures. Due to the shortening of the radius, the load transmitted through the wrist to the ulnar side may increase. Ulnar shortening osteotomy (USO) is a decompression of the operation of the carpal compartment of the ulna, which can reduce the stress distribution on the articular surface of the distal ulna and the distal radius. A study evaluated the distribution of mineralization density of 10 patients who underwent USO due to UIS. Preoperatively, the high-density area (%HDA) of subchondral bone was presented on the distal surface of the ulna in all patients, but no obvious %HDA was found at the last follow-up postoperatively. The %HDA of ulna, radius, navicular fossa and lunate fossa all decreased postoperatively. The analysis of the subchondral bone density distribution showed that USO reduced the stress on the surface of the distal ulna (Hasegawa et al., 2020). The percentage of radius/ulna held an increasing trend, which may due to different mechanisms. For example, the tension on the triangular fibrocartilage complex can absorb the load of the distal ulna surface. Some studies have also evaluated the stress

distribution pattern of the distal radioulnar joint (DRUJ) before and after USO for treating UIS. In the linear of the sigmoid notch, the preoperative stress distribution in the DRUJ of the distal radioulnar joint was concentrated on the distal dorsal side, while the postoperative stress distribution is relatively homogeneous. In the arcuate of the sigmoid notch, the preoperative internal stress of the radioulnar joint was concentrated on the distal palmar side, the postoperative stress concentration tended to move to the proximal (Hontani et al., 2021). These results suggest that USO may reduce the risk of degenerative changes in the dorsal side of the sigmoid incision, while the risk of degenerative changes in the proximal palmar side of arcuate the sigmoid incision may increase. Therefore, the morphological evaluation of the sigmoid notch on the transverse plane can predict the location on DRUJ with degenerative changes in patients with accept USO for treating UIS.

5.1.2 Lower limb joints

Sacroiliac joint arthrodesis (SIJ), as the final choice of sacroiliac joint dysfunction (SIJD), can greatly limit the motion of sacroiliac joint and provide lasting pain relief for releasing the tension of sacroiliac joint structure (Buchowski et al., 2005; Foley and Buschbacher, 2006; Murakami et al., 2018a; Poilliot et al., 2021). Surgical SIJ fusion significantly reduced joint motion by more than 50% on the three anatomical planes of the sacroiliac joint (Soriano-Baron et al., 2015). The decrease of sacroiliac joint motion can reduce the pressure of ligaments, muscles and bones around the sacroiliac joint, thereby alleviate SIJ pain to a certain extent (Szadek et al., 2008; Szadek et al., 2010). In addition, SIJ arthrodesis can also change the abnormal loading on auricularis ossis ilii and subchondral bone plate of SIJ, then consequently affecting the mineralization mode. Some authors used CTOAM technology to analyze the bone mineral density of the subchondral bone of SIJ in 18 patients before and after sacroiliac dysfunction. It was found that after surgery, compared with the data of the healthy control cohort (n = 39), the stress and load changes caused by SIJ fixation after arthrodesis led to an increase in the subchondral bone mineral density of the sacrum auricular surface, which was manifested by an increase in the morphological and mechanical integration of the front and lower parts, changes in the overall kinematics of the sacroiliac joint, and different morphological mechanical density patterns (Poilliot et al., 2021). The mineralization changes in sacroiliac joint auricular surface may be related to the surgical approach and screw placement, which provides time-related information about the overall appearance of SIJ and its dysfunction status. As sacroiliac joint fusion changes the stress distribution of the sacroiliac joint and optimizes the mechanical properties of the sacroiliac joint shape, the stress distribution is different from that of normal people, which reflects the adaptability of the human body to the surgery.

Knee osteoarthritis (KOA) and the related malalignment of genu varum change the gait pattern of knee and lower limb kinematics. For example, in the standing phase of gait, the ground reaction force is transmitted from the inner side of the foot to the center of the knee joint, and the medial compartment bears the maximum proportional load (Baliunas et al., 2002; Shelburne et al., 2006). Long-term varus deformity may further aggravate this medial compartment stress distribution. If the deformity is not corrected, the OA will be worsening (Hernigou et al., 1987;

Sharma et al., 2001). The common anatomical morphology of KOA with varus deformity includes narrow medial knee joint space of the knee, osteophyte (Teichtahl et al., 2006) and subchondral osteosclerosis. For the single compartment KOA, the medial KOA occupies the most. For end-stage KOA, total knee arthroplasty (TKA) is effective and most recognized treatment. For medial KOA, there are some special surgical options, such as unicompartmental knee arthroplasty (UKA), high tibial osteotomy (HTO) and fibular osteotomy. (Pendleton et al., 2000; van Raaij et al., 2010; McAlindon et al., 2014). The surgery can correct the malalignment thereby reverse the abnormal status of the lower limb, which is of profound biomechanical and clinical significance for treating KOA.

High tibial osteotomy (HTO) surgery (JACKSON and WAUGH, 1961; Liu et al., 2019; Primeau et al., 2021) correct the varus deformity and reduce the load of the medial compartment by laterally shifting the bearing axis. It can release the knee pain, improve the knee function, and delay the progression of KOA. CTOAM technology can observe the pre- and postoperative stress distribution of patients with knee osteoarthritis, and determine the location and severity of KOA through the area of high-density area and upper limit of density of the tibial plateau. Chu et al. found that in the subchondral bone of osteoporosis osteoarthritis (OP-OA), abnormal bone reconstruction leads to the deterioration of bone microstructure and biomechanical properties, potentially affecting the transmission of load stress from cartilage to subchondral bone, accelerating the progression of OA in OP-OA patients (Liu et al., 2019). Therefore, the stress distribution in the knee joint significantly affects the progression of KOA. If the abnormal stress distribution is corrected, the progression of KOA can be delayed to a certain extent. High tibial osteotomy (HTO) surgery (JACKSON and WAUGH, 1961) was developed for correcting varus deformity and reducing the load of the medial compartment by laterally moving the bearing axis. CTOAM technology can observe the preoperative pre- and postoperative stress distribution of patients with KOA in real-time, estimate the location and severity of KOA through the area of high-density area and upper limit of density of the tibial plateau. Iwasaki et al. analyzed the CT data of 16 patients without OA (control group) and 17 patients with KOA before and 1.5 years after HTO. Preoperatively, the medial compartment ratio of %HDA in OA group was significantly higher than that of control group ($p < 0.001$). the medial ratio decreased significantly from preoperative 80.1% to postoperative 75.1% ($p = 0.035$). The change of medial ratio was significantly correlated with the change of hip-knee ankle angle ($r = 0.587$; $p = 0.035$). In the four subregions of medial compartment, after HTO, %HDA increased in the outermost subregion, and decreased in the three medial subregions (Iwasaki et al., 2021). This indicated HTO can transfer the excessive medial stress to the lateral compartment, thus reducing the stress in the medial compartment of the knee varus knee joint surface, shifting the excessive concentration of the medial compartment to the lateral compartment, and furtherly balancing the medial and lateral stress distribution. Miura et al. analyzed the X-ray and CT data of 20 patients with non-compound injuries of unilateral anterior cruciate ligament (ACL rupture group) and 19 patients with non-ACL injury (control group), %

HDA (mean: 21.6%) in the posterior medial area of ACL in the ACL rupture group was significantly higher than that in the control group (14.7%) (p = 0.002). In contrast, %HDA (9.4%) in the anterior medial area of ACL in the ACL rupture defect group was significantly lower than that in the control group (15.3%) (p = 0.048). The logarithm of the time from ACL injury to CT examination showed a significant correlation with HDA% in the posterior medial region (p = 0.032), which indicated that anterior cruciate ligament injury increases the stress in the posterior medial area of the proximal tibia, and long-term condition of ACL deficiency will lead to the accumulation of stress, which will lead to the beginning and progression OA (Miura et al., 2022).

The consistency of patellofemoral joint (PF) and the change of contact stress may lead to patellofemoral osteoarthritis (PFOA) (Goutallier et al., 1979). Some studies have measured the bone mineral density distribution of the femoral trochlear and patellofemoral articular surface of patients who underwent open wedge high tibial osteotomy (OWHTO) before and 1 year after surgery with CTOAM, and found the %HDA percentage of the lateral femoral notch, lateral trochlea and the medial portion of the lateral facet of the patella increased significantly, and the patella height and inclination angle decreased significantly. It shows that the distribution pattern of subchondral bone mineral density of PF articular surface after OWHTO should be laterally shifted compared with the preoperative condition (Kameda et al., 2021). HTO also affect the stress distribution of the ankle. Matsubara et al. used CTOAM technology to analyze the subchondral bone density of distal tibia in patients OWHTO, closed wedge high tibial osteotomy (CWHTO) and unilateral anterior cruciate ligament injury. Preoperatively, no significant difference was found in the %HDA of the distal tibial articular surface between the three groups. Postoperatively, in OWHTO group, the innermost %HDA increased (49.3%–53.0%; p = .011), and the outermost %HDA decreased (21.4%–17.2%; p = .003). In the CW group, the innermost %HDA of the distal tibial articular surface decreased significantly (55.7%–35.7%; p = .001), and the second lateral %HDA increased significantly (23.6%–29.2%; p = 0.002) (Matsubara et al., 2022). These results indicated that the distribution pattern of subchondral bone mineral density in the distal tibia shifted medially after OWHTO and laterally after CWHTO. When performing OWHTO on patients with ankle varus, attention should be paid to the inward shifting of ankle stress distribution, which will lead to the deterioration of ankle OA postoperatively.

5.2 Research on sports medicine

Sports training medicine is an emerging subject in recent years, including various fields like surgery, internal medicine and auxiliary diagnosis and treatment. For example, some factors, such as the recurrence of sports injury or the delay in returning to the field, make it difficult for clinicians to find an appropriate balance between the premature return of players and the serious injury of players (Blanch and Gabbett, 2016). According to the data from the London Olympic Games, about 11% of the athletes participating in the Olympic Games will face injuries. During Rio de Janeiro Olympic Games, bone stress injury, muscle, tendon, ligament, and glenoid lip injury were reported. These injuries are mostly seen in the knee joints of lower limbs, ankle joints and shoulder joints of upper limbs, and are most common in

track and field athletes. High-intensity sports training and competition are inevitable in Olympic sports. Therefore, it is very important to detect the precursor phenomenon of injury as soon as possible before the stress deformation reaction progresses to stress fracture, and this may be an achievable goal at present (Engebretsen et al., 2013; Murakami et al., 2018b; Hayashi et al., 2018; Heiss et al., 2019). CTOAM technology is also used in guiding sports training and rehabilitation. It can evaluate abnormal bone mineralization caused by long-term stress stimulation in the early stage to predict the force trend of bone and joint according to the stress distribution to prevent injury and correct wrong-training habits (Table 2).

5.2.1 Upper limb joint

Mochizuki et al. analyzed the bone mineralization of the shoulder glenoid of baseball pitchers, and found that baseball pitchers' long-term use of throw movement lead to over rotational load from the humeral head on the shoulder glenoid. The displacement of the humeral head due to frequent and rapid abduction external rotation of the humeral head leads to the high-density distribution in the front and rear of the glenoid of the shoulder, laxity and proliferation of the shoulder ligament, and forms a bicentric distribution pattern of the shoulder (Mochizuki et al., 2005). CTOAM can also furtherly diagnose the pathological changes in Bennett (shoulder) of throwing athletes, and help clinical sports medicine experts determine the therapeutic schedule. Shimizu et al. analyzed the bone mineralization of the dominant shoulder joints of 10 baseball fielders, 10 baseball pitchers and 10 non-athletes, and found that the percentage of the high-density area of shoulder joint surface of pitchers and fielders was higher than that of the non-athletes. There was no significant difference in the percentage of shoulder high-density area between baseball pitchers and fielders. Baseball pitchers and fielders have higher shoulder external rotation angles than the non-athletes (Shimizu et al., 2012). The double center high-density area of baseball players' shoulder joint is due to long-term joint internal stress (compressive stress and shear stress) and excessive joint rotation displacement caused by joint ligament relaxation. Numaguchi et al. analyzed the mineralization of the subchondral bone of the shoulder joint of college baseball players (CP, pitcher group and outfielder) and professional baseball players (PP, pitcher group and outfielder), and found that in the CP Group, the stress distribution pattern on the joint surface of the dominant side and the non-dominant side is different, and the same is true between the two college student groups and the PP group. In the CP Group, the average HU of the humeral head surface on the non-dominant side and the dominant side was greater (p = 0.035). On the dominant side, the average HU of humeral head surface and shoulder glenoid in the CP Group was larger than that in the PP group (Numaguchi et al., 2021).

As a high-risk competitive sport, rugby players need to break through the encirclement of their opponents and obtain winning points. Therefore, apart from strong lower limb strength rugby players also need to train strong strength of upper limb and shoulder to break through the encirclement through collision and other forms, which may increase the load of sports shoulder glenoid in long-term training and competition. Kawasaki et al. analyzed the distribution of bone mineral density in the shoulder glenoid of rugby players and found that the area of high bone mineral density in the

shoulder glenoid of rugby players is large, and the shoulder joint of rugby players is in a certain unstable state, resulting in a certain degree of degenerative changes in the shoulder joint (such as arthritis and shoulder glenoid lip tear) (Kawasaki et al., 2013).

Gymnastics is a professional competitive sport with high complexity and technical difficulty. Gymnasts usually use high jumping, high somersault, looping and other difficult actions to obtain technical scores, while athletes' limbs contact with instruments and produce stress during exercise. With the help of the movement inertia and reaction force generated by the action, the enhanced local pressure of athletes' joints may also be an important factor causing musculoskeletal injuries to athletes. Momma et al. analyzed the bone mineralization of the shoulder joint of male college gymnasts and found that the high-density area appeared in the superior articular surface of the glenohumeral joint (Momma et al., 2020). Because gymnastic athletes bear repeated exercise, high impact load, axial compression, torsion, and tension, accompanied with different degrees of shoulder joint position, athletes are vulnerable to high injury. It is reported that in gymnastic activities, the shoulder can bear a force up to 8.5 times the body weight (Brewin et al., 2000). Momma et al. also analyzed the bone mineralization of the subchondral bone of the wrist joint of college gymnasts. They found that in the control group, the high-density area (%HDAs) was mainly distributed in the lunate fossa (LF) and navicular fossa (SF); In the gymnast group, HDAS is mainly distributed in the dorsal part of the navicular fossa (DSF), the volar part of the navicular fossa (PSF) and the articular surface of the navicular bone (Momma et al., 2019). Repeated gymnastic activities distributed excessive stress through the carpal navicular fossa and the proximal articular surface of the carpal navicular bone.

Elbow injuries occur frequently in throwing sports. To reduce the probability of elbow sports injury, team doctors and coaches should pay attention to any discomfort in the elbow of athletes, especially the worsening pain of baseball pitchers under the corresponding throwing action. Generally, the reason for this kind of high-density differential distribution may be special training, but there are some significant differences in high-density distribution between comprehensive technical training, special technical training, and different training duration.

A study conducted subchondral bone mineralization analysis on the articular surface of the distal humerus of 30 baseball subjects (10 fielders; 10 pitchers; 10 non-athletes). All subjects had high-density areas in the distal trochlea posterior area of the humerus, but the area of high-density areas of baseball players increased more significantly. Besides, high-density distribution containing the part of the capitellum and part of the trochlea was presented in the baseball pitcher group. This subtle differential distribution may due to the surface stress loading between the radial head and the capitulum humeri in the pitching group during the upper arm elevation and acceleration stage of pitching led to the concentration of high-density areas in this part (Momma et al., 2011). However, it is noteworthy that the high-density and concentrated distribution of the capitulum of the distal humerus may be a potential inducing factor of EOCD, which occurs frequently in throwing sports. When baseball pitches, the strength of the elbow will produce a huge valgus and extension overload. This combined overload often leads to acute or chronic injury of the elbow. A specific example is the posterior medial side

of the olecranon of the ulna, which is located outside the humeral column at the posterior medial side. Momma et al. observed the distribution of bone mineralization on the articular surface of the ulna olecranon and the radial head of the elbow in baseball players. They found that the high-density area of the entire ulna olecranon and the head of the radius in the baseball group is higher than that in the control group, and the area of the high-density area at the rear of the ulna olecranon and the front of the radial head is more significant (Momma et al., 2012). The findings indicated that baseball pitching activities increase the actual stress on the articular surface at both the rear of the trochlear notch and the front of the radial head. The elbow flexion motion in the throwing action can make the olecranon of the ulna and the trochlear of the humerus come into contact in a large area thereby increasing contact stress. Especially, in the last third of the arm raising stage of the fast-ball and the changing ball throwing, the forearm changes from pronation to supination (Barrentine et al., 1998), which increases the probability of elbow joint injury.

CTOAM technology also explored the stress distribution pattern of symptomatic elbow valgus instability in baseball players. It was found that in the asymptomatic group and the symptomatic group, the high-density areas were in the anterolateral and posteromedial sides of the capitellum of the humerus, as well as the posteromedial and radial heads of the ulna. It indicates that dysfunction with ulnar collateral ligament (UCL) symptoms will produce excessive and accumulated stress in the elbow joint (Funakoshi et al., 2016). If the UCL is insufficient, as the main stabilizer of valgus stress with elbow flexion of 20°–120°, the distal end of ulnar humeral joint will produce high stress in the acceleration stage of throwing action. The functional insufficiency of UCL symptoms will lead to these abnormal stress patterns, which can make baseball pitchers have humeral capitulum exfoliative chondritis or ulnar olecranon stress fracture. Momma et al. found that the high-density area of the distal mobilization elbow joint in the Baseball Academy group and the professional group was mostly found in the anterior part of the glenoid of the scapula, the posterior part of the trochlear, and the head of the radius. The percentage of high-density areas in the anterior part of the capitulum, the posterior part of the trochlear, the radial head and the olecranon in the professional group was significantly higher than that in the college students' group (Momma et al., 2018).

5.2.2 Lower limb joints

Nishida et al. used CTOAM technology to analyze the bone mineralization of the patellofemoral articular surface of baseball players, and found that low-density areas appeared at the proximal end of the lateral trochlea of fielders, pitchers, and control groups. While at the distal part of the lateral notch both the proximal part of the medial notch and the distal part of the medial femoral trochlea have high-density areas (Nishida et al., 2012), indicating that the proximal part of the lateral trochlea of the femur bears less weight-bearing stress and can be chosen as the best part for autologous osteochondral transplantation for reducing the risk of postoperative symptoms of the patellofemoral joint. This provided an optimized treatment scheme for athletes with osteochondral injury.

Shiota et al. conducted bone mineralization analysis on the ankle joint surface of college football players. It was found that the high-density

areas are in the anteromedial and anterolateral parts of the distal tibia, the anteromedial and anterolateral parts of the proximal talus, and the distal fibula (Shiota et al., 2020). The results indicated that the excessive stress in football produces the anterior impact of the ankle joint, which led to the impact of the medial anterolateral front of the ankle joint of football players, forming a high-density distribution. Xu et al. Observed the CTOAM images of the feet of 10 normal people (control group) and 10 high-level Taekwondo athletes. Among Taekwondo athletes, the volume percentage of the distal tibia and talus with high and medium bone density was significantly higher than that of the control group. The force points on the articular surface of the ankle were areas 1, 4, and 7 of the distal tibia and areas 1, 3, 4, and 7 of the talus domes. Taekwondo Athletes' ankles are comprehensively stressed based on normal stress points to improve the high-density area near the low-stress area (Xu et al., 2022). It is believed that the special stress distribution patterns caused by Taekwondo (such as impact stress, ground reaction force, intra-articular stress), sports technology, lower limb muscle and tendon stress lead to ankle and bone tissue remodeling.

6 Advantages and limitation

6.1 Diagnostic accuracy and imaging sensitivity of CTOAM

CTOAM technology is sensitive to water because of its X-ray photons. Due to the high-density, the bone tissue can show an accurate image of stress distribution in joints. Many earlier studies have also confirmed that CTOAM technology has good data consistency with X-rays. Partial volume effect may affect the imaging effect of bone tissue to a certain extent, but it can be effectively resolved through setting the image layer thickness to a thin-layer image (such as 0.5 mm or 0.625 mm), which can improve the image resolution and describe the mineralization in the relatively thin bone plate under the soft bone more accurately (Muller-Gerbl et al., 1990a; Muller-Gerbl et al., 1990b; Eckstein et al., 1995a; Eckstein et al., 1995b). Therefore, CTOAM technology can be used as a reliable method for evaluating of joint bone mineral density and accessing joint internal stress distribution.

6.2 Time and money costs

According to the admission protocol of patients with joint diseases, patients with joint diseases are generally diagnosed by X-ray before admission. If the patient's X-ray results cannot accurately diagnose joint diseases, CT images, QCT images or MRI will be considered for the next diagnosis, so the time cost of diagnosis will be increased to a certain extent. However, as far as we know, the cost of QCT image and MRI image is high, the amount of ordinary CT image is low, and the results obtained by CTOAM technology are consistent and the image reconstruction efficiency is high. Therefore, CTOAM technology can be added to the daily CT image evaluation as an auxiliary post-treatment method to assist the orthopedic surgeon to estimate the risk of patient's disease progress, to optimize the treatment plan.

6.3 Limitation

Joint stress distribution cannot be directly measured using CTOAM. Only changes in bone density in the subchondral bone are measured by CTOAM. The pressure state of the bone's articular surface was inferred using Wolff's law from joint motion and partial material indentation experiments. CTOAM cannot directly measure changes in stress parameters corresponding to high-density regions of the articular surface.

CTOAM technology mainly focuses on the two-dimensional plane area changes in the joint surface of the subjects and specimens, and there is less research on the spatial distribution of intra-articular bone tissue (in the epiphyseal plate), which reduces the spatial visualization of the whole joint.

There are certain differences in the upper and lower limits of bone and joint density CT values (HU) in various parts of the human body. Except for the dark color for high-density pseudo (such as orange, red, dark red or black), the pseudo color distribution (low-density area and medium density area) in other studies is less consistent, and there is a lack of unified color card coding.

As HU is the attenuation coefficient calibrated according to water rather than absolute value, the data difference generated by HU may show different result data according to the difference in CT scanner KV parameters, CT scanner brand, algorithm or inspection conditions, resulting in the lack of repeatability of image measurement data.

The variety of scanning conditions is also a limitation. Due to the differences in bone algorithm and instrument parameters between different instrument manufacturers, there may be a certain degree of data output deviation between different periods, different types of CT scanning instruments, different scanning parameters, and different brands of CT scanning instruments. Of course, if just estimate the overall mode of bone mineral density distribution and the transformation characteristics, this deviation can be reduced to a certain extent by judging the overall trend of bone mineral density distribution and rise and fall changes.

7 Conclusion

CTOAM technology is a cost-effective tool technology for studying and diagnosing abnormal stress distribution in the subchondral bone. This method has good sensitivity and specificity in the distribution of subchondral bone stress in the joint. When subchondral bone stress distribution in the articular surface that cannot be identified by conventional X-ray and MRI images, CTOAM technology can be used to make the accurate clinical judgment and prognosis evaluation. This technology can identify the abnormal stress distribution of subchondral bone and osteoarthritis in early athletes and normal people, to achieve the effects of early prevention, early diagnosis, early intervention.

Author contributions

were all actively involved in the writing of the manuscript. All authors critically reviewed the manuscript, approved the final version to be published.

Funding

Conflict of interest

The authors declare that the research was conducted in the absence of any commercial or financial relationships that could be construed as a potential conflict of interest.

Publisher's note

All claims expressed in this article are solely those of the authors and do not necessarily represent those of their affiliated organizations, or those of the publisher, the editors and the reviewers. Any product that may be evaluated in this article, or claim that may be made by its manufacturer, is not guaranteed or endorsed by the publisher.

References

Anetzberger, H., Schulz, C., Pfahler, M., Refior, H. J., and Müller-Gerbl, M. (2002). Subchondral mineralization patterns of the glenoid after tear of the supraspinatus. *Clin. Orthop. Relat. R.* 404 (404), 263–268. doi:10.1097/00003086-200211000-00040

Baliunas, A. J., Hurwitz, D. E., Ryals, A. B., Karrar, A., Case, J. P., Block, J. A., et al. (2002). Increased knee joint loads during walking are present in subjects with knee osteoarthritis. *Osteoarthr. Cartil.* 10 (7), 573–579. doi:10.1053/joca.2002.0797

Barrentine, S. W., Matsuo, T., Escamilla, R. F., Fleisig, G. S., and Andrews, J. R. (1998). Kinematic analysis of the wrist and forearm during baseball pitching. *J. Appl. Biomech.* 14 (1), 24–39. doi:10.1123/jab.14.1.24

Blanch, P., and Gabbett, T. J. (2016). Has the athlete trained enough to return to play safely? The acute:chronic workload ratio permits clinicians to quantify a player's risk of subsequent injury. *BRIT J. SPORT Med.* 50 (8), 471–475. doi:10.1136/bjsports-2015-095445

Brewin, M. A., Yeadon, M. R., and Kerwin, D. G. (2000). Minimising peak forces at the shoulders during backward longswings on rings. *Hum. Mov. Sci.* 19 (5), 717–736. doi:10.1016/s0167-9457(00)00033-6

Buchowski, J. M., Kebaish, K. M., Sinkov, V., Cohen, D. B., Sieber, A. N., and Kostuik, J. P. (2005). Functional and radiographic outcome of sacroiliac arthrodesis for the disorders of the sacroiliac joint. *Spine J.* 5 (5), 520–528. doi:10.1016/j.spinee.2005.02.022

Deml, C., Kaiser, P., van Leeuwen, W. F., Zitterl, M., and Euler, S. A. (2016). The J-shaped bone graft for anatomic glenoid reconstruction: A 10-year clinical follow-up and computed tomography-osteoabsorptiometry study. *Am. J. Sports Med.* 44 (11), 2778–2783. doi:10.1177/0363546516665816

Eckstein, F., Merz, B., Muller-Gerbl, M., Holzknecht, N., Pleier, M., and Putz, R. (1995). Morphomechanics of the humero-ulnar joint: II. Concave incongruity determines the distribution of load and subchondral mineralization. *Anat. Rec.* 243 (3), 327–335. doi:10.1002/ar.1092430307

Eckstein, F., Muller-Gerbl, M., Steinlechner, M., Kierse, R., and Putz, R. (1995). Subchondral bone density in the human elbow assessed by computed tomography osteoabsorptiometry: A reflection of the loading history of the joint surfaces. *J. Orthop. Res.* 13 (2), 268–278. doi:10.1002/jor.1100130215

Engebretsen, L., Soligard, T., Steffen, K., Alonso, J. M., Aubry, M., Budgett, R., et al. (2013). Sports injuries and illnesses during the London summer olympic games 2012. *Br. J. Sports Med.* 47 (7), 407–414. doi:10.1136/bjsports-2013-092380

Foley, B. S., and Buschbacher, R. M. (2006). Sacroiliac joint pain: Anatomy, biomechanics, diagnosis, and treatment. *Am. J. Phys. Med. REHAB* 85 (12), 997–1006. doi:10.1097/01.phm.0000247633.68694.c1

Funakoshi, T., Furushima, K., Momma, D., Endo, K., Abe, Y., Itoh, Y., et al. (2016). Alteration of stress distribution patterns in symptomatic valgus instability of the elbow in baseball players: A computed tomography osteoabsorptiometry study. *Am. J. Sports Med.* 44 (4), 989–994. doi:10.1177/0363546515624916

Goldring, S. R., and Bianchi, G. (2012). Alterations in periarticular bone and cross talk between subchondral bone and articular cartilage in osteoarthritis. *Ther. Adv. MUSCULOSKEL* 4 (4), 249–258. doi:10.1177/1759720x12437353

Goutallier, D., Delépine, G., and Debeyre, J. (1979). The patello-femoral joint in osteoarthritis of the knee with genu varum (author's transl). *Revue de Chir. Orthop. Reparatrice de L'appareil Moteur.* 65 (1), 25–31.

Hadjidakis, D. J., and Androulakis, II (2006). Bone remodeling. *Ann. N. Y. Acad. Sci.* 1092 (1), 385–396. doi:10.1196/annals.1365.035

Hara, T., Ohara, Y., Abe, E., Takami, K., Orias, A. A. E., Arai, H., et al. (2021). Cervical endplate bone density distribution measured by CT osteoabsorptiometry and direct

comparison with mechanical properties of the endplate. *Eur. Spine J.* 30 (9), 2557–2564. doi:10.1007/s00586-021-06920-2

Harada, Y., Yokoya, S., Akiyama, Y., Mochizuki, Y., Ochi, M., and Adachi, N. (2018). Bone mineralization changes of the glenoid in shoulders with symptomatic rotator cuff tear. *Int. Orthop.* 42 (11), 2639–2644. doi:10.1007/s00264-018-4004-x

Hasegawa, Y., Matsui, Y., and Iwasaki, N. (2020). Computed tomography osteoabsorptiometry changes following ulnar shortening osteotomy: Observations in nine patients. *J. Hand Surg. Eur. Volume)* 45 (5), 527–529. doi:10.1177/1753193420908795

Hayashi, D., Jarraya, M., Engebretsen, L., D Crema, M., Roemer, W. F., Skaf, A., et al. (2018). Epidemiology of imaging-detected bone stress injuries in athletes participating in the Rio de Janeiro 2016 Summer Olympics. *BRIT J. SPORT Med.* 52 (7), 470–474. doi:10.1136/bjsports-2017-098189

Heiss, R., Guermazi, A., Jarraya, M., Engebretsen, L., Hotfiel, T., Parva, P., et al. (2019). Prevalence of MRI-detected ankle injuries in athletes in the rio de Janeiro 2016 summer olympics. *Acad. Radiol.* 26 (12), 1605–1617. doi:10.1016/j.acra.2019.02.001

Hernigou, P., Medevielle, D., Debeyre, J., and Goutallier, D. (1987). Proximal tibial osteotomy for osteoarthritis with varus deformity. A ten to thirteen-year follow-up study. *J. bone Jt. Surg. Am. volume* 69 (3), 332–354.

Hoechel, S., Alder, M., Wirz, D., and Müller-Gerbl, M. (2013). The human hip joint and its long-term load intake--how x-ray density distribution mirrors bone strength. *Hip Int.* 23 (6), 583–589. doi:10.5301/hipint.5000056

Hontani, K., Matsui, Y., Kawamura, D., Urita, A., Momma, D., Hamano, H., et al. (2021). Stress distribution pattern in the distal radioulnar joint before and after ulnar shortening osteotomy in patients with ulnar impaction syndrome. *Sci. REP-UK* 11 (1), . doi:10.1038/s41598-021-97398-x

Iwasaki, K., Kondo, E., Matsubara, S., Matsuoka, M., Endo, K., Yokota, I., et al. (2021). Effect of high tibial osteotomy on the distribution of subchondral bone density across the proximal tibial articular surface of the knee with medial compartment osteoarthritis. *Am. J. Sports Med.* 49 (6), 1561–1569. doi:10.1177/03635465211002537

Jackson, J. P., and Waugh, W. (1961). *Tibial osteotomy for osteoarthritis of the knee*, 746–751.

Kameda, T., Kondo, E., Onodera, T., Iwasaki, K., Onodera, J., Yasuda, K., et al. (2021). Changes in the contact stress distribution pattern of the patellofemoral joint after medial open-wedge high tibial osteotomy: An evaluation using computed tomography osteoabsorptiometry. *Orthop. J. Sports Med.* 9 (4), . doi:10.1177/2325967121998050

Kawasaki, T., Sashi, R., Moriya, S., Kaketa, T., Kobayashi, H., Itoigawa, Y., et al. (2013). Computed tomography osteoabsorptiometry for assessing the density distribution of subchondral bone as a measure of long-term mechanical stress in the "rugby shoulder". *J. SHOULDER Elb. Surg.* 22 (6), 800–806. doi:10.1016/j.jse.2012.07.015

Kemp, J. P., Medina-Gomez, C., Estrada, K., St, P. B., Heppe, D. H., Warrington, N. M., et al. (2014). Phenotypic dissection of bone mineral density reveals skeletal site specificity and facilitates the identification of novel loci in the genetic regulation of bone mass attainment. *PLOS Genet.* 10 (6), . doi:10.1371/journal.pgen.1004423

Kraljević, M., Zumstein, V., Wirz, D., Hügli, R., and Müller-Gerbl, M. (2011). Mineralisation and mechanical strength of the glenoid cavity subchondral bone plate. *Int. Orthop.* 35 (12), 1813–1819. doi:10.1007/s00264-011-1308-5

Layton, M. W., Goldstein, S. A., Goulet, R. W., Feldkamp, L. A., Kubinski, D. J., and Bole, G. G. (1988). Examination of subchondral bone architecture in experimental

osteoarthritis by microscopic computed axial tomography. *Arthritis rheumatism* 31 (11), 1400–1405. doi:10.1002/art.1780311109

Leumann, A., Valderrabano, V., Hoechel, S., Göpfert, B., and Müller-Gerbl, M. (2015). Mineral density and penetration strength of the subchondral bone plate of the talar dome: High correlation and specific distribution patterns. *J. Foot Ankle Surg.* 54 (1), 17–22. doi:10.1053/j.jfas.2014.09.035

Liu, X., Chen, Z., Gao, Y., Zhang, J., Jin, Z., and Affatato, S. (2019). High tibial osteotomy: Review of techniques and biomechanics. *J. Healthc. Eng.* 2019, 8363128–28. doi:10.1155/2019/8363128

Lochmuller, E. M., Maier, U., Anetzberger, H., Habermeyer, P., and Muller-Gerbl, M. (1997). Determination of subacromial space width and inferior acromial mineralization by 3D CT. Preliminary data from patients with unilateral supraspinatus outlet syndrome. *Surg. Radiol. Anat.* 19 (5), 329–337. doi:10.1007/s00276-997-0329-7

Madry, H. (2010). The subchondral bone: A new frontier in articular cartilage repair. *Knee Surg. sports traumatology, Arthrosc. official J. ESSKA* 18 (4), 417–418. doi:10.1007/s00167-010-1071-y

Matsubara, S., Onodera, T., Iwasaki, K., Hishimura, R., Matsuoka, M., Kondo, E., et al. (2022). Discrepancy in the distribution patterns of subchondral bone density across the ankle joint after medial opening-wedge and lateral closing-wedge high tibial osteotomy. *Am. J. Sports Med.* 50 (2), 478–485. doi:10.1177/03635465211062235

Matsui, Y., Funakoshi, T., Momma, D., Miyamoto, A., Endo, K., Furushima, K., et al. (2018). Variation in stress distribution patterns across the radial head fovea in osteochondritis dissecans: Predictive factors in radiographic findings. *J. SHOULDER Elb. Surg.* 27 (5), 923–930. doi:10.1016/j.jse.2017.12.023

McAlindon, T. E., Bannuru, R. R., Sullivan, M. C., Arden, N. K., Berenbaum, F., Bierma-Zeinstra, S. M., et al. (2014). OARSI guidelines for the non-surgical management of knee osteoarthritis. *Osteoarthr. Cartil.* 22 (3), 363–388. doi:10.1016/j.joca.2014.01.003

Miura, S., Iwasaki, K., Kondo, E., Endo, K., Matsubara, S., Matsuoka, M., et al. (2022). Stress on the posteromedial region of the proximal tibia increased over time after anterior cruciate ligament injury. *Knee Surg. Sports Traumatol. Arthrosc.* 30 (5), 1744–1751. doi:10.1007/s00167-021-06731-4

Mochizuki, Y., Natsu, K., Kashiwagi, K., Yasunaga, Y., and Ochi, M. (2005). Changes of the mineralization pattern in the subchondral bone plate of the glenoid cavity in the shoulder joints of the throwing athletes. *J. SHOULDER Elb. Surg.* 14 (6), 616–619. doi:10.1016/j.jse.2005.02.016

Momma, D., Funakoshi, T., Endo, K., Yokota, M., Fujisaki, K., and Iwasaki, N. (2018). Alteration in stress distribution patterns through the elbow joint in professional and college baseball pitchers: Using computed tomography osteoabsorptiometry. *J. Orthop. Sci.* 23 (6), 948–952. doi:10.1016/j.jos.2018.06.006

Momma, D., Iwamoto, W., Endo, K., Sato, K., and Iwasaki, N. (2020). Stress distribution patterns across the shoulder joint in gymnasts: A computed tomography osteoabsorptiometry study. *Orthop. J. Sports Med.* 8 (11), . doi:10.1177/2325967120962103

Momma, D., Iwamoto, W., and Iwasaki, N. (2019). Long-term stress distribution patterns across the wrist joint in gymnasts assessed by computed tomography osteoabsorptiometry. *J. Hand Surg. Eur. Volume)* 44 (10), 1098–1100. doi:10.1177/1753193419870037

Momma, D., Iwasaki, N., Oizumi, N., Funakoshi, T., Abe, Y., Minami, A., et al. (2012). Alterations in stress distribution patterns through the forearm joint surface of the elbow in baseball players assessed using computed tomography osteoabsorptiometry. *J. Orthop. Sci.* 17 (3), 253–260. doi:10.1007/s00776-012-0198-8

Momma, D., Iwasaki, N., Oizumi, N., Nakatsuchi, H., Funakoshi, T., Kamishima, T., et al. (2011). Long-term stress distribution patterns across the elbow joint in baseball players assessed by computed tomography osteoabsorptiometry. *Am. J. Sports Med.* 39 (2), 336–341. doi:10.1177/0363546510383487

Mühlhofer, H., Ercan, Y., Drews, S., Matsuura, M., Meissner, J., Linsenmaier, U., et al. (2009). Mineralisation and mechanical strength of the subchondral bone plate of the inferior tibial facies. *Surg. Radiol. Anat.* 31 (4), 237–243. doi:10.1007/s00276-008-0430-6

Muller-Gerbl, M., Putz, R., Hodapp, N., Schulte, E., and Wimme, B. (1990). Computed tomography-osteoaboorptiometry: A method of assessing the mechanical condition of the major joints in a living subject. *Clin. Biomech.* 5, 193–198. doi:10.1016/0268-0033(90)90002-n

Müller-Gerbl, M., Putz, R., Hodapp, N., Schulte, E., and Wimmer, B. (1989). Computed tomography-osteoabsorptiometry for assessing the density distribution of subchondral bone as a measure of long-term mechanical adaptation in individual joints. *Skelet. Radiol.* 18 (7), 507–512. doi:10.1007/bf00351749

Muller-Gerbl, M., Putz, R., Hodapp, N., Schulte, E., and Wimmer, B. (1990). Demonstration of subchondral density pattern using CT-osteoabsorptiometry (CT-OAM) for the assessment of individual joint stress in live patients. *Z Orthop. Ihre Grenzgeb* 128 (2), 128–133. doi:10.1055/s-2008-1039487

Murakami, A. M., Kompel, A. J., Engebretsen, L., Li, X., Forster, B. B., Crema, M. D., et al. (2018). The epidemiology of MRI detected shoulder injuries in athletes participating in the Rio de Janeiro 2016 Summer Olympics. *BMC MUSCULOSKEL Dis.* 19 (1), . doi:10.1186/s12891-018-2224-2

Murakami, E., Kurosawa, D., and Aizawa, T. (2018). Sacroiliac joint arthrodesis for chronic sacroiliac joint pain: An anterior approach and clinical outcomes with a minimum 5-year follow-up. *J. Neurosurg. Spine* 29 (3), 279–285. doi:10.3171/2018.1.spine17115

Nishida, K., Iwasaki, N., Fujisaki, K., Funakoshi, T., Kamishima, T., Tadano, S., et al. (2012). Distribution of bone mineral density at osteochondral donor sites in the patellofemoral joint among baseball players and controls. *Am. J. Sports Med.* 40 (4), 909–914. doi:10.1177/0363546511435085

Numaguchi, K., Momma, D., Matsui, Y., Yokota, M., Oohinata, J., Kondo, E., et al. (2021). Stress-distribution pattern across the glenohumeral joint in collegiate and professional baseball players: A computed tomography osteoabsorptiometry study. *Orthop. J. Sports Med.* 9 (6), . doi:10.1177/23259671211009185

Oettmeier, R., Arokoski, J., Roth, A. J., Helminen, H. J., Tammi, M., and Abendroth, K. (1992). Quantitative study of articular cartilage and subchondral bone remodeling in the knee joint of dogs after strenuous running training. *J. BONE Min. Res.* 7 (S2), S419–S424. doi:10.1002/jbmr.5650071410

Orías, A. A. E., Sheha, E., Zavras, A., John, P., Fitch, A. A., An, H. S., et al. (2021). CT osteoabsorptiometry assessment of subchondral bone density predicts intervertebral implant subsidence in a human ACDF cadaver model. *Glob. Spine J.*, 21925682211034845. doi:10.1177/21925682211034845

Pendleton, A., Arden, N., Dougados, M., Doherty, M., Bannwarth, B., Bijlsma, J. W. J., et al. (2000). EULAR recommendations for the management of knee osteoarthritis: Report of a task force of the standing committee for international clinical studies including therapeutic trials (ESCISIT). *Ann. Rheum. Dis.* 59 (12), 936–944. doi:10.1136/ard.59.12.936

Poilliot, A., Kurosawa, D., Toranelli, M., Zhang, M., Zwirner, J., Muller-Gerbl, M., et al. (2021). Subchondral bone changes following sacroiliac JointArthrodesis – a morpho-mechanical assessment ofSurgical treatment of the painful joint. *PAIN PHYSICIAN* 24 (3), E317–E326. doi:10.36076/ppj.2021/24/e317

Primeau, C. A., Birmingham, T. B., Leitch, K. M., Willits, K. R., Litchfield, R. B., Fowler, P. J., et al. (2021). Total knee replacement after high tibial osteotomy: Time-to-event analysis and predictors. *Can. Med. Assoc. J. (CMAJ)* 193 (5), E158–E166. doi:10.1503/cmaj.200934

Rhee, S. H., and Baek, G. H. (2012). A correlation exists between subchondral bone mineral density of the distal radius and systemic bone mineral density. *Clin. Orthop. Relat. Research®* 470 (6), 1682–1689. doi:10.1007/s11999-011-2168-4

Sharma, L., Song, J., Felson, D. T., Cahue, S., Shamiyeh, E., and Dunlop, D. D. (2001). The role of knee alignment in disease progression and functional decline in knee osteoarthritis. *JAMA* 286 (2), 188–195. doi:10.1001/jama.286.2.188

Shelburne, K. B., Torry, M. R., and Pandy, M. G. (2006). Contributions of muscles, ligaments, and the ground-reaction force to tibiofemoral joint loading during normal gait. *J. Orthop. Res.* 24 (10), 1983–1990. doi:10.1002/jor.20255

Shimizu, T., Iwasaki, N., Nishida, K., Minami, A., and Funakoshi, T. (2012). Glenoid stress distribution in baseball players using computed tomography osteoabsorptiometry: A pilot study. *Clin. Orthop. Relat. Research®* 470 (6), 1534–1539. doi:10.1007/s11999-012-2256-0

Shiota, J., Momma, D., Yamaguchi, T., and Iwasaki, N. (2020). Long-term stress distribution patterns across the ankle joint in soccer players: A computed tomography osteoabsorptiometry study. *Orthop. J. Sports Med.* 8 (11), . doi:10.1177/2325967120963085

Simon, P., Gupta, A., Pappou, I., Hussey, M. M., Santoni, B. G., Inoue, N., et al. (2015). Glenoid subchondral bone density distribution in male total shoulder arthroplasty subjects with eccentric and concentric wear. *J. SHOULDER Elb. Surg.* 24 (3), 416–424. doi:10.1016/j.jse.2014.06.054

Soriano-Baron, H., Lindsey, D. P., Rodriguez-Martinez, N., Reyes, P. M., Newcomb, A., Yerby, S. A., et al. (2015). The effect of implant placement on sacroiliac joint range of motion: Posterior versus transarticular. *Spine* 40(9), E525–E530. doi:10.1097/brs.0000000000000839

Szadek, K. M., Hoogland, P. V., Zuurmond, W. W., de Lange, J. J., and Perez, R. S. (2008). Nociceptive nerve fibers in the sacroiliac joint in humans. *Reg. Anesth. Pain Med.* 33 (1), 36–43. doi:10.1016/j.rapm.2007.07.011

Szadek, K. M., Hoogland, P. V. J. M., Zuurmond, W. W. A., De Lange, J. J., and Perez, R. S. G. M. (2010). Possible nociceptive structures in the sacroiliac joint cartilage: An immunohistochemical study. *Clin. Anat. (New York, N.Y.)* 23 (2), 192–198. doi:10.1002/ca.20908

Teichtahl, A. J., Cicuttini, F. M., Janakiramanan, N., Davis, S. R., and Wluka, A. E. (2006). Static knee alignment and its association with radiographic knee osteoarthritis. *Osteoarthr. Cartil.* 14 (9), 958–962. doi:10.1016/j.joca.2006.04.014

van Raaij, T. M., Reijman, M., Brouwer, R. W., Bierma Zeinstra, S., and Verhaar, J. (2010). Medial knee osteoarthritis treated by insoles or braces: A randomized trial. *Clin. Orthop. Relat. R.* 468 (7), 1926–1932. doi:10.1007/s11999-010-1274-z

von Eisenhart-Rothe, R., Eckstein, F., Müller-Gerbl, M., Landgraf, J., Rock, C., and Putz, R. (1997). Direct comparison of contact areas, contact stress and subchondral mineralization in human hip joint specimens. *Anat. Embryology* 195 (3), 279–288. doi:10.1007/s004290050047

Xu, G., Liu, H., and Zhang, L. (2022). Characterization of changes in subchondral bone tissue density of the ankle joint in Taekwondo players. *Front. Bioeng. Biotechnol.* 10, 872258. doi:10.3389/fbioe.2022.872258

Zumstein, V., Kraljević, M., Wirz, D., Hügli, R., and Müller-Gerbl, M. (2012). Correlation between mineralization and mechanical strength of the subchondral bone plate of the humeral head. *J. Shoulder Elb. Surg.* 21 (7), 887–893. doi:10.1016/j.jse.2011.05.018

Moving fluoroscopy-based analysis of THA kinematics during unrestricted activities of daily living

Fabio D'Isidoro[1], Clara Brockmann[1], Bernd Friesenbichler[2], Thomas Zumbrunn[1], Michael Leunig[2] and Stephen J. Ferguson[1]*

[1]Institute for Biomechanics, ETH Zurich, Zurich, Switzerland, [2]Schulthess Klinik, Zurich, Switzerland

Introduction: Knowledge of the accurate *in-vivo* kinematics of total hip arthroplasty (THA) during activities of daily living can potentially improve the *in-vitro* or computational wear and impingement prediction of hip implants. Fluoroscopy- based techniques provide more accurate kinematics compared to skin marker-based motion capture, which is affected by the soft tissue artefact. To date, stationary fluoroscopic machines allowed the measurement of only restricted movements, or only a portion of the whole motion cycle.

Methods: In this study, a moving fluoroscopic robot was used to measure the hip joint motion of 15 THA subjects during whole cycles of unrestricted activities of daily living, i.e., overground gait, stair descent, chair rise and putting on socks.

Results: The retrieved hip joint motions differed from the standard patterns applied for wear testing, demonstrating that current pre-clinical wear testing procedures do not reflect the experienced *in-vivo* daily motions of THA.

Discussion: The measured patient-specific kinematics may be used as input to *in vitro* and computational simulations, in order to investigate how individual motion patterns affect the predicted wear or impingement.

KEYWORDS

hip, kinematics, fluoroscopy, arthroplasty, daily activities

1 Introduction

Total hip arthroplasty (THA) is a well-accepted and successful solution for patients with end-stage osteoarthritis, and its demand is expected to rise as demographics reflect an ageing population (Szymanski and Barciszewski, 2017). Despite the positive outcomes (Fortina et al., 2005), the longevity of THA must be improved to counter the expected increase in number of revisions and to meet the needs of a broader and generally more active patient population. With improvements in THA technology and societal expectations for unencumbered life, indications are increasing for arthroplasty in both younger and older subjects. The downturn of metal-on-metal hip prostheses (Hart et al., 2012; Mellon et al., 2013), despite promising technical measures of performance, showed that current *in-vitro* wear testing procedures fail at predicting the true *in-vivo* performance of the hip prosthesis (Scholes and Unsworth, 2006). Comparisons between *ex-vivo* and *in vitro* implant surface textures revealed wider regions of marked wear patterns for retrievals (Manaka et al., 2004;

Affatato et al., 2012). These discrepancies were related to differences between *in vitro* and *in vivo* kinematics and kinetics.

Implant wear is currently tested with laboratory simulators, where standardized motion and loading patterns are applied on the hip prosthetic components (ISO 14242-1:2014, 2014). The standard loading pattern consists of a walking profile with a simplified axial loading twin-peak curve, with 3,000 N peak load at "heel strike" and "toe-off," and a 300 N swing phase. The ISO motion is standardized to +25°/−18° Flexion/Extension, +7°/−4° Adduction/Abduction and +2°/−10° Internal/External rotation, to represent a typical gait pattern 8. Researchers have found that altering the input parameters of wear simulators from the ISO standard can generate clinically relevant changes in wear predictions (Roter et al., 2002; Bowsher et al., 2006; Fabry et al., 2013), and that individual patient activity patterns affect wear of THA (Gao et al., 2011; Mellon et al., 2013).

In addition to laboratory wear testing, there is an increasing shift towards computational simulations of THA tribology and wear, in the interest of improving efficiency, decreasing costs, or exploring broader parameter spaces. Gait driven finite element analyses have been shown to accurately capture experimentally measured wear rates (Toh et al., 2021), and the specific importance of developing appropriate wear coefficients and analysing various daily living activities has been stressed (Wang et al., 2019). Computational wear predictions allow the exploration of unconventional articulating counter-surfaces, in the absence of prohibitive physical prototyping costs (Jamari et al., 2022) and facilitate a full parametric analysis of the contribution of implant geometry, properties and loading conditions on THA contact stresses and wear (Li et al., 2020). The maintenance of low-friction articulation is a requirement for limiting wear, and recently fully coupled simulation models have emerged which allow the prediction of both the evolution of a lubricating fluid film, taking into account implant deformation, and the consequent wear (Gao et al., 2017), and exploring the effect of fluid film depletion in, e.g., ceramic-on-ceramic systems (Meng et al., 2015). Kinematic data has also been used to drive musculoskeletal models, which then provide the boundary conditions for finite element simulations of contact pressure (Affatato et al., 2018).

Impingement, and a corresponding increased risk of joint subluxation, is a further potential cause of implant failure heavily influenced by joint kinematics. Geometry based models, or 3D parametric finite element models, of the implant and bone have been used to evaluate the impingement-free range of motion (ROM) of THA (Alastruey-Lopez et al., 2020; Pryce et al., 2022). Such simulations have provided ROM-to-impingement curves for challenging high flexion and pivot activities (McCarthy et al., 2021). Such predictions allow the pre-operative surgical plan to be adjusted to minimise impingement risk (Palit et al., 2019).

Therefore, the importance of testing the normal function and wear of THA based on motions and loadings from a broader spectrum of activities of daily living (ADL), as well as the need to identify adverse loading scenarios is increasingly acknowledged.

Kinematics and kinetics of THA during different ADLs have been analyzed by Bergmann et al. (2001) in four patients using motion analysis and instrumented prostheses. Skin marker-based motion capture (MC) has been adopted in several studies to measure implanted hip joint motion during gait (Perron et al., 2000; Bennett

et al., 2008), stair climbing and descending (Shrader et al., 2009; Lamontagne et al., 2011a), and sitting and standing from a chair (Lamontagne et al., 2012). However, MC-based kinematics are affected by errors due to soft tissue artefact, which is caused by the extensive movement of skin markers relative to the underlying bones (Leardini et al., 2005). The accuracy of MC may not allow to reliably capture kinematic aspects that have been observed to affect wear, such as hip micro separation (Nevelos et al., 2000), prosthetic hip impingement (Malik et al., 2007) and edge loading (Mellon et al., 2013).

Soft tissue artefact-free THA kinematics have been obtained with video-fluoroscopy (VF), a minimally invasive technique where the true motion of the prosthetic components is retrieved directly by 2D/3D registration of implant models with a sequence of X-ray images acquired dynamically during *in-vivo* activities. VF studies have analyzed gait on treadmill (Glaser et al., 2008; Tsai et al., 2013; Tsai et al., 2014), stair climbing (Dimitriou et al., 2015), squatting (Koyanagi et al., 2011), and isolated abduction (Lombardi et al., 2000). However, a constraint of these studies was the limited field of view using a stationary X-ray imaging system (List et al., 2013) that allowed the assessment of only restricted movements, or only a portion of the whole motion cycle. For this reason, gait using VF has only been evaluated on a treadmill. Although similarities in both kinematics and kinetics have been reported between treadmill and overground gait for healthy subjects after an accommodation period (Watt et al., 2010), there is evidence that elderly people may have difficulty accommodating to treadmill walking (Wass et al., 2005). Hence, overground gait is better suited to represent the daily walking of most THA patients.

Moving fluoroscopic systems have been developed in order to measure accurate unrestricted joint motions. ADLs of the prosthetic knee (List et al., 2017) and ankle (List et al., 2012) were analyzed *in-vivo* with moving single-plane fluoroscopy during ADLs. Recently, a moving biplane X-ray imaging system was tested *in-vitro* for total knee arthroplasty during simulated overground gait (Guan et al., 2016).
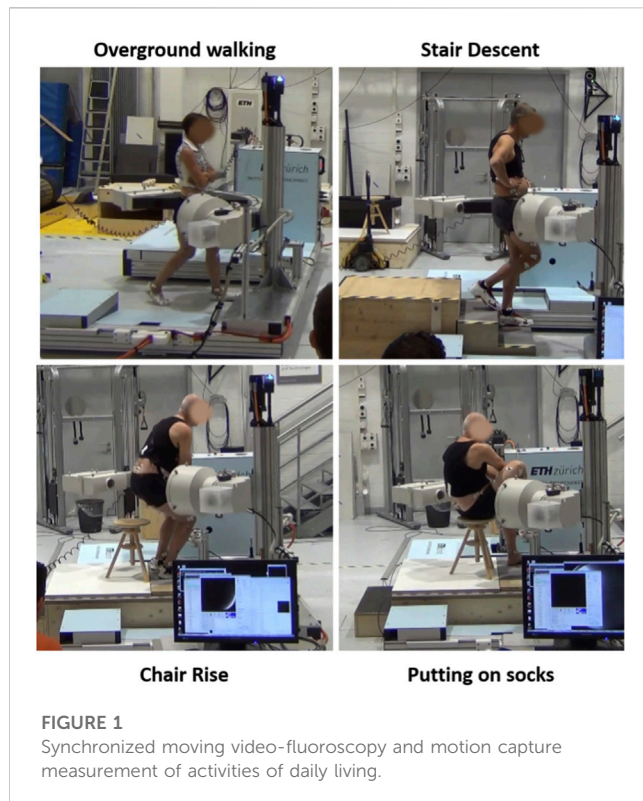
The present study is the first observational analysis of the *in-vivo* kinematics of THA measured with moving fluoroscopy in a sample population performing whole cycles of both routine and challenging activities of daily living, i.e., overground gait, stair descent, chair rise, and putting on socks.

2 Methods

This was an analytic, cross-sectional, observational, non-clinical research study for the collection of health-related data (Level of evidence III).

2.1 Subjects and activities

15 subjects with unilateral primary THA due to osteoarthritis (9 men, average age 65 ± 7.4, weight 77.4 kg ± 10.6, height 174.7 cm ± 9.1, BMI 25.3 kg/m² ± 2.2, average follow-up time from surgical date 31 months, cup sizes from 48 to 60 mm, femoral head sizes from 32 to 36 mm, all right implanted side) provided their written informed consent to the study, that was approved by the institutional review board and by the local cantonal

FIGURE 1
Synchronized moving video-fluoroscopy and motion capture measurement of activities of daily living.

ethics committee (BASEC-No. 2016-00438). All patients received a Smith & Nephew Polar Stem and R3 cup with a direct anterior approach, had an Oxford Hip Score >40, none or very low pain (VAS < 2) and standardized general health survey score (SF-12) within the normal range for people in their age group.

Each subject was measured with synchronized moving video-fluoroscopy and optical motion capture at a reference standing upright position and while performing four ADLs: overground walking, stair descent, chair rise, and putting on socks (Figure 1). Given the overall limitation on allowable radiation exposure, determined by the overall imaging time, and imaging angle for a desired accuracy (D'Isidoro et al., 2017), no more than four activities could be assessed. Five cycles per activity were chosen for analysis, based on the image quality. Force plates on the ground and on the stair steps were used to identify cycle events. Cycles were defined for gait between two consecutive right heel strikes, for stair descent between the right toe landing on the step and the following right heel strike on the ground, for chair rise from beginning of trunk flexion to standing position. Gait was performed with the arms crossed in front of the torso, to allow an unobstructed view of the hip for video fluoroscopy. It has been shown that even a partial weight-bearing constraint of the arms does not influence the motion patterns at the joints of the lower extremities during gait (Stephenson et al., 2010). Putting on socks was performed in a seated position until maximum hip flexion. Prior to each experiment, each subject was given sufficient time to get accustomed to the moving fluoroscope without being exposed to radiation. Measurements were done once the moving pattern of the patient was deemed consistent and unaffected by the presence of the machine.

2.2 Video-fluoroscopy measurement

The moving fluoroscope consisted of a modified video-fluoroscopy C-arm (BV Pulsera, Philips Medical Systems) mounted onto a motorized trolley that allows horizontal tracking up to 5 m/s velocity and 9 m/s^2 acceleration, and vertical tracking up to 1.33 m/s velocity and 4 m/s^2 acceleration. Tracking is achieved by positional feedback of the subject's joint using a wire sensor and a digital goniometer; the wire sensor is attached with a Velcro-strap to the waist of the subject for tracking the hip.

Specifically for the hip joint measurements, the C-arm was oriented such that the irradiation angle was 45° from the posterior side according to the guidelines described in a previous study for optimized accuracy of 2D/3D registration and low radiation dose delivered to the patient (D'Isidoro et al., 2017). Fluoroscopic images were acquired during motion at 30 Hz, with a standalone charge-coupled device camera (camera: IMPERX IPX-1M48-L, Imperx Inc., Boca Raton, United States; framegrabber: Matrox Solios eCL/XCL-B, Matrox Electronic Systems Ltd., Quebec, Canada) to allow a shutter time of 1 ms and an image resolution of 1,000 × 1,000 pixels with a grayscale resolution of 12 bit. The fluoroscopy system was operated at 8 ms pulse width, 100–110 kV and 12 mA*s. Due to the optimized irradiation angle, measurements were performed with a total radiation exposure below 5 mSv over all motion trials for each subject.

2.3 Motion capture

Optical motion capture was performed simultaneously to single-plane video-fluoroscopy. A Vicon MX system (Oxford Metrics Group, UK) using twenty-six MX40 and T160 infrared cameras recorded at 100 Hz the positions of skin markers, that were attached to the pelvis and the thigh of the patient according to the investigational site's marker-set for lower extremity assessments 28.

MC and VF were synchronized temporally with an external trigger and spatially with a calibration tool with known relative position between a grid of metal beads and fixed skin markers.

2.4 VF-based kinematics

Local coordinate systems were defined for the computer aided design (CAD) models of the acetabular cup and of the femoral stem (Figure 2) obtained from the manufacturer. For each acquired fluoroscopic image, the corresponding 3D pose of each implant model was retrieved with an in-house developed semi-automatic 2D/3D registration procedure. Automatic registration minimizes the difference between an input real fluoroscopic image and simulated images at predicted poses of the 3D model. Simulated images of the implant are fast generated as binary images with no-shading rendering from VTK Python graphics library, and subsequently blurred with Gaussian filter to simulate a real imaging system (Figure 2). Similarity between the de-noised input image and the simulated images is computed with a gradient correlation metric. The evolutionary strategy optimizer from the NLopt library is used to find the optimum 3D pose of the implant for which the similarity metric is maximum.
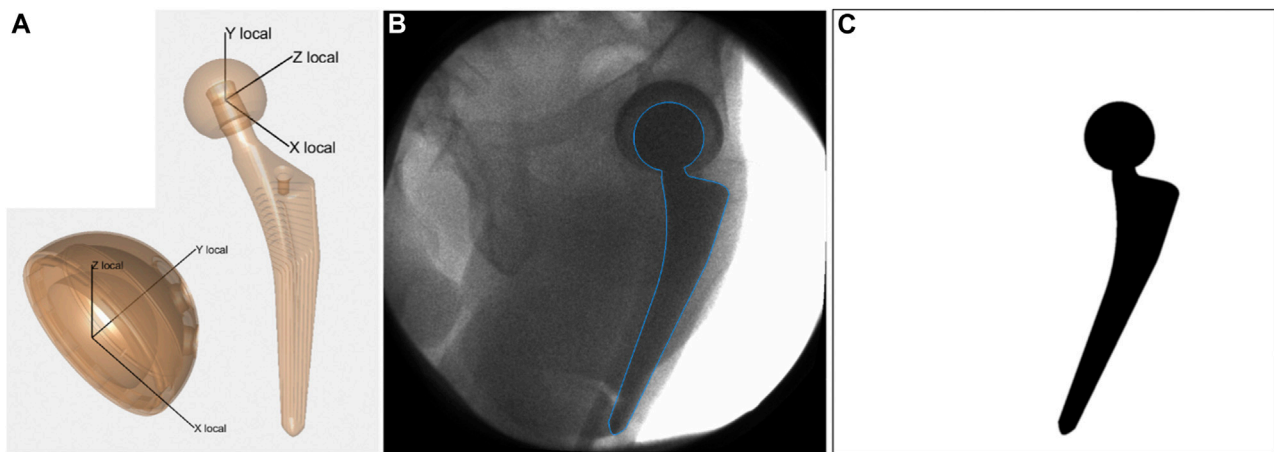
FIGURE 2
(A) Local coordinate systems defined for acetabular cup and femoral stem. **(B)** Acquired fluoroscopic image with overlay of registered femoral stem (blue line). **(C)** Simulated image of the femoral stem at the registered pose. It represents the simulated image that presented the highest similarity with the acquired fluoroscopic image, according to the gradient correlation similarity metric.
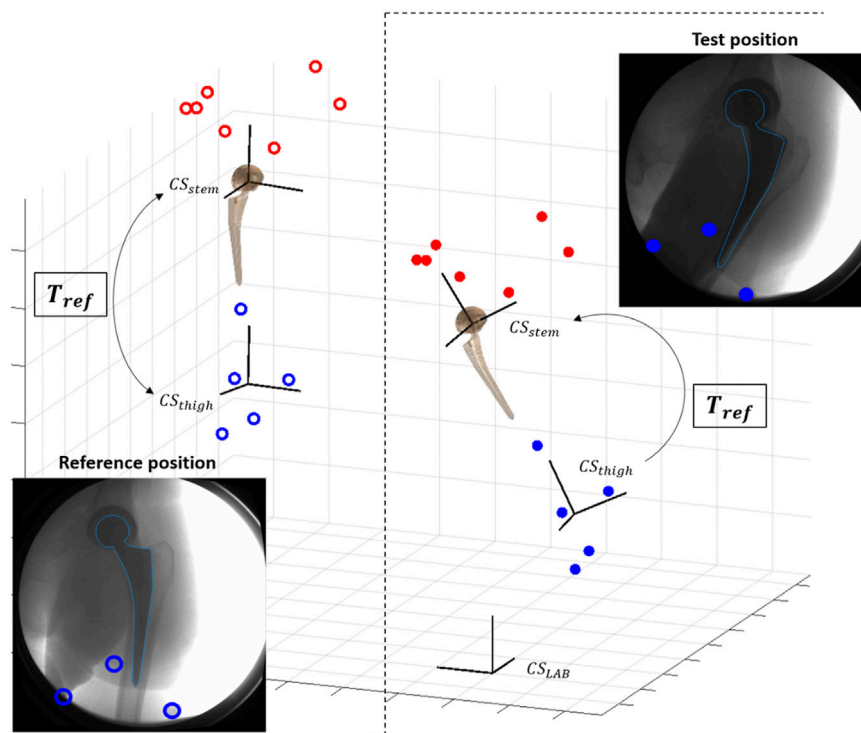

FIGURE 3
Scheme of pose initialization with skin markers (red for pelvis, blue for thigh): at reference standing position, the transformation T_{ref} between skin-marker based segment (CS_{thigh}) and prosthetic component (CS_{stem}) is computed. T_{ref} is used to initialize the pose of the prosthetic component for each new test position.

Convergence of the optimization to the optimum 3D pose was facilitated by providing a close initial guess that was derived from MC (Figure 3) in an automatic fashion. Reference skin marker-based segments of the hip joint were defined at the standing position, and

their relative position with respect to the corresponding prosthetic component was calculated. This relative position at the standing position was used to estimate the 3D pose of the prosthetic components for each acquired fluoroscopic image from the 3D

TABLE 1 Kinematic parameters extracted for 15 THA patients during four activities of daily living.

	Gait	Stairs	Chair rise	Socks on
Average speed [m/s] or duration [s]	1.13 m/s (0.19)	0.56 m/s (0.12)	2.15 s (0.391)	1.65 s (0.42)
Flexion [°]				
Mean ROM	41.10 (6.23)	28.27 (3.64)	93.35 (8.89)	53.02 (9.65)
Mean Peak	32.3 (8.37)	39.29 (8.73)	100.68 (13.36)	106.41 (12.3)
Mean Min	−8.7 (10.45)	11.11 (8.60)	7.56 (10.51)	53.33 (14.32)
Average Mean	14.33	22.01	61.89	80.56
Inter-patient dev	8.98	8.24	11.48	12.13
Intra-p mean dev	1.93	2.32	7.17	3.94
Adduction [°]				
Mean ROM	10.12 (2.22)	15.85 (3.836)	10.37 (2.08)	16.86 (4.10)
Mean Peak	6.9 (4.40)	10.29 (4.21)	5.85 (3.27)	11.0 (9.54)
Mean Min	−3.14 (3.32)	−5.46 (4.35)	−4.35 (3.27)	−5.24 (8.78)
Average Mean	2.22	2.76	1.03	1.69
Inter-patient dev	4.01	4.06	3.51	9.41
Intra-p mean dev	1.43	1.84	1.79	1.72
Internal rotation [°]				
Mean ROM	11.80 (2.90)	16.28 (4.03)	13.37 (3.30)	24.88 (5.68)
Mean Peak	1.75 (5.73)	2.18 (7.46)	3.26 (4.61)	−0.6 (6.85)
Mean Min	−9.98 (5.82)	−14.02 (7.17)	−9.97 (4.43)	−24.43 (7.52)
Average Mean	−3.92	−5.42	−3.12	−13.9
Inter-patient dev	5.59	6.56	4.21	8.24
Intra-p mean dev	2.04	2.91	2.26	1.95

Value in brackets indicate standard deviations. "Inter-patient dev" is the mean standard deviation calculated over the mean cycles for the 15 THA patients, while "Intra-p mean dev" is the average of the mean standard deviations calculated per patient over the five cycles per activity.

pose of the relative skin marker-based segment. The 3D pose for each acquired frame of the skin marker-based segments was computed by a least-square fit with the markers cloud at the reference standing position.

Since the acetabular cup is symmetric, its rotation around the symmetry axis cannot be uniquely determined by registration between image and implant model. This undetermined degree of freedom was then computed from the skin marker-based initialized value.

After automatic registration, manual correction of the 3D pose was performed by a trained user using a graphical user interface. The final registered 3D poses expressed in the local coordinate system of each prosthetic component were transformed into the anatomical coordinate systems. These were defined for both components based on the skin marker derived location of the relative joint segment at the reference upright standing position and according to the International Society of Biomechanics recommendations 35. Finally, kinematics curves obtained from the sequence of registered

poses were filtered using a fourth-order bidirectional low-pass Butterworth filter with a cutoff frequency of 6 Hz. Anatomical hip joint rotations were expressed as a ZXY Cardan sequence (Wu et al., 2002), corresponding to a sequence of consecutive flexion-extension (FE), adduction-abduction (AA) and internal-external rotation (IE).

The registration accuracy of single-plane fluoroscopy from a 45° irradiation angle was evaluated for the femoral stem in a previous study 34: RMS errors for FE, AA and, IE were 1.4°,1.2°,2.0° during simulated gait and 0.6°,0.8°,1.75° during simulated sitting down, respectively.

3 Results

The average speed of the 15 THA subjects was 1.13 m/s during level walking, 0.56 m/s during stair descent, while the average duration of the tasks of chair rise and putting on socks was 2.15 and 1.65 s, respectively (Table 1).
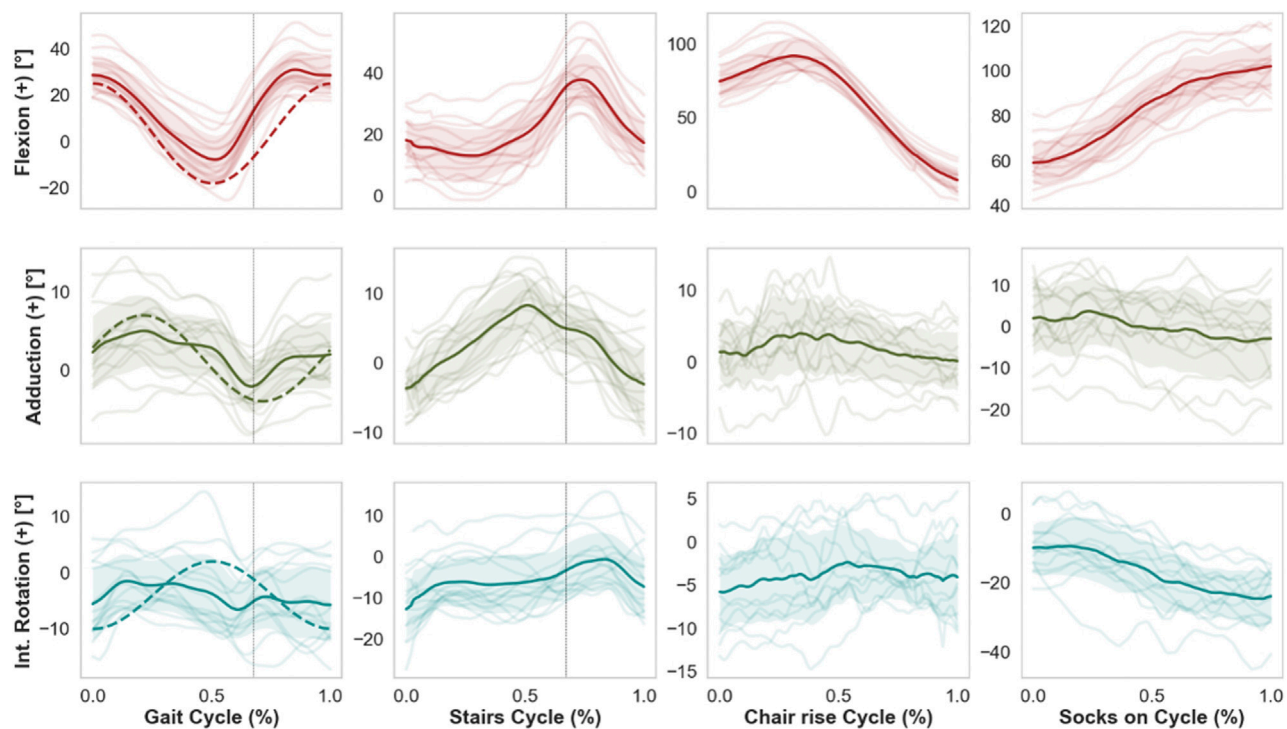
FIGURE 4
Mean kinematic curves (solid line) of 15 THA subjects during whole cycles of gait, stair descent, chair rise, and putting on socks. Shaded bands indicate standard deviations, while single semi-transparent lines refer to the individual per-subject kinematics averaged over five cycles. Dashed vertical lines indicate the time of toe-off for the kinematics of gait and stairs descent. Dashed curved lines superimposed on the activity of gait refer to the current ISO standard. Of note, the current ISO standard for wear testing fails to capture, e.g., the extensive range of flexion observed in specific daily activities such as chair rise or putting on socks, therefore these less frequent but potentially challenging activities are excluded from standard pre-clinical device tests.

During overground gait, the mean range of motion (ROM) was 41.1°, 10.1°, and 11.8° for FE, AA, and IE, respectively. The hip joint remained for the most part flexed, externally rotated and slightly adducted throughout the gait cycle (Figure 4), reaching extension up to a mean of 8.7° at late stance phase (ca. 56% gait cycle). The highest average hip flexion was 32.3° at terminal mid swing phase (ca. 85% gait cycle). The average external rotation was 3.9°.

Compared to gait, mean ROM for stair descent was smaller for FE and AA (28.3°, 15.9°, respectively) and larger for IE (16.3°). The average peak flexion was 39.3° at mid-swing phase of the descent (75% cycle). The hip reached higher peak adduction levels (10.3°) compared to gait around the toe-off. No particular trend was observed for IE, with average external rotation of 5.4°.

Starting from the seated position, the THA joint reached average peak flexion values of 100.7° (±13.36) for the sit-to-stand and 106.4° (±12.3) for the task of putting on socks, corresponding to average ranges of FE of 93.4° and 53.0°, respectively. Putting on socks was performed at average external rotation of 13.9°, with peak values of 24.4°.

For gait, average standard deviations from the mean cycles over all 15 subjects were 9.0°, 4.0°, and 5.6° for FE, AA and IE, respectively. Compared to gait, inter-subject variability was similar for stair descent, while larger for the FE during chair rise and putting on socks (Table 1). Intra-subject variability over the five cycles per

activity was generally below 3° on average for all anatomical rotations and for all motion tasks, with larger values of mean standard deviations for the flexion during chair rise and putting on socks.

No hip separations or impingement were observed for any of the 15 THA subjects during the measured activities.

4 Discussion

This study is the first to the authors' knowledge to measure with moving video-fluoroscopy the *in-vivo* THA kinematics during both routine and challenging activities of daily living performed in an unconstrained environment. The retrieved set of soft tissue artefact-free kinematics for 15 THA patients during four ADLs has been made publicly available (see Data Availability Statement). The observed patient-specific motions differed from the standard patterns applied for wear testing, supporting the statement that current pre-clinical wear test procedures do not reflect the experienced *in-vivo* daily motions and loadings and do not capture possible adverse loading scenarios such as separation, edge loading or hip impingement. The pre-clinical testing standards (e.g., ISO) allow a reliable comparison between devices in controlled conditions, and may indeed provide a reasonable estimate of long-term wear over millions of cycles. However, the

unique kinematic patterns observed in the present study for specific activities may be quite important for short-term phenomena related to fluid film response within the joint over a single loading cycle, or single adverse events causing joint subluxation.

Studies have pointed out the scarce amount of motion analyses for challenging activities that could contribute more to wear than gait (Kolk et al., 2014). The activity of stair descent was associated with the highest peak hip contact forces (260% BW) among several daily activities analyzed by Bergmann et al. (2001) for four patients with instrumented implants. Standing up is performed by older adults 65 times a day on average (Egerton and Brauer, 2009), and sitting was reported to be the most frequent daily activity from analysis over 31 THA patients (Morlock et al., 2001). Chair rise is challenging both for maintaining balance and for producing the force needed to complete the movement starting from a high degree of hip flexion (Lunn et al., 2016). Putting on socks is a challenging daily activity for patients with a hip implant and the ability to perform it is included in the Oxford Hip Score questionnaire to evaluate THA outcomes. Accurate measurement of hip kinematics with skin marker-based motion capture during high range of motion activities, such as stand up or putting on socks, is hampered by at least two factors. The skin deformation due to the large amount of soft tissue surrounding the hip joint contributes to soft tissue artefact. Secondly, the limited markers visibility due to the flexion of the trunk with respect to the lower limbs may reduce accuracy in motion retrieval. This study showed that moving fluoroscopy represents a valid solution for accurate kinematic analysis of the hip joint during challenging motion tasks besides gait.

The retrieved mean curves and ranges of motion of hip angles during level walking differed from those of the current ISO standard patterns for wear tests (ISO 14242-1:2014, 2014), with an offset towards a more extended hip throughout the cycle in the ISO standard. Moreover, the observed inter-subject variations (average standard deviations of 9.0°, 4.0°, 5.6° from the mean FE, AA, and IE rotation, respectively) indicate considerable deviations of the individual motions from the mean gait curves. We point out that the observed variations among patients stem solely from different motion patterns and not from different implant orientations, since kinematics were described based on anatomical coordinate systems. While the ISO pattern may approximate the gait motion of the mean THA population, wear predictions based on average profiles as input do not necessarily correspond to effective wear generated by the patient-specific kinematics (Cook and Robertson, 2016). The effect on wear of the individual motion paths of the femoral head articulating against the acetabular cup was discussed in several studies (Gao et al., 2011; Mellon et al., 2013). Some related the rate of polyethylene wear with the degree of multidirectional motion and the associated cross shear (Bragdon et al., 1996; Bennett et al., 2000; Budenberg et al., 2012), which are not realistically captured by the ISO pattern according to our results.

The angle curves retrieved for the other activities of daily living were different than the gait ISO profiles (Figure 1). Higher ranges were computed for AA and IE during stairs descent, and for FE and IE during chair rise. Given these differences, the present dataset of patient-specific kinematics may be used in combination with loading profiles to investigate the effect on wear of a range of daily activities broader than the current ISO standard. Moreover, a single representative daily cycle may be defined based on a combination of these activities and on their frequency, and the importance of the sequence of motions for wear can be further investigated.

A similar dataset was proposed by Fabry et al. (2013), based on the *in-vivo* kinematics and kinetics of four THA patients measured by Bergmann et al. (2001) with skin-marker motion capture and instrumented implants. Fabry et al. generated mean motion and loading profiles for walking, knee bending, stair climbing, and chair rising, and combined those into a single motion sequence that was suggested for wear tests under more comprehensive conditions. The mean profiles were produced from the measurements of only four patients, thus they cannot be generalized. Compared to the present study, the mean ranges of FE for level walking and for chair rise were almost 10° and 32° smaller, respectively. Reduced mean range of FE by 11° during chair rise was also reported by Lamontagne et al. (2012) in a motion capture study of 20 THA patients. These differences may be partly due to the less accurate motion analysis technique. In fact, a recent study by Fiorentino et al. (2017) evaluated the effects of soft tissue artefact on hip angles and reported statistically significant underestimation of the hip flexion and of the range of FE by skin marker-based technique, which we have also observed in our own ongoing measurements (D'Isidoro et al., 2020). In these measurements, during dynamic activities the hip joint appeared less flexed, more adducted and more internally rotated with motion capture, compared to video fluoroscopy. Overall errors for motion capture were on the order of 7%–11% of total ROM (D'Isidoro et al., 2020). The theoretical registration accuracy of single plane video fluoroscopy has been estimated in (D'Isidoro et al., 2017), ranging from RMS errors of sub-1° up to 2°, depending on imaging angle. For the oblique imaging angle in the present study, errors of up to 0.5° could be expected. The range and motion profiles reported by Lamontagne et al. (2011b) for stair descent are similar to those of the current analysis.

Since no previous fluoroscopy study of the hip was carried out for the four daily activities described here, comparison could only be performed between the overground gait presented in this research and the treadmill gait analyzed with dual-plane fluoroscopy by Tsai et al. (2014) (28 subjects) and Fiorentino et al. (2017) (11 subjects). While overall motion patterns were similar, some differences were found. Tsai et al. reported the prosthetic joint to remain flexed, adducted and externally rotated throughout the treadmill gait cycle. While a similar range of FE was found in the present study, the hip attained extension up to a maximum of 19.3° at terminal stance of the overground gait, indicating a more upright walking posture of the subjects. This discrepancy may originate from the higher walking speeds achieved with the moving fluoroscope (1.13 m/s versus 0.77 m/s), the different patient population, or the use of skin markers rather than bony landmarks for definition of the anatomical coordinate systems. Another reason may be the difference between treadmill and overground gait. However, kinematic equivalence between these two activities was found in a previous study (Watt et al., 2010). Furthermore, hip extension up to 20° was also observed in the analysis of Fiorentino et al., where ROM for flexion was even higher than in the present study.

Reduced ROM of implanted hip joints compared to healthy ones was reported during overground gait in a few motion capture-based studies (Perron et al., 2000; Bennett et al., 2008) and confirmed in the present one. For the fifteen measured subjects, the mean speed and range of hip FE and AA were lower compared to normal elderly subjects measured for a large cohort by Bennett et al. (2008); likewise, the range of hip FE, and the peak hip extension, adduction and internal rotation were smaller compared to the twenty healthy subject measured by Beaulieu et al. (2010). The latter study suggested that THA patients walk with reduced flexion and adduction in order to produce lower moments to stabilize the pelvis in the sagittal and the frontal plane, respectively. They speculated that this altered gait patterns result from a weakness of the hip flexors and adductors, which was developed either pre-operatively as a result of disuse atrophy to avoid pain or post-operatively as a result of surgery (Lamontagne et al., 2012).

For the activity of stair descent, the range and the peak values of hip FE observed in the present study were smaller compared to those of healthy subjects from the study by Lamontagne et al. (2011b); this supports the finding that THA patients flex their operated leg to a minimal degree necessary to clear the step, a tendency that might be a result of reduced activation of hip flexors. However for the chair rise activity, the reduction in hip sagittal plane range of motion and peak hip flexion of THA patient with respect to healthy controls was not observed in this study, where range of hip flexion was even higher than the one of healthy subjects reported by La Montagne et al. This higher range of hip flexion might be explained from a larger forward lean required to initiate the chair rise due to reduced force generating capacity.

No hip separations or impingement could be detected in the present study. Accuracy of single-plane fluoroscopy in retrieval of in-plane translations is comparable to accuracy of dual-plane techniques (Tsai et al., 2013), with estimated errors smaller than 0.47 ± 0.38 mm (mean and standard deviation) for the femoral stem and smaller than 0.84 ± 0.64 mm for the acetabular cup. Therefore, at least the in-plane components of the relative movement between the hip implant segments can be reliably considered smaller than 1 mm. Other dual-plane (Tsai et al., 2014) and single-plane (Glaser et al., 2008) fluoroscopy studies also reported small hip separation during gait (<0.72 and <0.9 mm, respectively), supporting the statement that only minimal "hip pistoning" occurs during the swing phase of gait. It was speculated that co-contraction may be responsible of the limited hip separation (Park et al., 1999; Tsai et al., 2014). In contrast, other studies reported larger hip separations during gait (2.8 mm) and hip abduction/adduction (3.0 mm) (Lombardi et al., 2000) and during pivoting activity (3.3 mm) (Blumenfeld et al., 2011). The results from the present study suggest that no relevant hip separations occur for stair descent, despite the longer leg trailing phase compared to gait, as well as for higher range of motion activities such as char rise and putting on socks. However, the accuracy of the present study did not allow to characterize micro-separation during daily activities. Studies have highlighted the importance of introducing micro-separation in the wear tests, as it affects the lubrication regime and the wear rate of the hip implant (Beadling et al., 2016).

Besides the low out-of-plane accuracy intrinsic to single-plane fluoroscopy, another limitation exists. The rotational degree of the acetabular cup around its symmetry axis could only be retrieved from the skin markers locations, thus its accuracy is affected by the soft tissue artefact. The resulting error propagates mostly to the internal rotation of the hip joint that is overestimated by skin marker-based techniques by an average of 5.8° during dynamic activities (Fiorentino et al., 2017). Other studies registered the pelvis segment with a model segmented from a CT scan that had not been acquired for the cohort of this study, as CT scans are not part of the standard routine procedure for total hip replacements. On the other hand, the present study showed a novel way to register the pelvis pose of an implanted hip without the need of a CT scan, thus with a considerable lower radiation dose delivered to the subjects at the expense of a lower accuracy. Another novelty was the use of skin markers to provide an initial guess of the 3D pose of the hip joint for each acquired fluoroscopic frame; this sped up the lengthy 2D/3D registration process and has not been reported in literature up to the author's knowledge. Finally, no previous study analyzed the activity of putting on socks for THA patients.

In conclusion, accurate *in-vivo* patient-specific kinematics of a sample THA population during four daily activities were produced and made publicly available. The importance of using individual patterns was highlighted by the inter-subject variability observed in the present study for different activities of daily living. The presented dataset can help to gain a better understanding of the *in-vivo* mechanisms of implant impingement and wear and could potentially improve the current range of motion and wear predictions performed with computational and laboratory simulators.

Data availability statement

The datasets presented in this study can be found in online repositories. The names of the repository/repositories and accession number(s) can be found below: https://www.research-collection.ethz.ch/handle/20.500.11850/404705.

Ethics statement

The studies involving human participants were reviewed and approved by Cantonal Ethics Commission Zurich (BASEC-No. 2017-00277). The patients/participants provided their written informed consent to participate in this study.

Author contributions

FD'I: Study design, ethics application, data collection, data analysis, manuscript preparation, manuscript revision, manuscript approval. CB: Data collection, data analysis, manuscript revision, manuscript approval. BF: Data collection, data analysis, manuscript revision, manuscript approval. TZ:

Conflict of interest

The authors declare that the research was conducted in the absence of any commercial or financial relationships that could be construed as a potential conflict of interest.

Publisher's note

All claims expressed in this article are solely those of the authors and do not necessarily represent those of their affiliated organizations, or those of the publisher, the editors and the reviewers. Any product that may be evaluated in this article, or claim that may be made by its manufacturer, is not guaranteed or endorsed by the publisher.

References

Affatato, S., Merola, M., and Ruggiero, A. (2018). Development of a novel *in silico* model to investigate the influence of radial clearance on the acetabular cup contact pressure in hip implants. *Materials* 11 (8), 1282. doi:10.3390/ma11081282

Affatato, S., Traina, F., De Fine, M., Carmignato, S., and Toni, A. (2012). Alumina-on-alumina hip implants: A wear study of retrieved components. *Bone Jt. J.* 94-B (1), 37–42. doi:10.1302/0301-620X.94B1.26956

Alastruey-Lopez, D., Ezquerra, L., Seral, B., and Perez, M. A. (2020). Using artificial neural networks to predict impingement and dislocation in total hip arthroplasty. *Comput. Methods Biomech. Biomed. Engin* 23 (10), 649–657. doi:10.1080/10255842.2020.1757661

Beadling, A. R., Bryant, M., Dowson, D., and Neville, A. (2016). Tribocorrosion of hard-on-hard total hip replacements with metal and ceramic counterfaces under standard and adverse loading conditions. *Tribol. Int.* 103, 359–367. doi:10.1016/j.triboint.2016.07.022

Beaulieu, M. L., Lamontagne, M., and Beaulé, P. E. (2010). Lower limb biomechanics during gait do not return to normal following total hip arthroplasty. *Gait Posture* 32, 269–273. doi:10.1016/j.gaitpost.2010.05.007

Bennett, D., Humphreys, L., O'Brien, S., Kelly, C., Orr, J. F., and Beverland, D. E. (2008). Gait kinematics of age-stratified hip replacement patients-A large scale, long-term follow-up study. *Gait Posture* 28 (2), 194–200. doi:10.1016/j.gaitpost.2007.11.010

Bennett, D. B., Orr, J. F., and Baker, R. (2000). Movement loci of selected points on the femoral head for individual total hip arthroplasty patients using three-dimensional computer simulation. *J. Arthroplasty* 15, 909–915. doi:10.1054/arth.2000.9195

Bergmann, G., Deuretzbacher, G., Heller, M., Graichen, F., Rohlmann, A., Strauss, J., et al. (2001). Hip contact forces and gait patterns from routine activities. *J. Biomech.* 34 (7), 859–871. doi:10.1016/S0021-9290(01)00040-9

Blumenfeld, T. J., Glaser, D. A., Bargar, W. L., Langston, G. D., Mahfouz, M. R., and Komistek, R. D. (2011). *In vivo* assessment of total hip femoral head separation from the acetabular cup during 4 common daily activities. *Orthopedics* 34 (6), 127. doi:10.3928/01477447-20110427-06

Bowsher, J. G., Hussain, A., Williams, P. A., and Shelton, J. C. (2006). Metal-on-metal hip simulator study of increased wear particle surface area due to "severe" patient activity. *Proc. Inst. Mech. Eng. Part H. J. Eng. Med.* 220 (2), 279–287. doi:10.1243/09544119JEIM93

Bragdon, C. R., O'Connor, D. O., Lowenstein, J. D., Jasty, M., and Syniuta, W. D. (1996). The importance of multidirectional motion on the wear of polyethylene. *Proc. Inst. Mech. Eng. Part H. J. Eng. Med.* 210, 157–165. doi:10.1243/PIME_PROC_1996_210_408_02

Budenberg, S., Redmond, A., White, D., Grainger, A., O'Connor, P., Stone, M. H., et al. (2012). Contact surface motion paths associated with leg length inequality following unilateral total hip replacement. *Proc. Inst. Mech. Eng. Part H. J. Eng. Med.* 226 (12), 968–974. doi:10.1177/0954411912453245

Cook, D. D., and Robertson, D. J. (2016). The generic modeling fallacy: Average biomechanical models often produce non-average results. *J. Biomech.* 49 (15), 3609–3615. doi:10.1016/j.jbiomech.2016.10.004

D'Isidoro, F., Brockmann, C., and Ferguson, S. J. (2020). Effects of the soft tissue artefact on the hip joint kinematics during unrestricted activities of daily living. *J. Biomech.* 104, 109717. doi:10.1016/j.jbiomech.2020.109717

Dimitriou, D., Tsai, T. Y., Li, J. S., Nam, K. W., Park, K. K., and Kwon, Y. M. (2015). *In vivo* kinematic evaluation of total hip arthroplasty during stair climbing. *J. Orthop. Res.* 33 (7), 1087–1093. doi:10.1002/jor.22837

D'Isidoro, F., Eschle, P., Zumbrunn, T., Sommer, C., Scheidegger, S., and Ferguson, S. J. (2017). Determining 3D kinematics of the hip using video fluoroscopy: Guidelines for balancing radiation dose and registration accuracy. *J. Arthroplasty* 32 (10), 3213–3218. doi:10.1016/j.arth.2017.05.036

Egerton, T., and Brauer, S. G. (2009). Temporal characteristics of habitual physical activity periods among older adults. *J. Phys. Act. Health* 6 (5), 644–650. doi:10.1123/jpah.6.5.644

Fabry, C., Herrmann, S., Kaehler, M., Klinkenberg, E. D., Woernle, C., and Bader, R. (2013). Generation of physiological parameter sets for hip joint motions and loads during daily life activities for application in wear simulators of the artificial hip joint. *Med. Eng. Phys.* 35 (1), 131–139. doi:10.1016/j.medengphy.2012.07.014

Fiorentino, N. M., Atkins, P. R., Kutschke, M. J., Goebel, J. M., Foreman, K. B., and Anderson, A. E. (2017). Soft tissue artifact causes significant errors in the calculation of joint angles and range of motion at the hip. *Gait Posture* 55, 184–190. doi:10.1016/j.gaitpost.2017.03.033

Fortina, M., Carta, S., Gambera, D., Crainz, E., Ferrata, P., and Maniscalco, P. (2005). Recovery of physical function and patient's satisfaction after Total Hip Replacement (THR) surgery supported by a tailored guide-book. *Acta Biomed. l'Ateneo Parm.* 76 (3), 152–156.

Gao, L., Dowson, D., and Hewson, R. W. (2017). Predictive wear modeling of the articulating metal-on-metal hip replacements. *J. Biomed. Mater Res. B Appl. Biomater.* 105 (3), 497–506. doi:10.1002/jbm.b.33568

Gao, L., Fisher, J., and Jin, Z. (2011). Effect of walking patterns on the elastohydrodynamic lubrication of metal-on-metal total hip replacements. *Proc. Inst. Mech. Eng. Part J. J. Eng. Tribol.* 225 (6), 515–525. doi:10.1177/1350650110396802

Glaser, D., Dennis, D. A., Komistek, R. D., and Miner, T. M. (2008). *In vivo* comparison of hip mechanics for minimally invasive versus traditional total hip arthroplasty. *Clin. Biomech.* 23 (2), 127–134. doi:10.1016/j.clinbiomech.2007.09.015

Guan, S., Gray, H. A., Keynejad, F., and Pandy, M. G. (2016). Mobile biplane X-ray imaging system for measuring 3D dynamic joint motion during overground gait. *IEEE Trans. Med. Imaging* 35 (1), 326–336. doi:10.1109/TMI.2015.2473168

Hart, A. J., Quinn, P. D., Lali, F., Sampson, B., Skinner, J. A., Powell, J. J., et al. (2012). Cobalt from metal-on-metal hip replacements may be the clinically relevant active agent responsible for periprosthetic tissue reactions. *Acta Biomater.* 8 (10), 3865–3873. doi:10.1016/j.actbio.2012.05.003

ISO 14242-1:2014 (2014). Implants for surgery—Wear of total hip-joint prostheses—Part 1: Loading and displacement parameters for wear-testing machines and corresponding environmental conditions for test. Available at: https://www.iso.org/standard/63073.html.

Jamari, J., Ammarullah, M. I., Santoso, G., Sugiharto, S., Supriyono, T., Prakoso, A. T., et al. (2022). Computational contact pressure prediction of CoCrMo, SS 316L and Ti6Al4V femoral head against UHMWPE acetabular cup under gait cycle. *J. Funct. Biomater.* 13 (2), 64. doi:10.3390/jfb13020064

Kolk, S., Minten, M. J. M., Van Bon, G. E. A., Rijnen, W. H., Geurts, A. C., Verdonschot, N., et al. (2014). Gait and gait-related activities of daily living after total hip arthroplasty: A systematic review. *Clin. Biomech.* 29, 705–718. doi:10.1016/j.clinbiomech.2014.05.008

Koyanagi, J., Sakai, T., Yamazaki, T., Watanabe, T., Akiyama, K., Sugano, N., et al. (2011). *In vivo* kinematic analysis of squatting after total hip arthroplasty. *Clin. Biomech.* 26 (5), 477–483. doi:10.1016/j.clinbiomech.2010.11.006

Lamontagne, M., Beaulieu, M. L., and Beaulé, P. E. (2011). Comparison of joint mechanics of both lower limbs of tha patients with healthy participants during stair ascent and descent. *J. Orthop. Res.* 29 (3), 305–311. doi:10.1002/jor.21248

Lamontagne, M., Beaulieu, M. L., Varin, D., and Beaulé, P. E. (2012). Lower-limb joint mechanics after total hip arthroplasty during sitting and standing tasks. *J. Orthop. Res.* 30 (10), 1611–1617. doi:10.1002/jor.22127

Lamontagne, M., Varin, D., and Beaulé, P. E. (2011). Does the anterior approach for total hip arthroplasty better restore stair climbing gait mechanics? *J. Orthop. Res.* 29 (9), 1412–1417. doi:10.1002/jor.21392

Leardini, A., Chiari, A., Della Croce, U., and Cappozzo, A. (2005). Human movement analysis using stereophotogrammetry. *Gait Posture* 21 (2), 212–225. doi:10.1016/j.gaitpost.2004.05.002

Li, G., Peng, Y., Zhou, C., Jin, Z., and Bedair, H. (2020). The effect of structural parameters of total hip arthroplasty on polyethylene liner wear behavior: A theoretical model analysis. *J. Orthop. Res.* 38 (7), 1587–1595. doi:10.1002/jor.24577

List, R., Gerber, H., Foresti, M., Rippstein, P., and Goldhahn, J. (2012). A functional outcome study comparing total ankle arthroplasty (TAA) subjects with pain to subjects with absent level of pain by means of videofluoroscopy. *Foot Ankle Surg.* 18 (4), 270–276. doi:10.1016/j.fas.2012.04.001

List, R., Gülay, T., Stoop, M., and Lorenzetti, S. (2013). Kinematics of the trunk and the lower extremities during restricted and unrestricted squats. *J. Strength Cond. Res.* 27 (6), 1529–1538. doi:10.1519/JSC.0b013e3182736034

List, R., Postolka, B., Schütz, P., Hitz, M., Schwilch, P., Gerber, H., et al. (2017). A moving fluoroscope to capture tibiofemoral kinematics during complete cycles of free level and downhill walking as well as stair descent. *PLoS One* 12 (10), e0185952. doi:10.1371/journal.pone.0185952

Lombardi, A. V., Mallory, T. H., Dennis, D. A., Komistek, R. D., Fada, R. A., and Northcut, E. J. (2000). An *in vivo* determination of total hip arthroplasty pistoning during activity. *J. Arthroplasty* 15 (6), 702–709. doi:10.1054/arth.2000.6637

Lunn, D. E., Lampropoulos, A., and Stewart, T. D. (2016). Basic biomechanics of the hip. *Orthop. Trauma* 30, 239–246. doi:10.1016/j.mporth.2016.04.014

Malik, A., Maheshwari, A., and Dorr, L. D. (2007). Impingement with total hip replacement. *J. Bone Jt. Surg. Am.* 89, 1832–1842. doi:10.2106/JBJS.F.01313

Manaka, M., Clarke, I. C., Yamamoto, K., Shishido, T., Gustafson, A., and Imakiire, A. (2004). Stripe wear rates in alumina THR - comparison of microseparation simulator study with retrieved implants. *J. Biomed. Mater Res. - Part B Appl. Biomater.* 69 (2), 149–157. doi:10.1002/jbm.b.20033

McCarthy, T. F., Thompson, M. T., Nevelos, J., Salem, H. S., Naylor, B. H., and Mont, M. A. (2021). Range of motion to impingement curves create a new patient-specific impingement-free zone for acetabular cup placement. *Surg. Technol. Int.* 38, 400–406. doi:10.52198/21.STI.38.OS1399

Mellon, S. J., Grammatopoulos, G., Andersen, M. S., Pegg, E. C., Pandit, H. G., Murray, D. W., et al. (2013). Individual motion patterns during gait and sit-to-stand contribute to edge-loading risk in metal-on-metal hip resurfacing. *Proc. Inst. Mech. Eng. Part H. J. Eng. Med.* 227 (7), 799–810. doi:10.1177/0954411913483639

Meng, Q., Wang, J., Yang, P., Jin, Z., and Fisher, J. (2015). The lubrication performance of the ceramic-on-ceramic hip implant under starved conditions. *J. Mech. Behav. Biomed. Mater* 50, 70–76. doi:10.1016/j.jmbbm.2015.06.001

Morlock, M., Schneider, E., Bluhm, A., Vollmer, M., Bergmann, G., Müller, V., et al. (2001). Duration and frequency of every day activities in total hip patients. *J. Biomech.* 34 (7), 873–881. doi:10.1016/s0021-9290(01)00035-5

Nevelos, J., Ingham, E., Doyle, C., Streicher, R., Nevelos, A., Walter, W., et al. (2000). Microseparation of the centers of alumina-alumina artificial hip joints during simulator testing produces clinically relevant wear rates and patterns. *J. Arthroplasty* 15 (6), 793–795. doi:10.1054/arth.2000.8100

Palit, A., King, R., Gu, Y., Pierrepont, J., Simpson, D., and Williams, M. A. (2019). Subject-specific surgical planning for hip replacement: A novel 2D graphical representation of 3D hip motion and prosthetic impingement information. *Ann. Biomed. Eng.* 47 (7), 1642–1656. doi:10.1007/s10439-019-02260-x

Park, S., Krebs, D. E., and Mann, R. W. (1999). Hip muscle co-contraction: Evidence from concurrent *in vivo* pressure measurement and force estimation. *Gait Posture* 10, 211–222. doi:10.1016/S0966-6362(99)00033-8

Perron, M., Malouin, F., Moffet, H., and McFadyen, B. J. (2000). Three-dimensional gait analysis in women with a total hip arthroplasty. *Clin. Biomech.* 15 (7), 504–515. doi:10.1016/S0268-0033(00)00002-4

Pryce, G. M., Sabu, B., Al-Hajjar, M., Wilcox, R. K., Thompson, J., Isaac, G. H., et al. (2022). Impingement in total hip arthroplasty: A geometric model. *Proc. Inst. Mech. Eng. H.* 236 (4), 504–514. doi:10.1177/09544119211069472

Roter, G. E., Medley, J. B., Bobyn, J. D., Krygier, J. J., and Chan, F. W. (2002). Stop-dwell-start motion: A novel simulator protocol for the wear of metal-on-metal hip implants. *Tribol. Ser.* 40. 367. doi:10.1016/S0167-8922(02)80041-4

Scholes, S. C., and Unsworth, A. (2006). The tribology of metal-on-metal total hip replacements. *Proc. Inst. Mech. Eng. Part H. J. Eng. Med.* 220 (2), 183–194. doi:10.1243/09544119JEIM40

Shrader, M. W., Bhowmik-Stoker, M., Jacofsky, M. C., and Jacofsky, D. J. (2009). Gait and stair function in total and resurfacing hip arthroplasty: A pilot study. *Clin. Orthop. Relat. Res.* 467, 1476–1484. doi:10.1007/s11999-009-0791-0

Stephenson, J. L., De Serres, S. J., and Lamontagne, A. (2010). The effect of arm movements on the lower limb during gait after a stroke. *Gait Posture* 31 (1), 109–115. doi:10.1016/j.gaitpost.2009.09.008

Szymanski, M., and Barciszewski, J. (2017). The path to the genetic code. *Biochim. Biophys. Acta - Gen. Subj.* 1861 (11), 2674–2679. doi:10.1016/j.bbagen.2017.07.009

Toh, S. M. S., Ashkanfar, A., English, R., and Rothwell, G. (2021). Computational method for bearing surface wear prediction in total hip replacements. *J. Mech. Behav. Biomed. Mater* 119, 104507. doi:10.1016/j.jmbbm.2021.104507

Tsai, T. Y., Li, J. S., Wang, S., Lin, H., Malchau, H., Li, G., et al. (2013). A novel dual fluoroscopic imaging method for determination of THA kinematics: *In-vitro* and *in-vivo* study. *J. Biomech.* 46 (7), 1300–1304. doi:10.1016/j.jbiomech.2013.02.010

Tsai, T. Y., Li, J. S., Wang, S., Scarborough, D., and Kwon, Y. M. (2014). *In-vivo* 6 degrees-of-freedom kinematics of metal-on-polyethylene total hip arthroplasty during gait. *J. Biomech.* 47 (7), 1572–1576. doi:10.1016/j.jbiomech.2014.03.012

Wang, L., Isaac, G., Wilcox, R., Jones, A., and Thompson, J. (2019). Finite element analysis of polyethylene wear in total hip replacement: A literature review. *Proc. Inst. Mech. Eng. H.* 233 (11), 1067–1088. doi:10.1177/0954411919872630

Wass, E., Taylor, N. F., and Matsas, A. (2005). Familiarisation to treadmill walking in unimpaired older people. *Gait Posture* 21 (1), 72–79. doi:10.1016/j.gaitpost.2004.01.003

Watt, J. R., Franz, J. R., Jackson, K., Dicharry, J., Riley, P. O., and Kerrigan, D. C. (2010). A three-dimensional kinematic and kinetic comparison of overground and treadmill walking in healthy elderly subjects. *Clin. Biomech.* 25 (5), 444–449. doi:10.1016/j.clinbiomech.2009.09.002

Wu, G., Siegler, S., Allard, P., Kirtley, C., Leardini, A., Rosenbaum, D., et al. (2002). ISB recommendation on definitions of joint coordinate system of various joints for the reporting of human joint motion—part I: Ankle, hip, and spine. *J. Biomech.* 35 (4), 543–548. doi:10.1016/S0021-9290(01)00222-6

Frontiers in **Bioengineering and Biotechnology**

Check for updates

Improvements of tooth movement efficiency and torque control in expanding the arch with clear aligners: a finite element analysis

Song Yao[1,2,3], Wei Jiang[1,2,3], Chunjuan Wang[1,2,3], Yao He[1,2,3], Chao Wang[1,4] and Lan Huang[1,2,3]*

[1]Stomatological Hospital of Chongqing Medical University, Chongqing, China, [2]Chongqing Key Laboratory of Oral Diseases and Biomedical Sciences, Chongqing, China, [3]Chongqing Municipal Key Laboratory of Oral Biomedical Engineering of Higher Education, Chongqing, China, [4]Key Laboratory of Biomechanics and Mechanobiology, Ministry of Education, Beijing Advanced Innovation Center for Biomedical Engineering, School of Biological Science and Medical Engineering, School of Engineering Medicine, Beihang University, Beijing, China

Objectives: The purpose of this study was to analyze the effect of different movement strategies, embossment structures, and torque compensation of the aligner on tooth movement during arch expansion using clear aligners by finite element analysis.

Methods: Models comprising the maxilla, dentition, periodontal ligament, and aligners were created and imported into a finite element analysis software. The tests were performed using the following: three orders of tooth movement (including alternating movement with the first premolar and first molar, whole movement with second premolar and first molar or premolars and first molar), four different shapes of embossment structures (ball, double ball, cuboid, cylinder, with 0.05, 0.1, 0.15-mm interference) and torque compensation (0°, 1°, 2°, 3°, 4°, and 5°).

Results: The expansion of clear aligners caused the target tooth to move obliquely. Alternating movement resulted in higher movement efficiency with lower anchorage loss as compared with whole movement. Embossment increased the efficiency of crown movement but did not contribute positively to torque control. As the angle of compensation increased, the tendency of oblique tooth movement was gradually controlled; however, the movement efficiency decreased concurrently, and stress distribution on the periodontal ligament became more even. For each 1° increase in compensation, the torque per millimeter of the first premolar would decrease by 0.26°/mm, and the crown movement efficiency eliminate decreased by 4.32%.

Conclusion: Alternating movement increases the efficiency of the arch expansion by the aligner and reduces anchorage loss. Torque compensation should be designed to enhance torque control in arch expansion using an aligner.

1 Introduction

Clear aligner therapy (CAT) is becoming increasingly popular owing to its esthetic, clean, and comfortable features, which are preferred by clinicians and patients (Shokeen et al., 2022). CAT divides the tooth movement process into a series of tiny sequential movements that ultimately help achieve the targeted movement of the tooth. The slight offset of the clear aligner from the dentition creates an elastic force that further applies an orthodontic force to the tooth, causing it to move towards the target position (Cortona et al., 2020). Currently, CAT is available for a wide range of tooth movements, such as intrusion (Liu et al., 2021), molar distalization (Ji et al., 2022), and root torque (Liu et al., 2022), expanding clinical opportunities to treat complex orthodontic cases (Inchingolo et al., 2022).

Insufficient width of the maxillary arch results in narrowing of the dentition and a molar crossbite, which will then affect occlusal function and esthetics (Lee, 1999). Many studies have confirmed the ability of CAT to expand the arch; however, the actual efficiency of CAT is lower than the preset value (Solano-Mendoza et al., 2017) and decreases gradually by moving from the premolar to molar (Houle et al., 2017; Lione et al., 2021). A quantitative analysis of a change in torque of arch expansion using CAT is yet to be reported. Moreover, the type of tooth movement in CAT tends to be buccal tilt (Houle et al., 2017), and a less predictable buccal tilt is associated with a risk of severe periodontal destruction, including buccal gingival recession (Morris et al., 2017) and bone dehiscence (Sulewska et al., 2021). Therefore, it is worthwhile to further investigate how CAT can improve tooth movement efficiency and torque control.

Finite element analysis (FEA) is a computer simulation technique that can be used for complex biomechanical analyses. The advantages of this technique include the ability to create many different simulations with tightly controlled variables and high reproducibility, to provide an appropriate database for future clinical trials, helping to avoid unnecessary duplication of clinical trials (Romanyk et al., 2020; Liu et al., 2022).

Therefore, the aim of this paper is to evaluate the effect of different tooth movement strategies on movement efficiency during arch expansion using CAT and to compare the effects of different embossment designs and torque compensation on movement efficiency and torque control by FEA (Supplementary Table S1).

2 Materials and methods

2.1 Construction of an orthodontic model

This study was approved by the Stomatological Hospital of Chongqing Medical University Ethics Committee (NO. 2022-038). The study participant was a healthy adult orthodontic patient with a narrow dental arch. For starters, the maxilla and dentition data of the participant were acquired using cone-beam computed tomography (CBCT, Kava, Biberach, Germany) and intraoral scanning (iTero, Invisalign, United States), and three-dimensional models of the maxilla and dentition were constructed (Barone et al., 2017) using Mimics Research (19.0; Materialise, Leuven, Belgium), 3-Matic (11.0; Materialise, Leuven, Belgium), and Geomagic Warp (3D systems, Rock Hill, SC) software. Additionally, the right maxilla and dentition were
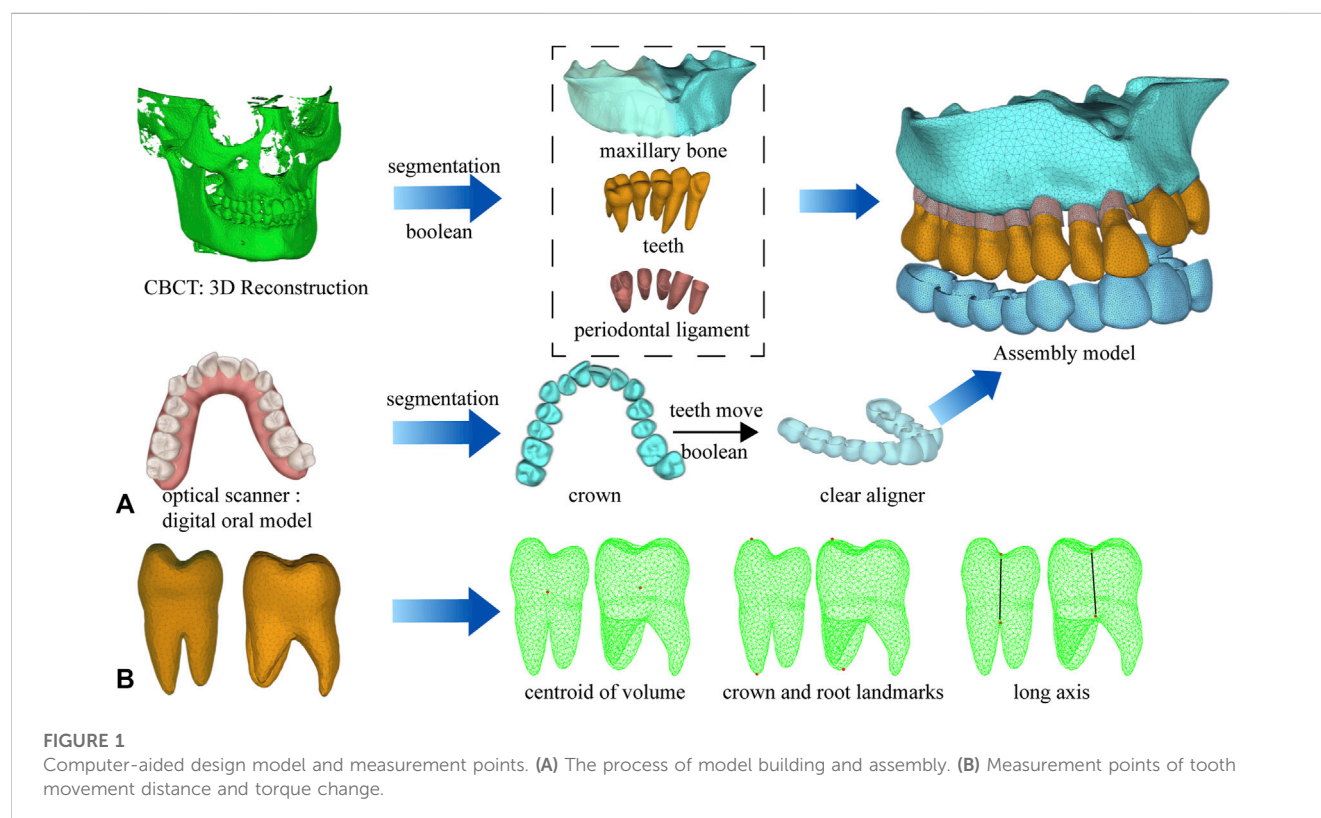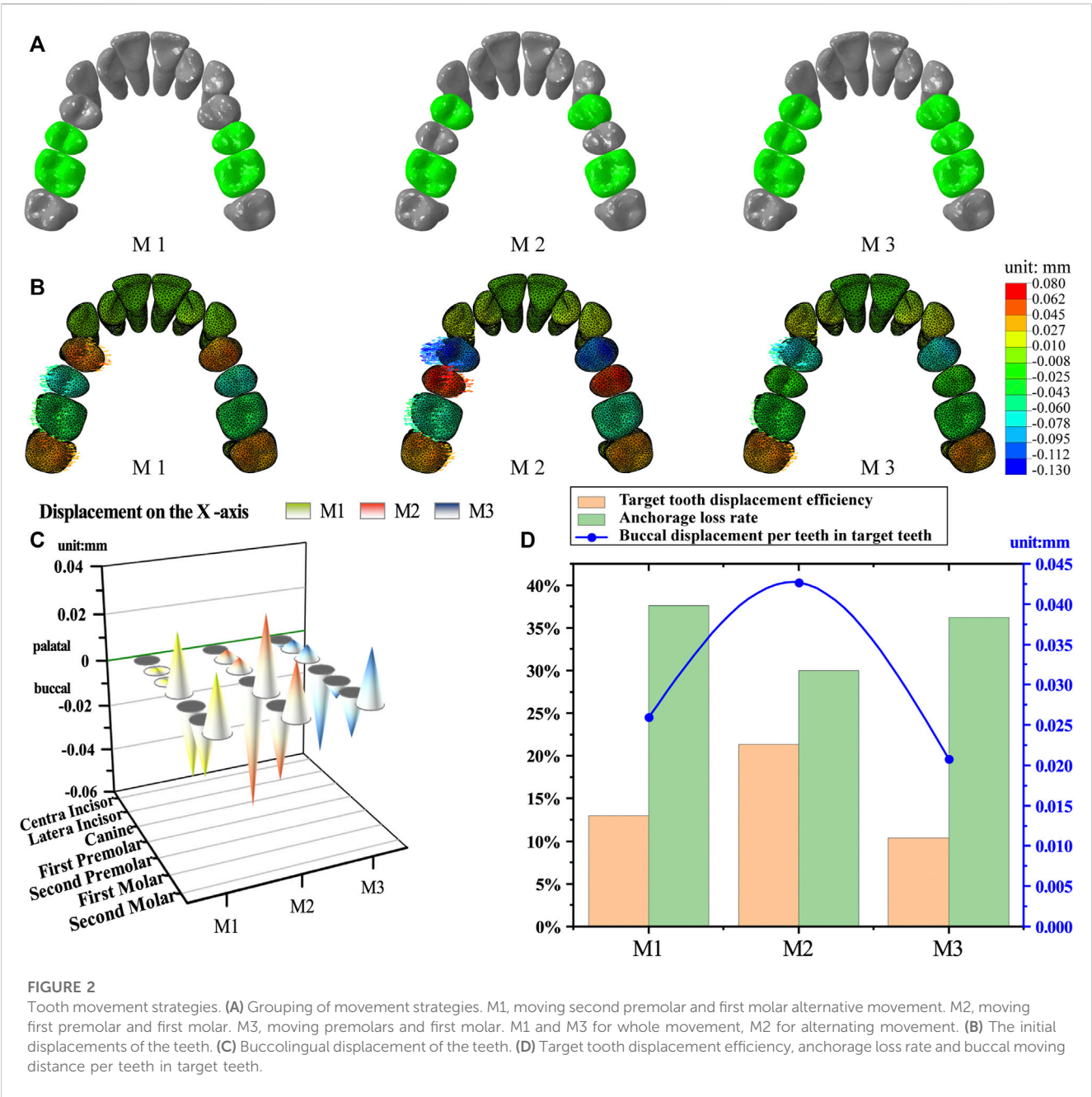

FIGURE 1
Computer-aided design model and measurement points. **(A)** The process of model building and assembly. **(B)** Measurement points of tooth movement distance and torque change.

TABLE 1 Material properties and number of nodes and elements of the components of the finite element model.

Component	Young's modulus (MPa)	Poisson's ratio	Nodes	Elements
Teeth	18,600	0.31	178752	123439
PDL	0.68	0.49	152139	76970
Bone	13,700	0.3	137197	81737
Clear aligner	816.31	0.3	313998–342416	203691–224513

FIGURE 2
Tooth movement strategies. **(A)** Grouping of movement strategies. M1, moving second premolar and first molar alternative movement. M2, moving first premolar and first molar. M3, moving premolars and first molar. M1 and M3 for whole movement, M2 for alternating movement. **(B)** The initial displacements of the teeth. **(C)** Buccolingual displacement of the teeth. **(D)** Target tooth displacement efficiency, anchorage loss rate and buccal moving distance per teeth in target teeth.

mirrored to establish a symmetric model to improve the efficiency of the subsequent FEA and guarantee a realistic model (Jia et al., 2022). After having established a symmetric model, each tooth was offset along the normal line outward by 0.2 mm (Seo et al., 2021). Moreover, through a Boolean operation, the PDL, also known as periodontal ligament model was acquired (Liu et al.,
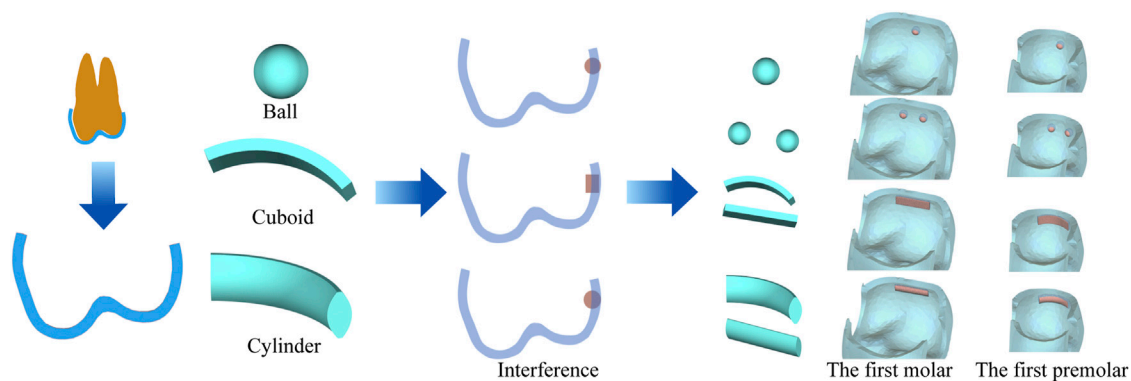
FIGURE 3
Embossment of aligner, including ball (diameter: 0.8 mm, 0.85 mm, 0.90 mm), double-ball (diameter: 0.90 mm), cuboid (3.5*1*0.85 mm, 3.5*1*0.9 mm), cylinder (3.5*1*0.85 mm, 3.5*1*0.9 mm). The interference (0.05, 0.10, and 0.15 mm) is equal to the difference between the thickness of the auxiliary shapes and the aligner (0.75 mm).

2022). After having obtained the PDL, we were able to obtain the maxillary alveolar socket by subtracting the teeth and PDL models from the maxilla using Boolean operations (Supplementary Figure S1). Finally, the maxillary, PDL, dentition, and clear aligner models were assembled in 3-Matic software to produce an FEA solid model with unstructured 4-noded tetrahedral elements in Figure 1A. Specifically, the dimensions of the mesh divisions were 1.0 mm for the tooth, 2.0 mm for the maxilla, 0.2 mm for the PDL, and 0.5 mm for the aligners. The maxilla, teeth, PDL, and aligners were set as linearly elastic (Kojima and Fukui, 2012). The material properties (Gomez et al., 2015) and the approximate number of nodes and mesh are listed in Table 1. Following, these operations were completed using the MIMICS, 3-Matic and ABAQUS (2020; SIMULIA, Providence, RI) software.

2.2 Design of aligner model

2.2.1 Order of teeth movement

We selected several different tooth movement patterns for expanding the arch. The optimal tooth movement strategy was filtered based on the movement efficiency of the target teeth and the loss of anchors. The strategies of the different tooth movement are the following: M1 moves the second premolar and first molar. M2 moves the first premolar and first molar. M3 moves premolars and the first molar. The target teeth are moved buccally by 0.2 mm. We refer to the intraoral scanning to trim the dentition along the gingival margin, mark it as the inner surface of clear aligner, and then offset by 0.75 mm (Xia et al., 2022) outward according to the surface normal direction to generate the clear aligner model (Figure 2A). M2 represents alternating movement, M1 and M3 represent whole movement.

2.2.2 Embossment of aligner

For starters, the effects of different embossments on tooth movement, including movement efficiency and torque control, were measured. The structure of the embossment in the aligner,

that we measured is formed by means of aligner and auxiliary shapes (Figure 3). Moreover, we added auxiliary shapes on the inner surface of the aligner at a site corresponding to the cervical portion of the palatal surface of the crown, including balls, double balls, cuboids, and cylinders. Once we added the auxiliary shapes, the aligner no longer fit tightly to the crown surface, and the embossment generated an interference contact, which simulated a buccal push to the tooth. Subsequently we designed a buccal movement of 0.2 mm for the first premolar and first molar to create an aligner with no embossment as a blank control (this strategy had shown higher movement efficiency in the previous part of the experiment and was therefore used as a blank control in this part, as is explained in the Results section). Based on the blank control, the aforementioned embossment structures were added to the aligners. The experimental groups were named according to the extent of interference and shape of the embossment.

2.2.3 Torque compensation of aligner

We designed different torque compensations ($\theta = 0°$, $1°$, $2°$, $3°$, $4°$, and $5°$) based on a 0.2 mm buccal shift of the target tooth to measure the tooth torque generated when the aligner expanded the arch. Torque compensation was achieved by rotating the target tooth anticlockwise (crown to the palatal side and root to the buccal side) at the center of the tooth volume and then designing the aligner with the repositioned dentition.

2.3 Coordinate system setting

A global coordinate system was used to define the orientation of the x-, y-, and z-axes. The x-axis represented the intersection of the coronal and occlusal planes. The positive direction pointed to the left side of the patient. The y-axis was perpendicular to the x-axis, with the positive direction pointing posteriorly. The z-axis was perpendicular to the x- and y-axes, with the positive direction pointing apically.

TABLE 2 *X*-axis movement per tooth in group M1, M2, and M3 (unit: mm).

Group	Central incisor	Lateral incisor	Canine	First premolar	Second premolar	First molar	Second molar
M1	−0.00038	0.000785	0.000587	0.02508	−0.02907	−0.02288	0.022754
M2	−0.00058	0.004576	0.005551	−0.05474	0.031878	−0.03071	0.02259
M3	−0.0035	0.004349	0.006471	−0.03603	−0.0076	−0.01865	0.02278

X-axis, posterior teeth are buccolingual (buccal side is negative direction), anterior teeth are proximo-distal (distal side is negative direction). Target teeth of M1 group are the second premolar and first molar. Target teeth of M2 group are first premolar and first molar. Target teeth of M3 group are premolars and first molar.

2.4 Measurement and analysis

The initial displacement tendencies of the target and anchorage teeth and the equivalent stress of the PDL were measured. The anchor loss rate (Figure 2D) was used to evaluate the efficiency of different movement strategies, which is shown in the following equations. We further describe the movement of the target teeth based on the target tooth displacement efficiency (the ratio of the actual value of the sum of the buccal positions of the target teeth to the present value) and the buccal moving distance per target tooth.

$$\text{The anchor loss rate} = \frac{\text{Tooth} - \text{average anchor loss}}{\text{Tooth} - \text{average arch expansion}}$$

$$
\begin{aligned}
&\text{Tooth−average anchor loss} \\
&= \frac{\text{Sum of the buccolingual displacement of the anchorage teeth}}{\text{The number of anchorage teeth during arch expansion}}
\end{aligned}
$$

$$
\begin{aligned}
&\text{Tooth} - \text{average arch expansion} \\
&= \frac{\text{Sum of the buccal displacement of the target teeth}}{\text{The number of target teeth during arch expansion}}
\end{aligned}
$$

The centroid of the tooth volume, buccal cusp, and buccal root were used as measurement points to observe tooth movement. The angular variation of the long axis of the tooth in the coronal plane was measured to evaluate torque change (Figure 1B).

3 Results

3.1 Alternating movement is more efficient than whole movement

The target teeth moved buccally, and the posterior anchored teeth moved palatally with all strategies (M1, M2, and M3). The cuspids and incisors tended to move with a labial tilt, but this movement was significantly less than that of the posterior teeth (Figure 2B, Supplementary Videos S1–S3).

The M2 group showed the greatest buccal displacement of the target teeth as well as the greatest undesirable palatal displacement of the anchorage teeth in all groups. Although the second premolar in the M3 group moved buccally as planned, its displacement was one order of magnitude lower than that of the other target teeth (Figure 2C; Table 2).

As shown in Figure 2D, the M2 group had the highest target tooth displacement efficiency (21.35%), which was greater than that in M1 (13%) and M3 (10.38%) groups, while the M2 group showed the greatest

buccal movement per tooth in the target teeth (0.0427 mm), which was greater than that in the M1 (0.026 mm) and M3 (0.0208 mm) groups. The lowest anchorage loss rate was found in the M2 group (30.02%), followed by M3 (36.24%) and M1 (37.62%) groups.

3.2 Embossment increases efficiency based on the excessive tilting movement

As the diameter of the ball-like embossment increased, the crown-root movement of both first premolar and first molar increased. However, the tooth movement was oblique (Figures 4A, E), and the crown point movement efficiency and torque per millimeter also increased (Figure 4B). This trend previously explained, was more prominent in the double-ball group than in the ball group, with the same interference. Crown point movement efficiency of the first premolar in the blank group was 62.05% and the torque per millimeter was 3.93°/mm, which was greater than those in the ball 0.05 and 0.1 interference groups but less than those in the ball 0.15 and double ball 0.15 interference groups (Figure 4B). Equally important, the movement of the first molar was similar, and the crown point movement efficiency of first molar in the blank group was 30.7% and torque per millimeter was 2.39°/mm (Figures 5A, B, E).

Cuboid and cylinder groups were also similar because as interference increased, the crown-root movement increased for both the first premolar and first molar (Figures 4C, E, 5C, E), the crown point movement efficiency and torque per millimeter also increased along with the tendency of oblique movement (Figure 4D; Figure 5D). The performance of the first premolar in the cylinder group was similar to that in the cuboid group, but the measurements of the first molar in the cylinder group were greater than those in the cuboid group (cylinder 0.15> cylinder 0.1> cuboid 0.15> cuboid 0.1) (Figure 5D).

3.3 Torque compensation reduces the tendency of tilting

As the angle of compensation increased, the crown-root point movement of the first premolar decreased. Similarly, the torque per millimeter and crown point movement efficiency also decreased. Torque per millimeter of the first premolar decreased by 0.26°/mm, and crown point movement efficiency decreased by 4.32% for approximately every 1° increase, within 1°–5° of the compensation angle (Figures 6A, B). As the angle increased, buccal movement of the first premolar decreased, and the changes of the palatal root changed from extrusion to intrusion (Figure 6C).
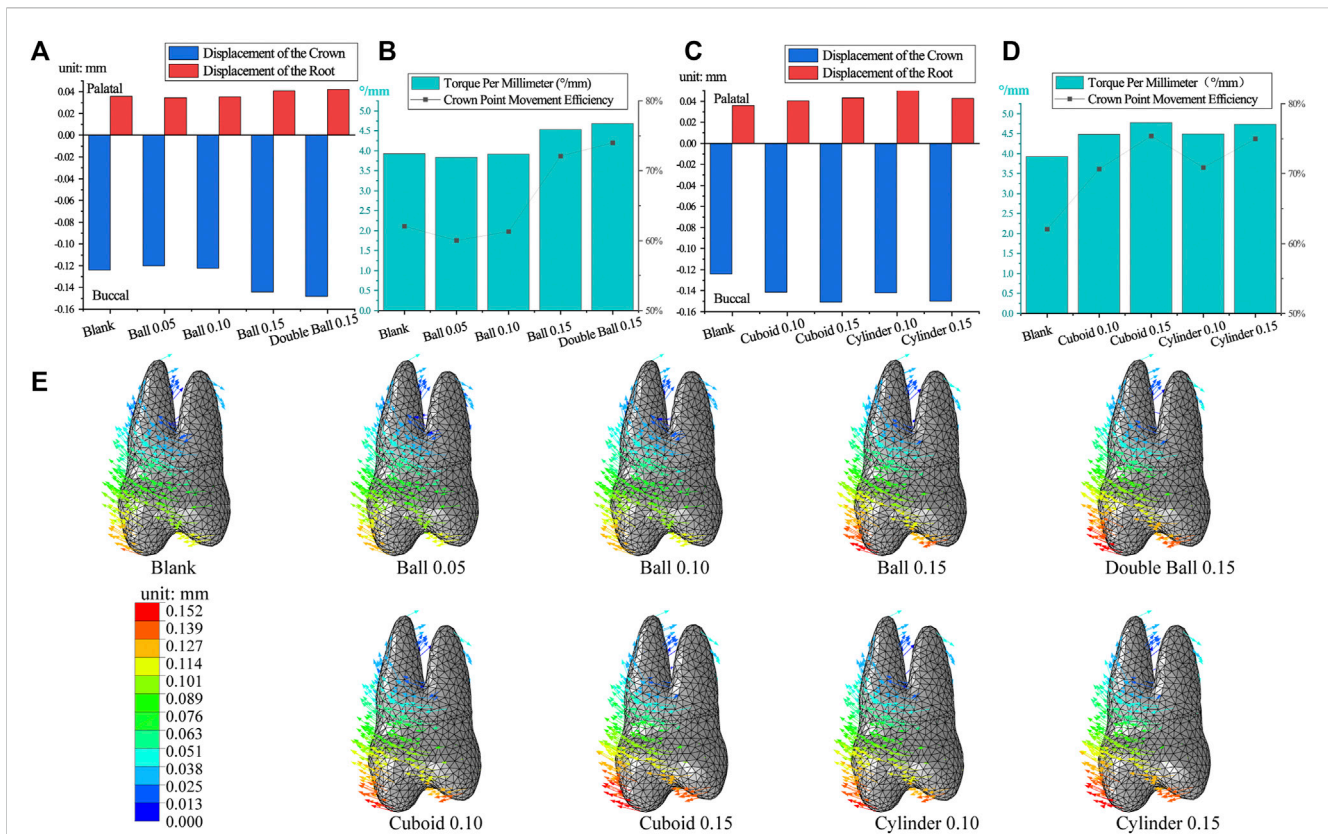
FIGURE 4
The movement of the first premolar in embossment groups. **(A,C)** The crown-root movement in embossment groups. **(B,D)** The torque per millimeter and crown movement efficiency in embossment groups. **(E)** The displacement tendencies of the first premolar in embossment groups.

Based on a linear regression model ($R^2 > 0.99$) matched to the measured data, it was predicted that when the angle of compensation is approximately 13°, the crown and root of first premolar are displaced equally and towards the buccal side, achieving bodily movement (Figure 6D). However, the predicted result of crown point movement efficiency dropped almost to 5.6% (Figure 6E).

Torque compensation reduced the torque per millimeter of molar but lacked predictability. As the angle of compensation increased, the torque per millimeter and crown point movement efficiency of the first molar decreased (Figures 7A, B). However, the above data did not show linear relationships, as in the case of the first premolar. The first molar showed minimum torque per millimeter at 2° compensation, within 1–5° compensation. As compensation increased, the tendency of the crown to move buccally decreased, the magnitude of buccal root intrusion decreased, and the tendency of the palatal root to extrude palatally did not change significantly (Figure 7C).

Owing to the poor linear correlation of the first molar movement data, the regression model had a lower prediction reliability (Figures 7D, E).

Orthodontic force induces remodeling of periodontal tissues, resulting in bone resorption on the compressive side and bone deposition on the tensile side. Therefore, the distribution of compressive and tensile stresses on the surface of the periodontal ligament is utilized as an observational indicator of periodontal tissue remodeling and as an auxiliary predictor of tooth movement

trends. For the first premolar and first molar with no torque compensation, aligners produced compressive stress in the buccal root neck and palatal root apex and tensile stress in the palatal root neck and buccal root apex. As the torque compensation increased, the equivalent stress was more evenly distributed over the PDL (Figure 8).

4 Discussion

The comfort and esthetic properties of CAT deserve recognition; however, numerous studies (Houle et al., 2017; Zhou and Guo, 2020) have found that CAT exhibits lower efficiency and predominantly utilizes tipping movements during arch expansion. Consequently, our research investigates the biomechanical effects of movement strategies, embossment, and torque compensation designs in CAT to enhance the efficiency and anchorage control of aligners. The results reveal that alternating movements outperform whole movements in terms of movement efficiency, while torque compensation demonstrates superior torque control compared to embossment.

We proposed an anchorage loss rate based on target and anchorage teeth displacement to evaluate different movement strategies. Among all groups, alternating movement M2 demonstrated the lowest anchorage loss rate, indicating its
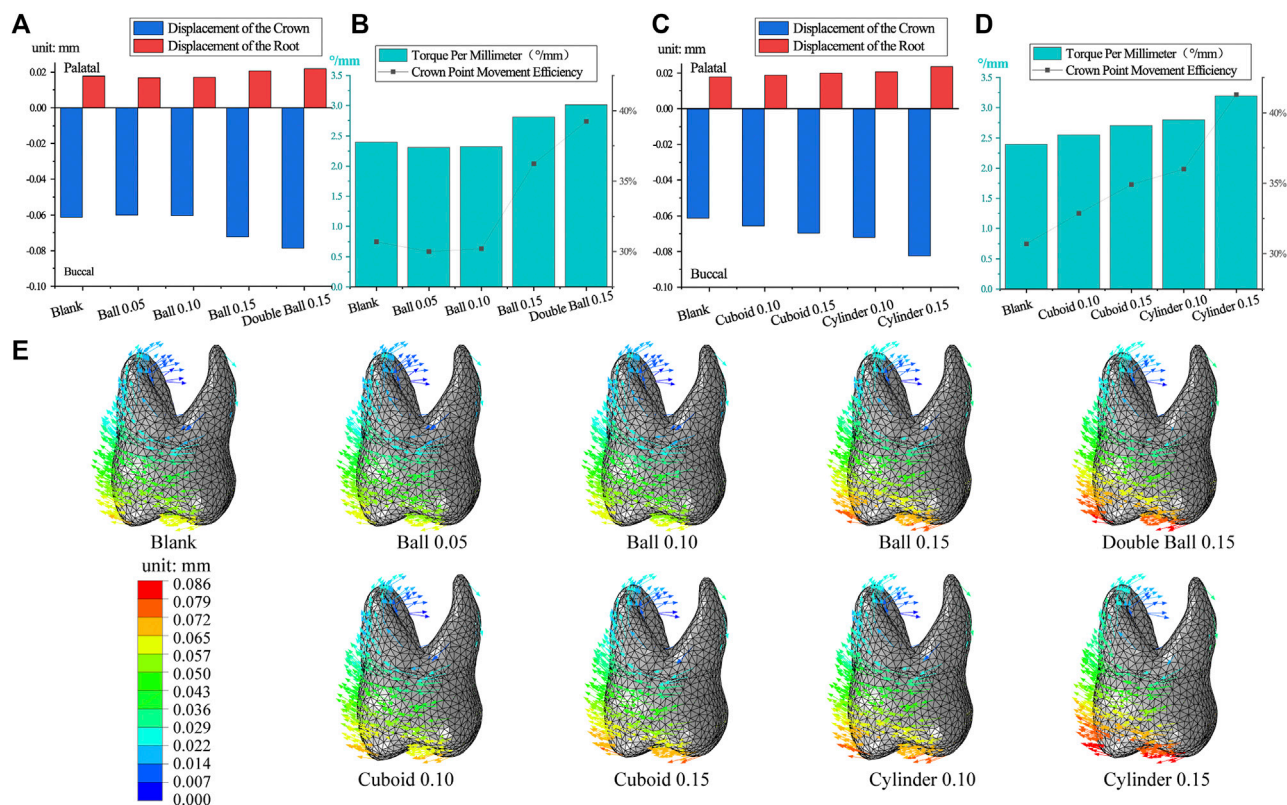
FIGURE 5
The movement of the first molar in embossment groups. **(A,C)** The crown-root movement in embossment groups. **(B,D)** Torque per millimeter and crown movement efficiency in embossment groups. **(E)**, displacement tendencies of the first molar in embossment groups.

effectiveness in achieving target tooth displacement with minimal anchorage loss.

The CAT-expanded arch's anchorage design involves intra-maxillary anchorage, including bilateral posterior tooth mutual anchorage and adjacent tooth anchorage (Wu et al., 2019). In the M3 group, premolars and the first molar were designed to be moved buccally. However, a displacement difference between the second premolar and the aligner hindered adjacent tooth anchorage, resulting in lower actual anchorage for the second premolar. This explains the minimal buccal displacement of the second premolar in the M3 group (Figure 2C; Table 2). In contrast, the M2 group achieved adjacent tooth anchorage for both the first premolar and first molar. Consequently, M2 exhibited the lowest anchorage loss rate and highest target tooth displacement efficiency. Groups M1 and M3 had only partial adjacent tooth anchorage, resulting in lower buccal displacement compared to M2.

To achieve efficient buccal movement with minimal anchorage loss, it is advisable to use alternating movements in CAT for arch expansion. Alternating movement resembles staging support control in aligners, such as frog pattern intrusion of anterior teeth and sequenced molar distalization. (Rossini et al., 2015; Ravera et al., 2016).

To mitigate the risk of buccal gingival recession and bone dehiscence (Kraus et al., 2014) caused by oblique buccal tooth movement (Lione et al., 2021), we incorporated various types of embossments on the aligner to enhance torque control. The embossment structures in posterior teeth aimed to exert pressure on the cervical part of the crown, similar to the power ridge in anterior teeth, facilitating torque control (Simon et al., 2014; Cheng et al., 2022a). Different shapes and thicknesses of embossments were designed based on mechanical principles, considering the extent of pressure generated by interference (Cheng et al., 2022b).

While the embossment structure improved movement efficiency, it primarily resulted in excessive tilting movements due to uncontrolled torque. Unfortunately, the embossment failed to provide beneficial torque control for posterior teeth, similar to the power ridge on anterior teeth (Cheng et al., 2022b). This failure could be attributed to the aligner material's limited force generation, unable to support buccal bodily movement of posterior teeth adequately (Zhou and Guo, 2020). Consequently, the aligner's support on the buccal aspect of posterior crowns was insufficient (Elkholy et al., 2015), leading to pronounced tilting movements instead of desired torque control through embossment.

Compared to cuboid and ball structures, cylindrical embossments caused more noticeable tilting movements. Conversely, ball embossments had a smaller impact on crown movement efficiency compared to cylindrical and cuboid embossments, likely due to differences in the contact area between the embossment and crown. The domed structure of the cylinder provided more resistance to compression, similar to the preference for domed structures in buildings, resulting in a more significant effect on first molar movement (Paris et al., 2020). For the first premolar, both cylinder and cuboid
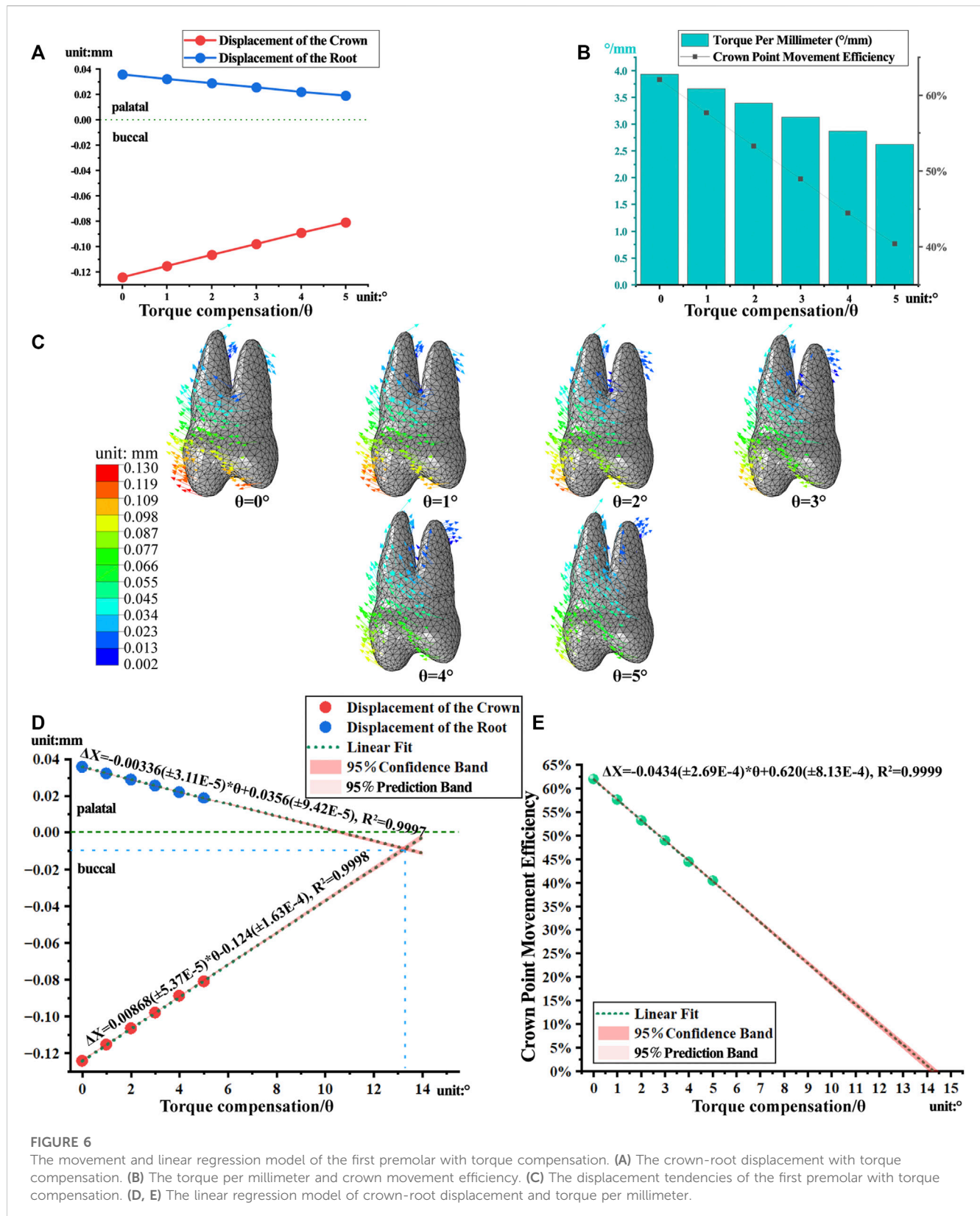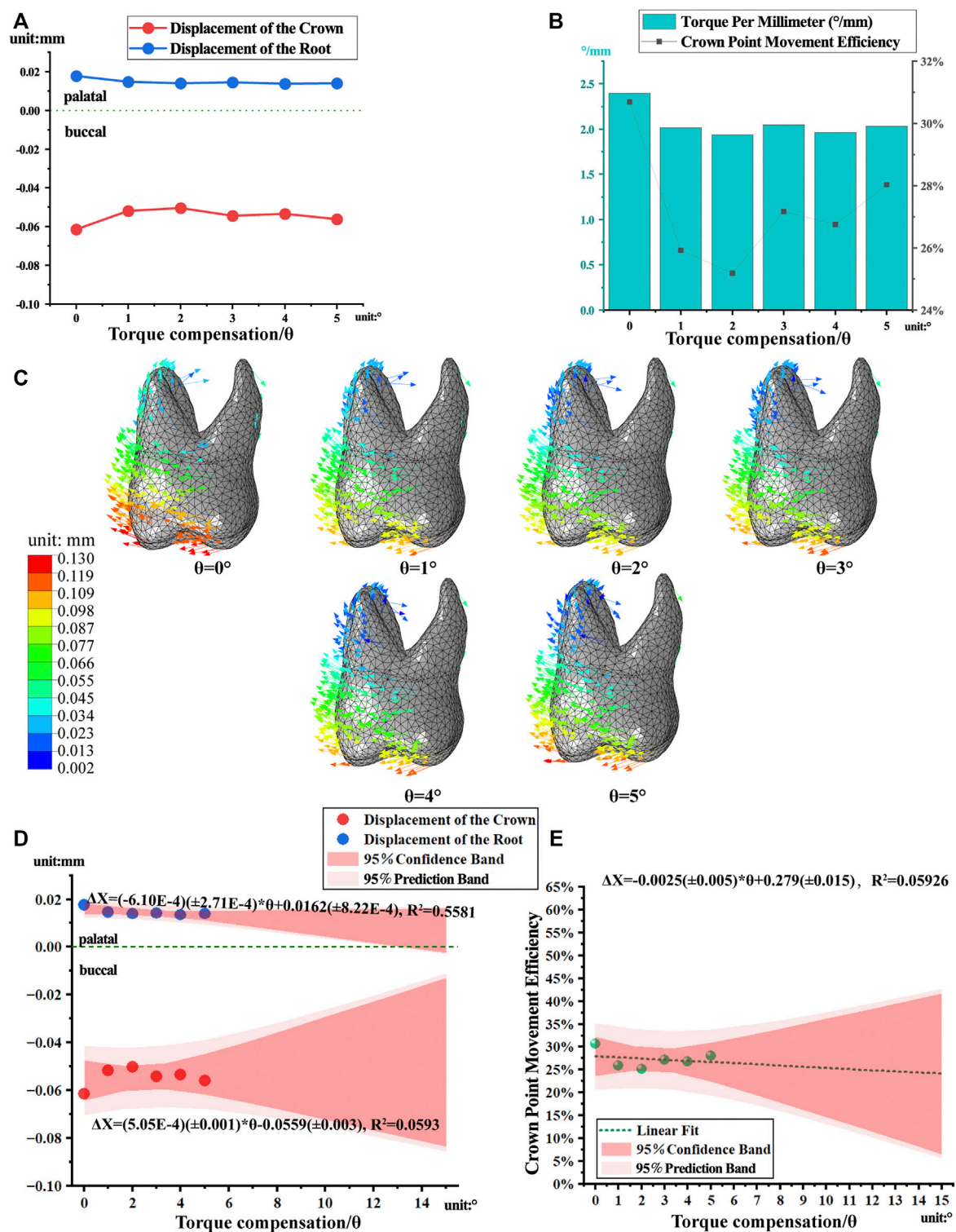
FIGURE 6
The movement and linear regression model of the first premolar with torque compensation. **(A)** The crown-root displacement with torque compensation. **(B)** The torque per millimeter and crown movement efficiency. **(C)** The displacement tendencies of the first premolar with torque compensation. **(D, E)** The linear regression model of crown-root displacement and torque per millimeter.

embossments exhibited similar performance, possibly due to differences in crown curvature affecting the distribution of resistance. Further investigation based on mechanical knowledge is required to explore this aspect.

Furthermore, torque compensation could enhance the torque control in buccal movement of the posterior teeth. We found that the tendency for tilting movement was gradually controlled as the degree of torque compensation increased, as shown in Figure 6B.

FIGURE 7

The movement and linear regression model of the first molar with torque compensation. **(A)** The crown-root displacement with torque compensation. **(B)** The torque per millimeter and crown movement efficiency. **(C)** The displacement tendencies of the first molar with torque compensation. **(D, E)** The linear regression model of crown-root displacement and torque per millimeter.

Based on the principle of action and reaction, the gradual homogenization of surface stress distribution on the PDL indicates an increasingly improved tendency towards tilting movement of teeth with increasing compensation angle, as shown in Figure 8A. According to the prediction by the regression model, when the compensation angle was approximately 13°, bodily
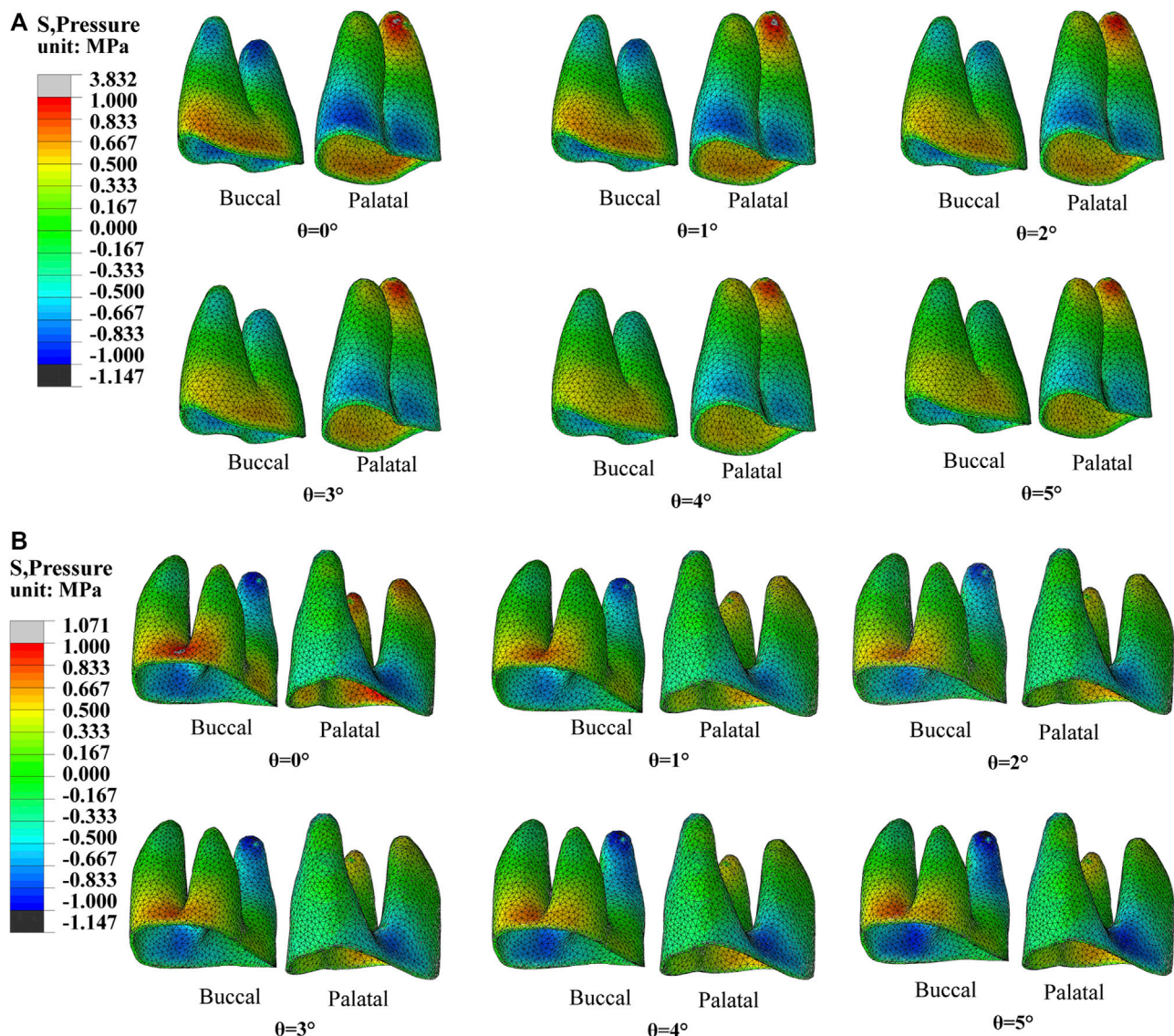
FIGURE 8
The equivalent stress of PDL with different torque compensation. **(A)** PDL of the first premolar. **(B)** PDL of the first molar.

movement of the first premolar was achieved; however, the crown point movement efficiency decreased to 5.6%, as shown in Figures 6D, E. Although these findings are only based on simulations, it was difficult to achieve both good torque control and good movement efficiency during arch expansion through CAT. This may be attributable to the limited force exerted by the aligner (Zhou and Guo, 2020).

For arch expansion, we should first observe the relationship between teeth and alveolar bone and then estimate the extent of movement of the crown and root while maintaining appropriate torque compensation. In fact, in many cases of dental arch narrowing, the posterior teeth are inclined to the palatal side, which necessitates buccal inclination of the teeth rather than bodily movement. In addition, in cases of excessive buccal inclination of posterior teeth, when the compensation limit has been reached and the use of aligners for arch expansion

may not be conducive for the root-bone relationship, micro-implant-assisted rapid palatal expansion (de Oliveira et al., 2021) or surgically assisted rapid maxillary expansion (Lin et al., 2022) should be considered. In addition, the attachment of CAT was not designed in our study because aligner wrapping around the buccolingual aspect of the crown provides better force for buccal-palatal movement. A related previous study found no significant effect of attachment on the efficiency of arch expansion (Zhao et al., 2017). However, based on clinical experience, attachments can increase the fit of the aligner and thus allow persistent orthodontic forces; therefore, we recommend their routine application in clinical practice.

FEA is one of the most suitable methods for studying the biomechanics of aligners. Our study provides valuable reference information for arch expansion with aligners in the clinic; however, some limitations cannot be ignored. Although FEA

involves transient biomechanical simulation, it cannot fully simulate the real oral environment and material properties. Moreover, FEA is incapable of directly observing the precise biological remodeling of alveolar bone. In this experiment, the direction of periodontal tissue remodeling can only be inferred through stress distribution, thus constituting a limitation of the present study. Further improvements in parameters and optimization of methods are required to create a more realistic simulation of clinical situations through FEA.

5 Conclusion

Improvements of tooth movement efficiency and torque control during arch expansion with clear aligners were analyzed and investigated. With the limitations of this study, the following conclusions were drawn.

- During arch expansion with CAT, alternating movement could result in higher movement efficiency with lower anchorage loss as compared with whole movement.
- The embossment structure could improve movement efficiency during arch expansion with CAT, but it is insufficient to produce torque control; thus, exhibiting a more marked tilting movement.
- Embossment of the cylindrical structure could result in a higher movement efficiency than that with cuboid and ball structures.
- Torque compensation could enhance torque control. The torque per millimeter of the first premolar decreased by $0.26°/mm$ for approximately every $1°$ increase in compensation.

Data availability statement

The original contributions presented in the study are included in the article/Supplementary Material, further inquiries can be directed to the corresponding author.

Ethics statement

This study was approved by the Stomatological Hospital of Chongqing Medical University Ethics Committee (NO. 2022-038). The patients/participants provided their written informed consent to participate in this study.

Author contributions

SY: software, methodology, validation, data collection and analysis, writing original draft. WJ: methodology, data collection. CW: software, methodology, validation, data analysis. YH: methodology, resources. CW: methodology, conceptualization, resources. LH: conceptualization, writing review and editing, resources. All authors contributed to the article and approved the submitted version.

Funding

Conflict of interest

The authors declare that the research was conducted in the absence of any commercial or financial relationships that could be construed as a potential conflict of interest.

Publisher's note

All claims expressed in this article are solely those of the authors and do not necessarily represent those of their affiliated organizations, or those of the publisher, the editors and the reviewers. Any product that may be evaluated in this article, or claim that may be made by its manufacturer, is not guaranteed or endorsed by the publisher.

Supplementary material

The Supplementary Material for this article can be found online at: https://www.frontiersin.org/articles/10.3389/fbioe.2023.1120535/full#supplementary-material

References

Barone, S., Paoli, A., Razionale, A. V., and Savignano, R. (2017). Computational design and engineering of polymeric orthodontic aligners. *Int. J. Numer. Method Biomed. Eng.* 33, e2839. doi:10.1002/cnm.2839

Cheng, Y., Gao, J., Fang, S., Wang, W., Ma, Y., and Jin, Z. (2022a). Torque movement of the upper anterior teeth using a clear aligner in cases of extraction: A finite element study. *Prog. Orthod.* 23, 26. doi:10.1186/s40510-022-00421-8

Cheng, Y., Liu, X., Chen, X., Li, X., Fang, S., Wang, W., et al. (2022b). The three-dimensional displacement tendency of teeth depending on incisor torque compensation with clear aligners of different thicknesses in cases of extraction: A finite element study. *BMC oral health* 22, 499. doi:10.1186/s12903-022-02521-7

Cortona, A., Rossini, G., Parrini, S., Deregibus, A., and Castroflorio, T. (2020). Clear aligner orthodontic therapy of rotated mandibular round-shaped teeth: A finite element study. *Angle Orthod.* 90, 247–254. doi:10.2319/020719-86.1

De Oliveira, C. B., Ayub, P., Ledra, I. M., Murata, W. H., Suzuki, S. S., Ravelli, D. B., et al. (2021). Microimplant assisted rapid palatal expansion vs surgically assisted rapid palatal expansion for maxillary transverse discrepancy treatment. *Am. J. Orthod. Dentofac. Orthop.* 159, 733–742. doi:10.1016/j.ajodo.2020.03.024

Elkholy, F., Panchaphongsaphak, T., Kilic, F., Schmidt, F., and Lapatki, B. G. (2015). Forces and moments delivered by PET-G aligners to an upper central incisor for labial and palatal translation. *J. Orofac. Orthop.* 76, 460–475. doi:10.1007/s00056-015-0307-3

Gomez, J. P., PeñA, F. M., MartíNEZ, V., Giraldo, D. C., and Cardona, C. I. (2015). Initial force systems during bodily tooth movement with plastic aligners and composite attachments: A three-dimensional finite element analysis. *Angle Orthod.* 85, 454–460. doi:10.2319/050714-330.1

Houle, J. P., Piedade, L., Todescan, R., JR., and Pinheiro, F. H. (2017). The predictability of transverse changes with Invisalign. *Angle Orthod.* 87, 19–24. doi:10.2319/122115-875.1

Inchingolo, A. D., Patano, A., Coloccia, G., Ceci, S., Inchingolo, A. M., Marinelli, G., et al. (2022). Treatment of class III malocclusion and anterior crossbite with aligners: A case report. *Med. Kaunas.* 58, 603. doi:10.3390/medicina58050603

Ji, L., Li, B., and Wu, X. (2022). Evaluation of biomechanics using different traction devices in distalization of maxillary molar with clear aligners: A finite element study. *Comput. methods biomechanics Biomed. Eng.* 26, 559–567. doi:10.1080/10255842.2022.2073789

Jia, L., Wang, C., Wang, C., Song, J., and Fan, Y. (2022). Efficacy of various multi-layers of orthodontic clear aligners: A simulated study. *Comput. Methods Biomech. Biomed. Engin* 25, 1710–1721. doi:10.1080/10255842.2022.2034794

Kojima, Y., and Fukui, H. (2012). Numerical simulations of canine retraction with T-loop springs based on the updated moment-to-force ratio. *Eur. J. Orthod.* 34, 10–18. doi:10.1093/ejo/cjq164

Kraus, C. D., Campbell, P. M., Spears, R., Taylor, R. W., and Buschang, P. H. (2014). Bony adaptation after expansion with light-to-moderate continuous forces. *Am. J. Orthod. Dentofac. Orthop.* 145, 655–666. doi:10.1016/j.ajodo.2014.01.017

Lee, R. T. (1999). Arch width and form: A review. *Am. J. Orthod. Dentofac. Orthop.* 115, 305–313. doi:10.1016/s0889-5406(99)70334-3

Lin, J., Li, C., Wong, H., Chamberland, S., Le, A., and Chung, C. (2022). Asymmetric maxillary expansion introduced by surgically assisted rapid palatal expansion: A systematic review. *J. oral Maxillofac. Surg.* 80, 1902–1911. doi:10.1016/j.joms.2022.08.008

Lione, R., Paoloni, V., Bartolommei, L., Gazzani, F., Meuli, S., Pavoni, C., et al. (2021). Maxillary arch development with Invisalign system. *Angle Orthod.* 91, 433–440. doi:10.2319/080520-687.1

Liu, L., Song, Q., Zhou, J., Kuang, Q., Yan, X., Zhang, X., et al. (2022). The effects of aligner overtreatment on torque control and intrusion of incisors for anterior retraction with clear aligners: A finite-element study. *Am. J. Orthod. Dentofac. Orthop.* 162, 33–41. doi:10.1016/j.ajodo.2021.02.020

Liu, L., Zhan, Q., Zhou, J., Kuang, Q., Yan, X., Zhang, X., et al. (2021). Effectiveness of an anterior mini-screw in achieving incisor intrusion and palatal root torque for anterior retraction with clear aligners. *Angle Orthod.* 91, 794–803. doi:10.2319/120420-982.1

Morris, J. W., Campbell, P. M., Tadlock, L. P., Boley, J., and Buschang, P. H. (2017). Prevalence of gingival recession after orthodontic tooth movements. *Am. J. Orthod. Dentofac. Orthop.* 151, 851–859. doi:10.1016/j.ajodo.2016.09.027

Paris, V., Pizzigoni, A., and Adriaenssens, S. (2020). Statics of self-balancing masonry domes constructed with a cross-herringbone spiraling pattern. *Eng. Struct.* 215, 110440. doi:10.1016/j.engstruct.2020.110440

Ravera, S., Castroflorio, T., Garino, F., Daher, S., Cugliari, G., and Deregibus, A. (2016). Maxillary molar distalization with aligners in adult patients: A multicenter retrospective study. *Prog. Orthod.* 17, 12. doi:10.1186/s40510-016-0126-0

Romanyk, D. L., Vafaeian, B., Addison, O., and Adeeb, S. (2020). The use of finite element analysis in dentistry and orthodontics: Critical points for model development and interpreting results. *Seminars Orthod.* 26, 162–173. doi:10.1053/j.sodo.2020.06.014

Rossini, G., Parrini, S., Castroflorio, T., Deregibus, A., and Debernardi, C. L. (2015). Efficacy of clear aligners in controlling orthodontic tooth movement: A systematic review. *Angle Orthod.* 85, 881–889. doi:10.2319/061614-436.1

Seo, J. H., Eghan-Acquah, E., Kim, M. S., Lee, J. H., Jeong, Y. H., Jung, T. G., et al. (2021). Comparative analysis of stress in the periodontal ligament and center of rotation in the tooth after orthodontic treatment depending on clear aligner thickness-finite element analysis study. *Mater. (Basel)* 14, 324. doi:10.3390/ma14020324

Shokeen, B., Viloria, E., Duong, E., Rizvi, M., Murillo, G., Mullen, J., et al. (2022). The impact of fixed orthodontic appliances and clear aligners on the oral microbiome and the association with clinical parameters: A longitudinal comparative study. *Am. J. Orthod. Dentofac. Orthop.* 161, e475–e485. doi:10.1016/j.ajodo.2021.10.015

Simon, M., Keilig, L., Schwarze, J., Jung, B. A., and Bourauel, C. (2014). Forces and moments generated by removable thermoplastic aligners: Incisor torque, premolar derotation, and molar distalization. *Am. J. Orthod. Dentofac. Orthop.* 145, 728–736. doi:10.1016/j.ajodo.2014.03.015

Solano-Mendoza, B., Sonnemberg, B., Solano-Reina, E., and Iglesias-Linares, A. (2017). How effective is the Invisalign® system in expansion movement with Ex30' aligners? *Clin. Oral Investig.* 21, 1475–1484. doi:10.1007/s00784-016-1908-y

Sulewska, M., Baczewska, A., Bugała-Musiatowicz, B., Waszkiewicz-Sewastianik, E., Pietruski, J., and Pietruska, M. (2021). Long-term assessment of periodontal tissues after corticotomy-assisted orthodontic arch expansion. *J. Clin. Med.* 10, 5588. doi:10.3390/jcm10235588

Wu, J., Lu, A. D., Zhang, L. P., Zuo, Y. X., and Jia, Y. P. (2019). Study of clinical outcome and prognosis in pediatric core binding factor-acute myeloid leukemia. *Zhonghua Xue Ye Xue Za Zhi* 40, 52–57. doi:10.3760/cma.j.issn.0253-2727.2019.01.010

Xia, Q., He, Y., Jia, L., Wang, C., Wang, W., Wang, C., et al. (2022). Assessment of labially impacted canines traction mode with clear aligners vs. fixed appliance: A comparative study based on 3D finite element analysis. *Front. Bioeng. Biotechnol.* 10, 1004223. doi:10.3389/fbioe.2022.1004223

Zhao, X., Wang, H. H., Yang, Y. M., and Tang, G. H. (2017). Maxillary expansion efficiency with clear aligner and its possible influencing factors. *Zhonghua Kou Qiang Yi Xue Za Zhi* 52, 543–548. doi:10.3760/cma.j.issn.1002-0098.2017.09.006

Zhou, N., and Guo, J. (2020). Efficiency of upper arch expansion with the Invisalign system. *Angle Orthod.* 90, 23–30. doi:10.2319/022719-151.1

Check for updates

Does a novel bridging collar in endoprosthetic replacement optimise the mechanical environment for osseointegration? A finite element study

Giulia Fraterrigo[1], Enrico Schileo[1]*, David Simpson[2],
Jonathan Stevenson[3,4], Ben Kendrick[5,6] and Fulvia Taddei[1]

[1]IRCCS Istituto Ortopedico Rizzoli, Laboratorio di Bioingegneria Computazionale, Bologna, Italy, [2]Adler
Ortho S.p.A., Cormano, Italy, [3]Royal Orthopaedic Hospital NHS Foundation Trust, Birmingham,
United Kingdom, [4]Aston University Medical School, Aston University, Birmingham, United Kingdom,
[5]Nuffield Orthopaedic Centre, Oxford University Hospitals Trust, Oxford, United Kingdom, [6]Nuffield
Department of Orthopaedics, Rheumatology and Musculo-skeletal Science, University of Oxford, Oxford,
England

Introduction: Limb-salvage surgery using endoprosthetic replacements (EPRs) is frequently used to reconstruct segmental bone defects, but the reconstruction longevity is still a major concern. In EPRs, the stem-collar junction is the most critical region for bone resorption. We hypothesised that an in-lay collar would be more likely to promote bone ongrowth in Proximal Femur Reconstruction (PFR), and we tested this hypothesis through validated Finite Element (FE) analyses simulating the maximum load during walking.

Methods: We simulated three different femur reconstruction lengths (proximal, mid-diaphyseal, and distal). For each reconstruction length one in-lay and one traditional on-lay collar model was built and compared. All reconstructions were virtually implanted in a population-average femur. Personalised Finite Element models were built from Computed Tomography for the intact case and for all reconstruction cases, including contact interfaces where appropriate. We compared the mechanical environment in the in-lay and on-lay collar configurations, through metrics of reconstruction safety, osseointegration potential, and risk of long-term bone resorption due to stress-shielding.

Results: In all models, differences with respect to intact conditions were localized at the inner bone-implant interface, being more marked in the collar-bone interface. In proximal and mid-diaphyseal reconstructions, the in-lay configuration doubled the area in contact at the bone-collar interface with respect to the on-lay configuration, showed less critical values and trends of contact micromotions, and consistently showed higher (roughly double) volume percentages of predicted bone apposition and reduced (up to one-third) percentages of predicted bone resorption. In the most distal reconstruction, results for the in-lay and on-lay configurations were generally similar and showed overall less favourable maps of the bone remodelling tendency.

Discussion: In summary, the models corroborate the hypothesis that an in-lay collar, by realising a more uniform load transfer into the bone with a more

physiological pattern, creates an advantageous mechanical environment at the bone-collar interface, compared to an on-lay design. Therefore, it could significantly increase the survivorship of endo-prosthetic replacements.

1 Introduction

Limb-salvage surgery using endoprosthetic replacements (EPRs) are frequently used to reconstruct segmental bone defects after *en-bloc* excision of malignant bone tumours of the proximal and distal femur and are also increasingly used for failed osteosynthesis and arthroplasty with significant bone loss (Chao et al., 2004; Myers et al., 2007; Jeys et al., 2008; Dean et al., 2012). Longevity of the reconstruction is, however, a major concern, especially in young and active patients who place high demands on their prostheses (Jeys et al., 2008; Farfalli et al., 2009).

In bone sarcoma, advances in chemotherapy have led to prolonged life expectancy meaning that reconstructions must be long-lasting if they are to avoid multiple revision operations (Grimer et al., 2016). EPRs permit early weight-bearing and are associated with shorter operative times and without the disease transmission risk associated with allograft reconstructions also indicated for segmental bone loss, thus EPRs are an attractive option for elderly, co-morbid patients (Khajuria et al., 2018).

Complications are common after EPRs due to multiple patient and surgery factors not limited to long surgical procedures, large soft-tissue resections, neo-adjuvant chemo-radiotherapy. Although these implants are widely used the rate of complications for any reason remains five to ten times higher than rates seen following routine total joint arthroplasties (Parvizi et al., 2007; Coathup et al., 2015). In any case, as classified by Henderson et al. (2014) complications across revision and sarcoma surgery with EPRs, both mechanical (soft tissue failure, aseptic loosening, structural failure) and non-mechanical (local recurrence, infections) are common (Jeys et al., 2008; Farfalli et al., 2009; Shehadeh et al., 2010). Aseptic loosening is a common mode of failure, accounting for 25% of revisions in a series of 661 EPRs for oncological indications (Jeys et al., 2008). Other studies have highlighted the rate of aseptic loosening ranges from 2.9% to 28.6% after four to 10 years (Unwin et al., 1996; Torbert et al., 2005).

Loosening of EPRs is associated with loss of cortical bone, initially at the point of contact between the bone and the collar of the prosthesis, then progressing along the stem (Mumith et al., 2017). Having a region of ingrowth on the prosthesis next to the bone at the site of transection promotes extracortical bone bridging (ECBB) (Chao et al., 2004; Mumith et al., 2017). Bone from the cortex at this site grows out and over the collar of the prosthesis. Osseointegration at the collar of the EPR has the potential to reduce the risk of aseptic loosening by improving stress transfer between the implant and bone. It is also thought that ECBB reduces aseptic loosening by sealing the bone/prosthesis interface, which in turn can prevent wear debris and synovial fluid from gaining access to the interface, decreasing the risk of osteolysis (Ward et al., 1993; Mumith et al., 2017).

A more porous collar structure might permit greater ingrowth of bone directly from the transected cortex thereby improving osseointegration (Bram et al., 2006). Although block porous metal has been used successfully to treat metaphyseal defects around revision arthroplasty of the knee (Kamath et al., 2015) it has not been used to encourage ECBB with EPRs. In animal models, a porous collar allows the direct ingrowth of more bone and is superior to current designs which rely on surface ongrowth and ECBB (Mumith et al., 2017). Conventional collars rely on bone bridging externally to the collar because these collars sit on top of the bone at the resection site, described as 'on-lay' collars. A novel collar design utilising a porous on-lay collar with a porous endosteal 'in-lay' sleeve has the theoretical advantage of immediate primary stability from the press-fit of the endosteal sleeve and early osseointegration *via* endosteal cellular growth. The mechanical environment is hypothesised to be further optimised with an in-lay collar and thereby maximising ECBB at the implant-bone interface.

Finite element analysis (FEA) has demonstrated that the stem-collar junction is the region subjected to the highest stresses (Fromme et al., 2017) and clinical studies indicate this region to be the most common site of mechanical failure (Agarwal et al., 2010). In addition, the mechanical environment around the collar is a key factor on whether bone will grow onto the collar, or resorb, leading to aseptic loosening. A lack of osseointegration can lead to stress shielding whereby more of the stress is transferred from the collar of the implant into the tip of the stem. This can lead to bone resorption at the implant-collar interface and ultimately in stem fracture and complex revision surgery. ECBB where it integrates with the surface of the implant allows for a more physiological load transfer and reduced stress shielding (Fromme et al., 2017). Therefore, maximising the ECBB at the implant collar to reduce the incidence of aseptic loosening and increase EPR longevity would be beneficial to patients.

It is not practical to use experimental measurements to directly measure the strain distributions in the bone *in-vivo*, but experimental limitations can be overcome by using Finite Element (FE) analysis. FE models can be used to optimise implant design and verify the design intent of a new prosthesis before long-term clinical data has been recorded. Our study hypothesis was that an in-lay collar would demonstrate advantageous biomechanics around the collar and would be more likely to promote bone ongrowth. The analysis was carried out using a fully validated FE model simulating an instance during a high intensity functional activity.

2 Methods

2.1 Overview

We simulated three different reconstruction lengths (proximal, mid-diaphyseal, and distal) covering almost all possible PFR cases (Figure 1). For each reconstruction length one in-lay and one on-lay
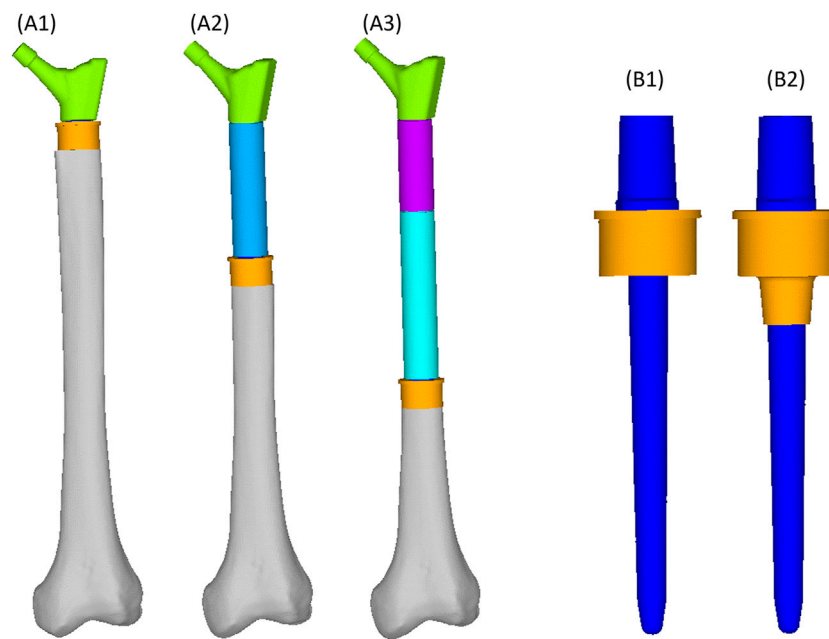
FIGURE 1
Geometry of the femoral reconstructions and concept of the two collar configurations investigated in this study. From left to right: Proximal PFR **(A1)**, Mid-diaphyseal PFR **(A2)**, Distal PFR **(A3)**; Prosthesis stem (blue) joined with on-lay **(B1)** and in-lay **(B2)** collar (orange).

collar model was built and compared. All reconstructions were virtually implanted in a single femur, carefully chosen to represent the average of the population that may receive a PFR. Personalised FE models were built for the intact case and for all simulated PFR cases. In the implanted models we simulated immediate post-operative conditions. The FE models were derived from CT data and virtual implantation information, according to a validated modelling procedure (Schileo et al., 2008; Schileo et al., 2014) that included contact interfaces where applicable (Viceconti et al., 2000; Taddei et al., 2010). Results were analysed to compare the mechanical environment in the in-lay and on-lay collar configurations, deriving metrics of post-operative reconstruction safety/osseointegration potential, and of long-term bone resorption due to stress-shielding.

2.2 Average femur

The average representative femur from this study was chosen from an already presented CT database (Taddei et al., 2014) of 200 femurs showing normal anatomy and absence of visible osteoarthritis signs (Grade 0 according to Altman and Gold (2007)). That database was already shown to be representative of the anatomical proximal femur variability in terms of diaphysis biomechanical length (from intertrochanteric to condylar saddles), femoral neck length, cervico-diaphyseal (CCD) angle, anteversion angle, compared to the widest available reports (Noble et al., 1995; Sugano et al., 1999; Toogood et al., 2009) (Table 1). Given that the PFR interface with bone happens in the diaphysis, we complemented these metrics adding two parameters measured on the diaphyseal bone cortex, i.e., cortical thickness and estimated periosteal radius.

We measured these two additional parameters with an in-house software application developed from an open-source framework (ALBA, https://github.com/IOR-BIC/ALBA), averaging measurements from four radial profiles traced from the centroid of on a horizontal section at the femoral isthmus, excluding the linea aspera. Then, since clinical cases for PFR (oncologic or trauma) are prevalent at young age, we first restricted the database to young (18–40 years old) and densitometrically normal (CT-derived DXA T-score close to zero) cases, then chose the subject with the closest-to-average femoral geometry (Table 1; Figure 2B).

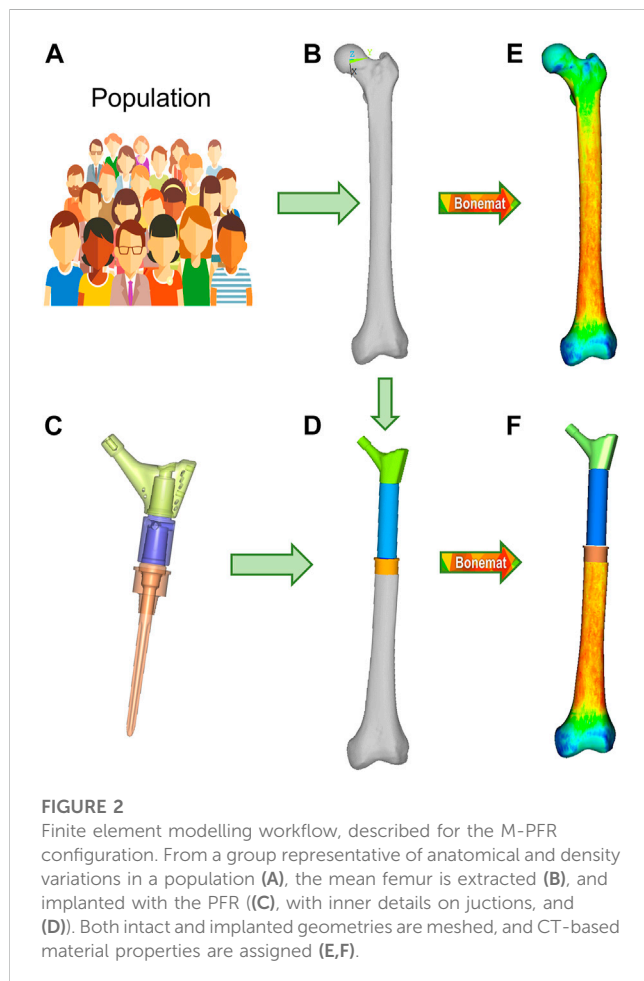## 2.3 Proximal femur reconstruction (PFR)

The Pantheon Proximal Femoral Reconstruction system (Adler Ortho S.p.A, Italy) was used in this study. Virtual implantation of all PFR cases (in-lay and on-lay collar configurations for proximal, mid-diaphyseal and distal reconstructions) was performed on CT data, with the aim to prioritise the best possible fit of prosthetic and intact femoral head centre and hence maximise the similarity of lever arms in the intact and implanted configurations (Figure 2D). A fit of the femoral head centre always below 4 mm could be achieved.

The PFRs in this study have a modular concept, therefore: the proximal reconstruction (P-PFR) was assembled with a femoral neck component, directly linked to the collar and stem (which are also two separate components, assembled through a taper junction); a shaft was added to achieve the mid-diaphyseal reconstruction (M-PFR); two shaft components were used to realize the distal reconstruction (D-PFR).

Cemented fixation of the prosthesis stem (not of the in-lay or of the on-lay collar) was simulated for all PFRs, through a uniform

TABLE 1 Femur geometry: basic descriptive statistics of population distribution over 200 normal anatomies from (Taddei et al., 2014), and values of the femur used in this study.

	Biomech. Length (mm)	Neck Length (mm)	Anteversion Angle (°)	CCD angle (°)	Cortical Thickness (mm)	Diaphyseal radius (mm)
Mean (SD)	407 (29)	39.2 (4.7)	13.3 (8.4)	126.5 (7.3)	5.0 (0.8)	12.1 (1.2)
Min-Max	348–490	26.9–51.5	0.6–45.5	104.1–145.0	3.8–7.1	9.4–14.4
This study	409.5	38.7	7.6	121.8	5.8	12.8

FIGURE 2
Finite element modelling workflow, described for the M-PFR configuration. From a group representative of anatomical and density variations in a population (A), the mean femur is extracted (B), and implanted with the PFR ((C), with inner details on juctions, and (D)). Both intact and implanted geometries are meshed, and CT-based material properties are assigned (E,F).

polymethylmethacrylate (PMMA) cement layer of 1 mm (equal to the nominal thickness indicated by the manufacturer for the implants) surrounding the stem from the collar end to just distal to the stem tip.

2.4 Finite element modelling

2.4.1 PFR

The geometry files of the virtual implantation in NURBS format were defeatured to permit a smooth meshing phase, without omitting any mechanically relevant detail apart from the deletion

of shallow recesses around the stem intended to host cement and thus act as anti-rotational features. These were accounted for in the contact model (Section 2.4.4 below).

A 10-node tetrahedral mesh was generated with an average edge length of 1.5 mm (Hypermesh v.21.0, Altair Engineering Inc., United States). To model the real assembly condition of the PFRs and avoid the simulation of innaturally bulky and stiff prostheses, nodes of the modular components (neck—shaft(s) where applicable—collar—stem) were tied at the actual sites where taper junctions occur (reflecting a condition of stable taper junctions). Titanium alloy material properties (Ti6Al4V, Young's modulus 110 GPa, Poisson's ratio 0.36) were assigned to PFR elements. The thin layer of trabecular titanium covering the surface of the on-lay collar was not assigned specific reduced properties because: i) its thinness hinders a real effect on the overall resistant section of the collar; ii) its osteoconductive and osteointegrating effects are likely due to its surface organisation rather than to the reduction of the elastic modulus towards a bone-like material, as trabecular titanium cells produced by the same manufacturer for custom made 3D reconstructions showed an effective elastic modulus of 97 GPa (i.e., not far from that of the bulk alloy) when mechanically tested (La Barbera et al., 2019).

2.4.2 Femur

We developed six models of the femoral host bone to be coupled to P-PFR, M-PFR and D-PFR in the on-lay and in-lay collar configurations. To permit an element-by-element comparison of implanted and intact conditions, we built six corresponding intact models, isotopological to PFR models in the part where the PFR is inserted into the diaphysis.

Contours of the whole femur were identified through segmentation of the original CT data (Mimics 21, Materialise NV, BE) and then used to obtain a mathematical representation of the surfaces (Geomagic Studio v.7, Raindrop Geomagic Inc., United States). To generate the femur models, we resected the intact femur and subtracted the stem, collar, and cement components with a Boolean operation. A 10-node tetrahedral mesh was generated, setting an average element edge length of 1.5 mm on the surface (HyperMesh 21, Altair Engineering, Inc., United States). Subject-specific bone properties were assigned to bone elements: radiological density was obtained by CT calibration (European Spine Phantom, QRM Gmbh, DE), followed by radiological-to-ash density (linear relationship (Schileo et al., 2008) and ash-to-wet density transitions (fixed 0.6 ratio (Schileo et al., 2008)); wet apparent density was then transformed in Young's modulus based on a density-elasticity
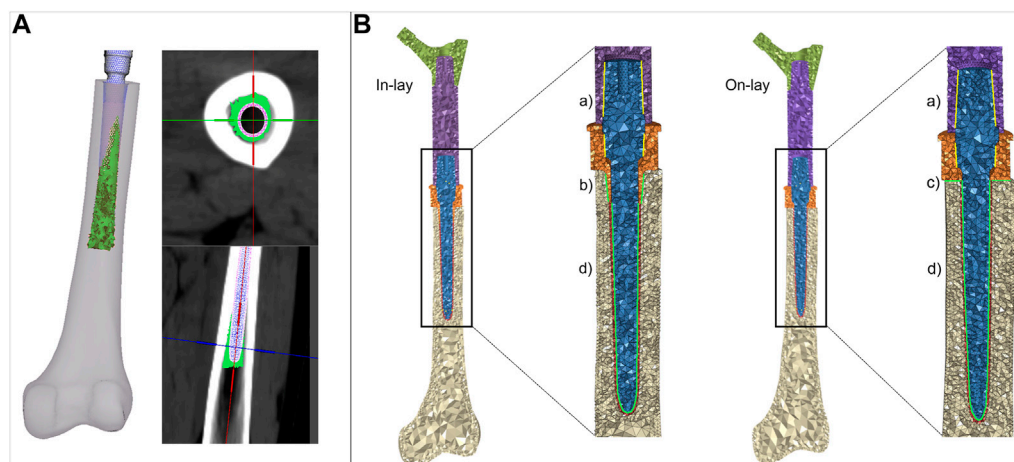
FIGURE 3
(A) details of the procedure to simulate cement interdigitation with porous bone. **(B)** details of contact interfaces for the in -lay and on-lay designs, representing bonded interfaces within the PFR **(Ba)**, and frictional interfaces between in-lay collar and bone **(Bb)**, on-lay collar and bone **(Bc)**, and stem and cement **(Bd)**.

relationship (Morgan et al., 2003). A homogeneous/constant Poisson ratio of 0.3 was set to all the mesh elements (Schileo et al., 2008). Material mapping from CT voxels to finite elements was performed with the Bonemat algorithm (freely available at www.bonemat.org), that provides an average Young's modulus for each element of the mesh, performing a numerical integration of voxel properties extracted from the CT images (Taddei et al., 2007) (Figures 2E,F).

2.4.3 Cement

The uniform 1 mm cement layer was meshed with 10-node tetrahedral elements. An exact match of cement/bone and cement/implant interfaces could be achieved proximally at the resection site, but as the stem extended inwards the uniform 1 mm cement layer was only sparsely in direct contact with the endosteum. To mimic the actual distribution of bone cement in the diaphysis canal, we allowed cement to i) circumferentially expand around the stem, interdigitating with bone elements of the endosteal surface that had a Young's modulus lower than 2 GPa, ii) distally expand down to 5 mm from the stem tip (Figure 3A). Cement elements were assigned a Young's modulus of 2.5 GPa and a Poisson ratio of 0.4.

2.4.4 Interfaces

We intended to simulate a short term post-operative condition, where osseointegration is still to be achieved. Consequently: i) we modelled frictional contact interactions between collar and bone as a function of the surface characteristics of the collar material; ii) we modelled contact between stem and cement but considered bone and cement bonded. A schematic of contact interfaces is provided in Figure 3B.

Contact was numerically implemented in ANSYS (ANSYS APDL v.2020 R1, Ansys Inc., United States), where all models were solved. We adopted an augmented Lagrangian approach and used face-to-face contact elements with large sliding formulation (Viceconti et al., 2000). We built meshes ensuring isotopology of contact and target faces, and we forced a perfect

initial match between contact surfaces neglecting any gap or penetration at the beginning of the loading step.

2.4.4.1 Collar-bone

For the traditional on-lay collar design, which usually has a moderately rough surface finish we set a friction coefficient of 0.5 (as derived from Biemond et al. (2011) for sandblasted coatings) at the interface between the collar and the resected bone surface. For the new in-lay collar: i) we set the friction coefficient to 0.7 to simulate a metal trabecular surface (Biemond et al., 2011); ii) we simulated initial contact between the bone and the sleeve portion of the collar inserted into the diaphysis, leaving the collar ring facing the bone resection plane initially detached from it. This contact setting was intended to replicate the actual condition, which is most likely to occur, where an ideal fit of both the ring and sleeve portion of the collar is almost impossible to be obtained, and the collar fit would likely be privileged operationally.

2.4.4.2 Stem-cement

Contact between the PFR stem and surrounding cement was assumed to have a friction coefficient of 0.3 (Nuño et al., 2006). To compensate for the defeaturing of the anti-rotational features we defined a local cylindric reference system and implemented an orthotropic coefficient of friction, increasing the circumferential coefficient to 0.9, and leaving the axial and transversal ones to 0.3.

2.4.5 Model verification

The chosen average element size of 1.5 mm permitted an accurate discretisation of bone-implant interfaces and can be considered at convergence in the computation of: i) bone strains, as a mesh size of 3 mm showed convergence in a similar study (Helgason et al., 2008); ii) contact results, as a mesh size of 2 mm was used in a previous validation work in a contact model of implanted bone conditions (Taddei et al., 2010).

Mesh quality check in the bone (complex shape, heterogeneous) and cement components showed an aspect ratio over 3 and/or volumetric skew over 0.6 only in 1% of elements, with all angles
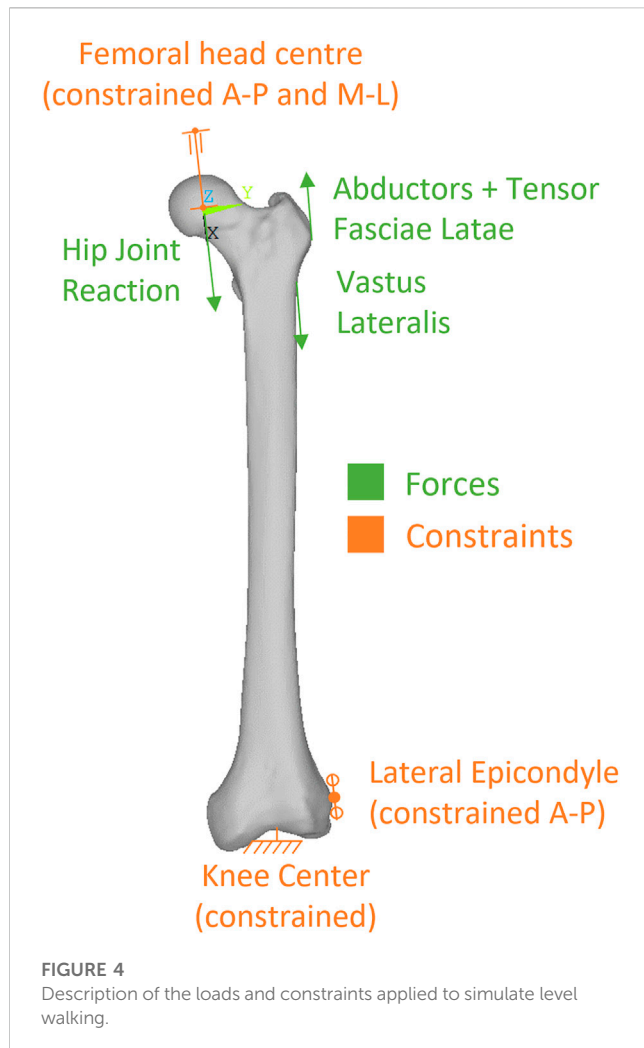
FIGURE 4
Description of the loads and constraints applied to simulate level walking.

between edges in the range 15°–125°. Mesh quality was optimal also at contact interfaces (only 2 elements with aspect ratio over 3, all angles between edges in the range 15°–125°). Mesh quality was slightly worse in the prosthesis, but deemed acceptable as the 1% of elements with aspect ratio over 5 or volumetric skew over 0.7 did not belong to interfaces as internal taper junctions or stem and were located in areas of little interest to our study.

At contact interfaces, residual penetrations at the end of the solution step were checked to be at least one order of magnitude lower than the observed contact sliding.

All material models were linear elastic. We did not include a post-elastic phase in material modelling as we were interested in the elastic response during regular exercise, and in verifying that no component would exceed the elastic limit. Also, validated models from which the modelling procedure was taken had used linear elastic materials.

2.5 Boundary conditions

2.5.1 Constraints

Physiological-like constraints were applied to femur models according to the scheme proposed by (Speirs et al., 2007), that

our research group has already applied to another femur reconstruction study (Valente et al., 2017). Knee stability in that scheme is obtained constraining in antero-posterior direction a single node at the lateral epicondyle, and fully constraining a single node in the knee centre (midpoint between epicondyles) (Figure 4). To permit femoral bending, the femoral head centre was constrained to move along the biomechanical axis of the femur that ideally joins the hip (femoral head) centre with the knee centre.

2.5.2 Loads

We simulated loads on the bone from a standard level walking task, because walking is likely to be the most frequent motor task performed, thus the most suitable to investigate bone remodelling around the implant. An average estimate of physiological loads during walking was obtained from the work of Heller et al. (2005). We adopted the schematization of musculoskeletal loads proposed by Heller et al. (2005) because it is rather simple, yet validated against loads from instrumented prostheses, and already used in preclinical testing of joint prosthesis (Martelli et al., 2011a). In brief, a hip reaction force is applied (at the femoral head centre), equilibrated by muscle forces from abductor and tensor fascia latae (acting at the greater trochanter), and vastus lateralis (acting on the proximal femur diaphysis) (Figure 4). As muscles are usually successfully reattached to metal surfaces or adjacent tissues at the end of the surgical reconstruction trying to reproduce their original position, attachment locations were kept also in the PFR models. Force values in the original work were given in percentage of bodyweight and we thus scaled them to the weight (86 kg) of the modelled subject (Table 2).

2.6 Analysis metrics

For each simulated PFR configuration we computed, according to the classification proposed by Martelli et al. (2011b): i) the percentage of interface area in contact under load and the interfacial sliding micromovements to quantify the risk of short-term aseptic loosening (risk thresholds set at 50 μm for implant-cement (Zhou et al., 1989) and 150 μm for implant-bone interfaces (Pilliar et al., 1986) respectively); ii) the longitudinal, principal and circumferential (hoop) bone strains around the implant to quantify the risk of bone failure (damage thresholds set at 0.73% for tensile and hoop strains, at 1.04% for compressive strains (Bayraktar et al., 2004); iii) the Von Mises equivalent stress on the whole PFR to verify its fatigue safety (fatigue limit set to 400 MPa as a conservative estimate from the data in Long and Rack, (1998)); iv) a strain-energy based indicator of possible positive (apposition) or negative (resorption) bone remodelling around the collar-bone interface. The indicator of bone remodelling tendency was defined (Martelli et al., 2011b) as:

$$R_{BRES} = \frac{\frac{(S-S_{ref})*100}{S_{ref}}}{75}$$

where:

S = strain energy density per unit of mass.

TABLE 2 Applied loads.

Force (Application point)	Med-Lat (N | BW%)	Ant-Post (N | BW%)	Vertical (N | BW%)
Hip Joint Reaction (Femoral head centre)	456 N | 54%	−277 N | −32.8%	1934 N | 229.2%
Abductors + Tensor Fasciae Latae (Greater Trochanter)	−546 N | −64.7%	128 N | 15.2%	−681 N | −80.7%
Vastus Lateralis (Lateral lip of the linea aspera)	8 N | 0.9%	156 N | 18.5%	784 N | 92.9%

S_{ref} = homeostatic reference (i.e., the S of intact femur) (Huiskes et al., 1992).

According to Kuiper and Huiskes (1997) values of R_{BRES} higher than 100 (i.e., strain energy densities over 175% of the intact reference) were considered indicative of bone apposition, values lower than −100 (i.e., strain energy densities lower than 25% of the intact reference) of bone resorption, and values between −100 and 100 (i.e., strain energy densities between 25% and 175% of the intact reference) of homeostasis.

An element-specific calculation was possible as for each PFR model we had built a corresponding isotopological intact model. This indicator was evaluated considering bone volumes of interest around the collar, as depicted in Table 4. A first VOI A) comprised the whole volume of interest around the sleeve portion of the in-lay collar (and corresponding volume in the on-lay configuration). This VOI was then eroded to consider B) the first two layers of bone elements extending radially from the implant, and then C) only the first layer of elements in contact with the implant.

For all PFR lengths, we compared the in-lay and on-lay collar configuration to each other, and each one to the intact femur condition when analysing bone strains and bone remodelling.

3 Results

3.1 Contact status

Contact status results are summarised in Table 3. In the P-PFR and M-PFR, the in-lay configuration doubled the area in contact at the bone-collar interface with respect to the on-lay configuration (32% vs. 16% in P-PFR, 38% vs. 19% in M-PFR). Collar contact areas

always below 40% indicated that the lever exerted by the stiffer overlaying PFR did not permit to evenly distribute load all around the collar. Nonetheless, the larger area in contact in the in-lay collar translated in a more even distribution of load in the in-lay stem, so that larger in-lay than on-lay stem portions were in contact with cement. As a result, the total area in contact under load (summing the collar-bone and stem-cement interfaces) was >60% for the in-lay, and <40% for the on-lay configuration. Full contact maps for each PFR configuration can be found in Supplementary Appendix S1.

Conversely, in D-PFR the on-lay collar showed larger contact area at the collar-bone interface, so that the overall area in contact was similar for both models. Notably, the overall area in contact was not higher than 33% of the total surface, and the contact area in the stem was concentrated for both configurations around the stem tip.

3.2 Contact sliding micromotions

Contact sliding micromotions results are summarised in Table 3 and Figure 5. In the P-PFR and M-PFR models of the on-lay configuration, the small collar ring area in contact with bone in the medial and posterior aspect of the osteotomy experienced limited sliding, which was however concentrated in a medial spot, raising a concern for the development of high shear strains nearby (Section 3.3). The stem was subjected to a larger sliding that locally, in the proximal portion, reached values slightly higher than the 50 μm risk threshold for cemented interfaces. P-PFR and M-PFR models of the in-lay configurations showed a smoother contact interaction, with no regions exceeding alert values and a more uniform distribution of micromotions over the stem, likely thanks to the larger area in contact.

TABLE 3 Percentage of area in contact under load and maximum sliding micromotion at bone-implant and stem-cement interfaces.

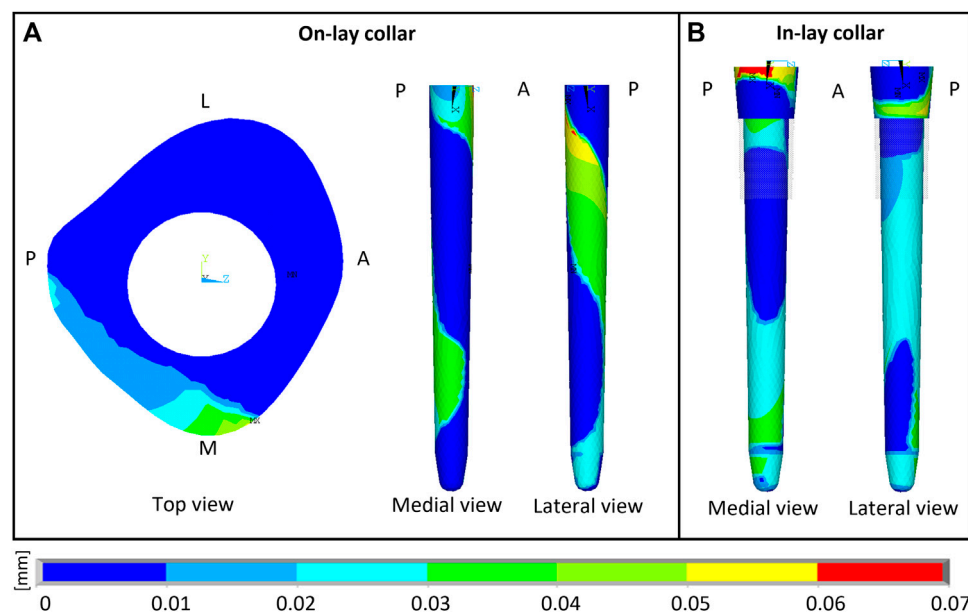|		On-lay collar			In-lay collar		
		Ring/Bone	Stem/Cement	Total	Sleeve/Bone	Stem/Cement	Total
P-PFR (Proximal)	% area in contact	16	38	36	32	73	64
	Max. sliding micromotion (μm)	46	77	—	76	37	—
M-PFR (Mid-diaphysis)	% area in contact	19	40	38	38	64	60
	Max. sliding micromotion (μm)	52	68	—	69	34	—
D-PFR (Distal)	% area in contact	34	31	31	16	37	33
	Max. sliding micromotion (μm)	26	26	—	54	33	—

FIGURE 5
Sliding micromotion resulting from the contact simulation of M-PFR in On-lay **(A)** and In-lay **(B)** collar configurations. A, P, M, L, superscripts indicate Anterior, Posterior, Medial and Lateral aspects, respectively.

D-PFR models showed not alerting levels of micromotions all over the interfaces, both for the in-lay and on-lay configurations. This behaviour, combined with the contact status results, likely indicates that load transfer to bone in D-PFR happens mostly through the stem at its tip.

3.3 PFR stresses

The modular PFR assembly relying on relatively short taper junctions helped reducing the PFR stiffness with respect to a monolithic construct, so that flexibility in the coronal plane was maintained, although grossly halved with respect to the intact bone. As expected, peak stresses occurred at the taper junction surfaces and at the distal collar-bone interface, but were maintained at relatively low levels. In all configurations, the maximum nodal Von Mises stress was around 290 MPa at the distal end of the collar-bone interface, which has the narrowest resisting section. This value is well below the fatigue limit we assumed for the titanium alloy the PFR is made of. However, as i) the maximum value arose in a small location close to an edge and ii) we neither modelled the fine details of the geometry (e.g., fillets, which may decrease stress concentration) nor the trabecular titanium surface (which may instead increase stress concentration especially if residual stresses are not relieved), the final conclusions about prosthesis safety should be left to experimental fatigue testing.
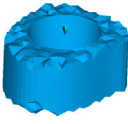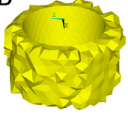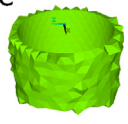
3.4 Bone strains

For all PFR configurations, the superficial strain field in the distal portion of the femur was almost equal to that of the intact bone. The normal stress distribution due to medio-lateral bending, developing postero-medial compressive and antero-lateral tensile strains was maintained, apart from a few unloaded millimeters distal to the osteotomy in the in-lay configuration (see longitudinal strain maps in Supplementary Appendix S1) within the physiological range of ±0.3% (Burr et al., 1996), where instead a significant, but still physiological hoop strain arose, more evidently for the in-lay design in the P-PFR and M-PFR configurations (see hoop strain maps in Supplementary Appendix S1). Differences in strain with respect to intact conditions were localized at the inner bone-PFR interface, being more marked in the collar-bone interface and levelling off moving distally (longitudinal strain maps in Supplementary Appendix S1). Differences between in-lay and on-lay collar configurations could be also observed when looking at longitudinal, hoop or principal strains at sections corresponding to the collar-bone interface (Supplementary Appendix S1). Principal strains never exceeded damage thresholds, although some concern was raised by unusual strain peaks in the medial part of the on-lay collar-bone interface. In fact, consequently to the sliding-sticking behaviour in the small area of the osteotomy in contact with the on-lay collar, a compressive peak exceeding physiological levels appeared in the postero-medial edge of the osteotomy, and a peak due to high shear strain nearby (shear strain at on-lay collar interface in Supplementary Appendix S1, see also Section 3.3).

3.5 Remodelling tendency

Remodelling tendency results are summarised in Table 4 and Figure 6. For all configurations, deviations from homeostasis (i.e., the strain energy density field of the intact bone) increased restricting the VOI towards the implant interface.

TABLE 4 Estimated percentage volumes of bone around (In-lay) or just below (On-lay) the collar region that are likely to undergo bone resorption, homeostasis or apposition according to the strain energy density criterion adopted. Results are presented for three regions of interest progressively reducing the volume of interest from the external surface (A) to two (B) or one (C) finite element layers close to the bone-implant interface.

		On-lay collar			In-lay collar			
		Resorption	Homeostasis	Apposition	Resorption	Homeostasis	Apposition	
P-PFR	A	38	50	12	23	56	21	A
	B	24	54	22	7	44	49	
	C	19	48	33	5	27	68	
M-PFR	A	32	47	21	22	56	22	B
	B	24	53	23	7	49	44	
	C	14	60	26	7	32	61	
D-PFR	A	47	48	5	53	38	9	C
	B	40	51	9	35	50	15	
	C	38	50	12	28	47	25	

In the P-PFR and M-PFR, in-lay configurations consistently showed higher (roughly double) volume percentages of predicted bone apposition and reduced (up to one-third) percentages of predicted bone resorption. Predicted appositional behaviour was predominant in the in-lay models, where a few millimetres distal to the osteotomy might undergo resorption but moving distally bone apposition is likely to happen almost all around the interface with the collar sleeve. On-lay models VOIs showed similar percentages of predicted apposition and resorption but indicated possible generalised resorption due to stress-shielding in the outermost lateral aspect.

D-PFR showed generally less favourable maps of the bone remodelling tendency. Overall numbers were similar for in-lay and on-lay configurations. Half of the whole VOI around the sleeve collar was predicted at risk of resorption. Moving closer to the bone-implant interface, this risk tended to decrease. However, the in-lay design seemed to offer a slight advantage also in this case, as the decrease of resorption risk was more marked, and more uniform around the collar interface, while the whole lateral aspect in the on-lay design remained at risk of resorption.

4 Discussion

It has previously been demonstrated that osteointegration with extracortical bone-bridging to the implant collar of EPRs improves prosthesis fixation, especially when HA coated collars are used (Chao et al., 2004; Myers et al., 2007). When bone is osseointegrated onto the collar of the prosthesis, survival at 10 years is increased by more than 20% (Coathup et al., 2013).

In this study we investigated the mechanical environment around a proximal femoral (endoprosthetic) replacement (PFR) for two different designs of collar using FE analysis: a novel fully porous bridging collar with a combined endosteal sleeve (in-lay) and a conventional collar without an endosteal sleeve (on-lay). The study examined different reconstruction lengths with the PFR and compared the mechanical environment between the two collar types.

There have been no reported studies investigating the overall mechanical environment around the stem and collar using a complete proximal femur constructed into a validated femur model. The present study used a finite element model to compare a novel in-lay
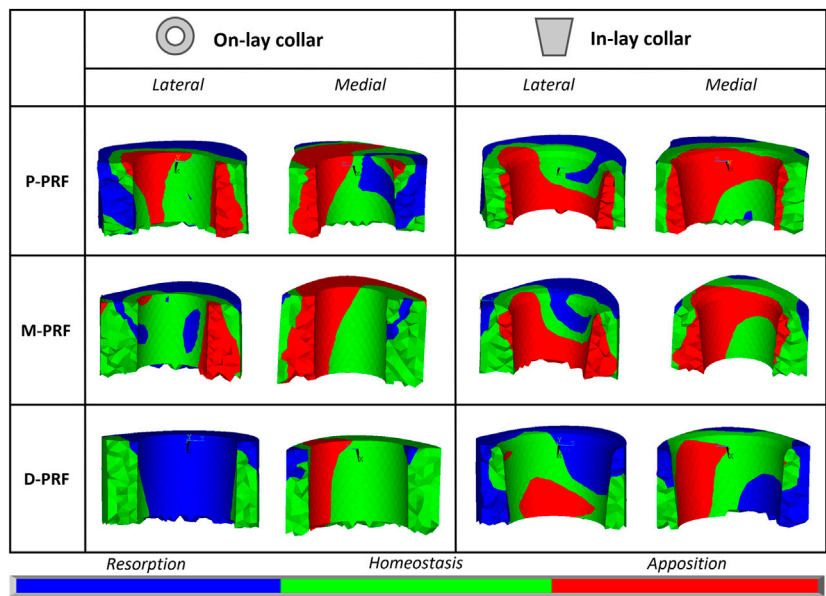
FIGURE 6
Visual maps of estimated bone resorption, homeostasis or apposition in the volume of interest around (In-lay) or just below (On-lay) the collar region.

collar to a conventional on-lay collar, in three different conditions for a proximal femoral (endoprosthetic) replacement (PFR) with proximal, mid-diaphysis and distal reconstructions.

We have demonstrated that an in-lay collar creates an advantageous mechanical environment at the bone-collar interface, compared to an on-lay design. The contact area around the collar was significantly increased for the in-lay collar compared to the on-lay collar (60% vs. 40%). The in-lay collar demonstrated more uniform load transfer into the bone with a more physiological pattern, and the predictions of bone apposition were double than with an on-lay collar. The in-lay collar induced a significant hoop strain in the bone cortex, but estimated strain levels remain within the physiological limit, suggesting a condition similar to conventional uncemented stems. Lastly, resorption was reduced by a third utilising an in-lay collar. The main differences in the mechanical environment induced by the on-lay and in-lay designs were found at the collar region, and more evident close to the interface between the bone and collar. Although neither of the designs realise full contact around the collar due to the high stiffness of the overall reconstruction, the in-lay collar may stimulate apposition of bone all around it, while results for the on-lay collar were more polarised.

The on-lay collar suffered significantly greater stem-cement micromotions, non-physiological localised shear and compressive strains at the bone-implant interface and a much larger volume at risk of resorption. These findings may indicate increased risk of prosthetic fractures clinically.

The greatest differences between the in-lay and on-lay designs were identified in the proximal and mid-diaphyseal reconstructions. In more distal reconstructions, results for on-lay and in-lay designs were similar, and overall, less favourable to positive bone remodelling around the implant. Unwin et al. theorised that longer resection in PFRs was protective as the mechanical offset decreases with greater resection length, which may explain the reduced stresses in the distal femur (Unwin et al., 1996).

Few studies have investigated the mechanical environment surrounding the collar and stem in endoprosthetic reconstruction. Fromme et al. (2017) used a finite element model to describe load transfer at the collar-bone interface and confirmed that the stem-collar junction is the region subjected to the highest stresses and crucially that the stresses are greatest when there was no ECBB onto the collar; the authors concluded that this would promote stem fracture under normal walking loads. They showed that bone ongrowth reduced stresses due to more physiological loading thus protecting against implant failure.

The results from this study would indicate that an in-lay collar design would be more likely to achieve ECBB at the collar of the implant and could potentially reduce the likelihood of aseptic loosening. All conventional collars are the on-lay design, and aseptic loosening rates for these devices are reportedly high. Although there are no published reports for the in-lay design, two of the authors of this study have been using the in-lay design for the last 5 years and to date and have observed zero cases of aseptic loosening in a series of over 100 PFRs. This study in combination with excellent short-term clinical data would suggest that a fully porous in-lay collar design could significantly increase the survivorship of endo-prosthetic replacements.

There are several limitations to this study.

A single femur instance was modelled with one load condition. However, the verified mean geometry and clinically relevant density distribution, with a single load condition is a useful way of investigating the relative comparison between the in-lay and on-lay design.

Only cemented fixation was modelled in this study, and although we would like to extend the analysis to cementless fixation, the use of cement is very common with proximal femoral (endoprosthetic) replacements. In the virtual implantation process, we assumed a perfect match between implant and bone; and we did not model a possible press-fit due to the insertion process of the collar in the reamed cavity. Modelling these surgical conditions and variabilities was out of the scope of the study and

would have required modelling of inelastic phenomena, for which the modelling procedure was not verified and validated. A direct validation against experimental data for the studied prosthetic configuration could not be produced. We however used a modelling procedure that has been extensively validated in the estimate of bone strains, bone failure, and bone-implant interaction (although in a different femoral prosthesis design). This same procedure had also been used previously to successfully revise an implant design (Martelli et al., 2011a).

The validated modelling procedure adopted neglects bone anisotropy, while the mechanical response of cortical bone of the femoral diaphysis, where the studied reconstructions insist on, is acknowledged to be anisotropic. To verify the strong assumption of bone isotropy we developed an additional anisotropic model of the intact bone and of the mid-diaphyseal reconstruction, computing bone strain and strain energy metrics. This additional activity, fully reported in Supplementary Appendix S2, highlighted: i) the limited robustness of anisotropic material parameters, and ii) the limited changes in the classification of the risk of bone damage in exercise and of bone weakening over time when anisotropic material properties were introduced (to our best estimate) in the model. We therefore corroborated the use of a validated isotropic model, even though the development of a validated anisotropic model would be desirable to further increase the accuracy and biofidelity of the analysis.

We did not develop or implement a model of the bone remodelling process. However, validated bone remodelling models for human bones from continuum level imaging data are not available, to our knowledge. Validated models are available only from microCT images in specific mice breeds, which have limited genetic (and age) variability, contrarily to humans. Therefore, we preferred limiting to give an indication of a potential remodelling signal based on strain energy density trends.

Finally, the porosity of the trabecular titanium layer of the in-lay collar was not modelled explicitly, but indirectly through a higher coefficient of friction with the surrounding bone. Future research could model in more detail ingrowth throughout the porous collar. A more porous structure might permit swifter ingrowth of bone directly from the transected cortex thereby improving osseointegration (Bram et al., 2006) as has been shown in animal modelling (Mumith et al., 2017).

In summary, the novel design in-lay collar provides an advantageous mechanical environment at the resection level compared to the existing on-lay design, with approximately twice as much bony apposition and significantly lower bony resorption. This has clear potential benefits in the clinical setting.

Data availability statement

The datasets presented in this article are not readily available because the implant models were generated using proprietary designs of Adler Ortho S.p.A. Request to access these data should be addressed to info@adlerortho.com. Access to the anonymised images used to build the bone models is available by request to the corresponding author. Requests to access the datasets should be directed to ES, enrico.schileo@ior.it.

Author contributions

Funding

Conflict of interest

Author DS is an employee of Adler Ortho S.p.A.

The remaining authors declare that the research was conducted in the absence of any commercial or financial relationships that could be construed as a potential conflict of interest.

Publisher's note

Supplementary material

The Supplementary Material for this article can be found online at: https://www.frontiersin.org/articles/10.3389/fbioe.2023.1120430/full#supplementary-material

References

Agarwal, M., Gulia, A., Ravi, B., Ghyar, R., and Puri, A. (2010). Revision of broken knee megaprostheses: New solution to old problems. *Clin. Orthop. Relat. Res.* 468, 2904–2913. doi:10.1007/s11999-010-1409-2

Altman, R. D., and Gold, G. E. (2007). Atlas of individual radiographic features in osteoarthritis, revised. *Osteoarthr. Cartil.* 15, A1–A56. doi:10.1016/j.joca.2006.11.009

Bayraktar, H. H., Morgan, E. F., Niebur, G. L., Morris, G. E., Wong, E. K., and Keaveny, T. M. (2004). Comparison of the elastic and yield properties of human femoral trabecular and cortical bone tissue. *J. Biomechanics* 37, 27–35. doi:10.1016/S0021-9290(03)00257-4

Biemond, J. E., Aquarius, R., Verdonschot, N., and Buma, P. (2011). Frictional and bone ingrowth properties of engineered surface topographies produced by electron beam technology. *Arch. Orthop. Trauma Surg.* 131, 711–718. doi:10.1007/s00402-010-1218-9

Bram, M., Schiefer, H., Bogdanski, D., Köller, M., Buchkremer, H., and Stöver, D. (2006). Implant surgery: How bone bonds to PM titanium. *Metal. Powder Rep.* 61, 26–31. doi:10.1016/S0026-0657(06)70603-8

Burr, D. B., Milgrom, C., Fyhrie, D., Forwood, M., Nyska, M., Finestone, A., et al. (1996). *In vivo* measurement of human tibial strains during vigorous activity. *Bone* 18, 405–410. doi:10.1016/8756-3282(96)00028-2

Chao, E. Y. S., Fuchs, B., Rowland, C. M., Ilstrup, D. M., Pritchard, D. J., and Sim, F. H. (2004). Long-term results of segmental prosthesis fixation by extracortical bone-bridging and ingrowth. *J. Bone and Jt. Surg.* 86, 948–955. doi:10.2106/00004623-200405000-00010

Coathup, M. J., Batta, V., Pollock, R. C., Aston, W. J., Cannon, S. R., Skinner, J. A., et al. (2013). Long-term survival of cemented distal femoral endoprostheses with a hydroxyapatite-coated collar: A histological study and a radiographic follow-up. *J. Bone Jt. Surg.* 95, 1569–1575. doi:10.2106/JBJS.L.00362

Coathup, M. J., Sanghrajka, A., Aston, W. J., Gikas, P. D., Pollock, R. C., Cannon, S. R., et al. (2015). Hydroxyapatite-coated collars reduce radiolucent line progression in cemented distal femoral bone tumor implants. *Clin. Orthop. Relat. Res.* 473, 1505–1514. doi:10.1007/s11999-014-4116-6

Dean, B. J. F., Matthews, J. J., Price, A., Stubbs, D., Whitwell, D., and Gibbons, C. M. L. H. (2012). Modular endoprosthetic replacement for failed internal fixation of the proximal femur following trauma. *Int. Orthop. (SICOT)* 36, 731–734. doi:10.1007/s00264-011-1332-5

Farfalli, G. L., Boland, P. J., Morris, C. D., Athanasian, E. A., and Healey, J. H. (2009). Early equivalence of uncemented press-fit and Compress® femoral fixation. *Clin. Orthop. Relat. Res.* 467, 2792–2799. doi:10.1007/s11999-009-0912-9

Fromme, P., Blunn, G. W., Aston, W. J., Abdoola, T., Koris, J., and Coathup, M. J. (2017). The effect of bone growth onto massive prostheses collars in protecting the implant from fracture. *Med. Eng. Phys.* 41, 19–25. doi:10.1016/j.medengphy.2016.12.007

Grimer, R. J., Aydin, B. K., Wafa, H., Carter, S. R., Jeys, L., Abudu, A., et al. (2016). Very long-term outcomes after endoprosthetic replacement for malignant tumours of bone. *Bone and Jt. J.* 98-B, 857–864. doi:10.1302/0301-620X.98B6.37417

Helgason, B., Taddei, F., Pálsson, H., Schileo, E., Cristofolini, L., Viceconti, M., et al. (2008). A modified method for assigning material properties to FE models of bones. *Med. Eng. Phys.* 30, 444–453. doi:10.1016/j.medengphy.2007.05.006

Heller, M. O., Bergmann, G., Kassi, J.-P., Claes, L., Haas, N. P., and Duda, G. N. (2005). Determination of muscle loading at the hip joint for use in pre-clinical testing. *J. Biomechanics* 38, 1155–1163. doi:10.1016/j.jbiomech.2004.05.022

Henderson, E. R., O'Connor, M. I., Ruggieri, P., Windhager, R., Funovics, P. T., Gibbons, C. L., et al. (2014). Classification of failure of limb salvage after reconstructive surgery for bone tumours: A modified system including biological and expandable reconstructions. *Bone and Jt. J.* 96-B, 1436–1440. doi:10.1302/0301-620X.96B11.34747

Huiskes, R., Weinans, H., and Rietbergen, B. V. (1992). The relationship between stress shielding and bone resorption around total hip stems and the effects of flexible materials. *Clin. Orthop. Relat. Res.* 274, 124–134. doi:10.1097/00003086-199201000-00014

Jeys, L. M., Kulkarni, A., Grimer, R. J., Carter, S. R., Tillman, R. M., and Abudu, A. (2008). Endoprosthetic reconstruction for the treatment of musculoskeletal tumors of the appendicular skeleton and pelvis. *J. Bone and Jt. Surg.* 90, 1265–1271. doi:10.2106/JBJS.F.01324

Kamath, A. F., Lewallen, D. G., and Hanssen, A. D. (2015). Porous tantalum metaphyseal cones for severe tibial bone loss in revision knee arthroplasty: A five to nine-year follow-up. *J. Bone Jt. Surgery-American* 97, 216–223. doi:10.2106/JBJS.N.00540

Khajuria, A., Ward, J., Cooper, G., Stevenson, J., Parry, M., and Jeys, L. (2018). Is endoprosthetic replacement of the proximal femur appropriate in the comorbid patient? *HIP Int.* 28, 68–73. doi:10.5301/hipint.5000520

Kuiper, J. H., and Huiskes, R. (1997). The predictive value of stress shielding for quantification of adaptive bone resorption around hip replacements. *J. Biomechanical Eng.* 119, 228–231. doi:10.1115/1.2796084

La Barbera, L., Trabace, M., Pennati, G., and Rodríguez Matas, J. F. (2019). Modeling three-dimensional-printed trabecular metal structures with a homogenization approach: Application to hemipelvis reconstruction. *Int. J. Artif. Organs* 42, 575–585. doi:10.1177/0391398819848001

Long, M., and Rack, H. J. (1998). Titanium alloys in total joint replacement—A materials science perspective. *Biomaterials* 19, 1621–1639. doi:10.1016/S0142-9612(97)00146-4

Martelli, S., Taddei, F., Cristofolini, L., Gill, H. S., and Viceconti, M. (2011a). Extensive risk analysis of mechanical failure for an epiphyseal hip prothesis: A combined numerical—experimental approach. *Proc. Inst. Mech. Eng. H.* 225, 126–140. doi:10.1243/09544119JEIM728

Martelli, S., Taddei, F., Cristofolini, L., Schileo, E., Rushton, N., and Viceconti, M. (2011b). A new hip epiphyseal prosthesis: Design revision driven by a validated numerical procedure. *Med. Eng. Phys.* 33, 1203–1211. doi:10.1016/j.medengphy.2011.05.010

Morgan, E. F., Bayraktar, H. H., and Keaveny, T. M. (2003). Trabecular bone modulus–density relationships depend on anatomic site. *J. Biomechanics* 36, 897–904. doi:10.1016/S0021-9290(03)00071-X

Mumith, A., Coathup, M., Chimutengwende-Gordon, M., Aston, W., Briggs, T., and Blunn, G. (2017). Augmenting the osseointegration of endoprostheses using laser-sintered porous collars: An *in vivo* study. *Bone and Jt. J.* 99-B, 276–282. doi:10.1302/0301-620X.99B2.BJJ-2016-0584.R1

Myers, G. J. C., Abudu, A. T., Carter, S. R., Tillman, R. M., and Grimer, R. J. (2007). Endoprosthetic replacement of the distal femur for bone tumours. *J. BONE Jt. Surg.* 89, 521–526. doi:10.1302/0301-620x.89b4.18631

Noble, P. C., Box, G. G., Kamaric, E., Fink, M. J., Alexander, J. W., and Tullos, H. S. (1995). *The effect of aging on the shape of the proximal femur.* Clinical Orthopaedics and Related Research NA, 31–44. doi:10.1097/00003086-199507000-00006

Nuño, N., Groppetti, R., and Senin, N. (2006). Static coefficient of friction between stainless steel and PMMA used in cemented hip and knee implants. *Clin. Biomech.* 21, 956–962. doi:10.1016/j.clinbiomech.2006.05.008

Parvizi, J., Tarity, T. D., Slenker, N., Wade, F., Trappler, R., Hozack, W. J., et al. (2007). Proximal femoral replacement in patients with non-neoplastic conditions. *J. Bone and Jt. Surg.* 89, 1036–1043. doi:10.2106/JBJS.F.00241

Pilliar, R. M., Lee, J. M., and Maniatopoulos, C. (1986). Observations on the effect of movement on bone ingrowth into porous-surfaced implants. *Clin. Orthop. Relat. Res.* 208, 108–113. doi:10.1097/00003086-198607000-00023

Schileo, E., Balistreri, L., Grassi, L., Cristofolini, L., and Taddei, F. (2014). To what extent can linear finite element models of human femora predict failure under stance and fall loading configurations? *J. Biomechanics* 47, 3531–3538. doi:10.1016/j.jbiomech.2014.08.024

Schileo, E., Dall'Ara, E., Taddei, F., Malandrino, A., Schotkamp, T., Baleani, M., et al. (2008). An accurate estimation of bone density improves the accuracy of subject-specific finite element models. *J. Biomechanics* 41, 2483–2491. doi:10.1016/j.jbiomech.2008.05.017

Shehadeh, A., Noveau, J., Malawer, M., and Henshaw, R. (2010). Late complications and survival of endoprosthetic reconstruction after resection of bone tumors. *Clin. Orthop. Relat. Res.* 468, 2885–2895. doi:10.1007/s11999-010-1454-x

Speirs, A. D., Heller, M. O., Duda, G. N., and Taylor, W. R. (2007). Physiologically based boundary conditions in finite element modelling. *J. Biomechanics* 40, 2318–2323. doi:10.1016/j.jbiomech.2006.10.038

Sugano, N., Noble, P. C., and Kamaric, E. (1999). Predicting the position of the femoral head center. *J. Arthroplasty* 14, 102–107. doi:10.1016/S0883-5403(99)90210-3

Taddei, F., Martelli, S., Gill, H. S., Cristofolini, L., and Viceconti, M. (2010). Finite element modeling of resurfacing hip prosthesis: Estimation of accuracy through experimental validation. *J. Biomechanical Eng.* 132, 021002. doi:10.1115/1.4000065

Taddei, F., Palmadori, I., Taylor, W. R., Heller, M. O., Bordini, B., Toni, A., et al. (2014). European society of biomechanics S.M. Perren award 2014: Safety factor of the proximal femur during gait: A population-based finite element study. *J. Biomechanics* 47, 3433–3440. doi:10.1016/j.jbiomech.2014.08.030

Taddei, F., Schileo, E., Helgason, B., Cristofolini, L., and Viceconti, M. (2007). The material mapping strategy influences the accuracy of CT-based finite element models of bones: An evaluation against experimental measurements. *Med. Eng. Phys.* 29, 973–979. doi:10.1016/j.medengphy.2006.10.014

Toogood, P. A., Skalak, A., and Cooperman, D. R. (2009). Proximal femoral anatomy in the normal human population. *Clin. Orthop. Relat. Res.* 467, 876–885. doi:10.1007/s11999-008-0473-3

Torbert, J. T., Fox, E. J., Hosalkar, H. S., Ogilvie, C. M., and Lackman, R. D. (2005). Endoprosthetic reconstructions: Results of long-term followup of 139 patients. *Clin. Orthop. Relat. Res.* NA 438, 51–59. doi:10.1097/01.blo.0000179735.37089.c2

Unwin, P. S., Cannon, S. R., Grimer, R. J., Kemp, H. B., Sneath, R. S., and Walker, P. S. (1996). Aseptic loosening in cemented custom-made prosthetic replacements for bone tumours of the lower limb. *J. Bone Jt. Surg. Br.* 78, 5–13. doi:10.1302/0301-620x.78b1.0780005

Valente, G., Pitto, L., Schileo, E., Piroddi, S., Leardini, A., Manfrini, M., et al. (2017). Relationship between bone adaptation and *in-vivo* mechanical stimulus in biological reconstructions after bone tumor: A biomechanical modeling analysis. *Clin. Biomech.* 42, 99–107. doi:10.1016/j.clinbiomech.2017.01.017

Viceconti, M., Muccini, R., Bernakiewicz, M., Baleani, M., and Cristofolini, L. (2000). Large-sliding contact elements accurately predict levels of bone–implant micromotion relevant to osseointegration. *J. Biomechanics* 33, 1611–1618. doi:10.1016/S0021-9290(00)00140-8

Ward, W. G., Johnston, K. S., Dorey, F. J., and Eckardt, J. J. (1993). Extramedullary porous coating to prevent diaphyseal osteolysis and radiolucent lines around proximal tibial replacements. A preliminary report. *J. Bone and Jt. Surg.* 75, 976–987. doi:10.2106/00004623-199307000-00003

Zhou, Z. R., Pellerin, V., and Vincent, L. (1989). "Fretting –wear of aluminium and titanium alloys." In *Titanium and aluminium*. Editor P. A. Coulon (I.I.T.T. International), 145–153.

An automated system for polymer wear debris analysis in total disc arthroplasty using convolution neural network

Sushil Kandel[1], Steven Su[1,2]*, Richard M. Hall[3] and Joanne L. Tipper[1,3]

[1]Faculty of Engineering and IT, University of Technology, Sydney, NSW, Australia, [2]College of Artificial Intelligence and Big Data for Medical Science, Shandong First Medical University & Shandong Academy of Medical Sciences, Taian, China, [3]School of Mechanical Engineering, University of Leeds, Leeds, United Kingdom

Introduction: Polymer wear debris is one of the major concerns in total joint replacements due to wear-induced biological reactions which can lead to osteolysis and joint failure. The wear-induced biological reactions depend on the wear volume, shape and size of the wear debris and their volumetric concentration. The study of wear particles is crucial in analysing the failure modes of the total joint replacements to ensure improved designs and materials are introduced for the next generation of devices. Existing methods of wear debris analysis follow a traditional approach of computer-aided manual identification and segmentation of wear debris which encounters problems such as significant manual effort, time consumption, low accuracy due to user errors and biases, and overall lack of insight into the wear regime.

Methods: This study proposes an automatic particle segmentation algorithm using adaptive thresholding followed by classification using Convolution Neural Network (CNN) to classify ultra-high molecular weight polyethylene polymer wear debris generated from total disc replacements tested in a spine simulator. A CNN takes object pixels as numeric input and uses convolution operations to create feature maps which are used to classify objects.

Results: Classification accuracies of up to 96.49% were achieved for the identification of wear particles. Particle characteristics such as shape, size and area were estimated to generate size and volumetric distribution graphs.

Discussion: The use of computer algorithms and CNN facilitates the analysis of a wider range of wear debris with complex characteristics with significantly fewer resources which results in robust size and volume distribution graphs for the estimation of the osteolytic potential of devices using functional biological activity estimates.

1 Introduction

Wear particles result from frictional interaction between two surfaces in motion against each other. With the ever-increasing number of complex mechanical equipment in the industrial and medical sectors, the study of wear particle characteristics and their effects on the system's overall performance has gathered significant interest in recent years, given that wear is an inherent part of a mechanical system. Total joint replacement (TJR) procedures are performed to replace a problematic natural joint and they aim to preserve the natural range of motion. Motion preservation is achieved using an articulating mechanism which provides motion around the desired axes. These articulating components are made of various materials such as metals, polymers and ceramics. The three major joint replacements in the human body which are total hip replacement (THR), total knee replacements (TKR) and total disc replacements (TDR), use similar design principles but differ in their mechanical operation, which include different ranges of motion and different loading conditions. The difference in kinematic conditions and material choices have been shown to affect the characteristics of the wear debris produced (Milošev et al., 2012).

The study of wear debris and the potential problems it can cause in joint replacements have been carried out since the late 1960s (Lewis, 2001b). Since then, multiple studies have established cytotoxic reactions, inflammation and osteolysis as major side effects of the wear particles released from joint replacements (Harris, 1995; Ingham and Fisher, 1997; Kobayashi et al., 1997; Green et al., 2000; Lewis, 2001a; Cunningham et al., 2013). Early studies found that sub-micrometre particles were associated with macrophage responses releasing several osteolytic cytokines that cause osteolysis and aseptic loosening of the joint [13]. The level of cytokine release and the subsequent bone resorption depends on the characteristics of wear, such as particle size, shape and volumetric concentration (Green et al., 1998). Wear characteristics such as the type of wear, the rate, and its severity are the main defining characteristics of polyethylene wear. The corresponding features of wear particles that define the wear characteristics include quantity, shape, size, and composition. Various factors such as the loading conditions, polishing of the surface material, oxidative state and the level of cross-linking of polyethylene have been shown to affect the wear characteristics (Peng, 2002).

Hence, it is crucial to explore the wear characteristics to understand the biological activity of the wear particles to minimize the causes of failures, whether it be *via* a change in material choice or by the use of a different design. Numerous studies have been performed in the last 3 decades to analyse the characteristics and biological compatibility of wear debris in TJRs. Apart from the analysis of failure modes in artificial joints, wear particle analysis is one of the crucial features in the condition monitoring of industrial machines and the prediction of their imminent behaviour [6]. Unlike the online monitoring and analysis of wear debris in an industrial setup, most of the wear analysis in joint replacements is done offline by taking images of wear debris from an *in vitro* simulation. Despite similar wear modes present in joint replacements and industrial machines, the nature of wear particles is quite different in terms of the particle size and the wear volume where the particles of interest in an industrial setup are in the order of micrometers. In contrast, the particles of concern in
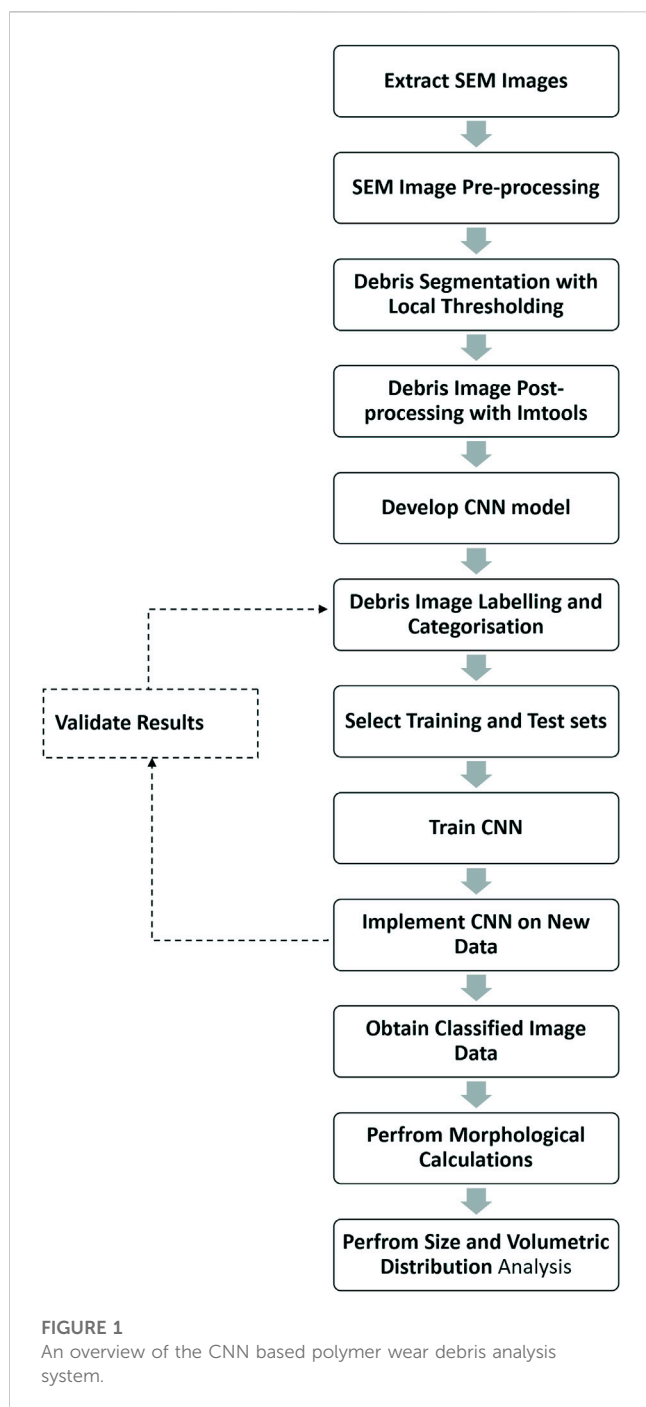
joint replacements are in the range of nanometers to millimeters (Charnley et al., 1968).

Wear debris analysis is a time-consuming process due to the complex nature of the wear particles generated from a joint replacement. Particle sizes range from less than 50 nm to greater than 100 μm and are morphologically complex due to a lack of uniformity in size, shape and intensity (McKellop et al., 1995). Smaller particles are hard to identify due to contamination by protein structures and low resolution of imaging. Until recently, the quantitative analysis of wear debris was performed manually, adding to the time constraint. The use of computer vision and machine learning for structural and morphological analysis of the wear debris is more efficient in terms of resources and time, which allows for a larger set of data to be analysed, potentially improving the distribution functions of wear particle size and volume.

The extraction and classification of the wear debris is a major step in determining the characteristics of the wear particles. There have been a small number of attempts to classify the wear particles generated from the use of machinery in the late 1990s using neural networks (Myshkin et al., 1997; Peng and Kirk, 1998). These methods use a discrete set of values, known as features, to classify the data into different categories. The features can be any data parameter such as the area, perimeter, length, shape, Fourier descriptors and fractal dimensions. These methods can perform basic classification but fail when the dataset is complex, and the features of two datasets become similar. Classification attempts have been made using a support vector machine (SVM) classifier with dissimilarity measures as the feature descriptors to detect the progression of wear in a tribological setup with a classification accuracy of 97% for wear particle images in different stages of the simulation, without considering their morphology (Podsiadlo and Stachowiak, 2005). Their main achievement was to distinguish if a debris sample is at the initial or mid stages of wear. However, in addition to the results not being explicit about the wear regimes, the results of this study are constricted due to the use of wear debris that was uniform and carefully selected.

Eckold et al. (Eckold et al., 2015) used a scale-invariant feature transform (SIFT) to extract features from the wear particle images obtained from a total disc replacement setup, using Charite TDR implant and then used SVM to classify the wear particles based on their morphology into five different categories with an accuracy of 77.6%. Juranek et al. (Juránek et al., 2011) used a machine learning algorithm called AdaBoost as a classifier on a four-bit feature vector produced using centre-symmetric local binary patterns to classify wear particles produced in an industrial machine into four classes based on the mechanism of wear with an average classification accuracy of 91.8%.

Recent studies on the classification of wear debris produced in industrial machines have used a convolution neural network (CNN) to determine the wear phenomenon according to the type of wear debris present. In a study by Wang et al. (Wang H et al., 2019), accuracies of up to 96% were achieved in detecting the presence of wear debris with disregard to the type and quantity of wear debris. Another study used CNN to detect the wear condition present in a mechanical setup without classifying the wear debris, with an accuracy of 90% (Wang et al., 2020). However, for the detailed quantitative analysis of wear debris, the average classification accuracies for different types of wear debris ranges from 77% to

FIGURE 1
An overview of the CNN based polymer wear debris analysis system.

can not be said for medical applications mainly because of the difference in size and number of the wear particles due to the difference in the dynamics of the two systems. The size of wear debris of interest in the industrial condition monitoring ranges from 20 μm to hundreds of micrometres (Wang H et al., 2019; Wang S et al., 2019), which can cause mechanical failure due to equipment breakages on a dynamic system. On the contrary, wear debris of a few micrometres, or less is more problematic in joint replacements as they are more biologically active and cause macrophage activation resulting in osteolysis. This difference in the size of wear particles correlates to the performance of a classifier and thus results in a significant difference in classification accuracies. Aside from that, the wear debris in the mechanical system are suspended in a lubricating medium which can be filtered, replaced, and monitored online. Whereas, the wear debris in artificial joints are in a closed loop system which cannot be monitored in real-time and replacing the lubricating medium is also not a possibility which imposes significantly more challanges in wear analysis and fault prevention. Since the biological reactions due to the wear debris depend not only on the type of wear present but also on the volume and size of the wear debris, determining just the wear mechanism is not enough for understanding adverse reactions. Hence a more complex method of wear particle identification is required for comprehensive quantitative analysis.

One of the major problems associated with wear debris analysis in joint replacements is the time required to perform image analysis and characterise wear debris, which can take up to a year for trained professionals. Another major issue is the segmentation and separation of wear debris from the non-particles present in the image. In most cases, the non-particles consist of images of filter pores. In some cases, the filter pores are well-defined and are easily identifiable. However, in other cases, the filter pores are almost identical to the wear debris and are hard to detect using traditional methods. A unique approach to tackle this issue is to use a hybrid model of wear analysis with a classical method of image segmentation and a CNN-based image classification system. To address the issues with time and the complex nature of the data, we designed a simple yet robust segmentation algorithm using adaptive thresholding to segment the image into the foreground and background. Then we used CNN to classify the objects defined by their bounding boxes into two categories of particle and non-particle. Threshold-based image segmentation is frequently used to analyse microscopic objects due to its capability to use local threshold values to identify objects in uneven illumination (Ma et al., 2023). Threshold-based segmentation is faster than machine learning-based segmentation significantly reducing the time required to perform wear debris analysis. On the other hand, a CNN is resilient to the distortion in the input image and can extract features directly from the image data, allowing better classification of particles and non-particles obtained from the SEM images. Since CNN automatically learns features from the images, the performance is significantly better, and this has been proven the case in multiple studies (Wang H et al., 2019; Wang et al., 2020; Wang S et al., 2019). With the segmentation and classification results, we then performed statistical analysis on the wear debris to perform size and volume distribution analysis. An overview of this paper is presented as a flowchart in Figure 1.

83% across multiple studies (Wang H et al., 2019; Wang et al., 2020; Wang S et al., 2019). CNN-based identification and classification of wear debris in joint arthroplasty have been shown to have very high accuracies in multi-class morphological classifications as shown in (Hu et al., 2022). However, the wear debris collected in this study was specific and constrained as they were collected from a 50 nm filter membrane Song et al. (2020) which does not accurately represent the vast number of particles generated in a joint replacement in terms of size and frequency.

Wear debris classification in the industrial setup has come a long way, with significant improvements in classification accuracy and detection of the underlying wear mechanism. However, the same
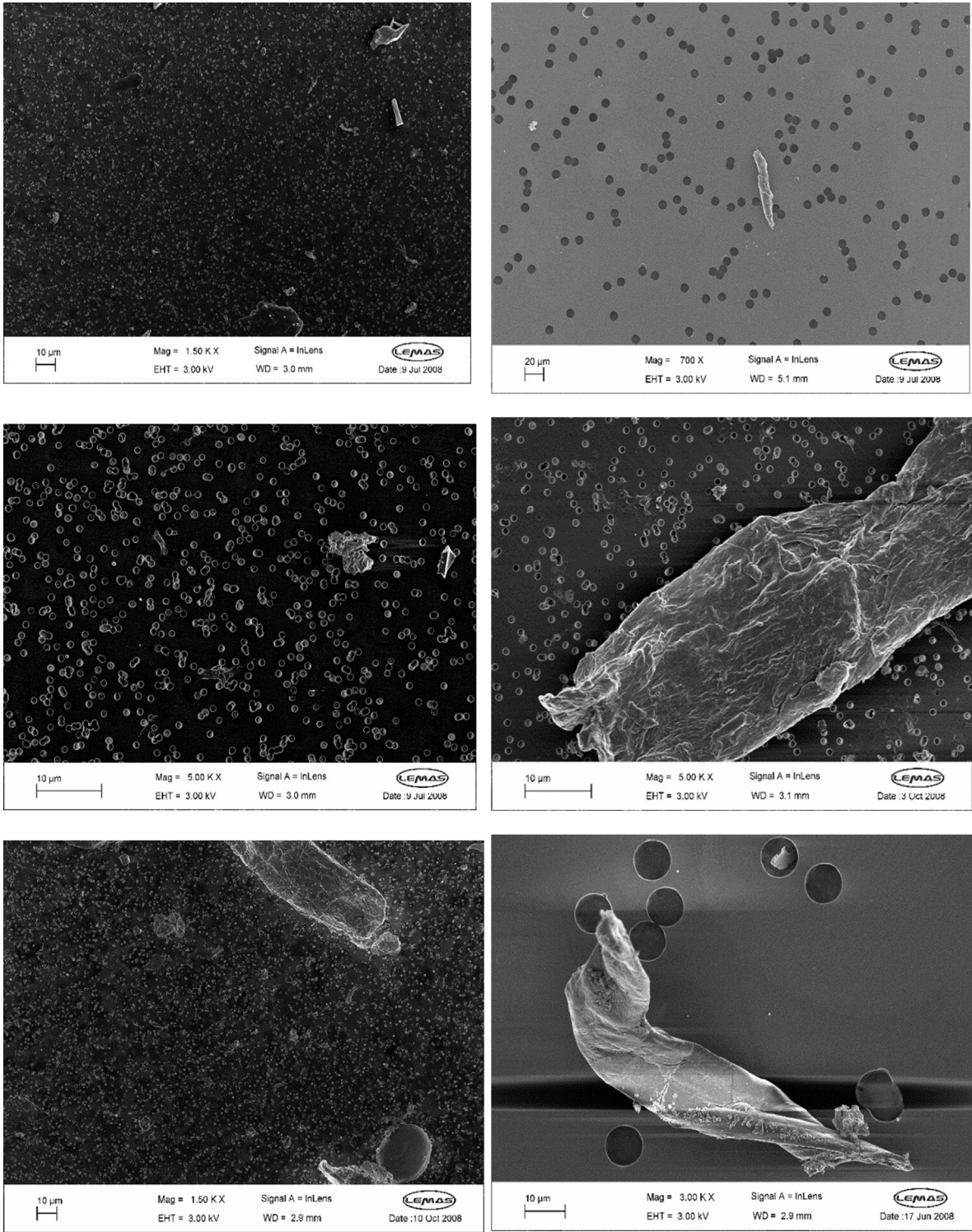
FIGURE 2
FEGSEM images of different magnification levels with different level of complexity.

2 Methodology

2.1 Wear particle generation

Similar to Vicars et al. (Vicars et al., 2010), we performed a study to compare the results of wear of the ProDisc-L TDR from 4 degrees of freedom (DOF) and 5 DOF movement. Six ProDisc-L devices were fixed into the test cells of the Prosim 5 DOF spine simulator, and tests were carried out for 5 million cycles (MC) according to the ISO 18192-1 4DOF protocol. The lubricating solution of 25% (v/v) Bovine serum, containing the wear debris, was extracted from the test setup every third of a million cycles and stored at −20°C for analysis.

2.2 Debris isolation

Wear particles were isolated from the serum Lubricant according to Richards et al. (Richards et al., 2008). An alkaline digestion procedure was employed to isolate and collect the wear particles by successive filtration through 10 μm, 1 μm and 0.015 μm filters. Tipper et al. (Tipper et al., 2012) captured the images of each filter using high-resolution field emission gun scanning electron microscopy (FEGSEM) at different levels of magnifications ranging from ×400 to 120000 x. A total of 1233 FEGSEM images from 4 simulator stations were analysed. Figure 2 shows SEM images taken at different magnification levels containing wear debris with varying levels of complexity.

2.3 Debris segmentation

MATLAB (MathWorks) image processing toolbox was used to analyse the FEGSEM images. Wear particles were segmented and measured using the Regionprops MATLAB function. Local adaptive thresholding was used to separate the foreground objects from the background. Before segmentation, a Gaussian filter was used to reduce the salt and pepper noise from the image, followed by a Laplacian filter which reduces the grey levels from the image and enhances the contrast and dynamic range. The dense clusters of bright pixels in the image indicated the wear particles, and the clusters of dark pixels in circular and semi-circular shapes indicated the filter pores. The segmented objects were classified into particle and non-particle with a CNN classifier. The region properties of each bright pixel cluster and black pixel cluster were calculated, including area, diameter, perimeter, mean intensity, and centroid.

2.4 Performance evaluation

The performance of the custom method was compared to the results obtained from image analysis using commericially available software, ImageJ. While there are other commercially available scientific image analysis software with proprietary algorithms for debris analysis, ImageJ was selected based on the better user interface. Moreover, there have been no studies establishing significant performance differences among different image analysis software. To evaluate the performance of the segmentation and pixel measurements, uniform synthetic images with varying levels of complexity of morphological and intensity features, including triangle, circle, pentagon and dodecagon, were used. The synthetic images were segmented and measured using two comparative analysis methods. The total number of pixels in an enclosed area indicated by a single object was used as the parameter for performance evaluation, as the volume estimation is primarily based on the area of the particles. Inbuilt image processing and segmentation techniques available in ImageJ were used to segment and characterise the objects.

2.5 Classification

Images extracted from the SEM image were manually labelled as wear particles and non-particles which mostly included filter pores as well as some foreign particles and non-objects which were isolated due to high-intensity areas as a result of light interference. The ratio of the number of wear particles to the filter pores was significant, and thus this affected the data analysis. However, the presence of foreign objects and non-objects was relatively low and did not affect the parameter distribution. Pre-established CNN models with high levels of accuracy are available to use in the classification task, but they are more complicated and require more resources. The parameters of CNN depend on the input data type and can be tailored according to the need to design a simpler architecture that uses lower resources and less time with high accuracy.
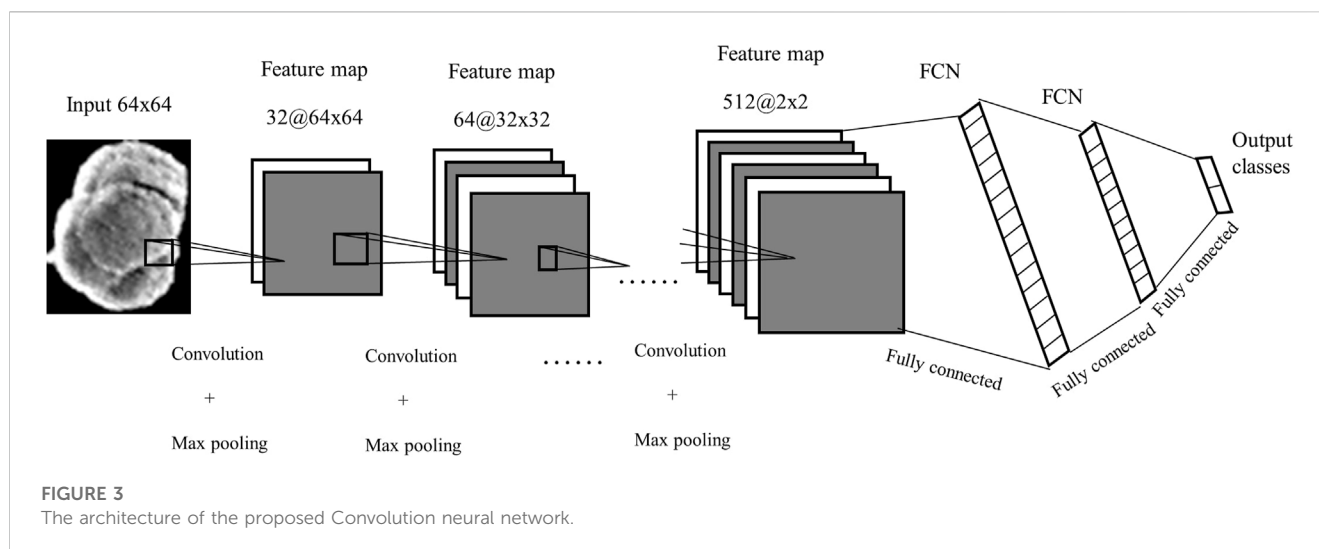
We designed a simple CNN structure with six convolutions and three fully connected layers. Batch normalisation and dropout techniques were used to make the CNN faster and more robust and prevent the network from overfitting. The segmented object was normalised to a size of 64×64 pixels and was sent as an input to the network. Six Convolution operations followed by batch normalisation, ReLu activation operations, and five max pooling operations were performed to create an output feature map of $2 \times 2 \times 512$. Three fully connected neural networks with 2048, 1,024 and 2 neural, nodes respectively, were used to classify the information from the feature maps into two categories which indicate wear particles and non-particles. Each fully connected layer was followed by a dropout layer with a 50% probability, to avoid overfitting. A SoftMax activation function followed the fully connected layer. A simple structure of the proposed CNN is shown in Figure 3.

2.6 Morphological calculations

The equivalent circular diameter (ECD), Circularity (C), and elongation (E) of the particles were calculated using Eqs 1–3. The size of the particles was determined by using the length and equivalent circular diameter (ECD). The bright pixel count debotes the area of the particle and thus can be multiplied by the scale factor to convert it into micrometres square (μm^2).
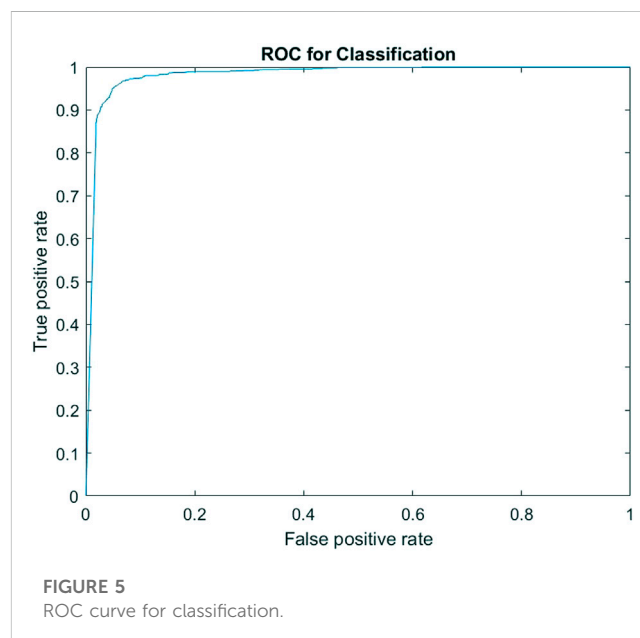
$$ECD = \sqrt{\frac{4 * Area}{\pi}} \tag{1}$$

The circularity of the particle (C) was calculated using Eq 2:

FIGURE 3
The architecture of the proposed Convolution neural network.

FIGURE 4
Confusion Matrix for classification.

FIGURE 5
ROC curve for classification.

$$C = 4 * Area/P^2 \qquad (2)$$

Elongation (E) was calculated using Eq 3:

$$E = Maxdia/Mindia \qquad (3)$$

Where, P = perimeter, MaxDia = Maximum diameter, MinDia = Minimum Diameter.

The wear particles volume was calculated by using area and wear particle thickness. Since SEM is a two-dimensional analysis, it can only provide the area of the wear particle, which is insufficient for volume analysis. Mean particle thickness can be estimated using two-dimensional area estimate and mass of the wear particles obtained by gravimetric analysis (Tipper et al., 2000). However, this method assumes a constant particle thickness which may introduce errors in volume estimations for larger particles. Another method of estimating particle thickness is using Atomic Force Microscopy (AFM) to directly measure the thickness of the particle (Wu et al., 2013). Thickness estimations for the size range < 0.1 μm, 0.1 μm–1 μm and1 μm to 10 μm were made using the width-to-thickness ratio obtained from a previous experiment that used AFM to measure the third dimension of the UHMWPE wear particles obtained from a six station pin-on-plate simulator (Wu et al., 2013). The width-to-thickness ratio used was 2.27, 1.32, 3.1 and 3.1 for the respective size ranges, which ensured a unique thickness estimation for every particle.

2.7 Experimental setup

Experiments conducted during this study were performed using MATLAB software on a computer with configurations: CPU i7 8,700 six cores 3.2 GHz, RAM 16 GB, GPU NVIDIA GeForce GTX

FIGURE 6
Wear particle size frequency distribution.
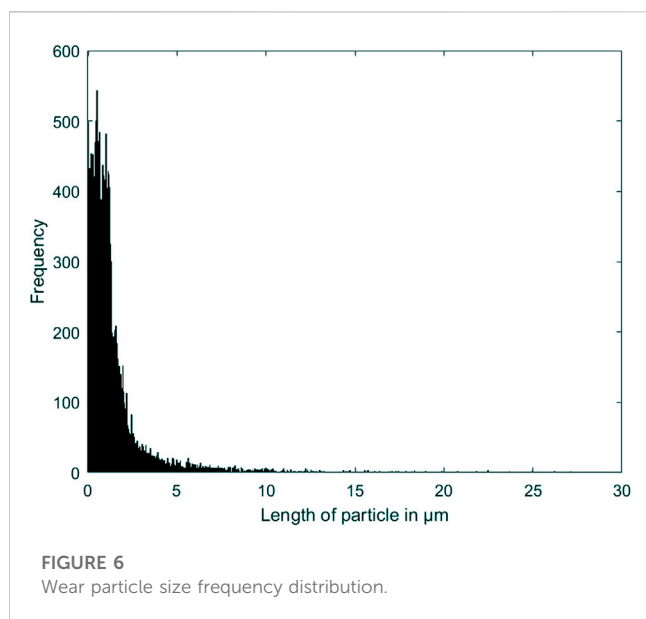
3 Results

The custom image segmentation and analysis method was more accurate than ImageJ across all the synthetic objects, with a mean absolute percentage error of 4.04% and 14.02%, respectively. The maximum error encountered was 9.3% and 31.3%, respectively. The custom analysis method performed significantly better on objects with intensity levels close to the background intensity levels.

Four thousand four hundred objects with 2,200 particles and 2,200 non-particles were selected from a pool of labelled data for the classification. The classification results are shown in Figures 4, 5. Once the classifier was trained, it was exported to the file directory as a matrix and then used to classify newly extracted objects from the FEGSEM images for all four stations of the spine simulator. Figure 4 shows the classification confusion matrix for the respective classes. The true positive and true negative rates for both subclasses were high, suggesting an even prediction success on both classes. Figure 5 shows the

FIGURE 7
(A) Wear particle size distribution, **(B)** Wear particle volume distribution.
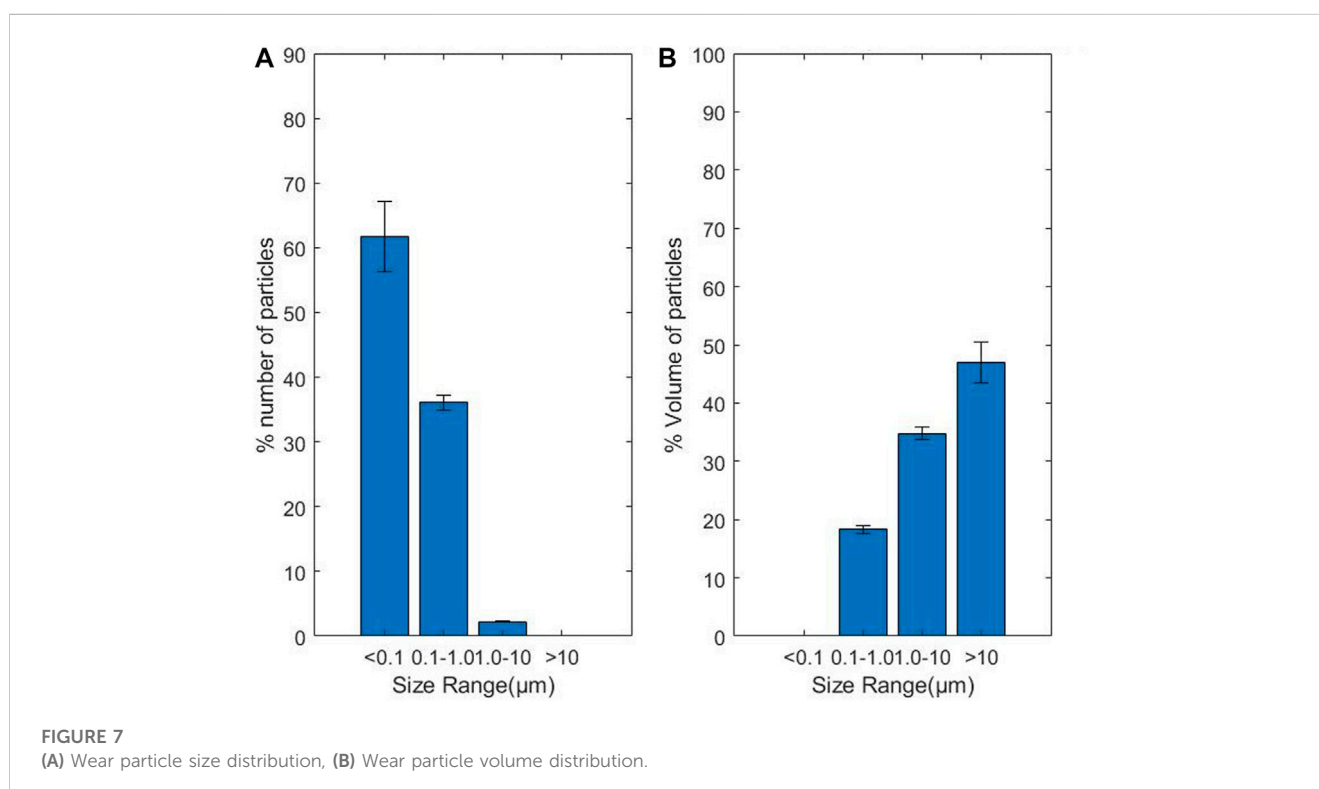
2070 8 GB. MATLAB's built-in image processing toolbox and deep learning toolbox were used to write the segmentation and the CNN algorithms. A learning rate of 0.01, Max epochs 30, the total number of iterations 1,300, and stochastic gradient descent with momentum (sgdm) optimiser were used as training parameters. A total of 4,440 images were used in the classification, and the data was divided into 80% training and 20% test set.

ROC curve for one instance of classification with 98.17% area under the curve (AUC).

The CNN classifier was trained and tested on a prelabelled dataset. An accuracy of 95.61% ± 0.57% was observed, with a maximum accuracy of 96.49%. The frequency distribution of the particle size follows a log-normal distribution as shown in Figure 6. The average size of the particles was 1.699 μm with a modal size of 0.92 μm.

4 Discussion

This study has shown that computer vision methods can significantly improve the efficiency of wear debris analysis. The use of a convolution neural network for image classification was found to be very effective and efficient. The accuracy of the CNN classifier, as shown in Figures 4, 5, is in line with other wear-related implementations (Wang H et al., 2019; Wang et al., 2020; Wang S et al., 2019). This is a very high rate of classification accuracy, which is required to accurately measure the size and number of particles for the whole experiment. The classification accuracy was found to fluctuate between training because of the random selection of training images, which suggests that the images' quality significantly affects the classification results. The confusion matrix, as shown in Figure 4, and ROC, as shown in Figure 5, suggest that the classifier's performance was equal in both classes, which points to a robust classification.

The size and volume distribution of particles, as shown in Figure 7, were similar to results from other studies (Tipper et al., 2012). Most of the particles were found to be less than 0.1 μm in length, followed by particles of size 0.1–1 μm, which are the most problematic, as established previously. Particles of size 0.1–10 μm were found to contribute more to the total area of the particles, which contradicts other similar studies (Fisher et al., 2001; Hyde et al., 2015). This difference in the area distribution may be attributed to the fact that this method relies heavily on segmentation techniques. Any error in the segmentation of large particles can a have huge effect on the area distribution. Since particles greater than 10 μm are very few, the variation in their numbers and pixel counts significantly affects the result. The area of a wear particle can vary significantly based on the accuracy of pixel detection, as demonstrated by the comparison analysis using ImageJ with uniform known shapes. The complexity of the wear particles in terms of shape and intensity levels and the intensity of the background are crucial factors to consider in improving the accuracy of the wear debris characterisation.

The accurate volume distribution is critical for analysing the biological reactivity of the implant material. The volume distribution relies heavily on the accuracy of particle area estimation and particle thickness estimation. Thickness estimation for a large number of particles is a tedious and time-consuming task. Moreover, current thickness estimation techniques, such as AFM, cannot measure the thickness of larger particles. SEM has been the standard choice for analysing large numbers of particles, as the images can be analysed later using computer-aided techniques. The accuracy of the various thickness estimation methods in past studies are debatable due to unrealistic assumptions of constant thickness across a wide range of sizes of particles obtained from different filter membranes. In this study, this problem was mitigated by using empirical thickness calculated using morphological parameters from a previous study. We have shown that the speed and accuracy of the wear particle analysis can significantly be improved by using CNN-based

image analysis. However, there is still room for improvement in volume estimation.

5 Conclusion

Using a convolution neural network with thresholding-based segmentation can produce accurate results in segmenting and classifying wear particles with relatively low resource consumption. This segmentation and classification can be used to build a functional biological activity model for all types of wear debris under different loading conditions. However, the discrepancies in the area parameter and the lack of three-dimensional information of the particles demand improvements in the segmentation and three-dimensional particle characterisation techniques.

Data availability statement

The data analyzed in this study is subject to the following licenses/restrictions: Copyrighted material. Requests to access these datasets should be directed to JT, joanne.tipper@uts.edu.au.

Author contributions

SK carried out the particle image analysis and drafted the manuscript under the supervision of JT and SS. All authors contributed to the article and approved the submitted version.

Conflict of interest

The authors declare that the research was conducted in the absence of any commercial or financial relationships that could be construed as a potential conflict of interest.

Publisher's note

All claims expressed in this article are solely those of the authors and do not necessarily represent those of their affiliated organizations, or those of the publisher, the editors and the reviewers. Any product that may be evaluated in this article, or claim that may be made by its manufacturer, is not guaranteed or endorsed by the publisher.

References

Charnley, J., Follacci, F., and Hammond, B. (1968). The long-term reaction of bone to self-curing acrylic cement. *J. Bone Jt. Surg. Br. volume* 50, 822–829. doi:10.1302/0301-620x.50b4.822

Cunningham, B. W., Hallab, N. J., Hu, N., and McAfee, P. C. (2013). Epidural application of spinal instrumentation particulate wear debris: A comprehensive evaluation of neurotoxicity using an *in vivo* animal model. *J. Neurosurg. Spine* 19, 336–350. doi:10.3171/2013.5.spine13166

Eckold, D., Dearn, K., and Shepherd, D. (2015). The evolution of polymer wear debris from total disc arthroplasty. *Biotribology* 1, 42–50. doi:10.1016/j.biotri.2015.04.002

Fisher, J., Bell, J., Barbour, P., Tipper, J., Mattews, J., Besong, A., et al. (2001). A novel method for the prediction of functional biological activity of polyethylene wear debris. *Proc. Institution Mech. Eng. Part H J. Eng. Med.* 215, 127–132. doi:10.1243/0954411011533599

Green, T., Fisher, J., Stone, M., Wroblewski, B., and Ingham, E. (1998). Polyethylene particles of a 'critical size'are necessary for the induction of cytokines by macrophages *in vitro*. *Biomaterials* 19, 2297–2302. doi:10.1016/s0142-9612(98)00140-9

Green, T. R., Fisher, J., Matthews, J. B., Stone, M. H., and Ingham, E. (2000). "Effect of size and dose on bone resorption activity of macrophages by *in vitro* clinically relevant ultra high molecular weight polyethylene particles," in *Journal of biomedical materials research: An official journal of the society for biomaterials*, 53. The Japanese Society for Biomaterials, and The Australian Society for Biomaterials and the Korean Society for Biomaterials, 490–497.

Harris, W. H. (1995). The problem is osteolysis. *Clin. Orthop. Relat. Res.*, 46–53.

Hu, X., Song, J., Liao, Z., Liu, Y., Gao, J., Menze, B., et al. (2022). Morphological residual convolutional neural network (m-rcnn) for intelligent recognition of wear particles from artificial joints. *Friction* 10, 560–572. doi:10.1007/s40544-021-0516-2

Hyde, P., Tipper, J., Fisher, J., and Hall, R. (2015). Wear and biological effects of a semi-constrained total disc replacement subject to modified iso standard test conditions. *J. Mech. Behav. Biomed. Mater.* 44, 43–52. doi:10.1016/j.jmbbm.2014.12.001

Ingham, E., and Fisher, J. (1997). Biological reactions to wear debris in total joint replacement. *J. Biomed. Mater. Res.* 38, 21–37. doi:10.1243/0954411001535219

Juránek, R., Machalík, S., and Zemčík, P. (2011). "Analysis of wear debris through classification," in *International conference on advanced concepts for intelligent vision systems* (Springer), 273–283.

Kobayashi, A., Freeman, M., Bonfield, W., Kadoya, Y., Yamac, T., Al-Saffar, N., et al. (1997). Number of polyethylene particles and osteolysis in total joint replacements: A quantitative study using a tissue-digestion method. *J. bone Jt. Surg. Br. volume* 79, 844–848. doi:10.1302/0301-620x.79b5.0790844

Lewis, G. (2001a). Polyethylene wear in total hip and knee arthroplasties. *Biomaterials* 22, 371–401. doi:10.1002/(sici)1097-4636(199721)38:1<55:aid-jbm8>3.0.co;2-g

Lewis, G. (2001b). Properties of crosslinked ultra-high-molecular-weight polyethylene. *Biomaterials* 22, 371–401. doi:10.1016/S0142-9612(00)00195-2

Ma, P., Li, C., Rahaman, M. M., Yao, Y., Zhang, J., Zou, S., et al. (2023). A state-of-the-art survey of object detection techniques in microorganism image analysis: From classical methods to deep learning approaches. *Artif. Intell. Rev.* 56, 1627–1698. doi:10.1007/s10462-022-10209-1

McKellop, H. A., Campbell, P., Park, S.-H., Schmalzried, T. P., Grigoris, P., Amstutz, H. C., et al. (1995). The origin of submicron polyethylene wear debris in total hip arthroplasty. *Clin. Orthop. Relat. Res.*, 3–20.

Milošev, I., Kovac, S., Trebše, R., Levašic, V., and Pišot, V. (2012). Comparison of ten-year survivorship of hip prostheses with use of conventional polyethylene, metal-on-metal, or ceramic-on-ceramic bearings. *JBJS* 94, 1756–1763. doi:10.2106/JBJS.J.01858

Myshkin, N., Kwon, O., Grigoriev, A. Y., Ahn, H.-S., and Kong, H. (1997). Classification of wear debris using a neural network. *Wear* 203, 658–662. doi:10.1016/s0043-1648(96)07432-7

Peng, Z. (2002). An integrated intelligence system for wear debris analysis. *Wear* 252, 730–743. doi:10.1016/s0043-1648(02)00031-5

Peng, Z., and Kirk, T. (1998). Automatic wear-particle classification using neural networks. *Tribol. Lett.* 5, 249–257. doi:10.1023/a:1019126732337

Podsiadlo, P., and Stachowiak, G. (2005). Development of advanced quantitative analysis methods for wear particle characterization and classification to aid tribological system diagnosis. *Tribol. Int.* 38, 887–897. doi:10.1016/j.triboint.2005.03.008

Richards, L., Brown, C., Stone, M., Fisher, J., Ingham, E., and Tipper, J. (2008). Identification of nanometre-sized ultra-high molecular weight polyethylene wear particles in samples retrieved *in vivo*. *J. bone Jt. Surg. Br. volume* 90, 1106–1113. doi:10.1302/0301-620x.90b8.20737

Song, J., Chen, F., Liu, Y., Wang, S., He, X., Liao, Z., et al. (2020). Insight into the wear particles of peek and cfrpeek against uhmwpe for artificial cervical disc application: Morphology and immunoreaction. *Tribol. Int.* 144, 106093. doi:10.1016/j.triboint.2019.106093

Tipper, J., Ingham, E., Hailey, J., Besong, A., Fisher, J., Wroblewski, B., et al. (2000). Quantitative analysis of polyethylene wear debris, wear rate and head damage in retrieved charnley hip prostheses. *J. Mater. Sci. Mater. Med.* 11, 117–124. doi:10.1023/a:1008901302646

Tipper, J., Vicars, R., Brown, T., Ingham, E., Fisher, J., and Hall, R. (2012). Quantitative comparison of uhmwpe wear particles from prodisc-l total disc replacements tested under iso and iso plus ap shear. Orthop. Proc. *(The British Editorial Society of Bone and Joint Surgery)* 94, 11.

Vicars, R., Hyde, P., Brown, T., Tipper, J., Ingham, E., Fisher, J., et al. (2010). The effect of anterior–posterior shear load on the wear of prodisc-l tdr. *European Spine Journal* 19, 1356–1362. doi:10.1007/s00586-010-1396-8

Wang H, H., Yuan, F., Gao, L., Huang, R., and Wang, W. (2019). "Wear debris classification and quantity and size calculation using convolutional neural network," in *Cyberspace data and intelligence, and cyber-living, syndrome, and health* (Springer), 470–486.

Wang, J., Liu, X., Wu, M., and Wang, X. (2020). Direct detection of wear conditions by classification of ferrograph images. *Journal of the Brazilian Society of Mechanical Sciences and Engineering* 42, 152–210. doi:10.1007/s40430-020-2235-4

Wang S, S., Wu, T., Shao, T., and Peng, Z. (2019). Integrated model of bp neural network and cnn algorithm for automatic wear debris classification. *Wear* 426, 1761–1770. doi:10.1016/j.wear.2018.12.087

Wu, J., Peng, Z., and Tipper, J. (2013). Mechanical properties and three-dimensional topological characterisation of micron, submicron and nanoparticles from artificial joints. *Tribology Letters* 52, 449–460. doi:10.1007/s11249-013-0228-5

Frontiers in
Bioengineering and Biotechnology

Accelerates the development of therapies, devices, and technologies to improve our lives

A multidisciplinary journal that accelerates the development of biological therapies, devices, processes and technologies to improve our lives by bridging the gap between discoveries and their application.

Discover the latest Research Topics

See more →

Frontiers in
Bioengineering
and Biotechnology

![frontiers logo] **frontiers** | Research Topics